LAWRENCE
LIVERMORE
NATIONAL
LABORATORY

UCRL-ID-142744-02

Laser Science and Technology Program Annual Report-2002 NIF Programs Directorate

L. A. Hackel, H. L. Chen

March 1, 2003

This document was prepared as an account of work sponsored by an agency of the United States Government. Neither the United States Government nor the University of California nor any of their employees, makes any warranty, express or implied, or assumes any legal liability or responsibility for the accuracy, completeness, or usefulness of any information, apparatus, product, or process disclosed, or represents that its use would not infringe privately owned rights. Reference herein to any specific commercial product, process, or service by trade name, trademark, manufacturer, or otherwise, does not necessarily constitute or imply its endorsement, recommendation, or favoring by the United States Government or the University of California. The views and opinions of authors expressed herein do not necessarily state or reflect those of the United States Government or the University of California, and shall not be used for advertising or product endorsement purposes.

This work was performed under the auspices of the U.S. Department of Energy by University of California, Lawrence Livermore National Laboratory under Contract W-7405-Eng-48.

Laser Science & Technology Program

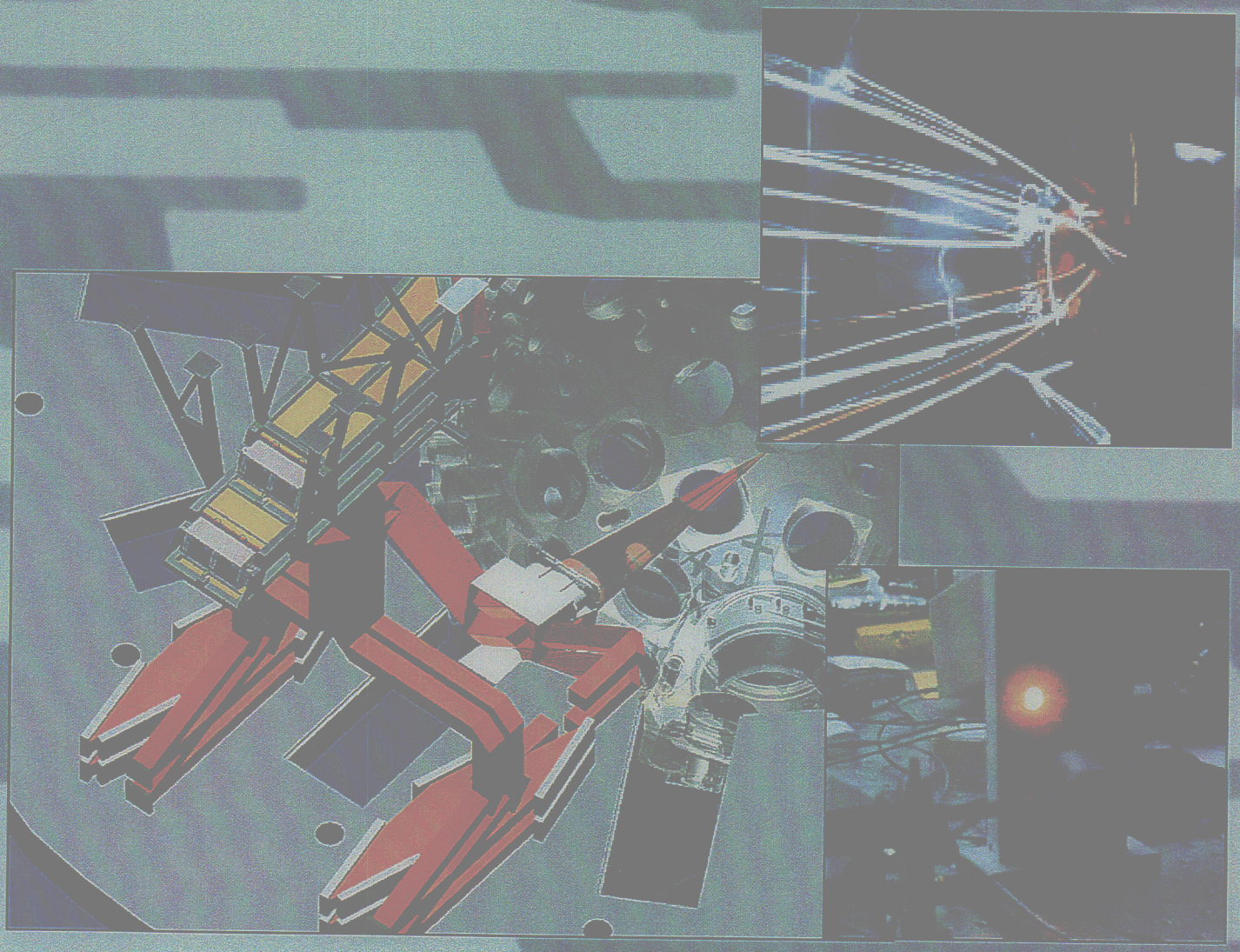

Annual Report — 2002
NIF Programs Directorate

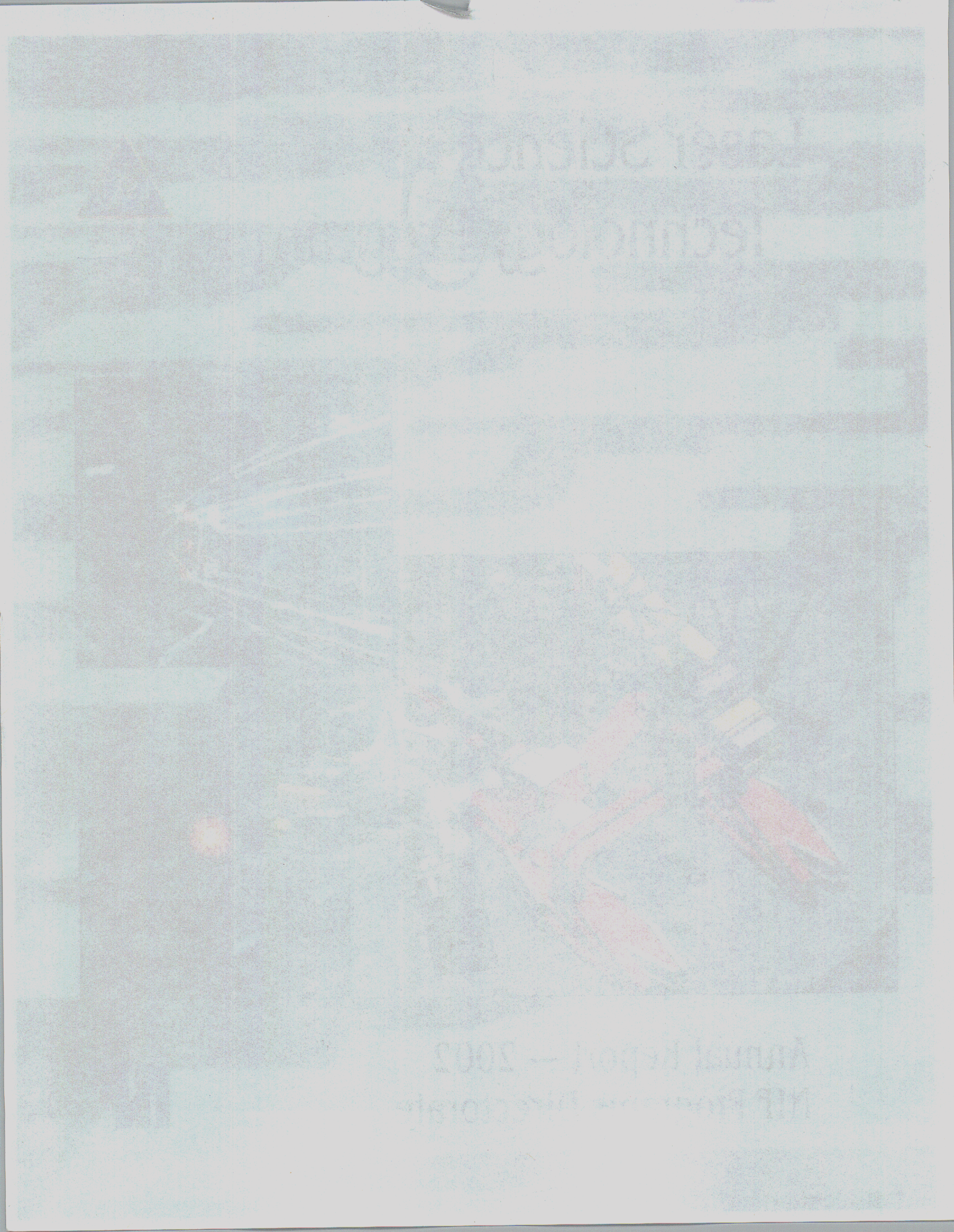

LASER SCIENCE AND TECHNOLOGY ANNUAL REPORT—2002

L. A. HACKEL AND H. L. CHEN

March 2003

LAWRENCE LIVERMORE NATIONAL LABORATORY
University of California • Livermore, California • 94550

Table of Contents

1. Overview of the Laser Science and Technology Program 1–1
   - Improving NIF Laser Optics and Material Performance 1-2
   - High-Energy Petawatt Laser Sciences and Technologies 1-5
   - Fabrication of a 5-m-Diameter Diffractive Fresnel Lens for Space-Based Applications 1-9
   - Advanced Solid-State Lasers and Components 1-10
   - Solid-State Heat Capacity Laser for Defense 1-16
   - Material Processing Using Pulsed Solid-State Lasers 1-18
2. Laser Optics and Materials Research Activity Highlights 2–1
   - OSL Upgraded to 1.5 kJ 2-1
   - Beam Sampling Gratings for Power Measurement and Balance of NIF Beams 2-2
   - Installation and Activation of the Beamlet PDS on NIF 2-3
   - Qualification of 3ω Optics Using Slab and OSL Lasers 2-4
3. Short Pulse Lasers, Applications and Technology Research Activity Highlights 3–1
   - Short-Pulse, High-Average-Power Laser System for Micromachining . . 3-1
   - Precision Optical Figuring with Wet-Etch Figuring 3-2
   - Fabrication of a 5-Meter-Diameter Diffractive Fresnel Lens 3-4
   - Laser Drilling of High-Aspect-Ratio Micron-Scale Holes for NIF Fusion Targets 3-5
   - Ultrafast Laser Micro-Sculpting of Materials 3-7
4. Advanced Lasers and Components Research Activity Highlights 4–1
   - Phase-Locked, Antiguided Multiple-Core Ribbon Fiber Laser 4-1
   - First Light From the Mercury Laser: a Diode-Pumped, Solid-State, Gas-Cooled Laser for Fusion Energy Applications 4-2
   - First Light from Diode-Pumpable Rubidium Laser 4-4
   - Activation of the XAPPER Experiment 4-5
   - Developing Advanced Fiber Lasers for Guide Star Applications and Petawatt Laser Front Ends 4-6
   - JANUS Update 4-9
5. Solid-State Heat-Capacity Laser Research Activity Highlights 5–1
   - Diode-Pumped Nd:GGG Laser–First Light 5-1
   - Compact Microchannel-Cooled Laser-Diode Arrays Deliver over Tens of kW/cm^2 onto the Working Surface 5-2
6. Special Project: Laser Material Processing Research Activity 6–1
   - Laser Peening Improves Corrosion Resistance and Mitigates Tensile Residual Stresses in Alloy 22 6-1
   - Laser Peening Improves Fatigue Life of Aluminum Components for USAF 6-2

1. OVERVIEW OF THE LASER SCIENCE AND TECHNOLOGY PROGRAM

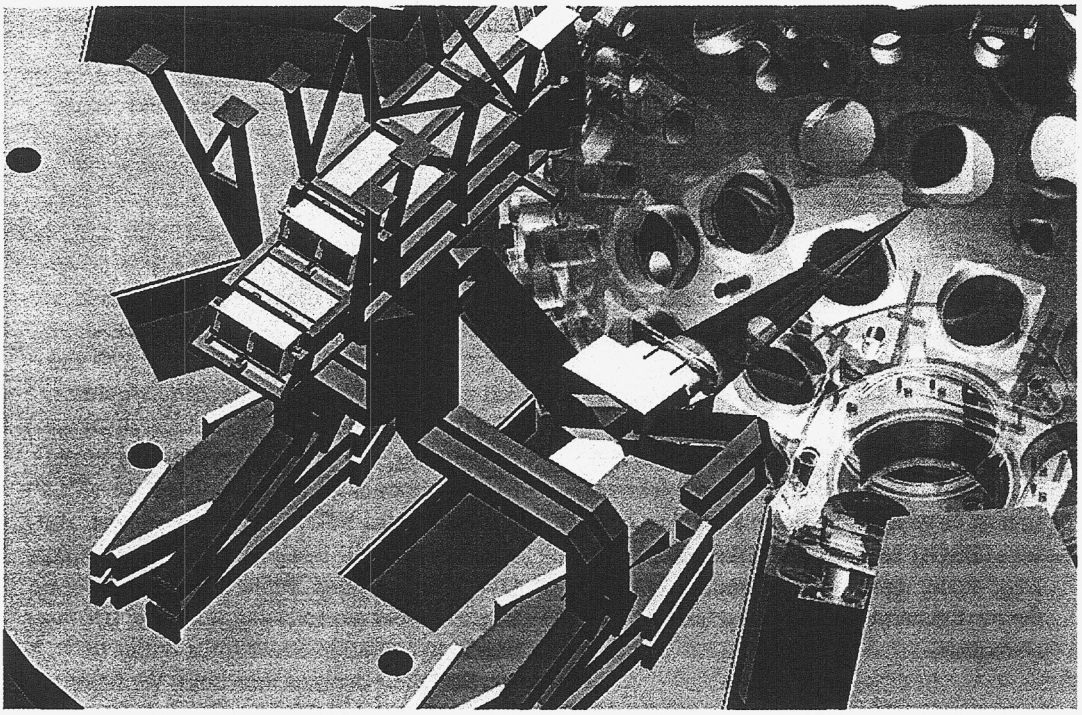

High-energy petawatt laser on NIF simulated in the target bay.

OVERVIEW

The Laser Science and Technology (LS&T) Program's mission is to develop advanced lasers, optics, materials technologies, and applications to solve problems and create new capabilities of importance to the nation and the Laboratory. A top, near-term priority is to provide technical support in the deployment and upgrade of the National Ignition Facility (NIF). Our other program activities synergistically develop technologies that are consistent with the goals of the NIF Directorate and develop state-of-the-art capabilities.

The primary objectives of LS&T activities in 2002 have been fourfold—(a) to support deployment of hardware and to enhance laser and optics performance for NIF, (b) to develop high-energy petawatt laser science and technology for the Department of Energy (DOE), (c) to develop advanced solid-state laser systems and optical components for the Department of Defense (DoD), and (d) to invent, develop, and deliver improved concepts and hardware for other government agencies and industry.

LS&T activities during 2002 focused on seven major areas:

1. NIF Project—LS&T led major advances in the deployment of NIF Final Optics Assembly (FOA) and the development of 3ω optics processing and treatment technologies to enhance NIF's operations and performance capabilities.
2. Stockpile Stewardship Program (SSP)—LS&T personnel continued development of ultrashort-pulse lasers and high-power, large-aperture optics for applications in SSP, extreme-field science and national defense. To enhance the high-energy petawatt

(HEPW) capability in NIF, LS&T continued development of advanced compressor-grating and front-end laser technologies utilizing optical-parametric chirped-pulse amplification (OPCPA).

3. High-energy-density physics and inertial fusion energy—LS&T continued development of kW- to MW-class, diode-pumped, solid-state laser (DPSSL).
4. Department of Defense (DoD)—LS&T continued development of a 100 kW-class solid-state heat-capacity laser (SSHCL) for missile defense.
5. Nuclear energy applications—LS&T continued to develop laser-shock peening technology to improve the service lifetime of metal nuclear waste containment canisters designed for DOE's Yucca Mountain Project.
6. Materials processing—Under cooperative research and development agreements (CRADA) with U.S. industry, LS&T developed and delivered kW-class solid-state lasers for shock peening and hole drilling of metals.
7. Diffractive optics for space telescopes and petawatt lasers—LS&T continued fabrication of large-aperture beam sampling gratings (BSGs) for NIF, and development of large-scale, lightweight diffractive optics for the next generation of space telescope (Eyeglass).

IMPROVING NIF LASER OPTICS AND MATERIAL PERFORMANCE

LS&T work on NIF has achieved major strides leading to the deployment of NIF Final Optics Assembly (FOA) and the development of 3ω optics processing, treatment, and testing technologies to enhance the performance of optics in the FOA. To extend optics lifetimes in the laser chain, we have successfully developed detailed optics processing and treatment procedures. We have completed construction of a preproduction facility (named Phoenix) for conditioning and repairing surface damage on full-scale NIF optics using ultraviolet (UV) and infrared (IR) lasers. We have also upgraded the Optical Sciences Laser (OSL) facility to 1.5 kJ per pulse to perform optical damage tests on 3ω optics for NIF. Ten large-aperture beam-sampling gratings (BSGs) have already been fabricated and four were installed on NIF. We are installing and commissioning a precision diagnostic system (PDS) for the characterization and commissioning of the beamlines during NIF's early light (NEL). We are also improving advanced optical fabrication technologies to fabricate continuous phase plates (CPP) for NIF.

Enhanced Optical Damage Resistance of NIF Optics Using UV and IR Lasers

The output fluences that can be attained on NIF and other megajoule-class solid-state lasers are ultimately limited by laser-induced damage to optical components within the chain. When damage reaches performance-limiting levels, optics must be replaced leading to higher operating expense and longer laser downtime. Because the laser damage threshold of optics decreases with decreasing laser wavelength, the final optics operating at 527 and 351 nm are the most susceptible to damage. The final optics on the NIF consist of frequency-doubling and -tripling crystals fabricated from potassium dihydrogen phosphate (KDP) and deuterated KDP, final focusing lens, BSG, and debris shield fabricated from fused silica. Over the past years, we have developed optic treatment techniques using scanning UV laser beams to condition fused silica optics to increase their damage threshold. We have also demonstrated that CO_2 lasers can be used to stabilize damage sites on optics and control the size of damage sites to less than few tens of microns, thereby greatly increasing the lifetime of an optic through reuse.

With the activation of NIF proceeding, the ability to process full-scale 43-cm × 43-cm optics is timely. We have successfully activated Phoenix to condition and repair surface damage on full-scale NIF optics. This new facility is equipped with two UV conditioning lasers—a 50-Hz Nd:YAG laser operating at 355 nm, with a pulse width of 3.7 ns and a 100-Hz XeF excimer laser operating at 351 nm with 23-ns pulse width. The facility also includes a CO_2 laser for damage mitigation, an optics stage for raster scanning full-scale optics, two microscopes to image damage sites with ≈5-μm resolution, and a damage mapping system (DMS) that can detect damage sites or precursors as small as ≈15 μm to image full-scale optics. The optics are handled in a class 100 clean room

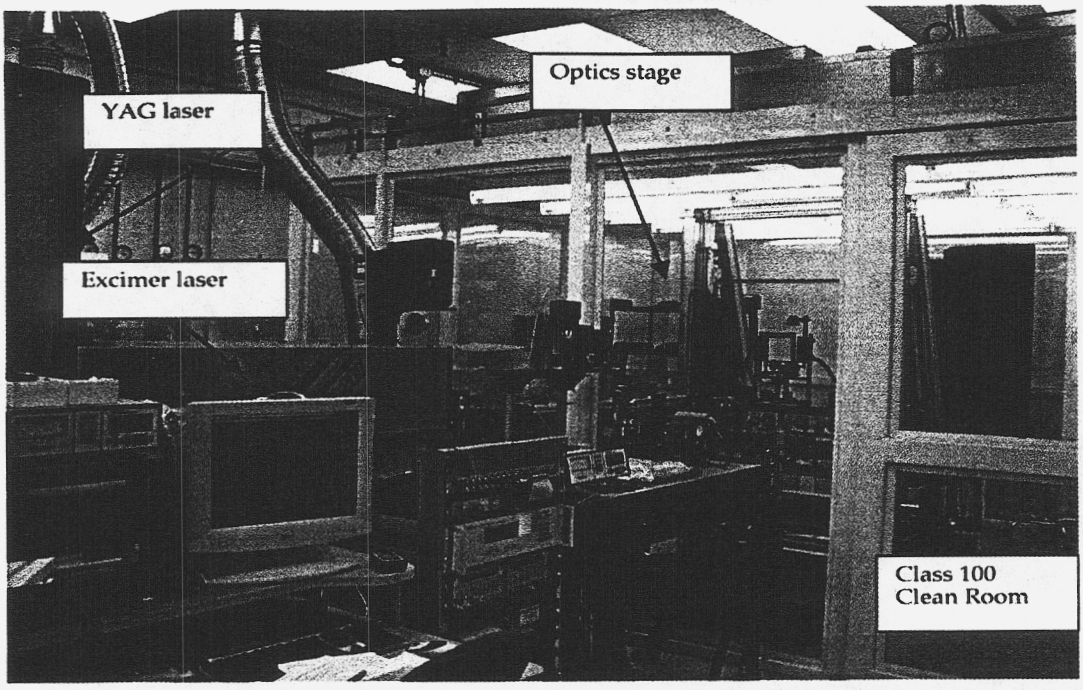

Phoenix, a preproduction facility for conditioning and repairing surface damages on NIF optics.

within the facility that is maintained at better than class 10000.

Three full-scale NIF optics were conditioned in Phoenix, including two wedged final focus lenses fabricated from inclusion-free fused silica. The XeF excimer laser puts out 280 mJ/pulse. It uses a one-dimensional beam homogenizer to tailor the beam profile that converts the 24-mm × 12-mm beam from the laser into a 1.5-mm by 0.3-mm focal spot. Due to the relatively small f-number of the optical system (f/13), the beam cannot be focused at both front and rear surfaces of the optic simultaneously. We thus condition the optic in two steps: output surface first and then the input surface. The first scan is performed at 11 J/cm^2 (which is equivalent to a fluence of 4 J/cm^2 for 3-ns pulses, using $\tau^{0.5}$ scaling). A damage map is acquired to identify new sites or sites that have grown in size. These sites are then spot-treated with the CO_2 laser to eliminate their potential for damage growth. The UV laser treatment process is repeated at 6, 8, and 10 J/cm^2 (all in 3-ns equivalent) for an optic to be used at 6 J/cm^2 and further at 12 and 14 J/cm^2 for an optic destined for 8 J/cm^2 operation. Using UV laser conditioning and IR laser annealing processes, we have been able to maintain <1 defect (or damage site) per fused silica optic at 14 J/cm^2, a 100× improvement compared to last year's result obtained from subscale optics processed in Phoenix. The design goal for 3ω optics is 50 defects per optic. We are designing a production facility to condition and mitigate damage on NIF optics. This facility is planned to be commissioned in 2004.

Qualification of 3ω Optics Using Slab and OSL Lasers

LS&T has established two laser facilities to test FOA optics and certify finishing and post-treatment processes. Optical damage tests on small optics are typically performed using a small laser beam (<1 mm diameter, Gaussian) to raster over the surface of the optics at high repetition rate. To test NIF optics that have relatively large apertures (40 × 40 cm), a large-area, high-energy and high-intensity laser beam that can cover many square millimeters in one shot is required. The OSL and Slab laser facilities were modified to provide such large-area, high-power optical testing capability.

The OSL's 10-cm disk amplifier system delivers up to 12 J/cm^2 of 0.351-μm, 3-ns laser light in a round 3-cm-diameter, flat-top beam at a repetition rate of 2 shots/hour. The flexible pulse shaping and excellent beam quality of this laser make it uniquely suitable for simulating NIF laser conditions on subscale parts of up to 15 cm in size. A main focus during this past year has been the characterization and quantification of surface damage on diamond-turned deuterated potassium dihydrogen

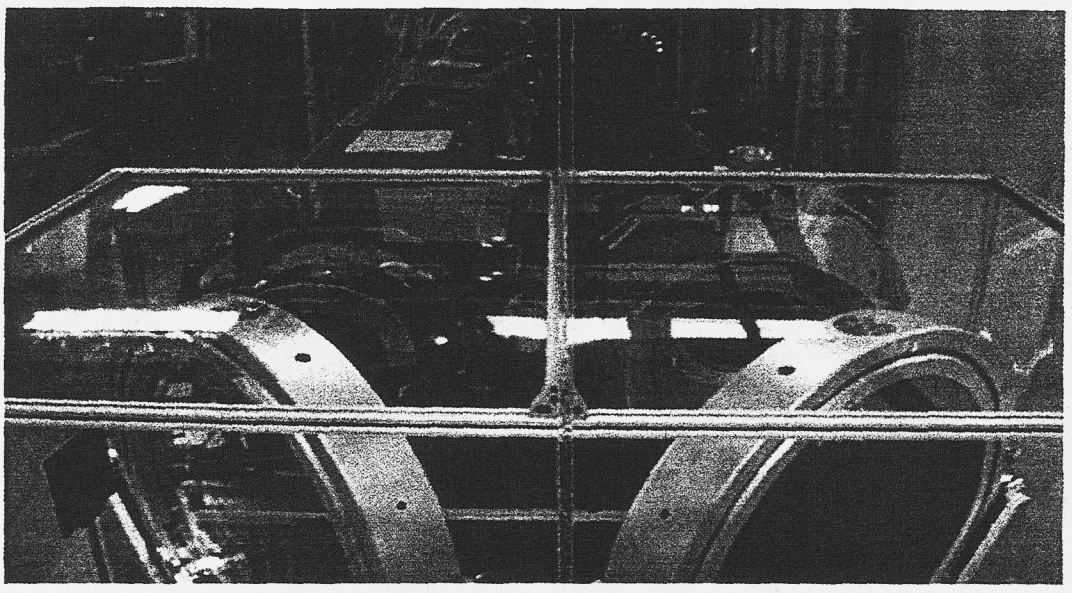

Optical Sciences Laser facility, 20-cm amplifiers on the left and spatial filter telescope on the right.

phosphate (DKDP). Extensive testing of 15-cm material was performed to correlate surface damage to specific defects on the surface of the DKDP (incurred during the diamond finishing process).

The finishing protocol has since been refined to effectively eliminate damage due to these defects. Other work included validation of damage mitigation and stabilization techniques applied to DKDP and fused silica surfaces, validation of small-beam laser conditioning protocols for surface and bulk damage, and the testing of fused silica contaminated with NIF-like shrapnel and target debris for establishing debris shield lifetime.

In 2002, LS&T upgraded the OSL laser to generate 1.5 kJ of 1053-nm light for testing of NIF final optics at full scale. OSL Upgrade uses a double-pass architecture containing four 20-cm aperture disk amplifiers (twelve disks total). The first-article Integrated Optics Module (IOM) has been installed and experiments are under way to verify the frequency converter operation and to test performance at various 3ω fluence levels.

The Slab laser can deliver up to 12 J/cm^2 of 0.351-μm, 11-ns laser light in a square 5-mm flat-top beam at a repetition rate of 30 shots/minute. The repetition rate of this laser enables a NIF lifetime-of-shots to be applied to a test sample in less than a day. Recent work has focused on quantifying the damage growth rate on fused silica surfaces at the individual and combined harmonic wavelengths of Nd:glass, and validating damage mitigation techniques for DKDP surfaces. Current techniques for mitigating damage on the surface of DKDP involve the use of a high-speed diamond-tipped rotary tool to excavate the damage site. The Slab facility has also played an important role in certifying "non-optical" materials for 1ω and 3ω laser exposure. Many engineering applications on the NIF require the use of materials able to withstand diffuse or scattered laser fluences of up to a few joules/cm^2 without generating particles or volatile by-products that can put nearby optical components at risk. Slab experiments were instrumental in providing NIF engineers with a plastic alternative to absorbing glass for protecting the beam transport system from stray 1ω light at fluences up to 1 J/cm^2.

Installation and Activation of the Precision Diagnostic System (PDS) on NIF

LS&T personnel are also commissioning an optical Precision Diagnostic System (PDS) to characterize NIF output beams during the NEL campaign. This system makes use of the 1ω and 3ω diagnostics from Beamlet, where they were used to demonstrate that the NIF laser architecture could produce the 3ω energy and far-field beam quality needed for its missions. The PDS will provide a full complement of 1ω and 3ω diagnostics and make possible the first full-power and full-aperture test of an Individual Optics Module (IOM)—the optical system that mounts directly to the target cham-

ber for each beamline and contains the vacuum window, harmonic conversion crystals, focus lens, diagnostic grating, wave plates, and debris shields. The major components of the PDS consist of turning mirrors that transport the laser beam from the output of the transport spatial filter to the PDS, a roving mirror diagnostic assembly (RMDA) that contains remotely operated robotic handlers and mirrors, a prime focus vessel (PFV), and a target diagnostic chamber (TDC). The TDC is an 8-foot-diameter by 40-foot-long vacuum vessel that contains the beam splitters and down-conversion optics. The entire RMDA enclosure and the beamline to the IOM is sealed and filled with Ar to suppress stimulated rotational Raman scattering during high-power laser shots in PDS. Full activation of the RMDA will allow any one of the 96 beamlines in NIF Switchyard 2 to be transported and analyzed. Commissioning of NIF beamlines using PDS will start in 2003.

HIGH-ENERGY PETAWATT LASER SCIENCES AND TECHNOLOGIES

Development of chirped pulse amplification has made possible production of unprecedented peak power from lasers. With NIF scheduled to produce first light in 2003, there is an increasing interest in the scientific potential of high-energy petawatt (HEPW) pulse production at NIF and other high-energy laser facilities in the U.S. A high-energy petawatt laser initiative has recently been initiated by the DOE to evaluate this frontier technology. LS&T has accomplished a number of major milestones in the development of ultrashort-pulse lasers and high-power, large-aperture optics for applications in SSP, extreme-field science, and national defense.

Petawatt Science and Technology for DOE

With support from the LDRD Program, we are leading an effort to develop a multi-kJ HEPW laser on NIF. The addition of HEPW to NIF will enable the acceleration of data collection for the Stockpile Stewardship Program and new high-energy-density science (HEDS) experiments for advanced inertial confinement fusion (ICF). Several NIF missions benefiting from HEPW capability have been evaluated. These experiments include: fast ignition, high photon energy (10-keV to >10-MeV x-ray) backlighters for large, massive targets, unique Equation of State (EOS) studies, 10- to 50-MeV proton backlighting for electric and magnetic field measurements, ultrahot hohlraums for spectral opacity studies and isochoric heating of inertially confined matter using either the relativistic electrons or ballistically focused protons. Our near-term goal is to develop a 2- to 5-kJ, 5- to 50-ps petawatt laser source for performing HEDS experiments with irradiance in the 10^{19}- to 10^{20}-W/cm^2 range. Our effort in 2002 has focused mainly on designing of advanced laser and optics technologies required to field HEPW beamlines on NIF using existing beamline design for ns-pulse operation. A conceptual design for installing HEPW capability on NIF was completed. To achieve this goal, some modifications to NIF's injection laser system and target areas will be made.

LS&T is developing a stable and correctly phased seed laser as the front end of the HEPW system. We plan to add a short-pulse oscillator and stretcher to the NIF master oscillator room. Output from the oscillator is delivered to a short-pulse preamplifier module to provide a high-contrast chirped pulse for injection to the main NIF amplifier chain. The short-pulse preamplifier module is a line replaceable unit with the capacity to convert from 1 to 4 beams in a NIF quad to short-pulse operation. Dispersion compensation is also added in the preamplifier beam transport system to allow high-order phase adjustment on individual beamlines. To enhance the performance of the Nd-glass laser amplifier, an efficient broadband preamplifier technology utilizing optical parametric chirped-pulse amplification (OPCPA) was developed and evaluated as a possible front end for the HEPW. We are also constructing a compact, ultrahigh-stability, 100-fs mode-locked fiber laser as master oscillator. A large-magnitude, chirped fiber Bragg grating was designed and procured to stretch the seed pulses to multi-nanoseconds. A large-flat-mode (LMF), high-energy (>1-mJ) fiber preamplifier is also being evaluated.

To enable HEPW on NIF, LS&T is also developing high-energy, short-pulse compatible gratings and focusing optics for the back-end system. Four gratings would be used to compensate for both temporal and spatial chirp during pulse compression. Since the laser pulse is shortest and energy is highest on the final

grating and focusing optic, optical damage of these components is a potential problem. Major effort was focused on developing high-damage-resistance, large-aperture multilayer dielectric reflection gratings for compression of the amplified pulses. Initial tests indicate that multilayer dielectric (MLD) coated gratings made with a fused silica (SiO_2) top layer hold promise for high-energy (~5 kJ) operation of a NIF HEPW. The reflection grating developed for HEPW was made with a multilayer stack of dielectric oxides that provide reflectivity at wavelength and angle of use and a SiO_2 grating layer with width and height of grooves designed for maximum efficiency and lowest electric field structure at a specific incidence angle. Using photoresist and holographic exposure tools and a large-area ion beam etcher, we were able to generate the grating grooves with high precision. The key to high-damage-fluence MLD gratings is to minimize the E-field enhancement at the groove surface. We are currently fabricating and damage testing sample gratings compatible with kJ-level short pulse production. Our goal is to build 2-meter aperture grating structure with 75% compressor efficiency and individual grating efficiency >94%. A schematic of the pulse compressors and parabolic focusing optics is shown in the figure (orange color) on page 1.

Generation of X-Rays by Thomson Scattering between an Ultrashort Laser Pulse and a Picosecond Electron Bunch

With funding from the LDRD Program and in partnership with the Physics and Advanced Technologies (PAT) and the Engineering Directorates, LS&T continues to develop an ultrafast x-ray source based on Thomson scattering of fs laser pulses from relativistic-electron bunches from a linear accelerator (linac). After years of intensive R&D, the experimental setup for Thomson scattering is returning results. In recent experiments, we successfully generated 70-keV x-rays with extremely high brightness. The immediate application of this intense x-ray source (20–100 keV) will be in pump-probe experiments for the Stockpile Stewardship Program to temporally resolve structural dynamics and atomic motion in high-Z materials with ps-resolution.

The PLEIADES facility (Picosecond Laser Electron InterAction for Dynamic Evaluation of Structures) is located in Bldg.194 where PAT's high current, rf, electron linac and LS&T's fs-laser facility (FALCON, femtosecond accelerator laser concept) are installed. We have recently completed construction and synchronization of a dual-beam Ti-sapphire laser

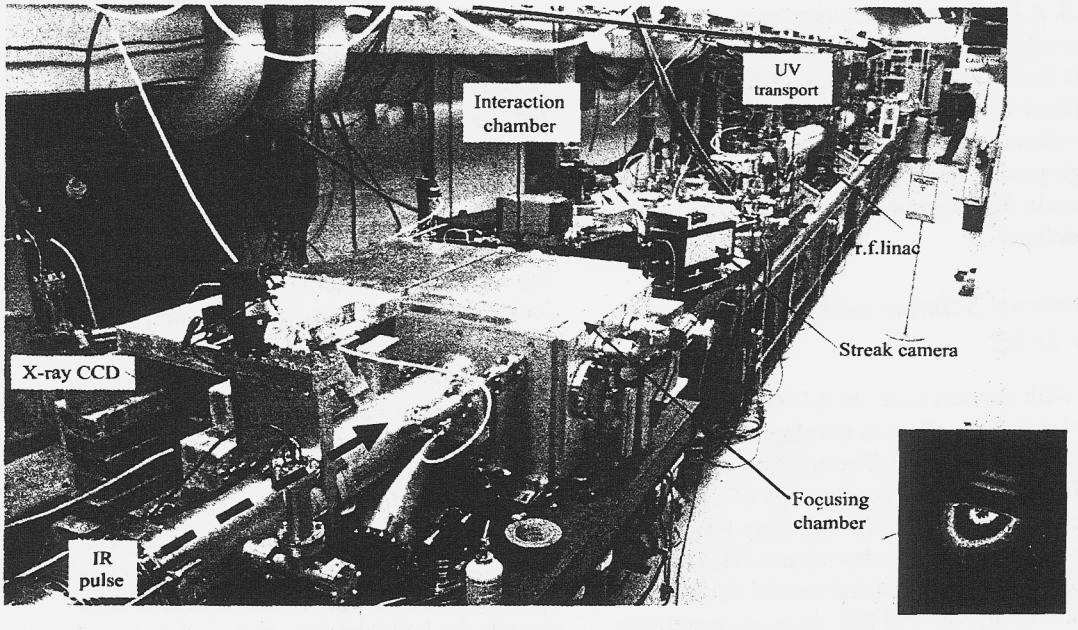

Short-pulse Thomson x-ray source. IR laser photons scatter off electron bunch in the interaction chamber located in Bldg. 194 where LS&T's fs-TW laser facility and PAT's electron linac are located. An x-ray image from a Thomson CCD camera is also shown. Top of beam is occluded by x-ray photodiode.

system for photon-electron counterpropagation experiments. A single, mode-locked oscillator is used to seed both the main IR laser system (the source of fs photons) and the photoinjector laser system (PLS, which seeds the linac). The laser master oscillator is phase-locked to an rf crystal oscillator to drive the klystrons that power the linac. The PLS consists of a regenerative amplifier (regen) and single 4-pass amplifier that yields an IR output of ~100 mJ. The amplifier output pulse is compressed using a small, dual grating compressor. The compressor output pulse is frequency-tripled to 266 nm and transported to the photogun to produce photoelectrons from a polished copper cathode. The photoelectrons are accelerated to 5 MeV and injected into the linac and accelerated between 50 to 80 MeV.

In the main IR laser, after the grating stretcher, the 600-ps pulse is amplified to 1 J by three stages: a regen, a 4-pass-preamplifier and a second 4-pass power amplifier, and then transported to a vacuum grating compressor. The 600-ps, 1-J pulse is compressed to ~50 fs and propagated (in vacuum) to the interaction region. Inside the interaction chamber, the electron pulse is focused by a magnetic lens to a 50-μm spot. The laser pulse is delivered and focused to the same interaction point from the opposite direction to collide with the electron bunch at an ~180° angle.

In the scattering chamber, the laser photon energy, E_L, is upshifted by an amount proportional to the square of the relativistic energy of the electrons. In our current experimental arrangement, the electron energy is 54 MeV, the energy of 800-nm photons (E_L) is 1.55 eV, and so the energy of x-ray photons (E_x) is calculated to be 70 keV. Initial experiments were performed with the laser pulse and electrons interacting head-on. We are also designing experiments for 90° scattering between the electrons and photons, which will produce subpicosecond x-ray pulses.

Several diagnostic tools were developed to monitor the Thomson x-rays. The image of the Thomson x-ray beam monitored by an x-ray charge-coupled device (ccd) camera was also recorded. The top portion of the beam was occluded by one of the x-ray photodiode packages. The estimated x-ray flux for this shot was 10^5 photons at an average energy of 70 keV. This is the highest single-pulse ps x-ray flux ever produced at this energy. Two other groups, one at LBL and the other in Japan, have produced comparable x-ray fluxes at lower energy, 30 keV and 14 keV respectively. With straightforward improvements to the laser focal fluence and focused electron spot, we expect an ~1000-fold improvement in the x-ray flux in future experiments.

Short-Pulse, High-Average-Power Laser System for Micromachining

Under a work-for-others contract, LS&T is developing a 100-W class picosecond, kHz, solid-state laser system for rapid, precision drilling of small (μm-scale) holes in metal and alloys. We have recently completed the assembly and initial testing of this advanced laser drilling system and were able to deliver over 35 W in a 2-ps, 4-kHz pulse train to the workpiece for material processing application.

Below: Large dielectric diffraction grating used in the 50-W-psec-pulse machining laser has a diffraction efficiency of 97% and rms wavefront of 1/40th of a wave.

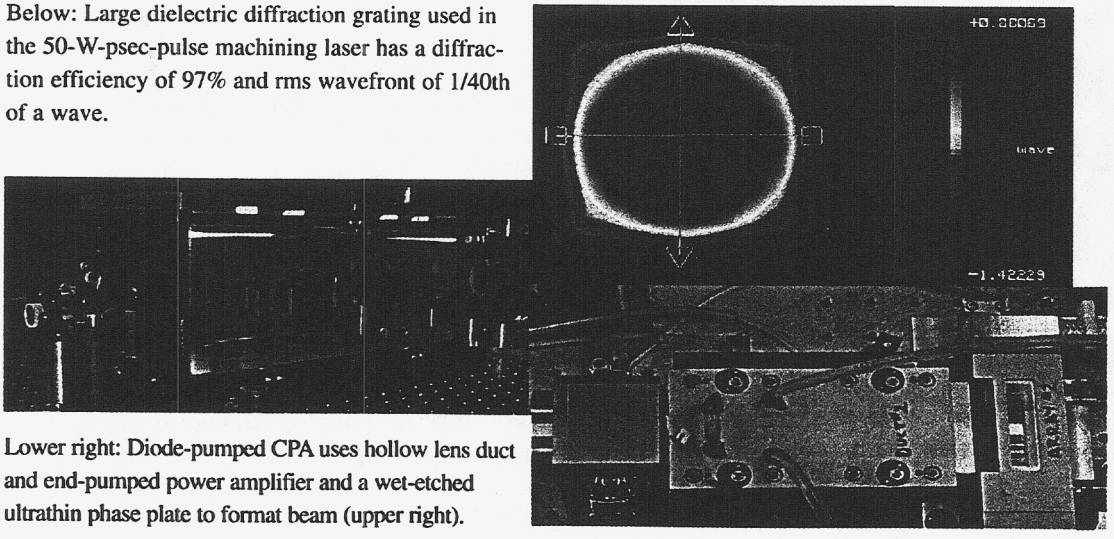

Lower right: Diode-pumped CPA uses hollow lens duct and end-pumped power amplifier and a wet-etched ultrathin phase plate to format beam (upper right).

This short-pulse, high-average-power laser employs numerous advanced technologies of the LS&T program. These technologies include fiber mode-locked oscillators, solid-state regenerative and power chirped-pulse amplifiers using diode-pumped Yb:YAG as the gain medium, and a high-power multilayer dielectric grating. The laser system architecture is based on chirped-pulse amplification (CPA). It starts with a mode-locked Yb-doped fiber laser, which was developed by Imra Corporation specifically for this application. This mode-locked oscillator produces 8-psec pulse trains and has an average power of 120 mW (2.4 nJ/pulse at 50 MHz). The spectral bandwidth of the oscillator pulses is 2 nm. The psec pulses from the fiber oscillator are stretched in time to 2 nsec using a diffraction grating pulse stretcher, amplified by 90 dB, then recompressed to 2-psec duration before being sent to the target chamber. Between each of these laser subsystems, we use computer-based pointing and centering loops to precisely control laser beam alignment.

The stretching-and-compressing process that is the crux of the CPA architecture is accomplished using a high-efficiency dielectric diffraction grating manufactured by LS&T's Diffractive Optics Group. This large (150 × 335 mm^2) multilayer dielectric grating has a diffraction efficiency of >97% at 1030 nm. Whereas a typical CPA-based laser system architecture may use 4 diffraction gratings (2 for the stretcher and 2 for the compressor), the current design employs a single grating that is shared by both the stretcher and compressor.

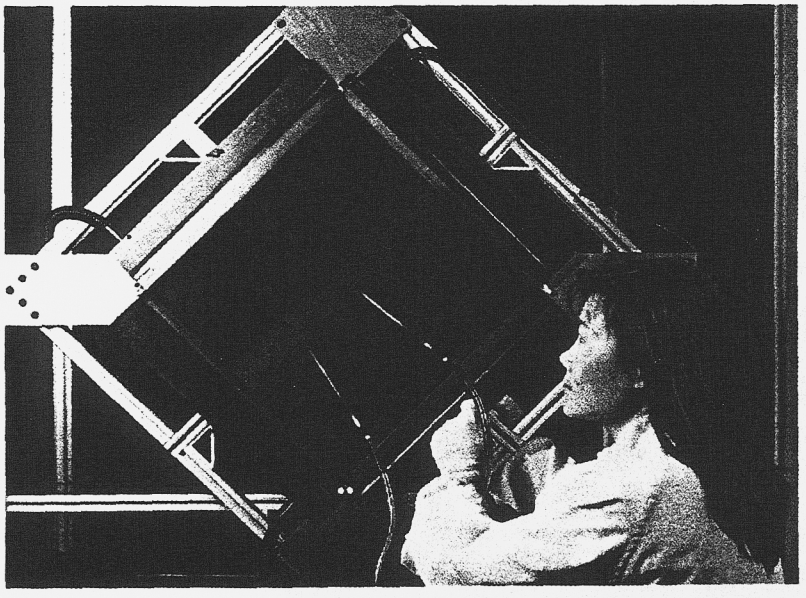

Large fused silica Beam Sampling Grating fabricated for NIF.

This single-grating stretcher/compressor design enabled us to combine two of the laser subsystems in a compact unit that can readily be incorporated into a hardened system that can withstand the harsh conditions typically encountered on the factory floor. The 90 dB of amplification between the pulse stretcher and compressor is accomplished by two subsystems: a linear-cavity regenerative amplifier and a power amplifier. Both amplifiers use Yb-YAG as the gain medium, and the power amplifier is pumped with microchannel-cooled diode laser arrays (operated at 940 nm). The regen amplifies the 1-nJ stretched pulses up to 750 μJ and converts the pulsing frequency from 50 MHz to 4 kHz (using a Pockels cell). The power amplifier has two heads. It boosts the regen output from 3 W to 50 W in two passes. With the use of a grating compressor, the pulse width of the amplified beam from the power amplifier is compressed from 2 ns back to 2 psec, multiplying the laser peak power by a factor of a thousand.

For drilling or material processing, the output from the compressor is delivered directly to the workpiece in the target chamber. Online beam diagnostics are developed to record and control the output power, beam quality, and wavefront of the laser. We have made good progress in the drilling of sub-μm holes in metals and alloys as required by our industrial partner. Under the support of ICF's Target Science and Technologies group, we have also built a new cutting station and coupled to an existing short-pulse machining laser to drill high-aspect-ratio, micron-scale holes for fusion target fabrication. Early trials of the system have demonstrated the feasibility of drilling holes that extend more than 100 times beyond the system's Rayleigh range. Holes with 3-μm diameter have been drilled in 125-μm-thick Be and Al foils as well as thin-walled Be capsules.

Fabrication of Beam Sampling Gratings (BSGs) for Power Balancing of NIF Laser Beams

Balancing the power on all the NIF beams requires a precise power measurement on each individual beam. This measurement has to be stable to ±1% over a period of time and should

be directly relatable to the energy on target without additional ambiguities or uncertainties. This requires that the measurement be done as close to the end of the laser chain as possible. Using a Fresnel reflection off an optical surface does not provide the required stability because the antireflection coatings degrade over a period of time, and because a reflected sample beam does not travel through all of the optical surfaces. A transmissive diffraction grating inserted in the beam path provides a stable sample of the beam for the power measurements. The requirements on this beam sampling grating for NIF are that the grating diffract in transmission a small fraction (~0.3%) of the incident high-power laser beam and bring it to focus at a distance of approximately 1.2 m from the optic. This requires a shallow grating structure (~15 to 20 nm deep) with concentric grooves. The grating period ranges from 1 to 3 μm. LS&T personnel assembled a wet-chemical processing machine and a patterning-and-illumination station to fabricate full-size BSGs with 5- to 30-nm groove depth for power balance diagnostics on NIF. We have completed building and testing of production hardware for fabricating BSGs. Ten full-aperture fused silica BSGs have been fabricated for use on the NIF to be used on NIF early light campaign.

Development of Continuous Phase Plates for NIF with Wet-Etch Figuring

With support from the Laboratory Directed Research and Development (LDRD) Program, we continued to develop a low-cost wet-etching tool for precision optical figuring and finishing of full-aperture optics for NIF. Wet-etch figuring (WEF), is a method for generating arbitrarily shaped optical surfaces using wet chemical etching. During the fabrication process, the etching region on the optic is confined to a stable droplet size through the use of surface tension gradients (called Marangoni confinement), and is moved in a controlled fashion over the optic surface to precisely generate the desired optical figure on very thin glass substrates. Real-time measurement of the surface wavefront during the etching process and feedback allows for a close-loop figuring operation. Over the course of this year, we further refined the process and applied it to fabricate subscale continuous phase plates (CPPs) for testing. A small-aperture (30- × 30-mm) CPP was fabricated on 1-mm-thick borosilicate substrates. This optic is designed as a beam homogenizer to generate a smooth, super-Gaussian focal spot at target. The surface height gradients for this optic are 0.5 μm/mm. Our ultimate goal is to produce full-aperture (40-cm × 40-cm) CPPs for NIF in the future. For precision material processing using short-pulse lasers, we have also fabricated ultrathin (1-mm) phase plates for modifying the focal spot on the workpiece.

FABRICATION OF A 5-m-DIAMETER DIFFRACTIVE FRESNEL LENS FOR SPACE-BASED APPLICATIONS

Detection and imaging of distant objects, such as the exosolar (outside our solar system) planets, require optical telescopes with large-aperture primary optics. Large apertures gather

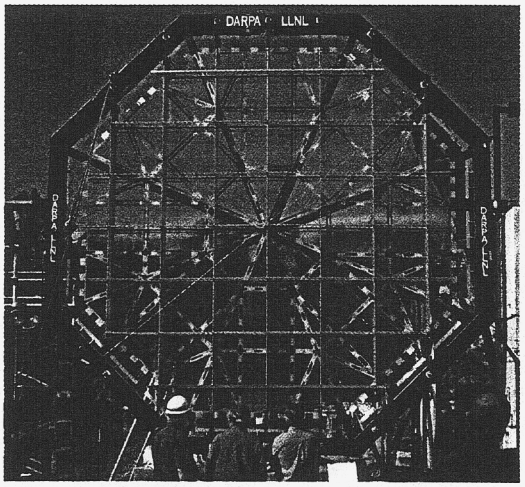

Five-meter foldable, ultrathin, lightweight Fresnel lens for space-based applications.

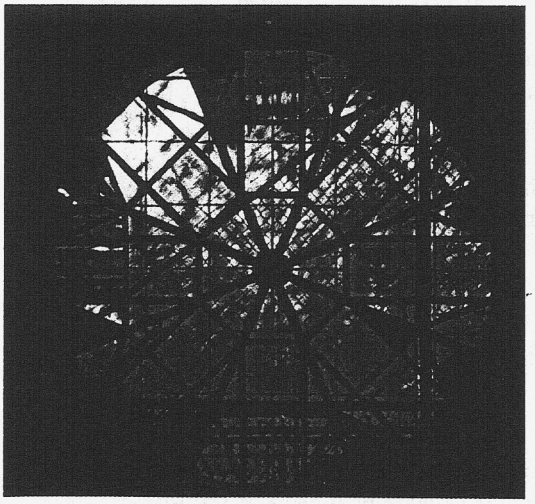

Focal spot produced by the 5-m Fresnel lens when illuminated with 532-nm light. Inscribed is a 2.5-cm-diameter circle. The central portion of the image is saturated.

more light from these objects, thereby increasing the signal-to-noise ratio. Space deployment of such telescopes severely limits the weight of the optical components and requires that the primary optic be thin, lightweight, and compact for deployment. Transmissive optics (lenses) are less sensitive to surface ripples and pointing errors than reflective optics (mirrors). Lenses can be made lightweight by replacing conventional lenses with diffractive Fresnel lenses.

Funded by LDRD, LS&T continues to develop large-aperture Fresnel lenses for space telescopes (Eyeglass project). In an early effort, we built diffractive telescopes at apertures up to 20 cm diameter and demonstrated their color-corrected operation over a 470- to 700-nm-wide bandwidth. We also successfully built large-aperture, space-deployable optics that can be packaged into a small volume for launch. For our first assembly, we built a 75-cm-diameter Fresnel lens made up of six segments and assembled it using 2.5-cm-wide metal hinges. After fabrication, this lens was shown to produce a diffraction-limited focal spot unaffected by folding and unfolding operations.

To further demonstrate the feasibility of scaling this concept to larger sizes, we have recently built and operated a 5-m-diameter Fresnel lens. This lens consists of 72 segments of 0.7-mm-thick glass panels that are glued together using 5-cm-wide metal hinges. The particular layout of the pattern was chosen to allow the lens to be folded into a cylinder of ~1/3 its diameter. The glass panels used for this lens are mass produced for flat-panel displays, making them very inexpensive. Optical testing consisted of hoisting the lens in a vertical position (see top photo on page 1-9), illuminating it with monochromatic light from a laser and observing the focal spot produced by the lens. We successfully tested the lens at 405-, 532-, and 670-nm wavelengths. The focal spot size and shape are dominated by the aberrations inherent in the glass panels and the reduced precision in the alignment of the panels. Both these limitations will be overcome in the future.

ADVANCED SOLID-STATE LASERS AND COMPONENTS

LS&T provided development and expertise for a number of DOE and DoD projects. These include developing advanced 100-kW-class high-power diode-laser arrays for the Mercury laser and Solid-State Heat-Capacity Laser (SSHCL) projects, developing advanced fiber lasers for petawatt and laser guide star applications, building high-energy lasers in collaboration with PAT and the University of Nevada, Reno, activating x-ray ablation experiments to evaluate IFE optics, and beginning activation of the Mercury laser. Mercury is a kW-class, diode-pumped, solid-state laser (DPSSL), intended to serve as driver for high-energy-density physics and inertial fusion energy.

Mercury Laser: a Diode-Pumped, Gas-Cooled, Solid-State Slab Laser for Inertial Fusion Energy (IFE)

Diode-pumped solid-state lasers are one of four driver technologies being considered for inertial fusion energy power plants. Each driver development project, including solid-state laser, heavy ions, Z-pinch and gas laser (KrF), is currently focused on demonstrating several proof-of-principle design concepts. The Mercury laser is being activated and will test key technologies including high-power laser diodes, crystals, and gas cooling within an architecture that is modular and scalable to multi-kilojoule apertures with minimal beamline reengineering.

The design requirements of the laser are to operate at 10 Hz and 100 J/shot within a 10% efficiency envelope. To meet this goal, we explored numerous gain materials and architectural options to best fit the design space of a fusion energy class laser. $Yb^{3+}:Sr_5(PO_4)_3F$ or Yb:S-FAP was chosen as the gain medium based on its long energy storage lifetime, moderately high cross section, and good thermal conductivity. The primary challenge has been in growing large aperture slabs of 4×6 cm^2 in area. However, the growth techniques employed to eliminate or reduce the crystalline defects produced boules that were difficult to cut due to the high thermal gradients required during the growth process. Using stress models developed in conjunction with a research group at the University of California, Davis, we chose an off-center cut geometry with a high-pressure water jet to overcome the high probability of boule-fracture during fabrication. This method has proven successful and five S-FAP slabs have been mounted onto the first amplifier. Four additional slabs are in fabrication and seven crystalline boules are waiting to be cut. The slabs are mounted onto aerodynamic aluminum structures called "vanes" that are separated by

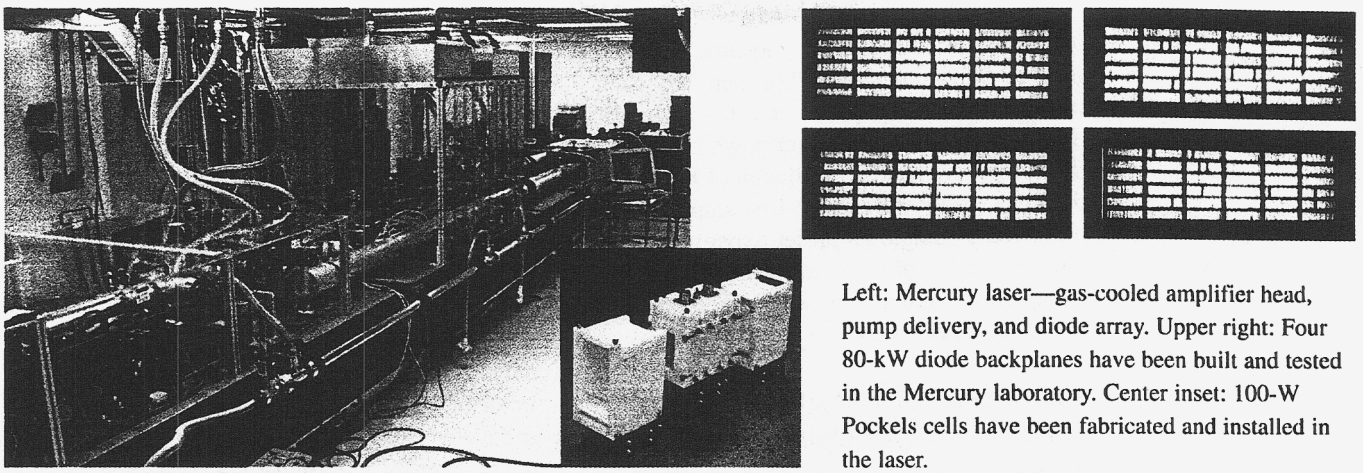

Left: Mercury laser—gas-cooled amplifier head, pump delivery, and diode array. Upper right: Four 80-kW diode backplanes have been built and tested in the Mercury laboratory. Center inset: 100-W Pockels cells have been fabricated and installed in the laser.

1-mm helium gas cooling channels. Recent measurements of Yb:S-FAP indicate damage thresholds of greater than 30 J/cm^2.

The laser diodes at 900 nm are precision mounted onto etched silicon heatsinks with microlenses to help reduce the light divergence, and then secured onto large copper blocks or arrays that provide the cooling and electrical power to the diodes. Each amplifier assembly is pumped by four 80-kW diode arrays. Four arrays have already been built and are currently being exercised in the system. Together they have accumulated over 10^5 shots. Several sets of diode array backplanes have been qualified and will be used for the second amplifier assembly. The diode array light is guided to the amplifier through multiple reflections within a hollow lens duct and homogenizer.

The amplifier was assembled with five Yb:S-FAP slabs and two undoped glass slabs. The undoped slabs serve as placeholders in the amplifier until the remaining S-FAP slabs can be fabricated. With 200 mJ of injected energy, we were able to extract up to 31.6 J of energy at 1.047 μm in single-shot mode. At 10 Hz, we measured an average energy of 20.6 J. Wavefront data was taken for static (no diode pumping) and full pumping conditions. The static wavefront data show 2.7 waves of peak distortion due to bonding phase discontinuities incurred during the fabrication process. New fabrication techniques are being tested to eliminate these distortions. In the interim, a static conjugate phase plate, using the wet-etch technology developed by LS&T, was used to correct for the distortion when placed directly adjacent to the amplifier assembly. We measured a factor of three improvement in the energy within a diffraction-limited spot for unpumped conditions. The conjugate phase plate will be used in the system until the slabs can be replaced with ones with higher optical quality.

The overall architecture employs an angularly multiplexed, four-pass beam layout. Relay imaging of the laser beam with telescopes between the amplifiers helps to greatly reduce the intensity modulation at the crystalline amplifiers. A100-W, large-aperture birefringence-compensated Pockels cell is used after two passes at low fluence (<1 J/cm^2) to help suppress parasitic beams. The laser system, diode laser power conditioning, and utilities are computer controlled. A full suite of sensor packages is used to diagnose the beam after

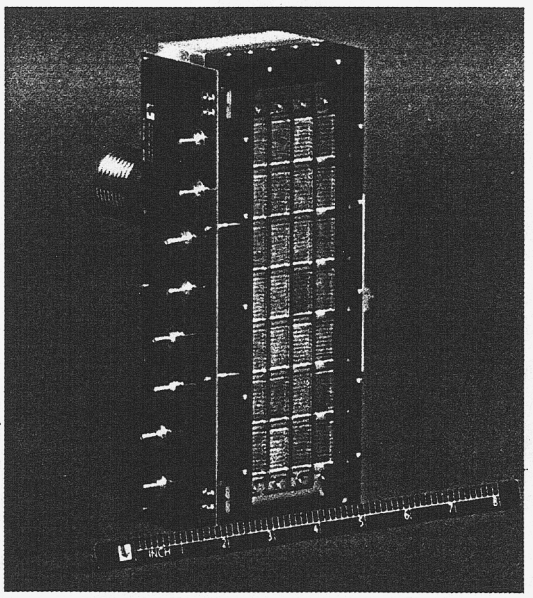

Pump module constructed from 28 closely packed SiMMs tiles arrayed in 4 rows of 7 tiles. This pump module is designed to deliver 42 kW of pump radiation.

each pass. A dark field diagnostic allows detection of damage on every shot such that when a damage site >100-μm is detected in the dark field image, the laser is shut down immediately. Future plans include installation of the remaining two S-FAP slabs in the first amplifier head, followed by single-amplifier experiments and then activation of the second amplifier. When complete, Mercury laser will yield up to 100 J /pulse at 10 Hz.

Fabrication of 100-kW-Class Laser Diode Arrays for Optical Pumping of Lasers

LS&T continues to develop diode laser arrays packaging technologies for optical pumping of kW-class and heat-capacity lasers. In 2002, we fabricated two 42-kW peak-power packaged arrays for the solid-state heat-capacity laser (SSHCL) and eight 80-kW packaged arrays (backplanes) for Mercury laser projects.

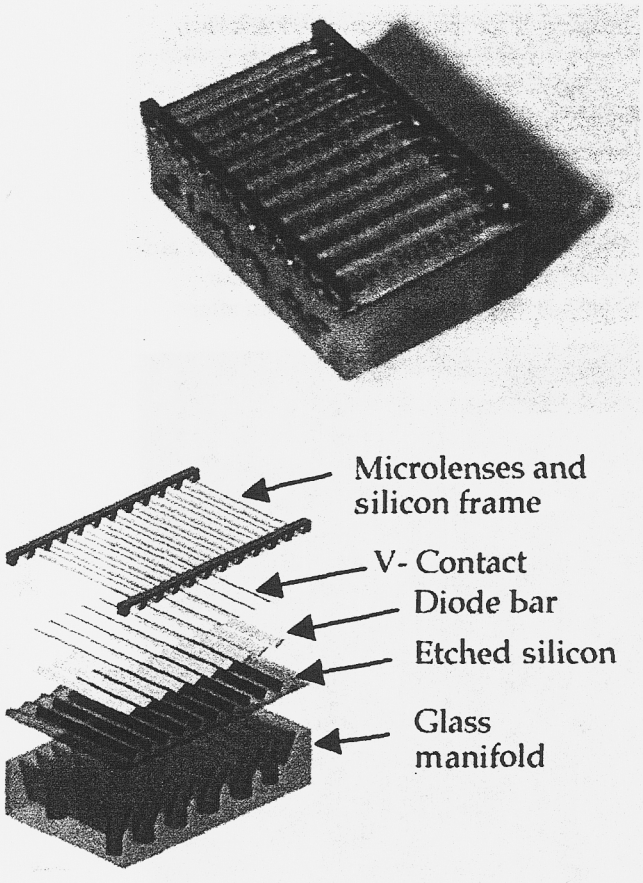

The SiMMs package holds 10 individual laser diode bars in a single monolithically cooled silicon tile. Top: Photograph of an individual SiMMs package. Bottom: Assembly drawing showing the various SiMMs package components in an exploded view.

To imagine 100-kW diode arrays becoming a common reality, two key elements of the technology need to fall into place: (1) high-performance, reliable diode bars and (2) heatsinks that offer excellent thermal management and precision diode bar mounting. Rapid cooling of diode laser arrays is achieved using silicon microchannels. Photolithography and etching techniques are applied to produce tens of thousands of 30-micron-wide channels in silicon substrates. Water flowing through these microchannels aggressively cools the laser diode bars, which are mounted on the silicon at location less than 200 microns from the channels. By combining 10 diode bars onto a single heatsink, a 10-bar package, referenced as a tile, serves as the unit cell from which large two-dimensional diode arrays can be built up through tiling. We have recently completed packaging of several diode arrays. Each package is capable of generating in excess of 40 kW of optical power. Noteworthy is that the brightness (i.e., W/cm^2-str) of the array is extremely high, by virtue of the compact tiling of the heatsinks and the precision placement of 10-element microlens arrays on each tile.

The individual tiles that are used to make up these large arrays are called SiMMs for Silicon Monolithic Microchannels. The considerations that drove the SiMMs package design were ease of fabrication and the ability to construct large laser diode arrays with output power capabilities of 10 to 100 kW. Of paramount importance in the design of the SiMMs package was the requirement that the same aggressive heat removal capability that characterized our original rack-and-stack silicon microchannel-cooled package be preserved in the SiMMs. This requirement was met by incorporating microchannels into the silicon directly below the location of the attached laser diode bars. The SiMMs design has a very tight thermal circuit with only 177 microns of silicon separating the heat-generating laser diode bars and the microchannel fins that define the cooling channels.

Since almost all applications at LLNL now require microlensed arrays, the development of an easy and efficient microlensing attachment technology was an important consideration during the design phase of the SiMMs package. Easy and efficient microlens attachment translated into a requirement that an entire SiMMs

package be microlensed in a single step. Single-step microlensing of an entire tile eliminates the production steps necessary to individually attach a microlens to each diode bar as we do in our rack-and-stack package. From our previous experience with the rack-and-stack package, we know that microlenses must be placed with a positional tolerance of a few microns relative to the diode bar emitter facets to achieve good optical performance. This implies that the single-step microlensing of an entire SiMMs tile will require the individual diode bars within a tile be positioned relative to one another with at least the same few-micron accuracy.

The precision placement of the laser diode bars on the SiMMs package is accomplished by using a V-groove technology on the front surface of the package. These V-grooves are generated using the same etching technology that is used to fabricate the microchannels into the backside of the silicon. The emission direction of the diodes at 55° to the normal of the SiMMs front face is due to the orientation of the V-grooves that serve as pads for the laser diode bars. With the diode bars precision located, the microlenses can be held in precision frames fabricated in the form of silicon runners using the same anisotropic etching technology that is used to fabricate the V-grooves and the microchannels. Shaped cylindrical microlenses are preloaded and glued into these silicon runners, forming a ladder-like structure consisting of 10 lenses as shown in the photo. The entire 10-lens assembly is then attached to the SiMMs package in a single step. The microlens array serves to collimate the fast axis radiation of the laser diode bars from its original 30° divergence angle into a collimated beam with a divergence angle of <1°.

The backing glass blocks of the SiMMs package are designed to sit side by side on a backplane structure containing cooling water source and drains. The package is specifically designed for close packing to give high effective fill factors. The array shown above has an effective fill fraction of 0.7. This pump module generates 42 kW of pump radiation at an effective irradiance, including the hit from the less than unity fill of the backplane, of 1 kW/cm^2 when viewed in the direction of the emitted radiation. The SiMMs package represents a significant breakthrough in high-power diode-array packaging technology and enables the scaling of power from 2-D diode arrays to100 kW or larger with extremely high brightness. A total of 840 kW arrays have been installed for the heat-capacity laser program. These are the most powerful average-power diode arrays in existence.

Advanced Fiber Lasers for Laser Guide Star Applications and Petawatt Laser Front Ends

Since their "rediscovery" by the University of Southampton in 1985, fiber lasers and amplifiers have steadily increased in importance and output power. They are popular solutions to many problems because they typically have high wall-plug efficiency and are easy to package into robust, reliable turnkey devices that virtually anyone can operate. A cursory analysis of fiber laser development history shows that its average output has been increasing by a factor of 10 every 3 years for roughly the last 18 years and is now reaching output powers of interest to DOE and DoD applications.

Two advanced fiber lasers were investigated by LS&T in 2002: a high-power 938-nm cladding pumped fiber laser to generate 589-nm light for laser guide star application and an ultrastable mode-locked fiber laser as the front end of high-energy petawatt laser system in NIF.

In the laser guide star effort, we are developing a 10-W, compact, all-solid-state laser to be operated at 589 nm. Our design is based on sum-frequency mixing of a 10-W erbium fiber laser (operated at 1583 nm) with a 10-W

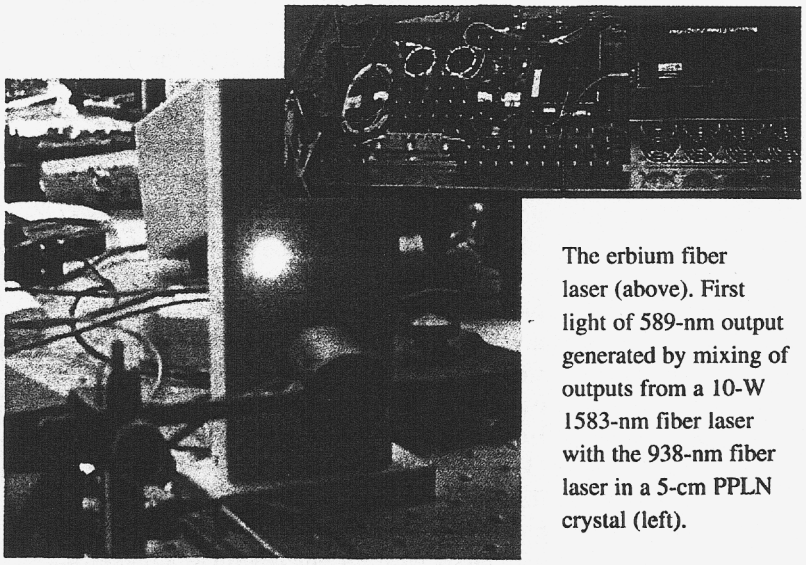

The erbium fiber laser (above). First light of 589-nm output generated by mixing of outputs from a 10-W 1583-nm fiber laser with the 938-nm fiber laser in a 5-cm PPLN crystal (left).

neodymium fiber laser (operated at 938 nm) in a periodically poled nonlinear optical material. We have made significant progress this year. A 10-W erbium fiber laser was successfully assembled using a master oscillator power amplifier configuration. To achieve this output, a 3-mW fiber DFB laser is phase modulated to broaden its linewidth and then amplified in a commercial L-band erbium-doped fiber amplifier.

A cladding pumped neodymium fiber laser was developed and has generated over 2 W of output power. Operation of neodymium-doped glass at 938 nm works best in a nearly pure silica glass, which limits the maximum doping concentration of the neodymium. Fiber lasers are particularly well suited to this application because they are a natural medium for achieving long interaction lengths at high power density. Physics relating to the operation of neodymium at 938 nm were investigated including excited-state quenching as a function of concentration, stimulated Brillouin scattering, ground state absorption, and competition from the1088-nm laser line. The fiber offers a natural mechanism for suppressing light at longer wavelengths as the waveguide is subject to a wavelength-dependent bend loss. By winding the fiber on an appropriately sized mandrel, we were able to create a distributed filter in the gain medium to suppress 1088-nm light and pass 938-nm light. We plan to scale the 2-W 938-nm fiber amplifier to 10-W level in the near future. First light of 589-nm laser was generated by frequency-mixing of outputs from these two fiber lasers (at 1583 nm and 938 nm) in a 5-cm-long periodically poled lithium niobate (PPLN) crystal. We plan to scale the 589-nm output to 10-W level in 2003 for laser guide star application.

We are also developing an advanced fiber laser to be used as the front end for a high-energy petawatt (HEPW) laser system. Our goal is to generate an all-fiber laser source of <200-fs pulses that can be stretched to 3 ns and amplified to output energies to 10 mJ completely within the optical fiber. The effort is divided into three tasks that include (1) construction of the fiber laser mode-locked master oscillator, (2) investigation of a chirped fiber Bragg grating for pulse stretching, and (3) demonstration of a large mode-area optical fiber amplifier, with a specialty refractive index profile designed to amplify and transmit pulses with up to 2.5 times the energy of optical fiber amplifiers with similar core sizes and beam qualities. We have constructed a working prototype of the mode-locked fiber oscillator. We have also designed and procured large-magnitude chirped fiber Bragg gratings for multi-ns pulse stretching. We are continuously investigating the large flattened mode fiber amplifier, with the goal of amplifying laser pulses to energies >10 mJ for HEPW on NIF.

X-Ray Ablation and Neutron Damage Experiments on Optical Materials for IFE

Under the support of the Defense Program's High Average Power Laser Program, LS&T is building a facility, named XAPPER, for x-ray ablation and damage experiments. The primary objective of these experiments is to study pulsed x-ray damage production in candidate inertial fusion energy (IFE) chamber wall (tungsten and carbon composites) and final optic (aluminum and dielectric mirrors, as well as fused silica) materials. XAPPER is also of interest to the heavy-ion fusion program for liquid ablation/condensation studies.

XAPPER (built by PLEX LLC of Brookline, Massachusetts) uses a star pinch to produce soft x-rays. The star pinch is driven by current supplied by six thyratrons that could be switched at 10 Hz or higher. An ellipsoidal condensing optic is used to collect x-rays and bring them to focus on the sample. When

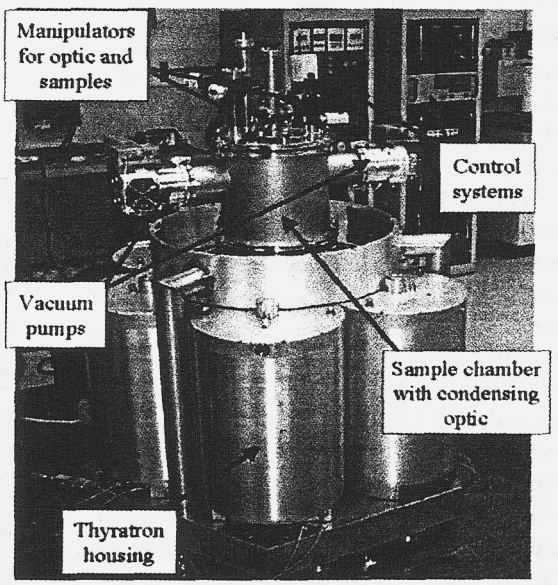

XAPPER facility uses a star pinch to produce soft x-rays at 10 Hz. The star pinch is driven by current supplied by 6 thyratrons.

operated with xenon, XAPPER will provide 113-eV x-rays at fluences of ≥7 J/cm^2. For operation with nitrogen, the peak fluence falls to ~0.25 J/cm^2, but the x-ray energy increases to 430 eV. Use of the condensing optic not only allows for higher fluences, it also greatly reduces the debris loading on the sample. Several million pulses of x-rays can be generated before minor maintenance is required. With x-ray fluence of several J/cm^2 and the short mean free path of the soft x-rays, XAPPER is capable of providing x-ray doses that exceed those expected in laser-IFE power plants. Current diagnostics include a photodiode, a vacuum calorimeter, and an extreme ultraviolet (EUV) spectrometer.

To qualify optical materials for IFE, we have performed a series of radiation experiments on fused silica. The survivability of the final optic, which must sit in the line of sight of high-energy neutrons and gamma rays, is a key issue for any laser-driven IFE concept. Previous work has concentrated on the use of reflective optics. We have introduced and analyzed the use of a transmissive final optic for the IFE application. Neutron damage experiments have been conducted at a range of doses and dose rates, including those comparable to the conditions at the IFE final optic. The experimental work, in conjunction with detailed analysis, suggests that a thin (<1 mm), fused silica Fresnel lens, such as those created for the Eyeglass Project, may be an attractive option when used at a wavelength of 351 nm. Our measurements and molecular dynamics simulations provide convincing evidence that the radiation damage, which leads to optical absorption, not only saturates but that a "radiation annealing" effect is observed. Neutron-induced optical absorption equilibrates at ~5% for a 500-μm-thick fused silica Fresnel lens operated at 300°C. By intentionally operating the optic at an elevated temperature of 500°C, the optical absorption would be reduced to only 0.6%.

Advanced High-Power Lasers for High-Energy Density Plasma Physics Experiments

Under the support of the DOE's NNSA/NV Cooperative Agreement, we are developing a 20 TW / 20 J laser at the Nevada Terawatt Facility of the University of Nevada at Reno to perform high-energy-density plasma physics experiments. The purpose of this laser system is to develop proton and x-ray radiography backlighting techniques, to study plasmas in z-pinches and magnetically insulated transmission lines, and to study deposition of energy from high-intensity laser pulses into plasmas. The performance requirements of this laser are: peak irradiance on target >10^{19} W/cm^2, prepulse irradiance <10^{11} W/cm^2, pointing accuracy of ± 25 μm, timing jitter relative to the Zebra z-pinch facility of <10 ns and shot rate >2/hr. Major efforts were focused on conceptual design of the laser system, which uses an optical parametric chirped-pulse amplifier (OPCPA) for preamplification, and phosphate Nd:glass rod amplifiers for final amplification. A mode-locked Nd:glass oscillator is used to generate 2 nJ, 250 fs-long pulses which are subsequently expanded to 1.5-ns duration using a grating stretcher. Two OPCPA stages will be used to amplify the pulse to 70 mJ. Two double-passed Nd:glass rod amplifiers will provide the final amplification to 30 J. After reflective gratings recompress the pulse to <1 ps, an f/3 off-axis parabolic mirror focuses the beam to a ~10 μm spot. Faraday isolators are used to protect the laser chain from damage. Analysis shows our design meets energy requirements with acceptable nonlinear phase shift and damage margins. The laser system activation is scheduled in 2004.

LS&T is also collaborating with the Physics and Advanced Technologies Directorate (PAT) in an upgrade of the Janus system to achieve 1 kJ in each of its 2 beamlines. Janus is a high-energy Nd:glass laser system operated by PAT to perform high-energy density experiments. The upgraded laser will enable significant new experimental capabilities, including pressures of 20 Mbar, compression to 2–3 times solid density, electron temperatures of >10 keV, and large area shock waves. Major effort was focused on the design of the high-energy amplifiers and beam transport periscopes. Our design codes verified that 1-kJ laser energy could be achieved at the pulse duration of 3 ns, using rod amplifiers, and 10-cm and 15-cm phosphate glass disk amplifiers. The frequency conversion efficiency is expected to be >70%. The installation of the upgraded beamline is scheduled for 2003. When completed, it will provide significant support capability for NIF, including testing and calibrating of diagnostics and training new physicists and engineers to perform high-energy-density experiments.

SOLID-STATE HEAT-CAPACITY LASER FOR DEFENSE

Under the support of the U.S. Army's Space and Missile Defense Command, and in collaboration with industrial partners including Decade Optical Systems (DOS), General Atomics (GA), PEI Electronics, Northrup/Grumman Polyscientific, and others, we are developing high-average-power (100 kW-class), diode-pumped, solid-state heat capacity laser (SSHCL) technology for applications in tactical short-range air defense missions. As a proof-of-principle, we have built and delivered a 10 kW-class (13 kW actual) heat-capacity laser to White Sands Missile Range. This laser employed flashlamp pumping of the laser media and Nd:glass laser slabs. In order to advance to a 100 kW-class laser, it is necessary to make a transition to laser-diode pumping (for increased power and efficiency), and crystalline laser media (for better thermal characteristics). The baseline design for such a laser uses Nd:doped gallium gadolinium garnet (GGG) as the laser medium and laser-diode pumping at 808 nm.

The technical and engineering basis required for SSHCL have been established. A mobile, compact, lightweight laser system capable of being deployed on a hybrid electric vehicle is currently under development. When complete, this laser system would be capable of defending against short-range rockets, guided missiles, artillery and mortar fire, and unmanned aerial vehicles (UAV). Power for both the vehicle and laser system would come from the vehicle's diesel generator and onboard high-energy lithium ion batteries.

High-Average-Power Pulsed Laser-Material Interaction

The flashlamp-pumped heat-capacity demonstrator laser was delivered to the High Energy Laser System Test Facility (HELSTF) at the White Sands Missile Range in August 2001 and was operated in support of material interaction testing. In its present configuration using a stable optical resonator, it is capable of generating laser pulse energies between 500 and 1000 J/pulse and an average power of up to 13 kW for 10-s burst duration. This combination of high pulse energy at high average power has never been achieved from a solid-state laser system. In 2002, an experimental program was undertaken to study the interaction between this beam and target samples made of aluminum and steel. Detailed numerical modeling was developed to guide the experiments and to help interpret the results. We investigated a number of significant interaction effects that are unique to the high-energy, pulsed-beam format. Initial test data indicate that laser–material interactions under high peak irradiance conditions using a small focusing spot result in rapid penetration due to hydrodynamic forces driven by vaporization. Due to transient surface temperature rise

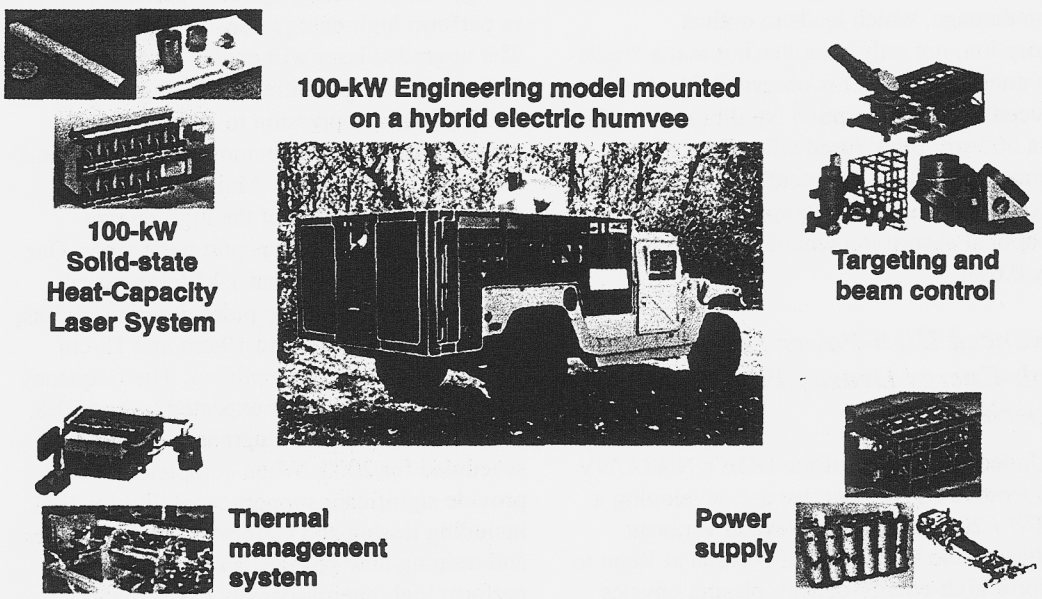

The 100-kW Solid-State Heat-Capacity Laser will have a 10% electrical efficiency, and the required 1-MW input is supplied by the vehicle traction battery mounted on a conceptual system using a hybrid electric humvee.

Courtesy of General Atomics and PEI Electronics.

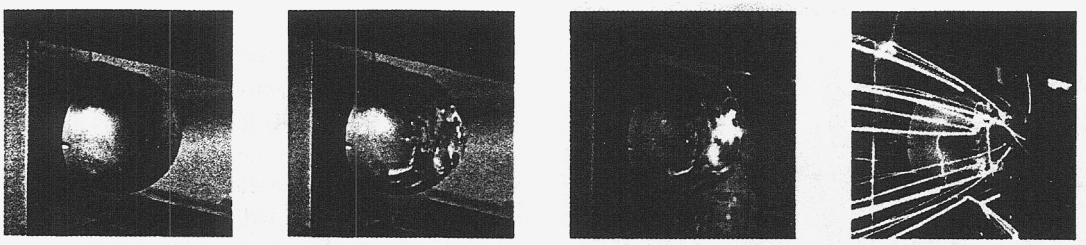

Frames taken from a movie showing the interaction of the laser beam with a steel coupon. The beam has punched through the coupon at this point.

during each laser pulse, increased heating over that achieved from a CW laser of the same average power is observed. High peak surface temperatures during each laser pulse also drive the combustion of the metal target under high-speed air flow conditions, providing additional energy deposition and heating.

In 2002, we had the opportunity to irradiate an antitank guided munition (ATGM) with the 10-W SSHCL. A video sequence of the actual ATGM crushing is shown above. The crush fuse on the ATGM is made from an aluminum alloy. The mechanism used to trigger the ATGM fuse was straightforward. The nose of the ATGM is a crush switch consisting of inner and outer domes. When heated by the laser, the fuse is weakened and collapses under the aerodynamic air flow load. When the two domes contact, the fuse is activated. The total fluence required to compromise the ATGM was 702 J/cm^2, a figure almost 10 times less than the value that has been used in the battlefield simulations using an existing Directed Energy (DE) laser system.

Adaptive Resonator Control for High Beam Quality Operation

Low divergence is necessary to propagate a high-average beam from an SSHCL to target. To do this, the relatively small thermally induced optical distortions in the heat-capacity amplifier of the laser system must be corrected. An unstable resonator that incorporates an intracavity deformable mirror has been incorporated to make these corrections. LS&T successfully demonstrated lasing from an SSHCL with wavefront correction using the 3-slab flashlamp-pumped testbed amplifier. A new mirror, built to tighter specifications was developed to achieve wavefront correction at full average power. A complete understanding of the impact of small-scale structure (ripple) of only 25 nm rms is now in hand and a combination of laboratory measurements and numerical simulation has validated a new mirror design. We have recently demonstrated <1.5 times the diffraction-limited divergence in active lasing low-energy experiments using a full-scale resonator and 3-slab flashlamp-pumped amplifier with the original deformable mirror. The full 10-kW amplifier head has now been returned from HELSTF to LLNL where it is being integrated with the adaptive resonator to demonstrate high-beam-quality operation for a 10-s burst at full power.

Diode-Pumped 3-Slab Nd:GGG Amplifier

The scaling from the 10-kW flashlamp-pumped demonstrator laser to 100-kW will use diode-pumped neodymium-doped gadolinium gallium garnet (Nd:GGG) as gain medium. LS&T is building a 3-slab amplifier testbed as the first conceptual submodule of the 100-kW laser design. The 3-slab testbed will use three full-aperture Nd:GGG crystals. To establish a solid technical basis for such a laser, we are also developing a half-scale testbed that utilizes a single Nd:GGG slab with an active region measuring 5 × 10 cm^2 in size and pumped by four half-size laser diode arrays. The diode arrays consist of 28 SiMMs (Silicon Monolithic Microchannels) "tiles" arranged in a 4 × 7 configuration that produce an average optical power of 4.2 kW/array. The pulse width is nominally 500 μs. We performed a series of experiments to verify the design of the100-kW SSHCL system with respect to pulse energy, efficiency, and run time. Optical gain coefficient, pump uniformity, output wavefront, and temperature rise in the lasing medium were also measured to benchmark the temperature-dependent energetic model.

Using a stable resonator with low output coupling, we obtained kW output from the half-scale system. At 200 Hz, over a 10-s run, we achieved an average power of 2.8 kW with an initial output in excess of 3 kW. The average diode-array optical pump power used for this experiment was 13.3 kW, and the overall diode electrical efficiency was 45%. Initial laser testing has demonstrated 9% electrical-to-

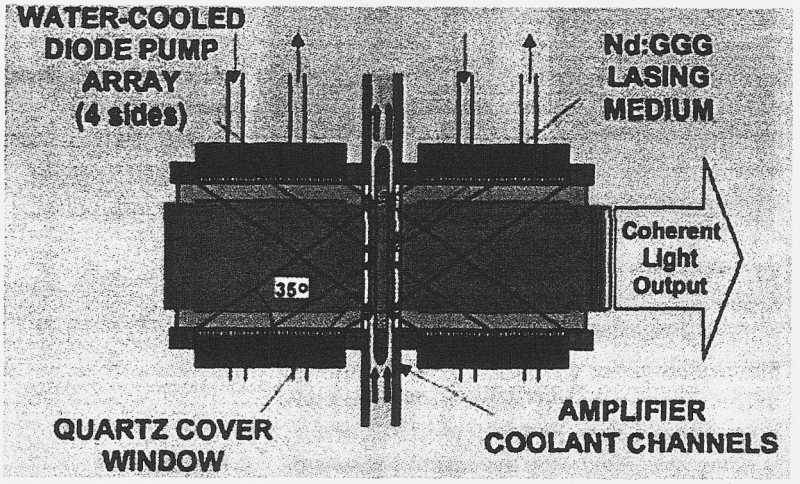

Schematic of the half-scale SSHCL. This is the fundamental building block of the diode-pumped Nd:GGG laser system.

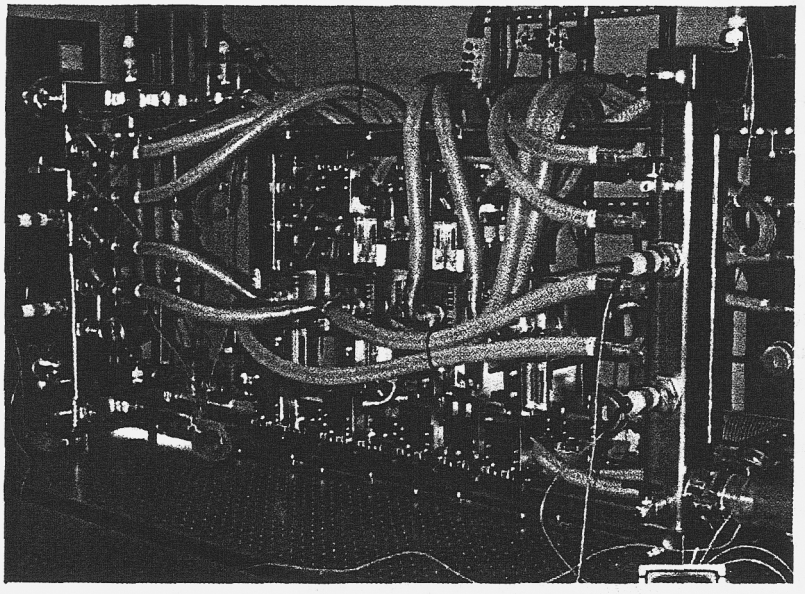

Installed 3-slab diode-pumped SSHCL head assembly hardware.

optical efficiency, a figure very near the 10% goal designed for the 100-kW mobile laser system.

Using the output beam from the half-scale system, we were able to penetrate a 1.5-mm-thick steel coupon in a matter of a few seconds. The mechanical structure of the 3-slab testbed is nearing completion, and the diode-array thermal management system is fully activated. Six of the required 12 full-scale diode arrays (80-kW peak each) manufactured by Armstrong Laser Technology have been tested and qualified. Six additional arrays have been manufactured and are undergoing testing. Fabrication of the three Nd:GGG slabs, including diffusion-bonded edge cladding and optical coating, is complete. We plan to activate the three-slab diode-pumped Nd:GGG testbed in 2003 as a scientific prototype for the 100-kW system to be developed for battlefield defense. It is anticipated that this system will generate an output power in excess of 15 kW—greater than the nine-slab flashlamp-pumped system currently in operation at the Army's HELSTF.

For the first time we have now demonstrated high-efficiency operation of a diode-pumped Nd:GGG SSHCL and are poised to operate the first conceptual submodule of a 100-kW objective laser system.

Material Processing Using Pulsed Solid-State Lasers

Laser peening is an emerging surface treatment technology for metals that places deep residual compressive stress into the surface, greatly improving resistance to fatigue failure and stress corrosion cracking. A laser system appropriate for peening at an industrial level requires an average power in the hundred-watt to kilowatt range, a pulse energy of around 25 to 100 J per pulse and a pulse duration of 10 to 30 ns. A solid-state laser with such capability was first developed for a DoD mission in 1996 by Drs. Lloyd Hackel and Brent Dane of LLNL. In order to complete the chain required for technology commercialization, we successfully established a Cooperative Research and Development Agreement (CRADA) with the Metal Improvement Company (MIC) of Parnasus, NJ. During the past year, we demonstrated key process performance, supported assembly of several high-rate, production-type laser-peening systems, and MIC began peening of commercial jet engine components. LS&T is currently developing the laser peening process to improve fatigue and corrosion lifetimes of metals and alloys in several project areas: (1) for DoE's Civilian Radioactive Waste Management System program, Yucca Mountain Project (YMP), to improve the service lifetime of metal canisters designed for long-term disposal of high-level radioactive waste generated by commercial nuclear power plants and government reactors, (2) for the U.S. military to improve the fatigue lifetime and reliability of aircraft structures as well as gears, bearings, and drive trains used in rotorcraft and combat vehicles and other energy-generation equipment in the DoD's weapon system, (3) for oil

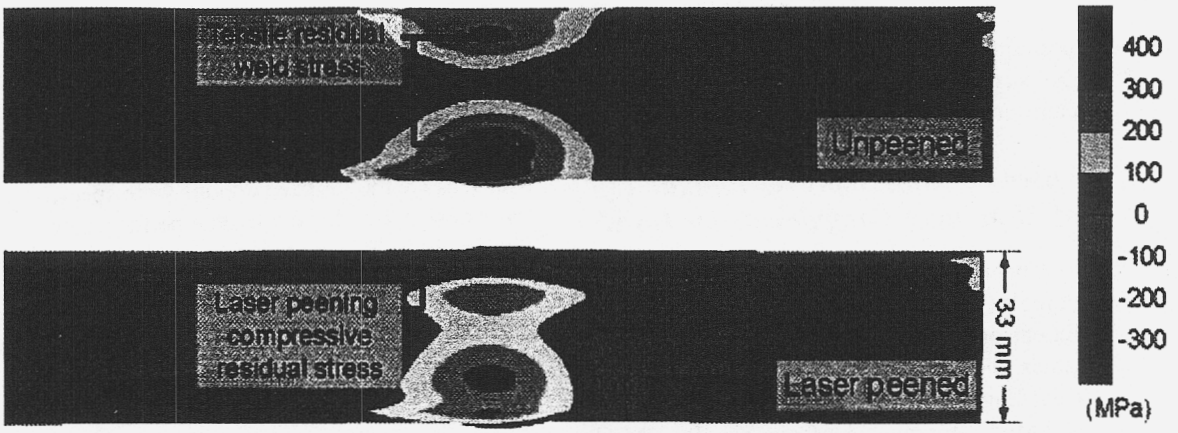

Results of contour residual stress measurement in a peened and unpeened Alloy 22 weld. Laser peening turned high tensile residual stress into near-yield-level compressive residual stress at the part surface.

and gas exploration and production, to improve the performance and reliability of structural materials. Spin-off technologies also demonstrate that pulse lasers are making an impact on U.S. industry in general; for example, technology like laser peenmarking, which provides an easy way to identify parts, and peenforming, which enables complex contouring of problematic thick metal components such as parts of large aircraft wings. We have recently partnered with the Material Performance Laboratory at the University of California, Davis, to further the development of laser peening.

Laser Peening Improves Corrosion Resistance and Mitigates Tensile Residual Stresses in Alloy 22

Under the support of Bechtel SAIC, and in collaboration with UC Davis and Metal Improvement Company, we are developing a laser peening process for application to radioactive waste storage. DOE has been charged with designing, constructing and operating a facility at the Yucca Mountain Project's (YMP) Nevada site to permanently store the nation's high-level civilian and military radioactive waste. In addition to the natural barriers at the Nevada site, a number of engineered barriers are being designed to help the facility meet its containment goal. Foremost among these is the waste package, which will be fabricated from Alloy 22, which is one of the materials known to be most highly resistant to corrosion. Our current work has focused on mitigating the potential for stress corrosion cracking (SCC) by eliminating the near-surface tensile residual stresses resulting from welding processes and evaluating the corrosion resistance of laser-peened Alloy 22.

Parametric studies covering many of the laser peening conditions have resulted in an improved treatment plan and the deepest residual stresses we have produced to date. Examples of two-dimensional residual stress fields in peened and unpeened Alloy 22 weldments, measured with the contour method, are shown above.

The effects of laser peening are dramatically demonstrated, with the near-surface longitudinal (along the weld) tensile residual stress present in the unpeened plate converted into deep, compressive residual stress with the application of laser peening.

Measurements of residual stress were made for various coupon thickness (from 5 to 35 mm). The depth of compressive residual stress appears to increase with coupon thickness.

These depths of residual stress, on the order of 20% of the part thickness for the range tested, far exceed the capabilities of conventional shot peening and other methods used in industry. This deep compressive stress serves to inhibit the process of SCC, which occurs in a tensile stress field. We have also measured the corrosion rate of peened and unpeened Alloy 22 coupons. Preliminary results have shown that laser-peened Alloy 22 will corrode more slowly than Alloy 22 alone. Because of the large depth of residual compressive stress, laser-peened material will continue to inhibit SCC even after several millimeters of material are removed through general corrosion. These beneficial characteristics, in conjunction with its noncontact, "hands off" nature, make laser

peening a good candidate for YMP to improve the corrosion resistance and lifetime of storage canisters.

Laser Peening Improves Fatigue Life of Aluminum Components for USAF

Under the support of the United States Air Force's (USAF's) Aging Landing Gear Life Extension Program, LS&T is working with UC Davis, the Ogden Air Logistics Center Landing Gear Engineering Branch (OO-ALC/LILE), and Metal Improvement Company, Inc. (MIC) to evaluate the advantages of applying laser peening (LP) to improve the performance of landing gear components for the USAF. Using test coupons made from the same high-strength aluminum alloy (7049-T73) as the trunnion, we systematically studied the effects of laser peening on the fatigue life and SCC characteristics of a trunnion, which is a part of the main landing gear on the USAF's T-38 aircraft. The results clearly show that laser peening can significantly improve the fatigue life of this component and its resistance to SCC.

Since the trunnions are currently treated with a shot peening (SP) treatment, an additional goal of this study was to compare the two surface treatments (LP and SP) and to also investigate the potential effects of applying laser peening to previously shot-peened specimens. Fatigue tests at various load levels near the service stress were performed. All three surface treatment techniques (laser peening LP, shot peening SP, and laser peening on top of the shot peening process LS+SP) increased the fatigue life of the test specimen but the greatest benefits appear to come from the laser peening treatment. Additionally, the benefits of each of the surface treatments increased at longer fatigue lives (lower maximum stress).

Stress corrosion cracking tests were performed on C-ring specimens made from 7075-T6 aluminum. The same surface treatments as above were used for the SCC tests (LP, SP, SP+LP) along with a control case of no surface treatment. The untreated C-ring specimens all showed clear evidence of SCC and cracked in half in the caustic environment after a few days (11, 13, and 23 days) while none of the treated specimens cracked throughout the entire test duration of 60 days. Although this test was not conclusive in ranking the benefits of LP over SP with regard to SCC, it did clearly show that LP is an effective tool to enhance the SCC performance of untreated specimens.

We are currently performing similar laser peening and fatigue tests on actual T-38 trunnions. Since the fatigue coupons were specifically designed to have a fatigue performance similar to the T-38 trunnion, it is expected that a similar life extension is achievable on the actual part. The estimated cost savings to the USAF (due to a reduction in the replacement costs and maintenance and inspection time) will be on the order of tens of millions of dollars.

Commercialization of Laser Peening Process and Tool

While the YMP and USAF development work continues, laser peening was also introduced this past year into commercial production by Metal Improvement Company, our CRADA partner. The laser peening system was deployed to solve an important fatigue failure problem in high-value commercial jet engine components. Since commercial introduction in May 2002, aircraft worth billions of dollars are now in service with laser-peened parts—saving millions of dollars per month in aircraft maintenance costs, millions more in parts replacement costs, and all the while greatly enhancing safety.

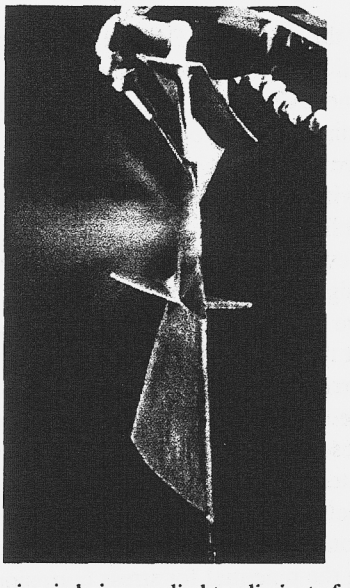

Laser peening is being applied to eliminate fatigue failure in high-value commercial jet engines.

2. LASER OPTICS AND MATERIALS RESEARCH ACTIVITY HIGHLIGHTS

OSL UPGRADED TO 1.5 KJ

The Optical Sciences Laser (OSL) achieved an output energy of 1.5 kJ on Aug. 2, 2002, culminating an accelerated 10-month program to upgrade the laser to a kJ-class facility. Originally constructed as a 100-J, 10-cm disk amplifier system in 1990, OSL has had a distinguished history as a laser-physics test bed for the National Ignition Facility (NIF) related technologies.

OSL fielded important experiments on a variety of nonlinear optical problems including frequency conversion, optical self-focusing, stimulated optical scattering, pinhole closure, short-pulse propagation in optical fibers, and laser-induced damage of both optical and nonoptical materials. With the new capability provided by the upgrade, OSL will be able to expand its mission to include integrated testing of the NIF final optics assembly.

The upgraded laser facility, shown in Figure 1, is located in a separate room adjacent to the original OSL facility. The main element is an angularly multiplexed, double-pass Nd:glass amplifier system consisting of one 9.5-m-long vacuum relay telescope and four 20-cm amplifiers recycled from the Nova laser. Each amplifier contains three 3-cm-thick disks fabricated from NIF-surplus, platinum-free Schott LG770 laser glass. The input pulse is generated in the original OSL facility and amplified through a 5-cm rod system, after which a kinematic mirror provides a choice between further amplification in the pre-existing 10-cm system or transport to the new 20-cm system.

The pulse is injected into the 20-cm system off a small injection mirror located near the focal plane of the vacuum relay telescope, after which it passes through a spatial-filter pinhole and is collimated at a beam size of ~15 cm by the first spatial filter lens. It then undergoes two gain passes through the 20-cm amplifiers, with the second being offset

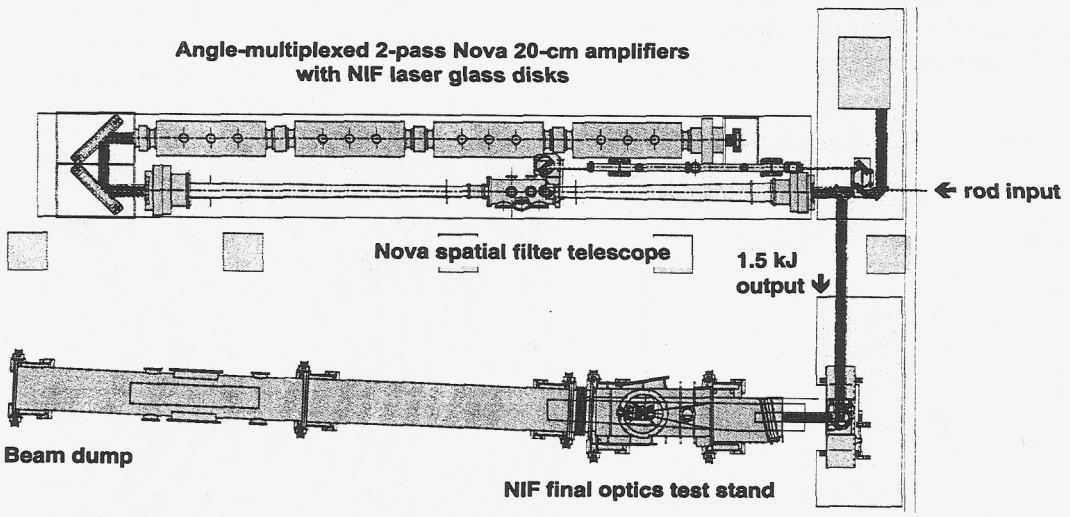

Figure 1. OSL Upgrade uses a double-pass architecture containing four 20-cm aperture disk amplifiers (twelve disks total) to deliver 1.5 kJ of 1ω energy in 3 ns for NIF final optics testing.

in angle relative to the first to allow the pulse to miss the injection mirror and exit the amplifier system through the second lens of the relay telescope. The second telescope lens demagnifies the beam by a factor of 0.83 to allow experiments to be conducted up to the fluence limits of the transport optics without stressing the optics in the amplifier cavity.

The OSL upgrade has successfully met all 1w performance objectives. CW gain tests have been conducted up to a maximum bank voltage of 22 kV, demonstrating a net round-trip, small-signal gain of ~900 with no evidence of parasitics. At 22 kV, and at the normal operating voltage of 20 kV, the small-signal gain coefficients for the LG770 disks are 8.5%/cm and 8.1%/cm respectively. System energetics are demonstrated in Figure 2, which plots measured output energy of the system vs the output energy of the 5-cm rod amplifier. At 20-kV bank voltage, the 1.5-kJ design energy is readily achieved at a 5-cm rod energy of 10 J (3 ns). Modeling results are also plotted for 20 and 22 kV, which show the potential for reaching output energies approaching 2 kJ.

The near-field beam quality of the system is also quite good, with measured whole-beam fluence contrasts (defined as the standard deviation of the fluence divided by the mean) of 7%. This level of beam quality is a critically important aspect of the NIF final optics test mission that will involve validating the damage resistance of 3ω optical components at NIF fluence levels. After completion of the new facility, the first-article final optics package was installed, and preparations are under way to begin experiments.

— P. Wegner, J. Caird, J. Murray, K. Skulina, S. Mills, G. Beer, T. Weiland, and D. Roberts

BEAM SAMPLING GRATINGS FOR POWER MEASUREMENT AND BALANCE OF NIF BEAMS

Balancing the power on all the National Ignition Facility (NIF) beams requires a precise power measurement on each individual beam. This measurement has to be stable to ±1% over a period of time and should be directly relatable to the energy on target without additional ambiguities or uncertainties. This requires that the measurement be done as close to the end of the laser chain as possible. Using a Fresnel reflection off an optical surface does not provide the required stability because the antireflection coatings degrade over a period of time.

A transmissive diffraction grating inserted in the beam path provides a stable sample of the beam for the power measurements. The requirements on this beam sampling grating (BSG) for NIF are that the grating diffract a small fraction (~ 0.2%) of the incident high-power laser beam and bring it to focus at a distance of approximately 1.2 m from the optic. This requires a shallow grating structure (~15 nm deep) with concentric grooves

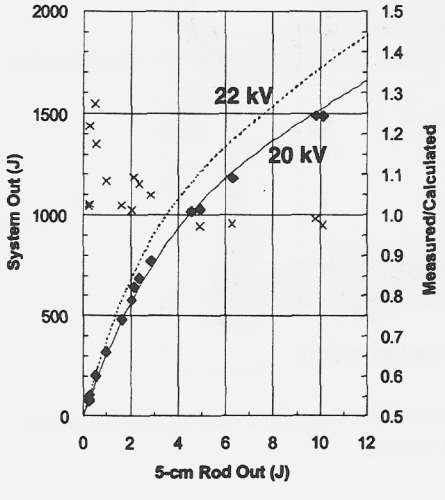

Figure 2. Plot of output energy vs. injected energy (the latter measured at the output of the 5-cm rod) demonstrating operation of the system at 20-kV bank voltage up to the full design energy of 1.5 kJ.

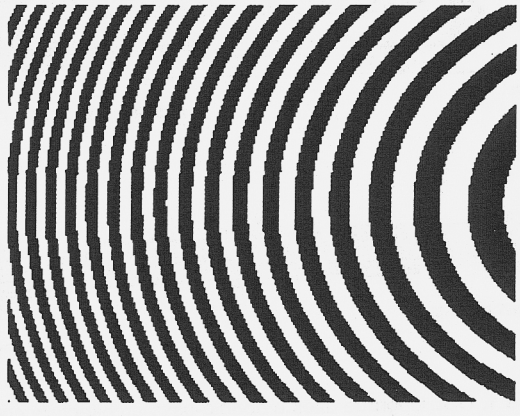

Figure 3. Schematic of the beam sampling grating (BSG) groove profile.

as shown schematically in Figure 3. The grating period ranges from 1 to 3 μm.

We use interference lithography to fabricate the beam sampling gratings. The exposure system for fabricating the beam sampling gratings is shown in Figure 4. Here a layer of photoresist deposited over the fused silica substrate is exposed to the interference pattern of two diverging beams at 351 nm originating from the main focus and the sampled focus. After exposure, the exposed photoresist is developed off, leaving photoresist grooves separated by clear areas. At this stage, we transfer the grating pattern into the fused silica substrate by etching clear areas using a buffered hydrofluoric acid solution. Finally the remaining resist is washed off, leaving a clear fused silica optic with ~15-nm deep grating profile. The automated wet-processing machine for BSG production is shown in Figure 5.

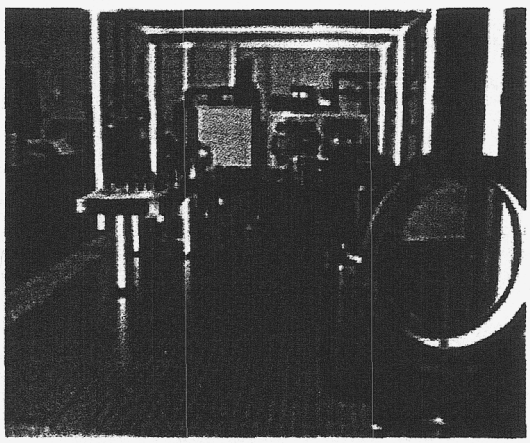

Figure 4. Beam sampling grating patterning station.

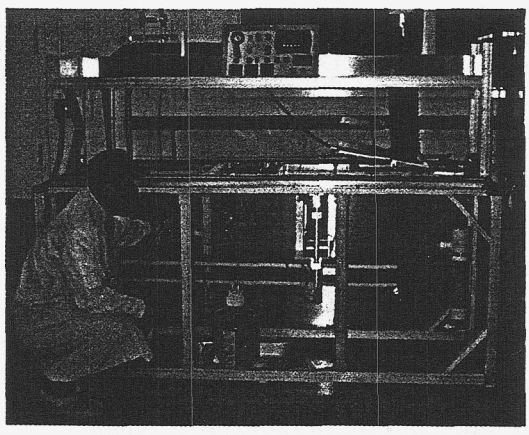

Figure 5. Automated wet-processing machine for beam sampling grating production.

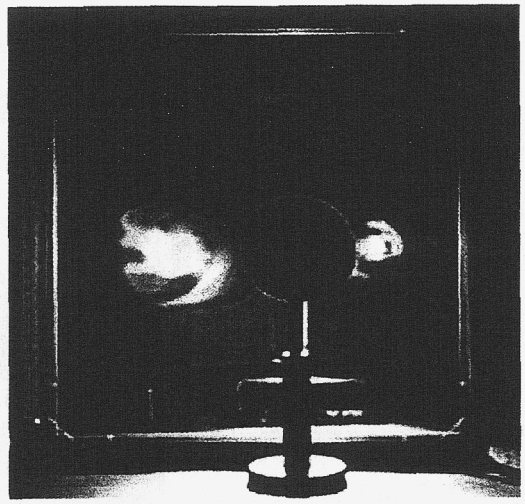

Figure 6. A 40-cm-aperature BSG prototype in operation. A white-light source located behind the black circle in the center of the picture illuminates the grating. The converging and the diverging diffracted orders are seen at the screen located behind the optic.

Figure 6 illustrates the operation of a 40-cm-aperture beam sampling grating. Here the grating is illuminated with a white-light source (hidden behind the screen), and the converging and the diverging diffracted orders are seen on the screen past the grating. A wet-chemical processing machine and a patterning-and-illumination station were assembled to fabricate full-size BSGs with 5- to 30-nm groove depth for damage testing in NIF. We completed building and testing of production hardware for fabricating NIF BSGs that will be used to perform critical power balance of the 192 NIF beamlines. We are currently fabricating full-aperture BSGs for NIF to be used on NIF early light.

— S. Dixit, J. Britten, and J. Yu

INSTALLATION AND ACTIVATION OF THE BEAMLET PDS ON NIF

A diagnostic system for detailed characterization of a NIF output beam is being activated for use in the NIF Early Light campaign. This facility, called the Precision Diagnostic System (PDS), makes use of the 1ω and 3ω diagnostics from Beamlet, where they were used to demonstrate that the NIF laser architecture could produce the 3ω energy and far-field beam quality needed for NIF's missions. The PDS will provide a full compliment of 1ω and 3ω diagnostics and make possible the first full-power and full-aperture test of an Individual

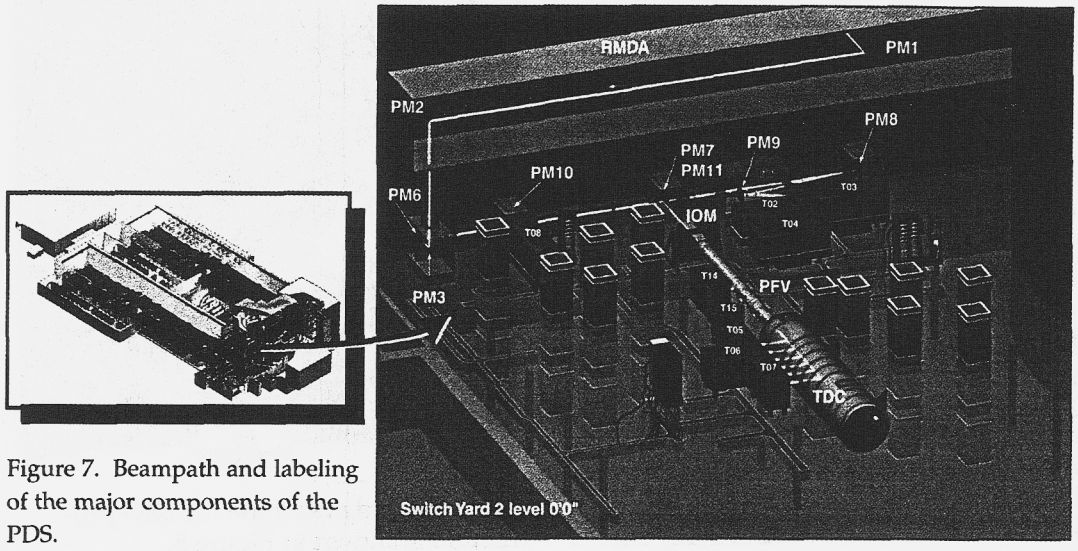

Figure 7. Beampath and labeling of the major components of the PDS.

Optics Module (IOM) -- the optical system that mounts directly to the target chamber for each beamline and contains the vacuum window, harmonic conversion crystals, focus lens, diagnostic grating, wave plates, and debris shields.

The PDS is located in Switchyard 2 on level 0'0". Figure 7 shows the turning mirrors that transport the beam to PDS from the output of the Transport Spatial Filter and the layout of the major components of the system. The Roving Mirror Diagnostic Assembly (RMDA) contains remotely operated robotic handlers that can position mirrors PM1 and PM2 to select one of the beamlines in quad 31B, the first quad to be activated, and send it to PDS. Full implementation of the RMDA will allow any one of the 96 beamlines in Switchyard 2 to be transported to the PDS. The entire RMDA enclosure and the beamline to the IOM is sealed so that it can be filled with Ar to suppress Stimulated Rotational Raman scattering during high-power shots to PDS.

The 1ω beam follows the beamline shown schematically in the figure from PM1 to PM7, where most (~96.5%) is reflected toward the IOM. The remaining fraction is transmitted through PM7 to PM8 and PM9, which point and center it into the 1ω diagnostics on Tables T03, T02, and T04. The majority of the beam reflects from PM7 into the harmonic conversion crystals and focusing lens in the IOM, passes through the Prime Focus Vessel (PFV), and enters the Target Diagnostic Chamber (TDC), an 8-foot-diameter by 40-foot-long vacuum vessel that contains the beam splitters and down-conversion optics required to handle the full NIF 3ω beam fluence.

Commissioning of NIF beamlines using PDS will start in 2003.

— J. Murray

QUALIFICATION OF 3ω OPTICS USING SLAB AND OSL LASERS

Laser-induced damage to optical components poses an upper bound to the energy that can be produced by high-fluence laser systems such as the National Ignition Facility. As a result, materials and finishing processes must undergo rigorous damage testing prior to being approved for use in the production of NIF optical components. On the NIF, the components most susceptible to damage reside in the final optics assembly, where the laser pulse is frequency converted from the infrared (1.053 μm) to the ultraviolet (0.351 μm) in precision-machined crystals of KDP and DKDP, and transported to the target through a fused silica lens, diffractive optics plates, and a debris shield. While much of the recent research in this area has focused on the role of third harmonic light in the formation of optical damage, damage due to the combined presence of first and second harmonic light has not been overlooked. In addition, the search for

inexpensive materials that can be used to protect the final optics assemblies and upstream beam transport system.

Laser damage testing is typically performed with small Gaussian beams rastered over the surface of the sample at high repetition rate. NIF laser conditions, on the other hand, are more appropriately simulated with large beams that can cover many square millimeters in a single shot of uniform fluence. The OSL and Slab laser facilities provide such large-beam capabilities. The OSL 10-cm disk amplifier system delivers up to 12 J/cm^2 of 0.351-μm light at 3 ns in a round 3-cm diameter, flat-top beam at a repetition rate of 2 shots/hour. The flexible pulse shaping and excellent beam quality of this laser make it uniquely suitable for simulating NIF laser conditions on subscale parts of up to 15 cm in size. The Slab laser can deliver up to 12 J/cm^2 of 0.351-μm light at 11 ns in a square 5-mm flat-top beam at a repetition rate of 30 shots/minute. The repetition rate of this laser enables a NIF lifetime of shots to be applied to a test sample in less than a day.

A main focus of OSL this past year has been the characterization and quantification of surface damage on diamond-turned DKDP. Extensive testing of 15-cm material was successful in correlating surface damage to specific defects on the surface of the DKDP incurred during the single-point diamond finishing process. The finishing protocol has since been revised to effectively eliminate damage due to these defects. Other work in OSL has included validation of damage mitigation and stabilization techniques applied to DKDP and fused silica surfaces, validation of small-beam laser conditioning protocols for surface and bulk damage, and the testing of fused silica contaminated with NIF-like shrapnel and target debris for the purpose of establishing debris shield lifetime.

This past year the OSL facility was also upgraded to produce 1.5 kJ of 1053-nm light for the purpose of integrated testing of NIF final optics at full scale. The first-article Integrated Optics Module (IOM) was installed and activated in August (see Figure 8), the frequency converter operation verified, and testing at a 3ω fluence level of 1 J/cm^2 begun in late September. These initial tests uncovered a number of mechanical problems with the manufacturing of the final optics cell and the diagnostic sampling grating that allowed engineers to correct the problems prior installation on NIF.

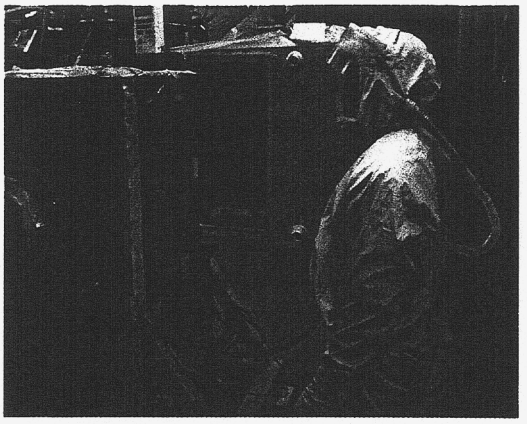

Figure 8. Insertion of the Final Optics Cell into the Integrated Optics Module installed in the OSL Upgrade facility.

Recent work in the Slab facility has focused on quantifying the growth rate of damage on fused silica surfaces at the individual and combined harmonic wavelengths of Nd:glass, and validating damage mitigation techniques for DKDP surfaces. Current techniques for mitigating damage on the surface of DKDP involve the use of a high-speed diamond-tipped rotary tool to excavate the

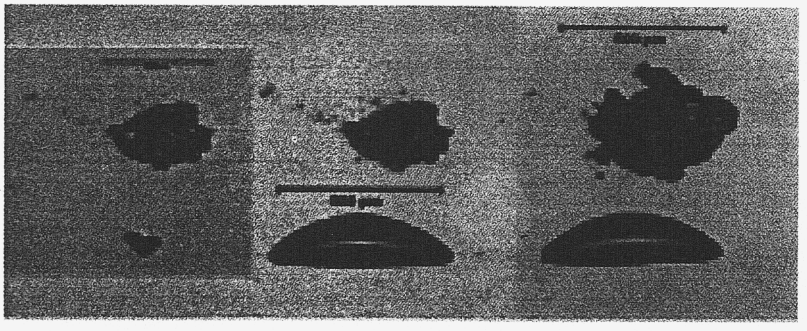

Figure 9. Results from the SLAB facility on DKDP show that a mitigated site (lower) survives 600 laser shots (12 J/cm^2, 11 ns), while an unmitigated site shows growth. The scale bar is 500 μm.

damage site. Resistance of this type of mitigation to laser radiation has been tested on samples where the mitigation technique has been applied to bare surfaces, mechanically initiated damage sites, and damage sites initiated at high fluence on the OSL laser. Results indicate the technique is promising (see Figure 9).

The Slab facility has also played an important role in certifying 'non-optical' materials for 1ω and 3ω laser exposure. Many engineering applications on the NIF require the use of materials able to withstand diffuse or scattered laser fluences of up to a few joules/cm^2 without generating particles or volatile by-products that can put near-by optical components at risk. Slab experiments were instrumental in providing NIF engineers with a plastic alternative to absorbing glass for protecting beam transport system components from stray 1ω light at fluences up to 1 J/cm^2.

— M. Norstrand, P. Wegner

Mechanisms of CO_2 laser mitigation of laser damage growth in fused silica*

M.D. Feit* and A.M. Rubenchik
Lawrence Livermore National Laboratory, P.O. Box 808- L-491, Livermore, CA 94550

ABSTRACT

Theoretical models for heating, evaporation, material flow, and stress and strain generation accompanying CO_2 laser damage mitigation and surface treatment of fused silica are developed to aid understanding of scaling with process parameters. We find that lateral nonlinear heat transport is an important cooling mechanism, more significant than evaporative cooling. Scaling laws relating experiments with different set of parameters are presented. Transverse conduction, together with the increased thermal conductivity at high temperatures, allows a gentle evaporation regime at low laser intensity in which the rate can be controlled via laser fluence. For higher laser intensity, recoil momentum imparted by rapid evaporation generates pressure, which can lead to transverse flow of the melted material. Only a very thin layer can flow because viscosity increases rapidly with depth. Evaporation and flow are subject to instabilities that can impact surface quality, especially surface flatness, if large areas are processed. Also material flow can heal cracks and improve material quality. Analysis of stress indicates that maximal tensile stresses of order 0.1 GPa, comparable to the tensile strength, can be generated.

Keywords: laser damage growth, fused silica, laser mitigation

1. INTRODUCTION

Since the discovery[1] that the transverse size of laser-induced damage in fused silica grows exponentially with repeated laser exposures, it has been evident that damage growth is the key factor in determining beam obscuration and scattering losses resulting from laser-induced damage. Growth mitigation is needed to limit these losses for the large optics used in high-power lasers. Various approaches have been investigated[2] including chemical etch, plasma etch, and CO_2 laser treatment. The CO_2 treatment of individual damage sites has proven the most effective. It was noted[3] by the end of the 1970's that exposure of fused silica to CO_2 laser radiation could lead to increased damage resistance. It was concluded this effect probably implied healing of sub-surface fracture. This conclusion was strengthened by the observation[4] that increased damage resistance occurred at a fairly sharp laser power transition and probably corresponded to temperatures at which flow begins as evidenced by residual strains left in the material. This early work dealt with small beam damage. It is interesting to note that both the above[5] [6]and other[7] early workers in laser cleaning noted that CO_2 laser processed silica surfaces had reduced water and hydrocarbon content compared with mechanically polished surfaces.

More recent experiments[2] have demonstrated successful mitigation of growth of laser-initiated damage spots on large silica optics using CO_2 laser irradiation. Indeed, the optical strength of material around the mitigated spot can be even higher than in the pristine material. These results make this mitigation method attractive for large-scale mitigation of NIF optics and motivate theoretical studies of the mitigation process to determine process scaling and optimization. We find that the laser radiation not only evaporates the damaged material, but also heals microcracks. The present paper summarizes our theoretical understanding of CO_2 laser-damage mitigation.

Growth of the damage spot is associated with enhanced absorption in material modified after previous laser shots. The ideal mitigation scheme must include local heating of the damage spot, melting and evaporation or revitrification of the modified material. Even if the transformation of heated modified material back to

Correspondence: Email: feit1@llnl.gov; Telephone: 925-422-2418: Fax: 925-422-5718

fused silica is quick, some time is required for closure of voids and microcracks. Due to the large viscosity of fused silica, such closure is made possible only by heating the material up to high temperature: temperature high enough that significant evaporation of material is inevitable. Both evaporation and material healing are very sensitive to temperature, so temperature modeling is essential for an evaluation of the mitigation process.

In most of the experiments done to date, the laser pulse is too short for the steady state to be reached so the nonstationarity of the temperature distribution is important. The effects of nonstationarity will be discussed in the next section of the paper.

The evaporation rate is very sensitive to the surface temperature, which therefore must be evaluated as accurately as possible. As a result, the nonlinearity (temperature dependent conductivity) of thermal conduction must be taken into account[8]. We will discuss a convenient scaling law to relate experiments with different parameters.

The enhanced optical strength of mitigated spots can be attributed to the healing of microcracks in the surrounding material. We will estimate the extent of the zone where material improvement takes place. We discuss thermal stresses induced by laser heating and the way to minimize their detrimental effects.

Finally, implications of these results for optimal mitigation strategy will be discussed.

2. NONSTATIONARY TEMPERATURE EFFECTS

We discuss here the role of temperature nonstationarity disregarding the temperature dependence of the thermal conductivity. The role of such nonlinearity will be discussed semi-quantitatively later.

The temperature distribution on the surface of an optic induced by a Gaussian laser beam is given by the expression[9]

$$T(r,t)=\frac{Aa^2}{D}\sqrt{\frac{\kappa}{\pi}}\int_0^t \frac{I(t-\tau)}{\sqrt{\tau}\left(a^2+4D\tau\right)} e^{-\frac{r^2}{a^2+4D\tau}} d\tau \qquad (1)$$

where A is the absorbed fraction, A=0.85 for fused silica irradiated by a CO_2 laser, D is the thermal diffusivity and κ is the thermal conduction coefficient. The intensity of the laser beam is $I(r,t)=I(t)\exp[-r^2/a^2]$. For a flat-top temporal pulse with duration τ and constant intensity I, the temperature at the center of the laser spot is

$$T=\frac{0.85P}{(\pi)^{3/2}a\kappa}Arc\tan(\sqrt{\frac{t}{\tau}}) \quad with \quad \tau=\frac{a^2}{4D} \qquad (2)$$

Here $P = I\pi a^2$ is the beam power. Asymptotically, the temperature in the center of the laser spot approaches the stationary value T_s.

$$T_s=\frac{0.85P}{2a\kappa\sqrt{\pi}}=0.24\frac{P}{a\kappa} \qquad (3)$$

The surface temperature determines the ablation rate[10]. The velocity of the evaporation front is given by the expression[10]

$$V=V_0 e^{-U/kT} \qquad (4)$$

where U is the latent heat of evaporation per atom, U=3.6 eV for fused silica and $V_0=3.8 \times 10^5$ cm/s.

Temporal evolution of temperature and ablation rates are shown in Fig.(1) for the case where the steady-state temperature is 2245°K and the steady state ablation rate is 50μ/s. One can see that the onset of the steady state regime for temperature is fast, about 10 $a^2/4D$. Of course, the temperature is slightly different from the asymptotic value for a long time. Even at t=100 $a^2/4D$, the temperature reaches only 0.94 of the steady state value. The ablation rate, however, is very sensitive to temperature, and, at the temperature at t=100 $a^2/4D$, is only 14.4 μm/s compared to 50 μm/s at steady state. Thus, the ablation steady state is much harder to reach than the temperature steady state.

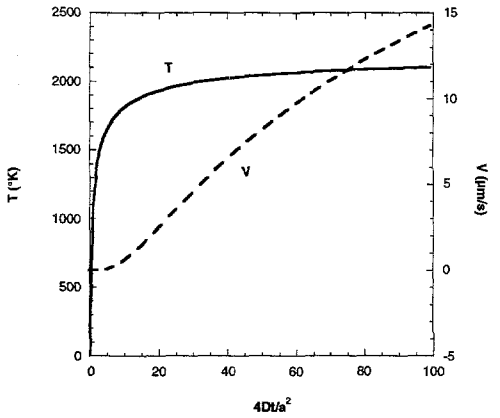

Fig.1: Temporal evolution of the temperature and ablation rate at the center of the laser spot. Time is measured in units of the thermal time $a^2/4D$.

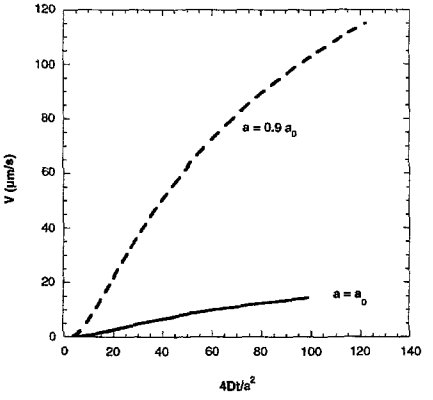

Fig.2: Ablation rate evolution for beam radii a_0 and $0.9a_0$ for same conditions as above.

As a result, the ablation rate is very sensitive to small variations of beam parameters, i.e. spot size and power. The temperature is dependent on beam size of course. The larger sensitivity of the ablation rate to small variations in beam size is shown in Fig(2).

An important effect not taken into account thus far is the nonlinearity of thermal conduction, which reduces the sensitivity of the ablation rate to variation in the processing parameters[8]. Increase of thermal conductivity at high temperatures shortens the onset of the steady state; nevertheless, one can expect that the mitigation process typically will take place in the nonstationary ablation regime.

3. NONLINEARITY OF THERMAL CONDUCTION AND SCALING LAW

The thermal conductivity of silica increases with temperature. Above about 800K, the effective conductivity (rate at which thermal energy is lost) is determined mostly by radiation transport[11]. We will use the following empirical interpolation formula for the thermal conductivity of fused silica:

$$\kappa(T)=\kappa_0+\beta T^3=0.01(1+1.7\cdot 10^{-9}T^3)(W/cmK)=\kappa_0 f(\frac{T}{T_0}) \qquad (5)$$

The coefficient β is determined from experimental data, κ_0=0.01 W/cm°K at room temperature, κ~0.04 W/cm°K at T_0=1200°K. It must be mentioned that the experimental data is not very detailed. As far as the contribution of radiation transport is concerned, some photons traverse the sample without absorption and the effective thermal conduction can then depend on sample shape. As a result, experimental information on effective thermal conduction is not very reliable and should be used for qualitative estimates only. For

simplicity below, we disregard the temperature dependence of density and specific heat, which is not essential.

For $T \ll T_0$ thermal transport can be treated as linear, i.e. $\kappa(T) = \kappa_0$. In the opposite case one can put

$$\kappa(T) = \beta T^3 = 0.01(1.7x10^{-9}T^3)(W/cmK) = \kappa_0(\frac{T}{T_0})^3 \tag{6}$$

The simple power law dependence of Eq.(6) affords a chance to find a scaling relation even in the highly nonlinear regime.

We must solve the thermal diffusion equation

$$\rho c\frac{\partial T}{\partial t} = \nabla \bullet (\kappa(T)\nabla T) \tag{7}$$

with the boundary condition

$$-\kappa(T)\frac{\partial T}{\partial z} = AIe^{-\frac{r^2}{a^2}} \qquad at \quad z = 0 \tag{8}$$

If we normalize spatial scales by the beam radius a, and introduce the dimensionless diffusion time Dt/a^2, where $D=\kappa_0/\rho c$, one sees that the problem will be characterized by one dimensionless parameter $s= AIa/\kappa_0 T_0$. Here T_0 is a specific temperature scale introduced in Eq.(5). This implies that the surface temperature and the ablation rate are functions of P/a and dimensionless time only. That is, surface temperature can be written in the form

$$T = T_0 f(\frac{AP}{a\kappa_0 T_0}, \frac{r}{a}, \frac{Dt}{a^2}) \tag{9}$$

where the structure of the function f is determined by the nonlinearity of thermal conduction. Let parameter s be the ratio of the surface temperature to T_0 for the case of linear thermal conduction. In the regime with nonlinear thermal conduction, $s \gg 1$, the relation Eq.(9) then offers the possibility to rescale experiments with different parameters. For example, to have the same processed crater for a beam spot two times larger, one must not only increase the power two times, but also increase pulse duration four times.

For $s \gg 1$, when thermal conduction can be adequately described by Eq.(6) instead of Eq.(9) one can derive a simpler scaling

$$T = T_0 s^{1/4} f\left(\frac{r}{a}, \frac{Dts^{3/4}}{a^2}\right); \qquad s = \frac{AP}{aT_0\kappa_0} \tag{10}$$

One can think of this as an increase of the effective thermal diffusivity at high power.
For thermal conduction of a more general type, $\kappa=\kappa_0(T/T_0)^n$ the scaling takes the form

$$T = T_0 s^{1/n+1} f\left(\frac{r}{a}, \frac{Dts^{n/n+1}}{a^2}\right); \qquad s = \frac{AP}{aT_0\kappa_0}$$

From Eq.(10), one sees that as power increases, surface temperature increases as $P^{1/4}$ and time for the temperature onset decreases as $P^{-3/4}$.

We introduce the new variable u,

$$\kappa_0 u = \int_0^T \kappa(T) dT \tag{11}$$

Equation (11), with boundary condition Eq.(8), can be rewritten as

$$\frac{\partial T}{\partial t} = D\Delta u; \qquad -\kappa_0 \frac{\partial u}{\partial z} = AI(r)\,|_{z=0} \tag{12}$$

One can see that in the steady-state situation the equations for u and for the temperature with temperature independent thermal conduction are identical, and for u in the center of the laser spot we have the analog of Eq.(3)

$$u_s = \frac{0.85P}{2ak_0\sqrt{\pi}} = 0.24\frac{P}{ak_0} \tag{13}$$

For the thermal conduction law (2.2) we find for the temperature in the center of the laser spot

$$T = 0.75T_0\left(\frac{P}{a\kappa_0 T_0}\right)^{1/4}$$

In Fig.(3) we compare the calculated evaporation rates vs. beam power both for linear thermal conduction, and for thermal transport described by Eq.(5) with experiment. The beam size was used as a fit parameter at a power of 50 W. The steepness of the curves is at issue here. One sees that Eq.(5) gives a better fit to experiment.

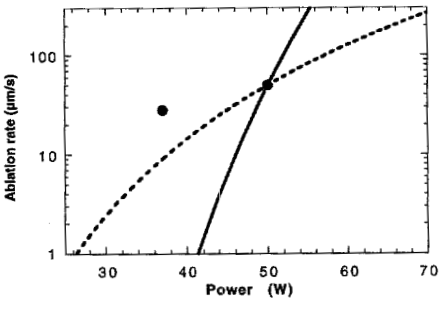

Fig.3: Ablation rate calculated with linear and nonlinear thermal is transport. Dots are experimental values. Solid line is calculated with linear thermal conduction, dotted line is calculated with thermal conductivity given by Eq.(5)

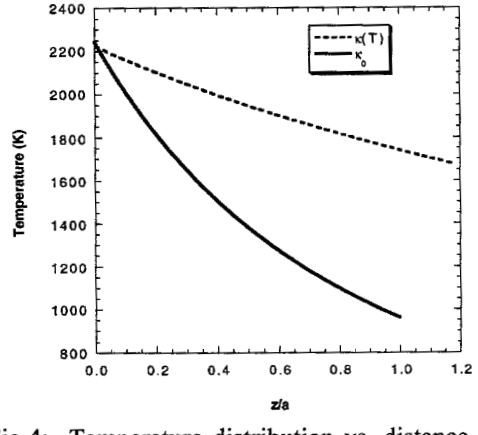

Fig.4: Temperature distribution vs. distance from the surface. Dashed line corresponds to temperature dependent thermal conductivity, solid line corresponds to constant thermal conductivity. Surface temperature of 2245 °K corresponds to the experimentally observed ablation rate of 50 µm/sec.

4. TEMPERATURE DISTRIBUTION

One must know the temperature distribution in the material to estimate the extent of the microcrack healing process. For the case of linear conduction and temporally flat top laser pulse, the temperature distribution is given by the expression

$$T(r,t)=\frac{Aa^2I}{D}\sqrt{\frac{\kappa}{\pi}}\int_0^t\frac{e^{\frac{-z^2}{4D\tau}}}{\sqrt{\tau}\left(a^2+4D\tau\right)}e^{-\frac{r^2}{a^2+4D\tau}}d\tau \tag{14}$$

At the center of the laser spot at r=0, the steady state temperature is given by the expression

$$T=\frac{AP}{(\pi)^{3/2}ak}\int_0\frac{e^{-\frac{z^2\varsigma^2}{a^2}}}{1+\varsigma^2}d\varsigma=\frac{AP}{2a\kappa_0\sqrt{\pi}}[1-erf[z/a]]e^{\frac{z^2}{a^2}} \tag{15}$$

When thermal conduction is nonlinear, however, according to the general result of the previous section we have

$$u(T)=\frac{AP}{2a\kappa_0\sqrt{\pi}}[1-erf[z/a]]e^{\frac{z^2}{a^2}} \tag{16}$$

for the quantity u defined in Eq.(11).

Temperature distributions for linear and nonlinear thermal conduction are shown in Fig.(4). One can see that the nonlinearity flattens the temperature distribution.

Typically, we are interested in cracks healing in a thin subsurface layer. For small z/a, by expanding Eq.(16) we obtain

$$T(z)=T_s-\frac{AP}{\pi a\kappa_0}(1+3\left(\frac{T_s}{T_0}\right)^3)^{-1}\frac{z}{a} \tag{17}$$

As already discussed, the steady state temperature onset takes a long time and in many situations the temperature evolution is nonstationary. In the linear regime the temperature evolution can be found from Eq.(14). To evaluate temperature in the nonlinear regime, we mention that we are mainly interested in rectification of a thin layer near the surface. On a short time scale, the temperature evolution can be treated by a 1D model and the expression Eq.(6) can be used for thermal conduction. The specific result for heat propagation in a medium with nonlinear heat conduction of form $\kappa=\beta T^n$ is the existence of a sharp temperature front with coordinate $z_f(t)$. Near the front the temperature variation behaves as

$$T=\left(\frac{nv}{\beta}|z-z_f|\right)^{1/n}$$

where v is the velocity of the thermal wave. The evolution of the temperature for the problem with fixed thermal flux q=AI on the boundary can be found from the following estimates[8].

For thermal conduction given by Eq.(6) the flux can be estimated as

$$q \sim \frac{\beta T^{n+1}}{z_f} = \frac{3\kappa_0 T_0}{z_f}\left(\frac{T}{T_0}\right)^4 \tag{18}$$

From the thermal conduction equation we have

$$T/t = q/z_f \tag{19}$$

From these relations we can find the temperature and thermal front coordinates

$$T = \frac{q^{\frac{1}{n+2}} t^{\frac{1}{n+2}}}{\beta^{\frac{1}{n+2}}} = q^{2/5} t^{1/5}\left(\frac{T_0^3}{3\kappa_0}\right)^{1/5}$$

$$z_f = \beta^{1/n+2} q^{\frac{n}{n+2}} t^{\frac{n+1}{n+2}} = \left(\frac{3\kappa_0}{T_0^3}\right)^{1/5} q^{3/5} t^{4/5}$$

Temperature increases relatively slowly. With propagation of the thermal front, the gradient drop and the temperature increase must satisfy conservation of the thermal flux.

5. MATERIAL REMOVAL

Heating of the surface induces material evaporation at a rate described by expression Eq.(4). The experimentally observed value is the crater depth

$$d = \int V dt \tag{20}$$

If the pulse duration is much longer than the thermal diffusion time, then the surface temperature is approximately equal to the steady state value T_s well before pulse termination and the crater depth is

$$d = V_0 e^{-\frac{U}{kT_s}\tau}$$

where τ is the pulse duration. For short pulses, when the temperature increases until the end of the pulse, the crater depth is determined mainly by the temperature at the end of the pulse $T(\tau)$. We can expand the temperature around $t=\tau$ to first order

$$T(t) = T(\tau) + T@\tau)(t-\tau) \tag{21}$$

Calculating the integral in Eq.(20) we find

$$d = V_0 \frac{T(\tau)^2}{UT@\tau)} e^{-\frac{U}{kT(\tau)}} \tag{22}$$

In both cases the depth is determined by the temperature at the end of the pulse and the dependence is exponential. A small change in temperature results in a large variation of depth. To increase the depth by a factor of e, one needs to vary the temperature by

$$\frac{\delta T}{T} = \frac{kT}{U} \approx 0.05$$

Thus, for linear thermal conduction, when temperature is proportional to laser power, a 5% variation of power will nearly triple the crater depth. For nonlinear thermal conduction, variations of power cause less extreme depth changes. For the thermal conductivity of Eq.(6), the variation of laser power must be four times larger to cause the same depth variation.

Since the evaporation rate is very temperature dependent, the steady state crater size can be estimated by expanding the surface temperature distribution of Eq.1) around r=0 and integrating over time. This yields a quadratic temperature distribution

$$T(r) = T_s (1 - r^2 / 2 a^2)$$

Substituting this temperature distribution into the expression for the evaporation rate, Eq.(4), leads to an evaporation rate with Gaussian spatial shape. The 1/e radius of this evaporation rate is found to be

$$R = \sqrt{\frac{2kT_s}{U}} a$$

Thus, for the parameters given above, the crater radius is predicted to be 3 times smaller than the laser beam radius. This prediction is consistent with experimental observations.

In all our calculations, we disregarded cooling by evaporation. This is justified for the steady state regime[8]. For non-stationary processing, evaporative cooling can be important and would again make the processing less sensitive to power variations.

6. CRACK HEALING

The high-temperature induced by absorption of infrared radiation not only evaporates material, but also reduces the viscosity of fused silica so that surface tension is able to close cracks, thereby annealing the material and increasing its optical strength. As pointed out above, the increase of optical damage resistance after CO_2 laser processing has been known for several decades. What is new here is local application to heal specific defects.

The typical time τ for relaxation of a surface disturbance with scale l can be estimated from the hydrodynamics of an extremely viscous liquid[12] and is given by

$$\tau \sim \frac{\eta l}{\sigma} \qquad (23)$$

The surface tension σ for glass is about 300 dyne/cm[13] and not very sensitive to temperature. In the range of 1600-2000°C, the viscosity η is given by the expression[14]

$$\eta = 1.05 * 10^{-9} e^{\frac{E}{kT}} \quad poise \qquad (24)$$

where E is an activation energy, E~6.44 eV. For a deep crack, we must use the crack depth for *l*. If we know the crack depth and the acceptable annealing time, we can determine from Eqs.(23) and (24) the annealing temperature T.

We consider crack mitigation by local heating. The time for crack healing is given by Eq.(23). During this time $d = V\tau$ of material will be ablated. The total amount of ablated material is given by the expression

$$d = \frac{\eta_0 l V_0}{\sigma} e^{\frac{E-U}{kT}} = 1.75 * 10^{-6} e^{\frac{32944}{T}}$$

Here d and l are in microns, T in degrees Kelvin. The numerical value is for a one-micron scale crack. The amount of material ablated during the crack healing process as a function of surface temperature is shown in Fig.(5). One can see that for the temperature 2245K used above, ablation of more than 4 μm guarantees that cracks in the subsurface layer will be annealed.

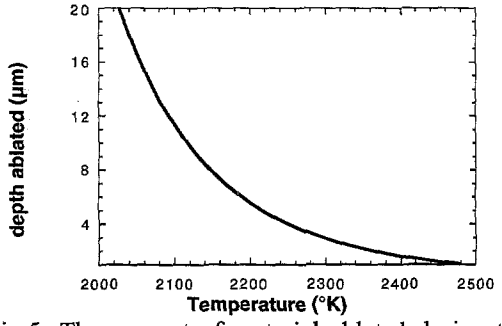

Fig.5: The amount of material ablated during the crack healing procedure.

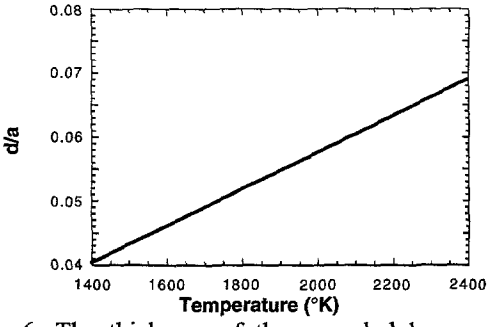

Fig.6: The thickness of the annealed layer as a function of the surface temperature.

Hence, in experiments[2] the laser-induced temperature must be high enough to heal the subsurface layer around the damage spot. Due to the nonlinearity of thermal conduction, the temperature distribution around the heated spot is reasonably flat and a wide zone of microcracks can be annealed.

We next estimate the extent of the annealed zone assuming the stationary temperature distribution. The temperature decrease inward into the heated material is given by Eq.(17), which can be rewritten as

$$T(z) = T_s - \delta T = T_s - \frac{2u(T_s)}{u(T_s)\sqrt{\pi}} \frac{z}{a}$$

where u(T) is given by expression Eq.(11). The crack healing time is

$$\tau(z) = \tau(0) e^{\frac{E\delta T}{kT_s^2}} = \tau(0) e^{\frac{2EU(T_s)}{\sqrt{\pi} U'(T_s) kT_s^2} \frac{z}{a}}$$

and the thickness of the zone d in which cracks are healed is given by

$$d = \frac{\sqrt{\pi}\, kT_s^2 u(T_s)}{2Eu(T_s)} a$$

The temperature dependence of d(T) is shown graphically in Fig.(6). For high temperatures

$$d \approx \frac{2\sqrt{\pi}\, kT_s}{E} a$$

For T_s =2245 K d~0.1a. One can see that the healing time is a strong function of the temperature while the thickness of the annealed layer is not very sensitive to surface temperature. If the crack is annealed near the surface, the thickness of the annealed layer will be thick enough to guarantee effective damage mitigation.

7. LASER INDUCED STRESSES

The laser-heated glass generates stress and strain due to thermal expansion. These strains can distort the initial flat glass surface, thus degrading the optical surface quality. Stresses can cause the glass to fail, producing cracks which act as centers for subsequent damage growth. The heated fused silica is soft and thermally-induced stresses are released by small material displacements. When the material cools, viscosity rapidly increases and material is then unable to move to further release stresses. The transition from "soft" to solid material is determined by many factors including the cooling rate. But due to the very strong viscosity temperature dependence, it is convenient to introduce the softening temperature T_{soft}. For temperatures below T_{soft} the stresses will be treated as imprinted into the material. For fused silica T_{soft} is 1585C.

One sees that if the heating of the glass is stationary, i.e. v<D/a where v is the scan velocity and D the thermal diffusivity, the time for buildup of stresses is $\tau_\sigma \sim a/s$ (s is the sound speed). This time is much smaller than the time to scan over the spot $a/v \sim a^2/D$. In this regime, stresses and strains can be treated as stationary.

To make an estimate, consider a model spherically symmetrical temperature distribution T(r). At large r, for steady state temperature distribution, the heat equation gives $T \sim T_0 a/r$. The temperature gradually drops from $T \sim T_0$ at the spot center with spatial scale ~a. The material displacement u in this case has only a radial component $u_r(r) = u(r)$ given by

$$u = \alpha \frac{1+\nu}{(1-\nu)} \frac{1}{r^2} \int_0^r T(r) r^2 dr$$

Here $\alpha = 7*10^{-7}\ ^\circ K^{-1}$ is the linear thermal expansion coefficient; $\upsilon = 0.17$ is the Poisson ratio. The maximum displacement occurs at r~a where $u \sim \alpha T a$. That is, the displacement is proportional to the spot size. For T~2000 °K and a=1mm, this displacement is about 1 μm. The residual deformation remaining after the glass freezes can be expected to be of the same order because of the high viscosity. It is clear that deformations of this scale can seriously affect the part's optical quality. The danger to surface quality for large-area scanning is apparent.

The resulting strains and stresses can be calculated from the above displacement u
Strains:

$$u_{\theta\theta} = u_{\varphi\varphi} = \frac{u}{r}$$
$$u_{rr} = \frac{\partial u}{\partial r} = -2\frac{u}{r} + \frac{\alpha(1+\nu)}{(1-\nu)} T(r) \qquad (25)$$

Stresses

$$\sigma_{ik} = \frac{E}{1+\nu}\left(u_{ik} + \frac{\nu}{1-2\nu} u_{ll} \delta_{ik} \right)$$

Here E is Young's modulus, E=74 GPa for fused silica
Hoop tensile stresses are the most dangerous:

$$\sigma_{\theta\theta} = \frac{\alpha E}{(1-\nu)(1-2\nu)}\left((1-2\nu)\tilde{T}(r) + \nu T(r) \right) \tag{26}$$

$$where \quad \tilde{T} = \frac{\int_0^r T(r) r^2 dr}{r^3}$$

Maximal hoop stress occurs at r~a and is given by

$$\sigma \sim \alpha E T \tag{27}$$

Hoop stress is independent of beam size and for T~2000 °C, σ~0.1GPa which is comparable with the silica tensile strength~0.05 GPa. Of course, we cannot conclude that the silica will inevitably crack as a result of processing. These estimates are uncertain by a factor of a few. Also, the maximum stress occurs where the glass is hot and ductile, cracking takes place during the cooling stage when thermal gradients are somewhat smoothed so stresses at that point will be smaller. But the above estimate does point out the possibility of cracking during the mitigation process.

To open a crack of length l, one must apply the stress $\sigma=K/\sqrt{l}$, where K is the toughness of the material. K=0.75 MPa $m^{1/2}$ for fused silica. The stress amplitude is determined by the maximum temperature only, but the extent of the zone of the maximal stress is about equal to the spot size. Hence, mitigation with a bigger spot size and the same peak temperature is more dangerous in terms of cracking.

The previous discussion deals with the steady state temperature distribution. As discussed above, the stresses are relaxed in hot material, and imprinted only when the temperature drops to $T=T_{soft}$. At this moment, the temperature distribution extends a large distance and the initial temperature distribution can be treated as a point source

$$T=B\delta(r) \tag{28}$$

The constant A can be found from the energy balance

$$\rho c \int T(r) dV = AP\tau; \qquad B = 2\frac{AP\tau}{\rho c}$$

The initial distribution in Eq.(28) evolves in time as

$$T(r,t) = \frac{B}{8(\pi D t)^{3/2}} e^{-\frac{r^2}{4Dt}}$$

When the temperature in the center is equal to T_{soft} the typical size of the distribution is

$$(4Dt)^{1/2} = \left(\frac{B}{T_{soft}}\right)^{1/3} = \left(\frac{AP\tau}{\rho c T_{soft}}\right)^{1/3} \tag{29}$$

For stress calculations, one can use Eqs.(25)-(28). The value of the imprinted hoop stress is

$$\sigma \sim \alpha E T_{soft}$$

ınd the size of the stressed zone is given by Eq.(29)

8. SUMMARY

We have presented above an analysis of thermal processes associated with laser mitigation of damaged spots. The results are a semi-quantitative description of the mitigation process, including some possible pitfalls.

·We obtained scalings which can, in principle, relate experiments with operational parameters. The main conclusions of the analysis are in good correlation with recent experiments[15].
·The observed pit depth is predicted to be very sensitive to process parameters due to the strong dependence of evaporation rate on temperature.
·Best results were predicted for processing with short pulses. Surface temperature will be higher for short pulse mitigation, and this also aids crack healing.

There are some effects left out of our description. We disregarded the melt motion under the effect of reciprocal momentum produced by evaporation. Also we didn't take into account the cooling due to evaporation. For typical mitigation parameters, these effects are not expected to be important[8], but may play a role for short, intense pulses when the surface temperature is high.

Finally, we note that the experiments[6,15] reveals noticeable debris deposition around the processed spot. The nature and the effect of this debris on damage need additional study.

ACKNOWLEDGEMENTS

This work was performed under the auspices of the U.S. Department of Energy by University of California, Lawrence Livermore National Laboratory under Contract W7405-Eng.48.

9. REFERENCES

1. M.A. Norton, L.W. Hrubesh, Z. Wu, E.E. Donohue, M.D. Feit, M.R. Kozlowski, D. Milam, K.P. Neeb, W.A. Molander, A.M. Rubenchik, W.D.. Sell and P. Wegner, "Growth of laser initiated damage in fused silica at 351 nm", *Laser-Induced Damage in Optical Materials: 2000* , Proc. SPIE **4347,**. 468-468 (2001).

2. L.W.Hrubesh, M.A.Norton, W.A.Molander, E.E.Donohue, S.M.Maricle, B.M.Penetrante, R.M.Brusasco, W.Grundler, J.A.Butler, J.W.Carr, R.M.Hill, L.J.Summers, M.D.Feit, A.Rubenchik, M.H.Key, P.J.Wegner, A.K.Burnham, L.A. Hackel and M.R.Kozlowski, "Methods for mitigating surface damage growth on NIF final optics", *Laser-Induced Damage in Optical Materials: 2001*, Proc. SPIE **4679**, 2002).

3. P. A. Temple, D. Milam and W. H. Lowdermilk, "CO2 laser polishing of fused silica surfaces for increased laser damage resistance at 1.06 μm",Nat. Bur. Stand. (U.S.) *Spec. Publ.* **568,** 229-36 (1979).

4. P. A. Temple and M. J. Soileau," 1.06 nm laser-induced breakdown of CO2-laser-polished fused SiO2", Nat. Bur. Stand. (U.S.) *Spec. Publ.* **620**, 180-89 (1981).

5. P.A. Temple, W.H. Lowdermilk, D. Milam, "Carbon dioxide laser polishing of fused silica surfaces for increased laser-damage resistance at 1064 nm", *Appl. Opt.* **21**, 3249-55 (1982).

6. P. A. Temple, S. C. Seitel, and D. L. Gate," CO2 Laser Polishing of Fused Silica: Recent Progress", Nat. Bur. Stand. (U.S.) *Spec. Publ.* **669**, 130-37 (1984).

7. T. Raj, D. E. McCready and C. K. Carniglia ,"Substrate Cleaning in Vacuum by Laser Irradiation, "NIST U.S.) *Spec. Publ.* **775,** 152-64 (1989).

8. M.D. Feit and A.M. Rubenchik, "Glass polishing by CO2 laser", LLNL memo NIF-0059084 (December 13, 2000).
9. M.Bass, "Laser-materials interactions", in *Encyclopedia of Lasers and Optical Technology*, R.Meyers, ed., *Academic Press*, (San Diego,1991).
10. S.I. Anisimov, V.A.Khokhlov, "Instabilities in Laser-matter interaction", *CRC Press* (1999).
11. H.Schoize, *Glass*, Springer-Verlag (1991).
12. H.Lamb," Hydrodynamics", *Dover Publications*, (New York 1945), pp. 624-626.
13. "The Handbook of Glass Manufacture", 3rd ed.v.2, p.930 *Ashlee Publishing Co.* (N.Y. 1984).
14. D.Hewak, Ed., "Properties, processing and applications of glass and rare earth-doped glasses for optical fibres", *INSPEC* (London, 1998).
15. W.Molander, "Laser parameter optimization and process design for CO_2 laser mitigation of fused-silica optics", LLNL memo NIF-0075949 (January 16,2002).

Analysis of raster scanning damage and conditioning experiments

M.D. Feit and A.M. Rubenchik*

Lawrence Livermore National Laboratory,
P.O. Box 808-L399, Livermore, CA. 94550

ABSTRACT

he raster scan technique is used for large optics damage tests and laser conditioning. We show that the "effective rea" concept enables the possibility to compare various scanning schemes and to use raster scan experiments for IF optics damage prediction. It is shown that the hexagonal lattice of laser beam imprints yields optimal use of ach shot for most of the typically used parameters. The effects of beam fluence fluctuations and pointing naccuracies on experiments are evaluated. To analyze raster scan conditioning experiments, we introduce the oncept of "effective dose", i.e. total dose averaged over a unit cell of the scan lattice. This allows various scanning chemes to be compared quantitatively.

INTRODUCTION

The high quality UV optics which will be used in high power laser systems such as NIF and LMJ are expected to have as little as 1 damaging defect per 100 cm^2 at operating fluences [1]. To have reliable characterization of damage susceptibility of such optics, an area of a few hundreds cm^2 must be tested. Even after NIF and LMJ are completed, their shots will be too valuable to use for damage testing. The natural way to test a large optic is to scan it with a small, high repetition rate beam. Most available lasers for scan experiments have a Gaussian beamshape.

To relate results of tests with small Gaussian beams to expected results for flat top large beams, some assumptions must be made. For damage tests, we usually ignore any effect of conditioning. Some conditioning[1] can take place at high fluences F>10 J/cm^2 and this situation must be taken into account. It is assumed that the damage density at a point is a function of the maximum fluence observed at this point over the number of shots in the test. This assumption is reasonably adequate for fused silica, but questionable for KDP where conditioning is a strong effect[3].

A second typical assumption is the Weibull distribution (power law) for damage density $c(F)\sim F^m$. Here c(F) is the density of damage sites produced by irradiation with fluence up to F. The Weibull index m for surface damage in fused silica is typically large, m~5-10. It should be noted that this assumption is not strictly necessary and has been adopted mainly because of scarcity of data. If damage tests are carried out at a number of test fluences with all conditions being held constant (particularly overlap spacing), then more general distributions can be derived from the measurements.

In raster scanning, the goal is to irradiate a large area with a small laser beam. The beam imprints form a scan lattice covering the plane. The way to relate this variable intensity lattice structure to flat top beam irradiation is the calculation of the effective beam area [2]. That is, the variable fluence exposure is equivalent to a flat top irradiation of the same peak fluence over a fraction of the total area. Calculations of effective area for different scan patterns in damage tests will be discussed in the first part of the paper.

Actual test beams exhibit intensity and pointing fluctuations. We consider the effects of fluence fluctuations and pointing accuracy on raster scan experiments in the second section.

DKDP and KDP damage experiments clearly demonstrate a strong conditioning effect[3,4]. Preliminary irradiation of the sample by increasing the fluence of UV pulses results in a substantial increase of the subsequent damage threshold. Thus, the history of laser exposure is important. For experiments on conditioning, we assume

*Correspondence: Email: rubenchik1@llnl.gov, Telephone: 925-422-6131, Fax: 925-422-5099

that the important parameter is dose, i.e. the integral fluence at some point. Within an elementary cell of the raster lattice, the irradiation dose is due not only to the beam centered in the cell, but also to nearby neighbors. For experiments with large beam overlap, the input of many neighbors is important. To compare experiments made under different conditions, we will calculate the dose averaged over the elementary cell as a function of the overlap fraction f. It is not clear that the dose is the sole important parameter for conditioning, but comparison of results of experiments with known doses can, at least, test this hypothesis.

It is desirable to have a numerical measure to compare different raster scan patterns. The ratio of minimum to peak fluence in a scan lattice cell can be used as a measure of variability [5]. This approach is simple and useful, but it takes into account neither the spatial distribution of intensity inside the cell nor the specific experimental setup. Damage experiments in fused silica are very sensitive to any local field maxima, and conditioning experiments are sensitive to the integrated dose We originally introduced the concept of "effective area"[2] to quantitatively measure the relative effectiveness of flat top and non-flat top beams in illuminating a sample in damage tests. This same definition is used in the present paper. The concept of effective area provides the means to compare different scan schemes and to select the most efficient one with respect to use of sample area. In the same way, the dose defined in the present work allows comparison of Gaussian beam scan conditioning experiments with ideal, flat top beam conditioning.

In the conclusion, we summarize our results, and discuss the limits of the assumptions made.

1. THE LATTICE OF BEAM IMPRINTS AND EFFECTIVE AREA

Small beam raster scanning produces an array of beam imprints covering the plane with a periodic lattice. Consider first the simple square lattice shown in Fig.1. The beam centers are spaced by distance 2a in both the vertical and horizontal directions. For the Gaussian beam

$$F = F_0 e^{-\frac{r^2}{b^2}} \qquad (1.1)$$

it is convenient to relate lattice spacing a to the overlap fraction f and Gaussian beam radius b via $a = b\sqrt{\ln(1/f)}$. For example, f=0.9 means that the beams overlap at 90% of peak fluence F_0. In this case, a=0.325 b. The Gaussian beam has maximum fluence F_0 only at the beam center.

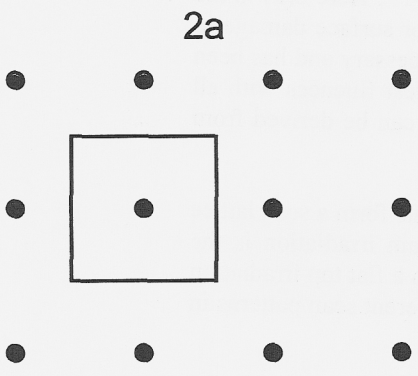

Fig.1: Square array of beam imprints. Dots signify beam centers. The distance between the centers is 2a in both the vertical and horizontal directions. Within each square unit (Wigner-Seitz) cell, every point gets its maximum fluence from the beam at its center.

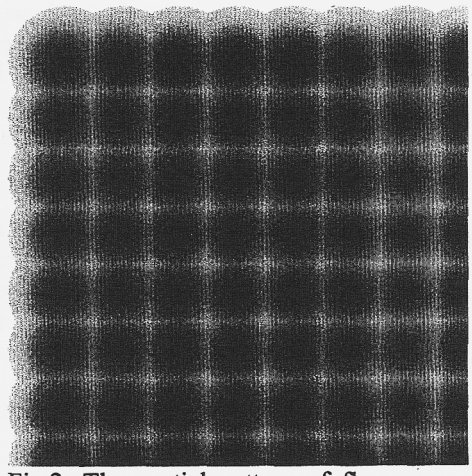

Fig.2: The spatial pattern of fluence produced by raster scan for a square lattice. One sees the square unit cells.

To relate the damage produced by raster scanning to that produced by a flat top beam, we will assume that the density of defect c(F) has the Weibull distribution.

$$c(F) = dF^m \tag{1.2}$$

with d being a constant. Typically, the Weibull index is large, m>5.
A flat top beam with fluence F_0 and area S produces $c(F_0)$ S damage sites. The Gaussian beam produces

$$\int c(F)dxdy \equiv c(F_0)S_{eff} \tag{1.3}$$

damage sites. Here F_0 is the peak fluence and the integral is over a unit cell, of area S, centered on a beam, so that this single beam provides the peak fluence for every point in the cell. Such cells are called Wigner-Seitz cells in condensed matter physics. The expression (1.3) defines the effective area S_{eff} , i.e., the fraction of the area S effectively illuminated by the Gaussian beam.

For an isolated Gaussian beam given by (1.1)

$$S_{eff} = \frac{\pi b^2}{m}$$

The meaning of this result is that the area one would expect for a Gaussian, πb^2, is reduced since the Gaussian 1/e radius of F^m is reduced from the radius b of F by a factor of $\sqrt{m}$.

We can easily carry out the calculation of effective area given by Eq.(1.3) for the square lattice of Fig.(1). The calculated effective area for this case is given by [2].

$$\frac{S_{eff}}{S} = \frac{\pi}{4}\left[\frac{Erf(u)}{u}\right]^2; \quad with \quad u = \sqrt{m\ln(1/f)} \tag{1.4}$$

Here $S=4a^2$ is the area of the elementary cell. The expression (1.4) indicates the fraction of the sample, which is effectively used in a raster scan experiment. The dependence of S_{eff}/S on overlap f for different Weibull indices m is shown in Fig.3. One sees that the curve is steeper for higher m so that small pointing (overlap) errors will result in larger variations of effective area, and thus affect damage density estimates, for larger m at high overlap.

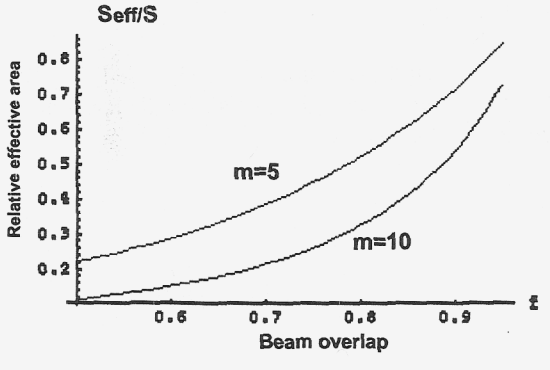

Fig.3: Relative effective area for square scan lattice as function of beam overlap f for Weibull indices 5 and 10. The curve with larger m is steeper.

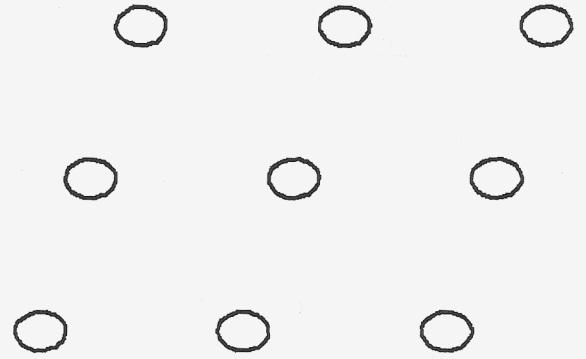

Fig.4: The array of beam imprints marking the position of the beam centers for a parallelogram lattice. The vertical distance between the rows is 2a.

It is natural to ask if another scan pattern has a higher effective area and thus uses the scanned area more efficiently. Besides the square lattice, we may consider rectangular, parallelogram and hexagonal lattices as candidates. It is easy to check that the most efficient rectangular lattice is the square one.

Similarly, the parallelogram lattice of equal cell area shown in Fig. 4 can be shown to be analogous to the rectangle. That is, maximum use of the scanned area is achieved when the parallelogram has height 2h equal to its base 2a when it has the same effective area as the square. The effective area is less for unequal height and base.

Consider now a hexagonal or triangular lattice (Fig.5). The distance between centers in every row is 2a as for the square lattice, but the distance between rows is smaller, $\sqrt{3}a$. The centers of even rows are positioned between the centers in odd rows (see Fig.6). The elementary cell is a hexagon. To calculate the effective area, the integral in (1.3) must be taken over this hexagon. To calculate this integral, we divide the hexagon into its six equilateral triangles. The integral over the triangles is conveniently calculated in polar coordinates as follows.

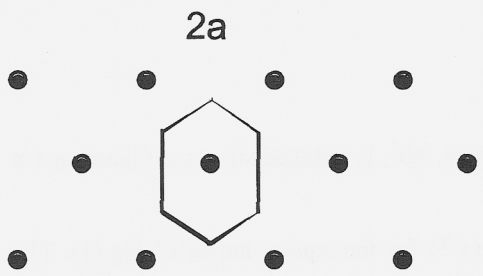

Fig.5: The hexagonal lattice. The Wigner-Seitz cell used to calculate the effective area is the hexagon, with width 2a and height $4a/\sqrt{3}$.

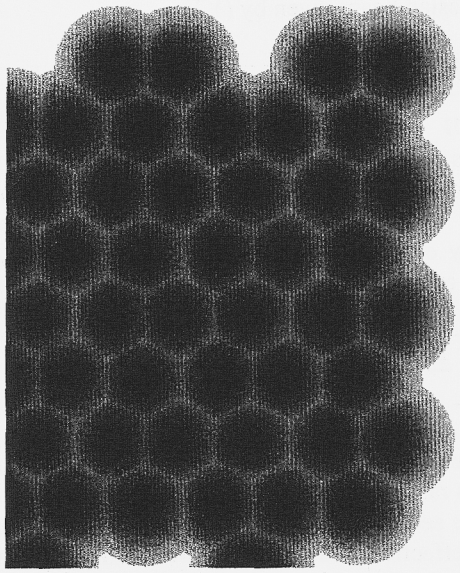

Fig.6: The spatial pattern of fluence produced by raster scan for the hexagonal lattice. The Wigner-Seitz structure is clearly seen.

Consider the representative triangle whose base is vertical. It's height is a and each side is $2a/\sqrt{3}$ in length. By symmetry, we need consider only the right triangle making up half the equilateral triangle. This triangle has area $S = a^2/2\sqrt{3}$. Note that for angle ϕ, the maximum radius is $r_{max}(\phi) = a/\cos(\phi)$. Then we have

$$S_{eff} = \int_0^{\pi/6} d\phi \int_0^{r_{max}} dr\ r\ \exp(-m\ r^2/b^2)$$

so (1.5)

$$S_{eff}/S = \frac{\sqrt{3}}{u^2} \int_0^{\pi/6} d\phi\ (1 - \exp[-u^2/\cos^2(\phi)])$$

where $u^2 = m \ln(1/f)$ as before.

The effective area is determined by the same parameter u as in the case of the square lattice. The plot of S_{eff}/S versus u for different Weibull indices is shown in Fig.7.

One sees that the dependence on u is different for square and hexagonal lattices and that the most efficient lattice depends on beam overlap f. The relative difference between the effective areas for square and hexagonal lattices as

a function of u is shown in Fig.8. More exactly we plot (S_{eff}(hex)-S_{eff}(square))/ S_{eff}(square) for equal spacing a. One can see that the hexagonal lattice is more efficient for most typical overlaps and Weibull indices. The relative difference can be large for small overlap, the hexagonal lattice can use 50% more sample surface than the square lattice does. One must also remember that the hexagonal lattice needs $2/\sqrt{3}\sim1.15$ times as many shots to cover the same scan area if the lattice spacing a is the same for both.

Effective areas for the square and hexagonal lattices for specific values of m and overlap are given in Table 2.

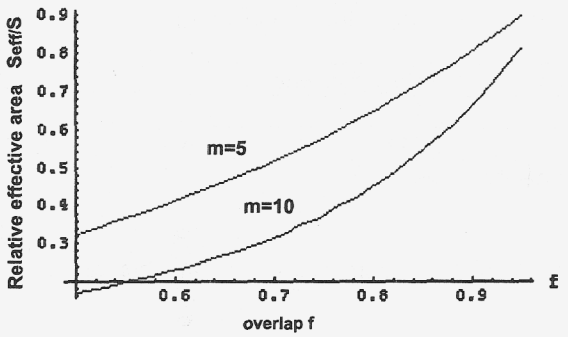

Fig.7: The effective area vs. overlap for hexagonal scan lattice. The green (lower) curve corresponds to m=10, red (upper) to m=5.

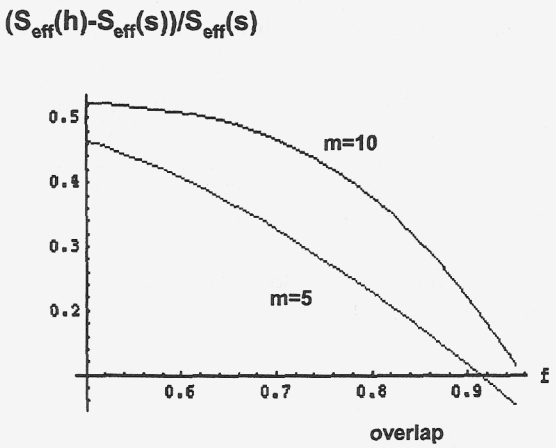

Fig.8 The difference in effective areas between hexagonal and square lattices with the same overlaps. The upper curve corresponds to m=10, lower to m=5.

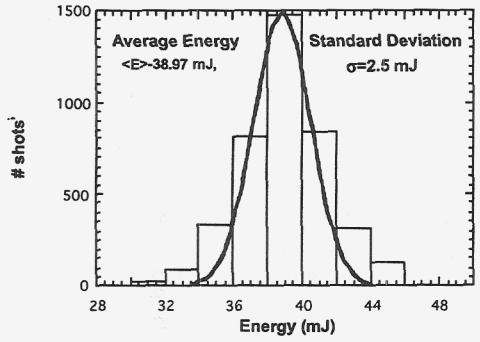

Fig.9: Measured energy fluctuations in the SOT beam. The mean energy is 38.97 mJ, and the rms deviation is σ=2.5 mJ. The curve is a normal distribution for these values of mean energy and σ (Courtesy of D.Hahn).

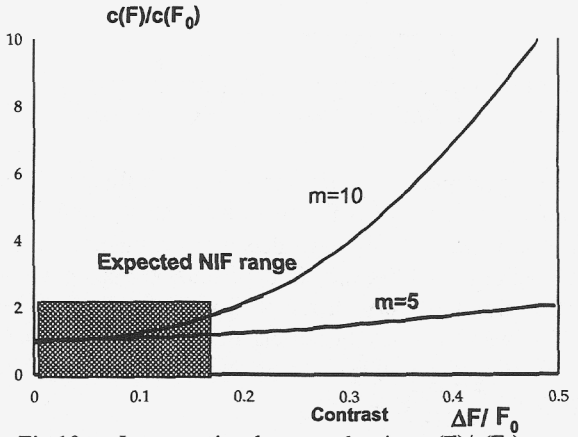

Fig.10: Increase in damage density $c(F)/c(F_0)$ as a function of rms energy fluctuations ΔF for m=5 and 10.

	m=5, f=0.9	m=5, f=0.5	m=10, f=0.9	M=10, f=0.5
u	0.478	1.227	0.676	1.735
S_{eff}/S (square)	0.863	0.439	0.750	0.253
S_{eff}/S (hex)	0.78	0.49	0.71	0.32

Table 2: Effective areas for different overlaps and Weibull indices for square and hexagonal lattices

2. BEAM ENERGY FLUCTUATIONS.

In our estimates above, we assumed that all shots have the same fluence and their positioning is perfect. Actual beam energy fluctuates and the pointing is not perfect. A histogram of the LLNL Small Optic Tester (SOT) laser

energy distribution in a 4000 shots series is shown in Fig.9. These fluctuations produce uncertainty in the determination of damage density. If P(F) is the probability to have a shot with fluence F, the observed damage density is given by the expression

$$c(<F>) = \int P(F)c(F)dF \qquad (2.1)$$

Here $c(F)\sim F^m$ is the damage density introduced above. The damage density for the normal distribution (Gaussian) fit and actual distributions are given in Table 3 normalized by the density corresponding to the mean fluence.

	Flat-top	Normal distribution	Actual distribution
m=5	1	1.021	1.155
m=10	1	1.095	1.544

Table 3: Relative damage density for flattop Gaussian and actual fluence distributions.
Mean energy is 38.97 mJ, σ= 2.5 mJ.

We see that the energy fluctuations result in an overestimate of damage density compared to a constant fluence beam. For the normal probability distribution

$$P(F) = \frac{1}{\Delta F\sqrt{\pi}} e^{-\frac{(F-F_0)^2}{\Delta F^2}} \qquad (2.2)$$

and Weibull defect density the integral (2.1) can be evaluated by the method of steepest descent [2] and the expected damage density are given by the expression:

$$c(F) = c(F_0)\sqrt{\frac{4b^2}{4b^2+2m}}\ Exp[\frac{m^2}{4b^2+2m}] \qquad (2.3)$$

Here $c(F_0)$ is the damage density for a flat top beam with fluence F_0, m is the Weibull index, $b= F_0/\Delta F$ is the inverse of the temporal "contrast", and ΔF is the rms distribution width. Fluctuations are tolerable when they change c(F) less than 2 times. The increase in damage density as a function of $\Delta F/F_0$ is shown in Fig.10. One can see that for temporal contrast smaller than 30%, the effect of fluctuations on damage density determination is minor. Let us note that this single shot result is very different from estimates of the effect on optics lifetime of spatial energy fluctuations [6]. The wandering of hot spots in the beam eventually produces a situation where every point is irradiated by the maximum possible fluence, and even a small beam contrast increase can greatly increase the amount of damage over many shots.

3. BEAM POINTING FLUCTUATIONS

Consider now fluctuations in beam pointing which lead to beam wander about the intended target at the center of the elementary cell. For simplicity we consider the square lattice only. We assume the mean displacement is small in comparison with the cell size a. For the square lattice, the effective area for a beam displaced by x and y from the cell center in the horizontal and vertical directions, respectively, is given by

$$\frac{S_{eff}}{S} = \frac{\pi}{16u^2}\left(Erf[u(1+\frac{x}{a})]+Erf[u(1-\frac{x}{a})]\right)\left(Erf[u(1+\frac{y}{a})]+Erf[u(1-\frac{y}{a})]\right) \qquad (3.1)$$

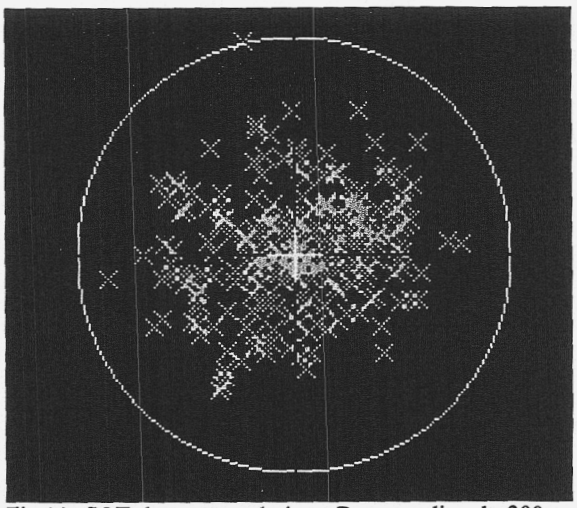

Fig.11 SOT beam wandering. Beam radius b=300μm, maximal deviation r =110 μm, rms deviation σ = 20 μm

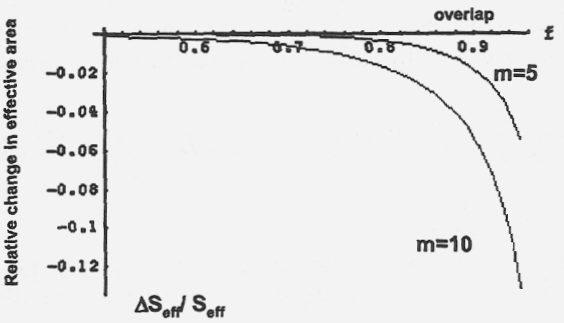

Fig.12 Variation of effective area as a function of overlap for σ / b=0.2

For small displacements, after expansion and averaging over the distribution of displacements we have

$$\frac{S_{eff}}{S} = \frac{\pi}{4}\left(\frac{Erf[u]}{u}\right)^2\left(1 - \frac{2}{\sqrt{\pi}}\frac{ue^{-u^2}}{Erf[u]}\frac{<x^2+y^2>}{a^2}\right) \tag{3.2}$$

where <x2 + y2> indicates the mean square displacement. One sees that beam wandering always decreases the effective area, hence leads to an underestimate of the defect density if wander is not taken into account in a damage experiment. The effect of pointing fluctuations is determined by the mean square displacement. This value is independent of details of the distribution function and can be directly measured in experiments, e.g. with burn paper. For the SOT laser, the measured value $\sqrt{<r^2>}$ is about 20 μm for beam radius ~300 μm . As a result, the variation of effective area due to beam wandering is less then 1% according to equation (3.2).

The variation of effective area with overlap is shown in Fig.12 for fixed level of beam wander σ/b=0.2.
We conclude that beam wander is more important for large overlap. For small wander, i.e. σ/b<<1, the variation of effective area is small for typical experimental parameters.

4. DKDP CONDITIONING AND EFFECTIVE DOSE

Unlike fused silica, surface damage measurements in DKDP are complicated by the requirement for laser conditioning to prevent unacceptable levels of bulk damage at NIF fluences. Unfortunately, we do not have a reliable theoretical description of DKDP conditioning, or even a qualitative understanding of the process. We can assume, however, that conditioning is the result of annealing of some absorbing centers. In this case, it is natural to assume that the degree of conditioning will be determined, in part, by the total energy dose irradiating a given point. The dose accumulates the effects of all shots that hit a given point. In practice, conditioning fluences must be low enough not to damage the sample and high enough to have an effect. For example, there may be an activation energy. Below, we calculate the sensitivity of the dose to beam overlap f., disregarding any restrictions on fluence and the influence of shot history. For illustration, we consider the square lattice only. Various conditioning schemes are discussed in [5, 7].

The total relative dose D, for a Gaussian beam with peak fluence F_0 and radius b on a square lattice of spacing 2a, relative to a flat-top beam of peak fluence F_0, can be calculated as follow

$$D = \frac{\int F(x,y)dxdy}{4a^2F_0} = \int_{-a}^{a}\int_{-a}^{a}\sum_{s=-\infty}^{\infty}\sum_{p=-\infty}^{\infty} e^{-\frac{(x-2sa)^2+(y-2pa)^2}{b^2}}dxdy \tag{4.1}$$

The sums over s and p include the contributions of neighboring cells. Integration is over the elementary cell. Physically, D denotes the number of shots with a flat top beam with fluence F_0 needed to get the same dose. Integration over x and y can be completed independently and we find

$$D=\frac{\pi}{16u^2}\sum_{s=-\infty}^{\infty}\sum_{p=-\infty}^{\infty}(Erf(u(1-2s))+Erf(u(1+2s)))(Erf(u(1-2p))+Erf(u(1+2p)))$$

$$where \quad u=\sqrt{\ln(1/f)}$$

The single term with s=p=0, the contribution of the central beam, is just the result (3.1) for m =1. Due to the even symmetry in s and p, we can write the summation over positive s and p values only:

$$\sum_{s=-\infty}^{\infty}(Erf(u(1-2s))+Erf(u(1+2s)))=2(Erfu+\sum_{s=1}^{\infty}(Erf(u(2s+1))-Erf(u(2s-1)))$$

Truncating the sum at some finite N we have

$$Erfu+\sum_{s=1}^{N}(Erf(u(2s+1))-Erf(u(2s-1)))=Erf(2N+1)u \qquad (4.2)$$

For large N, Erf(2Nu) ~ 1 and for the dose we find

$$D=\frac{\pi}{4u^2} \qquad (4.3)$$

A plot of the relative dose D, as a function of beam overlap f is given in Fig.13.

The result (4.3) allows estimation of the number of neighboring beams that contribute significantly for conditioning. Erf(x) is close to 1 at x~1 with accuracy~20%. Hence, the number of important neighbors is N~1/2u. For overlap f=0.9, N~2 and the total number of participating neighbors is ~13. The total relative dose D=8.2 in this case.

A planned experiment on DKDP conditioning with the excimer laser employs a highly elongated shape, with a near Gaussian profile in the transverse direction.[5]. The sample will be scanned by the laser beam with velocity v perpendicular to the long axis, providing a gradual increase in incident fluence desirable for conditioning. This situation is a near one-dimensional analog of the scheme discussed above. The distance between the beam centers is determined by the scan velocity v and repetition rate p:

$$2a=v/p. \qquad (4.4)$$

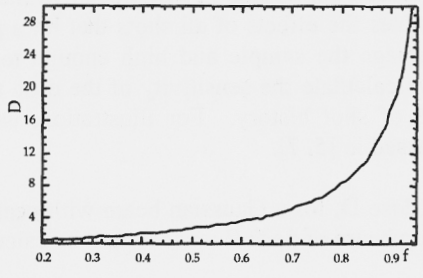

Fig.13: Relative dose as function of beam overlap fraction f for square lattice.

The calculation of the dose is similar to that presented above and gives

$$D = \frac{\sqrt{\pi}}{2u} \tag{4.5}$$

where a in the expression for u is now determined by (4.4). We emphasize that, due to geometrical reasons, the dose in the one-dimensional case is less sensitive to overlap.

5. CONCLUSION

Raster scan accelerated testing can be used to predict damage levels of large optics. Relating the results of scanning with a Gaussian beam to expected results for a flat top beam uses the effective area concept which indicates the equivalent flat top illuminated area. Different scanning schemes were considered. We demonstrated that for scans with fixed overlap and high Weibull index, the hexagonal lattice usually provides more efficient use of the sample (larger relative effective area) than the square lattice does. In our calculations, we assumed the Weibull model (power law) for the damage density as a function of fluence. This assumption is common for interpretation of our damage experiments, but extrapolation to fluence ranges not tested may not be reliable. The power law assumption is convenient, but not necessary. As long as the damage density distribution is of form c= g(F/<F>), and several experiments are carried out under the same conditions (overlap, etc), then the shape and scale can be determined separately. Here g(x) is an arbitrary function.

We assume implicitly a uniform distribution of defects over the optic. This is not necessarily true, of course, but no strong evidence to the contrary has come to light.

We showed that test beam fluence fluctuations are not a large problem for raster scanning. If the rms fluence variation is less than 10% of the mean fluence, these fluctuations do not substantially affect measurements of damage density, even for high Weibull indices.

We demonstrated that pointing fluctuations reduce the effective area, and the apparent damage density if not taken into account. The effect is most pronounced for scans with high overlap. But, for pointing fluctuations small in comparison with the beam radius, beam wandering is not dangerous.

For conditioning experiments, the important process parameter is not the maximum fluence at some point, but, rather, the total dose of irradiation. To characterize conditioning, we introduced the effective dose, i.e. the dose averaged over an elementary cell. As a result, we can now compare experiments done with different scanning schemes and laser parameters. Specifically, it should be possible to check the hypothesis that conditioning is largely determined by the irradiation dose.

ACKNOWLEDGEMENTS:

This work was performed under the auspices of the U.S. Department of Energy by University of California, Lawrence Livermore National Laboratory under Contract W7405-Eng.48. We would like to thank A. Burnham, M. Runkel, M. Nostrand, D. Hahn and P. Whitman for helpful discussions.

REFERENCES

1. J.A. Menapace, B. Penetrante, D. Golini, A. Slomba, P.E. Miller, T. Parham, M. Nichols and J. Peterson, "Combined advanced finishing and UV laser conditioning for producing UV-damage-resistant fused silica optics", *Proceedings XXXIII Annual Symposium on Optical Materials for High-Power Lasers* 2001, SPIE **4679**, 56-68 (2002).

2. M.D. Feit, A.M. Rubenchik, M.R. Kozlowski, F. Genin, L. Sheehan, S. Schwartz "Extrapolation of damage test data to predict performance of large-area NIF optics at 355 nm", *Proceedings XXX Annual Symposium on Optical Materials for High-Power Lasers 1998*, Proc. SPIE **3578**, 226-231, (1999).
3.R. Brusasco, B. Penetrante, J. Peterson, S. Maricle, J. Menapace," UV Laser conditioning for reduction of 351-nm damage initiation in fuse silica *Proceedings XXXIII Annual Symposium on Optical Materials for High-Power Lasers* 2001 SPIE **4679**, 48-55 (2002).
4. M. Runkel, J. DeYoreo, W. Sell, D. Milam, "Laser conditioning study of KDP on the Optical Sciences Laser using large area beams," *Proceedings XXIX Annual Symposium on Optical Materials for High-Power Lasers 1997*, SPIE **3244**, 51-63, (1998).
5. M. Runkel, M. Nostrand, "Overview of raster scanning for ICF-class laser optics", *Proceedings XXXIV Annual Symposium on Optical Materials for High-Power Lasers 2002* this proceedings.
6. M.D. Feit and A.M. Rubenchik, "Effect on estimated silica lifetimes of operating with average fluence near damage growth threshold and continued need for growth mitigation", LLNL memo NIF-0070225, (Aug. 27, 2001).; M.D. Feit, "Expected new damage initiation sites due to random beam contrast on LAT pre-initiated and mitigated fused silica operated at 5-8 J/cm^2", LLNL memo NIF-0073443, (Nov. 9, 2001).
7. C.J. Stolz, L.M. Sheehan, S.M. Maricle, S. Schwartz, "A study of laser conditioning methods of hafnia silica multilayer mirrors" *Proceedings XXX Annual Symposium on Optical Materials for High-Power Lasers 1998* SPIE **3578**, 144-152, (1998).

Conditioning and mitigation of Tinsley, inclusion-free, wedged focus lens

Rahul R. Prasad, Justin R. Bruere, John Peterson, John Halpin,
Lun Auyang and Michael Borden

Lawrence Livermore National Laboratory,
P.O. Box 808, Mail Stop L-479, Livermore, CA 94550

ABSTRACT

Fused silica optics to be used on NIF are conditioned using 3ˇ light and damage sites that occur are mitigated using a CO2 laser. This memorandum describes the conditioning/mitigation process as applied to a Tinsley, inclusion-free wedged focus lens (WFL), serial number 250200. The process was performed at the Phoenix laboratory. The lens is to be used in experiments on OSLII at fluences up to 6 J/cm2. Thus the lens was to be conditioned to 10 J/cm2, using the 351-nm, 23 ns pulse width excimer laser at Phoenix. However, since no damage was observed in these initial scans, it was decided to condition up to 14 J/cm2. No damage was observed on this lens, even at these higher fluences. This completes the milestone showing that the Phoenix facility is ready for conditioning and mitigating fused silica optics.

INTRODUCTION

Figure 1 shows the typical process cycle for a fused silica wedged focus lens that will be delivered to the NIF. Inclusion-free Lithosil Q fused silica is fabricated at Schott Lithotec into optic blanks. These blanks are then fabricated into the wedged focus lens and finished using proprietary processes at Tinsley in Richmond, CA. The lenses delivered to LLNL are then cleaned at the Optics Processing Laboratory (OPL) and transported to the Phoenix laboratory for conditioning and damage mitigation.

The WFL described in this memorandum was the first made from the Schott Lithosil Q inclusion-free fused silica. The fused silica is made using a process of deposition of organosilane, SiCl4, or powered quartz into cylinders or "telephone poles;" a process similar to that used to make optical fiber material. The "telephone poles" are slumped together in a graphite mold to produce optical blanks. Figure 2 shows damage maps of a conventional fused silica blank and an inclusion-free fused silica blank. There are no bubbles or inclusions or bulk damage

visible in the inclusion-free material, in contrast to the conventional material that shows typically 10-150 inclusions.

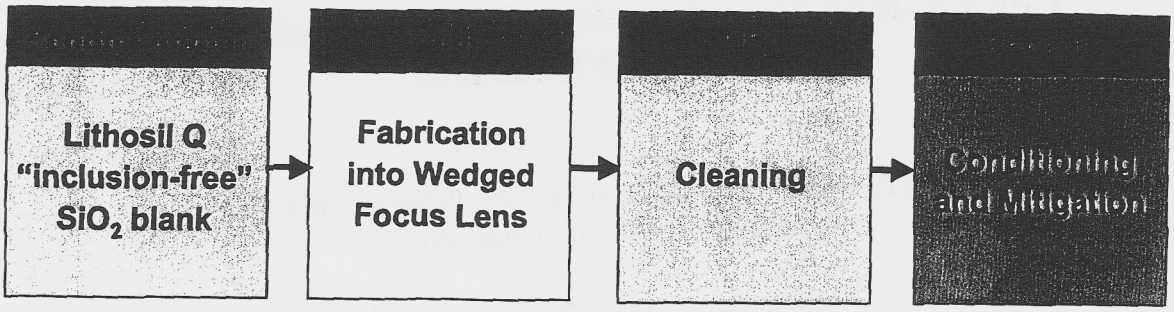

Figure 1: Typical process cycle for a wedged focus lens to be delivered to the National Ignition Facility.

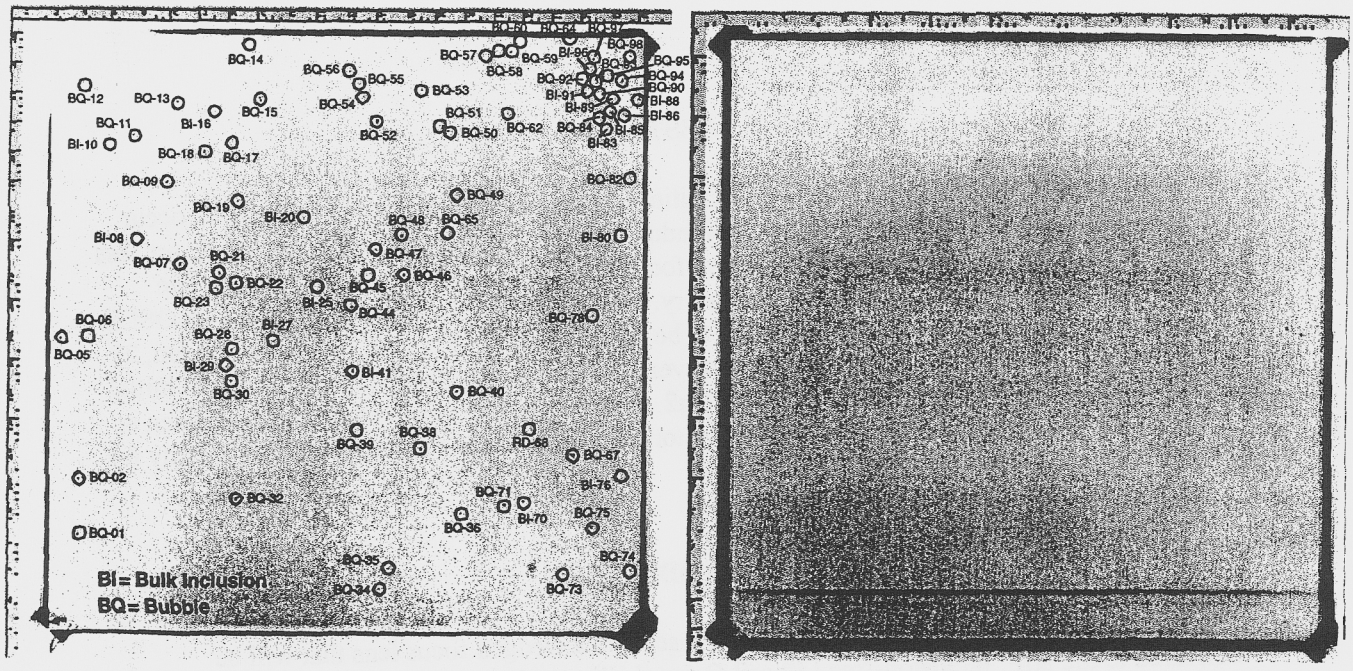

Figure 2: Damage map of a conventional fused silica blank (left) and an inclusion-free fused silica blank (right). The conventional material shows 63 bubbles and 18 solid inclusions while the inclusion-free material shows no bulk inclusions of any kind. Both blanks are 43 cm x 43 cm in dimension.

WFL serial number 250200 was fabricated at Tinsley. They use a proprietary 3ω final process that includes a non-ceria based polishing slurry and computer controlled optical surfacing. This controlled material removal at each process step reduces scratches and the removal of ceria from the polishing slurry eliminates laser damage from absorption of laser radiation within residue left from the polishing process. Figure 3 shows a part of the schematic drawing of the wedged focus lens, showing on the left a cross-section view that highlights the wedge (15 mm at the thin edge and 48 mm at the thick edge) and a front view that shows the dimensions of the finished part. Figure 4 shows a photograph of the lens while undergoing final inspection at Tinsley.

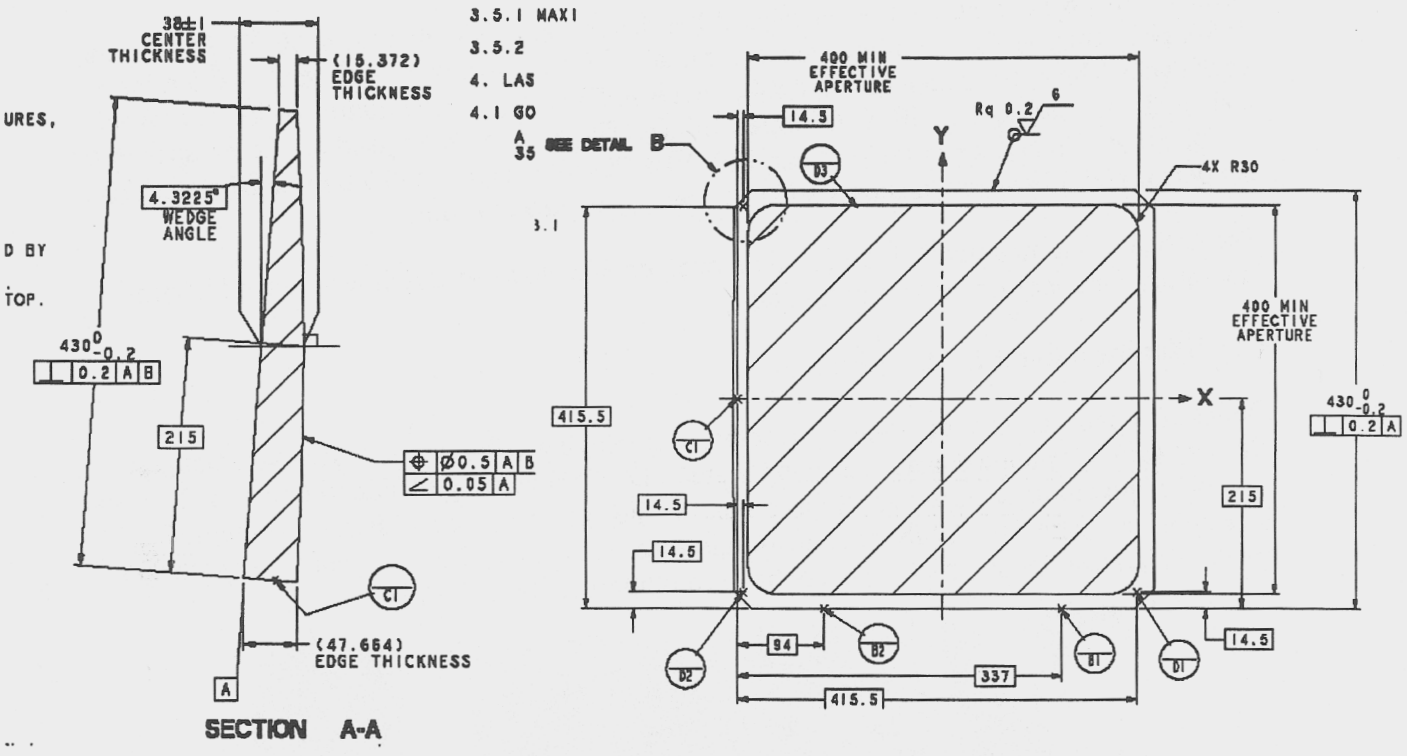

Figure 3: Schematic drawing of a WFL, AAA96-105252-OB.

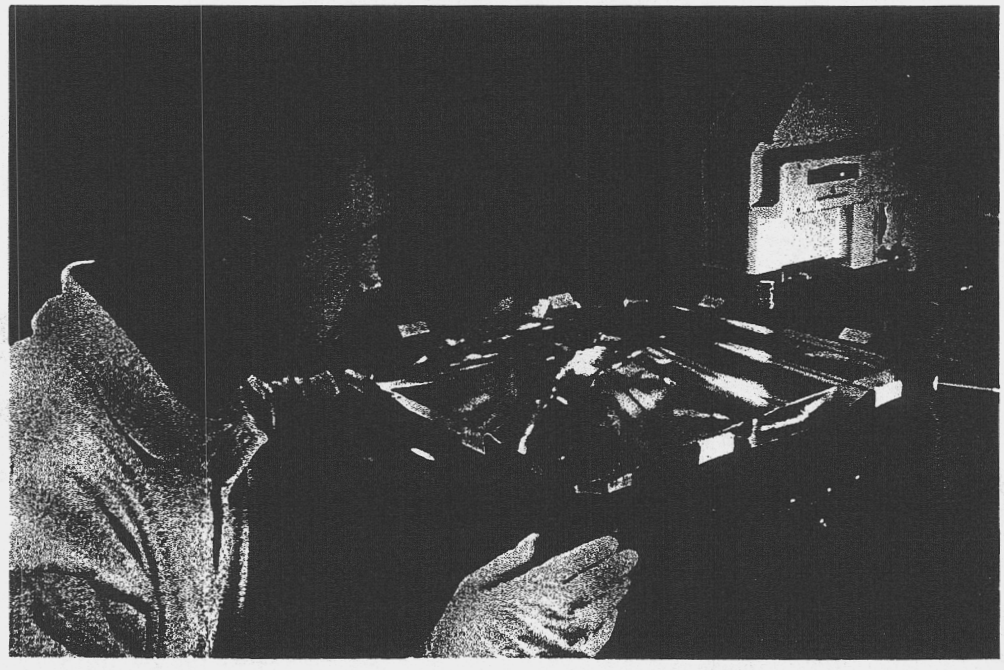

Figure 4: Photograph of WFL in final inspection at Tinsley.

Once the optic is delivered to LLNL it is cleaned at OPL. The OPL process consists of five steps. It begins with a de-ionized (DI) water rinse, a hand wipe clean with 10% FL-70 detergent and a 5 minute DI water rinse. Next the optic is soaked for 5 minute in a 20 °C, 10% NaOH bath

followed by an 11-minute DI water rinse. After this the optic is immersed in 50 °C, 1% Bruilin 1696PNC detergent for a 3 minute soak, 3 minute 104 kHz ultrasonic sonic soak and 5 minute soak cycle. The optic is then rinsed for 4 minutes in DI water. A 1.5 minute 104 kHz ultrasonic soak and 1 minute soak in 50 °C DI water follows. The optic is then rinsed for 5.5 minutes in 40 °C DI water. Finally, a hand wipe clean with 10% FL-70 detergent and 5 minute DI water rinse are performed, if inspection shows it to be necessary to clean the optic.

The optic is then mounted in the Phoenix mount, double wrapped and moved to the Phoenix laboratory for conditioning and mitigation.

Conditioning and mitigation process:

Optics are conditioned at the Phoenix laboratory employing a 351 nm excimer laser. Damage sites are located using a damage mapping system (DMS) consisting of side illumination bars and an 8000x1 pixel line scan camera. Figure 5 shows the optic mounted with the side illumination bars in place, ready for a DMS map. Scattering sites found using the DMS can be inspected in greater detail using a 65x telescope that has a resolution of about 5 μm.

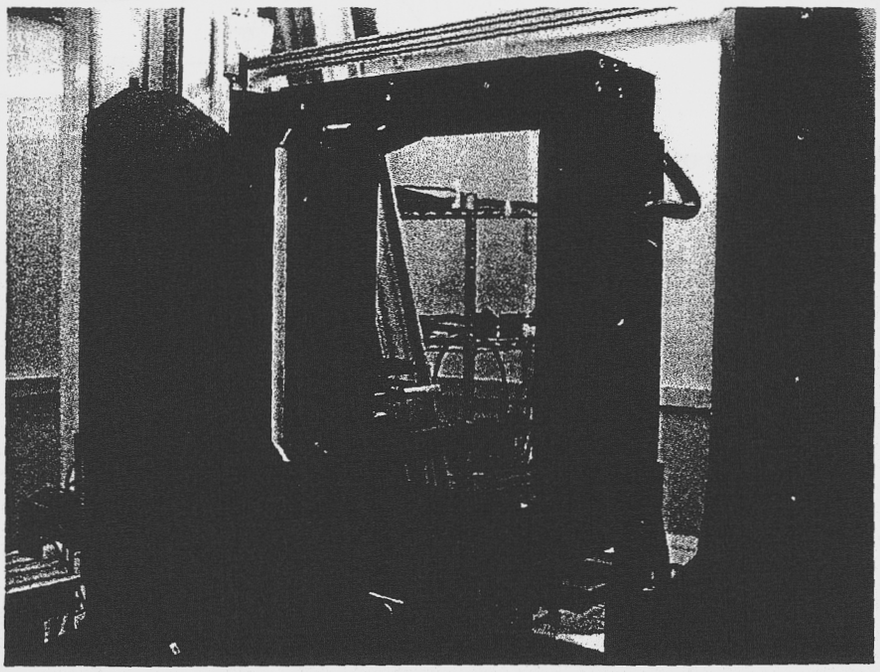

Figure 5: Optic mounted on the stage in Phoenix, ready for mapping, conditioning and mitigation.

The 351 nm, 23 ns pulse width, 280 J/pulse, 100 Hz repetition rate, XeF excimer laser in Phoenix uses a one-dimensional beam homogenizer. This homogenizer takes the 24 mm x 12 mm beam from the laser and converts it to a beam that is 1.5 mm by 0.3 mm at its focus. The intensity profile at the focus is a top hat along the long axis and a Gaussian along the short axis. Due to the relatively small f-number (f/13) of the optical system, the beam shape is not constant near the focus. The spatial profile as a function of distance near the beam focus was measured and the details have been reported in Ref. [1]. Reproduced from Ref. [1] are Figures 6 and 7 that show the full width at half maximum (FWHM) of the beam along the long and short axes.

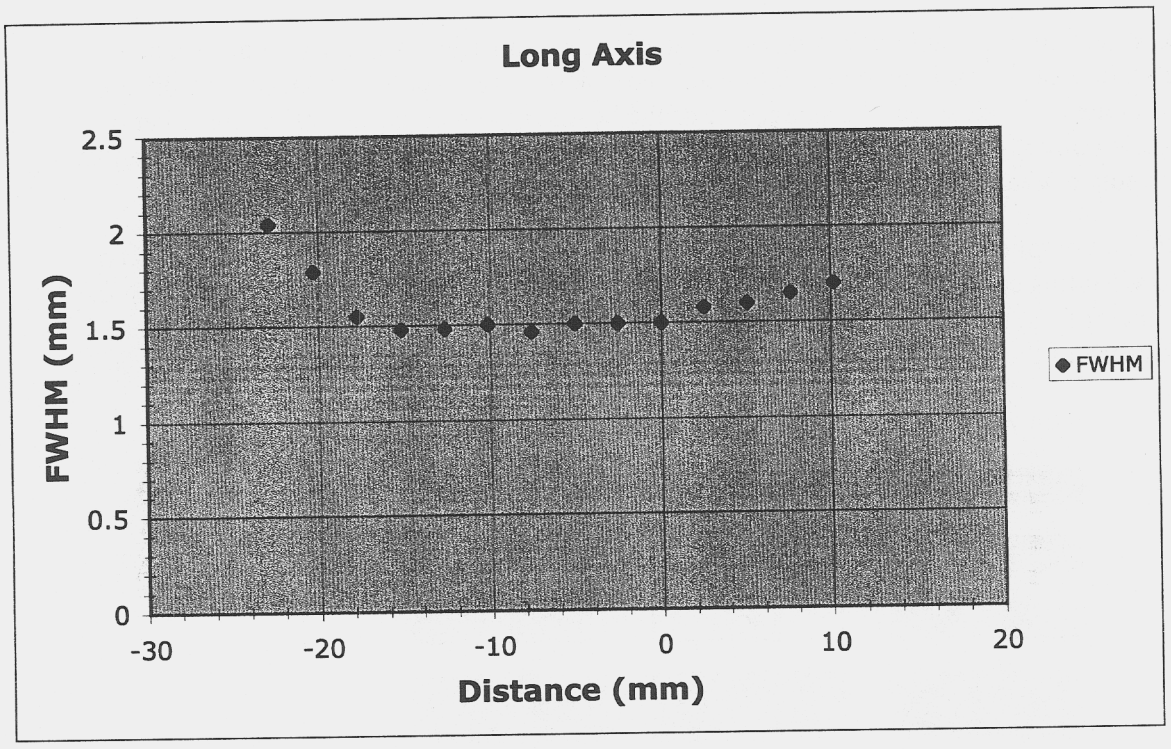

Figure 6: Full width at half maximum (FWHM) of the beam along the long axis as a function of distance from focus.

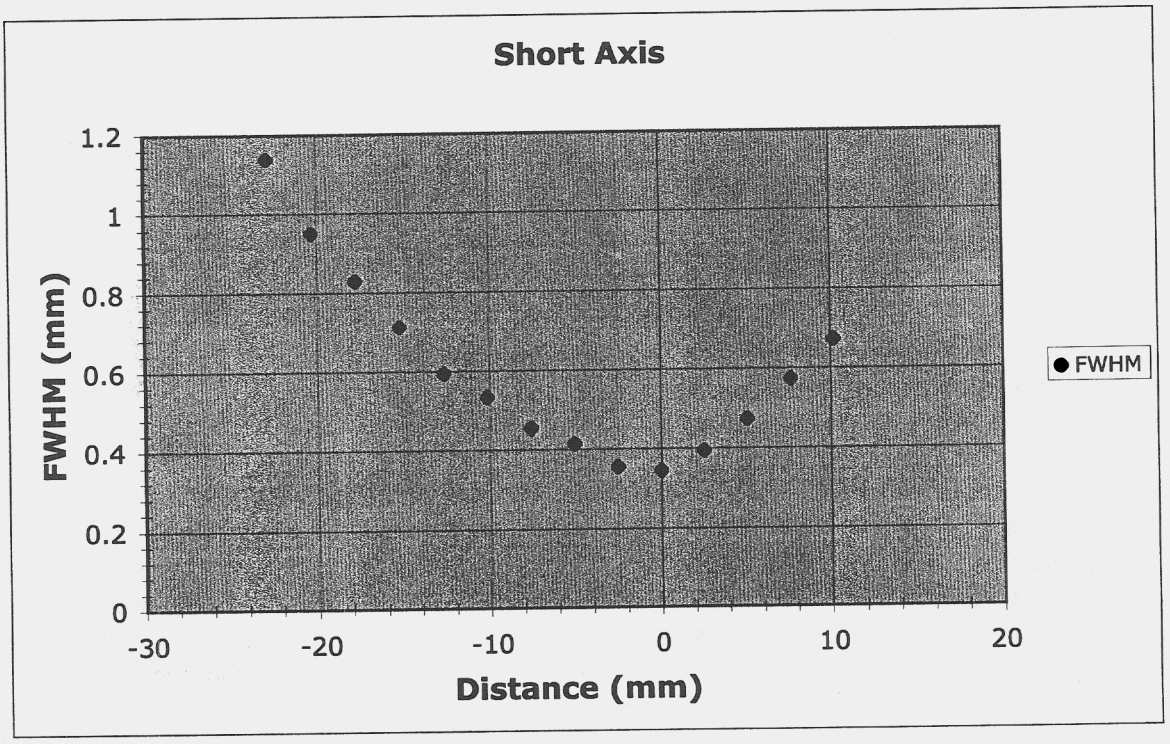

Figure 7: FWHM of the beam along the short axis as a function of distance from focus.

It is clearly seen from the above data that the size of the beam varies as a function of distance from the surface of the optic being conditioned. These data were taken in air. Due to the different refractive index of fused silica, the actual size of the beam at the rear surface of the optic cannot be determined directly from the data shown in figures 6 and 7 above. However, these data can be used to calculate what the size of the beam at the rear surface of the optic.

An additional complication in the case of the WFL is the fact that the rear surface is curved. To compensate for this curve and the wedge, the optic is moved along the z-axis (direction along the beam) as the optic is moved along the wedge. Measurements of the beam profile were taken on the rear surface of the optic showing that a uniform beam was obtained. Figure 8 shows the data.

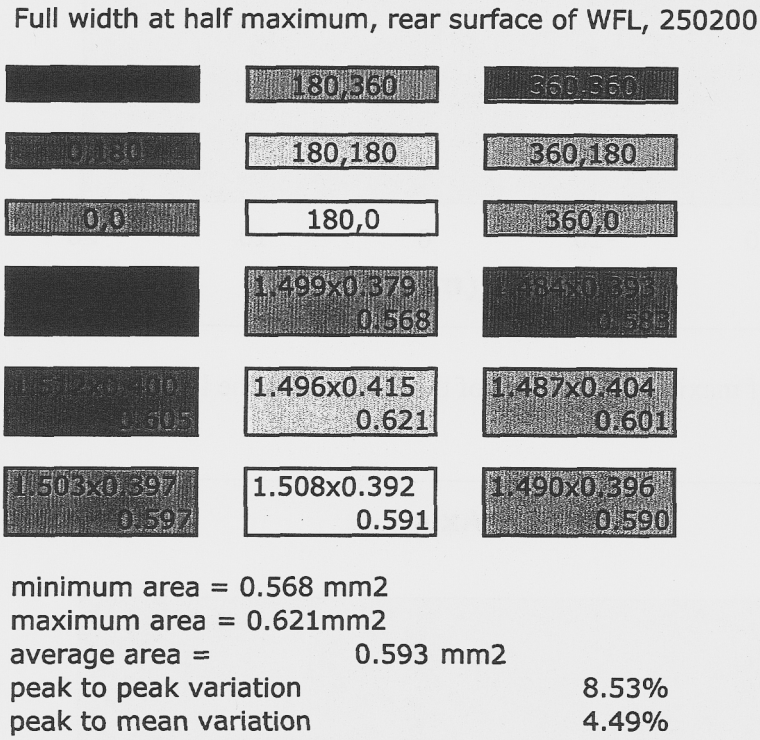

Figure 8: FWHM of the excimer beam at the rear of the WFL. The first 9 numbers show the location of the profile measurement in mm. The second 9, color-coded with the first 9, show the FWHM along the long axis, the short axis and the beam area. The variation is within the measurement accuracy, which is about 5%.

Figure 9 shows the damage map of the WFL prior to scanning. No precursors were visible in this map. However, closer inspection showed 6 sites that may have a potential to damage. Since the excimer beam focuses rather sharply the beam is not in focus at the front surface when focused on the rear surface of the WFL. We thus conditioned the rear surface first, then moved the optic and conditioned the front surface next. The first scan was performed at 4 J/cm^2 (3 ns equivalent, using $\tau^{0.5}$ scaling). The WFL was examined closely after this scan and it was found that the 6 sites, seen earlier, had been cleaned off by the laser, leaving a pristine surface.

Subsequent scans at 6, 8 and 10 J/cm^2 (on the rear surface) produced no damage. It was then decided to continue scanning the optic and scans at 12 and 14 J/cm^2 were also performed with no damage.

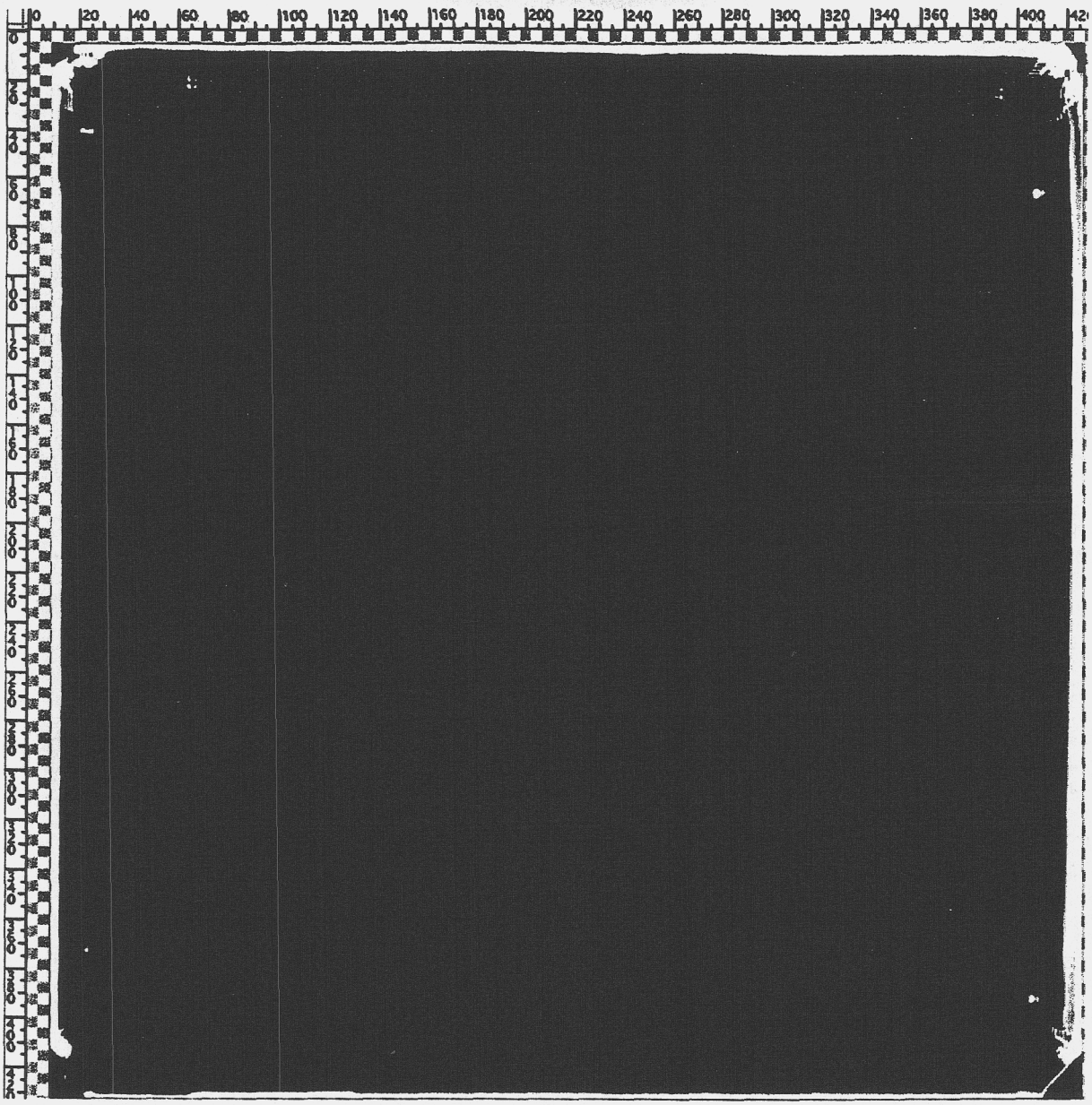

Figure 9: DMS map of WFL serial number 250200 prior to conditioning.

The part was then moved and the laser beam focused on the front surface. We did not scan the optic at 4 J/cm^2 since this fluence had already irradiated the entire front surface when performing the 14 J/cm^2 scan on the rear surface. It was scanned at 6, 8, 10, 12 and 14 J/cm^2, with no damage. Figure 10 shows a damage map taken after all scans were completed.

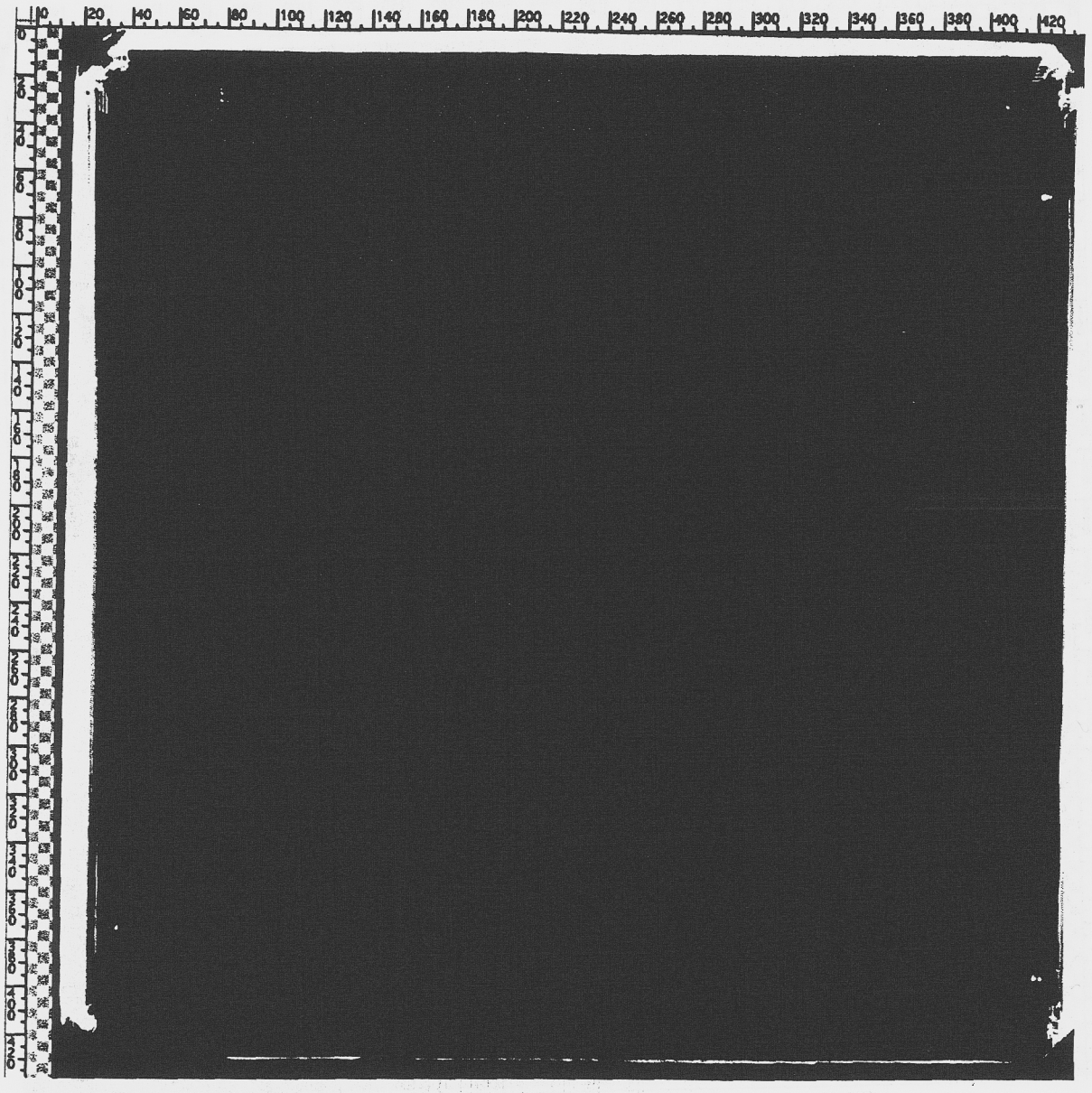

Figure 10: DMS map of WFL serial number 250200 after conditioning.

Figure 11 shows a plot of the damage density as a function of incident fluence on a number of optics. The pink square shows data from this optic. Since we saw no sites we have plotted the data as a half site over the 1550 cm^2 area that was scanned, with an error bar that ranged from 1 site on the high side and 0 sites on the low side. The blue diamonds represent the average of all Tinsley optics tested to date at LLNL. This WFL is at least 1000 times better at 14 J/cm^2. The orange triangles show the best Zygo MRF optic that has been processed at LLNL. This was a 6" optic. WFL 250200 is at least 100 times better than the Zygo optic as well.

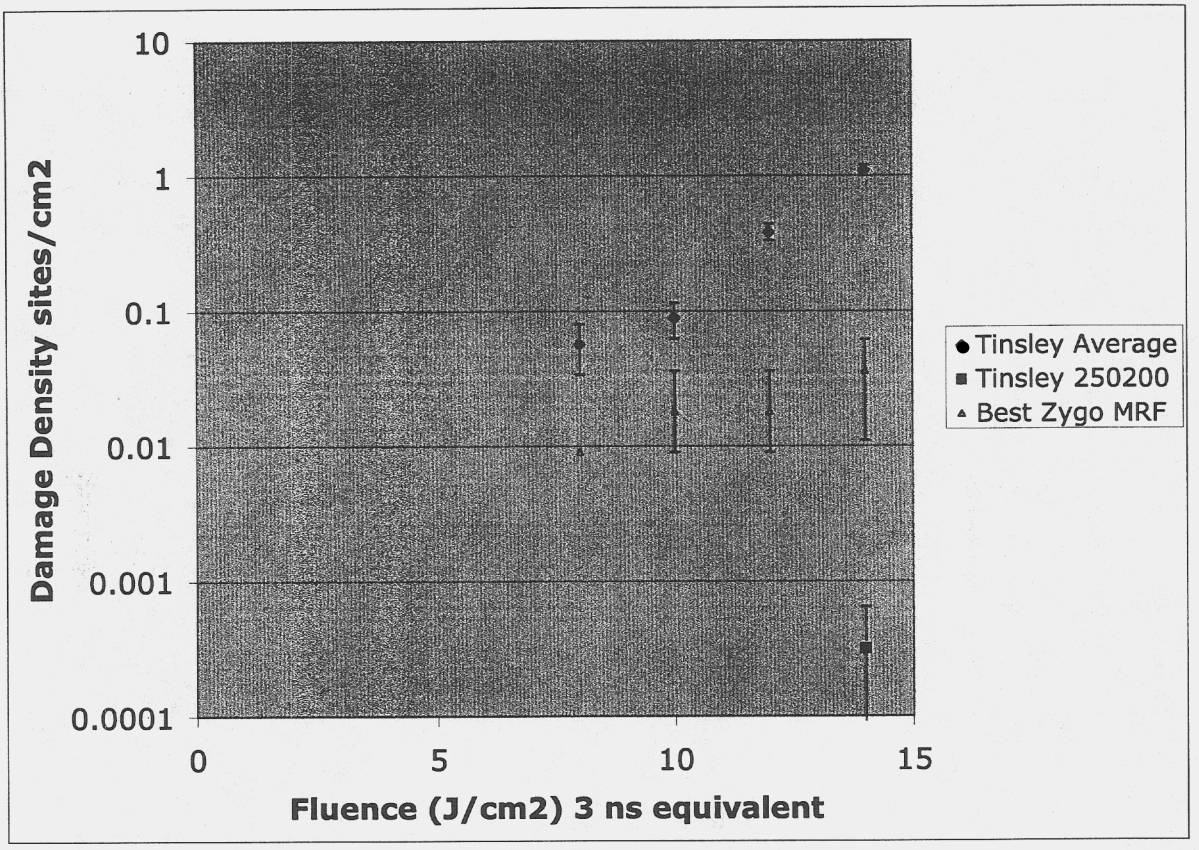

Figure 11: Damage density for Tinsley WFL 250200 compared with previously tested optics.

Even though the laser power had been measured using a calibrated power meter, the laser focal spot size verified and the pulse width measured using a fast photodiode there was some concern that perhaps the laser was not functioning properly. To allay this concern we installed a previously tested optic that had damaged at 10 J/cm^2 on the Phoenix excimer laser. This optic (Tinsley 2.5 cm thick, flat lens 240017-5) was scanned at 12 and 14 J/cm^2. The resulting damage map shown in Figure 12 reveals a result consistent with previous experiments. There are several new sites, evident as white dots and several old sites that exhibited growth (seen as white doughnuts). As a result, we concluded that the laser was working per specifications.

Conclusion:

It appears that the Tinsley process has eliminated damage precursors completely. Is this a one-time deal? Early indications suggest that this is not the case. The second inclusion-free optic, WFL serial number 250201 has been cleaned at OPL and sent to the Phoenix laboratory for conditioning and mitigation. It appears, at least before conditioning, to be as precursor-free as WFL 250200.

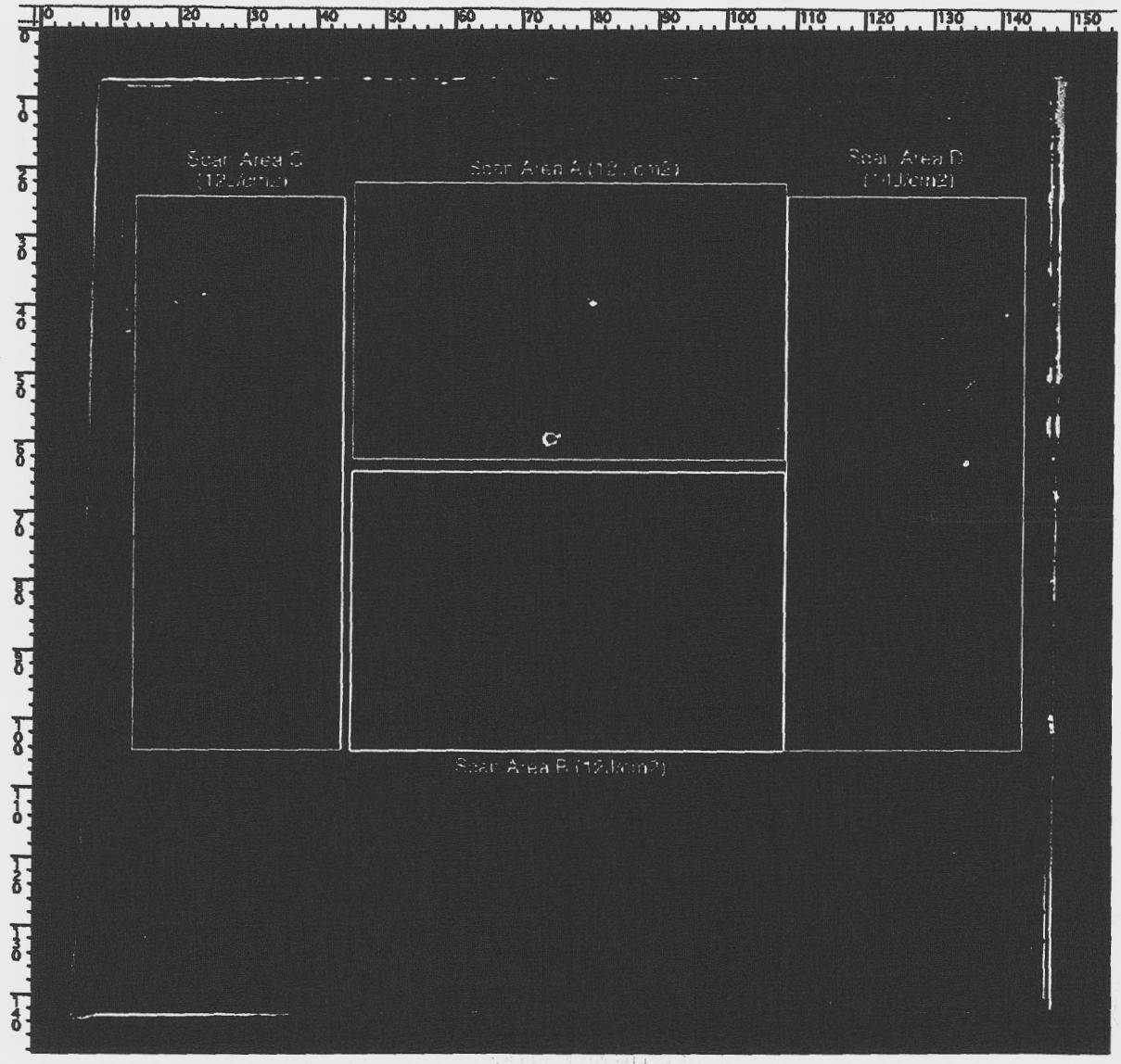

Figure 12: DMS map of Tinsley 240017-5 shows excimer laser damage at 12 and 14 J/cm^2.

The Zygo main debris shield that was conditioned and mitigated in Phoenix showed a quadrant with almost no damage. Could better control of the process at Zygo make better parts? Could the use of the controlled material removal and the non-ceria polishing slurry at Tinsley have made the difference and can Zygo develop a similar process?

After WFL serial number 250200 was conditioned it was returned to OPL for storage prior to AR coating. Further examination with bright lights showed extremely fine scratches and digs (~5-10 μm) that were speculated to have been a result of the conditioning process. Similar examination of the second inclusion-free optic, WFL serial number 250201, prior to processing in the Phoenix facility show similar features. Since these features did not grow in the first optic WFL 250200 when raster scanned in the Phoenix facility, they are unlikely to grow in use. The test on OSL shall confirm this hypothesis. It is possible that the quality of these WFLs is so good that we are looking at them with a much finer resolution?

To conclude, the first inclusion free wedged focus lens processed in the Phoenix laboratory. The conditioning process that has been validated on sub-scale optics was shown to work on a full size optic. The milestone to document the readiness of Phoenix as a facility for the conditioning and mitigation of optics has been met.

No damage was found over the full aperture of the optic at scan fluences as high as 14 J/cm^2. The second inclusion free WFL is being processed in Phoenix now. Results will be reported in a subsequent memorandum.

References:

[1] Rahul R. Prasad and Justin Bruere, "Spatial evolution of the XeF excimer laser beam," NIF memorandum, NIF0089170, October 9, 2002.

1.5 kJ Nd:glass laser system for large area damage testing†

J.A. Caird,* G.K. Beer, A.C. Erlandson, S.T. Mills, J.E. Murray, M.C. Nostrand, D.H. Roberts, K.M. Skulina, T.L. Weiland, and P. J. Wegner

Lawrence Livermore National Laboratory,
P.O. Box 808, Mail Stop L-479, Livermore, CA 94550

ABSTRACT

A new arm of LLNL's Optical Sciences Laser with twelve 20.8-cm aperture Nd:glass amplifier disks in double-pass configuration produces 1.5-kJ output with 10-J input. Net double-pass small-signal gain in disks is 900 at maximum pump energy. Active medium is 4-wt.% Nd-doped Schott LG-770 laser glass.

SUMMARY

LLNL's Optical Sciences Laser (OSL) produced output energy of 1.5-kJ after an accelerated 10-month program to upgrade the laser to a kJ-class facility. Originally constructed as a 100-J, 9.4-cm disk amplifier system in 1990, OSL has had a distinguished history as a laser-physics test bed for National Ignition Facility (NIF)-related technologies, fielding important experiments on a variety of non-linear optical problems including frequency conversion, optical self focusing, stimulated optical scattering, pinhole closure, short-pulse propagation in optical fibers, and laser-induced damage of both optical and non-optical materials. With new capability provided by the upgrade, OSL will expand its mission to include integrated testing of NIF final optics assemblies.

The new system shown in Fig. 1 is located in a laboratory adjacent to the original OSL facility. The design includes one 9.5-m long vacuum relay telescope and four 20.8-cm Nd:glass amplifiers recycled from Nova in an angle-multiplexed two-pass configuration. Each amplifier contains three 3-cm thick Brewster-angle disks. The original Nova laser glass has been replaced with 4-wt.% Nd-doped platinum-free Schott LG-770 laser glass developed for NIF. The higher damage threshold resulting from the lack of Pt-inclusions, along with higher neodymium concentration and the 2-pass geometry results in significantly higher output than these amplifiers were able to produce on Nova.

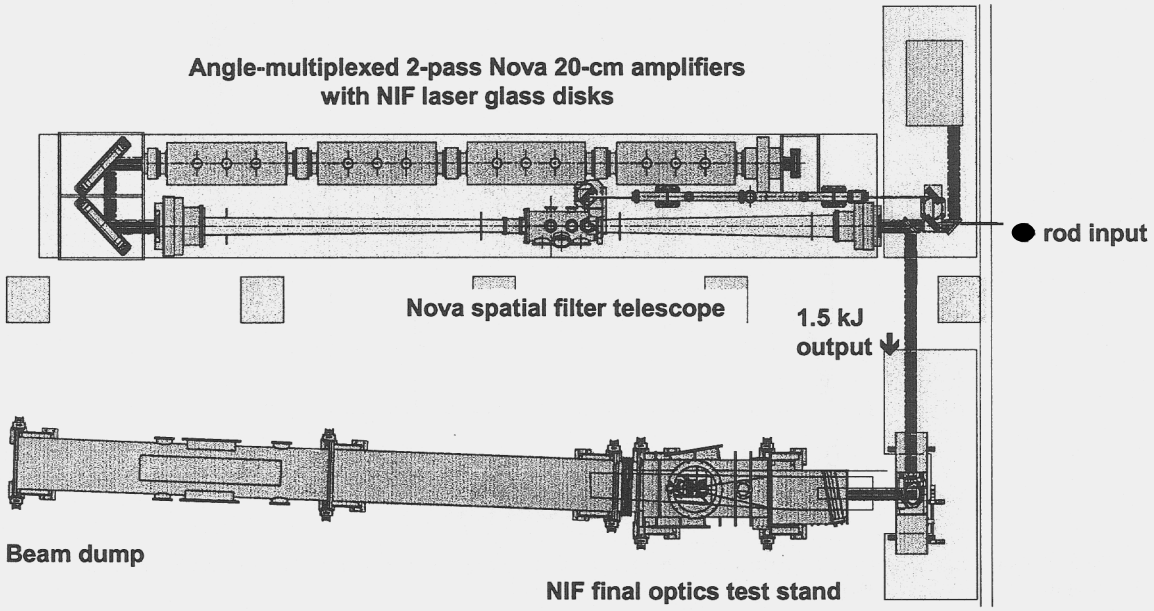

Fig. 1. OSL Upgrade delivers 1.5 kJ of 1ω energy using 2-passes in four 20.8-cm aperture disk amplifiers (12 disks total).

* Correspondence: Email: cairdl@llnl.gov, Telephone: 925-422-6159, FAX: 925-423-5517

The input pulse is generated in the original OSL master-oscillator power-amplifier (MOPA) chain through 1-cm, 2.5-cm and 5-cm Nd:glass laser rods. After the 5-cm rod a kinematic mirror provides a choice between further amplification in the pre-existing 9.4-cm disk amplifier system or transport to the new double-pass 20.8-cm disk amplifiers. The pulse is injected into the double-pass system using a small injection mirror located near the focal plane of the vacuum relay telescope, after which it passes through a spatial-filter pinhole and is collimated at a beam size of ~15-cm by the first spatial filter lens. It then undergoes two gain passes through the 20.8-cm amplifiers, with the second being offset in angle relative to the first to allow the pulse to miss the injection mirror and exit the amplifier system through the second lens of the relay telescope. The second telescope lens de-magnifies the beam by a factor of 0.83 to allow experiments to be conducted up to the fluence limits of the transport optics without stressing the optics in the amplifier cavity.

Small-signal gain tests were conducted using a continuous-wave probe beam up to a maximum capacitor bank voltage of 22-kV. The maximum net roundtrip gain of ~900 was obtained with no evidence of parasitics. At 22-kV, and at the normal operating voltage of 20-kV, the small-signal gain coefficients for the LG-770 disks were 8.5%/cm and 8.1%/cm respectively. Figure 2 shows measured output energy of the system versus the output energy of the 5-cm rod amplifier for high-energy 3.5-ns pulses. At 20 kV bank voltage, the desired 1.5 kJ energy is readily achieved at a 5-cm rod energy of 10-J (3 ns). Modeling results are also plotted for 20 and 22 kV, which show the potential for reaching output energies approaching 2 kJ. The near-field beam quality of the system is also quite good, with measured whole-beam fluence contrasts (defined as the standard deviation of the time-integrated fluence divided by the mean) of 7% (see Fig. 3). This level of beam quality is a critically important aspect of the NIF final optics test mission that will involve validating the damage resistance of optical components at NIF fluence levels. After completion of the new facility, the first-article final optics package was installed, and testing has begun.

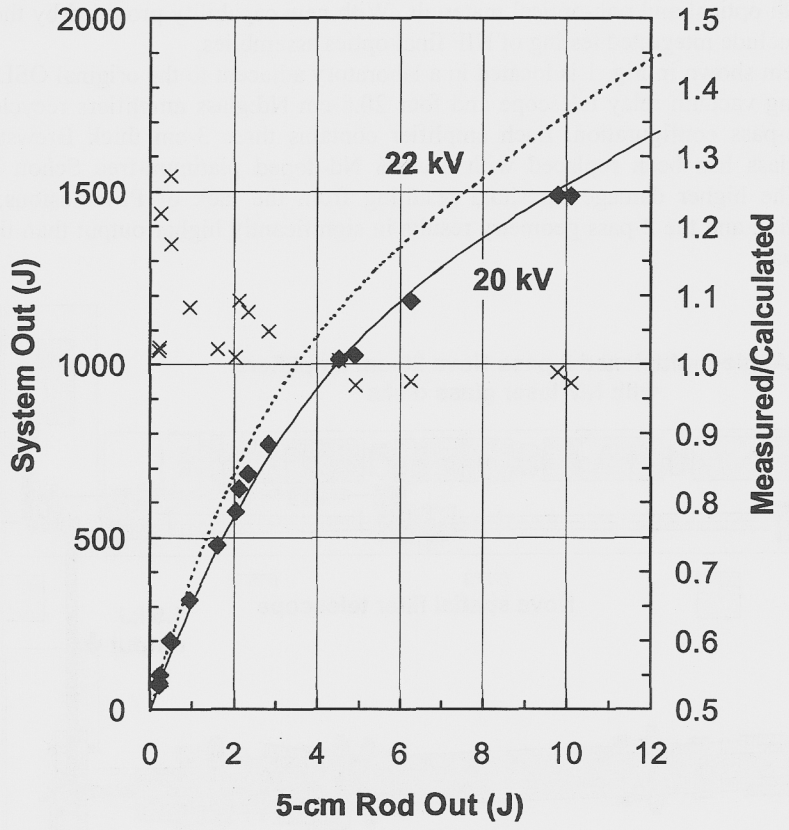

Fig 2. Output energy versus injected energy (the latter measured at the output of the 5-cm rod) demonstrating operation of the system at 20 kV bank voltage up to the full design energy of 1.5 kJ.

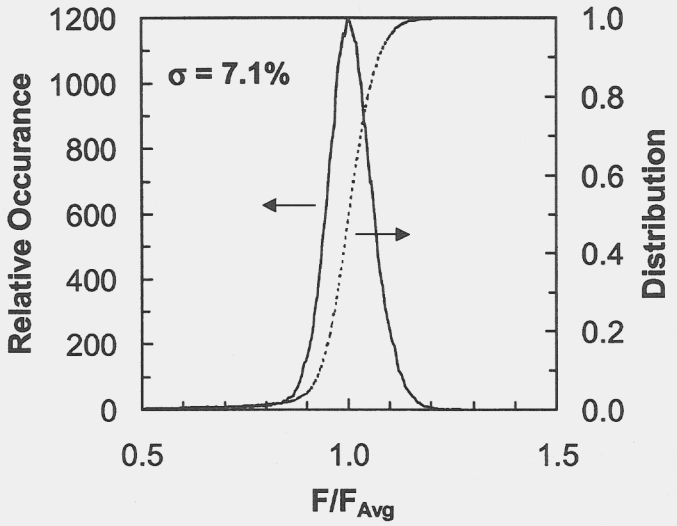

Fig. 3. Fluence histogram for 8-cm square patch centered on the 1.5 kJ output beam, showing high near-field beam quality.

†This work was performed under the auspices of the U. S. Department of Energy by the University of California, Lawrence Livermore National Laboratory under Contract No. W-7405-Eng-48.

3. SHORT PULSE LASERS, APPLICATIONS AND TECHNOLOGY RESEARCH ACTIVITY HIGHLIGHTS

SHORT-PULSE, HIGH-AVERAGE-POWER LASER SYSTEM FOR MICROMACHINING

Under a work-for-others contract, LS&T is developing a 100-W-class psec, kHz, solid-state laser system for rapid, precision machining of 100-mm-scale features in metals and alloys. This advanced laser drilling (ALD) system has recently been assembled and has undergone initial testing.

It delivered, for material processing application, over 50 W in a 2-psec, 4-kHz pulse train to the workpiece.

This short-pulse, high-average-power laser employs numerous advanced laser technologies of the LS&T program. These technologies include solid-state regenerative and power amplifiers using diode-pumped Yb:YAG as gain medium, a high-power multilayer dielectric grating, and a phase plate for conditioning the beam profile. A simpli-fied schematic of this laser is shown in Figure 1. The laser system architecture is based on chirped-pulse amplification (CPA). It starts with a mode-locked Yb-doped fiber laser, which was developed by Imra Corporation specifically for this applica-tion. This mode-locked oscillator produces a 4-kHz train of 8-psec, chirped pulses with an average power of 120 mW (2.4 nJ/pulse at 50 MHz). The spectral bandwidth of the oscillator pulses is 2 nm. The psec pulses from the fiber oscillator are stretched in time to 4 nsec using a diffraction grating pulse stretcher, amplified by 75 dB, then recompressed to 2-psec duration before being sent to the target chamber. Between each of these laser subsystems, computer-based pointing and centering loops are used to precisely control laser beam alignment.

The stretching-and-compressing process that is the basis of the CPA architecture is accomplished by using a high-efficiency dielectric diffraction grating (see Figure 2) manufactured by LS&T's Diffractive Optics Group. This large (150 × 335 mm) multilayer dielectric grating has a diffraction efficiency of >97% at 1030 nm. Whereas a typical CPA-based laser system architecture

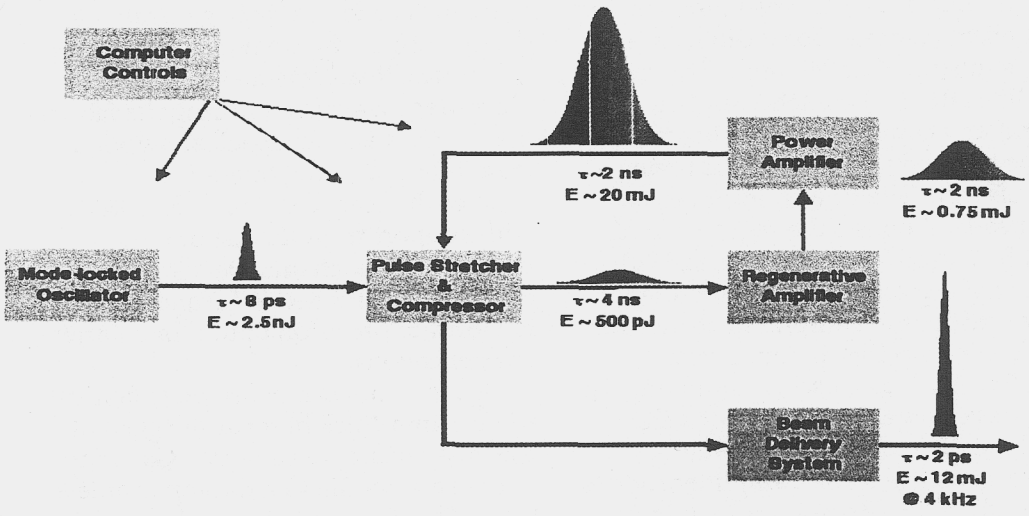

Figure 1. Laser system architecture uses chirped-pulse amplification to produce mJ-level short-pulse output.

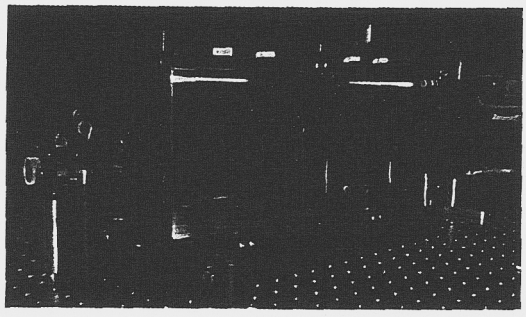

Figure 2. The large dielectric diffraction grating for the ALD laser has a diffraction efficiency of 97% and an rms wavefront of $1/40^{th}$ of a wave averaged over the surface.

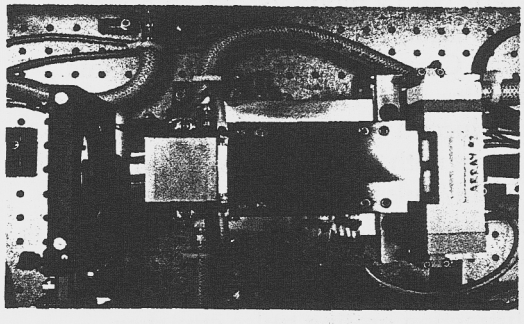

Figure 3. The Yb-YAG amplifier uses LS&T technologies: Tapered Yb-YAG rods with heat-diffusing end caps; hollow lens duct; repass pump mirrors; and a water-cooled jacket for the rod.

may use 4 diffraction gratings (2 for the stretcher and 2 for the compressor), the current design employs a single grating that is shared by both the stretcher and com-pressor. This single-grating stretcher/compressor design enabled the combination of two laser subsystems in a compact unit that can readily be incorporated into a hardened system that can withstand the harsh conditions on the factory floor.

The 75 dB of amplification between the pulse stretcher and compressor is accomplished by two subsystems: a linear-cavity regenerative amplifier (regen) and a power amplifier. Both amplifiers use Yb:YAG as the gain medium, pumped with micro-channel-cooled diode laser arrays (operated at 940 nm). The regen amplifies the 1-nJ stretched-pulses up to 750 mJ and converts the pulsing frequency from 50 MHz to 4 kHz (using a Pockels cell). The power amplifier has two heads. It boosts the regen output from 3 W to 50 W in two passes. With the use of a grating compressor, the pulse width of the amplified beam from the power amplifier is com-pressed from 2 ns back to 2 psec, multiplying the laser peak power by a factor of a thousand. We developed special water-cooled housings for the amplifier rods to efficiently dissipate heat and minimize amplified stimulated emission and parasitic losses in the laser cavity. The Yb-doped rods are also tapered to minimize parasitic oscil-lation. Undoped end caps are fused onto the end of each amplifier rod to minimize thermal gradients on the rods. A water-cooled hollow lens duct with precisely machined inner surfaces is used to efficiently couple pump light into the laser rods. Figure 3 shows the power amplifier assembly.

For material processing, the output from the compressor is delivered directly to the workpiece in the target chamber. Special phase plates manu-factured by the Diffractive Optics Group are used to produce a flat-top beam profile at the target. We have made good progress in the machining of ~100-mm features in metals and alloys as required by our industrial partner. We plan to transfer this high-average-power, solid-state laser technology to our industrial partner for applications in manufacturing.

— J. Crane, G. Huete, L. Shah, M. Shirk, B. Stuart, and S. Telford

PRECISION OPTICAL FIGURING WITH WET-ETCH FIGURING

Wet-etch figuring (WEF) is a method for generating arbitrarily shaped optical surfaces using wet chemical etching. In WEF, the etching region on the optic is confined to a stable droplet size through the use of surface tension gradients (called Marangoni confinement), and is moved in a controlled fashion over the optic surface to precisely generate the desired optical figure on very thin glass substrates. Real-time measurement of the surface wavefront during the fabrication process and feedback allow for a closed-loop figuring operation.

Over the course of this year LS&T, with support from the Laboratory Directed Research and Development Program, has refined WEF and applied it to fabricate precision optics for a variety of applications.

Figure 4 shows a phase plate fabricated on 1-mm-thick borosilicate glass at 1.2-cm aperture, to convert a Gaussian laser beam profile to a flat-top profile at focus. The transmitted wavefront of the

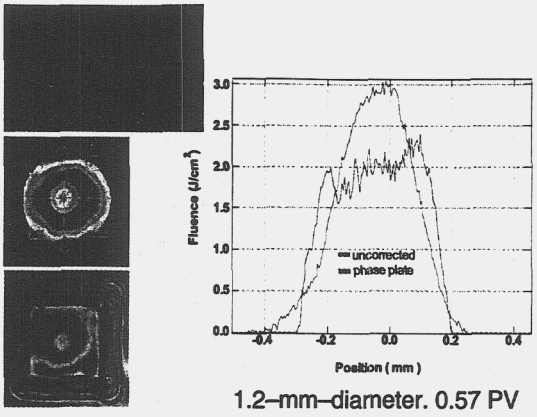

Figure 4. Contour map and interferogram of 1.2-mm-thick borosilicate glass. Also, lineout of intensity profile of laser focal spot before and after insertion of phase plate. (PV = peak-to-valley ratio.)

finished part as measured at 633 nm is shown in a false-color image as well as an inter-ferogram. Line-outs of the focal spot intensity with and without this phase plate are also shown illustrating the Gaussian to flat-top beam shaping. This optic has been successfully used in laser machining to increase the efficiency of drilling and the quality of the drilled holes.

Figure 5 demonstrates the effects of a thin (1-mm) static phase corrector optic

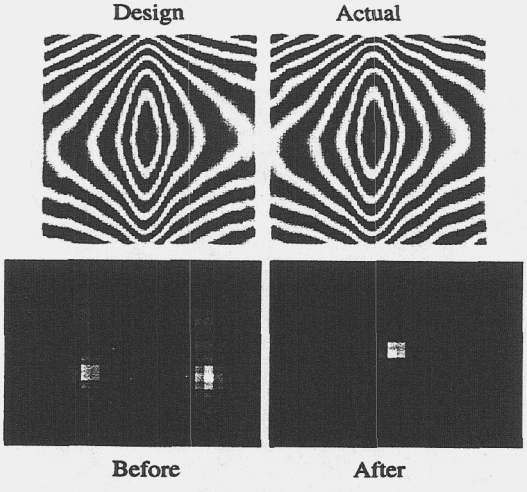

Figure 5. Design and actual transmitted wavefront interferogram of 30- × 40-mm aperature phase corrector plate fabricated for Mercury laser. Lower images show without (left) and with (right) phase plate.

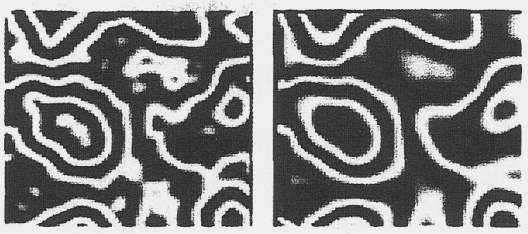

Figure 6. Design and actual transmitted wavefront interferogram of 30- × 30- × 1-mm-thick, WEF-fabricated continuous contour phase plate used for beam homogenization and spot size control for the NIF laser.

tailor-made to compensate for aberrations in the amplifier section of LLNL's Mercury laser. The beam aberrations were measured and were used to calculate the desired optical figure for the corrector. Interferograms of the desired and actual transmitted wavefront of the 30- × 40-mm optic are shown, along with the focal spot before and after insertion of this optic. The phase compensation allows the focal spot to approach the diffraction limit. Such phase correction optics could also be used on the National Ignition Facility (NIF) when a small focal spot is needed.

We are also fabricating continuous phase plates (CPP) for the NIF laser. Figure 6 shows the desired and actual transmitted wavefronts of a 30- × 30-mm aperture CPP fabricated on a 1-mm-thick borosilicate substrate. This optic, inserted upstream in the low-power section, is designed as a beam homogenizer to generate a smooth, super-Gaussian focal spot of a desired diameter at target. The surface height gradients for this optic are 0.5 μm/mm. Some experiments can utilize these small-aperture CPPs, while others require full-apperture CPPs. Our ultimate goal is to produce these optics at full aperture.

Figure 7 shows the transmitted wavefront of a multi-element, volume-phase holographic, dichromated gelatin (DCG) grating made for a telecommunication application. The DCG is sealed between two fused silica windows with optical cement. Stresses generated from the dried cement distort the overall optical

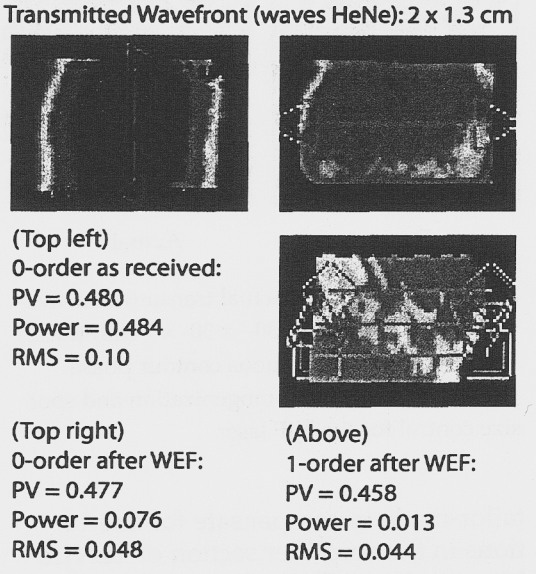

Figure 7. Transmitted zero-order wavefront of DCG grating with cover plate before and after WEF correction. Also shown is the 1st order transmitted wavefront over a 20- × 13-mm aperature. The WEF correction compensates for glue-induced distortion of this multi-element optic.

figure. We used WEF to figure one surface of the optic to restore a flat transmitted wavefront. The presence of multiple interfaces and the grating layer caused multiple fringes that required a filtering algorithm to be developed to measure the true optical figure in process. We corrected the figure based on measurement of the zero-order transmitted wavefront. The first two images in this figure show the 0-order wavefront before and after WEF. The corrected optic shows an improvement to better than 10th wave in power, and better than 20th wave in RMS figure, with the phase distortion concentrated in one corner of the optic. The bottom plot shows that correcting the 0-order is sufficient to bring the 1st order transmitted wavefront of this nominally 1-mm–period grating to an equivalent RMS value and even a better figure in terms of power.

— M. Rushford, S. Dixit, J. Britten, L. Summers, M. Aasen, and C.Hoaglan

Fabrication of a 5-Meter-Diameter Diffractive Fresnel Lens

Detection and imaging of distant objects, such as the exosolar (outside our solar system) planets, require optical telescopes with large-aperture primary optics. Large apertures gather more light from these objects, thereby increasing the signal to noise. Space deployment of such telescopes severely limits the weight of the optical components and requires that the primary optic be thin, lightweight, and deployable in space.

Transmissive optics (lenses) are less sensitive to surface ripples than reflective optics (mirrors). Lenses can be made lightweight by replacing conventional lenses with diffractive Fresnel lenses. The Eyeglass project, funded by the Laboratory Directed Research & Development Program, has been developing large-aperture Fresnel lenses for space telescopes. We have built diffractive telescopes at apertures up to 50 cm diameter and demonstrated their color-corrected operation over a 470- to 700-nm-wide bandwidth.

Space deployment of large-aperture optics requires that they be packageable into a small volume for launch. In our first attempt at this, we built a 75-cm-diameter Fresnel lens (shown in Figure 8) made up of six segments and assembled using 2.5-cm-wide metal hinges. After fabrication, this lens was folded, unfolded, and was shown to produce a diffraction-limited focal spot.

To demonstrate that this concept can be scaled up to larger sizes, we have recently built and operated a 5-m-diameter Fresnel lens (shown in Figure 9). This lens consists of 72 segments of 0.7-mm-thick glass panels that are joined togeth-

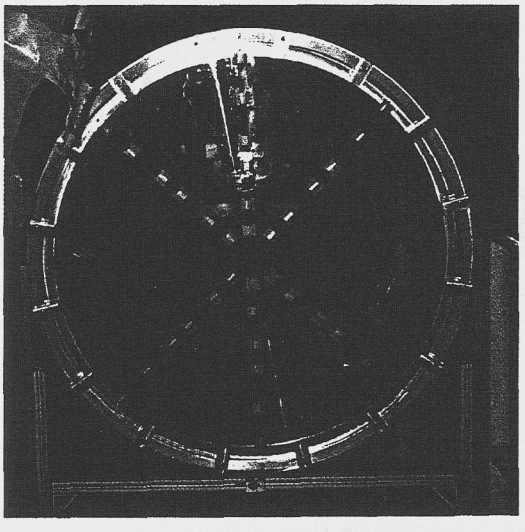

Figure 8. The 75-cm-diameter, six-panel folding lens.

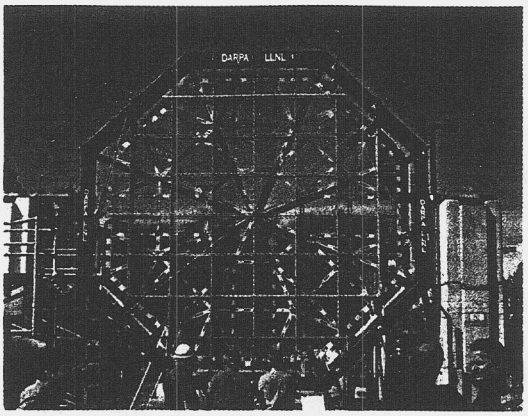

Figure 9. The 5-mFresnel lens mounted outdoors for optical testing.

er using 5-cm-wide metal hinges. The largest panel is about 600 × 770 mm in size. The particular layout of the pattern was chosen to allow the lens to be folded into a hatbox ~1/3 its size. The glass panels used for this lens are mass produced for flat-panel displays, which are inexpensive. A binary Fresnel lens pattern was applied to each panel separately using lithographic techniques. After patterning, the panels were cut to shape and the 72 pieces were glued together using a UV-curable adhesive. The assembled lens was then tension mounted in an octagonal frame and sandwiched between two metal meshes for transportation and protection against wind loading.

Optical testing of the lens consisted of hoisting the lens in a vertical position, illuminating it with monochromatic light from a laser and observing the focal spot produced by the lens. Such point-to-point tests require a minimum distance of four times the focal length between the source and the focus. We tested the lens at 405-, 532-, and 670-nm wavelengths. Figure 10a shows a focal spot produced by this lens. The focal spot size and shape are dominated by the aberrations inherent in the glass panels and the reduced precision in the alignment of the panels. Both these limitations will be overcome in the future. Figure 10b shows an image of the lens when viewed back from the focus. This confirms that light passing through the various panels reaches focus.

The next phases of the project involve improving the wavefront of the panels to improve the focal-spot quality and to fabricate Fresnel lenses of even larger sizes.

— S. Dixit, R. Hyde, and A. Weisberg

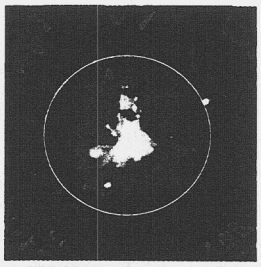

Figure 10a. Focal spot produced by the 5-m Fresnel lens when illuminated with 532-nm light. Inscribed is a 2.5-cm-diameter circle. The central portion of the image is saturated.

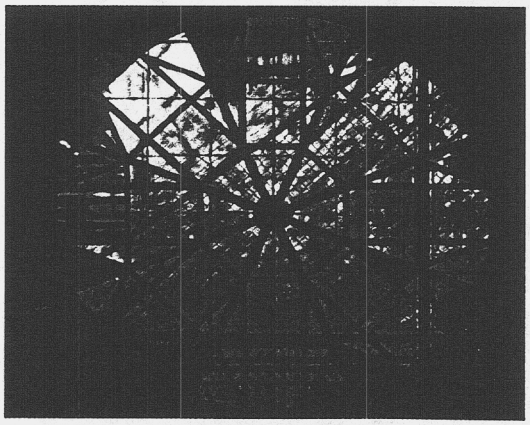

Figure 10b. View of the lens from the green-light focus.

LASER DRILLING OF HIGH-ASPECT-RATIO, MICRON-SCALE HOLES FOR NIF FUSION TARGETS

One of the leading ignition target design for the National Ignition Facility (NIF) requires a capsule with a copper-doped Be ablator. Unlike plastic or glass, this material is impermeable to hydrogen, requiring that a hole be used to fill the capsule with DT fuel. The requirements for this hole are quite stringent because density perturbations in the ablator can enhance Rayleigh-Taylor instability growth during an implosion, which in turn reduces the fusion yield. Recent calculations suggest that a 3-mm-diameter straight hole would probably be acceptable.

Several technologies have been explored in the past for drilling holes of similar dimensions. These techniques include electrical discharge machining (EDM) and

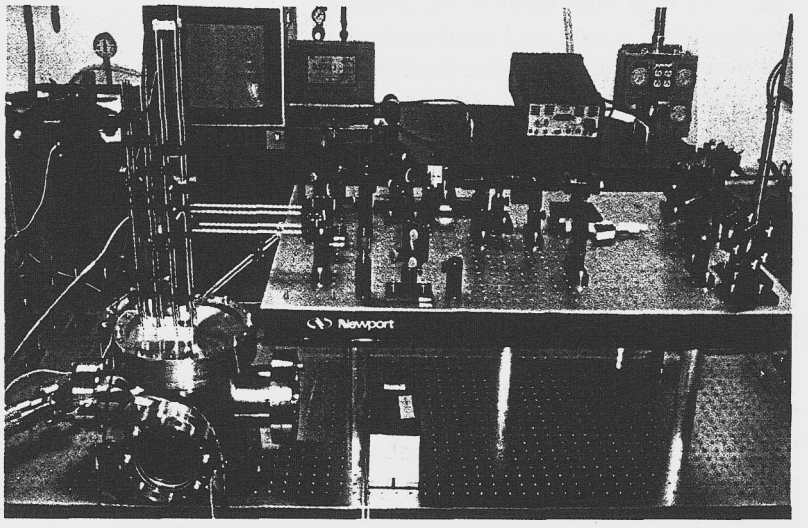

Figure 11. Cutting station for micron-scale hole drilling.

ion milling. The main problem encountered in these technologies is a limit in aspect ratio. For instance, EDM is able to drill through the thick material, but only if the hole is opened up to about 8 mm. Conversely, submicron-diameter holes can be made with an ion mill, but only through very thin material.

Under the support of ICF's Target Science and Technologies group, LS&T has recently built a new cutting station (Figure 11) and coupled it to an existing short-pulse machining laser. The short-pulse laser was selected to minimize the heat deposited in the area surrounding the hole and produce a sufficiently hot plasma such that the ablated material can escape the long, narrow channel.

In order to achieve the desired beam size on the front surface of the material, a high-numerical-aperture (NA) focusing system must be used. The large NA equates to a highly vergent beam into and out of the focal plane, yielding a very short depth of focus (≅1 μm). Gaussian beam propagation dictates that if the laser were focused to the diffraction-limited spot size on the front surface, the beam diameter at the exit of the capsule would be 135 μm. This is significantly larger than the size of hole required for this application.

A solution to the challenge of beam divergence is presented by the nature of the hole itself. As the hole begins to form, the walls of that hole become a metallic waveguide. This waveguide confines the propagating light in much the same way as an optical fiber.

The hole drilling system utilizes a Ti:sapphire laser that produces 1 mJ per pulse (before compression) at a 3.5-kHz repetition rate. The compressed pulse width is about 110 fs. This pulse is then spatially filtered and frequency doubled to a wavelength of 403 nm. The final available pulse energy is 1 mJ.

These laser pulses are injected into the collimated space of an infinite-conjugate-ratio microscope. The objective chosen for this project was a single-element aspheric lens with a focal length of 4 mm and a clear aperture of 4.6 mm, yielding an NA of 0.58. Due to the naturally high intensities of short-pulse lasers (about 10^{14} W/cm^2 in this application) and the small focal spot of this system, drilling must be done in vacuum. The lens is housed inside the cutting chamber and is protected from debris by a microscope cover slip.

Since the system was designed with infinite conjugates, the focal plane of the laser and the object plane of the microscope are at the same location. This allows seeing the hole as it is drilled. More importantly, it provides position feedback with sufficient resolution to reproducibly place the target precisely at focus. The microscope itself consists of a fiber-delivered laser illumination source, the aspheric objective and a 40-cm-focal-length tube lens to bring the image created by the objective to the plane of a charge-coupled device (CCD) camera. This microscope provides a field of view of about 75 mm with a resolution of 200 nm per pixel.

Early trials of the system have demonstrated the feasibility of drilling holes that extend more than 100 times beyond

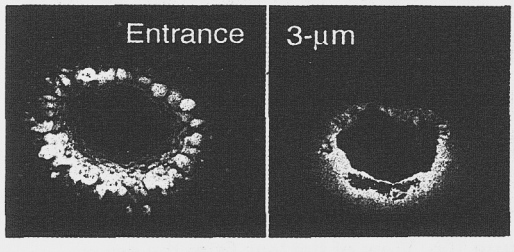

Figure 12. Laser-drilled hole through 125-μm-thick Be foil.

the system's Rayleigh range. Three-mm-diameter holes have been drilled in 125-mm-thick Be and Al foils, as well as thin-walled Be capsules. Figure 12 shows the typical entrance and exit of a hole in the Be foil.

— P. Armstrong, B. Stuart, and R. McEachern

ULTRAFAST LASER MICRO-SCULPTING OF MATERIALS

Several programs at LLNL have expressed an interest in having the surfaces of various parts to be machined to micron (and sub-micron) tolerances. Typically these parts are made of engineering materials that are very hard to machine due to their physical properties, and the process adds much value to the part. Potential materials include oxide ceramics, explosives, and refractory metals. Contact type machining techniques are undesirable due to factors such as tool wear and heat buildup. Ultrashort-pulsed laser ablation has previously shown that it can easily handle machining of these materials with extreme accuracy and very low thermal or mechanical distortion of a part. A prototype ultrafast laser machine tool has been fabricated and used to perform proof-of-principles work. We have demonstrated the capability to machine surfaces to arbitrary shape.

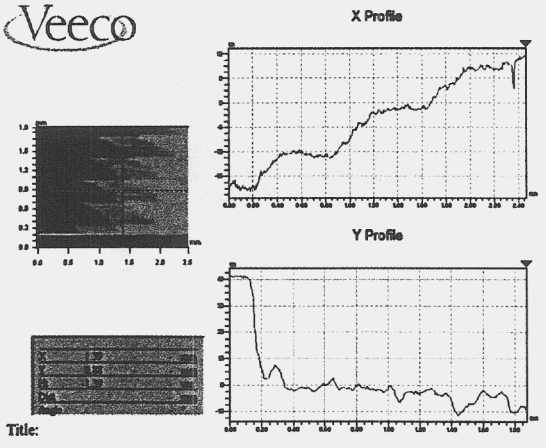

Figure 13. Profile of a Machined Alumina Surface. The parallelograms seen are expected from the control surface.

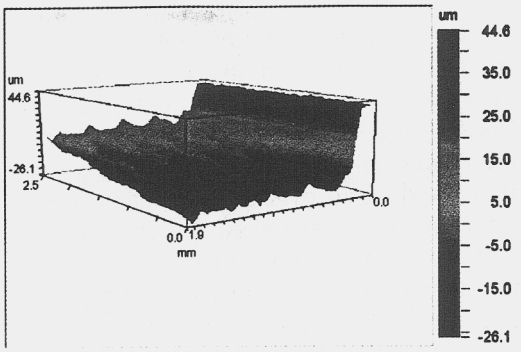

Figure 14. 3-D Perspective of the surface shown in Figure 13. Notice the depth of material ablated from the original surface is in excess of 70 μm in places.

The tool works by precisely measuring initial surface geometry to micron precision using an optical profilometer and an accurate 3-axis motion system to sub-micron accuracy in all dimensions. After the part is measured, the laser and motion system were automated to machine the part to the desired geometry using a Labview based control to precisely control material removal.

The first step in the development of this process was the characterization of laser machining of the desired material, alumina (Al_2O_3) under conditions similar to those expected during processing. This involved determination of material removal rates at various laser conditions (pulse energy, diameter, temporal width), and of the response of the target material with respect to variations in process parameters (feed-rate, shield gas). This information was then used to develop the machine tool so that it would operate at optimal accuracy and efficiency. The process consists of three steps. The initial geometry is mapped with a sub-micron accurate laser sensor. This surface is compared to one provided by the user that describes the desired final surface of the part. The computer based control system generates and executes a program that varies the power of the laser and operates the motion system to create 3-dimensional structure on the surface.

The tool consists of four principle components: sensor suite, motion system, laser and dynamic power control system, and automation hardware and software to control the process.

The power of the laser is varied by using a form of Pulse Width Modulation (PWM) to control the output. Specifically, the electronic pulses that switch open

the final Pockels cell optical gate are controlled by the system, in such a way as to vary the average power of the laser. Various shapes have been machined into alumina workpieces. These have shown that the desired precision of machining is possible, and that the surface finish is as smooth as, or smoother than that of the initial material, and with almost no heat affected zone. These shapes can be arbitrary in nature; such as a surface described with a function, or set of functions. In Figures 15 and 16, just such a surface is generated from a set of equations, in this case a sphere surrounded by a flat plane.

Now that a working prototype has been proven, a second, more advanced system is being considered, which will provide much greater capabilities. A rotational axis will be added to allow turning and milling operations. Also, encoders will be employed to get direct feedback from the motion system to increase accuracy. The laser used in the experiments will employ higher average power than the current one, thus increasing machining rates by 1 to 2 orders of magnitude. Another possible improvement includes simultaneous sensing and machining to eliminate the need for the 3-step process. Estimates show that the improved system will reach volume removal rates in excess of 0.3 mm^3/s.

The figures reference one particular trial, in which a tilted plane is to be machined. The plane is much longer than shown. The structure on the surface, seen as raised parallelograms, is a pattern exactly as expected according to the control algorithm. The surface is a terraced plane, with two dimensions of tilt and a contour line (iso-depth line) that is not normal to the machining direction. The resolution of the resulting surface is thus on the order of ± 0.001 mm. Concave structures similar to this one were also machined, but are not shown for brevity. The sphere shown in the figures intersects the surface such that the diameter of the rim is 2.5 mm, and is 250 microns deep.

We now have a tool, that when combined with a higher-average power laser, will be able to meet some very demanding precision machining requirements that were previously unachievable. The possible uses for this technology in wider industry will be pursued in the near future.

— M. Shirk and J. Furmanski

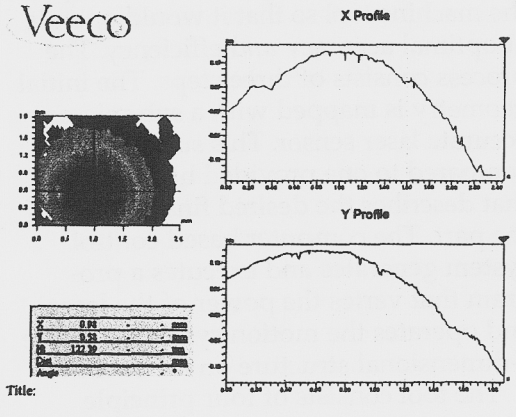

Figure 15. A convex spherical section machined onto a flat alumina surface.

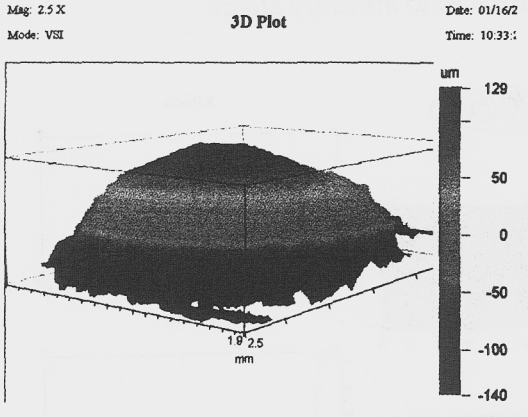

Figure 16. Perspective view of the spherical section machined onto an alumina surface.

Conceptual design for a high-energy petawatt laser on the National Ignition Facility

D. M. Pennington, M. Hermann, C. Barty, J. Caird, W. Clark, J. Dawson, A. Erlandson, I. Jovanovic, M. H. Key, K. Skulina, B. Wattellier

Lawrence Livermore National Laboratory
P.O. Box 808, L-477
Livermore, CA 94550
telephone:(925) 423-9234, fax:(925) 422-5537, e-mail address: pennington1@llnl.gov

Abstract: A conceptual design for implementing a high energy, short pulse capability on the National Ignition Facility has been developed. Details of the 2-5 kJ, 5-50 ps baseline design will be presented.

Summary:

Development of chirped pulse amplification has made possible unprecedented peak laser powers using large aperture lasers.[1] With the National Ignition Facility (NIF) scheduled to produce first light in 2003, there is increasing US interest in the scientific potential of high-energy petawatt (HEPW) pulse production at NIF and other high energy density facilities in the US. A national petawatt laser initiative has been started by the Department of Energy to evaluate the opportunities.

Several NIF missions benefiting from HEPW capability have been defined, requiring HEPW pulses with 2-5 kJ of energy and 5-50 ps duration. Within an HEPW laser-matter interaction, the electric and magnetic fields accelerate the plasma electrons to over 100 MeV. As the electrons collide with atoms in the target, they generate high energy x-rays (10 keV to > 10 MeV). These x-rays can serve as a source for high-energy back lighters for laser-matter interactions, as well as other radiographic applications. Other secondary effects of the electrons include heating and the formation of extremely high field Debye sheaths, which accelerate ions. Proton beams produced at the rear surface of thin flat targets have exceptional beam quality and intensity at energies ≥ 50 MeV. Advanced radiography at higher photon energies or using protons is of considerable interest for the study of larger scale laser-driven hydrodynamic experiments in ICF ignition experiments with NIF laser. Uniquely high energy densities can also be produced by isochoric heating of inertial confined matter using either the relativistic electrons or ballistically focused protons. Long term, fast ignition of fusion by electrons or protons is also an exciting possibility.

Technology R&D, including advanced grating and front-end development, is being undertaken to enable HEPW pulses as high as 5 kJ. In addition, we now have a conceptual system design for implementation of HEPW capability on NIF, in which only the injection laser system and target areas require modification. A short pulse oscillator and stretcher would be added to the NIF master oscillator room. This would be delivered to a short pulse preamplifier module to provide a high contrast chirped pulse for injection to the main NIF amplifier chain. The short pulse preamplifier module would be a line replaceable unit with the capability to convert from 1 to 4 beams in a NIF quad to short pulse operation. Dispersion compensation would be added in the preamplifier beam transport system to allow high-order phase adjustment on individual beam lines. Following amplification, the four beams would be diverted into two vacuum chambers, just prior to the NIF target chamber. Each chamber houses two compressor systems in a stacked geometry. The compact, four-grating compressor geometry compensates for both temporal and spatial chirp. High-dispersion multilayer dielectric gratings are required to minimize the grating separation and maximize damage resistance. Following compression, the beams are focused by an array of four, off-axis parabolas into the NIF target chamber via an equatorial port. Additional details of the design will be presented.

References :

1. D. M. Pennington, C. G. Brown, T. E. Cowan, W. Fountain, S. Hatchett, E. Henry, J. Johnson, M. Kartz, M. Key, J. Koch, M. Perry, T. Phillips, M. Roth, T. Sangster, R. Snavely, M. Stoyer, Y. Takahashi, "Petawatt laser system and experiments", IEEE J. Quantum. Electron. 6, 676-688 (2000).

This work was performed under the auspices of the U.S. Department of Energy by University of California, Lawrence Livermore National Laboratory under contract No. W-7405-Eng-48.

Optical parametric chirped-pulse amplifier as an alternative to Ti:sapphire regenerative amplifiers

Igor Jovanovic, Brian J. Comaskey, Christopher A. Ebbers, Randal A. Bonner, Deanna M. Pennington, and Edward C. Morse

We demonstrated a high-pulse energy, femtosecond-pulse source based on optical parametric chirped-pulse amplification. We successfully amplified 1-μm broadband oscillator pulses to 31 mJ and recompressed them to 310-fs pulse duration, at a 10-Hz repetition rate. The gain in our system is 6×10^7, achieved by the single passing of only 40 mm of gain material pumped by a commercial Q-switched Nd:YAG laser. This relatively simple system replaces a more complex Ti:sapphire regenerative-amplifier-based chirped-pulse amplification system. Numerous features in design and performance of optical parametric chirped-pulse amplifiers make them a preferred alternative to regenerative amplifiers based on Ti:sapphire in the front end of high-peak-power lasers.

1. Introduction

Chirped-pulse amplification[1] (CPA) is now routinely used to generate gigawatt, terawatt, and even petawatt[2] peak powers for applications such as short-pulse precision machining,[3] high-harmonic generation and time-resolved spectroscopy,[4] and fast ignitor drivers for inertial confinement fusion,[5] respectively. Typically, these sources consist of a short-pulse oscillator, a stretcher, a regenerative amplifier, a series of high-energy amplifiers, and a compressor. Bandwidth limitations of common laser gain media are partially circumvented by use of high-bandwidth materials such as Ti:sapphire in the system's front end, combined with high-energy storage materials such as Nd:glass in the final amplifiers. Different applications require different combinations of pulse energy and pulse width: Spectroscopic applications require μJ to mJ pulse energies with 65–100-fs pulse widths, machining applications require pulse energies in the range of 0.1–50 mJ with pulse widths between 0.5 and 2 ps, and fast ignitor drivers require relatively large pulse energies (1–10 kJ) with fairly long pulse widths (1–10 ps).

The existing technologies for short-pulse generation and amplification rely on laser hosts such as Cr:LiSAF, Ti:sapphire, or Yb:YAG. Yb:YAG is used when direct diode pumping of the source is desired. Otherwise, green-pumped Ti:sapphire is utilized. Nd:glass amplifiers find application when large pulse energies with relatively long pulse widths (hundreds of femtoseconds) are sought. Optical parametric amplification[6] was recently identified as an attractive amplification technology, and its use in CPA systems is referred to as optical parametric chirped-pulse amplification[7–9] (OPCPA). Optical parametric amplification is a nonlinear process that involves a signal wave, a pump wave, and an idler wave. In optical parametric amplifiers (OPAs), intense pulses essentially instantaneously interact in a nonlinear material through a nonlinear polarization wave generated at the difference frequency. Parametric gain is achieved over the coherence length, defined as the length over which the phase relationship among the three waves departs from the ideal condition $\phi_p - \phi_s - \phi_i = -\pi/2$ by $\Delta\phi = \pi$. An underappreciated feature of optical parametric amplification is that it results in a minimal heat deposition in the OPA crystal, allowing a different set of material constraints to limit the final energy. Combined with the demonstrated performance of existing doubled pump lasers,

When this research was performed, I. Jovanovic (jovanovic1@llnl.gov) was with both the Lawrence Livermore National Laboratory, mail code L-490, 7000 East Avenue, Livermore, California 94550 and the Department of Nuclear Engineering, University of California at Berkeley, Berkeley, California 94720. I. Jovanovic is now at only the Lawrence Livermore National Laboratory, as are B. J. Comaskey, C. A. Ebbers, R. A. Bonner, and D. M. Pennington. E. C. Morse is with the Department of Nuclear Engineering, University of California at Berkeley.

First, a changing beam diameter creates a nonuniform spatial intensity along the crystal. Second, angular dephasing leads to reduced gain that is due to finite angular acceptance of the nonlinear process. Both of these effects are insignificant with the weakly focused beams used in the nanosecond OPCPA and do not play an important role in the amplification process.

Equations (1) model the interaction of plane waves and have to be suitably modified to describe the situation in which the beam diameter is finite and the beam has a nonuniform transverse intensity profile. In addition, temporal and spectral modifications of the signal pulse occurs in OPCPA when the pump pulse intensity is not a constant with respect to time. Finally, the effect of Poynting vector walk-off for extraordinary waves in nonlinear crystals presents an additional effect that requires inclusion in the model. This is particularly important when the beam diameter is comparable with the total transverse walk-off over the nonlinear crystal length.

We evaluate those effects by solving Eqs. (1) numerically on a three-dimensional grid in space and time. We start with the assumed intensity distribution of the original waves at a point:

$$I_i(x, y, t) = 2n_i\left(\frac{\epsilon_0}{\mu_0}\right)^{1/2}|A_i(x, y, t)|^2, \qquad i = 1, 2, 3, \tag{2}$$

where I is the beam intensity, x and y are the two transverse coordinates, and t is the temporal coordinate. The intensity distribution is normalized in the following fashion:

$$\int_{-\infty}^{\infty}\int_{-\infty}^{\infty}\int_{-\infty}^{\infty} I_i(x, y, t)\mathrm{d}x\mathrm{d}y\mathrm{d}t = E_i, \qquad i = 1, 2, 3, \tag{3}$$

where E is the pulse energy. We assign a zero phase to the electric field of the seed and pump at the input face of the crystal ($z = 0$). This is consistent with the insensitivity of optical parametric amplification with respect to the initial phase relationship between the seed and the pump when an idler is not initially present. Additionally, we introduce the effect of the pump-beam walk-off angle, ρ, in one direction (x) and the noncollinear angle in two directions for the signal (Ω_{1x}, Ω_{1y}) and idler beams (Ω_{2x}, Ω_{2y}). We account for the appropriate transverse part of the signal, idler, and pump at the point z in the crystal by calculating the corrected transverse displacement:

$$x_1' = x_1 + \Omega_{1x}z, \qquad y_1' = y_1 + \Omega_{1y}z, \tag{4}$$

$$x_2' = x_2 + \Omega_{2x}z, \qquad y_2' = y_2 + \Omega_{2y}z, \tag{5}$$

$$x_3' = x_3 + \rho z, \tag{6}$$

where (x_1', y_1'), (x_2', y_2'), and x_3' represent the corrected transverse coordinates for the signal, idler, and pump, respectively.

In CPA the spectrum is linearly chirped in time, so the phase mismatch that is due to spectral bandwidth can be included by assignment of the appropriate value for wave-vector mismatch and its projection in the direction normal to the crystal surface:

$$\Delta\mathbf{k}(t) = \mathbf{k}_3 - \mathbf{k}_1(t) - \mathbf{k}_2(t), \tag{7}$$

$$\Delta k_z(t) \approx 2\pi\left[\frac{n_3}{\lambda_3} - \frac{n_1(t)}{\lambda_1(t)} - \frac{n_2(t)}{\lambda_2(t)}\right]. \tag{8}$$

Finally, the system of differential equations can be written as

$$\begin{aligned}
\frac{\mathrm{d}A_1(x_1', y_1', t)}{\mathrm{d}z} &= i\frac{2\omega_1(t)}{n_1(t)c}d_{\mathrm{eff}}A_2^*(x_2', y_2', t)\\
&\quad\times A_3(x_3', y, t)\exp[i\Delta k(t)z],\\
\frac{\mathrm{d}A_2(x_2', y_2', t)}{\mathrm{d}z} &= i\frac{2\omega_2(t)}{n_2(t)c}d_{\mathrm{eff}}A_1^*(x_1', y_1', t)\\
&\quad\times A_3(x_3', y, t)\exp[i\Delta k(t)z],\\
\frac{\mathrm{d}A_3(x_3', y, t)}{\mathrm{d}z} &= i\frac{2\omega_3(t)}{n_3(t)c}d_{\mathrm{eff}}A_1(x_1', y_1', t)\\
&\quad\times A_2(x_2', y_2', t)\exp[-i\Delta k(t)z].
\end{aligned} \tag{9}$$

We perform a discretization of the electric field on the grid of (DX, DY, DT) points with a spatial-and-temporal window size (WX, WY, WT), such that the following normalization applies:

$$2n_i\left(\frac{\epsilon_0}{\mu_0}\right)^{1/2}\frac{WX}{DX}\frac{WY}{DY}\frac{WT}{DT}\sum_{j=1}^{DX}\sum_{k=1}^{DY}\sum_{l=1}^{DT}|A_i(j, k, l)|^2 = E_i, \qquad i = 1, 2, 3. \tag{10}$$

The system (9) in discrete form is solved numerically with a fourth-order Runge–Kutta integration routine, yielding solutions for electric field amplitude and phase at the crystal output in a spatially and temporally resolved form. It is important to note that the model allows initial misalignment of the seed and pump beams at the input face of the nonlinear crystal. This is an experimental optimization procedure frequently required to achieve the best overlap of the beams inside a crystal that exhibits walk-off for one of the beams.

Our system uses a pump laser based on an unstable resonator, with a complicated spatiotemporal pulse evolution.[12] We recorded the pulse shape by use of a scanning pinhole in the image plane of the pump pulse. A numerical fit has been obtained for the pump pulse shape, as shown in Fig. 2 in a 4-ns temporal window centered at the peak of the pump pulse intensity. We use the obtained pump spatial-and-temporal pulse shape in our numerical model.

4. Results

With the injected signal of 0.5 nJ, the measured output from the first BBO crystal was 1.8 μJ, (gain = 3700), and from the second BBO crystal we obtained

Optical parametric chirped-pulse amplifier as an alternative to Ti:sapphire regenerative amplifiers

Igor Jovanovic, Brian J. Comaskey, Christopher A. Ebbers, Randal A. Bonner, Deanna M. Pennington, and Edward C. Morse

We demonstrated a high-pulse energy, femtosecond-pulse source based on optical parametric chirped-pulse amplification. We successfully amplified 1-μm broadband oscillator pulses to 31 mJ and recompressed them to 310-fs pulse duration, at a 10-Hz repetition rate. The gain in our system is 6×10^7, achieved by the single passing of only 40 mm of gain material pumped by a commercial Q-switched Nd:YAG laser. This relatively simple system replaces a more complex Ti:sapphire regenerative-amplifier-based chirped-pulse amplification system. Numerous features in design and performance of optical parametric chirped-pulse amplifiers make them a preferred alternative to regenerative amplifiers based on Ti:sapphire in the front end of high-peak-power lasers.

1. Introduction

Chirped-pulse amplification[1] (CPA) is now routinely used to generate gigawatt, terawatt, and even petawatt[2] peak powers for applications such as short-pulse precision machining,[3] high-harmonic generation and time-resolved spectroscopy,[4] and fast ignitor drivers for inertial confinement fusion,[5] respectively. Typically, these sources consist of a short-pulse oscillator, a stretcher, a regenerative amplifier, a series of high-energy amplifiers, and a compressor. Bandwidth limitations of common laser gain media are partially circumvented by use of high-bandwidth materials such as Ti:sapphire in the system's front end, combined with high-energy storage materials such as Nd:glass in the final amplifiers. Different applications require different combinations of pulse energy and pulse width: Spectroscopic applications require μJ to mJ pulse energies with 65–100-fs pulse widths, machining applications require pulse energies in the range of 0.1–50 mJ with pulse widths between 0.5 and 2 ps, and fast ignitor drivers require relatively large pulse energies (1–10 kJ) with fairly long pulse widths (1–10 ps).

The existing technologies for short-pulse generation and amplification rely on laser hosts such as Cr:LiSAF, Ti:sapphire, or Yb:YAG. Yb:YAG is used when direct diode pumping of the source is desired. Otherwise, green-pumped Ti:sapphire is utilized. Nd:glass amplifiers find application when large pulse energies with relatively long pulse widths (hundreds of femtoseconds) are sought. Optical parametric amplification[6] was recently identified as an attractive amplification technology, and its use in CPA systems is referred to as optical parametric chirped-pulse amplification[7–9] (OPCPA). Optical parametric amplification is a nonlinear process that involves a signal wave, a pump wave, and an idler wave. In optical parametric amplifiers (OPAs), intense pulses essentially instantaneously interact in a nonlinear material through a nonlinear polarization wave generated at the difference frequency. Parametric gain is achieved over the coherence length, defined as the length over which the phase relationship among the three waves departs from the ideal condition $\phi_p - \phi_s - \phi_i = -\pi/2$ by $\Delta\phi = \pi$. An underappreciated feature of optical parametric amplification is that it results in a minimal heat deposition in the OPA crystal, allowing a different set of material constraints to limit the final energy. Combined with the demonstrated performance of existing doubled pump lasers,

When this research was performed, I. Jovanovic (jovanovic1@llnl.gov) was with both the Lawrence Livermore National Laboratory, mail code L-490, 7000 East Avenue, Livermore, California 94550 and the Department of Nuclear Engineering, University of California at Berkeley, Berkeley, California 94720. I. Jovanovic is now at only the Lawrence Livermore National Laboratory, as are B. J. Comaskey, C. A. Ebbers, R. A. Bonner, and D. M. Pennington. E. C. Morse is with the Department of Nuclear Engineering, University of California at Berkeley.

OPCPA appears capable of extending CPA into the kilowatt-average power regime.[10]

OPCPA has the broad-bandwidth capability similar to Ti:sapphire but offers the flexibility of operating at an arbitrary wavelength, making OPAs more flexible than solid-state lasers. Broad bandwidth can be achieved in a collinear OPA operating near degeneracy or in a noncollinear nondegenerate OPA. High gain can be obtained from nanosecond OPCPA by the single passing of a relatively short length (several centimeters) of gain material, which eliminates the need for complicated regenerative multipass amplification and electro-optic switching. Because the total length of the gain material is short, the accumulated nonlinear phase (B integral) is substantially reduced, permitting good amplified pulse recompression without additional compensation for the B integral. A substantial reduction of the prepulse from a CPA system can be achieved by the elimination of the pulse leakage originating from the regenerative multipass cavity. In addition to the above-mentioned advantages of OPCPA when it is used to replace regenerative amplifiers, OPCPA also allows large energy scaling through large available apertures of potassium dihydrogen phosphate (KDP) crystals.

Another feature of an OPA makes it even more attractive for applications when the reduction of pulse aberrations is crucial. Optical parametric amplification is inherently a low-noise amplification process, allowing possible pump phase aberrations to be transferred to the idler wave while introducing a negligible modulation to the signal wave. The only noise that is introduced in the process is due to parametric superfluorescence,[11] a process analogous to amplified spontaneous emission in lasers, and is typically less intense than amplified spontaneous emission for similar gain.[8] The condition for signal amplification to occur with high fidelity is a good overlap between the signal and the idler waves in space and time. A reduced transverse beam overlap and pump-beam nonuniformity lead to spatial modulation of the signal, whereas a reduced temporal overlap can produce a modified chirped-pulse spectrum.

In this paper we report on an efficient chirped-pulse OPA pumped by a commercial Nd:YAG laser. We present a numerical model and design for an optical parametric chirped-pulse amplifier as a replacement for a regenerative amplifier. We evaluate the performance of our OPCPA system designed for the front end of a Nd:glass high-energy CPA system. In Section 2 we present the experimental setup. This is followed by a description of our numerical modeling in Section 3. Finally, we show the obtained results in Section 4 and follow with a discussion of these results and a conclusion. Our result represents, to our knowledge, the most efficient OPCPA to date pumped by a commercial Q-switched pump laser.

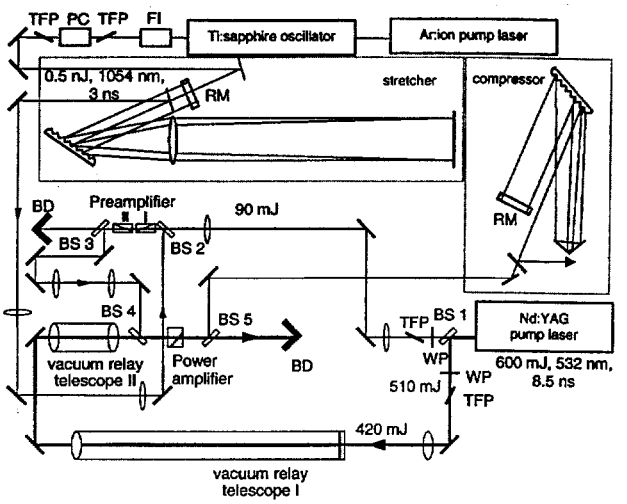

Fig. 1. Experimental OPCPA setup. BS, beam splitter; TFP, thin-film polarizer; WP, wave plate; BD, beam dump; FI, Faraday isolator; PC, Pockels cell; RM, roof mirror.

2. Experimental Setup

The design of our OPCPA system is presented in Fig. 1. A mode-locked Ti:sapphire oscillator (Spectra-Physics Tsunami) with a center wavelength of 1054 nm produces 100-fs transform-limited pulses. The pulse train consists of 2.5-nJ pulses at 84 MHz. A single pulse is selected from the oscillator by use of a Pockels cell and a pair of polarizers. The pulse is stretched in a four-pass stretcher that contains a 1480 lines/mm diffraction grating and a plano–convex lens, with the effective grating separation of 8 m. The stretcher is configured to clip the spectrum at its FWHM, with the bandwidth of 16.5 nm. The stretched pulse width is 3 ns, and the stretched pulse energy is 0.5 nJ. As noted in Section 4, spherical and chromatic aberrations in the stretcher limit the recompression of the seed pulse to 280 fs.

The stretched seed pulse is then relay imaged to the OPA. The OPA consists of three β-barium borate (BBO) crystals. The size of the first two crystals is $4 \times 4 \times 15$ mm^3 and that of the third crystal is $10 \times 10 \times 10$ mm^3, permitting scaling to large incident pump pulse energy when the pump-beam diameter is increased. The crystals are cut at 22.8° to allow type I angular phase matching, and they have a 2° wedge on their output faces to prevent intracrystal parasitic oscillation.

The pump source for the OPA is a Spectra-Physics GCR 270-10 Nd:YAG laser, operated in single longitudinal mode, producing 600 mJ of 532-nm output. The pulse width of Q-switched pulses is 8.5 ns, at a 10-Hz repetition rate. The transverse intensity profile of the pump beam is a super-Gaussian, whereas the temporal profile is Gaussian, with a characteristic pulse spatiotemporal evolution for an unstable resonator.[12] To maximize the gain, the relative temporal positions of the signal and pump pulses are adjusted so that the maximum intensity of the signal coincides with the maximum intensity of the pump transverse center.

The first two BBO crystals are configured as preamplifiers and separated by 2 mm. Walk-off compensation[13] is used to reduce the effect of the intrinsic 3.2° extraordinary-beam Poynting vector walk-off in BBO. The pump beam is split by a 15% beam splitter BSI into a 90-mJ beam and a 510-mJ beam. The super-Gaussian transverse intensity profile of the pump laser is relay imaged to a plane between the first two BBO crystals by means of a telescope, which simultaneously adjusts the pump-beam diameter in the first two crystals to 1.6 mm. The proximity of the two walk-off-compensated crystals in the preamplifier eliminates the need for separate imaging of the pump beam on each crystal, which is a significant simplification when compared with previous designs.[8,9] In addition, dephasing in the small air gap is calculated to produce only a small (<0.1%) modification of gain in the preamplifier. The peak intensity of the pump beam in the first and second BBO crystals is 450 MW/cm^2. The pump beam is collimated to minimize dephasing that is due to the small angular acceptance of BBO (0.4 mrad cm).

An additional source of dephasing is the beam quality from the pump source (we measured the pump-beam quality to be 1.6 × DL (diffraction limited) in the sensitive phase-matching plane and 1.8 × DL in the insensitive phase-matching plane). The measured deviation of the pump beam from the ideal beam quality has a negligible impact on parametric gain with the selected pump-beam diameter.

The size of the seed beam is dictated by the requirement to avoid spatial modulation on the signal beam that is due to transverse walk-off of the extraordinary polarized pump beam and is set to 0.4 mm in the first two BBO crystals. The center of the seed beam is displaced from the center of the pump beam by 0.4 mm in the sensitive phase-matching direction on the front face of the first BBO crystal, maximizing the spatial overlap of the beams in the preamplifier. We treat our first two crystals as large-gain preamplifiers and neglect the low conversion efficiency resulting from the small spatiotemporal overlap of the seed and the pump pulses. The seed beam is introduced into the crystal at a 1° external angle with respect to the pump beam, perpendicular to the crystal's principal plane. The amplified signal and the idler beams are spatially separated after propagating 30 cm out of the preamplifier, and the idler is subsequently blocked, leaving only the amplified signal.

We use the beam transmitted through the 15% beam splitter BS1 and relay image the super-Gaussian spatial profile of the pump beam onto the final BBO crystal (power amplifier). The pump imaging telescope consists of two vacuum image relays. The use of two vacuum relay telescopes in our system is necessary because of spatial constraints and the requirement for imaging, beam sizing, and temporal matching of the seed and pump between the preamplifier and the power amplifier. The pump-beam diameter in the power amplifier is 3.5 mm, with peak intensity of 430 MW/cm^2 on the crystal with 410-mJ incident pump energy used from the available 510 mJ. Operating at intensity near 0.5 GW/cm^2 is a compromise between the requirement for strong nonlinear drive and the reduction of the risk of crystal damage, leading to greater system reliability. At operating intensities near 1 GW/cm^2 we periodically observed crystal damage on antireflection-coated surfaces, which is unacceptable in a system with appreciable repetition rate. The signal beam is imaged from the preamplifier and introduced into the power amplifier by use of the beam splitter BS4. The signal and idler beams are separated spatially after 2 m of propagation out of the power amplifier crystal, given the larger diameter of the signal and idler beams in the power amplifier.

The amplified signal pulse is compressed by use of a single-grating, double-pass compressor. The compressor contains a 1480 lines/mm grating, set at a diffracted angle of 55.33° to match the stretcher angle. No spectral clipping occurs in the compressor as a result of the large size of the associated optics. The spectral range is limited by the hard spectral clip in the stretcher, which limits the size of the spectrally dispersed beam in the compressor. The measured compressor efficiency is 50%. The recompressed pulse-width measurement is performed with a scanning intensity autocorrelator for the recompressed seed and a single-shot intensity autocorrelator for the amplified signal pulse at 10 Hz.

3. Numerical Modeling

Numerical modeling was found to be an important step for optimizing the performance of the preamplifier and subsequent power amplifier. Our OPCPA model is based on a numerical solution for the system of coupled differential equations for difference-frequency generation. The system that describes traveling waves can be written in a concise form[6] as

$$\frac{dA_1}{dz} = i\frac{2\omega_1}{n_1 c} d_{\text{eff}} A_2^* A_3 \exp(i\Delta k z), \tag{1}$$

$$\frac{dA_2}{dz} = i\frac{2\omega_2}{n_2 c} d_{\text{eff}} A_1^* A_3 \exp(i\Delta k z),$$

$$\frac{dA_3}{dz} = i\frac{2\omega_3}{n_3 c} d_{\text{eff}} A_1 A_2 \exp(-i\Delta k z),$$

where A_1, A_2, and A_3 are the amplitudes of the electric field of the signal, idler, and pump, respectively, d_{eff} is effective nonlinearity, and Δk is the wave-vector mismatch. The temporal walk-off that is due to group-velocity dispersion is neglected because we are concerned with long (nanosecond) pulses. Group-velocity dispersion introduces negligible dephasing because the total spectral walk-off of signal, idler, and pump is small over the length of the nonlinear crystal. Diffraction effects were not included in the model explicitly owing to their weak relative impact compared with the temporal and spatial modulation. In particular, two effects arising from diffraction can influence gain and conversion efficiency in the optical parametric amplification.

First, a changing beam diameter creates a nonuniform spatial intensity along the crystal. Second, angular dephasing leads to reduced gain that is due to finite angular acceptance of the nonlinear process. Both of these effects are insignificant with the weakly focused beams used in the nanosecond OPCPA and do not play an important role in the amplification process.

Equations (1) model the interaction of plane waves and have to be suitably modified to describe the situation in which the beam diameter is finite and the beam has a nonuniform transverse intensity profile. In addition, temporal and spectral modifications of the signal pulse occurs in OPCPA when the pump pulse intensity is not a constant with respect to time. Finally, the effect of Poynting vector walk-off for extraordinary waves in nonlinear crystals presents an additional effect that requires inclusion in the model. This is particularly important when the beam diameter is comparable with the total transverse walk-off over the nonlinear crystal length.

We evaluate those effects by solving Eqs. (1) numerically on a three-dimensional grid in space and time. We start with the assumed intensity distribution of the original waves at a point:

$$I_i(x, y, t) = 2n_i\left(\frac{\epsilon_0}{\mu_0}\right)^{1/2}|A_i(x, y, t)|^2, \qquad i = 1, 2, 3, \tag{2}$$

where I is the beam intensity, x and y are the two transverse coordinates, and t is the temporal coordinate. The intensity distribution is normalized in the following fashion:

$$\int_{-\infty}^{\infty}\int_{-\infty}^{\infty}\int_{-\infty}^{\infty} I_i(x, y, t)\mathrm{d}x\mathrm{d}y\mathrm{d}t = E_i, \qquad i = 1, 2, 3, \tag{3}$$

where E is the pulse energy. We assign a zero phase to the electric field of the seed and pump at the input face of the crystal ($z = 0$). This is consistent with the insensitivity of optical parametric amplification with respect to the initial phase relationship between the seed and the pump when an idler is not initially present. Additionally, we introduce the effect of the pump-beam walk-off angle, ρ, in one direction (x) and the noncollinear angle in two directions for the signal (Ω_{1x}, Ω_{1y}) and idler beams (Ω_{2x}, Ω_{2y}). We account for the appropriate transverse part of the signal, idler, and pump at the point z in the crystal by calculating the corrected transverse displacement:

$$x_1' = x_1 + \Omega_{1x}z, \qquad y_1' = y_1 + \Omega_{1y}z, \tag{4}$$

$$x_2' = x_2 + \Omega_{2x}z, \qquad y_2' = y_2 + \Omega_{2y}z, \tag{5}$$

$$x_3' = x_3 + \rho z, \tag{6}$$

where (x_1', y_1'), (x_2', y_2'), and x_3' represent the corrected transverse coordinates for the signal, idler, and pump, respectively.

In CPA the spectrum is linearly chirped in time, so the phase mismatch that is due to spectral bandwidth can be included by assignment of the appropriate value for wave-vector mismatch and its projection in the direction normal to the crystal surface:

$$\Delta\mathbf{k}(t) = \mathbf{k}_3 - \mathbf{k}_1(t) - \mathbf{k}_2(t), \tag{7}$$

$$\Delta k_z(t) \approx 2\pi\left[\frac{n_3}{\lambda_3} - \frac{n_1(t)}{\lambda_1(t)} - \frac{n_2(t)}{\lambda_2(t)}\right]. \tag{8}$$

Finally, the system of differential equations can be written as

$$\begin{aligned}
\frac{\mathrm{d}A_1(x_1', y_1', t)}{\mathrm{d}z} &= i\frac{2\omega_1(t)}{n_1(t)c}d_{\mathrm{eff}}A_2^*(x_2', y_2', t) \\
&\quad \times A_3(x_3', y, t)\exp[i\Delta k(t)z], \\
\frac{\mathrm{d}A_2(x_2', y_2', t)}{\mathrm{d}z} &= i\frac{2\omega_2(t)}{n_2(t)c}d_{\mathrm{eff}}A_1^*(x_1', y_1', t) \\
&\quad \times A_3(x_3', y, t)\exp[i\Delta k(t)z], \\
\frac{\mathrm{d}A_3(x_3', y, t)}{\mathrm{d}z} &= i\frac{2\omega_3(t)}{n_3(t)c}d_{\mathrm{eff}}A_1(x_1', y_1', t) \\
&\quad \times A_2(x_2', y_2', t)\exp[-i\Delta k(t)z].
\end{aligned} \tag{9}$$

We perform a discretization of the electric field on the grid of (DX, DY, DT) points with a spatial-and-temporal window size (WX, WY, WT), such that the following normalization applies:

$$2n_i\left(\frac{\epsilon_0}{\mu_0}\right)^{1/2}\frac{WX}{DX}\frac{WY}{DY}\frac{WT}{DT}\sum_{j=1}^{DX}\sum_{k=1}^{DY}\sum_{l=1}^{DT}|A_i(j, k, l)|^2 = E_i, \qquad i = 1, 2, 3. \tag{10}$$

The system (9) in discrete form is solved numerically with a fourth-order Runge–Kutta integration routine, yielding solutions for electric field amplitude and phase at the crystal output in a spatially and temporally resolved form. It is important to note that the model allows initial misalignment of the seed and pump beams at the input face of the nonlinear crystal. This is an experimental optimization procedure frequently required to achieve the best overlap of the beams inside a crystal that exhibits walk-off for one of the beams.

Our system uses a pump laser based on an unstable resonator, with a complicated spatiotemporal pulse evolution.[12] We recorded the pulse shape by use of a scanning pinhole in the image plane of the pump pulse. A numerical fit has been obtained for the pump pulse shape, as shown in Fig. 2 in a 4-ns temporal window centered at the peak of the pump pulse intensity. We use the obtained pump spatial-and-temporal pulse shape in our numerical model.

4. Results

With the injected signal of 0.5 nJ, the measured output from the first BBO crystal was 1.8 μJ, (gain = 3700), and from the second BBO crystal we obtained

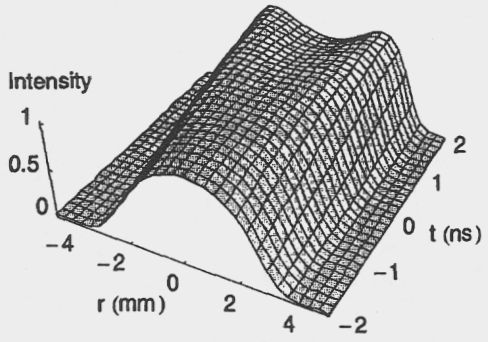

Fig. 2. Spatiotemporal evolution of the pump pulse originating in an unstable laser resonator. Shown is the normalized intensity as a function of the radial position r and time t, in a 4-ns time window.

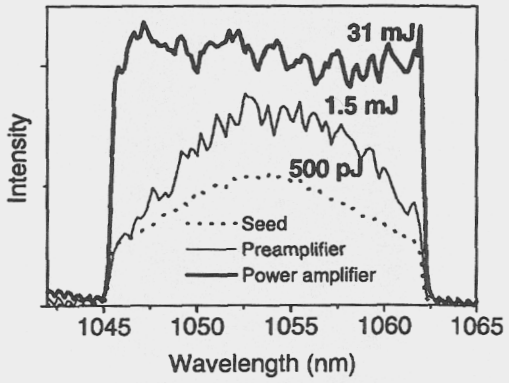

Fig. 4. Experimental extraction data from the final BBO amplifier. The lines are obtained from the numerical model.

1.5 mJ (gain = 830). Gain was optimized by adjustment of the transverse displacement between the seed and the pump on the front face of the first preamplifier crystal. The measured amplified signal pulse width, after passing through the preamplifier, was 3 ns at the clip points in the temporal domain. This is identical to the original stretched pulse width at its clip points in the temporal domain. Through adjustment of the wave plate, we could vary the amplified signal energy exiting the preamplifier by changing the pump intensity.

The expected small signal gain in the power amplifier is 160. We measured a maximum gain of 20 from the power amplifier operating in the regime of strong pump depletion. The signal beam is amplified to 31 mJ with 1.5 mJ of injected signal from the preamplifier. In Fig. 3 we show the extracted energy for several preamplifier outputs. The maximum pump-to-signal conversion efficiency in the power amplifier crystal is achieved when the preamplifier output is set to 1.5 mJ. The conversion efficiency of the pump to signal is 25%, by inclusion of only the pump energy contained in the temporal overlap of the pump with the signal. The overall pump-to-signal conversion efficiency in our OPCPA system is 6%.

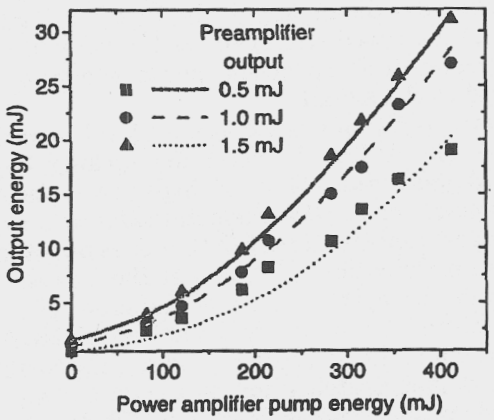

Fig. 3. Seed and amplified signal spectra from the preamplifier and the power amplifier. A spectral modification occurs in both preamplifier and power amplifier.

Our numerical model was applied to calculate the energy extraction in the final amplifier. We used the measured spatiotemporal characteristics of the pump and the signal in our calculation. The integration was performed on a 5-mm^2 spatial and 3-ns temporal window, on a grid of $50 \times 50 \times 1000$ points. The maximum intensity of the seed corresponded to the maximum intensity of the pump. The diameter of the signal in the final amplifier was 2.5 mm at its FWHM. As shown in Fig. 3, we observe fairly good agreement between the numerical model and the experimental results.

Figure 4 shows the measured spectra for stretched seed, the amplified signal from the preamplifier, and the amplified signal from the power amplifier. The measured bandwidth of the pulse is 16.5 nm at the spectral clip points in both the preamplifier and the power amplifier. This is consistent with the absence of bandwidth narrowing because of intrinsic OPA bandwidth. In our configuration we operate the power amplifier of the OPA in the depleted pump regime to obtain a large extracted energy. This is done at the expense of the recompressed pulse-contrast level, which remains limited by the hard clip on the spectrum occurring in the pulse stretcher. The amplified signal's spectral shape is modified by strong pump depletion in the power amplifier and resembles a top-hat shape in the central 70% of the beam diameter. The measured output stability of the signal is greatly improved in the regime of strong pump depletion,[14] reducing the effect of pump energy variation and temporal jitter. Because the stretched signal pulse width is relatively long, a timing jitter in excess of ~1 ns produces a significant modification of the amplified spectrum.

The near-field transverse intensity profiles for the pump, seed, and amplified signals are shown in Fig. 5. The incident seed beam's quality was $M^2 = 1.6 \pm 0.2$ in the sensitive direction and $M^2 = 1.2 \pm 0.2$ in the insensitive direction. The source of the measured imperfect beam quality of the seed is the hard beam clip that occurs on the stretcher lens and spherical and chromatic aberrations in the stretcher. We measured the beam quality of the signal and obtained

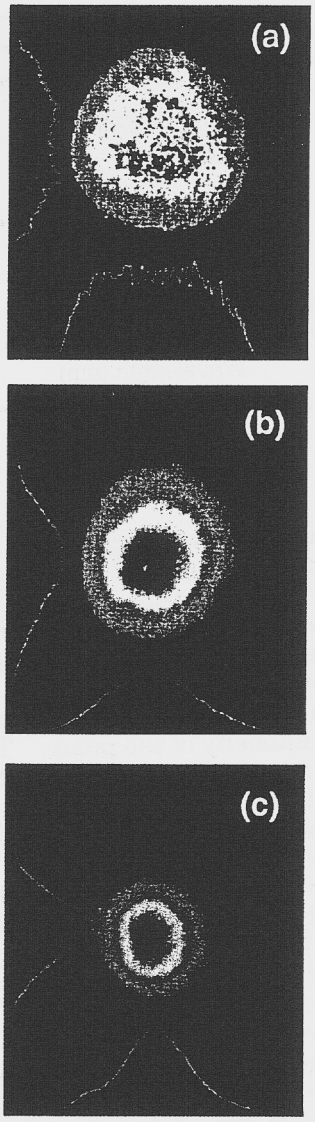

Fig. 5. Intensity profiles in the near field for (a) pump, (b) seed, and (c) amplified signals.

$M^2 = 2 \pm 0.2$ in the sensitive direction and $M^2 = 1.2 \pm 0.2$ in the insensitive direction. Optical parametric amplification is a process that conserves the signal beam quality to a high degree. However, the small diameter of the pump beam in the preamplifier leads to a strong effect of pump-beam walk-off in the crystal's sensitive direction. It is believed that this spatial modulation gives rise to the increase in the observed M^2 in the sensitive direction of the crystal.

As mentioned previously, we initially compressed the stretched 0.5-nJ seed pulses to 280-fs FWHM [Fig. 6(a)], limited by the spherical and chromatic aberrations occurring in the pulse stretcher, which contains a lens-based refractive telescope. The intensity autocorrelation of the recompressed pulse at an energy of 31 mJ is shown in Fig. 6(b). The recompressed amplified pulse duration is measured to be 310-fs FWHM, a 10% increase compared with the best-achieved seed recompression before amplification in the OPA. The recompressed pulse pedestal is decreased after amplification. This is probably the result of the modification of amplified spectrum in OPCPA operating in the regime of strong pump depletion. Because the exact impact of stretcher aberrations on the recompressed pulse shape is unknown, we used a conservative. Gaussian deconvolution factor to calculate the recompressed pulse width.

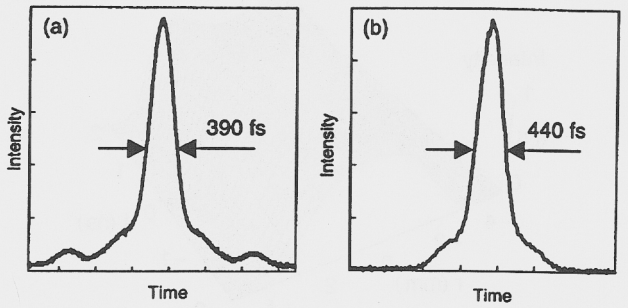

Fig 6. Recompressed pulse intensity autocorrelation for (a) seed pulses and (b) amplified pulses. Indicated is the FWHM of the autocorrelation trace. The deconvolved pulse width is (a) 280 fs and (b) 310 fs.

5. Conclusion

In summary, we demonstrated a successful use of optical parametric amplifiers for broadband, high-fidelity, chirped-pulse amplification. Our OPCPA produced a 50-fold increase in amplified pulse energy and a 10-fold improvement in efficiency compared with previous systems pumped by commercial Q-switched pump lasers.[15,16] Our improved efficiency is a result of several factors. Asymmetric splitting of the pump pulse is utilized to obtain a high gain from the preamplifier with a small fraction of the pump energy discarded. This is followed by the efficient power amplifier with a large pump beam and a short crystal, resulting in good spatial overlap between the pump and the signal. A walk-off-compensated double-crystal preamplifier design allows a relatively small pump beam to be used in the preamplifier. The pump beam is collimated to reduce the angular dephasing in the type I process in BBO. The increased stretched seed pulse width allows a greater fraction of the pump energy to be transferred to the signal.

The wavelength and pulse energy level from the demonstrated OPCPA is ideal for seeding high-energy Nd:glass amplifiers of high-power lasers. The peak power of 50 GW was obtained from a relatively compact and simple setup that does not utilize multipass amplification. We expect the focused intensity from our system to be of the order of 10^{16} W/cm^2. Although our system did not exploit the full bandwidth capabilities of type I nearly degenerate OPAs, we demonstrated high gain, conversion efficiency, and amplified pulse fidelity in OPCPA, which gives a viable cause for an all-OPA-based kilojoule-level ultrashort-pulse source.

We foresee several improvements that can lead to

better performance of our system. It is expected that a nondegenerate OPCPA at 800 nm will produce better efficiency because of the favorable splitting of the pump energy to the higher-frequency field. In addition, the availability of ultrashort-pulse sources will also permit the examination of the capability of OPCPA to produce pulses significantly shorter than those possible with our source. Finally, the development of appropriate pump lasers with a uniform spatial-and-temporal intensity profile and pulse width matched to the stretched pulse can produce better conversion efficiency. We are currently upgrading our system with an aberration-free, all-reflective stretcher, eliminating the bottleneck in our design that limits the recompressed pulse width. With a suitable high-energy pump laser and current compression grating technology, powers in excess of 10^{16} W are feasible with OPCPA.[8]

The authors thank M. D. Perry and P. S. Banks for their helpful comments. This research was performed under the auspices of the U.S. Department of Energy by Lawrence Livermore National Laboratory under contract W-7405-Eng-48.

References

1. D. Strickland and G. Mourou, "Compression of amplified chirped optical pulses," Opt. Commun. **56,** 219–221 (1985).
2. D. M. Pennington, C. G. Brown, T. E. Cowan, S. P. Hatchett, E. Henry, S. Herman, M. Kartz, M. Key, J. Koch, A. J. MacKinnon, M. D. Perry, T. W. Phillips, M. Roth, T. C. Sangster, M. Singh, R. A. Snavely, M. Stoyer, B. C. Stuart, and S. C. Wilks, "Petawatt laser system and experiments," IEEE J. Sel. Top. Quantum Electron. **6,** 676–688 (2000).
3. M. D. Perry, B. C. Stuart, P. S. Banks, M. D. Feit, V. Yanovsky, and A. M. Rubenchik, "Ultrashort-pulse laser machining of dielectric materials," J. Appl. Phys. **85,** 6803–6810 (1999).
4. D. Riedel, J. L. Hernandez-Pozos, R. E. Palmer, S. Baggott, K. W. Kolasinski, and J. S. Foord, "Tunable pulsed vacuum ultraviolet light source for surface science and materials spectroscopy based on high order harmonic generation," Rev. Sci. Instrum. **72,** 1977–1983 (2001).
5. M. Tabak, J. Hammer, M. E. Glinsky, W. L. Kruer, S. C. Wilks, J. Woodworth, E. M. Campbell, M. D. Perry, and R. J. Mason, "Ignition and high gain with ultrapowerful lasers," Phys. Plasmas **1,** 1626–1634 (1994).
6. R. A. Baumgartner and R. Byer, "Optical parametric amplification," IEEE J. Quantum Electron. **QE-15,** 432–444 (1979).
7. A. Dubietis, G. Jonušauskas, and. A. Piskarskas, "Powerful femtosecond pulse generation by chirped and stretched pulse parametric amplification in BBO crystal," Opt. Commun. **88,** 437–440 (1992).
8. I. N. Ross, P. Matousek, M. Towrie, A. J. Langley, and J. L. Collier, "The prospects for ultrashort pulse duration and ultrahigh intensity using optical parametric chirped pulse amplifiers," Opt. Commun. **144,** 125–133 (1997).
9. I. N. Ross, J. L. Collier, P. Matousek, C. N. Danson, D. Neely, R. M. Allott, D. A. Pepler, C. Hernandez-Gomez, and K. Osvay, "Generation of terawatt pulses by use of optical parametric chirped pulse amplification," Appl. Opt. **39,** 2422–2427 (2000).
10. S. P. Velsko and W. F. Krupke, "Applications of high-average power nonlinear optics," in *Nonlinear Frequency Generation and Conversion,* M. C. Gupta, W. J. Kozlowski, and D. C. MacPherson, eds., Proc. SPIE **2700,** 6–17 (1996).
11. D. A. Kleinman, "Theory of optical parametric noise," Phys. Rev. **174,** 1027–1040 (1968).
12. A. A. Isaev, M. A. Kazaryan, G. G. Petrash, S. G. Rautian, and A. M. Shalagin, "Evolution of Gaussian beams and pulse stimulated emission from lasers with unstable resonators," Sov. J. Quantum Electron. **5,** 607–614 (1975).
13. D. J. Armstrong, W. J. Alford, T. D. Raymond, and A. V. Smith, "Parametric amplification and oscillation with walkoff-compensating crystals," J. Opt. Soc. Am. B **14,** 460–474 (1997).
14. S. K. Zhang, M. Fujita, M. Yamanaka, M. Nakatsuka, Y. Izawa, and C. Yamanaka, "Study of the stability of optical parametric amplification," Opt. Commun. **184,** 451–455 (2000).
15. J. Collier, C. Hernandez-Gomez, I. N. Ross, P. Matousek, C. N. Danson, and J. Walczak, "Evaluation of an ultrabroadband high-gain amplification technique for chirped pulse amplification facilities," Appl. Opt. **38,** 7486–7493 (1999).
16. S. K. Zhang, M. Fujita, H. Yoshida, R. Kodama, H. Fujita, M. Nakatsuka, Y. Izawa, and C. Yamanaka, "Study on high gain broadband optical parametric chirped pulse amplification," in *High-Power Lasers in Energy Engineering,* K. Mima, G. L. Kulcinski, and W. Hogan, eds., Proc. SPIE **3886,** 588–595 (2000).

Cascaded-Optical Parametric Amplification for Extreme Contrast Enhancement

B. Wattellier, I. Jovanovic, and C. P. J. Barty
Lawrence Livermore National Laboratory, Mail Code L-490, 7000 East Avenue, Livermore, California 94550
wattellier1@llnl.gov and barty1@llnl.gov

Abstract: We demonstrate for the first time a straightforward technique for complete prepulse elimination in chirped pulse amplification systems, using two cascaded optical parametric amplifiers.

Prepulses are of great concern in high-power laser chains: if their intensity is high enough they can heat and/or destroy a target before the arrival of the main pulse. For petawatt-class lasers focal intensities can be of order 10^{21} W.cm^{-2} and above and thus a prepulse contrast of at least 10^8 is required to avoid preionization of solid targets.

Regenerative preamplification does not meet this requirement. A small fraction of the regeneratively amplified pulse energy leaks through the rejection polarizer before the main pulse. A typical contrast at the output of a regenerative amplifier is of the order of 10^3. Optical parametric chirped pulse amplification (OPCPA)[1] is well known to improve contrast during preamplification since amplification only occurs in the time window defined by the pump pulse. However, OPCPA does not remove prepulses but only decreases their relative peak intensity by a factor equal to its gain, typically 10^6 to 10^7.

Numerous techniques to enhance prepulse contrast have been investigated [2]. In most cases, they apply only to specific laser regimes. For example, Pockels cells, the most commonly used techniques to filter prepulses, are limited by the size and damage threshold of the crystal they use and require synchronized timing to be effective. Other techniques utilize non-linear effects which require high intensities and cannot be applied at low energy, such as just after an oscillator.

In this paper, we present for the first time a technique which is uniquely capable of selecting one pulse out of a stretched, mode-locked pulse train, in principle with near-infinite discrimination with respect to the remainder of the pulse train. The technique (see Fig. 1) is based on cascaded, 2-stage, optical parametric amplification in which the idler pulse generated in the first stage is spatially separated from the signal pulse and is used as the input signal pulse for the second stage.

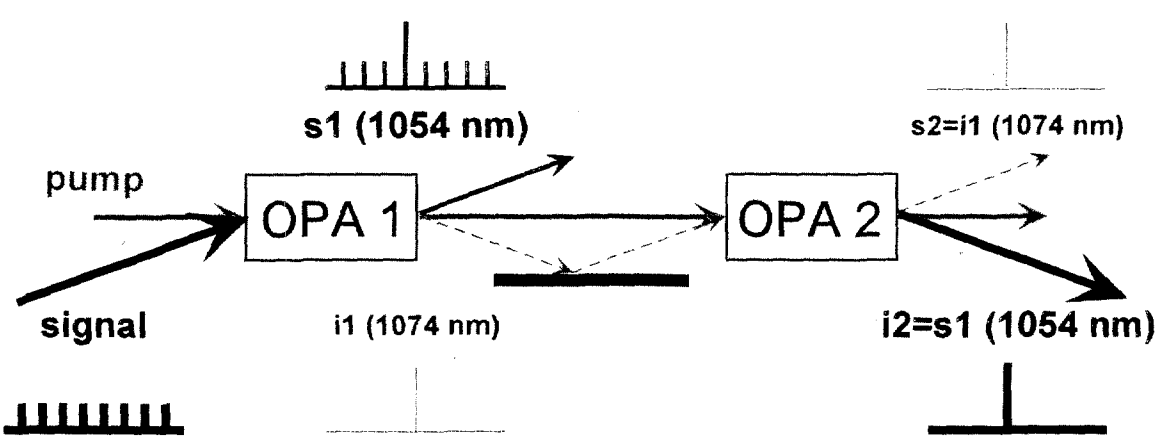

Fig. 1 – Principle of C-OPA. (s_1,i_1) and (s_2,i_2) represent signal and idler in two OPA stages.

This cascaded process reproduces the stretched-pulse duration and spectral phase of the 1st stage input signal pulse (see Fig. 2 and [3]). At once the process can provide significant, broad-bandwidth gain of several orders of magnitude and spatial separation of the output from the remainder of the input pulse train. This cascaded OPA (C-OPA) technique has potentially infinite contrast enhancement, limited only by parametric fluorescence and how well idler and signal can be separated after each of the two C-OPA stages.

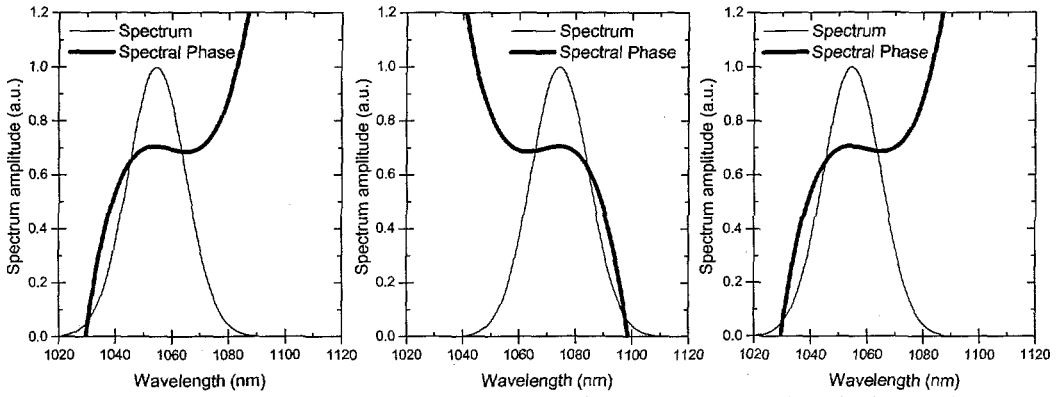

(a) signal 1 @ 1054 nm (b) idler 1=signal 2 @ 1074 nm (c) idler 2=signal 1 @ 1054 nm

Fig. 2 – Schematic of the evolution of spectral phase dispersion in C-OPA, with simulated input spectrum and exagerated spectral phases. Due to phase conjugation process, the sign of even orders of the spectral dispersion is inverted from the signal 1 (a) to the idler 1 (b), whereas the sign of dispersion of the odd orders is conserved. This makes the idler pulses not recompressible to Fourier transform-limited pulse durations. However, when this idler 1 is sent into a second OPA, the generated idler 2 (c) has only its even orders inverted back, so that it is potentially compressible to Fourier transform-limited pulse duration, just like the original signal pulse. The compressibility limit is determined by the phase accumulated from the pump phase aberrations in the two OPAs.

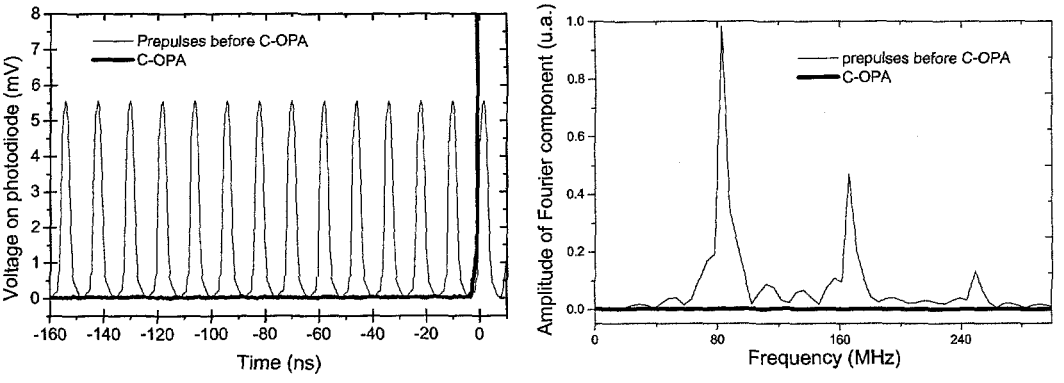

(a) oscilloscope traces (b) time-FFT of (a) traces

Fig. 3 – Experimental verification of C-OPA principle. (a) Direct measurement of prepulses before and after C-OPA. (b) A FFT of the oscilloscope traces shows that the ratio of the amplitudes at ~80 MHz (the repetition rate of the oscillator) to background noise is at least 33 dB. From the measured dynamic range of the intrusmentation and the gain of the C-OPA device, it is possible to estimate that prepulse contrast enhancement is greater than $6x10^8$, from this first measurement.

In order to evaluate the contrast enhancement, we measured the intensity on a photodiode at the output of our stretcher and at the output of our C-OPA. Starting from the 1:1 contrast of the oscillator pulse train, we measured a contrast enhancement of 10^9 with an OPA gain of 10^6. Our measurements were limited by the signal-to-noise ratio on the measurement of the oscillator pulse train (see Fig. 3).

In conclusion, we have demonstrated a new technique to remove all prepulses. The major attraction of this technique is its versatility: since it does not rely on non-linear effects on the signal pulse itself, it can be operated at any energy level and with either stretched or compressed pulses. It can be used as a preamplifcation stage or as a high-contrast, large-bandwidth pulse selector.

References

[1] A. Dubietis, G. Jonusauskas, and A. Piskarskas, "Powerful femtosecond pulse generation by chirped and stretched pulse parametric amplification in BBO crystal", Opt. Commun. 88(4-6), 437-40 (1992).

[2] W. Yanjie and B. Luther-Davies, "Optical-parametric-amplification-based prepulse eliminator for a chirped-pulse-amplification Nd:glass laser", J. Opt. Soc. Am. B 11(9), 1531-8 (1994).

[3] A. Yariv, D. Fekete, and D.M. Pepper, "Compensation for channel dispersion by nonlinear optical phase conjugation", Opt. Lett. 4(2), 52-4 (1979).

Feasibility study of thin Fresnel lens use in multi-kJ, short pulse laser systems

Igor Jovanovic, Sham N. Dixit, Benoit Wattellier, Mark R. Hermann, and C. P. J. Barty
Lawrence Livermore National Laboratory, Mail Code L-490, 7000 East Avenue, Livermore, California 94550
jovanovic@llnl.gov, barty1@llnl.gov

Abstract: Recently-developed, thin-Fresnel-lens technology offers the potential for transmissive focusing of high-peak-power, ultrashort-duration laser pulses. Calculations of spectral blurring effects of thin Fresnel lenses when used to focus ultrashort, high-energy laser pulses are presented.
©2003 Optical Society of America

High-peak-power, short-pulse laser systems have traditionally used reflective optics to focus laser pulses to avoid linear and nonlinear phase accumulation inherent to refractive optics. Typical recompressed pulses from a large Nd:glass laser have an unfocussed intensity of order 1 TW/cm^2. When incident on a transmissive fused silica optic, such pulses would produce a B-integral of ~20 cm^{-1}-200 cm^{-1}. High B-integral (>1) will lead to focal spot distortion, and possibly to self focusing and damage of the focusing optic. Reflective parabolic focusing optics eliminate the B-integral problem and are widely used in short pulse laser systems. However, the surface quality requirements for a reflective optic are typically much higher, and their tolerance to beam pointing and divergence is up to one order of magnitude lower than for a corresponding transmissive optic.

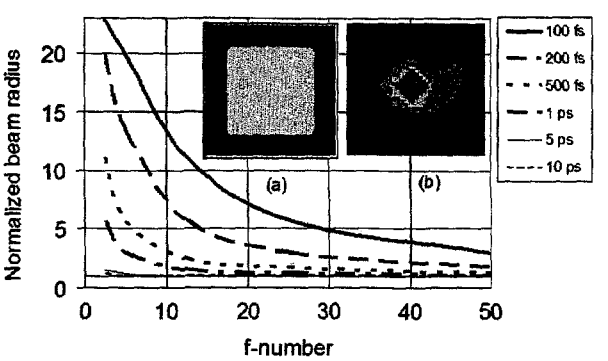

Fig. 1. Transverse focal spot blurring as a function of the Fresnel lens f-number, for several representative pulse widths. Calculated broadband beam radius is normalized to the monochromatic focused beam radius. Inset: (a) NIF near-field amplitude profile, (b) NIF focal spot, for f/#=10 and 100-fs pulse duration.

Recently, Lawrence Livermore National Laboratory has developed the capability to produce, high quality thin Fresnel lenses. [1] Lenses with thicknesses <200 μm and apertures up to 60 cm have been shown to be capable of producing diffraction-limited beam quality focal spots. Transmission through such lenses would produce negligible B-integral (<<1). However, chromatic aberrations inherent to Fresnel lenses will distort the focal spot size and pulse duration. Such distortions will be strong functions of the input pulse bandwidth and the f-number of the optical system. Next generation large laser systems such as the National Ignition Facility (NIF) in the US and the Laser MegaJoule (LMJ) in France have the potential to produce multi-kJ short pulses and operate with high f-number final optics. In this paper we numerically evaluate the feasibility of thin Fresnel lens use for focusing of high-power laser pulses.

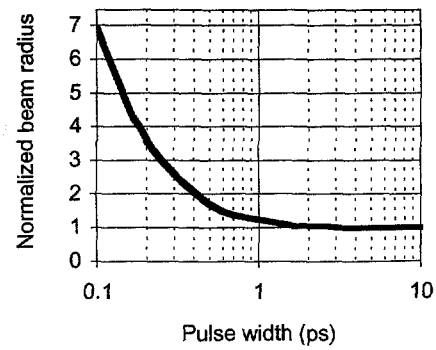

Fig. 2. Transverse focal spot blurring as a function of transform-limited pulse width, for f/#=17. Calculated broadband beam radius is normalized to the monochromatic focused beam radius.

The chromacity of the Fresnel lens results in reduced transverse focusability of a spectrally broadband beam. In Figs. 1 and 2 we show representative results of our calculations for transverse focal spot blurring assuming an input beam profile similar to that which will be produced by NIF or LMJ and a bandwidth corresponding to a 2-ps transform-limited pulse. A beam incident on a Fresnel lens also experiences radially variable transit time to focus. We calculated the pulse duration at focus for an incident Gaussian temporal pulse (Fig. 3).

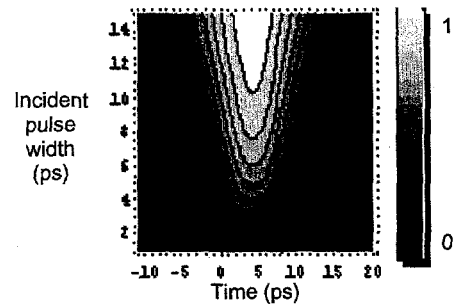

Fig. 3. Focused pulse intensity, for a range of incident pulse durations. Pulse intensity is normalized to the intensity of an ideally focused monochromatic beam.

If the criteria for acceptable pulse focusing is defined as <50% spatial blurring, the minimum acceptable f-number for focusing of 1-ps pulses is ~12.5. For a <50% decrease in peak intensity of an incident 0.4-m diameter, 1053-nm pulse, focused with f_0=8 m, the minimum pulse width allowed on the lens is ~4 ps. While those requirements may be too restrictive for some short-pulse laser systems, they are acceptable for applications such as hard x-ray generation with laser based relativistic electrons [2] and could be applicable to low energy applications such as precision micromachining, with high-average power CPA systems. Practical limits as a function of pulse bandwidth and lens f-number for a variety of short pulse systems will be presented.

References

1. I. M. Barton, J. A. Britten, S. N. Dixit, L. J. Summers, I. M. Thomas, M. C. Rushford, K. Lu, R. A. Hyde, and M. D. Perry, Fabrication of Large-Aperture Lightweight Diffractive Lenses For Use in Space, Appl. Opt. **40**, 447-451 (2001).
2. T. Guo, Ch. Spielmann, B. C. Walker, and C. P. J. Barty, Generation of hard X-rays by ultrafast terawatt lasers, Rev. Sci. Instrum. **72**, 41-47 (2001).

Large Aperture, High-Efficiency Multilayer Dielectric Reflection Gratings

J. A. Britten, S. J. Bryan, L. J. Summers, H. T. Nguyen, B. W. Shore
Lawrence Livermore National Laboratory, Livermore Ca 94550
(925) 423-7653, Fax (925) 422-5537, britten1@llnl.gov
O. Lyngnes
Cascade Optical Corporation, Santa Ana, CA 92705

Abstract: We have designed and fabricated a 355 x 150 mm multilayer dielectric diffraction grating, 1800 l/mm for 1030 nm light, that exhibits >99% diffraction efficiency and a diffracted wavefront flatness of <0.15 λ. This grating is an enabling component of a 2 ps, high rep-rate machining laser currently in operation at LLNL.
©2000 Optical Society of America
OCIS codes: (050.0050) Diffraction gratings, (220.0220) Optical fabrication, (140.0140) Laser optics

1. Introduction

The successful design and fabrication at the Lawrence Livermore National Laboratory (LLNL) of meter-sized high-efficiency reflection gratings was an important enabling technology for the pulse compressor of the LLNL Petawatt Laser [1,2]. These gratings, now becoming available for pulse compressors in other institutions, rely on the reflecting properties of a gold coating to achieve their needed high efficiency. As interest grows in increasing the intensity of laser pulses, the absorption of light by a metal surface becomes a limiting factor in the power obtainable from a pulse compressor. We have been working for some time to develop high-efficiency gratings from all-dielectric materials [3-7] .

2. Grating Design

The grating used for this particular high average-power laser system serves as the stretcher and compressor. The pitch (1800 l/mm), central wavelength (1030 nm) and incidence angle (63°) were specified as part of the overall system design. Design of the grating involves consideration of the reflective properties of the stack coupled with the diffractive properties of a surface relief grating etched into the uppermost layer of this stack. The overall design is optimized such that: 1) the MDG gives maximum diffraction efficiency into the –1 reflected order at use wavelength and angle, and 2) the multilayer stack exhibit antireflective or at least neutral reflective properties at the exposure wavelength and angle. This second criteria is to prevent back reflections from creating standing waves and resultant pattern degradation in the photoresist film during the laser interference lithography process.

Tantala/Silica were chosen as the high/low refractive index layers for the multilayer stack. The grating is etched into a top SiO_2 layer of a specified thickness. The layer immediately underlying this grating layer is of Al_2O_3, a material which is resistant to the etch process, thus providing more process latitude for the transfer etch. The thickness of the Al_2O_3 layer is determined by the optimized optical design.

Figure 1 shows a map of the –1 order diffraction efficiency as a function of angle and duty cycle (ratio of grating width to grating period)., for a fixed wavelength and groove height. The most sensitive parameter in terms of manufacturability is seen to be the duty cycle; a value of less than 0.35 is required to obtain the highest efficiency.

3. Grating Fabrication

Witness and production substrates were coated with a multilayer stack according to the optimized design using ion-assisted e-beam evaporation. These substrates were then vapor-primed with HMDS to promote resist adhesion, then coated with ~500 nm of a high-contrast photoresist, and softbaked at 100C for 90 min. in a convection oven. Witness parts were spin coated, and the large production parts were coated using a meniscus coater [8] . The parts were exposed to interfering collimated beams from a fringe-stabilized single-frequency 413nm Kr-ion laser, using LLNL's meter-scale laser interference lithography station. Exposure and development with a liquid base solution development, resulted in surface relief gratings in the resist layer, cleared to the top SiO_2 layer and of the proper duty cycle. Grating profiles were measured nondestructively using atomic force microscopy (AFM) at the end of

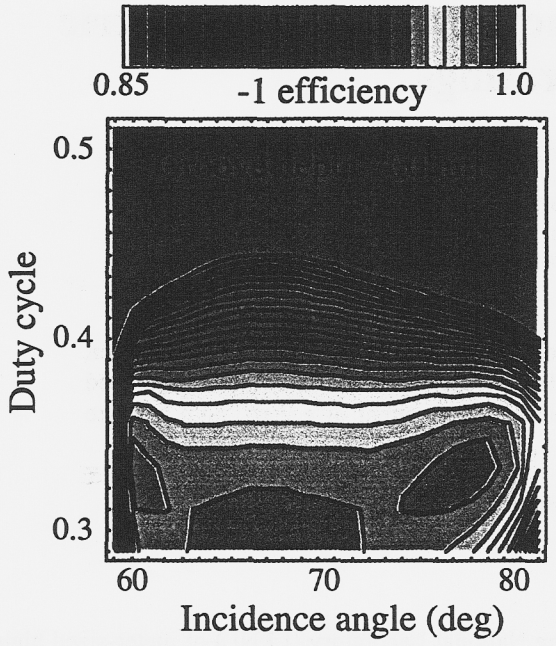

Figure 1. Theoretical efficiency of dielectric grating design as function of incidence angle and duty cycle, for fixed grating height of 700 nm.

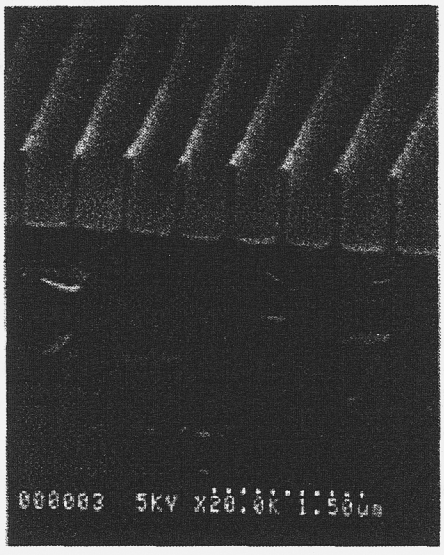

Figure 2. SEM of witness MDG.

the develop, step to assure clearance to the substrate and the correct duty cycle. Re-patterning could be done if grating profiles were not acceptable after the exposure/development step. Q/A'd parts were then hardbaked to cure the resist mask for subsequent transfer etching.

The grating profiles were transfer-etched into the topmost SiO_2 layer in an Oxford Instruments ion-beam etcher with a 40 cm ion gun. The procedure was optimized using planetary motion of the target platen and masking between the source and the platen to achieve ion-current uniformity over >30 cm radial aperture. The system was configured to run as a reactive ion beam etcher, by introducing the active chemical etching species along with Ar in the ion source. Prior to etching into the SiO_2 layer an O_2 /Ar 'descumming' process was performed in the etcher to ensure that the photoresist was completely removed in the grating grooves. This resist strip step was also performed subsequent to the etching to remove the remaining photoresist mask. The SiO_2 etching was performed using CHF_3 as the fluorine source. SiO_2 etch rates of ~2 nm/min were typically achieved in this system.

Ride-along witness parts coated with identical multilayer coatings were destructively examined using scanning electron microscopy (SEM). An example of the microstructure one ride-along part is shown in Figure 2

4. Grating Performance

A photograph of the finished grating is shown in Figure 3. Figure 4 shows the –1 order diffraction efficiency as a function of angle for 1030 nm, TE polarized light, taken as a series of spot measurements using a 2-channel ratioing power meter. Efficiencies of > 99% are measured near the use angle of 63° (the Littrow angle for this grating is 68° at 1030 nm). The spatial uniformity of the grating efficiency could not be measured at 1030, but a scanning photometric efficiency map was done using a portable 1064 laser at 71° incidence angle. This is shown in Figure 5. The average efficiency of 89.5 agrees well with model predictions for this wavelength and angle. The efficiency is extremely uniform spatially, exhibiting a standard deviation of 0.55%. This is attributable to the etch-stop layer and tight control of our areal exposure uniformity.

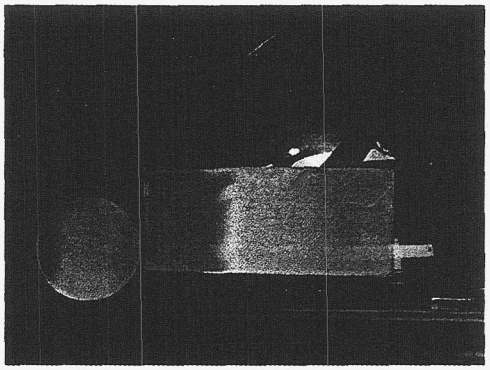

Figure 3. Photograph of 355x150 mm MDG also shown with 150 mm round grating of same design

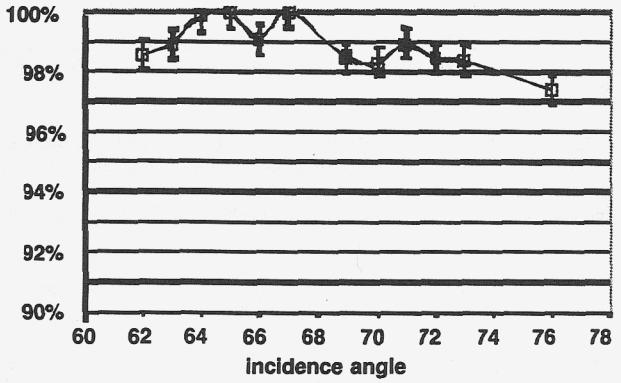

Figure 4. –1 order diffraction efficiency as function of angle for 130 nm, TE polarization.

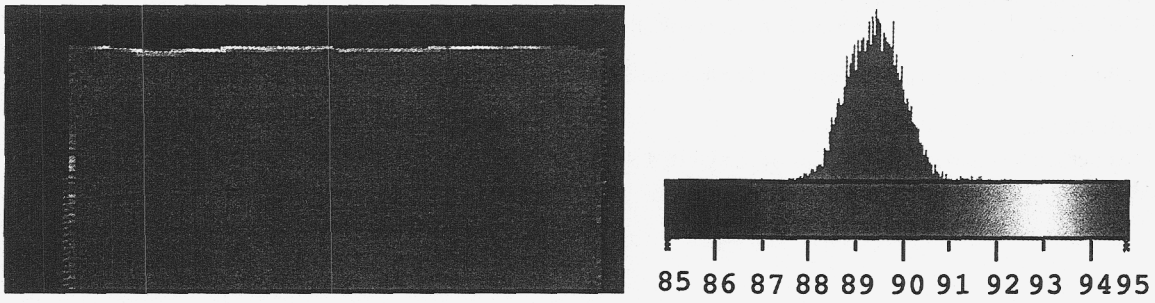

Figure 5. Diffraction efficiency map at 1064, 71 deg, TE polarization. Average = 89.%, σ = 0.55%, 9900 data points.

The –1 order diffracted surface figure of this part, measured at 632 nm, is shown in Figure 6. This data, converted to use wavelength, results in a diffracted wavefront of ~0.15λ based on an average of lineouts across the long axis of the grating.

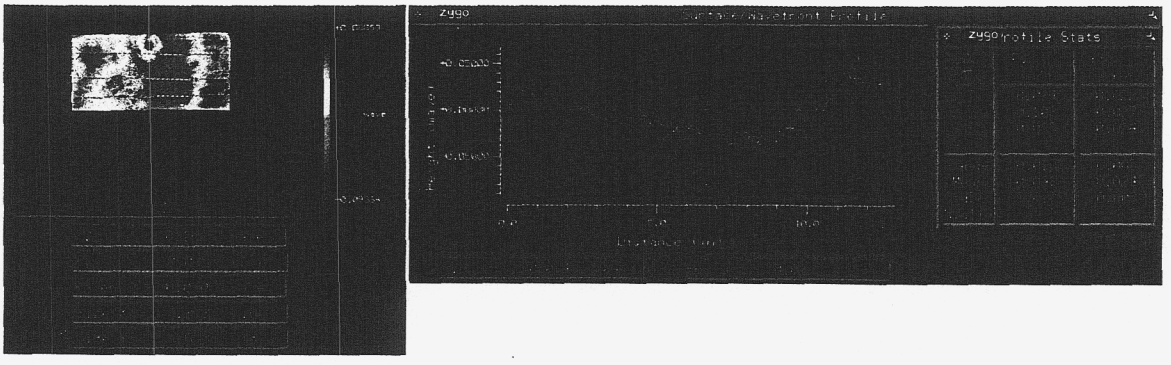

Figure 6. Full-aperture diffracted surface figure of grating at 633 nm.

4. Summary

This grating met or exceeded all specifications for its use in a short-pulse machining laser. The compressor throughput achieved by its high efficiency has allowed the realization of specified power to target without risk of thermal lensing in the upstream amplifiers.

5. References

[1] D. M. Pennington, M. D. Perry, B. C. Stuart, R. D. Boyd, J. A. Britten, C. G. Brown, S. M. Herman, J. L. Miller, H. T. Nguyen, B. W. Shore, G. L. Tietbohl and V. Yanovsky, "Petawatt laser system" Proceedings of the SPIE - The International Society for Optical Engineering **3047**, 490-500 (1997)

[2] M. D. Perry, D. Pennington, B. C. Stuart, G. Tietbohl, J. A. Britten, C. Brown, S. Herman, B. Golick, M. Kartz, J. Miller, H. T. Powell, M. Vergino and V. Yanovsky, "Petawatt laser pulses" Optics Letters **24**, 160-162 (1999)

[3] M. D. Perry, J. A. Britten, H. T. Nguyen, R. D. Boyd and B. W. Shore, U. S. Patent 5,907,436, "Multilayer Dielectric Diffraction Gratings" (1999)

[4] M. D. Perry, R. D. Boyd, J. A. Britten, D. Decker, B. W. Shore, C. Shannon, E. Shults and L. Li, "High-efficiency multilayer dielectric diffraction gratings" Optics Lett. **20**, 940-942 (1995)

[5] B. W. Shore, M. D. Feit, M. D. Perry, R. D. Boyd, J. A. Britten and L. Li, "Electric field enhancement in metallic and multilayer dielectric gratings", in *Solid State Lasers for Application to ICF*, ed. M. André and H. T. Powell, SPIE Proceedings **2633**, 709-713

[6] B. W. Shore, M. D. Perry, J. A. Britten, R. D. Boyd, M. D. Feit, H. Nguyen, R. Chow, G. Loomis and L. Li, "Design of high efficiency dielectric reflection gratings" JOSA A **14**, 1124-1136 (1996)

[7] J. A. Britten, M. d. Perry, B. W. Shore, R. D. Boyd, G. E. Loomis and R. Chow, "High-efficiency dielectric multilayer gratings optimized for manufacturability and laser damage threshold" in *27th Annual Boulder Damage Symposium: Laser-Induced Damage in Optical Materials* 2714, ed. H. E. Bennett, A. H. Guenther, M. R. K. Kozlowski, B. E. Newman and M. J. Soileau (Proc. SPIE, 1996), pp. 511-520

[8] J. A. Britten, "A simple theory for the entrained film thickness during meniscus coating" Chemical Eng. Commun. **120**, 59-71 (1993)

6. Acknowledgements

This work was performed under the auspices of the United States Department of Energy by the Lawrence Livermore National Laboratory under contract no. W-7405-Eng-48.

Fabrication of Beam Sampling Gratings for the National Ignition Facility (NIF)

June Yu, Jerald A. Britten, Leslie Summers, Sham Dixit,
Curly R. Hoaglan, Michael D. Aasen, Richard P. Hackel, Rahul R. Prasad
Lawrence Livermore National Laboratory
P.O.Box 808, L-482, Livermore, CA 94550
(925) 423-0418 (phone), (925) 424-2495 (fax), yu4@llnl.gov

Abstract: Beam sampling gratings (BSG) have been successfully fabricated to provide a small sample of the NIF 351nm high power laser beams. The sampled fraction will be used to determine the laser beam energy on target and to achieve power balance on all 192 NIF beams.

Achieving power balance on all 192 NIF beams requires precise power measurement of each individual beam of the 192-beam system. The BSG, which is a shallow focusing grating etched into a 43cm square fused silica substrate, has been developed to divert a small amount of the laser light into a diagnostic package containing the 351nm energy calorimeter and power sensor. It is located downstream of all the optical components with the exception of the debris shield. This location is selected to minimize laser damage threats to down-stream optics due to the beam modulations caused by the interference among various diffracted orders. Both main and sampled beams go through the same optics, thus ensuring a true measurement of energy-to-target. The BSG is specified to have 0.1-0.3% diffraction efficiency with less than 5% RMS diffraction uniformity in order to achieve laser power and energy balance requirements.

To fabricate the BSG, the NIF diffractive optics plate (DOP) is coated with photoresist. The DOP plates are 1cm thick, 43cm x 43cm fused silica substrates. A two-beam laser interference lithography exposure system is used to write the BSG pattern into the photoresist. In this exposure setup, a diverging F/11 beam is made to interfere with a diverging F/1.7 beam. The exposure geometry is an exact analog of the playback geometry in the NIF final optics assembly, and the exposure wavelength, 351nm AR-ion line, is sufficiently close to the NIF 3w wavelength to provide a diffraction-limited focal spot for the sample beam. Figure 1 is a schematic diagram of the BSG pattern.

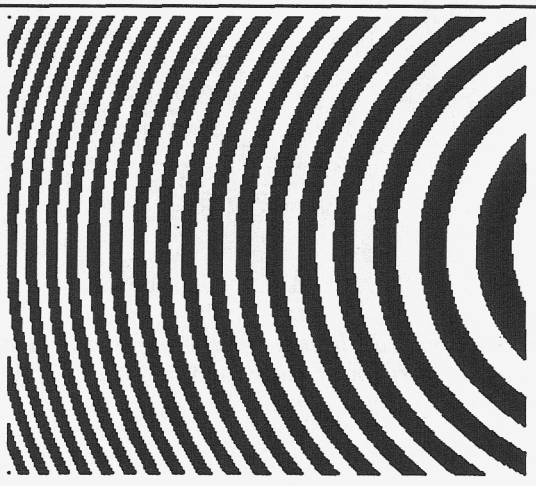

Figure 1. Schematic of the beam sampling grating groove profile

The grating period ranges from 1 to 3 microns. After exposure, the BSG pattern in photoresist is transferred into the fused silica substrate by exposing the substrate to buffered oxide etch solution. Following the etch step, the photoresist is finally removed from the substrate, leaving a very shallow grating (~20nm) in the fused silica substrate with ~ 0.3% diffraction efficiency. Meeting the 5%RMS diffraction efficiency uniformity specifications across the 43cm x 43cm part requires a number of innovative process developments. A novel wet processing machine has been designed and built to provide uniform photoresist coat and precision etch across the part (see Figure 2.) The ability to achieve better than 10% peak-to-valley intensity variation in the exposure beams is also crucial to obtaining diffraction uniformity across the substrate.

Figure 2. Wet processing machine used to apply uniform layer of photoresist to the 43cm x 43cm substrate and to obtain controlled etch with sub-nanometer uniformity into the fused silica substrates.

Figure 3 shows a fabricated BSG. After the grating has been imprinted, a scanning photometer is used to simultaneously measure the transmitted and diffracted energy. These measurements are used to verify the spatial uniformity of the diffraction grating and to accurately determine the sampling efficiency. Figure 4 illustrates the measurement result for a BSG with 0.27% diffraction efficiency and 3.3 % diffraction uniformity. Early laser damage tests done on sub-scale BSG's indicate that they will satisfy the NIF damage fluence requirements during initial activation. In addition, laser conditioning and mitigation processes are being developed for BSG's to ensure that the optics will meet the NIF lifetime operations goals of $8J/cm^2$ without compromising BSG performance.

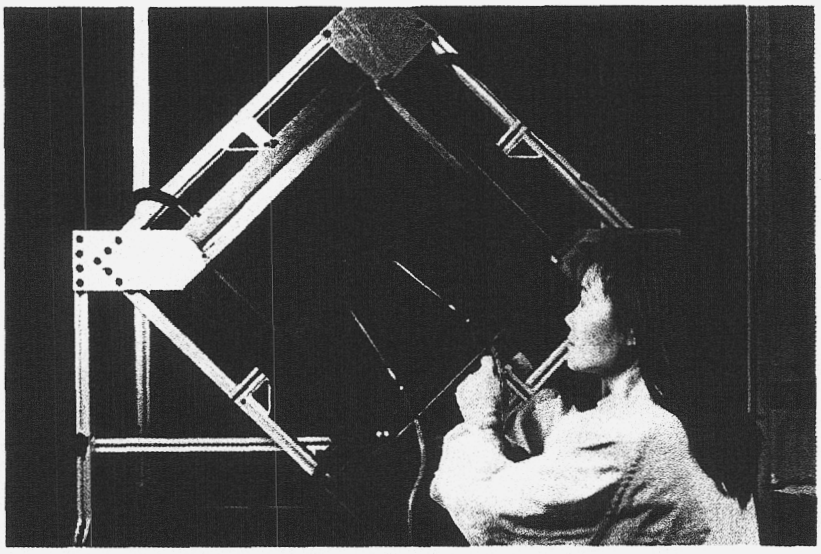

Figure 3. A completed BSG

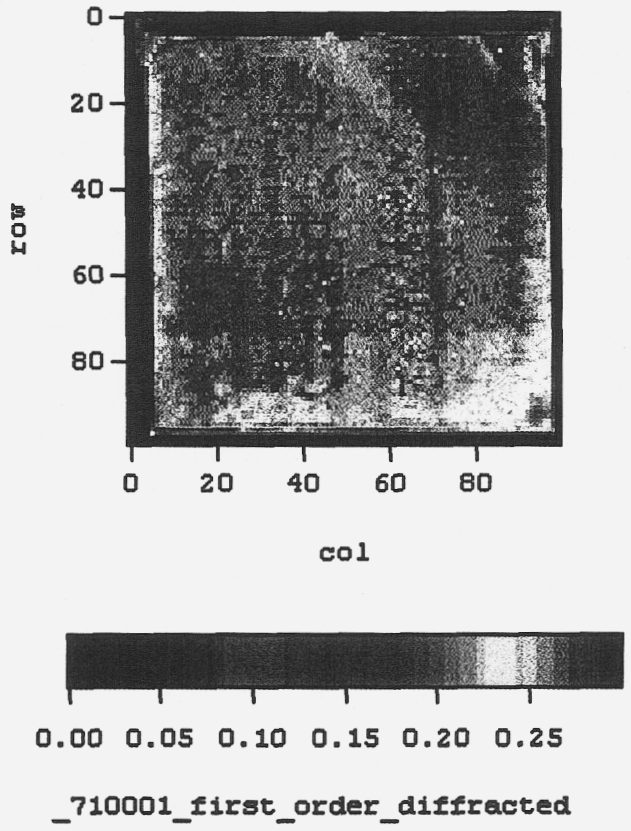

Figure 4. Photometer scan of the fabricated BSG shows the part to have 0.27% diffraction efficiency with 3.3% diffraction uniformity.

A.E. WYNNE
B.C. STUART✉

Rate dependence of short-pulse laser ablation of metals in air and vacuum

Lawrence Livermore National Laboratory, P.O. Box 808, L-477, Livermore, CA 94550, USA

ABSTRACT Ablation rates of aluminum and stainless steel are studied as a function of fluence, hole depth, pulse duration and ambient pressure (air vs vacuum). We find a weak rate dependence on pulse duration from 150 fs to 500 ps, and a strong rate dependence on hole depth due to surface roughness. Machining in air plays an important role in deep holes, but has a weaker influence on initial surface ablation rates. Oxidation greatly reduces drilling rates for deep holes in aluminum.

1 Introduction

Ultrashort-pulse lasers have been shown to be valuable tools for precise machining of many materials [1–13]. Due to the extremely short duration of the laser pulse, energy is locally deposited into the electrons on a timescale much faster than the transfer of this energy to the bulk of the material. The result is a cutting tool that can machine any material with minimal collateral damage or heat-affected zone.

Notwithstanding the success of these lasers in creating very clean and precise cuts in materials, there is still much to be understood about the details of the material removal. In metals, many interesting features appear in the progression of drilling holes or cutting slots with short-pulse lasers [14]. It is still extremely difficult to model the ablation process in metals, especially as the hole deepens and changes from a 1-D to 3-D problem. It is important to understand and include such effects as surface structure (atomic to macroscopic scale), temperature-dependent absorption, wall effects (waveguiding, eddy currents), hole geometry, background gas, and material redeposition.

In this paper, we examine some of the material removal rates and hole morphologies for short-pulse laser drilling in metals. We have chosen two common metals, 304 stainless steel and 7075 aluminum, for a full characterization of ablation rate as a function of pulse duration, fluence, hole depth and environment (air vs vacuum). These results are a start to being able to understand and model this very complicated ablation process.

✉ Fax: +1-925/422-5537, E-mail: stuart3@llnl.gov

2 Experimental set-up

For the following experiments, we used a chirped-pulse-amplification (CPA) [15] Ti:sapphire laser system. The system delivered pulses at a repetition rate of 1 kHz with energies up to 1.5 mJ at a wavelength of 810 nm. Because of the CPA configuration, the pulse width could be varied from 150 fs to 40 ps without changing any other parameters. When a 500-ps pulse was needed, the uncompressed pulse was intercepted and sent to the drilling chamber. We collected data at 150 fs, 1.5 ps, 20 ps and 500 ps.

We used a 34-cm-focal-length lens to focus the Gaussian beam to a nominally round spot. The part was placed before the beam focus in order to achieve an effective spot size of 150 μm diameter ($1/e^2$ intensity). We used circular polarization to avoid the uneven drilling effects of static linear polarization [16]. The beam hit the part at normal incidence, and the fluence was changed by adjusting the energy while the spot size remained constant. The materials used were 1-mm-thick coupons of 304 stainless steel and 7075 aluminum. When drilling in vacuum, the pressure in the chamber was approximately 10 mtorr. A fast mechanical shutter was used to select a defined number of pulses. For each fluence and pulse-width chosen, ten holes were drilled, two holes for each of five different time intervals (number of pulses). The times and corresponding number of pulses chosen varied with fluence to achieve similar depths at all fluences. The depths of the two holes for each number of pulses were averaged in each case and used to determine the drilling rate for that number of pulses. For breakthrough detection, an imaging set-up was installed at the rear end of the chamber. A lens imaged the plane of the part onto a CCD. Breakthrough was timed by first detection of light on the camera after the shutter was opened.

All holes were measured with a Nikon measuring microscope (MM-40) with an encoded Z-stage connected to a digital readout (Quadra-Chek 2000). Depths were measured by focusing at the surface of the part, zeroing the readout, and then focusing at the bottom of the deepest part of the hole. We estimated the error in depth to be ±3 μm. The fluence was determined by measuring the pulse energy and the spot size at an equivalent image plane. The absolute error in fluence was estimated to be 20% due to laser energy fluctuations and beam-diameter measurement error. Scanning electron micro-

scope (SEM) images were taken of selected holes to assess hole morphology and growth progression.

3 Ablation rate vs depth

We measured ablation rates as a function of depth at various fluence levels to determine the initial hole drilling progression. Instantaneous values of the drilling rate (nm/pulse) were found by measuring the hole depth as a function of the number of pulses (Fig. 1a), fitting the curve to a smooth function including (0 depth, 0 pulses), and differentiating the curve to obtain the rate (Fig. 1b). Figure 1 shows the data for 7075 aluminum in vacuum with 150-fs pulses at 0.5 J/cm^2. We did not try to measure depths greater than 150 μm (1:1 ratio) in order to approximate 1-D ablation conditions. As will be seen below, this assumption was not entirely valid.

Figure 2 shows the instantaneous ablation rate as a function of depth for 150-fs pulses on 7075 aluminum for various fluence levels in air (Fig. 2a) and vacuum (Fig. 2b). Several things can be noticed from these curves. At low fluence, the rates drop very rapidly over the first 10–20 μm. This may seem surprising since 10-μm depth over a 150-μm diameter should not make much of a difference. This, however, assumes that the surface remains relatively smooth. In reality, the surface roughens very quickly (within the first 100 pulses), as discussed below. The reduced effective fluence on the walls

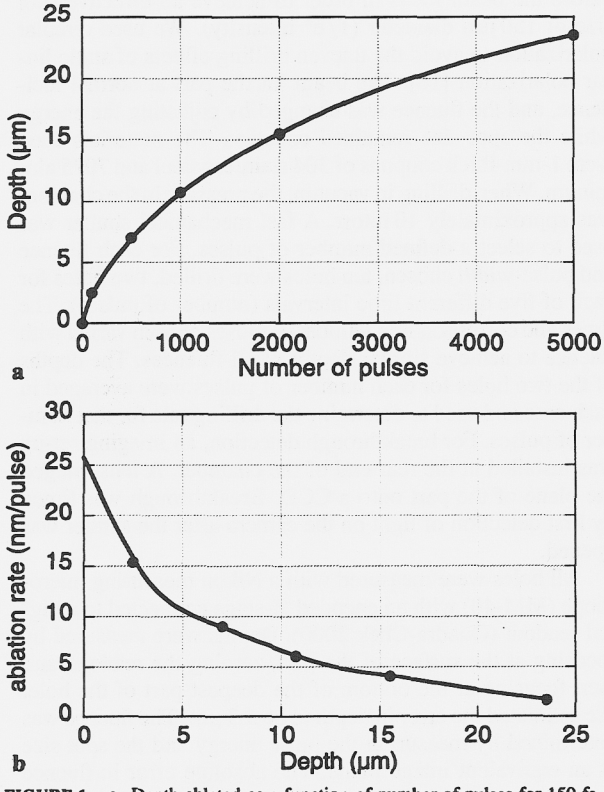

FIGURE 1 a Depth ablated as a function of number of pulses for 150-fs, 0.5-J/cm^2 pulses incident on 7075 aluminum. b Instantaneous rate of ablation as a function of depth derived from a

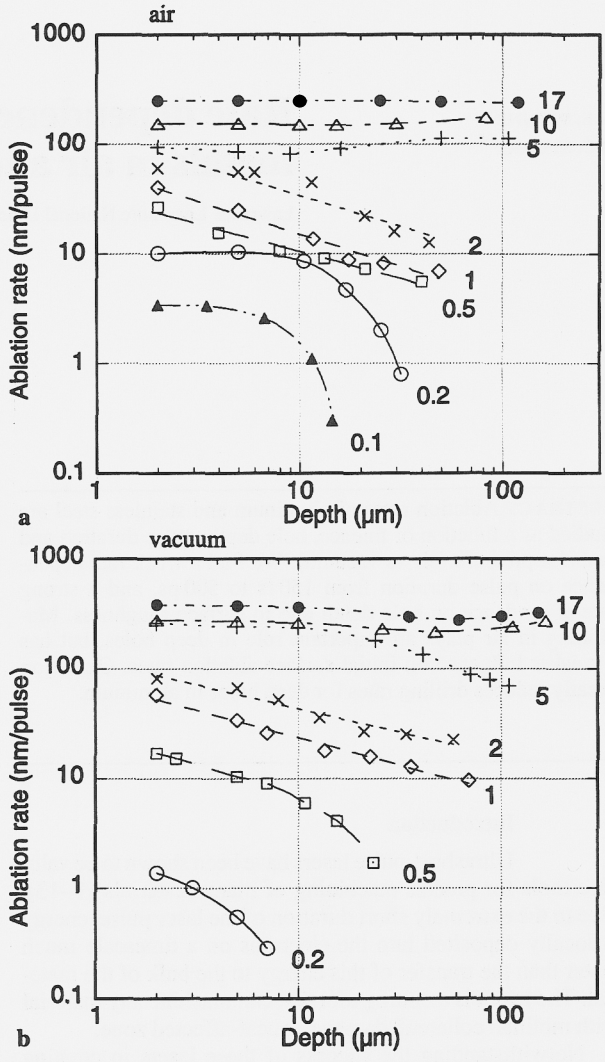

FIGURE 2 Rate of ablation as a function of depth for 150-fs pulses incident on 7075 aluminum in air (a), and vacuum (b). The incident fluence is indicated in units of J/cm^2

of the surface structure causes the rate to drop dramatically and then "stall-out", where material removal no longer occurs. In the intermediate fluence regions (few J/cm^2) the rate still drops off with depth and is well fitted by a power-law dependence. At high fluence, the rates are relatively constant. In some cases, the rate decreases up to a certain depth and then increases again. This is explained by the formation of channels in the bottom of the hole which have much faster ablation rates than the rest of the hole [14]. This occurs at depths greater than approximately 40 μm and at fluences greater than roughly 5 J/cm^2. In comparing the differences between air and vacuum, the removal rates at high fluence are faster in vacuum than air. This can be attributed to lack of breakdown (ionization) of the incident laser pulse in air, and to greater chance for the ablated atoms and ions to escape the surface into vacuum. For low fluence, the ablation rates are slightly higher in air than in vacuum. A clue to this behavior can be found by examining the surface structures formed during ab-

lation. The morphology of the low-fluence hole-drilling progression is shown in Fig. 3. These are SEM images of holes ablated in 7075 aluminum at 1 J/cm^2 for 100, 500, and 1000 pulses in air and vacuum. The craters ablated in vacuum exhibit sharper and more distinct features, while those ablated in air are smoother and contain many round micro-holes. It is these micro-holes that progress at a faster ablation rate than the structures formed in vacuum. The ablation morphologies in argon and nitrogen were similar to those in air. In this low-fluence regime, the presence of gas helps to accelerate the formation of these surface structures, leading to higher rates than in vacuum. Both morphologies are structured in a way that causes the ablation rate to drop as the light is scattered and trapped within the structures, eventually reaching an effective fluence that is unable to cause appreciable material removal. The hole morphology is very different at high fluence. Figure 4 shows the ablation of 7075 aluminum at 10 J/cm^2 in air and vacuum. The formation of a main central channel in the vacuum is clearly evident. This fluence level is too high for clean initial surface removal and results in material being ejected up from and to the sides of the hole. The structures in air are again smoother. As the holes become deeper, most of this initial structure is eventually ablated away. This results in a relatively clean hole, but usually with some residual slag due to the high initial fluence. The holes ablated in air were surrounded by aluminum oxide, while the holes drilled in vacuum were surrounded by aluminum particles and film. Although extremely important for deep holes, the role of oxidation on initial surface ablation was not defined in this set of experiments.

The ablation behavior as a function of depth we observed for aluminum at 150 fs is similar to that observed in stainless steel and for pulse durations of 1.5 ps, 20 ps and 500 ps, in air and vacuum. Figure 5 shows the removal rates as a function of depth for 304 stainless steel at 500 ps and different fluence levels in air (Fig. 5a) and vacuum (Fig. 5b). The same channel formation transition is evident above 40-μm depth and 5 J/cm^2. At low fluence, enhanced surface roughening and micro-hole formation were again evident in air, argon and nitrogen environments as compared with vacuum.

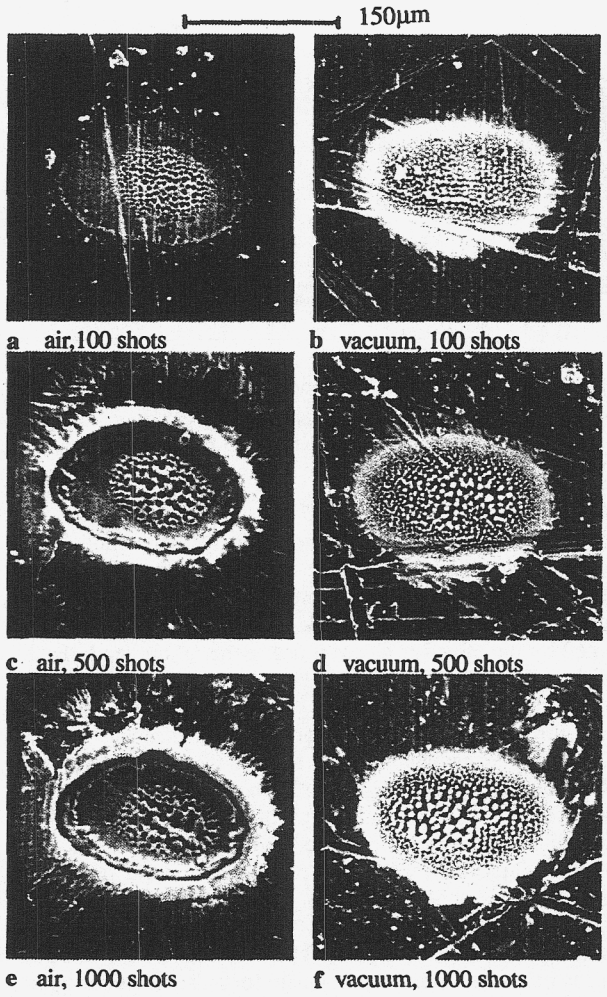

FIGURE 3 SEM images of initial hole progression in aluminum in vacuum and air at 150 fs, 1 J/cm^2 and 100, 500 and 1000 pulses

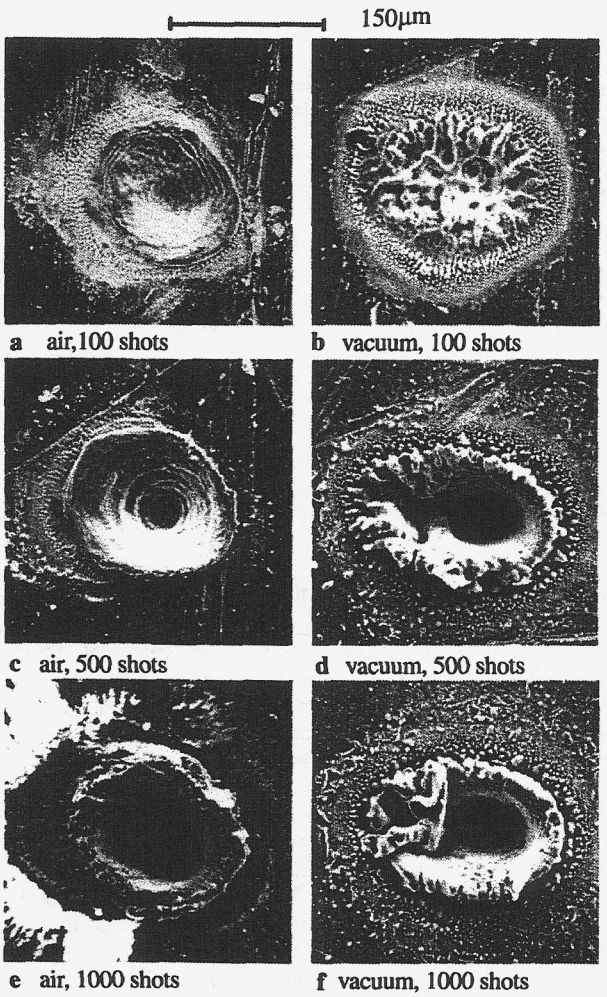

FIGURE 4 SEM images of initial hole progression in aluminum in vacuum and air at 150 fs, 10 J/cm^2 and 100, 500 and 1000 pulses. This fluence is too high to create holes with minimal slag

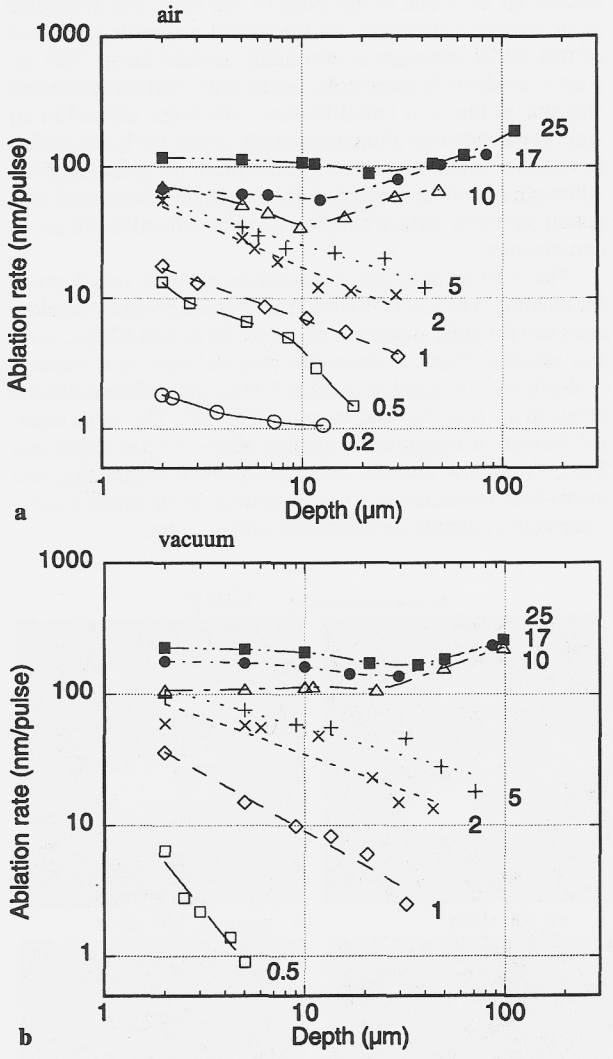

FIGURE 5 Rate of ablation as a function of depth for 500-ps pulses incident on 304 stainless steel in air (a), and vacuum (b). The incident fluence is indicated in units of J/cm^2

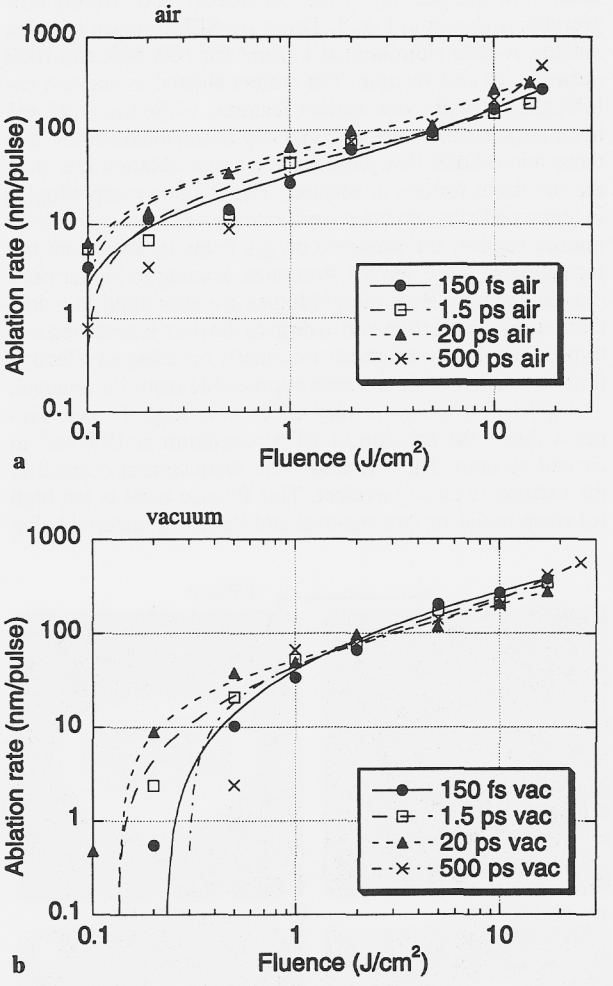

FIGURE 6 Ablation rate as a function of fluence at 5-μm depth for 150-fs, 1.5-ps, 20-ps and 500-ps pulses incident on 7075 aluminum in air (a), and vacuum (b)

4 Rate dependence on fluence and pulse width

Using the above data sets, we can now make a meaningful comparison of ablation rate as a function of fluence. This is done by comparing initial removal rates at similar depth. The depth chosen for comparison in Figs. 6 and 7 was 5 μm. Figure 6 shows ablation rates as a function of fluence of 7075 aluminum in air (a) and vacuum (b). Within the uncertainties (due in large part to the step of taking the derivative of the depth vs number of pulses), the initial ablation rates (at 5-μm depth) are similar as a function of pulse duration (within a factor of 2–3). For each pulse width, the curve of rate vs fluence has a similar shape that is characterized by a threshold value at low fluence (approximately 0.1 J/cm^2), with a sharp rise (log scale) in rate until approximately 0.5 J/cm^2, where it changes into something closer to a power-law fit. We do not have enough resolution in our data to discern the two regimes of short-pulse ablation derived in [7] for a two-temperature diffusion model: the lower fluence regime where the energy deposition is characterized by the optical penetration depth, and the high-fluence regime (> 0.7 J/cm^2 for Cu) where the deposition is governed by the effective electron heat penetration depth. Both of these regimes are described by a logarithmic dependence of ablation depth on fluence, $L \approx d \ln(F/F_{th})$, with only the high-fluence regime apparent for pulses longer than 1 ps [7]. Our high-fluence data indicates a faster-than-logarithmic dependence of ablation depth on fluence, augmented by the faster rates due to surface roughening and micro-hole formation. Initial rates are expected to be similar as a function of pulse duration over 0.1–500 ps because the thermal diffusion distances at 500 ps are 0.3 μm for 7075 aluminum and 0.09 μm for 304 stainless steel. Therefore, not much energy is lost to heat during the pulse. This insensitivity to pulse duration has been observed previously for pulse durations up to a few hundred picoseconds in other metals [6, 17]. The exact shape of these fluence-dependent rate curves will of course change as rates at different depths are considered.

In aluminum, the high-fluence rates are slightly higher in vacuum and the low-fluence rates are higher in air, as mentioned above for the 150-fs case. Stainless steel shows similar behavior (Fig. 7). The low- and intermediate-fluence rates are similar between air and vacuum, while the high-fluence rates are faster in vacuum due to the absence of the air breakdown and plume interactions. Overall, the ablation rates of aluminum are approximately three times those of stainless steel.

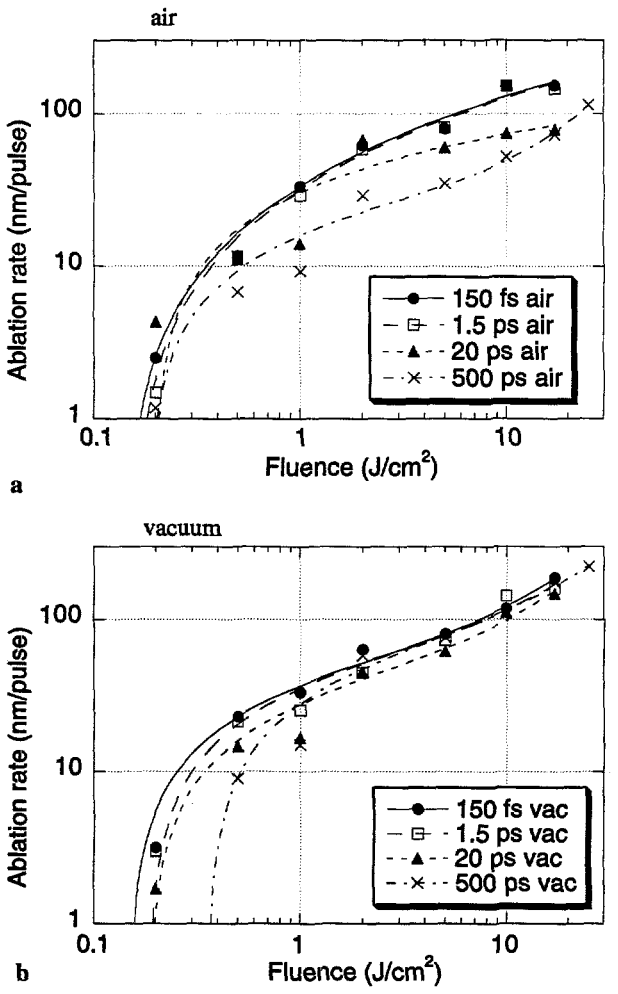

FIGURE 7 Ablation rate as a function of fluence at 5-μm depth for 150-fs, 1.5-ps, 20-ps and 500-ps pulses incident on 304 stainless steel in air (a), and vacuum (b)

5 Breakthrough times

Deep channel formation is a much more complicated process than initial surface removal. In addition to the difficulties in transporting and depositing the laser energy deep in a narrow hole, the contributions of redeposition, chemical reaction, surface morphology and overall geometry become increasingly important.

Although not significant for initial material removal, the difference between the air and vacuum environments was very pronounced in comparing times to drill holes all the way through the samples. We measured breakthrough times for 1-mm-thick samples of the two materials in order to study completion of high-aspect-ratio holes. Measured breakthrough times were noticeably shorter in vacuum than in air. Figure 8 shows plots of breakthrough time vs fluence for 7075 aluminum and Fig. 9 shows the results for 304 stainless steel. The limited number of data points are connected with the power-law fits. These give a general guide to the breakthrough times as a function of pulse duration and fluence: times for 150 fs, 1.5 ps and 20 ps are increasing but similar, while the 500-ps times are much longer for both air and vacuum. For aluminum in air below 8 J/cm^2, the drilling stalled and the holes did not break through.

Breakthrough times for the long pulses (500 ps) were consistently greater than for the shorter pulses, whether in air or

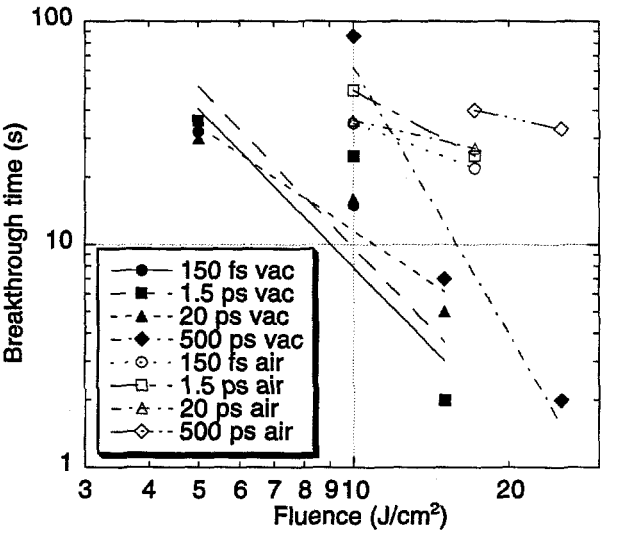

FIGURE 8 Breakthrough times as a function of fluence for 150-fs, 1.5-ps, 20-ps and 500-ps pulses in air and vacuum through 1-mm 7075 aluminum

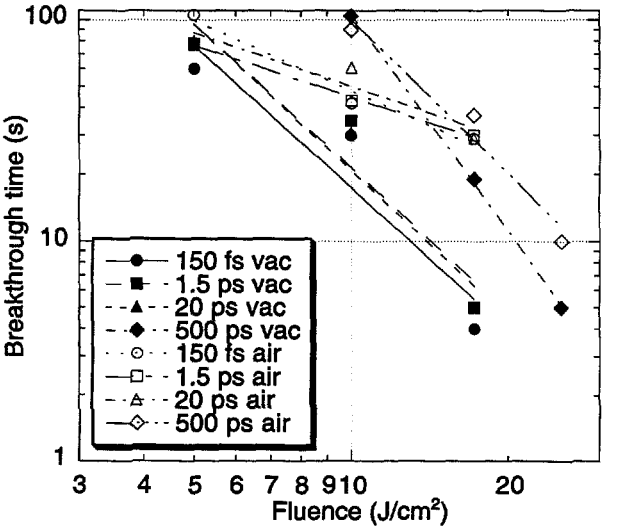

FIGURE 9 Breakthrough times as a function of fluence for 150-fs, 1.5-ps, 20-ps and 500-ps pulses in air and vacuum through 1-mm 304 stainless steel 1

vacuum. The longer pulses suffer from plasma shielding and thermal conduction losses during the pulse. The shorter pulses also impart a higher initial temperature to the ablated material, allowing a better chance of escape from the hole before being reabsorbed on the walls.

Oxidation plays a major role in increasing high-fluence drill times through thick aluminum and in preventing breakthrough for lower fluences. This was confirmed by comparing drill times in argon and nitrogen with 150-fs pulses. At 14 J/cm^2, breakthrough times were approximately 2 s for vacuum, 3 s for argon, 6 s for nitrogen and 23 s for air. On aluminum, the oxide layer forms almost immediately. This reduces the ablation rate as the oxide has a higher threshold for ablation than the metal. Oxygen also contributes to increased drill times in stainless steel, although to a lesser extent. Breakthrough times in stainless steel at 14 J/cm^2 were 6 s in vacuum, 9 s in argon and nitrogen and 14 s in air. Breakthrough times for either metal in argon and nitrogen in the high-fluence regime were slower than in vacuum, indicating contributions from gas breakdown and/or channel formation. The central channel formation is more apparent in vacuum than in air (see Fig. 4 for aluminum). This channel progresses and breaks through much faster than the rest of the hole. It appears that nitride formation also contributes to the slower rates in aluminum, as the breakthrough time is twice as long in nitrogen as argon, whereas in stainless steel the times are equal. A further consideration is the role of redeposition within the hole, which will occur at a higher rate in gas than in vacuum. Discerning the relative contributions of the various deep-hole effects is an area of considerable scientific interest and current research.

6 Conclusion

In summary, we find a very strong decrease in ablation rate with depth of hole, even over the first 10 μm of a 150-μm diameter area. We attribute this reduction in rate to the formation of 3-D structures within the ablation region. These structures are sharper and more defined under vacuum conditions and thus lead to a faster decline in rate than in air, where the structures are smoother and contain larger and deeper micro-holes. In terms of the difference between air and vacuum, we find that initial ablation rates are somewhat similar (with subtle differences) for both stainless steel and aluminum for all pulse widths in the range 150 fs to 500 ps. The rates tend to drop only slightly for the longer pulses. However, the rates do change significantly when drilling completely through a 1-mm-thick sample. In a vacuum, breakthrough times are much lower than in air for aluminum and slightly lower for stainless steel. Oxidation plays an important role in both metals, but has a much stronger effect on aluminum. Shorter pulses (150 fs–20 ps) also drill faster than 500-ps pulses. A compete understanding of deep-hole drilling will require the knowledge of initial surface ablation rates along with further investigation into the roles of redeposition, reaction dynamics, plasma formation, hole geometry, channel formation and surface morphology.

ACKNOWLEDGEMENTS We would like to acknowledge many helpful discussions with M. Feit, A. Rubenchik, A. Komashko, M. Shirk and F. Génin, and thank E. Lindsey for the SEM images. This work was performed under the auspices of the U.S. Department of Energy by Lawrence Livermore National Laboratory under Contract No. W-7405-ENG-48.

REFERENCES

1 W. Kautek, J. Krüger: SPIE **2207**, 600 (1994)
2 S. Preuss, A. Demchuk, M. Stuke: Appl. Phys. A **61**, 33 (1995)
3 J. Ihlemann, A. Scholl, H. Schmidt, B. Wolff-Rottke: Appl. Phys. A **60**, 411 (1995)
4 P.P. Pronko, S.K. Dutta, J. Squier, J.V. Rudd, D. Du, G. Mourou: Opt. Comm. **114**, 106 (1995)
5 B.N. Chichkov, C. Momma, S. Nolte, F. von Alvensleben, A. Tünnermann: Appl. Phys. A **63**, 109 (1996)
6 B.C. Stuart, M.D. Feit, S. Herman, A.M. Rubenchik, B.W. Shore, M.D. Perry: J. Opt. Soc. Am. B **13**, 459 (1996)
7 S. Nolte, C. Momma, H. Jacobs, A. Tünnermann, B.N. Chichkov, B. Wellegehausen, H. Welling: J. Opt. Soc. Am. B **14**, 2716 (1997)
8 D. Ashkenasi, A. Rosenfeld, H. Varel, M. Wähmer, E.E.B. Campbell: Appl. Surf. Sci. **120**, 65 (1997)
9 M. Lenzner, J. Krüger, W. Kautek, F. Kranz: Appl. Phys. A **68**, 369 (1999)
10 M.D. Perry, B.C. Stuart, P.S. Banks, M.D. Feit, V. Yanovsky, A.M. Rubenchik: J. Appl. Phys. **85**, 6803 (1999)
11 S. Nolte, G. Kamlage, F. Korte, T, Bauer, T. Wagner, A. Ostendorf, C. Fallnich, H. Welling: Adv. Eng. Mat. **2**, 23 (2000)
12 H.K. Tonshoff, C. Momma, A. Ostendorf, S. Nolte, G. Kamlage: J. Laser Appl. **12**, 23 (2000)
13 T. Juhasz, G. Djotyan, F.H. Loesel, R.M. Kurtz, C. Horvath, J.F. Bille, G. Mourou: Laser Phys. **10**, 495 (2000)
14 P.S. Banks, M.D. Feit, A.M. Rubenchik, B.C. Stuart, M.D. Perry: Appl. Phys. A **69**, S377 (1999)
15 D. Strickland, G. Mourou: Opt. Comm. **56**, 219 (1985)
16 S. Nolte, C. Momma, G. Kamlage, A. Ostendorf, C. Fallnich, F. von Alvensleben, H. Welling: Appl. Phys. A **68**, 563 (1999)
17 P.B. Corkum, F. Brunel, N.K. Sherman, T. Srinivasan-Rao: Phys. Rev. Lett. **61**, 2886 (1988); N. K Sherman, F. Brunel, P.B. Corkum, F.A. Hegmann: Opt. Eng. **28**, 1114 (1989)

Pressure wave generation and energy balance in ultrashort laser pulse surface ablation of water

Beop-Min Kim[1], Aleksey M. Komashko[2], Alexander M. Rubenchik[2], Michael D. Feit[2], Steffen Reidt[2], Luiz B. Da Silva[2], and Jürgen Eichler[3]

1: *Department of Biomedical Engineering, Yonsei University, 234 Maeji, Heungup, Wonjoo, Kangwon-Do 220-710, Korea*

2: *Lawrence Livermore National Laboratory, Livermore, California 94550*

3: *Technische Fachhochschule-Berlin, University of Applied Science, Seestr. 64, 13347 Berlin, Germany*

ABSTRACT

Experimental and theoretical study of the near threshold ablation of water surface by ultrashort laser pulses with duration in the 140fs-10ps range is presented. Using Mach-Zehnder interferometry, formation and propagation of spherical and, in ablation with longer pulses, combination of spherical and cylindrical pressure waves was observed. Theoretical modeling on the basis of the nonlinear ionization equation shows that the laser created surface plasma acts as a filter transmitting only a fixed energy leading edge of the laser pulse. For longer pulses this energy is larger, therefore generation of cylindrical waves is enabled. Measurements of the amplitude and dynamics of the pressure waves show that the conversion efficiency of laser energy to mechanical energy of the pressure waves is less than 1% thus justifying the claim that ultrashort laser pulse ablation induces low collateral damage and has a large potential in biomedical applications.

I. INTRODUCTION

Ultrashort laser pulse (USLP) ablation of transparent liquid dielectrics has been the subject of numerous studies[1-5]. This interest is partially due to the potential application of this technique in medicine[6-11]. It is claimed that femtosecond pulses are uniquely suited for such applications since low collateral damage can be obtained due to the specific nature of laser-material interactions in this regime. Breakdown of transparent material proceeds via electron avalanche initiated by "seed" conduction band electrons. For long pulses, sufficient seed electrons may be provided by impurities while for very short pulses the larger number of needed seed electrons may be provided by nonlinear absorption. Once the seed electrons are available, subsequent avalanche ionization produces more free electrons. When the density of the free electrons exceeds a certain threshold, enough energy is absorbed to produce macroscopic ablation.

The threshold intensity of ultra-short laser pulses needs to be high enough that multiphoton ionization (MPI) produces the needed initial electrons before the pulse ends. For very short (less than 100 fs) pulses, MPI can produce the initial electrons required for the breakdown. The resulting ablation process is controlled by intrinsic properties of the material such as the band-gap energy; therefore the whole process becomes highly deterministic. Any material can be processed with USLP independent of linear absorption.

Beyond threshold, the free electrons generated by MPI and avalanche ionization absorb and reflect all further incoming light energy and limit the energy deposition depth (< 100 nm). The energy deposition in a thin surface layer creates an extremely large energy density, which leads to the ejection of most of the absorbed energy with the plume. High pressure developed in the absorption zone generates intense shocks. But, due to the short pulse duration, a rarefaction wave starts to "eat" the shock rapidly and to decrease its amplitude. Both of these effects result in small collateral damage. Multiple publications have presented photographs demonstrating little or no residual damage in different materials[1,12,13].

In biological applications, the experimental outcome can be affected in a subtler and not readily visible way. One example is the case when generated shock waves are too weak to create obvious mechanical change, but

nevertheless strong enough to adversely modify or kill tissue cells[14]. Therefore one needs quantitative understanding of how pressure waves develop, propagate and decay in ablation with ultrashort pulses. Also, near threshold the critical electron density at which strong absorption and reflection takes place is formed well after the beginning of the USLP. The initial part of the pulse penetrates into the medium and can affect the tissue. The goal of this paper is to study the distribution of the incident laser energy between the transmission, reflection and absorption, to evaluate the localization of the absorbed energy and conversion efficiency in the shock waves. We first describe the experimental setup and present typical measurements. We measured ablation thresholds and performed theoretical modeling of laser energy propagation and deposition. USLP-induced pressure is measured and analyzed and the conversion into mechanical energy is presented.

We found that the USLP generated plasma serves as a shutter - with increase of the pulse energy the transmitted and absorbed energy saturates and only the reflected energy increases. For longer pulse duration the transmitted energy is larger, which is manifested in the cylindrical shock waves formation. The information on localization and efficiency of the absorption can be used for the optimization of USLP biomedical studies.

II. EXPERIMENTS

The ultrashort pulse laser system is composed of two pumping lasers, one oscillator, and a regenerative amplifier. The oscillator (Tsunami, Spectra Physics) is pumped by the frequency-doubled Nd:YAG laser beam (Millenia, Spectra Physics) operating in continuous mode with 5W of output power. The Ti:Sapphire oscillator beam is 80 fs in pulse width, 82 MHz in repetition rate, and 800 nm in wavelength. Low energy pulse from the oscillator is amplified using a regenerative amplifier (Spitfire, Positive Light) through chirped pulse amplification process. The amplifier is pumped by a Q switched Nd:YLF laser (Merlin, Positive Light). Final output of the laser has the maximum pulse energy of 1 mJ/pulse at 1 kHz with wavelength of 800 nm and the shortest pulse width is approximately 130fs. The pulse energy was controlled by rotating the half-wave plate placed immediately before the polarizing beam splitter and a matching mirror. Longer pulse widths were obtained from the shortest by changing the path length of the beam compressor inside the regenerative amplifier.

Pulse widths were measured using a scanning autocorrelator. The incoming laser beam was split into two beams with equal intensity and the path of one of the beams was adjustable. The beams were recombined within a KDP crystal generating the second harmonic at 400 nm in the direction of the intersection. The intensity, I, of the second harmonic beam was measured as a function of the path difference x. From the full width half maximum (FWHM) of the function $I = f(x)$, the pulse width of the first harmonic laser pulse was calculated assuming a Gaussian beam profile.

Previous experimental studies of laser induced shock waves in water used shadowgraphy diagnostics[4,5,9]. In these experiments the laser light is typically focused inside the liquid. As a result, the induced pressure is high and measurable deviation of the shock speed from the sound speed gives the information on pressure magnitude. In our case of surface ablation the expected pressure could be much smaller. Thus we used more sensitive interferometric diagnostics for pressure measurements.

For measurement of pressure induced by USLP ablation on water surface, a Mach Zehnder interferometer was devised (Fig. 1). A dye laser (LSI Inc.) at 480 nm, pumped with a Nitrogen laser, was used as a probing light source for the interferometer. The 5 ns dye laser pulse was split into two beams (test and reference beams) using a 50:50 beam splitter. A 1 cm x 1 cm x 5 cm cuvette filled with purified water was inserted into the test beam and was illuminated on one of the four long sides. Another water-filled cuvette was placed in the reference beam of the interferometer to compensate for the path difference. The two beams were recombined at another beam splitter and the path difference of the two beams created the uniform fringe patterns without the presence of USLP. The ultrashort laser pulse was vertically incident on the water surface and created the pressure waves, which resulted in the shift of the fringe patterns.

The 5 ns dye laser pulse was delayed with respect to the ablating USLP using a digital delay generator. A variable delay time from 0 to 200 ns was chosen so that the propagation of pressure waves could be observed at various times. The actual delay time was measured for each ablation pulse with a separate photodiode. This diode was illuminated simultaneously with the ultrashort laser pulse scattered from the water and the transmitted dye laser pulse. The two signals were displayed and saved in a digital oscilloscope for calculation of the actual delay times. The maximum diameters of the spherical pressure waves that we probed were approximately 300 μm.

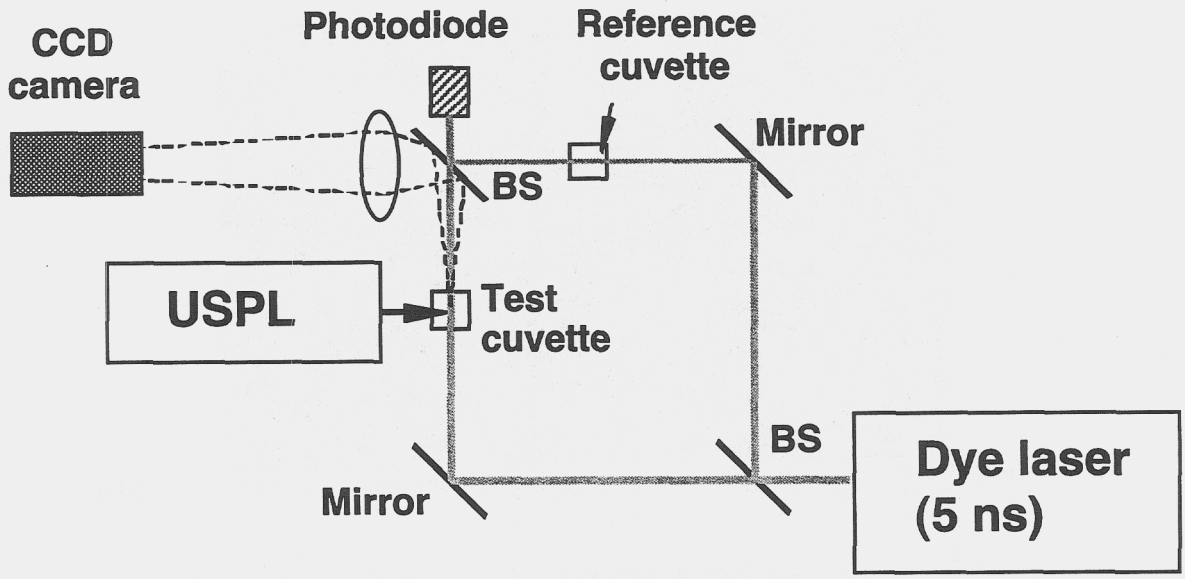

Fig. 1. Mach-Zehnder interferometer for analysis of USLP-induced pressure waves. The USLP is incident vertically at the top surface of the water contained in a cuvette.

The water surface in the test cuvette has the form of a concave meniscus. The USLP was focused on the centrum of the meniscus and the resultant pressure waves were imaged on a CCD camera with 512x512 pixels, each pixel measuring 48 μm. The shutter of the camera was synchronized with the ablation pulse. To magnify the images, a photo-objective with f = 57 mm with high numerical aperture was used. With magnification of 45, the resolution of the magnified images was approximately 1 μm/pixel. The magnification was measured by imaging a micrometer-scale resolution target. The images were processed in a computer using IPLab software. By adjustment of mirrors of the interferometer, vertical or horizontal fringes were obtained for analyses of different types of pressure waves. The pressure waves create density changes in water, which appear as a fringe shift on the interferograms. Recording interferograms at different time delays we could observe wave dynamics.

III. INTERFEROGRAMS

Fig. 2 shows a typical interferogram obtained using this setup. USLP is incident from the top onto the surface of water that coincides with the upper boundary of the fringes. In all of our experiments, the beam diameter was 56 μm (full width half maximum), which was measured separately. The dark area at the center near the surface seems to be a region where the heated water deflects the probing light beam. The thin, semi-circular structure is a fringe shift induced by the pressure wave. We see that laser energy absorption near the surface generates a shock wave in the form of a thin shell which expands with time. The amount of fringe shift caused by the wave depends on the density change and pressure and can be computed using a relationship based on an appropriate equation of state of water[15].

In our experiments, two different kinds of waves were observed. One was a spherical wave, propagating from the area around the focal spot on the water surface; the other was a cylindrical wave generated along the path of the laser beam propagation. Their presence depended on the fluence and pulse width as reported in a previous publication[16]. Fig. 3 shows interferograms of laser ablation with different pulse widths in the range from 0.12ps to 10ps and with laser fluence just high enough to generate spherical pressure waves. For the shorter pulses (τ < 1ps), only spherical waves were observed. When the pulse gets longer, we first saw the cylindrical wave and then, after increasing the fluence, the spherical wave appeared. We believe that the cylindrical channel structure seen in this case on the interferogram is a result of beam defocusing by the lens formed when the refractive index is changed by heating the water. For a typical time delay in these experiments, there is not enough time for this thermal energy to dissipate. Thus a cylinder with refractive index different from the bulk is formed. We estimate that a one-degree rise in temperature would create a lens with a focal length on the order of 15-20 cm – enough to deflect light and create dark channel visible on the interferogram.

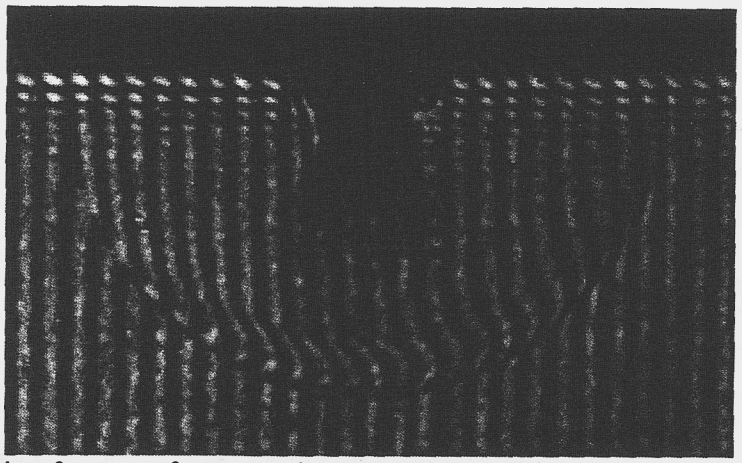

Fig. 2. Typical interferogram of a generated pressure wave. Laser beam was incident from the top

IV. LASER ENERGY ABSORPTION

The type and the amplitude of the generated pressure waves depend on many mutually interacting processes; however, we can notice that hydrodynamic motion is essentially decoupled from the ultrashort laser energy absorption. Pressure waves of moderate magnitude in water propagate with a velocity of a few km/s (sound speed in water is 1.5 km/s) and in 10ps they travel approximately 10-100 nm. Note that the skin depth of a metal is on the order of 10nm. In laser-induced breakdown of a dielectric, we can expect an even larger energy deposition zone, thus material expansion during absorption is not significant. All of the pressure wave formation takes place after the pulse is over. Understanding where and how much of the pulse energy gets absorbed is a first step in interpretation of the experimental results and it gives insight into mechanical aspects of material damage without solving the complex equations of hydrodynamics. In this section, we present results of absorption modeling and compare with experiment.

Interaction of an electromagnetic wave with a material is mostly controlled by the response of electrons. In high power laser ablation of transparent dielectrics a central role is played by the dynamics of free electron generation (elevation from the valence band to the conduction band). Since the intrinsic conduction electron density in dielectrics is very small, these new free electrons are primarily responsible for the laser energy absorption. To describe the ionization process we applied a simple rate equation derived from kinetic theory and successfully used in modeling ablation of solid dielectrics[17]

$$\frac{dn}{dt} = \alpha(I, n) + P(I) - \beta n^2. \qquad (1)$$

This equation describes the change in electron density $n(t)$ as being due to impact ionization at rate $\alpha(I,n)$, multiphoton ionization at rate $P(I)$, and recombination at rate βn^2. The first term describes collisional ionization by free energetic electrons - it depends on the electron density n, whereas the second term represents direct ionization by the laser light, and is only a function of the laser pulse intensity $I(t)$. Since water can be modeled as an amorphous dielectric with a bandgap energy of 6.5 ev[18], MPI is described with the Keldysh formulas[19]. At low intensities, the MPI rate has the simple form

$$P(I) \sim I^K, \qquad (2)$$

where k is the number of photons needed to bridge the energy bandgap - five for 800nm light. At high intensities the transition to the tunneling ionization regime takes place[19]. In our calculations, we used the more general nonlinear Eq. (37) of Keldysh's paper[19], since for light intensities greater than 1 TW/cm^2 the multiphoton approximation begins to break down. The studies of breakdown in fused silica indicate that the Keldysh formula provides a good

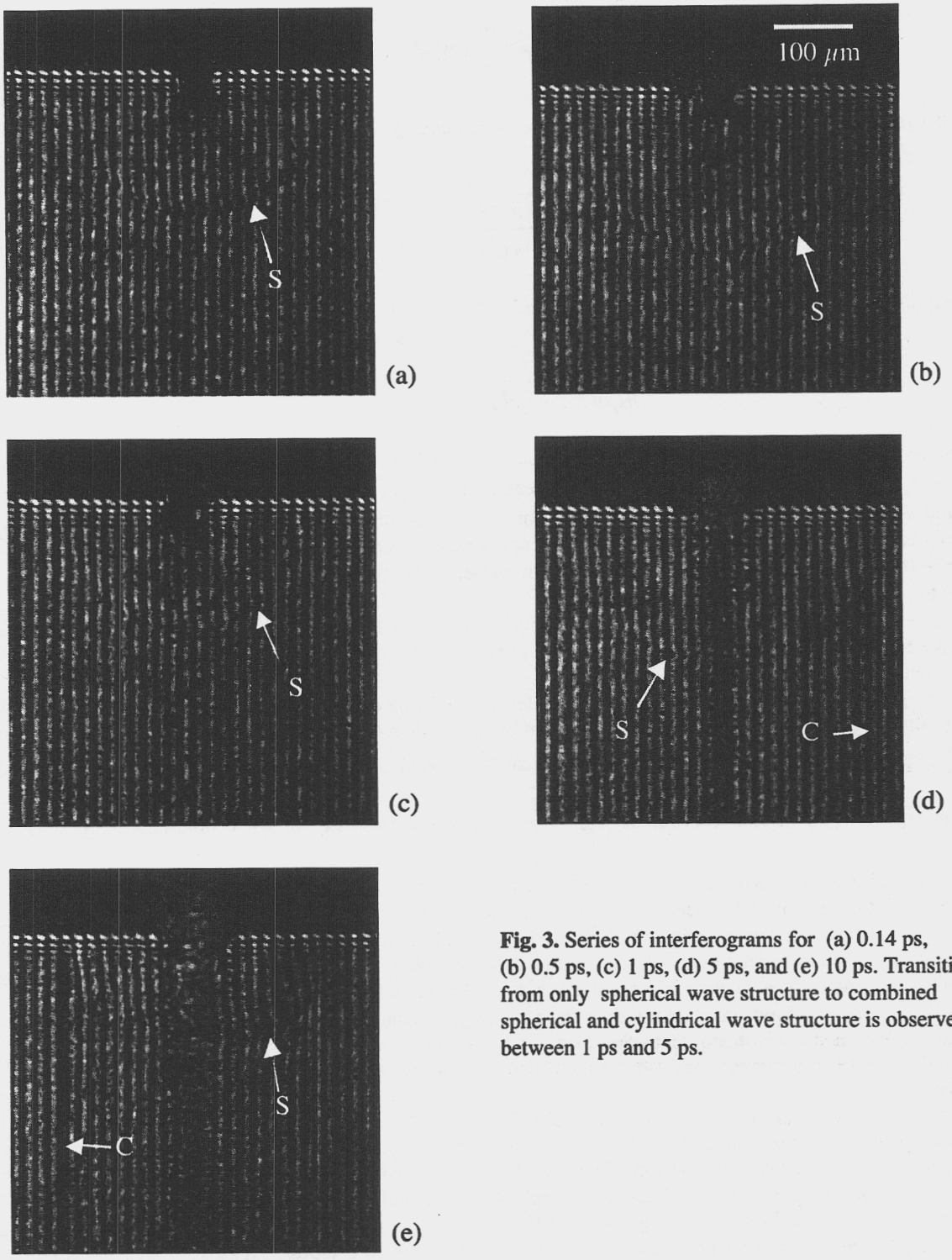

Fig. 3. Series of interferograms for (a) 0.14 ps, (b) 0.5 ps, (c) 1 ps, (d) 5 ps, and (e) 10 ps. Transition from only spherical wave structure to combined spherical and cylindrical wave structure is observed between 1 ps and 5 ps.

description of experimental data[17]. Assuming that a free electron produces another free electron once it acquires enough energy, the impact ionization rate $\alpha(I,n)$ can be deduced from the laser absorption of the plasma[17]. Energy conservation requires

$$(< e_e > + U)\left.\frac{dn}{dt}\right|_{impact} = -\frac{dI}{dz} = 2\frac{\omega}{c}\mathrm{Im}[\sqrt{\varepsilon}]I, \qquad (3)$$

where ω is the laser frequency, $<e_e>$ is the average free electron energy, U is the bandgap energy and $\varepsilon(n)$ is the dielectric function. As a result, the impact ionization rate is

$$\alpha(I,n) = 2\frac{\omega}{c}\frac{\mathrm{Im}(\sqrt{\varepsilon(n)})I}{(< e_e > + U)}. \qquad (4)$$

In the modeling, $\varepsilon(n)$ was calculated using the Drude formula

$$\varepsilon = \varepsilon_o - \frac{4\pi n e^2}{m_e \omega^2}\frac{1}{1 + i\nu/\omega}, \qquad (5)$$

where ν is the collision frequency and $\varepsilon_0=(1.33)^2$ is the dielectric constant of water. By expanding Eq. (4), we find that $\alpha(I,n) \sim n$. As expected, the higher the electron density, the larger the ionization rate. The proportionality between α and n leads to electron avalanche. The solution of the kinetic equation[17] shows that the average free electron energy can be taken as $0.5U$. The collision frequency ν depends on both electron temperature and density. However, since there is no significant expansion during the pulse, ν was set to a constant, chosen to give the best description of the experiment.

The last term of Eq. (1) describes electron recombination. The coefficient β was set to the value of $2\cdot10^{-9}$ cm^3/s that was deduced from plasma luminescence studies in water[20]. Our calculations show that the results are not very sensitive to this number.

Laser energy propagation and absorption were handled in the following way. The first step is the calculation of electron density evolution at the surface, which is driven by an incident Gaussian pulse with FWHM duration τ, i.e. $I(t) = I_0 \exp\left(-4\ln(2)(t/\tau)^2\right)$. Reflection from the surface is included by multiplying the incident intensity by the time dependent transmission coefficient $\frac{4\,\mathrm{Re}\sqrt{\varepsilon}}{\left|\sqrt{\varepsilon}+1\right|^2}$ determined from Eq. (5). The nonlinear Eq.(1) was solved numerically employing a Runge-Kutta method. Once the surface electron density $n(t)$ is known, we begin propagating beam into the bulk. The laser pulse with intensity $I(t,z)$ at depth z is advanced a distance δz by subtracting the energy lost to electron ionization (both by impact and multiphoton processes) given in Eq. (3). The size of the step was chosen to be small enough so that the absorbed energy is much smaller than the energy carried by the beam. Once the intensity is advanced from z to $z+\delta z$, Eq. (1) is solved again to find the electron density at the new location. Executing this algorithm as many times as necessary we can propagate the laser pulse to the desired depth z. In these calculations, we obtain deposited energy density and electron density as a function of depth, the total transmitted and reflected fluences and the temporal behavior of the laser fluence and electron density at the depth of interest.

Such calculations were carried out for a number of different pulse lengths between 140fs and 10ps and for a range of intensities at each pulse width. If the fluence was low, there was practically no absorption and the laser energy propagated unchanged through 1000μm of water. When the intensity increased, at some specific point for each pulse length, absorption and reflection increased sharply due to high electron density generation at the surface and reduced energy penetration in the bulk. Figs. 4 and 5 show simulation results for 140fs and 10ps that describe this situation. The figures show the temporal evolution of pulse intensity and electron density at three different positions – immediately after surface penetration, 25 μm deep and 1000 μm deep. For reference, the incident intensity profile is also included. Qualitatively, the pictures are quite similar. Pulse fluences are high enough (F(140fs) = 4.47 J/cm^2, F(10ps) = 31.9 J/cm^2) to generate significant electron densities. In fact, during the pulse the density exceeds $n_{cr}=3\cdot10^{21}$ cm^{-3} at the surface. If there were no collisions (in both cases $\nu=3\cdot10^{14}$s^{-1}) the dielectric function $\varepsilon(n_{cr})$ would vanish at this electron density and penetration of the laser radiation is arrested. The plasma effectively absorbs and reflects the radiation. For higher densities, it is also a good reflector. This is exactly what we see in the figures, once n_{cr} is reached, i.e. transmission drops sharply. In the case of the 10 ps pulse we can see this

effect occur twice. The pulse is long enough for recombination to reduce the electron density below the critical density when the intensity is decreasing. As a result there is a little bump in the intensity transmission.

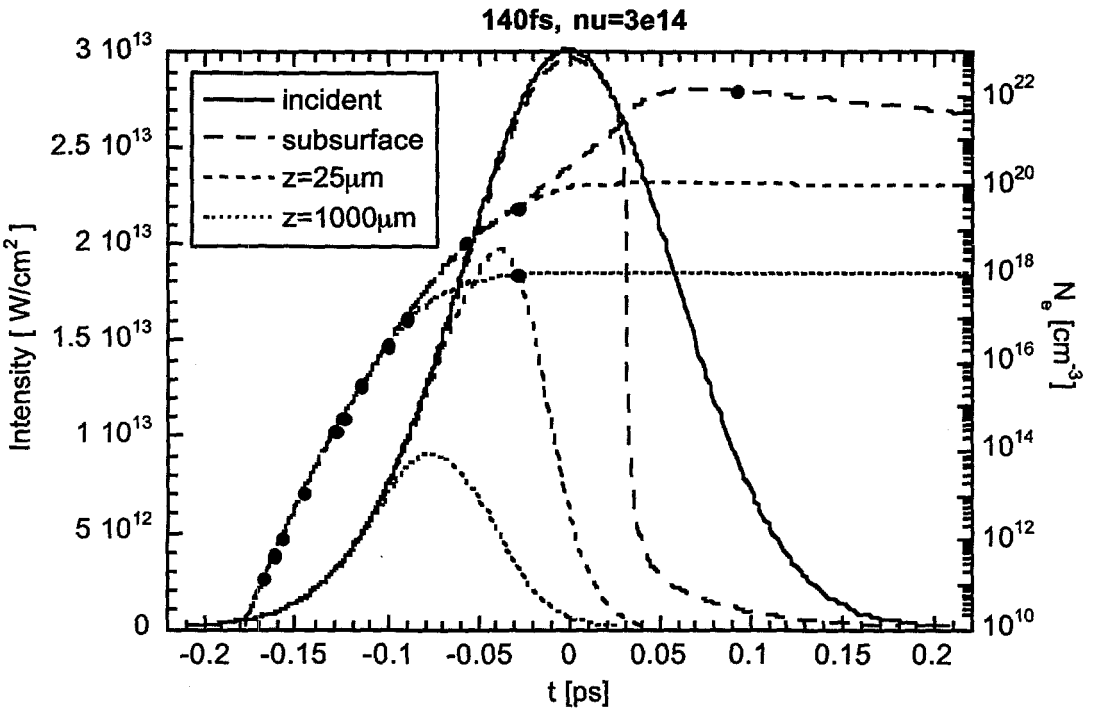

Fig. 4. Simulation of behavior of electron density and pulse intensity as a function of time for three different positions: at the surface, 25 μm deep and 1000 μm deep for an input laser pulse with intensity $3 \cdot 10^{13}$ W/cm^2 and length $\tau = 0.14$ ps. Collision frequency is $\nu = 3 \cdot 10^{14}$. Lines with solid points show evolution of electron density (log axis on the right) and lines without markers show evolution of intensity (axis on the left).

The region of above critical density has thickness on the order of 100nm for the shortest pulses (140 fs) while for longer pulses (10 ps) it decreases to 20-30nm. When laser pulse is propagated deeper into the bulk, the deposition rate decreases considerably. The modeling shows that most of the pulse energy is deposited within a surface layer 20-30 μm thick with the highest absorption at the surface where the electron density exceeds the critical n_{cr}. At the boundary of this region energy deposition density was approximately 100J/cm^3, which corresponds to the tissue temperature increase of 20-30°C when protein coagulation begins[21]. For the two cases presented in Figs. 4 and 5, the energy fraction absorbed in a 25 μm surface layer after propagation for 1000 μm is 0.8 for 10 ps pulse and 0.6 for 140 fs pulse.

To understand how laser energy is divided among reflection, absorption and transmission, we performed a number of calculations for different intensities at each pulse length. The results indicated that the qualitative behavior is independent of the pulse width. Fig. 6 shows results for the 140 fs pulse length. We plot the laser fluence splitting in different energy channels as a function of the incident fluence normalized by F^*=3 J/cm^2. We can see that absorption begins to appear for fluence $F \sim 0.5\ F^*$. The deposited energy increases until the pulse fluence reaches approximately F^*. Afterwards it starts to saturate, whereas the energy transmitted after propagation through a 25 μm surface layer stays about the same in the whole fluence range. Since energy deposition is saturated and transmission is not changed, all of the excess energy for incident pulse fluences above 3 J/cm^2 goes into reflection. Clearly F^*=3 J/cm^2 represents a threshold value F_{th}; indeed it is a fluence that allows the critical electron density n_{cr} to be reached at the surface. For longer pulses, the general picture is the same - fixed energy deposition, transmission and growing reflection for fluences above threshold. The only difference is in the value of F_{th} which increases with pulse width. For instance, the 10ps pulse has a threshold fluence F_{th}=10.9 J/cm^2. It is natural to consider the laser fluence that can generate critical electron density n_{cr} as the ablation threshold. There is clearly a

transition from no absorption and full transmission at lower fluences to a significant energy deposition at the surface for higher fluences, which should cause energetic material removal.

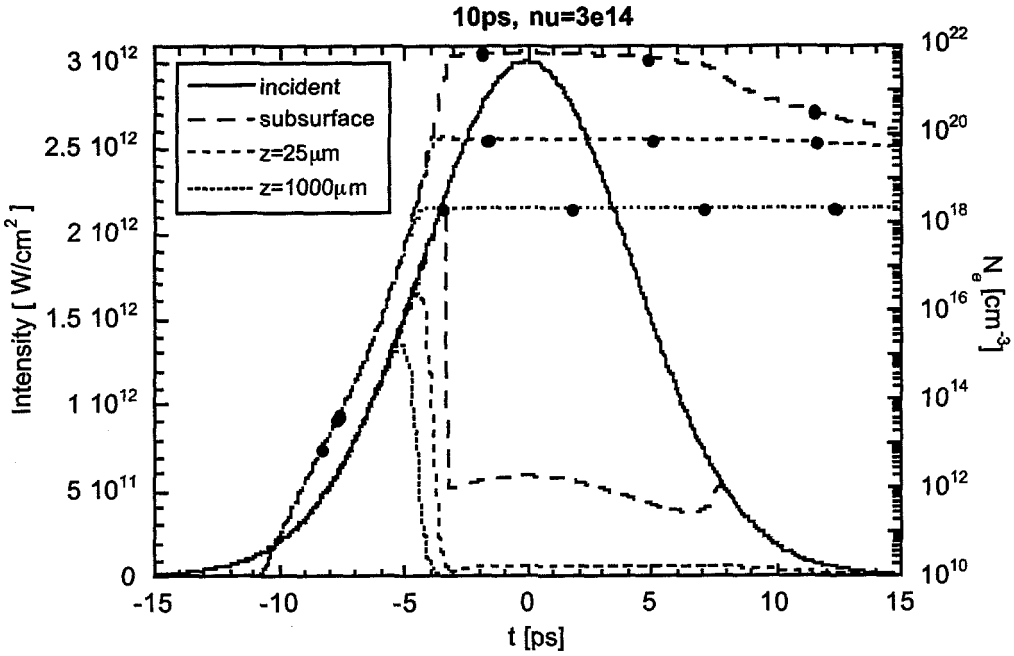

Fig. 5. Simulation of behavior of electron density and pulse intensity as a function of time for three different positions: at the surface, 25 μm deep and 1000 μm deep for input laser pulse with intensity $3 \cdot 10^{12}$ W/cm^2 and length $\tau = 10$ ps. Collision frequency is $\nu = 3 \cdot 10^{14}$. Lines with solid points show evolution of electron density (log axis on the right) and lines without markers show evolution of intensity (axis on the left).

Experimentally, it is difficult to measure energy deposition. Typically, the ablation threshold is defined by the appearance of some observable change such as visible material damage[17]. Since post pulse examination doesn't work for water, one has to look for some transitional changes, like generation of cavitation bubbles[22] or plasma formation[23]. In our experiments, the ablation threshold was defined as the fluence at which spherical pressure waves appeared - a sign of strong laser absorption at the water surface. Using this criterion, we measured the threshold fluence for a number of pulse lengths. Fig. 7 presents our data along with simulation results. For short pulses (~100 fs), the ablation threshold is about 3.5 J/cm^2. It increases with pulse width to approximately 18 J/cm^2 at 10ps pulse duration.. The calculated result, using the same criterion, is also presented in Fig. 7. Our model has one free parameter, the collision frequency ν. Typically, in this type of calculation[24,25] the collision frequency is set to the value proposed by Bloembergen[26] $\nu = 10^{15}$ s^{-1}.We adjusted this number to get the best description of the experimental result and $\nu = 3 \cdot 10^{14}$ s^{-1} seems to be the best fit. The general behavior of the theoretical curve stays the same, when the collision frequency is adjusted; the only change is the overall magnitude.

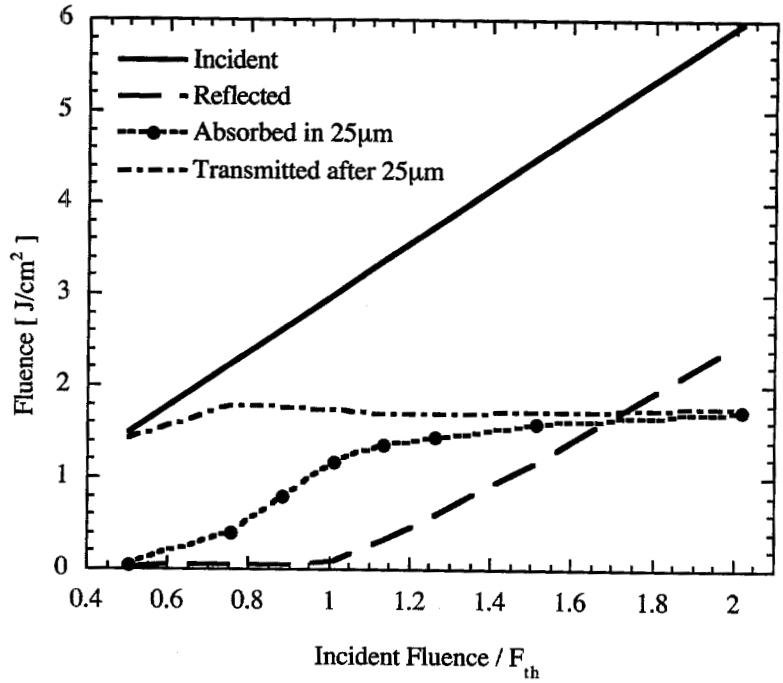

Fig. 6. Reflected, absorbed and transmitted fluence as a function of relative pulse energy for 140fs and surface layer 25 μm thick. The data is plotted versus normalized fluence F/F_{th}, where F_{th} is the fluence that allows laser pulse to just produce critical electron density $n_{cr}=3\cdot10^{21}$ cm^{-3} at the surface. Collision frequency is $\nu=3\cdot10^{14}$.

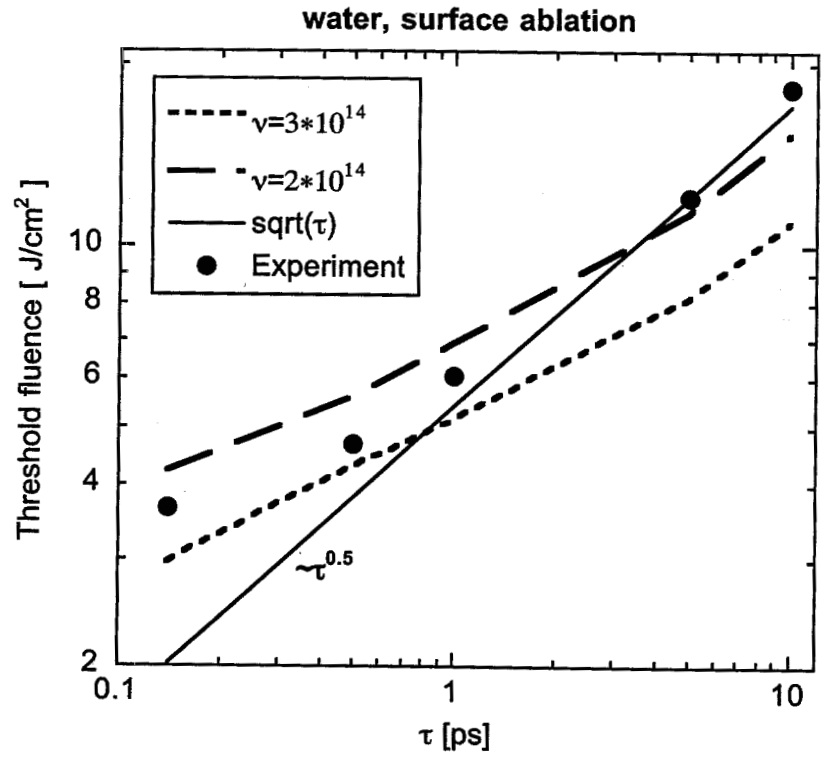

Fig. 7. Experimental measurements and theoretical calculations of ablation thresholds.

From these curves we see that a good match can be obtained for short pulses, whereas the experimental curve is a steeper function of τ for long pulses. This longer pulse disagreement cannot be compensated by adjustment of the collision frequency. The discrepancy may appear because our model does not include thermal transport, which lowers the energy deposition rate at the surface, thus allowing higher transmission in the material and requiring a larger fluence to reach the critical density. Thermal diffusion is more important for longer pulses. In fact experimental thresholds for longer pulses are well known to vary approximately in proportion to $\sqrt{\tau}$ representative of thermally controlled damage, when initial seed electrons are provided by small absorbers[27]. Another reason could be the effect of hydrodynamics - material expansion lowers the electron density at the surface for the longer pulses.

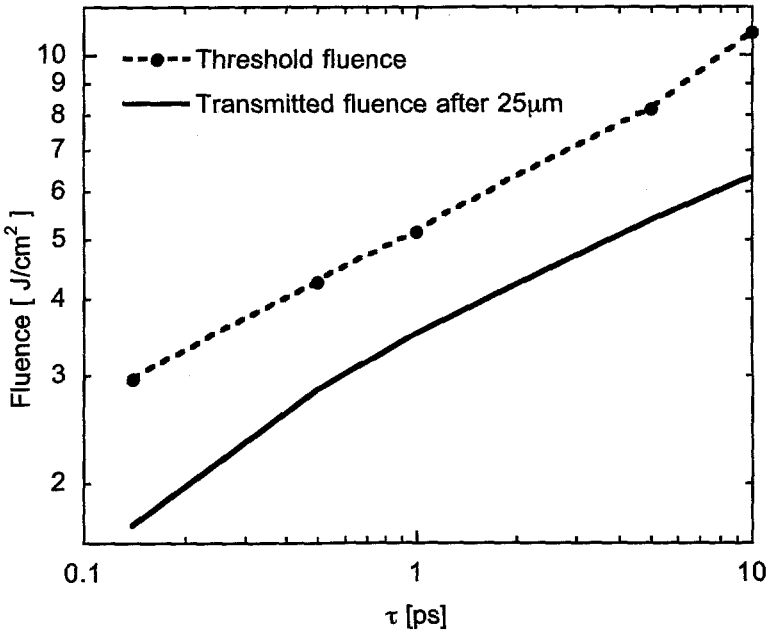

Fig. 8. Calculated threshold fluence and transmitted fluence after 25μm as a function of pulse length. Collision frequency is $\nu=3\cdot10^{14}$.

The following explanation, based on the simulations, emerges for the qualitative behavior of pressure waves shown in Fig. 3. The laser beam interacts with water generating significant electron density at the surface. This plasma acts as an energy absorber that generates spherical pressure waves, and also as a reflector that allows only the leading edge of the pulse to penetrate the surface layer. Fig. 8 shows a calculation of energy transmission as a function of pulse length. Since the ablation threshold is an increasing function of pulse width, the transmitted energy also increases for longer pulses. For instance, in our calculations the transmitted fluence is 6.5 J/cm^2 for the 10ps pulse versus 1.7 J/cm^2 for the 140 fs pulse. Therefore, the energy available for volumetric absorption along the beam path is noticeably larger for longer pulses. As a result, we see an observable effect of this larger energy deposition, viz. cylindrical pressure waves and a dark absorption channel.

V. PRESSURE WAVE DYNAMICS

Absorption of an ultrafast laser pulse creates a localized region with high temperature and pressure. Hot material begins to expand rapidly, thus generating shock waves propagating in the bulk of the material. These waves carry part of the laser deposited energy and can affect material far away from the absorption zone. Our purpose is to characterize this shock effect by measurement of the wave strength and dynamics.

To get an idea of what we are dealing with, the initial stage of shock propagation was modeled applying the one dimensional hydrocode HYADES previously used for simulation of USLP effects[28-30]. From our calculation of laser absorption, we know the distribution of deposited energy as a function of depth. Assuming absorption occurs before any noticeable expansion, we can deduce the initial material temperature using the equation of state of water[31]. The obtained temperature profile, together with the unchanged water density of 1g/cm^3 serve as initial conditions for the hydrocode. For the laser absorption case presented in Fig. 4, the initial surface temperature

calculated this way is 1.4 eV~16200K. This corresponds to a peak pressure of approximately 330 kbar. However, the simulation shows that the high pressure does not last very long. Since this is surface ablation and hot material is free to leave the surface, a rarefaction wave immediately sets in. Because the rarefaction moves faster than the shock, it starts lowering the wave pressure. After several nanoseconds, a triangular pressure pulse is formed and this pressure pulse leaves the absorption zone. Fig. 9 shows profiles of pressure and water density 10 ns after the absorption. Interaction of the shock and rarefaction develops a wave with a noticeably reduced peak of 6 kbar at this moment. Once the propagation becomes three dimensional, we can expect further lowering of pressure because of the geometrical effect. This part was done experimentally.

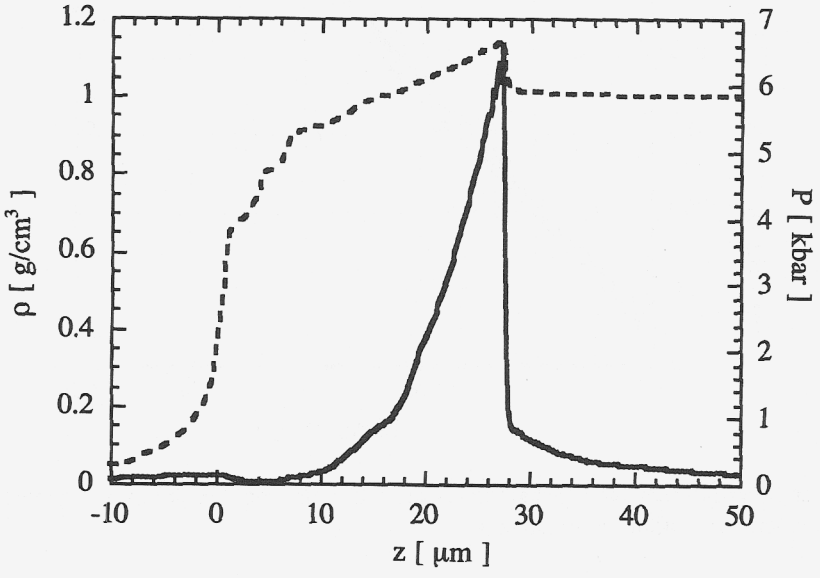

Fig. 9. Profiles of pressure and density calculated with hydrocode10ns after laser absorption described in Fig. 4. Solid line is pressure, dashed line is water density.

One of the ways to monitor pressure evolution is based on calculations of the shock speed[22]. Using interferograms taken at various delays after pulse absorption, we measured shock position for both spherical and cylindrical waves as a function of pulse fluence and width. The time derivative of the shock radius gives its velocity. Results for the radii measurement of the spherical waves are presented in Fig. 10.

First, there is no significant dependence on the laser pulse width, so the three curves presented are for $F=F_{th}$, $2F_{th}$, $3F_{th}$. The wave propagation distance is basically a linear function of time with slightly different initial radii for the three curves. The curves all have the same slope of 1.55 km/s, which is very close to the sound speed in water[4] of 1.48 km/s. The initial size changes from approximately 20 μm for low energy $F=F_{th}$ to 40 μm for the highest laser fluence. Since the laser pulse has a Gaussian spatial profile, higher beam energy makes the ablation spot larger, thus increasing the shock formation zone. Supersonic propagation during the initial stage also contributes to this change. Similar behavior was observed for the cylindrical waves – a constant propagation velocity close to the sound speed with an initial shock radius approximately equal to 30 μm (close to the beam radius).

This behavior is indicative of the wave strength. Despite formation of a shock, its velocity is practically constant at low pressures[4]. Since velocity measurement error becomes comparable to the expected pressure induced velocity variation, methods of pressure determination based on observation of the wave speed[22] do not work in the weak shock regime. Because pressure is always a strong function of density, which also directly affects the optical properties of water, we rely on interferometry to get more sensitive measurements of wave strength. We would like to emphasize that a major factor responsible for putting pressure generation in this weak shock regime is the configuration of ablation. If laser induced breakdown occurs inside of the material, ablation products are confined, and pressure pulses are stronger and last longer. On the other hand, for surface ablation, hot material is quickly ejected, taking with it a significant portion of the laser deposited energy and thus weakening the shock wave.

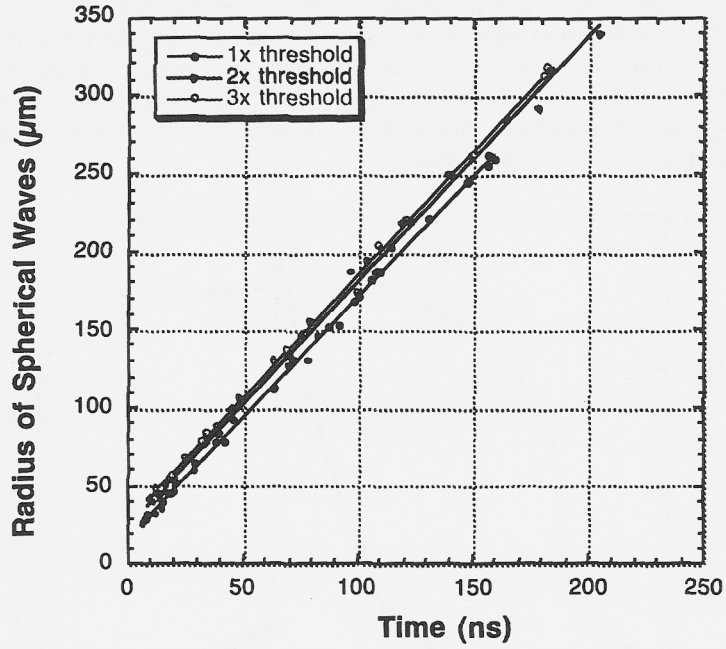

Fig. 10. Spherical pressure wave propagation as a function of time. Pressure wave generated by more intense energy is initially more advanced.

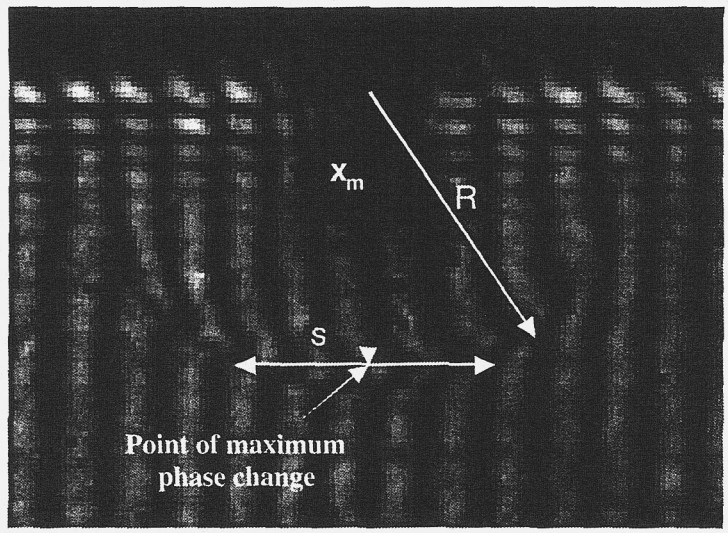

Fig. 11. Typical interferogram and parameters used for deducing the peak pressure.

interferograms provide us with information about the refractive index change, which can then be converted to pressure data using an appropriate formula for optical properties of water as a function of its state[15]. Theoretically, in the case of radial symmetry, one can recover optical properties for the whole wave. However this requires specialized software, which we did not have. Instead we adopted a simple method that allows us to estimate peak pressure and its evolution from several easily measurable wave parameters. Fig. 11 shows an interferogram of a spherical wave. We can see that the outer shock radius R, maximum phase shift $\delta\varphi_{max}$ and position of maximum phase shift x_m can be easily identified. For a simple dependence of refractive index on radius, these parameters can be used to calculate the maximum change in optical properties. Our modeling with the hydrocode (Fig. 9) shows that

a thin spherical shell with a triangular pulse profile would be a very reasonable assumption for the form of the refractive index. Therefore, calculating the phase shift $\delta\varphi$ from

$$\delta\varphi(x,a,R) = \frac{4\pi}{\lambda}\int_{\max(x,a)}^{R}\delta n(r,a,R)\frac{rdr}{\sqrt{r^2-x^2}}, \qquad (6)$$

where δn is the refractive index change, a is an inner wave radius, λ is wavelength, x is distance from the surface to the point of phase measurement and assuming the following variation of refractive index as a function of radius

$$\delta n(r) = \begin{cases} \delta n_{\max}\dfrac{r-a}{r}\dfrac{R}{R-a}, & a \le r \le R \\ 0, & r < a,\ r > R \end{cases}, \qquad (7)$$

we find the relationship between $\delta\varphi_{max}$ and δn_{max}:

$$\delta n_{\max} = \frac{\lambda\delta\varphi_{\max}}{2\pi s} f(s/2R), \qquad (8)$$

where $s = 2\sqrt{R^2 - x_m^2}$ is easily measured in the case of spherical geometry and f(s/2R) is a function depending on details of the integration. This function increases monotonically from 1.0 for thick pressure shells ($a<<R$, $s\sim R$) to 1.5 for thin shells ($a\sim R$, $s<<R$). Since the interferograms show that the latter is practically always the case, the value of this function is always set to 1.5. It is interesting to note that if we assumed a constant rectangular profile of δn, this function would have been equal to one identically.

Once δn_{max} is known, the peak pressure can be calculated. The formula describing the optical properties of water[15] has light wavelength, pressure and temperature as input parameters. However since shocks with pressure of a few kbars (the range we expect according to our modeling) heat water only by a few degrees, we assumed that constant temperature and very simple formula for refractive index change for 480nm light is obtained

$$\delta n \approx 1.154\cdot 10^{-5}\delta p + 1.93\cdot 10^{-9}\delta p^2, \qquad (9)$$

where pressure variation δp is in bars.

Fig. 12 shows the calculated spherical wave pressure as a function of radius for 140fs, 500fs and 1ps pulses. The pressure is strongly dependent on fluence, but only weakly dependent on the pulse width. The pressure decays from approximately 1000 bars at r ≈ 50 μm to about 100 bar at 300 μm for $F=F_{th}$, from 2500 bars to 250 bars for $F=2F_{th}$, and from 3000 bars to 300 bars for $F=3F_{th}$. The decay curves were fit to a r^{α} power law function and the α's were found to be in the range of 1.1 – 1.4. The pressure decay for a 5 ps pulse behaves differently from the shorter pulses. However, these results may not be reliable due to the interference of cylindrical waves with spherical waves at the longer pulse length.

We see that pressure decays a bit faster than inverse radius – the pressure behavior of sound waves in spherical geometry. There are two factors that may contribute to this behavior. First, even if the shock heating is small, after propagating a considerable distance, the wave does lose some energy. Second, since the symmetry is incomplete (the wave is hemispherical), the pressure must vanish at the water surface, and rarefaction waves launched at this boundary reduce the pressure.

The evolution of cylindrical waves is complicated by the fact that the laser beam deposits energy as a function of depth. Since this is a weak shock regime, the propagation speed is constant and the cylindrical shape is preserved. However, there is a constant flow of energy across the shock front that complicates the results. Our measurements at depth of 300μm indicate that cylindrical waves are noticeably weaker, evolving from approximately 400 bars at 40 μm to 100 bars at 200 μm. This decay is only a little bit slower than $1/r$, whereas according to energy conservation considerations it should be $1/\sqrt{r}$.

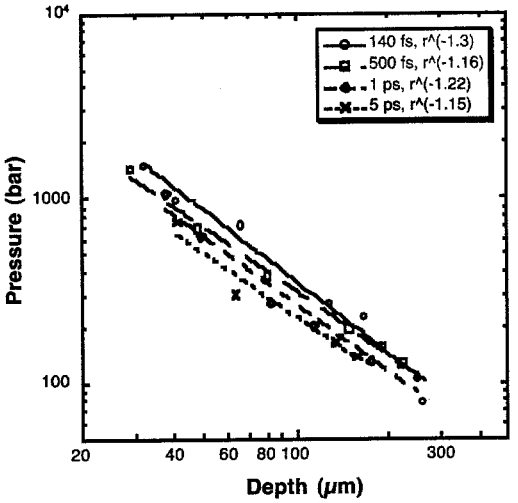

a)

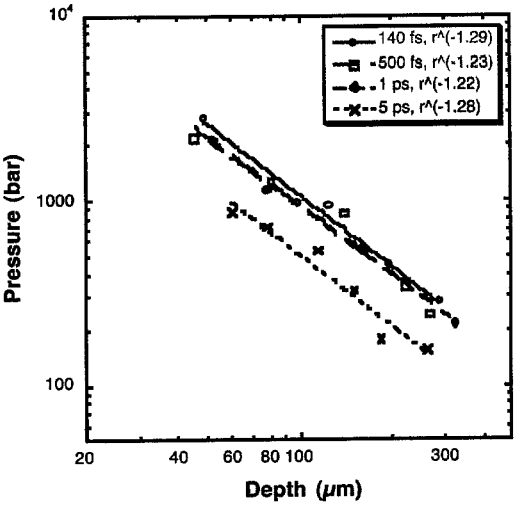

b)

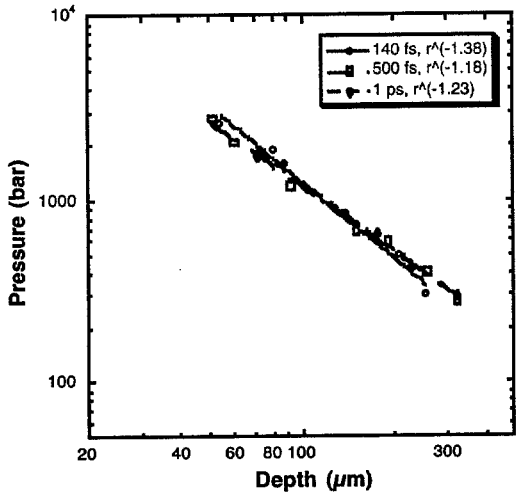

c)

Fig. 12. Estimated peak pressure as a function of depth for F/F_{th} = (a) 1, (b) 2, and (c) 3.

Once the pressure and wave profile are known, we can calculate the energy carried by the wave and estimate the conversion efficiency. For spherical symmetry, the energy can be calculated from[32]

$$E = 2\pi R^2 \int \frac{p(t)^2}{c_0 \rho_0} dt, \qquad (10)$$

where $p(t)$ is the pulse pressure, c_0 is the sound speed and ρ_0 is the normal density of water. Since we know the propagation velocity is equal to the sound speed, and the spatial profile of pressure is assumed to have a triangular form, a simple result is obtained

(11)

For a spherical wave with a triangular profile, the internal shell radius $a = x_m^2 / R$. If we simulate a rectangular profile, $a = R - x_m$.

Fig. 13 presents results of calculations of wave energy for shocks with 200 mm radius as a function of laser fluence. Measurements show that the fraction of beam energy deposited as mechanical energy (shock wave) is on the order of one percent. A similar calculation was done for the case of the simulated shock shown in Fig. 9. The energy carried by the wave at the moment of the onset of the triangle shape is 0.046 J/cm2. Since the modeling was done for energy deposition of a laser pulse with fluence 4.47 J/cm2 (Fig. 4), we calculate a similar conversion rate of one percent. In this case, about a third of the pulse energy was absorbed in the surface layer, thus conversion of absorbed energy is approximately 3%. This is much lower than the conversion efficiency of 90% found in volumetric laser induced breakdown of nanosecond pulses33 focused inside the liquid. It also appears to be lower than in the case of volumetric absorption of femtosecond pulses, which is on the order of 10%33,34.

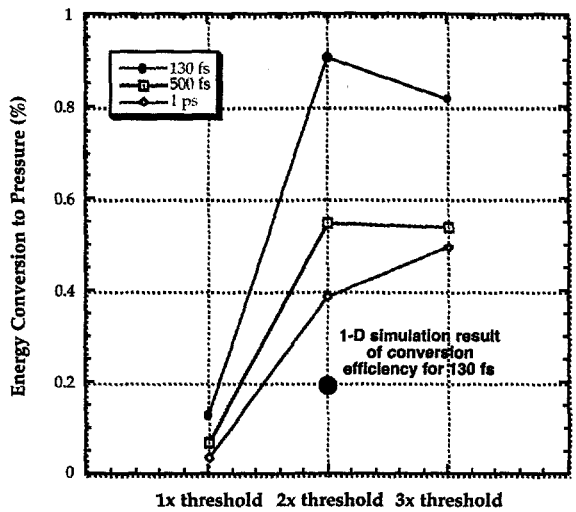

Fig. 13. Fraction of laser beam energy converted in the energy of the pressure wave for 140fs, 500fs and 1ps pulses.

VI. CONCLUSION

Laser ablation of water surface generates plasma that allows transmission in the bulk of only the leading edge of the laser pulse. Since the ablation fluence threshold is an increasing function of pulse width, this energy increases for longer pulses and may be large enough to cause deleterious effects. Laser ablation can affect the bulk of the material thermally and mechanically. However, for ultrashort pulses these effects are low, because breakdown occurs at relatively low laser fluence and absorption is very localized. Thickness of the plasma layer with density above critical is 100nm or less and energy deposition density quickly decreases with depth.

We also found experimentally and theoretically that the conversion efficiency of USLP laser energy into shock waves is on the order of one percent - noticeably smaller then in the case of radiation focused inside the liquid. A significant factor in decreasing the generated pressure is breakdown at the free surface of water. The surface allows a significant part of the laser deposited energy to escape with ejecta. Surface ablation creates pressure waves that

fall in the so-called weak shock regime. Their velocity is practically equal to the sound speed, therefore interferometry must be used to determine wave strength.

ACKNOWLEGMENT

This work was partially supported by Regional Research Center (RRC) Program of Ministry of Science and Technology (MOST) and Korea Science and Engineering Foundation (KOSEF).

REFERENCES

1. A. A. Oraevsky, L. B. DaSilva, A. M. Rubenchik, M. D. Feit, M. E. Glinsky, M. D. Perry, B. M. Mammini, W. Small, and B. C. Stuart, IEEE J. Sel. Top. Quantum Electron. **2**(4), 801 (1996).
2. D. X. Hammer, R. J. Thomas, G. D. Noojin, B. A. Rockwell, P. K. Kennedy, and W. P. Roach, IEEE J. Quantum Electron. **QE-32**(4), 670 (1996).
3. T. Juhasz, X.-H. Hu, L. Turi, and Z. Bor, Lasers Surg. Med. **15**(1), 91 (1994).
4. A. Vogel, S. Busch, and U. Parlitz, J. Acoust. Soc. Amer. **100**(1), 148 (1996).
5. E. N. Glezer, C. B. Schaffer, N. Nishimura, and E. Mazur, Opt. Lett. **22**(23), 1817 (1997).
6. A. Vogel, S. Busch, K. Jungnickel, and R. Birngruber, Lasers Surg. Med. **15**(1), 32 (1994).
7. A. Vogel, M.R.C. Capon, M. N. Asiyovogel, and R. Birngruber, Invest. Ophthalmol. Visual Sci. **35**(7), 3032 (1994).
8. X.-H. Hu, and T. Juhasz, Lasers Surg. Med. **18**(4), 373 (1996).
9. T. Juhasz, G. A. Kastis, C. Suarez, Z. Bor, and W. E. Bron, Lasers Surg. Med. **19**(1), 23 (1996).
10. B.-M. Kim, M. D. Feit, A. M. Rubenchik, B. M. Mammini, and L. B. Da Silva, Appl. Surf. Sci. **127-129**, 857 (1998).
11. B.-M. Kim, M. D. Feit, A. M. Rubenchik, E. J. Joslin, J. Eichler, P. C. Stoller, and L. B. Da Silva, Appl. Phys. Lett. **76**(26), 4001 (2000).
12. J. Neev, L. B. Da Silva, M. D. Feit, M. D. Perry, A. M. Rubenchik and B. C. Stuart, IEEE J. Sel. Top. Quantum Electron. **2**(4), 790 (1996).
13. M. Lenzner, J. Krüger, S. Sartania, Z. Cheng, Ch. Spielmann, G. Mourou, W. Kautek, and F. Krausz, Phys. Rev. Lett. **80**(18), 4076 (1998).
14. A. G. Doukas and T. J. Flotte, Ultrasound Med. Biol. **22**(2), 151 (1996).
15. I. Thormahlen, J. Straub, and U. Grigull, J. Phys. Chem. Ref. Data **14**(4), 933 (1985).
16. B.-M. Kim, M. D. Feit, A. M. Rubenchik, E. J. Joslin, P. M. Celliers, J. Eichler, and L. B. Da Silva, J. Biomed. Optics **6**(3), 332 (2001).
17. B. C. Stuart, M. D. Feit, S. Herman, A. M. Rubenchik, B. W. Shore, and M. D. Perry, Phys. Rev. B **53**(4), 1749 (1996).
18. F. Williams, S. P. Varma, and S. Hillenius, J. Chem. Phys. **64**(4), 1549 (1975).
19. L. V. Keldysh, Soviet Phys. JETP **20**(5), 1307 (1965).
20. F. Docchio, Europhys. Lett. **6**(5), 407 (1988).
21. J. Pearce and S. Thomsen, "Rate process analysis of thermal damage" in "Optical-thermal response of laser-irradiated tissue" ed. A. Welch and M. van Gemert, Plenum Press, 1995.
22. J. Noack and A. Vogel, Appl. Opt. **37**(19), 4092 (1998).
23. A. Vogel, K. Nahen, D. Theisen, and J. Noack, IEEE J. Sel. Top. Quantum Electron. **2**(4), 847 (1996).
24. P. K. Kennedy, IEEE J. Quantum Electron. **QE-31**(12), 2241 (1995).
25. J. Noack and A. Vogel, IEEE J. Quantum Electron. **QE-35**(8), 1156 (1999).
26. N. Bloembergen, IEEE J. Quantum Electron. **QE-10**(3), 375 (1974).
27. M. D. Feit, A. M. Rubenchik, and M. Runkel, Proc. SPIE **4347**, 383 (2001).
28. A. M. Rubenchik, M. D. Feit, M. D. Perry, and J. T. Larsen, Appl. Surf. Sci. **127-129**, 193 (1998).
29. A. M. Komashko, M. D. Feit, A. M. Rubenchik, M. D. Perry, and P. S. Banks, Appl. Phys. A **S69**, 95 (1999).
30. M. D. Feit, A. M. Rubenchik, Beop-Min Kim, L. B. Da Silva, and M. D. Perry, Appl. Surf. Sci., **127-129**, 869 (1998).
31. SESAME Report on the Los Alamos Equation of state Library, Report No. LALP-83-4, T4 Group, Los Alamos National Laboratory, Los Alamos, 1983. Equation of state for water #7150.
32. R. H. Cole, *Underwater Explosions* (Princeton University Press, Princeton, NJ, 1948).
33. A. Vogel, J. Noack, K. Nahen, D. Theisen, S. Busch, U. Parlitz, D.X. Hammer, G.D. Noojin, B.A. Rockwell, and R. Birngruber, Appl. Phys. B, **68**(2), 271 (1999).
34. J. Noack, D. X. Hammer, G. D. Noojin, B. A. Rockwell, A. Vogel, J. Appl. Phys., 83(12), 7488 (1998).

4. ADVANCED LASERS AND COMPONENTS RESEARCH ACTIVITY HIGHLIGHTS

PHASE-LOCKED, ANTIGUIDED MULTIPLE-CORE RIBBON FIBER LASER

Under the support of the Laboratory Directed Research & Development Program (LDRD) and U.S. Air Force Research Laboratory (AFRL), Albuquerque, N. M., we are developing a scalable multiple-core ribbon fiber laser to generate short-pulse, high-average-power (kW-scale) coherent light for possible applications in the military, material processing, and x-ray generation.

The development of double-clad fiber has brought fiber lasers to the forefront of possible approaches for high-beam-quality, high-average-power laser sources. Using a cladding-pumped geometry with a single-mode core, individual fibers have been demonstrated to yield greater than 100 W of average power. However, it is difficult to increase the outputs of these single-core fiber lasers to higher levels because of the onset of optical facet damage and deleterious nonlinear optical interactions at high irradiance. Critical to increasing the average power capability of fiber lasers is enlarging the aperture area of the laser radiation emerging from the fiber. One way to increase the aperture available to the laser radiation is to employ multiple cores that are phase-locked to yield a coherent output beam. The conventional power scaling techniques using evanescent coupling have not been very successful because of phase fidelity degradation between distant cores in large-diameter fibers.

During the course of this work, we successfully developed a new method to phase-lock multiple fiber cores in a fiber structure via radiative coupling (not evanescent coupling). This new method, known as antiguiding, which utilizes gain elements radiatively coupled in a "leaky" waveguide array, is analogous to the scheme used earlier for phase locking of laser diode elements. By selective placement of gain regions within a uniform index core, we were able to create a preferred single mode in the fiber.

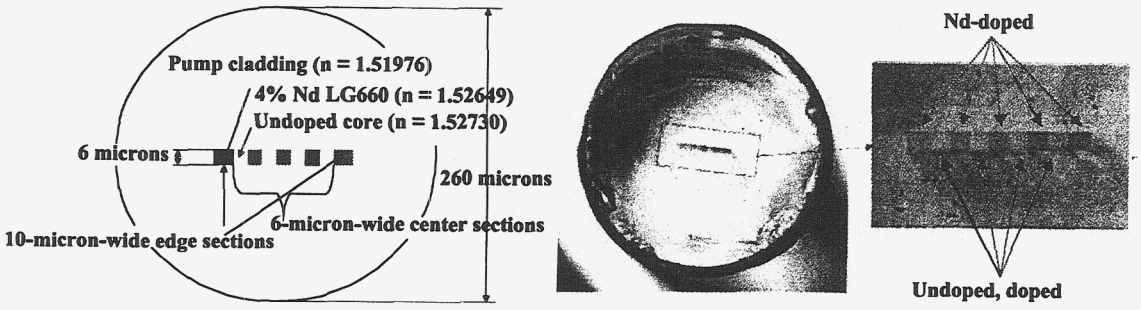

Figure 1. Sketch and photograph of LS&T's prototype five-core Nd fiber in which multiple-gain cores were phased using an antiguiding mechanism.

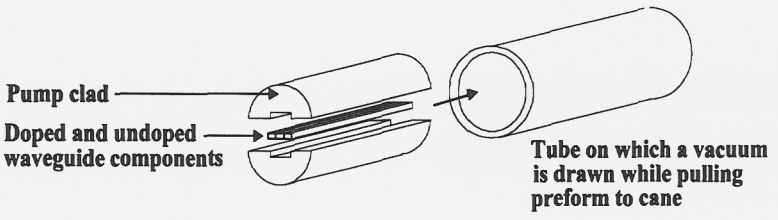

Figure 2. Sketch illustrating the rod-in-tube fabrication technology used to construct the preform for the prototype fiber shown in Figure 1.

Because the light field is evenly distributed across all cores in this scheme and all gain cores communicate with each other, we anticipate that the scalability of the device will be very favorable.

A cross-sectional view of the prototype ribbon laser is shown in Figure 1. The waveguide region is rectangular in shape and is comprised of a periodic sequence of gain and no-gain segments having nearly uniform refractive index. It is embedded in a lower-refractive-index cladding region used for diode pumping. Using an end-pumping geometry in which an 808-nm diode array served as the pump source, we were able to run the Ribbon laser predominately in two antiguided modes, as predicted by our modeling.

Figure 2 illustrates the novel "rod-in-tube" fabrication technique that was used to construct the preform for the prototype ribbon fiber. The same technique shows great promise in being able to scale to substantially higher-power-capability fibers.

By using antiguiding mechanism, we successfully demonstrated phase-locking in a five-core Nd-doped glass prototype structure that was fabricated using a novel soft glass fabrication technology. Due to the delocalized nature of their eigenmodes, antiguided structures similar to the ribbon fiber reported here are being evaluated as potential routes to extremely high-power, single-spatial-mode radiation. As an example of a power-scaled system, Figure 3 shows a conceptual design for a 30-kW ribbon fiber. By scaling from 5 cores to 100 cores with fused silica, it should be possible to achieve 30 kW from a single fiber. Achieving this power in laser weapons would be truly revolutionary for the military and, moreover, would have an enormous economic impact in laser material processing and x-ray generation.

— R. Beach, M. Feit, and S. Payne

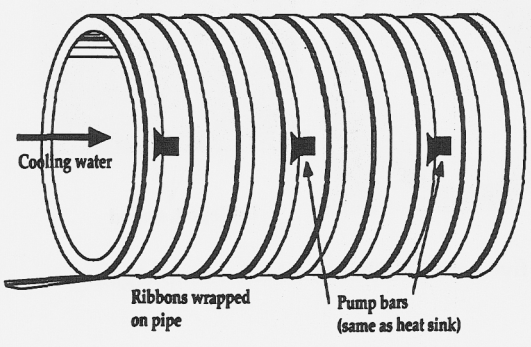

Figure 3. Conceptual design of 30-kW ribbon fiber laser in which a cooled mandrel is used for thermal management, and pump excitation light from diode bars is introduced into the side of the structure.

FIRST LIGHT FROM THE MERCURY LASER: A DIODE-PUMPED, SOLID-STATE, GAS-COOLED LASER FOR FUSION ENERGY APPLICATIONS

Diode-pumped solid-state lasers are one of four driver technologies being considered for inertial fusion energy systems. The competing technologies include heavy ions (Lawrence Livermore National Laboratory, Lawrence Berkeley Laboratory), Z-Pinch (Sandia) and KrF (Naval Research Laboratory). Each driver development program is currently focused on demonstrating several proof-of-principle design concepts.

Mercury is designed to be a 100-J, 10-Hz, 10% efficient prototype laser system, scalable to a 1-kJ aperture with minimal beamline reengineering. To achieve this goal, we explored numerous gain mate-

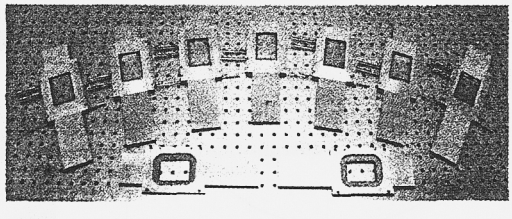

Figure 4. Gas-cooled amplifier vanes. Central three vanes are potted with surrogate Nd:Glass as placeholders until additional S-FAP slabs can be fabricated.

rials and architectural options to best fit the design space of a fusion energy class laser. Yb^3+$Sr_5(PO_4)_3F$, called Yb:S-FAP, was chosen as the gain medium based on its long energy storage lifetime, moderately high cross section, and good thermal conductivity.

The primary challenge has been in growing full-aperture slabs of 4×6 cm^2 in area. This past year, we developed a successful growth process to produce half-size slabs that can then be bonded together to form full-size slabs for the 100-J Mercury aperture. Four of these slabs have been mounted onto the first set amplifier cooling vanes as shown in Figure 4.

Four more slabs are in fabrication and six crystalline boules are waiting to be cut. We can anticipate having enough slabs by the end of the year to fill two amplifier cassettes. Recent measurements indicate surface damage thresholds of greater than 50 J/cm^2 when tested on a 3×5 cm^3 sample.

The pump diodes at 900 nm, fitted with microlenses, are mounted onto etched silicon heatsinks and then mounted onto large copper blocks that provide the cooling and electrical power to the diodes. The amplifier assembly in Figure 4 was pumped by four 80-kW diode arrays. The amplifiers and pump delivery optics are shown in Figure 5 along with the diode arrays.

The system was initially operated at modest repetition rates of 0.1 Hz to avoid excessive thermal loading on the Nd:Glass slabs. With 200 mJ of front

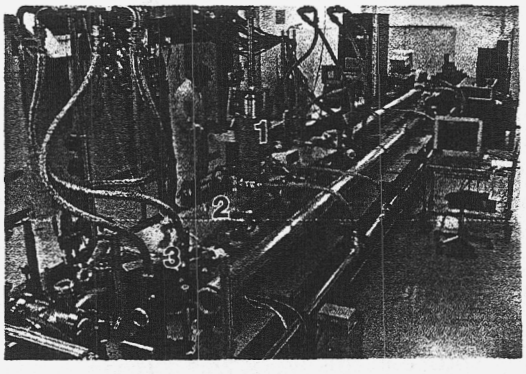

Figure 5. Mercury laboratory: (1) gas-cooled amplifier head, (2) pump delivery, and (3) diode array.

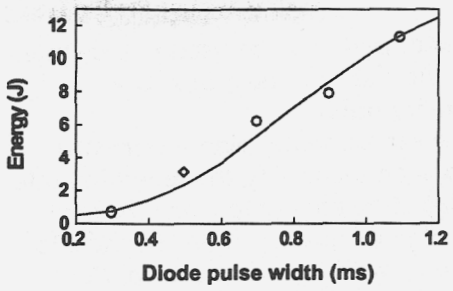

Figure 6. The energy extracted from a 4-pass S-FAP slab amplifier, using a Q-switched oscillator pulse as the seed.

energy in a 16-ns pulse, we were able to extract up to 11.8 J of energy at 1.047 μm in a 4-pass angularly multiplexed arrangement. An energetics code was used to model the data and energy-vs-time (see Figure 6). Wavefront data was also taken for static (no pumping) and full pumping conditions. The static wavefront data show 2.7 waves of peak distortion due to bonding phase discontinuities incurred during the fabrication process. New fabrication techniques are being tested to eliminate these distortions. In the interim, a static phase corrector plate using the wet-etch technology developed by Sham Dixit and Michael Rushford of the Short-Pulse Lasers, Applications, and Technology team, was tested and shown to compensate for the distortion when placed directly adjacent to the amplifier assembly.

Figure 7 shows the far-field spot with and without the corrector plate, indicating a factor of three improvement to reach a 2× diffraction-limited spot. The

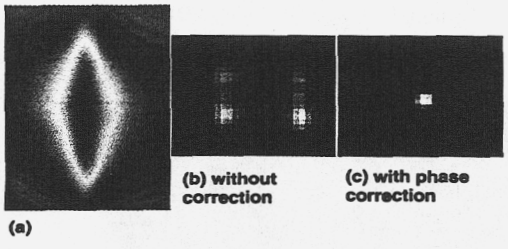

Figure 7. (a) The static wavefront of the amplifier with no diode pumping. (b) The corresponding far-field spot. (c) A phase corrector plate allows the far-field spot to reach a 2× diffraction limit.

corrector plate will be used in the system until the slabs can be replaced with higher quality units.

The experimental plan is currently focused on increasing the repetition rate and injection energy to reach the next level of performance of >3 Hz and >15 J of output with the current amplifier assembly. Additional slabs are expected later in the year and will allow for full 10-Hz operation and up to 30 J of energy output with one amplifier. Activation of a second amplifier that will yield up to 100 J at 10 Hz will occur in 2003.

— C. Bibeau, A. Bayramian, K. Skulina, and S. Payne

FIRST LIGHT FROM DIODE-PUMPABLE RUBIDIUM LASER

With support from the Laboratory Directed Research and Development (LDRD) Program, we have recently demonstrated and modeled for the first time a laser diode-pumpable rubidium (Rb) laser operating at its first resonance wavelength of 795 nm. While counterintuitive, our work shows that it is feasible to efficiently convert the relatively broadband (2–3 nm), low-brightness (M2 ~1000) output of commercial laser diode arrays into high-brightness emission using atomic vapor gain media (which are characterized by relatively narrowband optical transitions, ~0.1 nm, FWHM in the presence of buffer gas). Moreover, due to the uniquely favorable quantum characteristics of the alkali atoms as laser gain media, this energy conversion process can be affected with a remarkably small quantum energy defect ($1 - \lambda_{pump}/\lambda_{laser}$) of ~2%, compared to the well-known values for Nd (24%) and Yb (8%), even though a purely three-level laser scheme is employed.

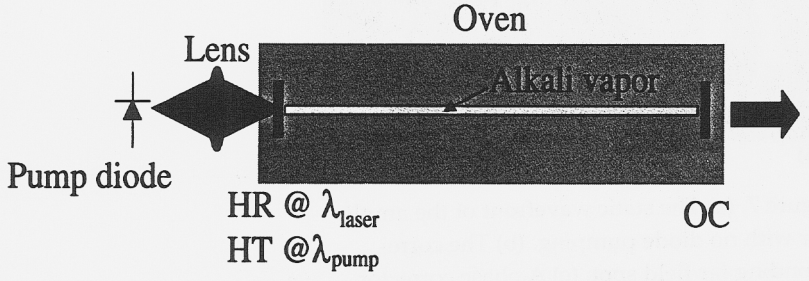

Figure 8. The diode-pumped alkali vapor laser (DPAL) concept. (HR = high-reflectivity optic; HT = high-transmission.)

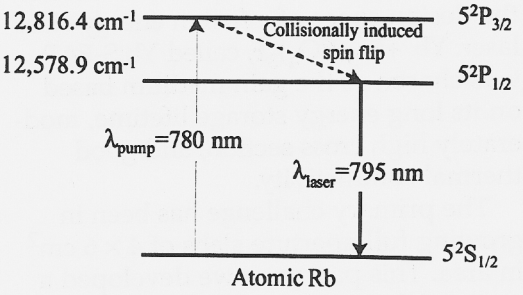

Figure 9. Energy levels of atomic Rb involved in the laser.

An initial demonstration of this Rb laser concept was performed using a Ti:sapphire laser as the pump source (see Figure 8). Figure 9 shows the energy levels of atomic Rb involved in this laser. The system is pumped on the D2 line at 780 nm and lase on the D1 line at 795 nm. It has been long recognized that population inversions can be produced on the D1 transition of alkali atoms. By resonantly pumping the D2 transition with a dye laser, amplified spontaneous emission (ASE) has been observed. However, up until now the extension of this optical experiment to laser output has been hampered by two issues: (1) Atomic lines (in GHz-to-tens of GHz) are much narrower than available practical optical pump excitation sources, such as semiconductor diode lasers with their emission linewidths of several nm (~103 GHz). (2) Kinetic relaxation time between the D line transitions is often too slow compared with its radiative lifetime (only 28 nsec for Rb $5^2P_{3/2}$). For this laser scheme to work, the rate of spin-flip transition ($5^2P_{3/2}$ to $5^2P_{1/2}$) must be sufficiently accelerated so that the excited-state population can be efficiently transferred into the initial $5^2P_{1/2}$ laser level before it is lost out of the $5^2P_{3/2}$ level through radiative decay.

Figure 10 shows a schematic diagram of the initial experimental setup. The pump source in this work was a Ti:sapphire laser capable of delivering 500 mW of 780-nm CW pump power into the Rb cell. The linewidth of the pump beam was measured to be 49 GHz FWHM. The

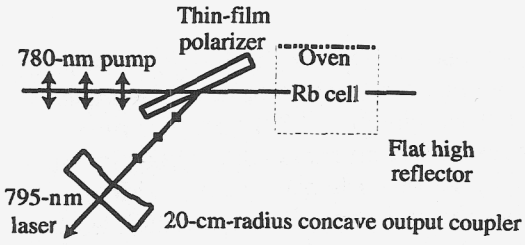

Figure 10. Schematic diagram of the atomic Rb vapor laser used in the demonstration. The overall cavity length of the laser was 19 cm, for the data presented within.

Rb was buffered with 525 torr of helium and 75 torr of ethane. Helium and ethane were added to broaden the atomic absorption band of Rb and to accelerate the rate of spin-flip transition (relaxation). The cell was contained in a closed oven (held at 120°C ± 1°C) with two AR-coated windows to allow access for both the pump and laser beams. The Rb density in the cell was held at $1.7 \times 10^{13}/cm^3$. Although the one-way loss for this cavity, excluding output coupling, was high at 20%, it was still low enough to allow lasing. During the initial experiment using a 50% reflectivity output coupler, we obtained over 50 mW of laser output, in good agreement with the result calculated from the energetics laser model. The emitted laser beam at 795 nm was found to be diffraction limited.

Total pump power absorbed in the lasing mode volume was estimated to be 179 mW. The reason for the good absorption of the pump radiation, which is 4× broader than the D2 absorption feature, is the very high absorption on line center. The on-line-center absorption is estimated to be ~20 nepers in a single pass through the cell. Because the line is homogeneously broadened in the presence of helium, pump photons absorbed in the wings are as useful to the laser as pump photons absorbed on line center, a fact that is critical to the efficient performance of this class of laser.

Using the energetics laser model, we were able to accurately predict the performance of an end-pumped DPAL system in which the pump beam freely propagates through a vapor cell. In this approach, a hollow lens duct is used to deliver the pump light to the laser and the pump light is double passed in the gain medium to improve pump absorption efficiency. Our model calculation shows that the DPAL concept can be scaled up to systems with output powers beyond 100 kW, with very high efficiency.

Experiments are continuing to optimize the performance of the Ti:sapphire laser-pumped Rb laser and to demonstrate an end-pumped DPAL. In addition to Rb, Cs is also a good candidate for a DPAL, being pumped at 852 nm and lasing at 895 nm. Besides Rb and Cs, other alkalis are also possible candidates. Based on our understanding of line broadening and published broadening rates, we are confident that a diode-pumped alkali laser (DPAL) could be developed to operate at high average power with exceptionally high efficiency (up to 70% optical-optical) and with high beam quality.

— W. Krupke, R. Beach, V. Kanz, and S. Payne

ACTIVATION OF THE XAPPER EXPERIMENT

System activation is under way for an x-ray ablation and damage experiment, XAPPER. XAPPER is supported by Defense Program's High Average Power Laser Program. The source uses an ellipsoidal condensing optic to collect x-rays and bring them to focus on the sample. XAPPER's mission includes study of pulsed x-ray damage production in can-

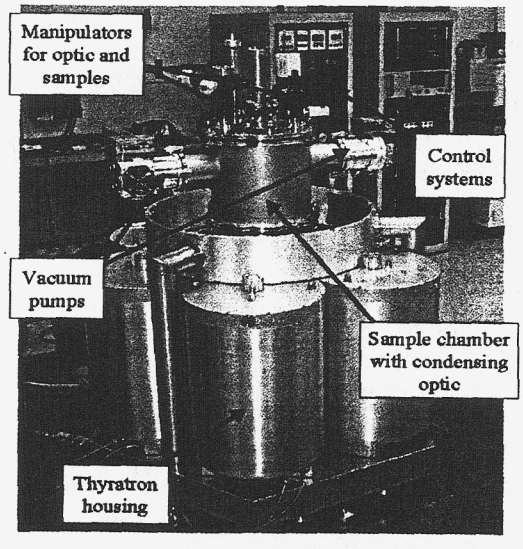

Figure 11. The XAPPER star pinch is driven by current supplied by six thyratrons. Both the condensing optic and sample tray can be manipulated.

didate inertial fusion energy chamber wall (tungsten and carbon composites) and final optic (aluminum and dielectric mirrors, as well as fused silica lenses) materials.

XAPPER uses a star pinch to produce soft x-rays at repetition rates of up to 10 Hz (see Figure 11). When operated with xenon, XAPPER will provide fluences of ≥7 J/cm^2 of 113 eV x-rays. For operation with nitrogen, the peak fluence falls to ~0.25 J/cm^2, but the x-ray energy increases to 430 eV. Use of the condensing optic not only allows for higher fluences, but it greatly reduces the debris loading on the sample. Several million pulses can be completed before minor maintenance is required. The XAPPER source was designed and built by PLEX LLC of Brookline, Massachusetts.

With x-ray fluences of several J/cm^2 and the short mean free path of the soft x-rays, XAPPER is capable of providing x-ray doses that exceed those expected in laser-IFE power plants. Current diagnostics include a photodiode, vacuum calorimeter, and EUV spectrometer. A fast optical thermometer will be added and a laser interferometer is being designed. In addition to its laser fusion energy mission, XAPPER may be of interest to the heavy-ion fusion program for liquid ablation/condensation studies. Inertial confinement fusion facilities, such as NIF, may be interested in performing low-fluence ablation study. XAPPER's pulsed nature would allow one to study the small levels of ablation expected at fluences at or above threshold.

The survivability of the final optic, which must sit in the line-of-sight of high-energy neutrons and gamma-rays, is a key issue for any laser-driven inertial fusion energy (IFE) concept. Previous work has concentrated on the use of reflective optics. We have introduced and analyzed the use of a transmissive final optic for the IFE application. Our experimental work has been conducted at a range of doses and dose rates, including those comparable to the conditions at the IFE final optic. The experimental work, in conjunction with detailed analysis, suggests that a thin (<1 mm), fused silica Fresnel lens, such as those created for the Eyeglass Project, may be an attractive option when used at a wavelength of 351 nm. Our measurements and molecular dynamics simulations provide convincing evidence that the radiation damage, which leads to optical absorption, not only saturates but that a "radiation annealing" effect is observed.

Neutron–induced optical absorption equilibrates at ~5% for a 500-mm-thick fused silica Fresnel lens operated at 300°C. By intentionally operating the optic at an elevated temperature of 500°C, the optical absorption would be reduced to only 0.6%.

— *J. Latkowski*

DEVELOPING ADVANCED FIBER LASERS FOR GUIDE STAR APPLICATIONS AND PETAWATT LASER FRONT ENDS

Since their "re-discovery" by the University of Southampton in 1985, fiber lasers and amplifiers have steadily increased in importance and output power. They are popular solutions to many problems because once demonstrated for a particular application they typically have high wall-plug efficiency and are easy to package into robust, reliable turn-key devices that virtually anyone can operate. Figure 12 below shows the increase in output power of this class of laser with time for CW lasers.

A cursory analysis of Figure 12 shows that fiber laser have been increasing in average power by a factor of 10 every 3 years for roughly the last 2 decades

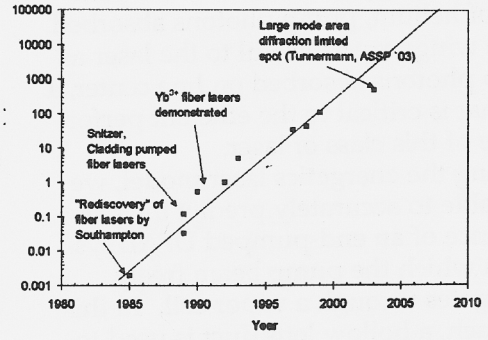

Figure 12. Output power increase with time from CW fiber lasers.

and are now reaching output powers of interest to DOE applications. In recognition of this we have begun an effort to investigate these lasers to a greater degree. This effort is project focused in two areas; an investigation of high power CW sources at novel laser wavelengths for application in laser guide stars sources and an investigation of high energy short pulses to create an all-fiber front end for peta-watt lasers compatible with the NIF fiber front end.

In the laser guide star effort, we are attempting to create a 10-W, turn-key, compact, robust all-solid state source of 589-nm light. Our scheme for doing this is based on sum-frequency mixing a 10-W erbium fiber laser at 1583 nm with a 10-W neodymium fiber laser operating at 938 nm in a periodically poled nonlinear material. In the last year we have made significant progress towards this goal. We have assembled a 10W source of 1583-nm light by using a master oscillator power amplifier configuration. A 3-mW fiber DFB laser is phase modulated to broaden the linewidth and then amplified in a commercial 10-W L-Band erbium doped fiber amplifier. This system and its output power with pump diode current are shown in Figure 13.

The 938-nm laser has proven to be more of a challenge, but significant progress has been made on this front also. Previous reports in the literature of fiber lasers at 938 nm claimed output powers less than 100 mW. We have constructed a cladding pumped fiber laser system operating at over 2W of output power this year and have made considerable progress in understanding the technical challenges involved in scaling this output power to 10W. Operation of neodymium doped glass at 938 nm works best in a nearly pure-silica glass composition; unfortunately these glass compositions limit the maximum doping concentration of the neodymium. Fiber lasers are particularly well suited to this type of problem because they are a natural medium for achieving long interaction lengths at high power density. Challenges relating to the operation of neodymium at 938 nm that were investigated in this year's efforts include the

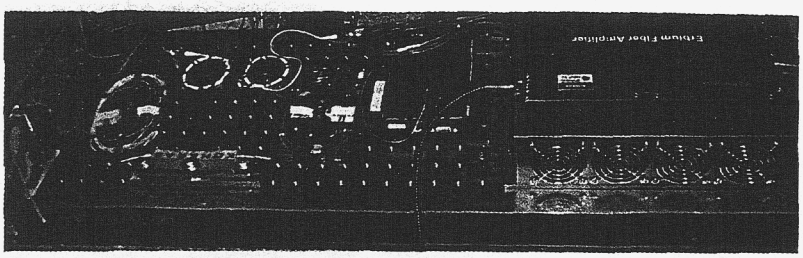

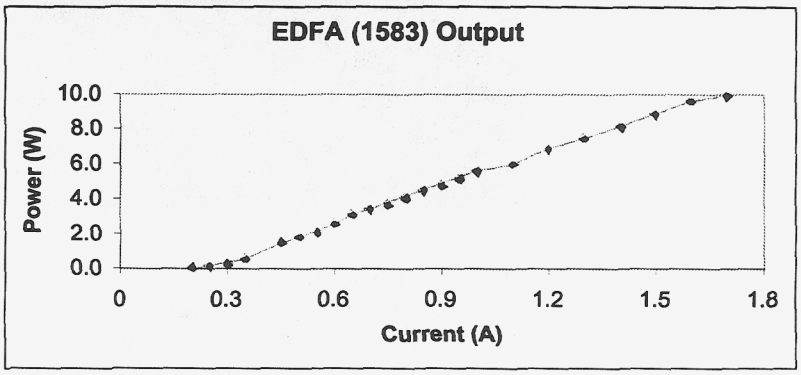

Figure 13. LHS: Picture of the 10W 1583-nm fiber laser source (for scale, the hole spacing is 1 inch, and no effort has been made to "package" the device to small size), RHS: Output power at 1583-nm vs. pump diode current.

effects of quenching as a function of concentration, understanding the impact of stimulated Brilliouin scattering on the amplifier performance, mitigation of ground state absorption and competition from the 1088-nm laser line. The fiber

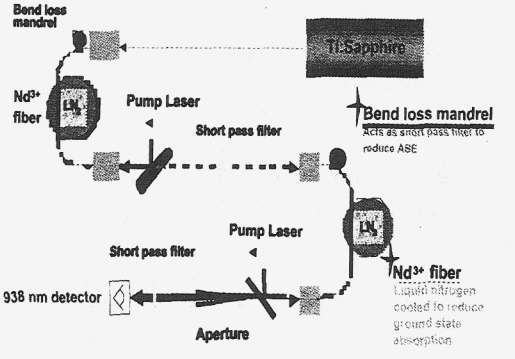

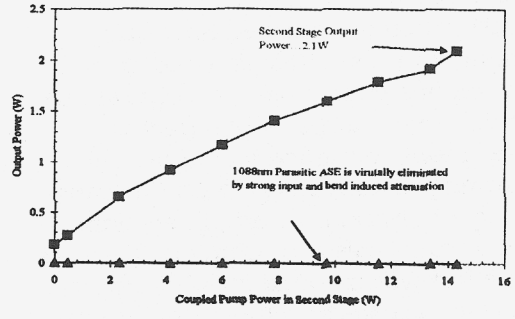

Figure 14. LHS: Schematic of the 938-nm fiber amplifier prototype, RHS: Output power curve from the second stage of the amplifier showing >2W of output power and near total suppression of competing 1088-nm light.

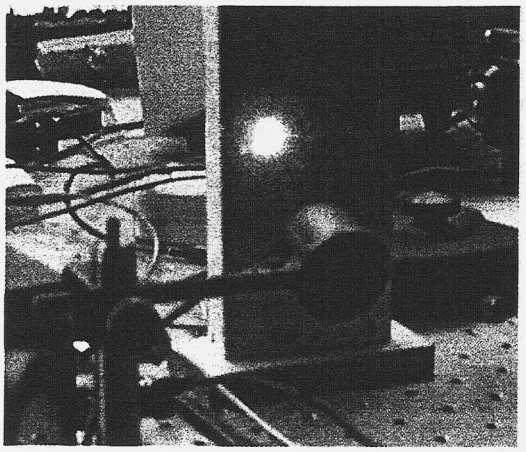

Figure 15. 589-nm output of the fiber laser system.

offers a natural mechanism for suppressing light at longer wavelengths as the waveguide is subject to a wavelength dependent bend loss. Thus by winding the fiber on an appropriately sized mandrel, it is possible to create a distributed filter in the gain medium that suppresses 1088nm light, and passes 938nm light. Understanding of these issues has permitted the construction of a 2-W prototype fiber amplifier shown in Figure 14 and design of an optical fiber, which we believe, will permit us to construct an efficient 10-W amplifier in 2003.

We recently combined these two sources in a 5-cm-long PPLN crystal and demonstrated the full system at 589 nm. A picture of the output of the full system is shown in Figure 15 above.

We have also begun an effort this year to look at fiber lasers as the front end for a high-energy petawatt laser system. This is a far-reaching effort with the goal of generating an all fiber laser source of <200fs pulses that can be stretched to 3 ns and amplified to output energies as high as 10mJ completely within the optical fiber. The effort is divided into three tasks which include construction of the fiber laser mode-locked master oscillator, investigation of a chirped fiber Bragg grating for pulse stretching and demonstration of a large mode-area optical fiber amplifier with a specialty refractive index profile designed to amplify and transmit pulses with up to 2.5 times the energy of optical fiber amplifiers with similar core-sizes and beam qualities. As this effort was initiated in 2002, progress thus far has consisted mostly of design and modeling efforts. However, we have demonstrated the basic physics of the "large flatten mode" (LFM) amplifier by having a sample fiber made and by purchasing a second fiber with a similar characteristics and a standard refractive index profile to use as a control sample. The LFM index profile is shown in Figure 16 below along with the intensity profile of the preferred mode and a comparison of it to the preferred mode found in a standard fiber of similar core size.

In the literature short pulses with energies as high as 1 mJ have been demonstrated. The limiting factor in these demonstrations has been stimulated Raman scattering, an effect which scales with peak power. Thus the large flattened mode fiber should provide an improvement in terms of the energy at which the onset of this effect occurs. To demonstrate this, we employed two

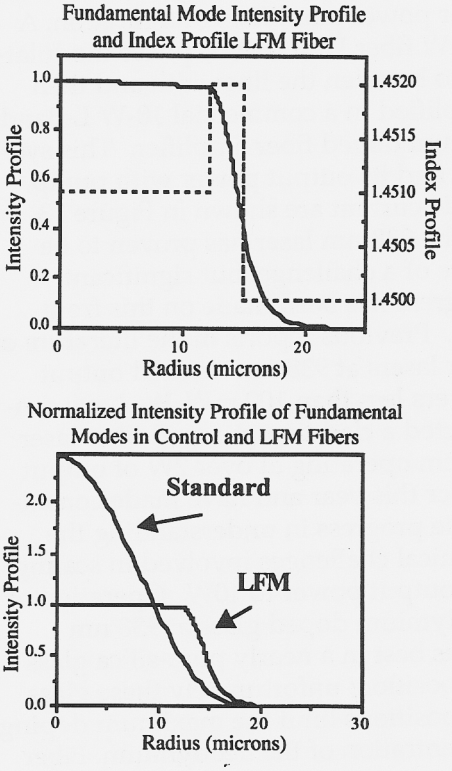

Figure 16. LHS: Radial refractive index profile of the large flattened mode fiber (dotted line) and the preferred mode (solid line), RHS: Normalized comparison of the large flattened mode to the mode found in a standard step-index fiber (the modes have been normalized such that they carry the same energy.)

fibers with 30-mm cores and a nominal numerical aperture of 0.06. One fiber had a standard step index design and one had the large flattened mode fiber design. Both fibers were doped with ytterbium, cladding pumped at 976nm and employed as amplifiers for stretched pulses with a 16nm bandwidth centered at 1070nm. The control fiber had a length of 9.1m and the large flattened mode fiber had a length of 8.3 m. A summary of the amplification results is shown in Figure 17 below, revealing the reduced Raman gain in an LFM fiber.

In 2003, we will be further investigating the large flattened mode fiber amplifier, with the goal of amplifying laser pulses to energies up to 10mJ or greater. We will also be working to demonstrate a mode-locked fiber laser that can be used as a front end for petawatt laser systems and investigate the usefulness of chirped fiber Bragg gratings as pulse stretchers. Finally, we will also be looking at the propagation dynamics of short pulses in specialty fibers used in NIF such as the polarizing optical fiber used to transport light from the master oscillator room to the glass amplifier chain.

— J. Dawson

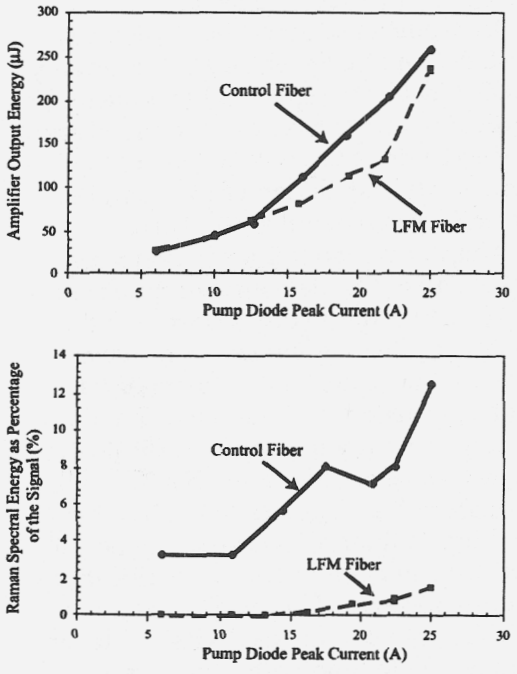

Figure 17. LHS: Output pulse energy vs. pump current for the two fibers, as expected they have about the same characteristic, RHS: Percentage of the total power contained in the Raman signal band to longer wavelength showing the large flattened mode fiber (LFM) having significantly less of a Raman component than the standard step index fiber.

JANUS UPDATE

The JANUS laser, a high-energy Nd:glass laser system operated by PAT, supports a variety of experiments such as equation-of-state studies and is used as a pump laser for the high-peak-power, ultrafast JANUSP laser. In operation since 1974, JANUS has undergone several upgrades, most recently in 1985, and currently has two beam lines capable of about 300 J each (see Figure 18.) LS&T is collaborating with PAT in a major upgrade of the JANUS system to achieve 1 kJ per beamline at a wavelength of ~1 mm and with the capability of frequency doubling with at least 70% conversion efficiency. The JANUS laser facility is located in Building 174.

The upgraded laser will enable significant new experimental capabilities. With a 1-kJ pulse energy, pressures of 20 Mbar can be achieved, compressing targets to 2-3 times solid density. Electron temperatures in the range >10eV will be possible. The higher energy pulse can drive larger area shock waves resulting in higher precision measurements. The upgraded laser will provide significant NIF support capabilities. Proof-of-principle experiments can be performed prior to scaling to NIF. Test and calibration of NIF diagnostics can be done. The system will also continue to serve an important hands-on facility for recruiting and training new physicists.

In addition to achieving a pulse energy of 1 kJ, the laser design was created to use as much as possible of existing hardware and architecture. This minimizes costs and downtime for conversion. The major changes in the laser design were to replace the current silicate laser glass with higher gain phosphate glass and to add 15-cm disk amplifiers. The 15-cm amplifier housings, as wells as some of the spatial filter components, are excess NOVA hardware.

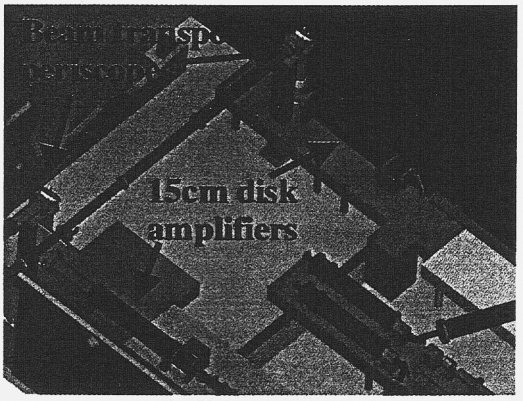

Figure 18. Janus laser bay.

The energetics of final design, comprising the front-end rod amplifiers, 10-cm amplifiers with phosphate glass and the final 15 cm amplifier, was analyzed using a Frantz-Nodvik model, which verified that energy of 1 kJ could be achieved at a pulse duration of 3 ns. The system will be capable of pulse durations from 0.1-10 ns, in some cases with lower pulse energy. The design limits DB to <2 and damage fluence to <0.67 times the damage limit. The modeling also verifies that square-pulse distortion and pre-pulse ASE are within acceptable limits. In addition, optical raytracing and diffraction modeling was used to insure image relaying and address ghost reflection issues. The frequency conversion was also modeled to verify the conversion efficiency of >70%.

To achieve the damage performance called for in the design, the laser glass for many of the disks must be free of Pt inclusions, which damage at fluences above 4 J/cm^2. The phosphate glass used in the 10-cm and 15-cm amplifiers in NOVA was not specified as Pt free. However, the glass used in the NOVA 46-cm slab amplifiers is Pt-free.

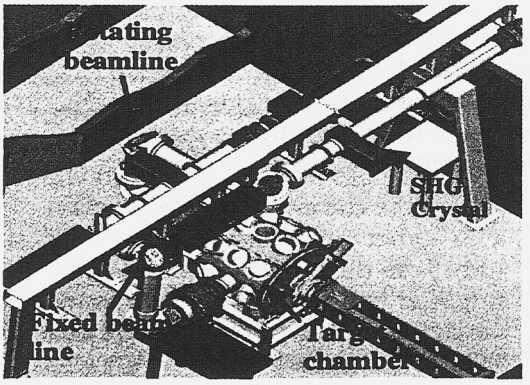

Figure 19. Janus target bay.

Therefore, the disks for the upgrade will be fabricated from glass from the 46-cm slabs. Elliptical disk blanks have been cut from the 46-cm laser slabs. Monolithic edge cladding for ASE suppression is being poured on.

The laser output is transported to the target chamber in another room with image-relaying vacuum spatial filters. The beam transport system from the spatial filters to the target chamber has a unique design. One beamline is fixed and one is on a rotating arm (see Figure 19). The rotating arm can be arranged to bring the second beam into one of three different target-chamber ports. This versatility allows for illumination of targets from opposing beams, backlighter experiments, X-ray Thompson scattering diagnostics and other experiments.

The detailed design began following a technical design review in November, 2001, and is now complete. Procurement of the mechanical hardware is virtually complete. Much of the beam

transport mechanical hardware was installed in December, 2002, and January, 2003. Most of the spherical and plano optical elements have been received and the aspheric optics will arrive in March. The finally installation of the upgraded beamlines is scheduled for April.

The 15-cm monolithically clad laser disks will not be delivered until summer of 2003. In order to begin operating the system and validating its performance prior to that time, NOVA 15-cm disks will be installed. Although they aren't Pt free, preliminary test results indicate that Pt inclusions are few enough and small enough so that selected disks placed in the highest fluence locations may permit operation at close to design specifications prior to the arrival of the new disks.

The name of the JANUS laser is taken from a Roman god with two faces, one looking to the past and one looking to the future. The name could not be more apt. The facility looks backward on more than a quarter century of service. With the current upgrade it will continue to be at the forefront of high-energy laser interaction research.

— J. Caird, C. Ebbers, A. Erlandson, G. Huete, B. Molander, and N. Nielsen

Activation of the Mercury laser, a diode-pumped, gas-cooled, solid-state slab laser

A.J. Bayramian, R.J. Beach, W. Behrendt, C. Bibeau, R. Campbell, S.N. Dixit, C.A. Ebbers, B.L. Freitas, V.K. Kanz, M.C. Rushford, S.A. Payne, J. Schmidt, K.I. Schaffers, K.M. Skulina, S. Telford, and J.B. Tassano

A. DeWald, J. Rankin, and M.R. Hill

Mechanical and Aeronautical Engineering, University of California, Davis, CA 95616 USA

Diode-pumped solid-state lasers are one of four driver technologies being considered for inertial fusion energy power plants. Each driver development program, including solid-state lasers, heavy ions, Z-Pinch and gas lasers (KrF) is currently focused on demonstrating several proof-of-principal design concepts. The Mercury Laser (see Fig. 1) is currently being activated and will test several key technologies including high power laser diodes, crystals, and gas cooling within an architecture that is modular and scalable to multi-kilojoule apertures with minimal beam line reengineering (Orth, Payne, and Krupke[1]).

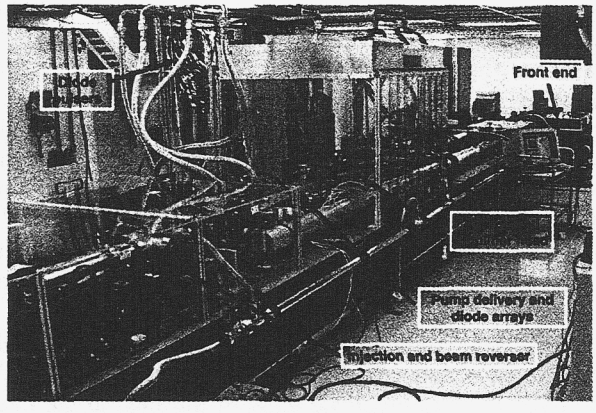

Figure 1. The Mercury laboratory

The design requirements of the laser are to operate at 10 Hz and 100 J/shot within a 10% efficiency envelope. To meet these goals, we explored numerous gain materials and architectural options to best fit the design space of a fusion energy class laser. $Yb^{3+}:Sr_5(PO_4)_3F$ or Yb:S-FAP was chosen as the gain media based on its long energy storage lifetime, moderately high cross section, and good thermal conductivity. The primary challenge has been in growing full aperture slabs of 4x6 cm^2 in area. However, the growth techniques employed to eliminate or reduce the crystalline defects, produced boules that were difficult to cut due to the high thermal gradients required during the growth process. Based stress models developed in conjunction with a research group at UC Davis, we chose an off-center cut geometry with a high pressure water jet to overcome the high probability of boule fracture during fabrication. This method has proven successful and five S-FAP slabs have been mounted into the first amplifier. The slabs are mounted into aerodynamic aluminum structures called "vanes" that are separated by 1 mm helium gas cooling channels. Four additional slabs are in fabrication and seven crystalline boules are waiting to be cut. We can anticipate having enough slabs (seven) by the end of the year to fill one amplifier assembly. Recent measurements of Yb:S-FAP indicate damage thresholds of greater than 50 J/cm^2 .

The laser diodes at 900 nm are precision mounted onto etched silicon heatsinks with microlenses to help reduce the light divergence, and then secured onto large copper blocks or arrays that provide the cooling and electrical power to the diodes. Each amplifier assembly is pumped by four 80 kW diode arrays. Four arrays have already been built and are currently being exercised in the system. Together they have accumulated over 10^5 shots. The next set of backplanes is being qualified and will be used for the second amplifier assembly (Figure 3). The diode array light is guided to the amplifier through multiple reflections within a hollow lens duct and homogenizer.

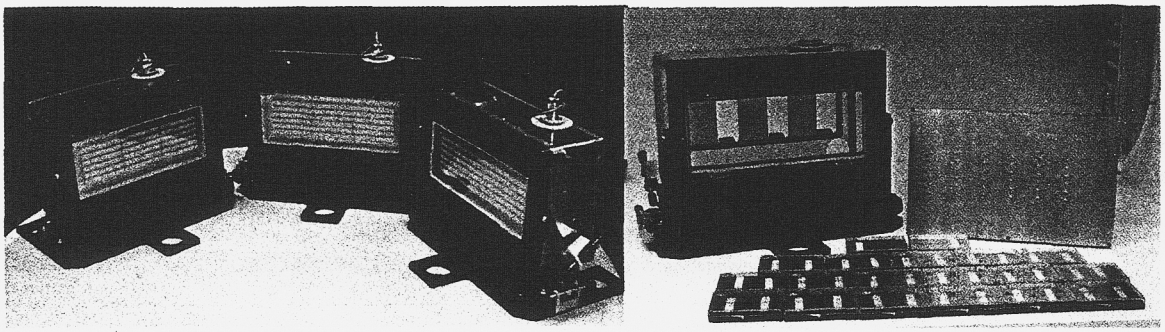

Figure 3. Three diode backplanes have been built and are in the laboratory being tested. The final backplane is in assembly.

The overall architecture employs an off-axis, four-pass beam layout. Relay imaging of the laser beam with telescopes between the amplifiers helps to greatly reduce the intensity modulation at the crystalline amplifiers. The propagation of the beam at a five milliradian off-axis angle to the telescopes allows the beam to pass through the system four times without the use of a final full-aperture optical switch. However, an average-power, birefringence-compensated Pockels cell [3] is used after two passes at low fluence (< 1 J/cm^2) to help suppress parasitic beams.

The laser system, diode laser power conditioning, and utilities are computer controlled. A full suite of sensor packages is being fielded to diagnose the beam after each pass. A dark field diagnostic allows detection of damage on every shot such that when the software algorithm detects a > 100 um damage site in the dark field image, the laser is shut down immediately.

The amplifier was assembled with five Yb:S-FAP slabs and two undoped glass slabs. The undoped slabs serve as placeholders in the amplifier until the remaining S-FAP slabs can be fabricated. With 200 mJ of front energy we were able to extract up to 31.6 joules of energy at 1.047 um in single shot mode. At 10 Hz, we measured an average energy of 20.6 joules. Due to a gas flow disturbance in the cooling channels from unevenness in the slab mounting compound, we developed a hot spot in the intensity profile. The modulated beam damaged a small mirror in the pass two section of the laser. We are in the process of correcting this problem and will repeat the above experiments under more stable flow conditions.

Wavefront data was taken for static (no diode pumping) and full pumping conditions. The static wavefront data show 2.7 waves of peak distortion due to bonding phase discontinuities incurred during the fabrication process. New fabrication techniques are being tested to eliminate these distortions. In the interim, a static conjugate phase plate, using the wet-etch technology developed at LLNL, was tested and shown to correct for the distortion when placed directly adjacent to the amplifier assembly. We measured a factor of three improvement in the energy within a diffraction limited spot for unpumped conditions. The conjugate phase plate will be used in the system until the slabs can be replaced with higher quality parts.

FY03 pans for the Mercury laser include: installation of the remaining two S-FAP slabs in the first amplifier head, followed by single amplifier experiments and then activation of the second amplifier head.

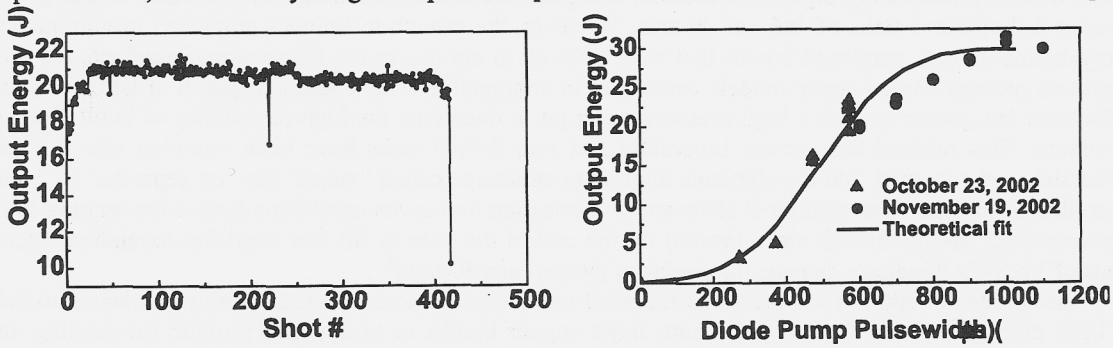

Figure 4 a) Burst mode operation at 20.6 joules and 10 Hz. b) Single shot data and energetics modeling

References

[1] C. D. Orth, S. A. Payne, and W. F. Krupke, "A diode pumped solid state laser driver for inertial fusion energy," *Nuc. Fus.* 36, 75-116, (1996).

[2] J.A. Skidmore, B.L. Freitas, J. Crawford, J. Satariano, E Utterback, L. DiMercurio, K. Cutter, and S. Sutton, "Silicon monolithic microchannel-cooled laser diode array," *Appl. Phys. Lett.*, 77, 10-12, (2000).

[3] C.A. Ebbers, K. Kanz, and H. Nakano," A thermally compensated, deuterated KDP Q-switch for high average power lasers," Conference for Lasers and Electro Optics, Baltimore Maryland, 2002.

[4] Dixit, S.N.; Feit, M.D.; Perry, M.D.; Powell, H.T. "Designing fully continuous phase screens for tailoring focal-plane irradiance profiles," *Opt. Lett.*, 21, 1715-17, (1996).

UCRL-JC-145598

Initial experiments on Mercury, a 100 J / 10 ns / 10 Hz / 10% efficiency diode pumped solid-state laser

A.J. Bayramian, R.J. Beach, W. Behrendt, C. Bibeau, C.A. Ebbers, B.L. Freitas, V.K. Kanz, S.A. Payne, K.I. Schaffers, K.M. Skulina, L.K. Smith, J.B. Tassano, and D. Van Lue
Lawrence Livermore National Laboratory, 7000 East Ave., L-482, Livermore, CA 94550-9234 USA
bayramian1@llnl.gov

H. Nakano
KINKI University, School of Science and Engineering, 3-4-1 Kowakae, Higashi-osaka, Osaka 577-8502

Abstract: We report the activation of four 80 kW diode arrays, fabrication of four full aperture (4 x 6 x 0.75 cm) S-FAP slabs, an average power Pockels cell, transmitted wavefront, and gain measurements on the Mercury laser system.
OCIS codes: (140.3580) Solid State Lasers; (140.3280) Laser Amplifiers

Introduction

The Mercury laser design is based on demonstrating a scalable architecture for inertial fusion energy applications (Orth and Payne[1]). To achieve the Mercury goals of 100 J in 2-10 ns at 10 Hz operation with 10 % electrical efficiency, three major technologies were developed: high-peak-power diode arrays, $Yb^{3+}:Sr_5(PO_4)_3F$ (Yb:S-FAP) crystalline slabs, and helium gas cooling of the gain media. Activation of the 80 kW pump arrays and propagation of the pump light through the amplifier have allowed us to benchmark our ray trace and extraction codes. In addition, experimental data taken with a subscale birefringence-compensated KD*P Pockels cell show that this technology can used for gating average power laser beams to help suppress parasitics from damaging the laser system. Finally, improvements in our crystal growth procedures and process controls have allowed us to fabricate 4x6 cm Yb:S-FAP crystalline slabs. Initial damage tests on Yb:S-FAP crystals show damage thresholds to be > 35 J/cm^2 at 10 ns.

Pump Architecture

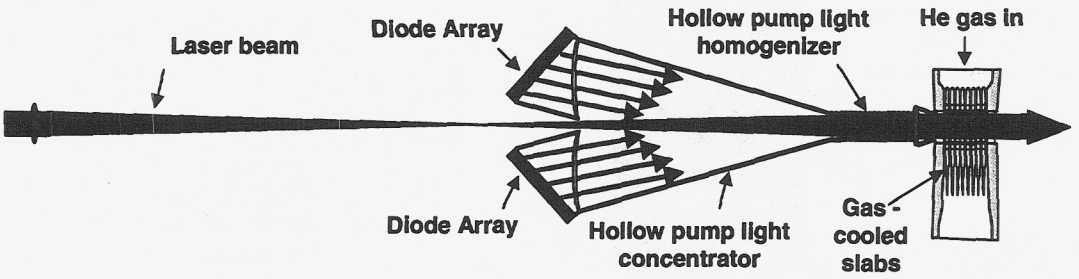

Fig. 1 The optical layout of the Mercury pumping scheme utilizes end pumping in conjunction with high-speed gas cooling to maximize pump efficiency while minimizing thermal distortion to the extraction laser beam.

We chose a pumping scheme in which the diode pump and extraction light are collinear. This design minimizes the number of optics in the beam line thereby lowering the overall B-integral of the laser extraction, while maximizing the pump transport efficiency. The optical layout of the amplifier

including pump delivery, optics, and relay telescopes is shown in fig. 1. The V-BASIS [2] packaging of the diode bars causes the diode light to exit at an angle of 55°. The diode arrays are tilted to compensate for this angle and are split into two elements to allow for the passage of the 1047 nm extraction beam through the center. The diode array light is guided to the amplifier through multiple reflections within a hollow lens duct and homogenizer. A ray tracing code was used to design the optical layout and sizing of the pump delivery optics.

Diode Pump Arrays

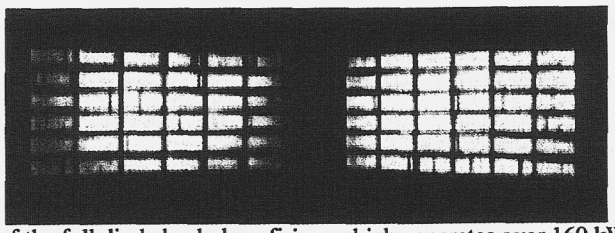

Fig. 2 A view of the full diode backplane firing, which generates over 160 kW peak power.

Currently four backplanes have been activated with each backplane delivering up to 85 kW of peak power in a 750 μs pulse (fig. 2). The backplane hardware provides water-cooling and pulsed power to the 36 "tiles", where each tile holds twenty-three 100 W diode bars. The monolithic packaging concept of the tiles was specifically developed for the Mercury Laser and is referred to as Bars And Springs In Slots (V-BASIS)[2]. In this scheme, diodes are soldered to a V-groove etched silicon wafer, which is then bonded to a molybdenum block for structural support and heat sinking. Next microlens arrays are precision mounted onto the tiles to increase brightness. The package is consistent with our low duty factor (1%) and the need for low cost packaging (6624 diode bars in the system). Initial backplane characterization indicates a measured power droop of 6 % in the temporal pulse, a linewidth of 4.2 nm in the output spectrum, and a far field divergence of 13 x 146 mrad for the full backplane, which meets the design point requirements. Wall plug efficiency experiments have demonstrated that these diodes (Coherent Inc.) can operate with an electrical efficiency of at least 45% per bar. Experimental tests of a tile at 10 Hz and 115 W yield a lifetime of greater than 10^8 shots.

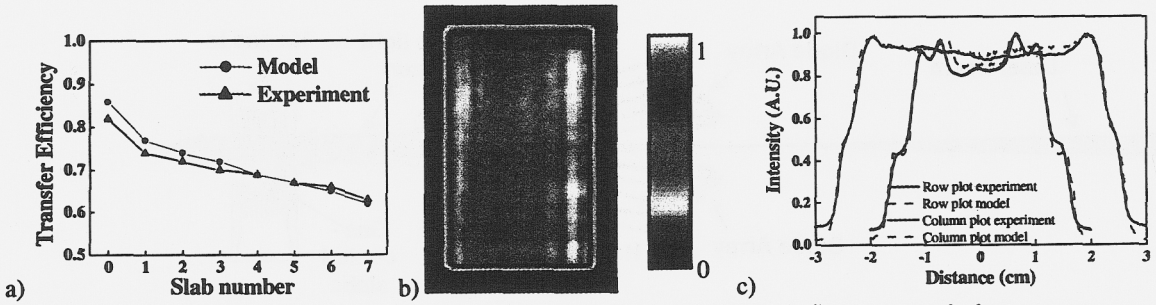

Fig. 3 a) An intensity plot of the output of the pump delivery system indicates a nearly homogeneous output. b) Transfer efficiency measurements from the diode backplane to each slab in the amplifier agree with the model c) Lineouts of the intensity in the first slab show smooth profiles and good agreement with ray-tracing models.

Energy measurements of the pump light tranmitted through the lens duct, homogenizer, and lenses yielded an efficiency of 83% which roughly agrees with the model prediction of 86% as shown in fig. 3a. A near field image of the pump beam at the output of the homogenizer is shown in fig. 3b.

Lineouts (shown fig. 3c) of the extractable (3x5 cm) area of the first amplifier slab in the horizontal and vertical directions are shown along with the ray trace model predictions. The model overlaps well with the experimental data for transfer efficiency and spatial profile, giving us confidence in our optical design codes.

Average power Pockels cell

Extensive ghost and amplified spontaneous emission analysis was performed, and motivated the need for a 100 W average power, low-loss Pockels cell to be located in the "reverser" (an image relay beam path which turns the beam and re-injects it for the 3 and 4th pass through the system). Though the Pockels cell sees relatively low energy pulses (< 0.5 J/cm2), the average power loading requires an advanced design since thermal birefringence could compromise the extinction ratio of the cell. A design was explored in which two nearly identical KD*P crystals (99% deuteration from Inrad, Inc.) are oriented with a 90° rotator between them such that the thermally induced birefringence is nearly cancelled. The average power Pockels cell shown in fig. 4a has an aperture of 1.5 x 2.5 cm, is capable of extinction of 200:1 at an incident power of 100 W (fig 4b), and will be used to prevent ghost beams from reaching high levels of amplification. A high voltage pulser, capable of 13 kV (which will be needed for the full size Pockels cell to be fabricated this year with an aperture of 3.5 x 6 cm), was used to switch the Pockels cell. By employing a load line technique, a minimum pulsewidth of 17.2 ns FWHM was achieved (fig. 4c).

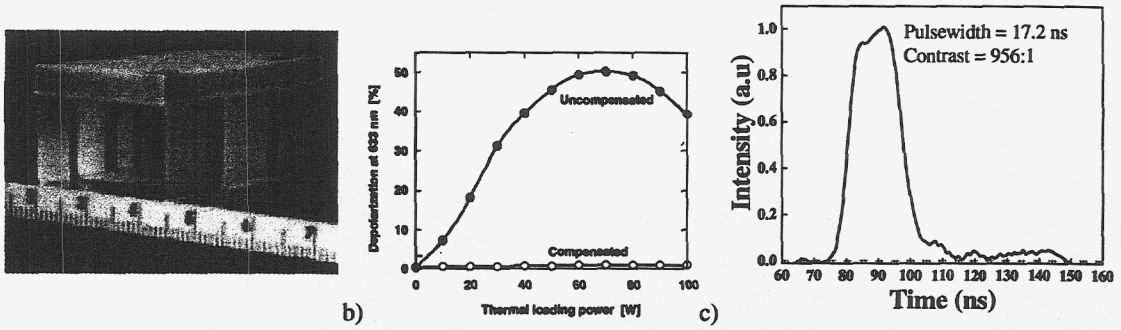

a) b) c)

Fig. 4 a) This thermal birefringence compensated KD*P Pockels cell switches with 200:1 extinction at 100 W average power, b) Extinction data taken on Pockels cells loaded up to 100 W average power 20X reduction in depolarization loss for the compensated design.

Crystal Growth

Significant improvements have been made in the growth of the ytterbium doped strontium fluorapatite (S-FAP) crystals. Current growths have produced nine 3.4 cm diameter boules free of major defects allowing fabrication of five amplifier slabs to date. The boules are cut into half size amplifier slabs, which are then diffusion bonded together by Onyx Optics to achieve full-scale 4 x 6 cm amplifier slabs (fig. 5a) [3]. These Czochralski grown crystals were initially plagued by a number of defects including: cracking, cloudiness, bubble core defects, grain boundaries or slip dislocations, anomalous absorption, and crystal inclusions. Careful control of temperature gradients and use of a SrF_2-rich melt have mainly resolved these issues. Our current method of fabricating half slabs allows us to use the current boule scale and work around the defects while continuing to explore ways to eliminate defects and scale the boules to larger diameter. Initial damage threshold experiments were performed using a Q-switched 1

micron laser with a 10 ns pulsewidth employing the N/1 method (Fluence is ramped on each spot until damage occurs). The measurements were made on several sub-aperture S-FAP samples from different boules. The damage threshold had some variability with a minimum threshold at 35 J/cm^2 and a maximum at 65 J/cm^2. Since all damage occurred at the surface, we are currently investigating improvements in surface finish. We currently have four bonded slabs being finished into laser slabs (fig. 5b).

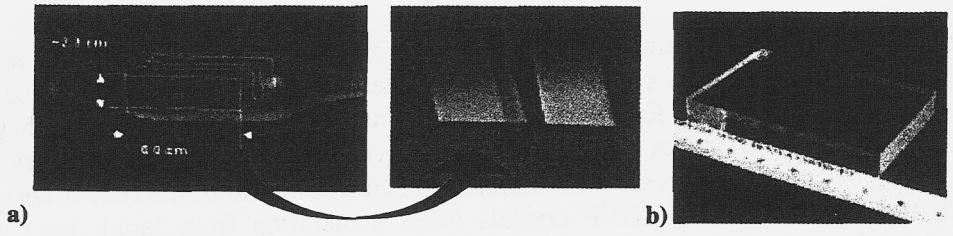

Fig. 5 a) Picture showing how the sub-slabs are cut from the boule and diffusion bonded to form a single slab, b) Picture of a full aperture 4 x 6 x 0.75 cm Yb:S-FAP slab

Gain Experiments and Propagation Modeling

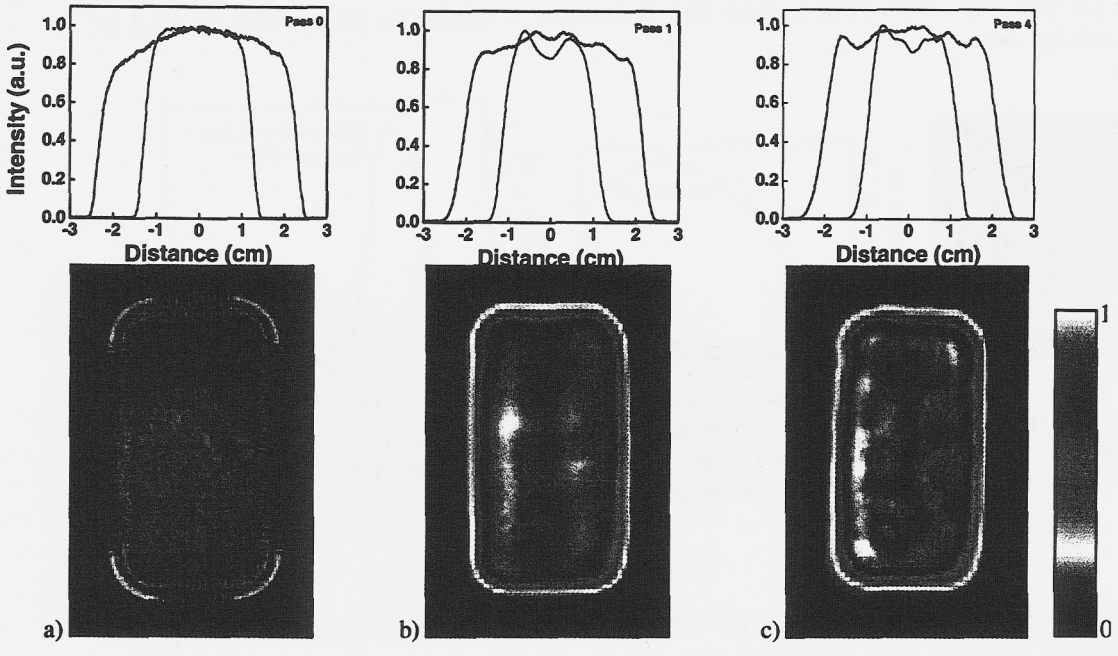

Fig. 6 a) Beam at the serrated aperture, b) alignment beam after 1 pass through the system showing some modulation due to pinhole size and optical homogeneity, c) alignment beam after 4 passes through the system showing some additional modulation due to clipping, optical homogeneity and larger pinholes.

System alignment and gain measurements were conducted using a small CW Nd:YLF laser made by Crystalaser, Inc. The 1 mm gaussian beam is expanded in a telescope, then passed through a serrated aperture which apodizes the beam to the proper aperture (fig. 6a). The high spatial frequency serrates are removed after passing through the first pinhole, leaving a smooth-edged supergaussian beam. This high-

contrast profile is required to efficiently extract the gain in the amplifier, while minimizing clipping and diffraction losses as well as intensity peaks caused by hard aperturing of beams. Initial alignment of the angularly multiplexed beam is difficult due to the out-of-plane injection system and the necessarily out-of-plane reverser which reinjects the beam at a multiplexing angle 90° from where it arrives. Beam rotation must be minimized to propagate the without diffraction or clipping through the homogenizer, which is only 1 mm larger than the extraction beam (3x5 cm). Single pass (Fig. 6b) and four-pass (Fig 6c) beam profiles are shown for the initial single head demonstration of the system. The next goal was so measure small signal gain of the system. Nd:glass slabs amplifiers are used as surrogate gain material until all of the S-FAP slabs are finished. The measurements were made in three independent experiments: CW pulse amplification and q-switched pulse amplification using a photodiode, and Q-switched amplification using a CCD to get full spatial gain uniformity. The average small signal gain for each was 1.55, 1.56, and 1.6 respectively, which agrees within experimental error to the modeled gain of 1.60.

Summary

Initial measurements are reported for the Mercury laser system, a scalable driver for inertial fusion energy. The first full diode backplane and pump delivery system was completed, tested, and found to meet or exceed all specifications with an overall transfer efficiency of 83% through the pump delivery system, and a homogeneity that matches models well. A birefringence compensated average power KD*P Pockels cell was designed and meets the 200:1 extinction requirement at 100 W average power. The first Yb:S-FAP crystals of sufficient size to fabricate full aperture amplifiers have been grown with five slabs currently in various stages of fabrication. The system with one amplifier was aligned and activated allowing 4-pass small signal gain measurements to be conducted with Nd:glass surrogate amplifiers. The technological breakthroughs of the past year and recent activation of the laser system will allow extraction up to 20 joules from the diode pumped Yb:S-FAP Mercury laser system in 2002, with plans to generate 100 J in the next two years.

Acknowledgement

We would like to thank the Steve Mills, John Lang, and Will Davis for their designing, fabricating, and assembly of the Mercury hardware. We would like to thank Larain Dimercurio, Jackie Crawford, Joe Sartariano, and Everett Utterback for assembly and testing of diode tiles. We would like to thank Peter Thelin for cutting and prefabricating S-FAP slabs for bonding at Onyx. This work was performed under the auspices of the U.S. Department of Energy by the University of California Lawrence Livermore National Laboratory under contract No. W-7405-Eng-48.

References

[1] C. D. Orth, S. A. Payne, and W. F. Krupke, "A diode pumped solid state laser driver for inertial fusion energy," *Nuc. Fus.* **36**, 75-116, (1996).

[2] J.A. Skidmore, B.L. Freitas, J. Crawford, J. Satariano, E Utterback, L. DiMercurio, K. Cutter, and S. Sutton, "Silicon monolithic microchannel-cooled laser diode array," *Appl. Phys. Lett.*, **77**, 10-12, (2000).

[3] A.J. Bayramian, C. Bibeau, K.I. Schaffers, J.K. Lawson, C.D. Marshall, and S.A. Payne, "Development of ytterbium doped $Sr_5(PO_4)_3F$ for the Mercury Laser Project," in *OSA Trends in Optics and Photonics Series*, M.M. Fejer, H. Injeyan, U. Keller, ed(s)., Vol. **26** of OSA Proceedings Series (Optical Society of America, Washington, D.C., 1999), 635-641.

Design of a 20 TW / 20 J chirped-pulse amplification laser for high-energy-density plasma physics experiments at the University of Nevada at Reno

A. C. Erlandson[1] *S. Batie*[2] *B. Bauer*[2]
J. A. Caird[1] *C. Ebbers*[1] *J. Glassman*[2]
V. Ivanov[2] *B. LeGalloudec*[2] *N. LeGalloudec*[2]
S. Letzring[3] *S. Payne*[1] *B. Stuart*[1]

[1] Lawrence Livermore National Laboratory, P.O. Box 808, L-479, Livermore, CA 94551
[2] Department of Physics, Nevada Terawatt Facility, University of Nevada, Reno, NV 89506
[3] Los Alamos National Laboratory, P.O. Box 1663, Los Alamos, NM 87545

ABSTRACT

We have developed a conceptual design for a 20 TW / 20 J laser for performing high-energy-density plasma physics experiments at the Nevada Terawatt Facility of the University of Nevada at Reno. The purpose of the laser is to develop proton and x-ray radiography techniques, to use these techniques to study plasmas in z-pinches and in zones surrounding magnetically-insulated transmission lines (MITLs), and to study deposition of energy from high-intensity laser pulses into both magnetized and unmagnetized plasmas.

OVERVIEW

The University of Nevada (UNR) has undertaken the construction and activation of a short pulse 20 TW / 20 J laser that will significantly enhance NTF capabilities. The purpose of this laser is threefold: 1) to provide sufficient focused intensity for the development of x-ray and proton-beam backlighting techniques; 2) to characterize z-pinch and MITL plasmas using laser backlighting; and 3) to study the deposition of high-intensity laser beams into magnetized and unmagnetized plasma. UNR has partnered with Lawrence Livermore National Laboratory for the design and construction of this laser, and with Los Alamos National Laboratory for the design and construction of the target area. Laser system activation is scheduled in 2004.

SYSTEM REQUIREMENTS

To achieve the planned experiments, a flexible laser system with sufficient irradiance on target to produce x-ray and proton sources for backlighting and interacting with the z-pinch plasma is required. The most essential performance requirements of the laser system, as driven by the needs of the planned experiments, are as follows:

- Peak irradiance on target > 10^{19} W/cm^2 to enable generation of energetic proton beams for proton radiography
- Pre-pulse irradiance < 10^{11} W/cm^2 to inhibit formation of plasma at the target prior to short pulse arrival and to enhance proton beam generation
- Pointing accuracy of – 25 μm to allow interaction with an imploded-liner pinch target
- Timing jitter relative to Zebra < 10 ns to ensure evolution of events driven by the z-pinch can be diagnosed with adequate temporal resolution and repeatability.
- Shot rate > 2 / hr to equal the maximum expected shot rate of the z-pinch (1 / hr) and to allow for at least one laser calibration shot between successive z-pinch shots

LASER DESIGN

Figure 1 shows a schematic diagram of our conceptual laser design, which uses a chirped-pulse amplification (CPA) laser architecture. A commercial mode-locked Nd:glass oscillator generates 2 nJ, 250 fs-long pulses that a grating stretcher expands to 1.5 ns duration. Two optical parametric chirped-pulse amplifier (OPCPA)[1-3] stages amplify the pulse to 70 mJ. Two double-passed Nd:glass rod amplifiers, provide final amplification to 30 J. After reflective gratings recompress the pulse to less than ~ 1 ps, an f/3 off-axis parabolic mirror focuses the beam to a ~10 μm spot. The energy and intensity delivered on target are expected to be at least 20 J and 10^{19} W/cm^2, respectively. Faraday isolators protect the laser chain from damage in the event of back reflections from the target.

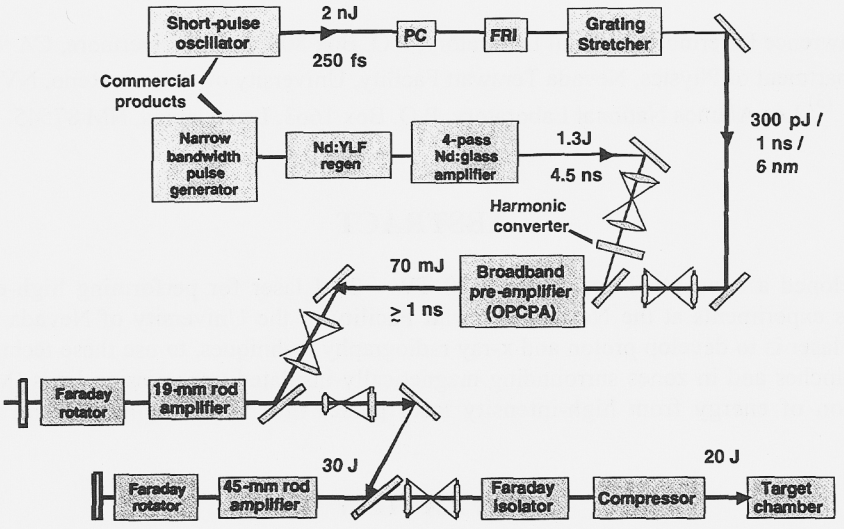

Figure 1. Our chirped-pulse amplification (CPA) laser design uses an optical parametric chirped-pulse amplifier (OPCPA) for pre-amplification, and phosphate Nd:glass rod amplifiers for final amplification.

Analysis shows our design meets energy requirements with acceptable non-linear phase shift and damage margins. Total non-linear phase shift, commonly referred to as ΣB, limits the size and quality of the focused beam as well as the duration and quality of the recompressed pulse. Non-linear phase shift accumulated between spatial filters, known as ΔB, is correlated with the growth of small-scale intensity features. In well-engineered chirped-pulse amplification systems, typical limits on ΣB and ΔB are both ~ 2 radians, depending on the beam quality required. Frantz-Nodvik modeling shows our design produces 20 J on target with ΣB and ΔB values of 2.0 radians and 1.1 radians, respectively. Average fluences throughout the chain are less than 50% of the rated damaged fluences. The rod amplifiers will contain high-damage-threshold, platinum-free Nd:glass rods.

Additionally, we estimate our system achieves a temporal contrast ratio greater than, 10^8, the minimum value needed to meet peak irradiance (10^{19} W/cm^2) and pre-pulse irradiance (< 10^{11} W/cm^2) requirements simultaneously. This estimate is based on a lower-limit measured for the contrast ratio for the mode-locked oscillator (> 10^4), multiplied by the gain of the OPCPA stages (~ 10^7). OPCPA gain acts as a temporal gate, as the OPCPA gain is present only during the pump pulse. In part, we chose OPCPA rather than Ti:sapphire regenerative amplifiers for the broadband preamplifier since Ti:sapphire regenerative amplifiers reduce contrast ratio by leaking light during round trips before the beam is switched out.

Our optical pulse compressor uses a roof mirror to double pass two parallel gratings that are enclosed in a vacuum chamber. The gratings are gold, have a groove density of 1749/mm, are separated by 1.3 m, and have an angle of incidence of 61¡ on the first grating. The chirp parameter is 312 ps/nm. The width of the

larger of the two gratings will be in the range 40-50 cm. A final grating size will be determined after the completion of cost-performance tradeoff studies that are now scheduled for 2003.

TARGET AREA DESIGN

Figure 2 shows our conceptual target area design. A 1-m-diameter vacuum target chamber rests atop the Zebra power conditioning system's pulse forming line and encloses a ~ 1 MA z-pinch and its associated MITL. The laser beam, which has a diameter of 10 cm, travels from the compressor to the target chamber in an evacuated tube and is focused onto a target by an off-axis parabolic reflector. Proton beams are generated by focusing the laser beam onto the back surfaces of thin sheets of metal? foil. X-rays are generated by focusing the laser beam onto the front surfaces of foils made of high-Z materials. Radiography of the z-pinch and MITL plasmas can be performed using either proton beams or x-rays. Radio-chromic film or plastic track detectors will be used to generate proton radiographs, while x-ray-sensitive film or charged-coupled-device (CCD) cameras will be used to make x-ray radiographs. Alternatively, the beam can be focused directly onto the z-pinch plasma to study laser energy deposition processes.

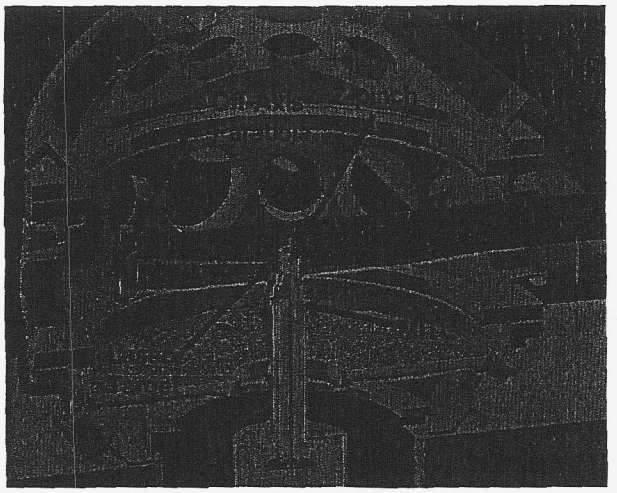

Figure 2. Our design uses a 1-m-diameter vacuum target chamber resting on top of the Zebra power conditioning system, which provides 1 MA / 1 MV pulses to an enclosed z-pinch through a magnetically-insulated transmission line (MITL). An off-axis parabola focuses a 10-cm-diameter, 20 TW, ~ 1 ps-long laser beam to 10^{19} W/cm^2, sufficient for generating proton beams or for generating x-rays with energy up to ~100 keV.

ACKNOWLEDGEMENTS

This work was performed under the auspices of the US Department of Energy by the University of California Lawrence Livermore National Laboratory under contract No. W-7405-Eng-48. This work was supported by the US Department of Energy NNSA/NV Cooperative Agreement No. DE-FC08-01NV14050 with the University of Nevada. Los Alamos National Laboratory, an affirmative action/equal opportunity employer, is operated by the University of California for the US Department of Energy under contract No. W-7405-ENG-36.

References

1. J. Collier, C. Hernanez-Gomez, I.N. Ross, P. Matousek, C. N. Danson, J. Walczak, Evaluation of an ultrabroadband high-gain amplification technique for chirped pulse amplification facilities, Appl. Opt. **38**, 7486-7493 (1999).
2. A. Dubeitis, G. Jonuaskas, and A. Piskarskas, Powerful femtosecond pulse generation by chirped and stretched pulse parameteric amplification in BBO crystal, Opt. Commun. **88**, 437-440 (1992).
3. I. Jovanovic, B. J. Comaskey, C. A. Ebbers, R. A. Bonner, D. M. Pennington, and E. C. Morse, Optical parametric chirped-pulse amplifier as an alternative to Ti : sapphire regenerative amplifiers, Applied Optics **41**, 2923-2929 (2002) .
4. D. M. Pennington, C. G. Brown, T. E. Cowan, S. P. Hatchett, E. Henry, S. Herman, M. Kartz, M. Key, J. Koch, A. J. MacKinnon, M. D. Perry, T. W. Phillips, M. Roth, T. C. Sangster, M. Singh, R. A. Snavely, M. Stoyer, B. C. Stuart, S. C. Wilks, Petawatt laser system and experiments, IEEE J. of Sel. Top. In Quant. Electron. **6**, 676-688 (2000).

A Thermally Compensated, Deuterated KDP Q-Switch for High Average Power Lasers

H. Nakano
Kinki University
Department of Electrical Engineering
Osaka 577-8502 JAPAN
Email: hitoshi@ex.ee.kindai.ac.jp
and
K. Kanz and C. A. Ebbers
Lawrence Livermore National Laboratory
Livermore, CA 94550 USA
Tel. (925) 423-9465 Email: ebbers1@llnl.gov

ABSTRACT

We have demonstrated a dual crystal, transverse electrode, DKDP Pockels cell that, in off-line testing, exhibits less than 0.5% depolarization near 1 mm over the 1.5x2.5 cm^2 aperture with 100 W of average power loading.

SUMMARY

Using dual-crystal, thermally compensated, $LiNbO_3$ and $KTiOPO_4$ (KTP) electro-optic modulators, we have demonstrated 250 and 65 watts, respectively, of Q-switched average power at thermal loadings approaching 1 kW/cm^2. [1-2] The low surface damage threshold of $LiNbO_3$ and the limited aperture of KTP poses a problem for devices operating at moderate fluences (3-5 J/cm^2) or requiring apertures greater than 2 cm^2. For these applications, KD_2PO_4 (DKDP) remains as the only electro-optic crystal available in large apertures with high optical homogeneity and with damage thresholds exceeding 10 J/cm^2. However, the relatively low thermal conductivity, high near-infrared optical absorption, and low fracture strength makes DKDP difficult to use for high average power applications. [3] The Mercury laser project at Lawrence Livermore National Laboratory is a 100 J, 10 Hz (1kW) prototype of a potential inertial fusion energy driver.[4] A moderate aperture (3x5 cm^2) electro-optic cell which can handle 100 W of average power is required for use as an isolation device. We have built and tested a scaleable, half-aperture, dual DKDP crystal Pockels cell, which, in off-line testing, exhibits less than 0.5% depolarization when thermally loaded with a 100 W near-infrared laser.

Figure 1 shows the arrangement of a pair of DKDP crystals in a thermally compensated Q-switch. The DKDP (1.5x2.5 cm^2 aperture) crystals and a 90 degree quartz rotator are thermally bonded to an alumina substrate, which provides a sink for the modest amount of heat (~2 W) deposited in the crystal. The DKDP crystals we utilized were polished to a flatness of l/15 with parallelism better than 5", as measured on a Zygo interferometer at 632.8 nm. In an ideal pair of identical length crystals, the static birefringence, thermally induced birefringence, and the stress-optic induced depolarization would vanish. When the ideal crystal arrangement of Figure 1 is placed between parallel polarizers (with polarization axis at 45° to the Z axis) no light would be transmitted across the aperture. If a 90° rotator is placed after the compensated crystal pair, the maximum intensity is transmitted. For a non-ideal crystal pair, the fraction of light which is depolarized due to uncompensated birefringence is determined from the expression:

$I_{depolarization} = I_{rotator\ removed} / (I_{rotator\ removed} + I_{rotator\ inserted})$

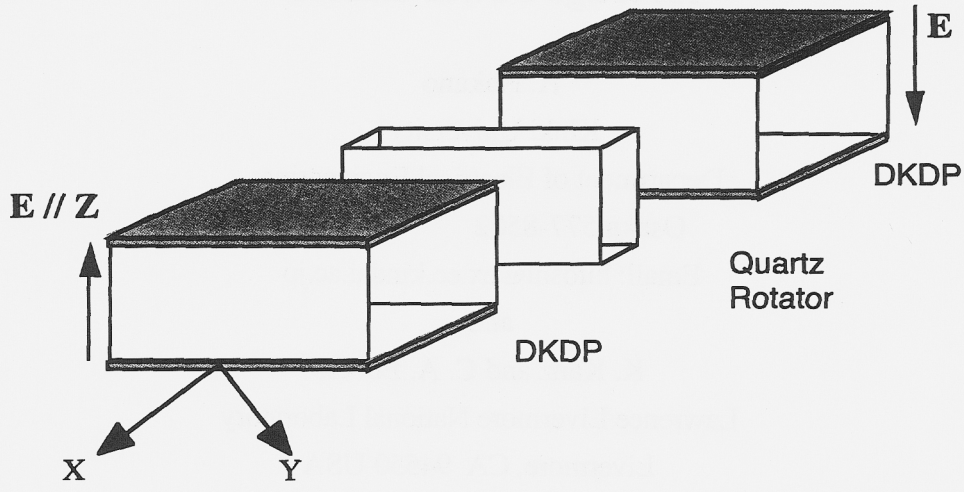

Figure 1. Transverse, bicrystal, thermally compensated switch consisting of DKDP crystals and 90 degree quartz rotator.

Our test setup, shown in Figure 2, utilizes a 633 nm source coincident with a multimode 100 W Nd:YAG laser. Depolarization is examined utilizing both a camera as well as a photodiode. The depolarization as a function of thermal loading is shown in Figure 3. At the maximum thermal loading, the compensated crystal pair exhibits less than 1% depolarization at 633 nm (less than 0.5% depolarization at 1 um). Finally, we have demonstrated optical switching at 633 nm and are currently in process of testing the higher voltage (13.5 kV) electro-optic pulser required for switching at 1.047 um.

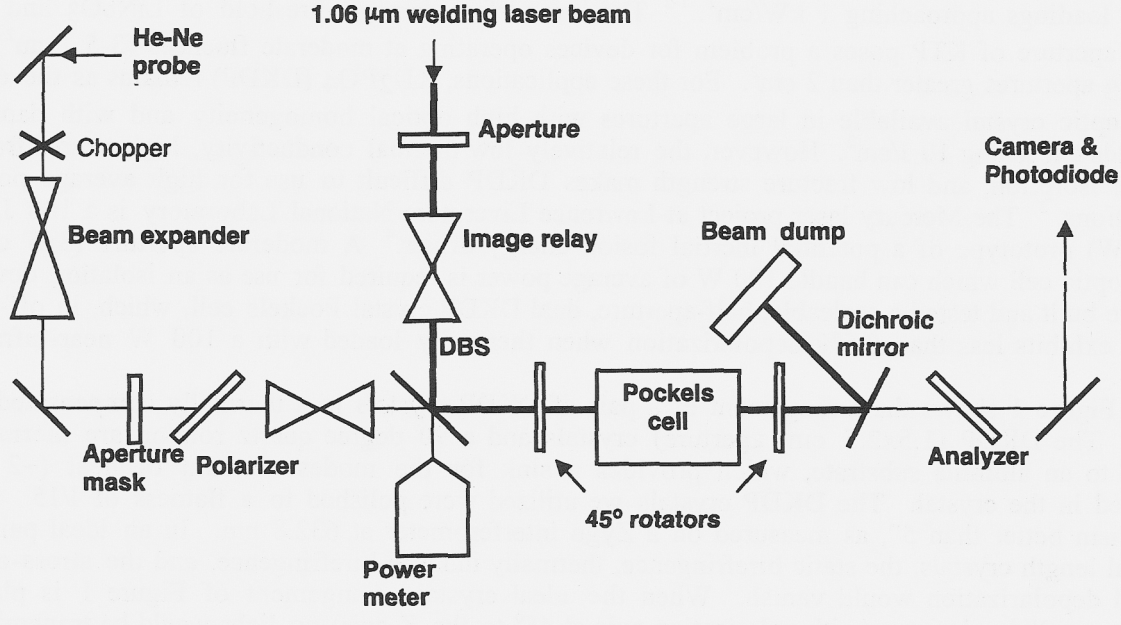

Figure 2. Apparatus used to thermally load Pockels cell assembly and examine depolarization.

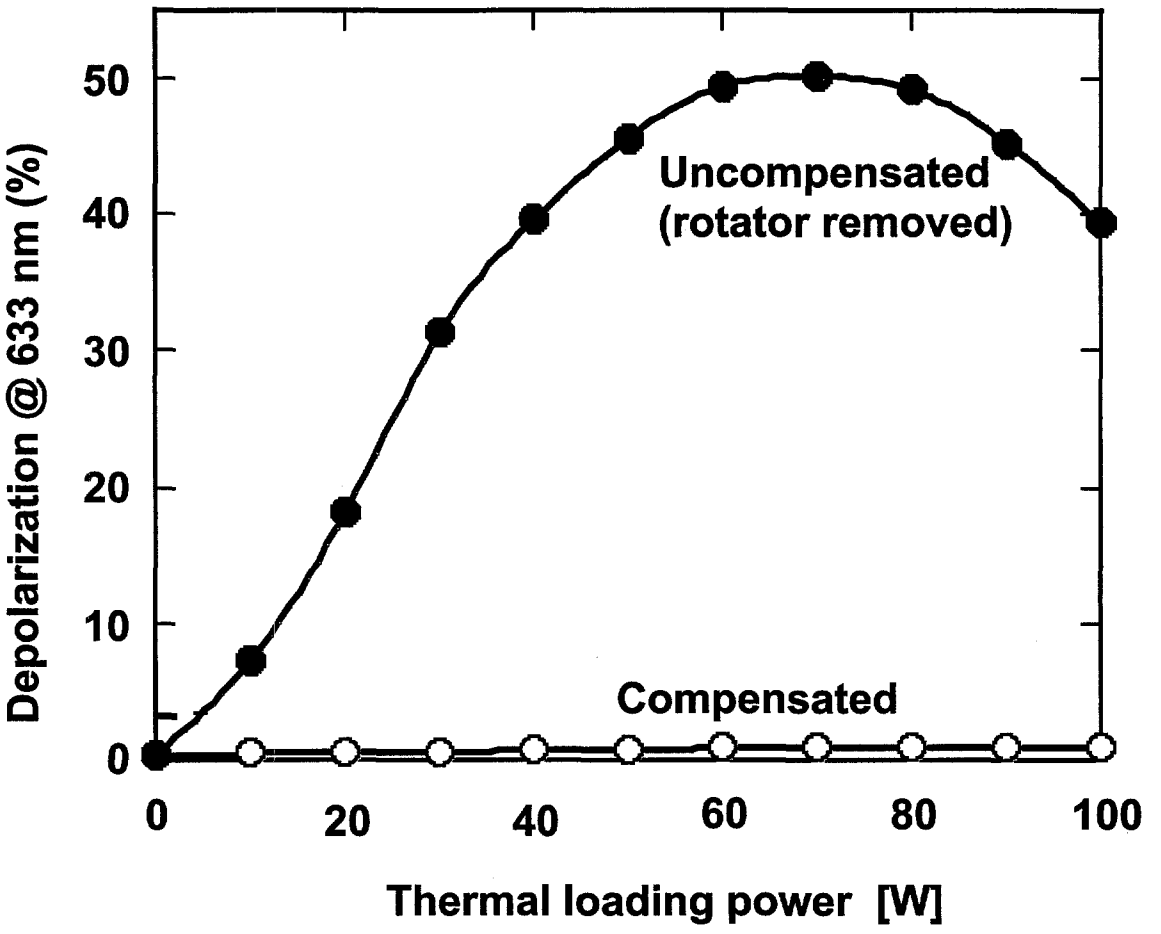

Figure 3. 633 nm depolarization of the uncompensated dual crystal device (90 degree rotator emoved) and thermally compensated device as a function of thermal loading.

REFERENCES

[1] S. P. Velsko et. al. "100 W Average Power at 0.53 um by external frequency conversion of an electro-optically Q-switched diode-pumped power oscillator", Applied Phys. Lett. 64 pp. 3086-3088 (1994).

[2] C.A. Ebbers, S.P. Velsko, "High average power KTP Electro-optic Q-switch", Applied Phys. Lett. 67 pp. 593-595 (1995).

[3] D. Eimerl, "Thermal aspects of high-average-power electro-optic switches", IEEE J. Quantum Electronics 23 pp. 2238-2251 (1987).

[4] A. Bayramian et. al., "Activation of the Mercury laser: A diode-pumped solid-state laser driver for inertial fusion" ASSL Conference, OSA Tops Volume 50, pp. 24-29 (2001).

* This work was performed under the auspices of the U. S. Department of Energy by the University of California, Lawrence Livermore National Laboratory under Contract No. W-7405-Eng-48.

Linear electro-optic properties of $YCa_4O(BO_3)_3$

J. J. Adams *C. A. Ebbers*

ABSTRACT

We have characterized the effective linear electro-optic coefficients of $YCa_4O(BO_3)_3$ (YCOB) relative to KH_2PO_4 (KDP) and KD_2PO_4 (DKDP) at 632.8 nm. We measured a maximum r_{eff} value of 10.8 ± 1.4 pm/V for YCOB in a transverse electric field configuration, for propagation along the X or α dielectric axis with the electric field applied along the Z or γ dielectric axis. We also find effective coefficients of 10.7 ± 1.0 pm/V and 3.4 ± 0.4 pm/V for YCOB in longitudinal configurations. The remaining r_{eff}'s for various transverse applied voltages were found to be less than 3 pm/V. The excellent thermo-mechanical properties of this crystal, coupled with the moderate electro-optic coefficients, make YCOB and its isomorphs potential candidates for high average power electro-optic switches.

INTRODUCTION

In spite of the relatively rapid discovery, development, and commercial deployment of several new nonlinear optical (NLO) crystals (YCOB [1,2] $CsLiB_6O_{10}$,[3] and BiB_3O_6 [4]), there remains little progress in expanding the suite of commercially available *electro-optic* (EO) crystals. One reason is that candidate NLO crystals must have the standard properties that make them useful as optical materials (high optical transparency, suitable crystal symmetry, favorable growth and fabrication properties) as well as possessing adequate nonlinear coupling for sum frequency generation processes. In the absence of an ionic contribution to the nonlinear polarizability via a ferroelectric phase transition, the electro-optic coefficient of a material is strictly proportional to the value of the nonlinear optical coefficient.[5] As a consequence, crystals without ferroelectric phase transitions must have substantial nonlinear optical coefficients to have merit as electro-optic crystals.

The half-wave voltage (the applied voltage required to rotate the incident polarization by 90 degrees), V_π, for an electro-optic crystal can be calculated from (1),

$$V_\pi = (l_{volt}/l_k)\, \lambda/r_{eff} \qquad (1)$$

where l_{volt} is the electrode spacing, l_k is the propagation length through the crystal, λ is the incident wavelength, and r_{eff} is the effective electro-optic coefficient. The form of the effective electro-optic coefficient is dependent upon the crystal symmetry, as well as the applied electric field and light propagation directions. In general, it is desirable to use applied voltages less than 15 kV to avoid coronal discharge or other electrode sputtering effects.[6] For longitudinal operation, l_k and l_{volt} are identical, leading to a fixed voltage, independent of crystal geometry. Half-wave voltages can be reduced for transverse field electrodes devices by increasing the propagation length and/or reducing the electrode spacing. In practice, aspect ratios in bulk devices larger than 10:1 (l_k:l_{volt}) become impractical from a propagation and fabrication point of

view. Considering these two constraints, crystals potentially useful for transverse 1 μm Q-switches should have effective electro-optic coefficients of at least 7 pm/V.

DKDP [7], $LiNbO_3$[8], BaB_2O_4 (BBO) [9,10], and $KTiOPO_4$ [11,12] are four of the most common commercially available electro-optic. Of these 4 crystals, only DKDP is routinely available with high optical homogeneity for apertures exceeding 2 cm. Unfortunately, due to relatively large stress-optic coefficients, low thermal conductivity, and the necessity of sol-gel coatings, DKDP is not well suited for high average power systems. Thus, it is of interest to characterize the electro-optic coefficients of promising nonlinear optical crystals with favorable growth, fabrication, and average power handling properties.

In our previous study [13] of the $GdCa_4O(BO_3)_3$ family, we determined that $GdCa_4O(BO_3)_3$, YCOB, and $LaCa_4O(BO_3)_3$ have equivalent $d_{\alpha\beta\beta}$ and $d_{\gamma\beta\beta}$ nonlinear optical coefficients with the $d_{\gamma\beta\beta}$ coefficient being of relatively large magnitude (1.69 pm/V). Though this coefficient, due to phasematching constraints, can not be utilized for second harmonic generation of near infrared radiation, a Miller's type scaling relating the d (NLO) coefficient to the r (EO) coefficient [5] suggests the existence of a correspondingly large electro-optic coefficient, namely $r_{\beta\beta\gamma}$. The robust mechanical and thermo-mechanical nature of the GdCOB family of crystals makes them attractive candidates for sum frequency generation of near infrared radiation. The existence of moderate electro-optic coefficients would also lead to potential application in large aperture, high average power 1 μm Q-switches. We report on the experimental measurement of the linear effective electro-optic coefficients along principal dielectric directions in YCOB.

EXPERIMENTAL TECHNIQUE

The apparatus used for the electro-optic measurements is similar to other electro-optic measurement techniques.[9,10] Measurements of r_{eff} were performed at 632.8 nm. Given the low dispersion of the refractive indices, r_{eff} is expected to be relatively constant over the visible wavelength range. The YCOB samples used were fabricated into slabs with polished faces cut perpendicular to the dielectric directions. Crystal faces across which the electric field was applied were sputter-coated with approximately 2 μm of gold for the transverse cases and 120 nm of gold (allowing ~20% optical transmission) for the longitudinal measurements.

A 20 V low frequency (5 kHz) sine wave was applied to the samples. The peak change in intensity was compared to that from either a KDP sample in the transverse experiments or to a DKDP (> 99% deuteration) sample in the longitudinal experiments, yielding a relative measurement of r_{eff} for the YCOB crystals. In addition, a DC power supply was utilized to apply 0-3 kV across the faces of the crystals. The change in light intensity as a function of applied voltage was also measured using the lock-in amplifier.

For a longitudinal arrangement with YCOB, with both the applied voltage, $\Delta V_{applied}$, and the light propagation along the γ dielectric direction, the modulation in light intensity, $\Delta I/I_o$, through the analyzer can be related to $\Delta V_{applied}$ (for $\Delta V_{applied} << V_\pi$ (half-wave voltage)) by (2), where Γ_c is the net retardation imparted by the compensator, $\Gamma_s = (2\pi\ell_\gamma/\lambda)(n_\alpha - n_\beta)$ is the background static

retardation of the crystal, n_α and n_β are principal refractive indices along the α and β-dielectric directions (where $n_\alpha < n_\beta < n_\gamma$), respectively, $\Delta V_{applied}$ is the applied voltage, and

$$\frac{\Delta I}{I_o} = 1 + \sin\Gamma_c \cos\Gamma_s - \sin\Gamma_c \sin\Gamma_s \frac{\pi}{\lambda}(r_{\beta\beta\gamma} n_\beta^3 - r_{\alpha\alpha\gamma} n_\alpha^3)\Delta V_{applied} \quad (2)$$

$r_{\beta\beta\gamma}$ and $r_{\alpha\alpha\gamma}$ are coefficients of the linear electro-optic tensor for YCOB (point group Cm, m $\perp$ β). Eq. (2), and similar equations, allow us to compute values for r_{eff}'s in both the AC and DC experiments. The DC measurement of $r_{eff} = (r_{\beta\beta\gamma} n_\beta^3 - r_{\alpha\alpha\gamma} n_\alpha^3)$ for YCOB was obtained from the parameters of the fit of Eq. (2) to the data as shown in Fig. 1.

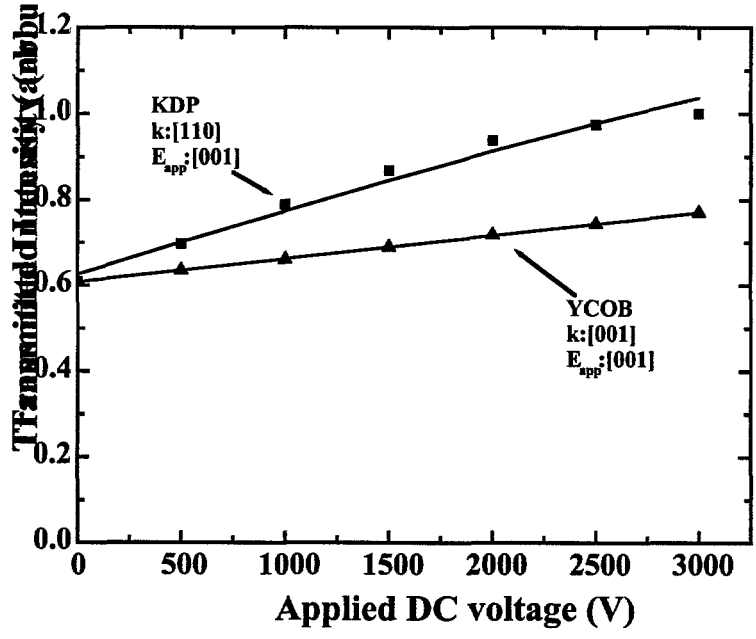

Fig. 1. Normalized intensity transmitted through the analyzer as a function of the applied DC voltage to the crystal. From the parameters of the fitted lines, we measure $r_{eff}^{KDP} = n_o^3 r_{63} = 35.8 \pm 4.4$ *pm/V and* $r_{eff}^{YCOB} = (r_{\beta\beta\gamma} n_\beta^3 - r_{\alpha\alpha\gamma} n_\alpha^3) = 10.7 \pm 1.0$ *pm/V.*

RESULT

The geometries of our measurements are indicated in Table I. $E_{applied}$ is the applied electric field, $E_{applied} = \Delta V_{applied}/l_{volt}$, k is the wavevector direction for the propagating light, l_k is the propagation length through the crystal, r_{eff} is the relevant effective electro-optic coefficient. $V_\pi^{1064\,nm}$ ($= \lambda/r_{eff}$) is the calculated half-wave switching voltage at 1064 nm using Eq. (1) with the r_{eff} values in Table I and assuming aspect ratios of 10 for each material (i.e. $l_k = 10 * l_{volt}$). Table I displays the AC and DC values for the effective coefficients for comparison. Values for r_{63} for KDP and DKDP were calculated from the r_{eff} values shown in Table I using $n_o = 1.51$, yielding

r_{63} = 10.4 ± 1.3 pm/V for KDP and r_{63} = 23.8 ± 0.9 pm/V for DKDP. Our DC result for KDP agrees within 1% of Ref. 7 (r_{63} = 10.5 pm/V) and our value for r_{63} for DKDP agrees with that of Ref. 14 (r_{63} = 23.8 pm/V).

Table I. Experimentally determined effective electro-optic coefficients and calculated half-wave voltages.

Crystal	EO experiment k and E_{app} configurations	Propagation length and Applied voltage length of measured crystals (mm)	r_{eff}	r_{eff} (5kHz AC values) (pm/V)	r_{eff} (DC values) (pm/V)	V_{π}^{1064nm} ($l_k = 10*l_{volt}$)
YCOB	**k:[100]** **E_{app}:[001]**	**l_k = 17.81** **l_{volt} = 6.48**	$(r_{\gamma\gamma\gamma}n_\gamma^3 - r_{\beta\beta\gamma}n_\beta^3)$	**10.8 ± 1.4**	**8.79 ± 1.46**	**9.8 kV**
YCOB	**k:[010]** **E_{app}:[100]**	**l_k = 14.26** **l_{volt} = 3.94**	$(r_{\gamma\gamma\alpha}n_\gamma^3 - r_{\alpha\alpha\alpha}n_\alpha^3)$	**≤ 0.20**	**≤ 0.27**	-
YCOB	**k:[010]** **E_{app}:[001]**	**l_k = 14.26** **l_{volt} = 7.36**	$(r_{\gamma\gamma\gamma}n_\gamma^3 - r_{\alpha\alpha\gamma}n_\alpha^3)$	**≤ 0.52**	**≤ 0.55**	-
YCOB	**k:[001]** **E_{app}:[100]**	**l_k = 7.98** **l_{volt} = 9.86**	$(r_{\beta\beta\alpha}n_\beta^3 - r_{\alpha\alpha\alpha}n_\alpha^3)$	**≤ 0.82**	**≤ 1.8**	-
YCOB	**k:[100]** **E_{app}:[100]**	**l_k = 9.60** **l_{volt} = 9.60**	$(r_{\gamma\gamma\alpha}n_\gamma^3 - r_{\beta\beta\alpha}n_\beta^3)$	**3.43± 0.49**	**3.4 ± 0.4**	**310 kV**
YCOB	**k:[001]** **E_{app}:[001]**	**l_k = 6.08** **l_{volt} = 6.08**	$(r_{\beta\beta\gamma}n_\beta^3 - r_{\alpha\alpha\gamma}n_\alpha^3)$	**10.3 ± 1.6**	**10.7 ± 1.0**	**99 kV**
KDP	**k:[110]** **E_{app}:[001]**	**l_k = 20.33** **l_{volt} = 10.05**	$n_o^3 r_{xyz}$	-	**35.8 ± 4.4**	**2.9 kV**
DKDP	**k:[001]** **E_{app}:[001]**	**l_k = 17.58** **l_{volt} = 17.58**	$2n_o^3 r_{xyz}$	-	**164.0 ± 6.8**	**6.5 kV**
BBO [9]	**k:[001]** **E_{app}:[010]**	-	$2n_o^3 r_{yyy}$	**23.3**	-	**4.6 kV**

As expected, we found one large effective coefficient for YCOB in the transverse cases with $r_{eff} = (r_{\gamma\gamma\gamma}n_\gamma^3 - r_{\beta\beta\gamma}n_\beta^3) = 10.8 \pm 1.4$ pm/V. A similar magnitude coefficient was found to exist for the longitudinal cases with $r_{eff} = (r_{\beta\beta\gamma}n_\beta^3 - r_{\alpha\alpha\gamma}n_\alpha^3) = 10.7 \pm 1.0$ pm/V. In general, we see good agreement between our AC and DC measurements, within the estimated experimental error.

The half-wave voltage for YCOB crystal with a 10:1 aspect ratio (lk:lvolt) in the transverse configuration is 9.8 kV, approximately twice that of BBO. This is consistent, in both crystals, with an electro-optic coefficient value proportional to the corresponding NLO coefficient. (Due to crystal symmetry, BBO gains an additional factor of 2 in the expression of r_{eff}.) Examination of the remaining transverse results reveals r_{eff} coefficients for YCOB that have small upper bounds. The results for the coefficients, $(r_{\beta\beta\gamma}n_\beta^3 - r_{\alpha\alpha\gamma}n_\alpha^3)$ and $(r_{\gamma\gamma\gamma}n_\gamma^3 - r_{\beta\beta\gamma}n_\beta^3)$, suggest that $r_{\alpha\alpha\gamma}$ and $r_{\gamma\gamma\gamma}$ are either both small and/or of equal magnitude.

CONCLUSION

We have characterized the electro-optical coefficients of YCOB for both transverse and longitudinal field geometries. The largest effective electro-optic coefficient found is 10.8 pm/V, consistent with that expected from Miller type scaling of the measured nonlinear optical coefficients. The ease of growth and handling makes multi-plate longitudinal arrangements using YCOB a possible alternative to single or multiple crystal BBO or multiple crystal DKDP electro-optic switches. A useful low-switching voltage arrangement could be realized using two identical YCOB crystals separated by a 90° rotator where opposite transverse voltages are applied to the crystals. This architecture has the advantages of compensating for the crystals' static and thermally induced birefringence and, for a 10:1 propagation to field length aspect ratio, has a half-wave voltage below 10 kV. YCOB may therefore have potential application as a 1 μm Q-switch in high average power applications where DKDP or BBO can not be utilized.

ACKNOWLEDGEMENTS

The authors would like to thank Denise Krol (UC Davis) for her comments and suggestions. The authors also express their gratitude to Bruce Chai (University of Central Florida) for the YCOB boule from which the crystals used in this study were obtained. This work was performed under the auspices of the U.S. Department of Energy by the University of California Lawrence Livermore National Laboratory under Contract No. W-7405-Eng-48.

REFERENCES

1. M. Iwai, T. Kobayashi, Y. Mori, T. Sasaki , *Japanese J. of Appl. Phys* **36**, L276 (1997)
2. Q. Ye and B. H. T. Chai, *J. Cryst. Growth* **197**, 228 (1999)
3. Y Mori, I Kuroda, S Nakajima, T Sasaki, S Nakai, Appl. Phys. Let. **67** 13 (1995)
4. H. Hellwig, J. Liebertz, and L. Bohaty, *Solid State Commun.* **109**, 249 (1998)
5. D. Eimerl, L. Davis, S. Velsko, E. K. Graham, and A. Zalkin, *J. Appl. Phys.* **62**, 1968 (1987)
6. L. Weaver, C. Petty, D. Eimerl, J. Appl. Phys. **68** 6 (1990)
7. R. O. Carpenter, *J. Opt. Soc. Am.* **40**, 225 (1950)
8. G. Peterson, A. A. Ballman, P. V. Lenzo, P. M. Bridenbaugh, *Appl. Phys. Lett.* **5**, 62 (1964)
9. C. A. Ebbers, *Appl. Phys. Lett.* **52**, 1948 (1988)

10. L. Bohaty, J. Liebertz, Zeit. Krist. **192** 91-95 (1990)
11. J. D. Bierlein C.B. Arweiler, Appl. Phys. Lett. **49** 15 (1986)
12. C. A. Ebbers, *J. Opt. Soc. Am. B* **12**, 1012 (1995)
13. J. J. Adams, C. A. Ebbers, K. I. Schaffers, and S. A. Payne, *Opt. Lett.* **26**, 217 (2001)
14. K. Onuki, N. Uchida, and T. Saku, *J. Opt. Soc. Am.* **62**, 1030 (1972)

Growth of Yb: S-FAP [Yb^{3+}:$Sr_5(PO_4)_3F$] crystals for the Mercury laser ☆

K.I. Schaffers*, J.B. Tassano, A.B. Bayramian, R.C. Morris[a]

Lawrence Livermore National Laboratory, PO Box 808, L-482 Livermore, CA 94551, USA, [a]Consultant

Abstract

Crystals of Yb:S-FAP [Yb^{3+}:$Sr_5(PO_4)_3F$] will be used as the gain medium for the Mercury Laser, a gas-cooled amplifier system intended to yield 100 J, 10 Hz and 10% efficiency in 3 ns when completed, for inertial fusion energy. Growing high optical quality crystals is a challenge due to a number of growth issues, including: cloudiness, bubble core defects, anomalous absorption, low-angle grain boundaries, cracking, and crystal inclusions. At this time, a growth process has been developed to simultaneously eliminate or diminish each of the defects.

Keywords: A1. Defects; Phase equilibria; A2. Czochralski method; B1. Oxides; B3. Solid state lasers

1. Introduction

To achieve the goals of the Mercury laser and have an architecture that can be scaled to higher energy for inertial fusion energy [1], three key technologies are incorporated into the system, specifically, diode pumping to replace flashlamp pumping in previous systems [2,3], active cooling of the amplifier medium with helium flowing over the faces of the slabs, and Yb:S-FAP crystals as the gain medium. Yb:S-FAP is well suited for diode pumping in moderate thermal load applications owing to the relaxed diode brightness requirements, long lifetime of 1.1 ms, and a suitable gain cross-section ($6.0 \times 10^{-20}\,cm^{-1}$) for ns pulse extraction. Many of the initial proof-of-principal measurements on Yb:S-FAP crystals were performed on material provided by Bruce Chai at CREOL in Orlando, Florida, who grew the first small, high quality boules suitable for laser measurements [4]. A list of thermomechanical and laser properties for Yb:S-FAP is provided in Table 1 [5–8]. Yb:S-FAP is a uniaxial crystal with a refractive index of approximately 1.61 at 1047 nm which is the emission wavelength. The large absorption cross section makes diode pumping more cost-feasible for large laser systems due to

☆This work was done under the auspices of the US Department of Energy by the University of California Lawrence Livermore National Laboratory under Contract W-7405-ENG-48.

*Corresponding author. Tel.: +1-925-422-5084; fax: +1-925-423-6195.

E-mail address: schaffers1@llnl.gov (K.I. Schaffers).

Table 1
Thermomechanical and laser properties of trivalent ytterbium doped $Sr_5(PO_4)_3F$ (S-FAP)

Property	Value
Hexagonal space group	$P6_3/m$
Density, ρ (g/cm^3)	4.14
Hardness (M ohs Scale)	~5
Heat capacity, C_p (J/g °C) @ 25°C	0.5
Thermal diffusivity (m^2/s)	9.8×10^{-7}
Thermal conductivity, κ (W/m °C)	2.0
Young's modulus E_{ave} (GPa)	109
Fracture toughness, K_{IC} (MPa m$^{1/2}$)	0.51
Poisson's ratio, ν	0.4
Extraordinary index of refraction, n_e (@ 1047 nm)	1.61262
Ordinary index of refraction, n_o (@ 1047 nm)	1.61760
dn_e/dT (°C^{-1})	-5×10^{-6}
dn_o/dT (°C^{-1})	0×10^{-6}
Sellmeier coefficients: $n = 1 + \Sigma A_i\lambda^2/\lambda^2 - \lambda_i^2$	
n_o: $\lambda_1 = 0.09722\,\mu m$, $A_1 =$	1.00838
$\lambda_2 = 0.09721\,\mu m$, $A_2 =$	0.60057
$\lambda_3 = 9.93370\,\mu m$, $A_3 =$	0.60892
n_e: $\lambda_1 = 0.08377\,\mu m$, $A_1 =$	1.0281
$\lambda_2 = 0.11671\,\mu m$, $A_2 =$	0.56498
$\lambda_3 = 10.12103\,\mu m$, $A_3 =$	0.61833
Photoelastic coefficient q_{33} ($\times 10^{-12}$ Pa)	0.308
Photoelastic coefficient q_{31} ($\times 10^{-12}$ Pa)	0.936
Thermal expansion α_e (°C^{-1})	8.4×10^{-6}
Thermal expansion α_o (°C^{-1})	9.5×10^{-6}
Typical Yb^{3+} dopant densities (ions/cm^3)	~1.3 x 10^{19}
Emission cross section @ 1047 nm (cm^2)	6.0 x 10^{-20}
Absorption cross section @ 900 nm (cm^2)	9×10^{-20}
Radiative lifetime (ms)	1.14
Damage threshold (J/cm^2)	$\geqslant 50$
Scatter loss (cm^{-1})	$1e^{-3}$
Absorptive loss (cm^{-1})	$5e^{-4}$
Calculated extrinsic thermal stress–resistance, R_T[a] (W/m) [assumes a crack size of 25 μm)	125

[a] Figure of merit: $R_T = K_{IC}\kappa(1-\nu)/a^{1/2}\alpha E_{ave}$; a = crack size radius.

the reduced requirement on the brightness and number of diode packages necessary. Yb^{3+} doped into S-FAP is pumped at the 900 nm absorption line and with a long, 1.14 ms lifetime, allowing for greater energy storage in the material. In addition to the aforementioned characteristics, a high damage threshold ($\geqslant 50\,J/cm^2$) and low losses ($\leqslant 0.1\%$/cm) make Yb:S-FAP a suitable material for the Mercury laser system.

The Mercury laser requires a minimum of 14 Yb:S-FAP slabs for operation. Each slab has dimensions $4 \times 6 \times 0.75$ cm in thickness, where the c-axis is oriented along the 6 cm length of the slab. Each slab requires a Yb-doping level of approximately 1.3×10^{19} ions/cm^3. With this requirement, crystal growth becomes challenging because only ~12% of Yb in the initial melt is incorporated into the S-FAP lattice ($C_s/C_l \sim 0.12$), Fig. 1. This low of a distribution coefficient for Yb gives rise to interface instabilities that could result in bubble core and second phase inclusions as will be discussed in Section 3 of this paper. Current crystal growth capabilities have produced high quality, low loss crystals with adequate wavefront as shown in Fig. 2. As of the writing of this article, the Mercury laser is producing 20 J at 10 Hz in a 20 ns pulse, based on partial activation of the system.

Yb:S-FAP crystals have a number of attractive properties for high average power applications. However, large enough size to produce laser slabs for Mercury are not yet commercially available and the growth of high optical quality, low loss crystals poses a challenge due to a number of crystal growth issues. Six possible defects that can occur in these crystals include cloudiness, bubbles in the core region, anomalous absorption, cracking, low-angle grain boundaries, and inclusions at

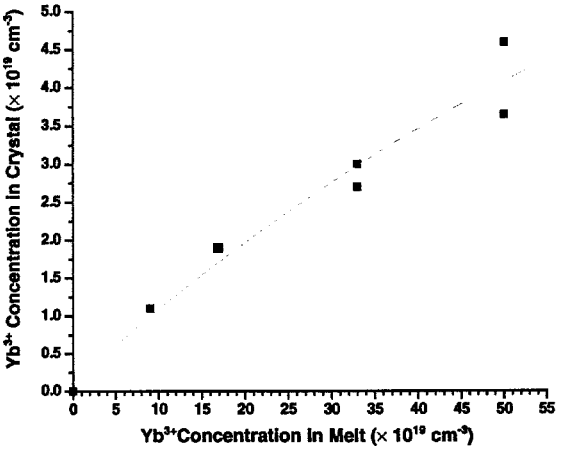

Fig. 1. Distribution coefficient of Yb in the melt composition versus the number density in the crystals.

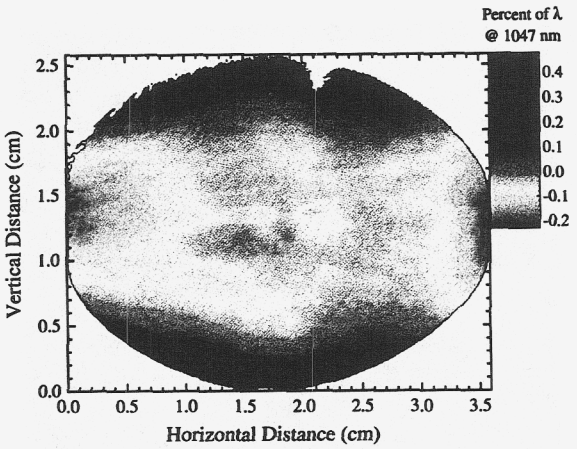

Fig. 2. Wavefront of an oval piece of Yb:S-FAP indicating approximately 0.1 waves of distortion.

the outer surface of the boule. A significant effort has been put forth to understand the nature of the defect chemistry in Yb:S-FAP crystals and to develop a growth process to yield crystals from which slabs can be fabricated.

This article describes the advances that have been made in the growth process for Yb:S-FAP and the current understanding of the defect chemistry. At this time crystal growth parameters are understood well enough to produce high quality crystals from which half-size slabs can be harvested for diffusion bonding to form full size slabs for the Mercury laser project.

2. Experimental procedure

High optical quality crystals of Yb:S-FAP have been grown in sizes up to 3.5 cm diameter by approximately 12 cm in length. These crystals are grown by using the Czochralski method in a high temperature oxide-type furnace. A 4-in diameter by 4-in tall iridium crucible is used for the growth because the melting temperature is approximately 1786°C [8]. The crucible is supported on two $\frac{1}{4}$in. thick zirconia plates and two $2\frac{1}{2}$in. thick zirconia ceramic disks; zirconia tubes and grog are used as the insulation for the furnace walls. Flowing nitrogen is necessary to create an inert environment for the crystal growth, preventing oxidation of both the melt components and the iridium crucible.

To prepare the melt for growth, the appropriate ratios of $SrHPO_4$ (Optical Grade, General Electric Corp.), $SrCO_3$ (Optical Grade, General Electric Corp.), and Yb_2O_3 (99.99%, All-Chemie Corp.) powders are well mixed and then melted in the crucible. In this reaction, the $SrHPO_4$ and $SrCO_3$ decompose giving off water and carbon dioxide and leaving the composition $Sr_3(PO_4)_2$:Yb in the crucible (1). This composition is kept molten for approximately 18 h to fully decompose the orthophosphate and the carbonate. SrF_2 (99.99%, GFI, Advanced Technologies) is then added to the decomposed melt to form the appropriate melt stoichiometry for growth (2). The pre-decomposition reaction prevents the SrF_2 from oxidizing to SrO thereby removing fluorine from the melt. The final melt is allowed to react and equilibrate for approximately 5 h before initiating the growth of a crystal.

$$3[2SrHPO_4 + SrCO_3 + xYb_2O_3 \rightarrow Sr_3(PO)_2\text{: } Yb + H_2O(g) + CO_2(g)], \quad (1)$$

$$3Sr_3(PO_4)_2\text{: } Yb + SrF_2 \rightarrow 2Yb : Sr_5(PO_4)_3F, \quad (2)$$

where Yb_2O_3 has been typically used as the dopant to aid in the charge compensation process where a Yb^{3+}–O^{2-} ion pair exchanges for a Sr^{2+}–F^- pair [8]. The solid-to-liquid composition ratio (C_s/C_l) of Yb^{3+} in the S-FAP crystal lattice is approximately 0.12 requiring that an excess of Yb_2O_3 be added to the melt.

The crystals are grown from seeds oriented along the [0 0 1] direction attached to a $\frac{1}{4}$in diameter iridium coupler and held by an alumina rod. Diameter control is maintained by a computer-based, closed-loop power control system that is based on weighing the crystal and calculating a growth rate per unit time. A motor generator power isolation unit is used to damp out power fluctuations to within ± 0.5 V on a 480 V input to the RF power supplies and chillers are used to control the variations that occur in water temperature. With these controls in place, outside perturbations to the crystal growth process are minimized.

Rotation rates of approximately 10–15 rpm have been effective for boule diameters up to 3.5 cm and a pull rate of 0.5 mm/h is typically used to reduce defect formation. Boules of dimension 3.5 cm diameter by 12 cm in length are grown with good optical quality.

3. Results and discussion

The growth of high optical quality crystals of Yb:S-FAP has proven very challenging due to a number of defect issues (cloudiness in as-grown crystals, an anomalous absorption, bubble core, low-angle grain boundaries, cracking from thermally induced stresses, and second phase inclusions around the perimeter of the boule).

3.1. Cloudiness

An excess of SrF_2 in the melt has been effective in controlling, and most times eliminating, the cloudiness in Yb:S-FAP crystals. Cloudiness in as-grown boules of Yb:S-FAP (Fig. 3) has been attributed to second phase precipitation on line defects in the crystal lattice. This is evident in Fig. 4 where the Scanning Electron Micrograph (SEM) shows spiral defects decorated with a whitish precipitate. The identity of the white precipitate has not yet been identified due to the small size of the particulates. However, the precipitate could be caused by slight incongruent melting in addition to significant evaporation of the fluoride from the melt surface at the 1786°C melt temperature. Efforts to use Tunneling Electron Microscopy (TEM) and SEM—X-ray thus far have been ineffective for identifying the white precipitate. Currently, a 33 mole% excess of SrF_2 is added to the melt as a flux to account for the possible incongruent melting behavior of the Yb:S-FAP composition. The excess also helps to compensate for evaporation losses over the 17 day growth period. Based on the known phase diagram of the $Ca_5(PO_4)_3F$ (C-FAP) derivative [9], the 33 mole% SrF_2 composition in the $Sr_3(PO_4)_2$:SrF_2 phase system would be equivalent to the compound $Sr_7(PO_4)_4F_2$. Even though this derivative exists in the C-FAP system, single crystal X-ray structure analysis and Inductively Coupled Plasma/Mass Spectrometry have identified the crystals grown from this composition to be the $Sr_5(PO_4)_3F$ phase. The full phase diagram for the $Sr_3(PO_4)_2$:SrF_2 system does not yet exist, however, based on NIST (National Institute of Standards and Technology) measurements and

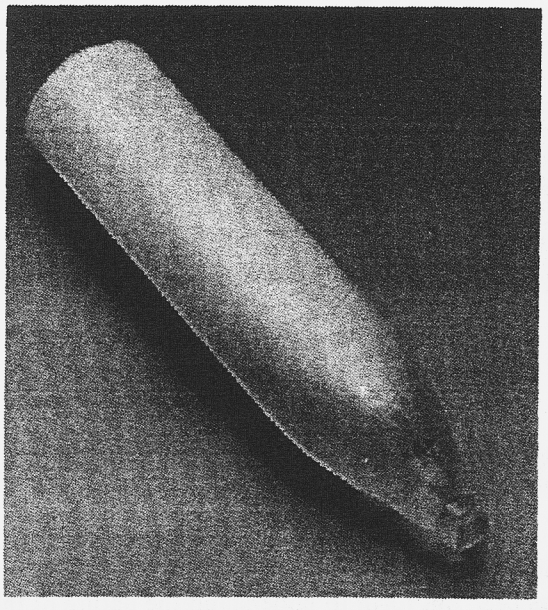

Fig. 3. As-grown boules of Yb:S-FAP near the stoichiometric composition have significant amounts of cloudiness.

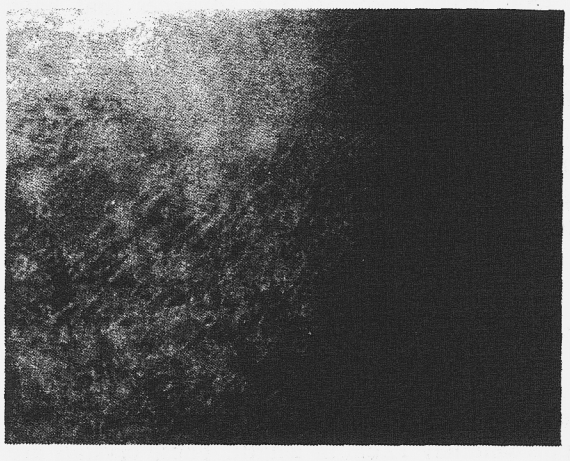

Fig. 4. Cloudiness in an as grown Yb:S-FAP crystal; approximately 75 × magnification.

crystal growth observations, an initial working phase diagram has been formulated, but has not been published at this time. It has also been found that the amount of excess SrF_2 is significant since compositions within 20 mole% excess of the stoichiometric composition yield crystals that are cloudy and large excesses above 33 mole% lead to the formation of new, elongated bubble defects that propagate down the *c* axis in the core region of the boule. However, melt compositions near 33 mole% SrF_2 yield crystals with limited or no cloudiness. Any remaining cloudiness appears near the bottom of the crystal where the melt has lost a significant amount of fluoride.

Alternatively, for boules grown at melt compositions closer to the stoichiometric composition, the cloudiness can be annealed away by suspending the boule over the melt directly following growth. The boule is raised to a temperature that is approximately 250°C below melting at the bottom of the boule and held there for 5–6 days. This procedure is very time consuming, but effective in dramatically reducing, or in many cases, eliminating the cloudiness in as-grown boules.

3.2. *Anomalous absorption*

Growth along the *c*-axis and axial thermal gradients of <60°C/cm above the melt, are critical for eliminating the anomalous absorption that occurs as a broad band from approximately 925–1000 nm with the largest peak at 975 nm, Fig. 5. Crystals grown along both the *a*-axis and 45° to the *c*-axis intermittently display the unwanted absorption whereas only *c*-axis crystals grown at very high gradients ($\geqslant 70$°C/cm) show evidence of this absorption. Based on excitation and emission spectra, this absorption behavior has been attributed to the presence of Yb^{3+} ions on a second site in the crystal lattice. XPS and XAS spectra taken at the Stanford Synchrotron Radiation Laboratory also indicate a second site for the Yb^{3+} ion in the Yb:S-FAP lattice [10]. This is a likely explanation as there are two crystallographic sites in the S-FAP lattice that Yb can occupy (Sr_I and Sr_{II}), as shown in Fig. 6. Also, the spectrum most closely resembles that of Yb^{3+} in a phosphate environment such as in $LuPO_4$ [11], where there

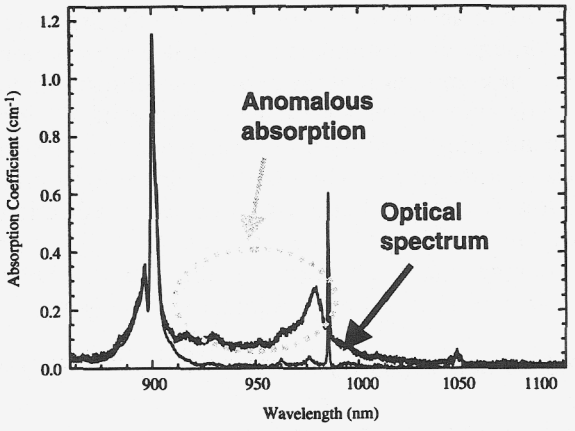

Fig. 5. Plot showing the anomalous absorption that can appear in Yb:S-FAP crystals.

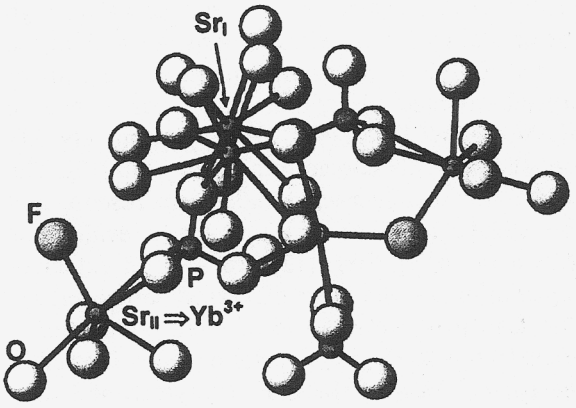

Fig. 6. Sketch of the two Sr sites in Yb:S-FAP, where the Yb prefers the Sr_{II} site and the F is replaced by O for charge compensation.

are no characteristics of the desired spectrum arising from the vibration interactions of the Yb^{3+}–O^{2-} charge compensation pair [8]. This natural charge compensation mechanism offers a preferential site (Sr_{II}) for the Yb^{3+} ion. However, at higher dopant concentrations and for growth directions other than the *c*-axis, the Yb can be pushed to occupy the second strontium site (Sr_I) in the lattice. In this case, the site is surrounded by seven oxygens associated with phosphate groups and there is no natural charge compensation mechanism available to the Yb. Under these conditions, a defect site is likely created in the

lattice to accommodate the Yb^{3+} on the Sr_I^{2+} site. Although unsubstantiated, a possible explanation for the elimination of the anomalous absorption in *c*-axis crystals relates to the presence of F^- ion "conduction" channels that parallel the *c*-axis in the apatite lattice. The preferred orientation may allow for easier charge compensated substitution of the Yb^{3+}–O^{2-} pair for the Sr^{2+}–F^- pair reducing the probability of the Yb achieving charge compensation by another mechanism.

3.3. *Grain boundaries*

Low-angle grain boundaries have been eliminated by growing "seed extensions" and choosing a small cone angle to maintain a stable growth interface. Grain boundaries appear as slight shifts in the refractive index or waves running through the crystal in sheets oriented perpendicular to the *c*-axis. To view the grain boundaries, a slab of crystal oriented along the *a*-axis was etched in $5H_2SO_4 + 1HCl$ at 110°C for approximately 30 s and then quickly cooled in a water bath [12]. The crystal was then inspected under a microscope and the etched boundaries were clearly evident as shown in Fig. 7. Ref. [12] provides an extensive explanation of the type of crystal lattice effects that lead to the formation of these grain boundaries. In this study, boundaries typically formed in the cone section of the C-FAP crystals and near the center of the full diameter section of the crystal. It is generally understood that these boundaries can propagate from the seed into the crystal and by strain-induced deformations resulting from an unstable growth interface [13]. To prevent grain boundaries from propagating from seed or forming during the seeding process, a seed extension technique is used. Here, the initial growth is constrained to approximately 3–5 mm in diameter for a 3 cm length so there is an opportunity for the boundaries to propagate to the outside of the crystal where they would terminate. This method has been very effective for all growth directions. In addition, a gradual increase in diameter in the cone section, with a cone angle of approximately 35°, helps to maintain stable growth conditions minimizing stress and preventing new grain boundaries from forming. Further,

Fig. 7. Grain boundaries are evident in an acid etched slab of Yb:S-FAP where the *c*-axis is perpendicular to the boundaries.

growth of crystals along the *c*-axis increases the probability that the grain boundaries will grow out, because the propagation direction is perpendicular to the growth direction. Even though this technique is effective in the initial part of the growth, boundaries can still form in the full diameter section of the crystal, typically where constitutional supercooling occurs and the bubble core defects form.

3.4. *Bubble core defects*

Crystals of Yb:S-FAP are grown in a high thermal gradient furnace to stabilize the growth interface and control the formation of bubble core defects. The bubble core is attributed to constitutional supercooling where a supercooled liquid is formed from concentration gradients of rejected melt components pushed along in front of the advancing interface. In the Yb:S-FAP system, SrF_2 is in excess to alleviate cloudiness. Also, an excess of Yb_2O_3 is added to account for the 0.12 distribution coefficient (C_s/C_l). Therefore, these components may be of higher concentration near

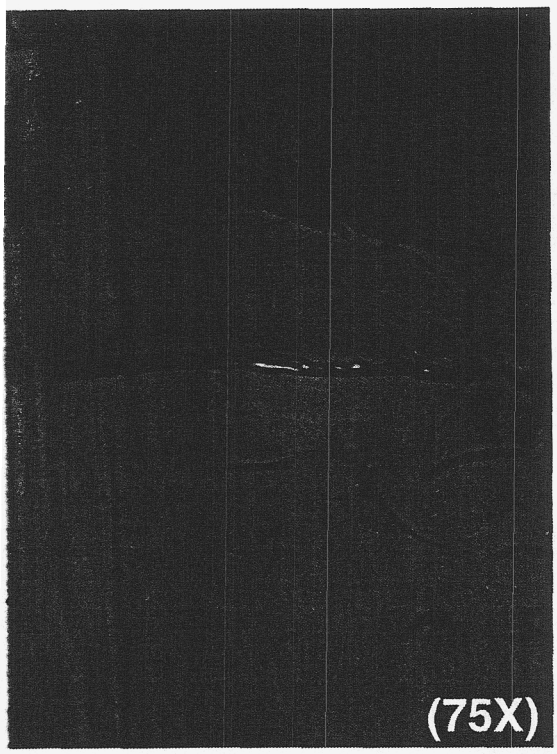

g. 8. Bubble core defects can result from constitutional ɔercooling.

e interface resulting in constitutional supercool-g under unstable growth conditions [14]. Bubbles e formed from trapped liquid that solidifies upon oling leaving an evacuated void (see Fig. 8). EM/EDX analysis has pinpointed the approx-ıate composition associated with the bubbles to Yb_2O_3 and $Sr_3(PO_4)_2$, suggesting a possible lack SrF_2 at the interface even though there is an cess in the melt . This might be explained from e vaporization of SrF_2 from the melt surface and elt convection driving a fluoride poor composi-ɔn to the growing interface. To prevent bubbles ɔm forming, we have increased the thermal adients in the furnace to stabilize the growth terface. Axial gradients of ~35–50°C/cm di-ctly above the melt have been effective. The dial gradients in the melt are currently not easured, due to lack of a compatible thermo-uple to insert into the melt. However, it is sumed that by increasing the axial gradient

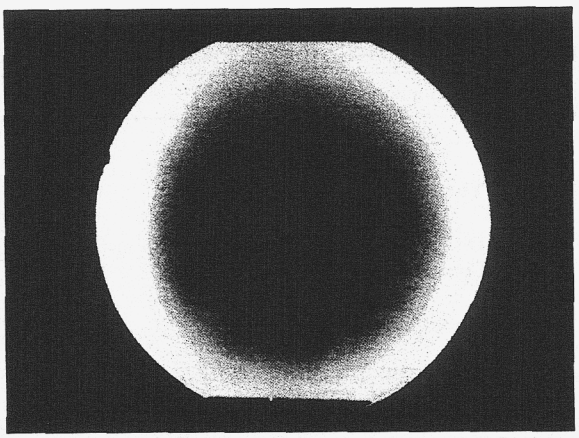

Fig. 9. Second phase inclusions propagate inward from the outside of the crystals under low thermal gradient conditions.

above the melt, the radial gradient in the melt will also be increased by an unknown factor.

3.5. *Inclusions*

Second phase inclusions (Fig. 9) can be pushed to within 1 mm of the skin of the boule by lowering the Yb-doping level and maintaining a higher axial thermal gradient above the melt as discussed for the core defects. In most cases, the defects appear to be denser in the upper region of the crystal and decrease down the length. Also, crystals can sometimes be grown with almost no inclusions under nominally identical conditions to previous growths. These inclusions have been identified by using transmission electron microscopy (TEM) as being rich in Yb, likely Yb_2O_3. Further analysis is necessary to determine the exact nature for the nucleation of the second phase at the outer rim of the crystal. At this time, however, the inclusions can be controlled well enough to allow for high optical quality crystals to be harvested inside of the inclusion perimeter.

3.6. *Cracking*

Cracking is reduced by not separating the crystals from the melt during the cooling process and by a significant reduction of defects causing strain. The main source of cracking was related to

Table 2
A summary of the possible defect issues in Yb:S-FAP as well as their fundamental cause and resolution

Issue	Fundamental cause	Resolution
Cloudiness	Precipitation on line defects	excess SrF2 in melt annealing over melt
Anomalous absorption	Yb^{3+} in a different site	*c*-axis along growth direction axial thermal gradients $<60°C/cm$
Grain boundaries	Dislocations from the seed or growth instabilities	seed extensions to grow out boundaries
Bubble core	Constitutional supercooling	growth stability maximize thermal gradients
Cracking	Internal stresses	cool crystals attached to melt reduce defects
Second phase inclusions	Limited Yb solubility in melt	Yb-doping of <0.75 at% in melt increase thermal gradients

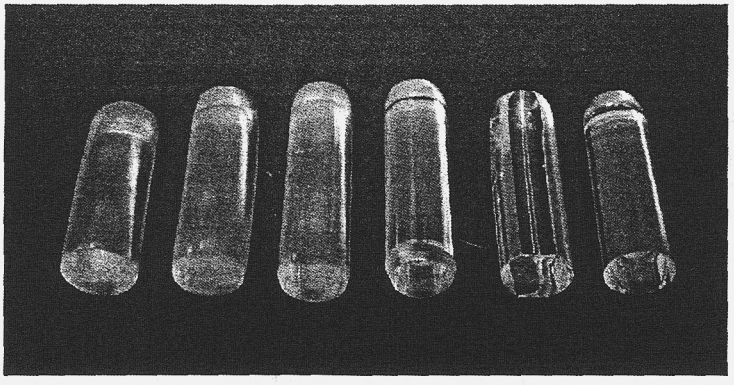

Fig. 10. High optical quality Yb:S-FAP boules produced by controlling each of the defects.

high thermal gradients in the crystals during cooling, especially at larger (5 cm) diameters, as well as numerous bubble core defects. Narrowing the diameter, before cooling the crystals still attached to the melt, reduces the thermal stress along the length of the boule by using the large thermal load of the melt to conduct heat into the crystal. Also, with a reduction in defects, cracking is no longer an issue in the growth of 3.5 cm diameter crystals.

4. Conclusions

A sufficient understanding of growth parameters has been achieved to manage or eliminate each of the six defects that can occur in Yb:S-FAP boules (Table 2) so that, for the first time, large, high optical quality crystals can be routinely grown (Fig. 10). Currently, Yb:S-FAP boules of approximate 3.5 cm diameter by 12 cm length are fabricated into slabs suitable for laser applications. Since the crystals are still too small to yield a full size slab, they are cut to yield two half slabs from either side of an approximate 5 mm diameter refractive index core. The two half-slabs are then held together by a diffusion bonding technology [15] to form a full size ($4 \times 6 \times 0.75$ cm) slab (Fig. 11) required for the laser design.

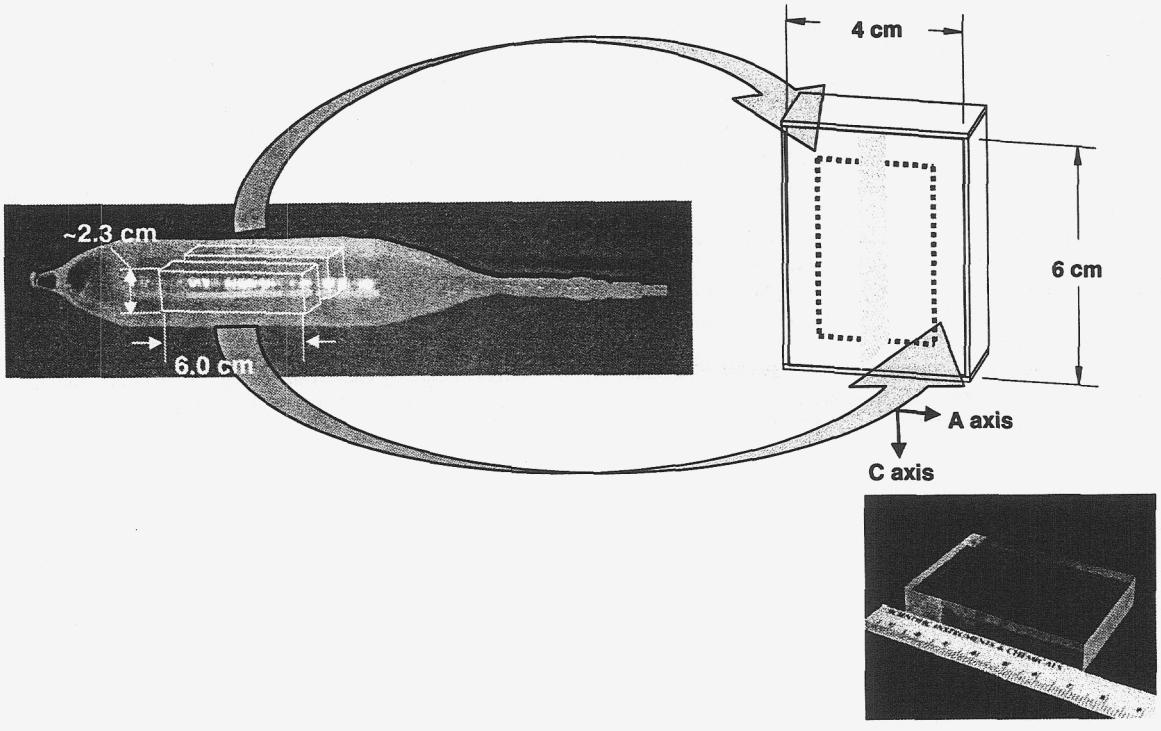

Fig. 11. Sketch to show the orientation of the half slabs that are harvested from the boule to form a full size 4 × 6 × 0.75 cm slab.

Acknowledgements

The authors especially thank Camille Bibeau and Jay Dawson for overseeing the development of diffusion bonding to permit the growth of half-slabs (in conjunction with Onyx Optics), and for establishing algorithms to assess optical quality. In addition, we acknowledge Northrop-Grumman, Space Technologies (Synoptics Division) for their collaborative efforts in growing Yb:S-FAP crystals on a contract with LLNL and providing useful material and discussions. Peter Thelin deserves great thanks for his tireless efforts in devising unique methods for cutting and polishing these extremely fragile crystals. We appreciate the contribution to this project by Scientific Materials, Inc., and their efforts in performing the SEM/EDX measurements that identified the bubble core defects. We recognize Mark Wall for performing the TEM measurements to determine the composition of the second phase inclusions. We also acknowledge NIST (specifically Larry Cook) for performing the measurements to obtain the first data points in defining an initial phase diagram for the $Sr_3(PO_4)_2$:SrF_2 system. Finally, the authors are indebted to Steve Payne for his invaluable insights and discussions throughout this work.

References

[1] C.D. Orth, S.A. Payne, W.F. Krupke, Nucl. Fusion 36 (1) (1996) 75.

[2] A.J. Bayramian, R.J. Beach, W. Behrendt, C. Bibeau, C.A. Ebbers, B.L. Freitas, V.K. Kanz, S.A. Payne, K.I. Schaffers, K. Skulina, L.K. Smith, J.B. Tassano, D. Van Lue, H. Nakano, in: M.E. Fermann, L.R. Marshall (Eds.), OSA Trends in Optics and Photonics on Advanced Solid State Lasers, January 2002 Conference, p. 139.

[3] A.J. Bayramian, R.J. Beach, W. Behrendt, C. Bibeau, C.A. Ebbers, B.L. Freitas, V.K. Kanz, S.A. Payne, K.I. Schaffers, K. Skulina, L.K. Smith, J.B. Tassano, in: K.A. Tanaka, D.D. Meyerhofer, J. Meyer-ter-Vehn (Eds.), International Fusion Science and Applications 2001, 2001 Conference, Vol. 459.

[4] C.D. Marshall, L.K. Smith, S. Sutton, M.A. Emanuel, K.I. Schaffers, S. Mills, S.A. Payne, W.F. Krupke, B.H.T. Chai, in: S.A. Payne, C.R. Pollock (Eds.), OSA Trens in Optics and Photonics on Advanced Solid State Lasers, Vol. 1, January 1996 Conference, p. 208.
[5] S.A. Payne, L.K. Smith, L.D. DeLoach, W.L. Kway, J.B. Tassano, W.F. Krupke, IEEE J. Quantum Electron. 30 (1994) 170.
[6] L.D. DeLoach, S.A. Payne, L.K. Smith, W.L. Kway, W.F. Krupke, J. Opt. Soc. Am. B. 11 (1994) 269.
[7] S.A. Payne, L.D. DeLoach, L.K. Smith, W.L. Kway, J.B. Tassano, W.F. Krupke, B.H.T. Chai, G. Loutts, J. Appl. Phys. 76 (1) (1994) 497.
[8] L.D. DeLoach, S.A. Payne, W.L. Kway, J.B. Tassano, S.N. Dixit, W.F. Krupke, J. Luminescence 62 (1994) 85.
[9] J. Berak, I. Tomczak-Hudyna, Rocz. Chem. 12 (1972) 2157.
[10] A.J. Nelson, T. van Buuren, C. Bostedt, K.I. Schaffers, L.J. Terminello, M. Engelhard, D. Baer, J. Appl. Phys. 91 (8) (2002) 5135.
[11] L.D. DeLoach, S.A. Payne, L.L. Chase, L.K. Smith, W.L. Kway, W.F. Krupke, IEEE J. Quantum Electron. 29 (1993) 1179.
[12] G.M. McManus, R.H. Hopkins, W.J. Takei, J. Appl. Phys. 40 (1) (1969) 180.
[13] Private communication with Robert Morris, consultant, 1998.
[14] B. Chalmers, Principles of Solidification, Wiley, New York, 1964, p. 150.
[15] H.E. Meissner, Diffusion bonding is done at Onyx Optics, Inc. in Dublin, California, Patent Number 5,441,803, Onyx Optics, Composites made from single crystal substrates, August 15, 1995.

PHOTOEMISSION AND PHOTOABSORPTION INVESTIGATION OF THE ELECTRONIC STRUCTURE OF YTTERBIUM DOPED STRONTIUM FLUOROAPATITE

A. J. Nelson, T. van Buuren, K. I. Schaffers, and Lou Terminello
Lawrence Livermore National Laboratory, Livermore, CA 94550 USA

X-ray photoemission and x-ray photoabsorption were used to study the composition and the electronic structure of ytterbium doped strontium fluoroapatite (Yb:S-FAP). High resolution photoemission measurements on the valence band electronic structure was used to evaluate the density of occupied states of this fluoroapatite. Element specific density of unoccupied electronic states in Yb:S-FAP were probed by x-ray absorption spectroscopy (XAS) at the Yb 4d ($N_{4,5}$-edge), Sr 3d ($M_{4,5}$-edge), P 2p ($L_{2,3}$-edge), F 1s and O 1s (K-edges) absorption edges. These results provide the first measurements of the electronic structure and surface chemistry of this material.

1. Introduction

Host materials doped with the Yb^{3+} ion have sparked a great deal of interest in the last several years for their use as diode-pumped solid-state lasers. Crystals of Yb Doped Strontium Fluoroapatite [Yb:S-FAP or $Yb^{3+}:Sr_5(PO_4)_3F$] are currently being studied for use in an average power 100 J, 10Hz, diode pumped laser operating at 1047 nm.[1] The Yb^{3+} dopant is a $4f^{13}$ ion and possesses only two relevant electronic states derived from the single 4f hole - the $^2F_{7/2}$ ground-state and the $^2F_{5/2}$ excited-state. An anomalous absorption has been observed in some Yb:S-FAP crystals that is thought to be related to the crystallographic site occupied by the Yb.

S-FAP has the hexagonal crystal structure shown in Figure 1(a), space group $P6_3/m$, a = 9.7078 Å and c = 7.2819 Å.[2] The unit cell contains two formula units. There are 6 PO_4 groups with their central P ions at the hexagonal corners on the reflection planes and the F ions are centered on the hexagonal faces. The ten divalent Sr^{2+} ions occupy two different crystallographic sites in the unit cell [Fig. 1(b)].[2,3] Site I has trigonal symmetry with four Sr^{2+} ions occupying a nine-coordinated oxygen polyhedron. Site II has six Sr^{2+} ions surrounded by six oxygen and one fluorine. The trivalent Yb dopant has a strong tendency to occupy the lower symmetry site II. The charge compensation mechanism for rare earth doping at site II involves substitution of the F^- with an O^{2-}, i.e. Sr^{2+}-F^- is replaced by Yb^{3+}-O^{2-}. The aforementioned anomalous absorption has been attributed to Yb^{3+} on a second site in the crystal.

This paper presents results from an x-ray photoemission (XPS) and x-ray photoabsorption (XAS) investigation of the composition and the electronic structure of ytterbium doped strontium fluoroapatite (Yb:S-FAP). Core-level spectroscopy and results for the occupied states in the valence band and unoccupied states in the conduction band reveal chemical differences associated with anomalous optical absorption.

2. Experimental

Crystals of Yb:S-FAP are grown in an inert atmosphere by the Czochralski (CZ) method. $SrHPO_4$, $SrCO_3$, SrF_2 and Yb_2O_3 powders are mixed and inductively heated to prepare the melt. Crystal growth runs were initiated with oriented single crystal seeds having the desired orientation, and with a pull rate of ~0.5 mm/hr and a rotation rate of ~20 rpm. Yb^{3+} doping concentration is ~1-2 x 10^{19} cm^{-3}.

The Yb:S-FAP samples examined were CZ171218, which exhibited anomalous optical absorption, and C200115, an optically 'clean' sample.

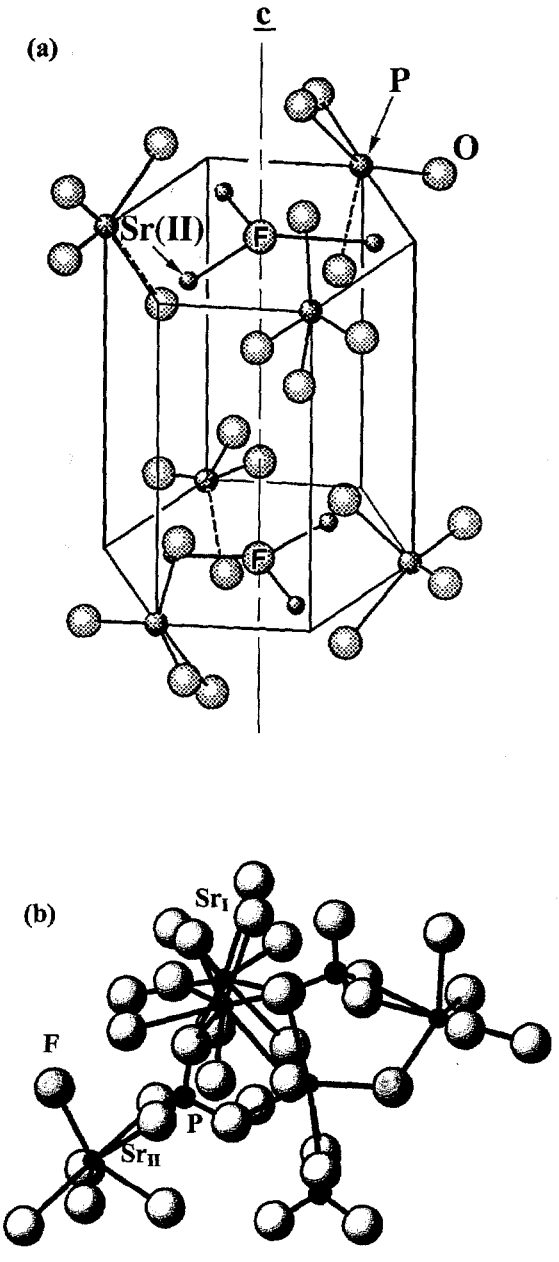

Figure 1. (a) Crystal structure of $Sr_5(PO_4)_3F$ and (b) the two Sr^{2+} sites for Yb-doping in the crystal.

Analytical results for these samples were compared to determine compositional and electronic differences. The starting compounds were also analyzed by XPS and XAS to provide a basis for quantitative analysis. The $SrHPO_4$, $SrCO_3$, SrF_2, Yb_2O_3 and YbF_3 powders were used as received and pressed into In foil for analysis.

XPS spectra were obtained using a focused monochromatic Al Kα x-ray (1486.7 eV) source for excitation and a spherical section analyzer. XAS analysis was performed at beamline 8.2 at the Stanford Synchrotron Radiation Laboratory (SSRL) by scanning the photon energy of the incoming monochromatic synchrotron radiation through the Yb 4d ($N_{4,5}$-edge), Sr 3d ($M_{4,5}$-edge), P 2p ($L_{2,3}$-edge), F 1s and O 1s (K-edges) core-level edges while monitoring the total electron yield (TEY, surface sensitive, 50-100Å).

3. Results and Discussion

The valence band (VB) spectra for the Yb:S-FAP crystals and model compounds are presented in Figure 2. The valence band for Yb:S-FAP is composed of overlapping P 3p, O 2p, and F 2p states. The localized Yb $4f^{13}$ states lie below the upper part of the O 2p density of states,[4-6] as can be seen in the expanded VB maximum region for the Yb_2O_3 model compound.

Figure 2. VB region for the Yb:S-FAP crystals and model compounds.

In addition, note the broadened peaks in the expanded VB maximum region for the YbF_3 model compound that is due to the overlapping F 2p valence band. Visual inspection of the expanded VB maximum region shows a similarity between the spectra of $SrHPO_4$ and the

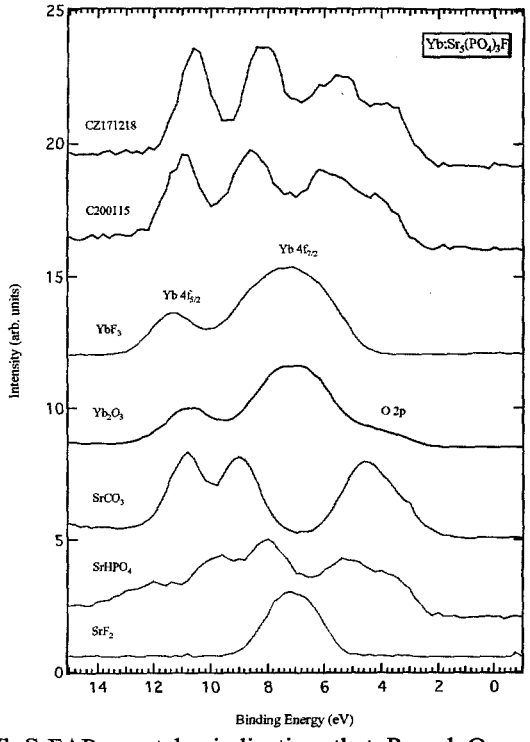

Yb:S-FAP crystals, indicating that P and O p-states dominate the valence band.

The XAS technique probes empty or unfilled electronic states and provides information on the local chemical environment. Transitions between the initial state ($4d^{10}5s^25p^64f^N$, N = 13 for Yb^{+3}) and a series of final states ($4d^95s^25p^64f^{N+1}$) yields numerous features at the Yb $N_{4,5}$-edge that can provide structural information. For 4d X-ray absorption, the dipole

allowed transitions are 4d → 4f and 4d→ 5p, with transitions to the 4f states dominant. The dipole forbidden 5p → 4f transition ($4d^{10}5p^64f^N \rightarrow 4d^95p^64f^{N+1} \rightarrow 4d^{10}5p^54f^{N+1}$) becomes weakly dipole-allowed due to spin-orbit interaction and manifests itself as pre-threshold features,[7] and is of course absent in the divalent $4f^{14}$ (Yb^{2+}) case. Enhancement of these transitions has been noted when valence electrons associated with oxygen bonding contribute.[5] The nature of the crystal field splitting in the $^2F_{7/2}$ and $^2F_{5/2}$ electronic states derived from the single 4f hole are affected by the symmetry of the two distinct crystallographic sites.

Figure 3 presents the Yb 4d core-level XAS of the Yb:S-FAP crystals and model compounds. The spectra have been normalized to the same edge-jump.[8] Note the lower energy separation and edge shift in the spectrum for the crystal with the anomalous absorption, thus indicating differences in the chemical environment of the Yb ion and associated changes in crystal field splitting. Also note that the pre-edge features (separated by 4 eV) are only present in the spectrum of the clean crystal. The enhancement of these features occurs when valence electrons associated with oxygen bonding contribute and thus are probably due to Yb^{3+}-O^{2-} complexes. The absence of these features and the edge shift in the spectrum for the Yb:S-FAP crystal exhibiting the anomalous absorption would seem to indicate incomplete replacement of Sr^{2+}-F^- by Yb^{3+}-O^{2-} at site II, and possibly mixed Yb^{2+}, Yb^{3+} valency.

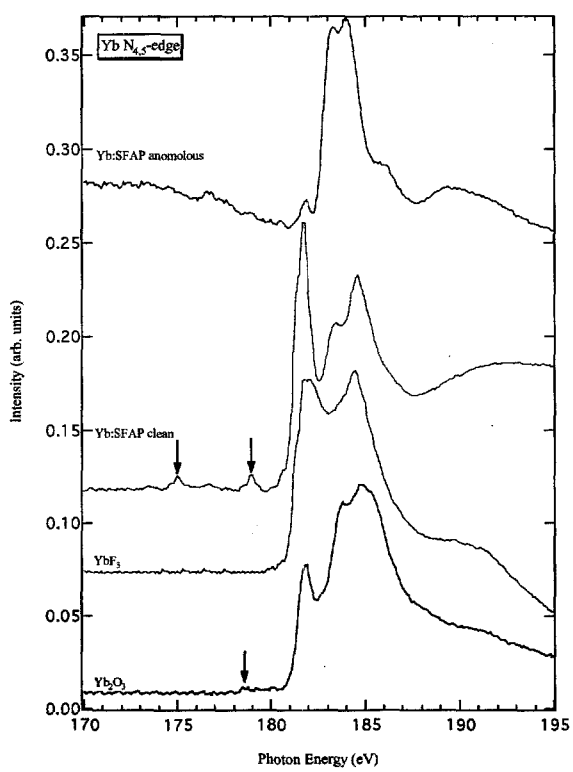

Figure 3. Yb $N_{4,5}$-edge photoabsorption spectra for the Yb:S-FAP crystals and Yb model compounds.

The overlapping Sr $M_{4,5}$-edge and P $L_{2,3}$-edge photoabsorption spectra for the Yb:S-FAP crystals and the $SrHPO_4$ model compound are shown in Figure 4. The weak dipole allowed Sr 3d → 4p transition has a lower energy than the P 2p → 3d transition. The spectrum for the $SrHPO_4$ represents the standard for Sr-O and $-PO_4$ bonding. Comparing the spectrum for the clean Yb:S-FAP crystal indicates similar Sr-O and $-PO_4$ bonding, however the anomalous crystal has a much more intense Sr $M_{4,5}$-edge signal.

Figure 5 presents the O K-edge photoabsorption spectra for the Yb:S-FAP crystals and the oxide model compounds. Again we see distinct similarities between the spectrum for $SrHPO_4$ and the Yb:S-FAP crystals. The presence of the π^* feature at ~530 eV indicates residual carbonaceous contamination. The major peak centered at 537 eV is

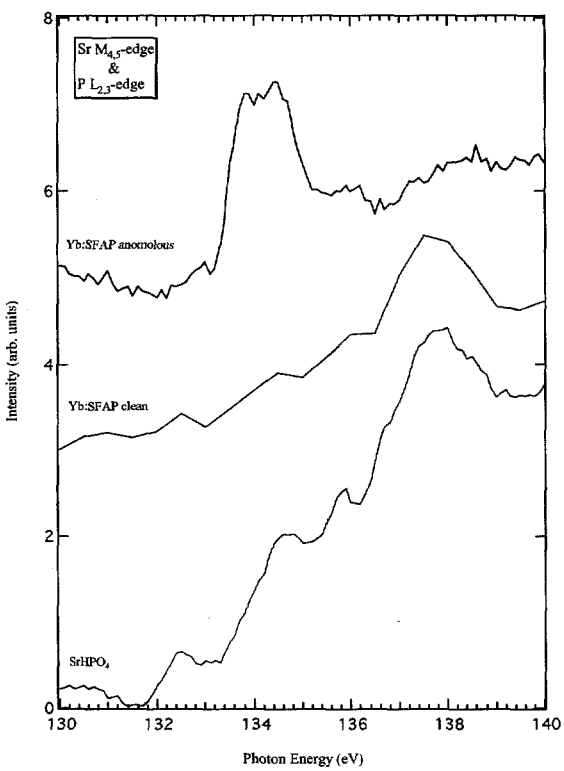

Figure 4. Sr $M_{4,5}$-edge and P $L_{2,3}$-edge photoabsorption spectra for the Yb:S-FAP crystals and Sr model compounds.

assigned to a transition from the O 1s core level to an unoccupied σ^* orbitals of the O-Sr and O–P bonds. A higher energy feature at ~543.6 eV is clearly visible in the spectra for clean Yb:S-FAP crsytal and Yb_2O_3 model compound, and is thus assigned to the presence of Yb^{3+}-O^{2-} complexes. This shoulder has a reduced intensity in the spectrum for the anomalous Yb:S-FAP crystal possibly indicating incomplete replacement of Sr^{2+}-F^- by Yb^{3+}-O^{2-} at site II.

4. Conclusions

X-ray photoemission (XPS) and x-ray photoabsorption (XAS) spectroscopy were used to examine the electronic structure of ytterbium doped strontium fluoroapatite (Yb:S-FAP) as a function of the crystallographic sites occupied by the Yb in the unit cell. Valence band photoemission results indicate that P

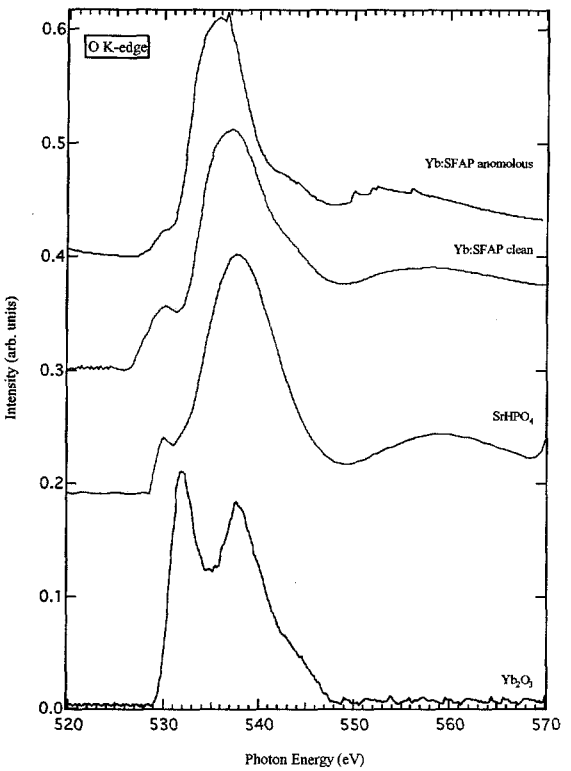

Figure 5. O K-edge photoabsorption spectra for the Yb:S-FAP crystals and the oxide model compounds.

and O p-states dominate the valence band electronic structure. XAS results show that both dipole allowed Yb 4d → 4f transitions and weakly allowed 5p → 4f transition are enhanced with the formation of Yb^{3+}-O^{2-} complexes. Yb $N_{4,5}$-edge results also indicate that the anomalous absorption may not only be due to Yb^{3+} at the high symmetry site I, but also to a mixed Yb^{2+}, Yb^{3+} valency. O K-edge results also indicate the presence of Yb^{3+}-O^{2-} complexes in the clean Yb:S-FAP.

Acknowledgements

We would like to thank the SSRL staff for their assistance during these experiments. This work was performed under the auspices of the U.S. Department of Energy by University of California, Lawrence Livermore National Laboratory under contract No. W-7405-ENG-48. This work was conducted at the Stanford Synchrotron Radiation Laboratory which is supported by the U.S. Department of Energy under contract No. DE-AC03-76SF00515.

References

1. Stephen A. Payne, Laura D. Deloach, Larry K. Smith, Wayne L. Kway, John B. Tassano, William F. Krupke, Bruce H. T. Chai and George Loutts, J. Appl. Phys. **76(l)**, 497 (1994).
2. R. F. Klevtsova, J. Structural Chem. **5**, 292 (1964).
3. St. Naray-Szabo, Z. Krist **75**, 387 (1930).
4. P.A.W. van der Heide, Q.D. Jiang, Y.S. Kim and J.W. Rabalais, Surf. Sci. **473**, 59 (2001).
5. J. Schmidt-May, F. Gerken, R. Nyholm and L.C. Davis, Phys. Rev. **B30(10)**, 5560 (1984).
6. L.I. Johansson, J.W. Allen, I. Lindau, M.H. Hecht, S.B.M. Hagström, Phys. Rev. **B21(4)**, 1408 (1980).
7. A. Kotani and S. Shin, Rev. Mod. Phys. **73**, 203 (2001).
8. J. Stöhr, *NEXAFS Spectroscopy* (Springer-Verlag, Berlin Heidelberg, 1992).

Large flattened mode optical fiber for high output energy pulsed fiber lasers

Jay W. Dawson, Raymond Beach, Igor Jovanovic, Benoit Wattellier, Zhi Liao, Steven Payne, C. P. J. Barty

National Ignition Facility, Lawrence Livermore National Laboratory, 7000 East Avenue, Livermore, CA 94550
Tel: 925-422-1617, FAX: 925-422-5928, e-mail: dawson17@llnl.gov

Abstract: An Yb^{3+}-doped optical fiber with a refractive index profile that distributes the intensity of light uniformly across the core of the fiber has been designed. A >2X decrease in stimulated Raman scattering was measured.
©2003 Optical Society of America
OCIS Codes: (060.2320) Fiber optics amplifiers and oscillators; (140.3510) Lasers, fiber

Femtosecond, chirped-pulse, fiber lasers with pulse energies greater than 1mJ have been demonstrated [1]. This output power was limited by the onset of stimulated Raman scattering. A common approach for scaling the output power and pulse energy of these fiber lasers is to increase the core size of the fiber and selectively excite only the fundamental mode [2]. The core size to which the fiber can be scaled before output beam quality begins to degrade is around 30-50μm. In this paper we pursue an alternative and complimentary approach which is to reduce the intensity of light propagating in the core by distributing it more evenly across the core area via careful design of the refractive index profile [3].

In figure 1, we show one such refractive index profile for creating a flat-topped fiber mode on the left hand side. On the right hand side of figure 1, we show the intensity distribution of a large flattened mode fiber design (LFM) and a standard step index profile fiber normalized such that the total power contained in the two modes is the same. (i.e. The two intensity distributions contain the same total power after the integration over the full cross sectional area is performed.) We see the LFM design decreases the peak intensity on axis by a factor of 2.46, which should lead to a significant decrease in the amount of stimulated Raman scattering for a given pulse energy, while not compromising the power handling capability.

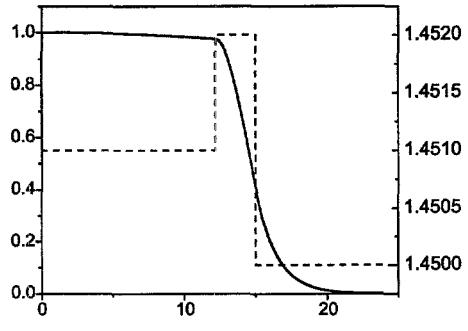

Figure 1: Left: refractive index profile and preferred mode of LFM fiber. Right: comparison of the intensity profiles of a step index fiber and an LFM fiber with the same total power.

We purchased a 30-μm core, 0.06-NA, step-index, control fiber (Nufern) with a 400μm hexagonal cladding with a low index polymer coating (pump clad NA=0.37). The core was doped with Yb^{3+} such that there was an effective core absorption of 120dB/m at 977nm. We also purchased a nearly identical fiber from Nufern, but with the raised ring that gives the LFM fiber its distinctive index profile. The inner core diameter of the LFM was 25.3μm and the outer core diameter was about 30-μm FWHM, the effective NA

of the structure was approximately 0.06. The outer cladding and Yb^{3+} doping were the same as for the control fiber.

We then coupled 1.2-ns, 1075-nm, 10-Hz stretched mode-locked laser pulses into 9.1m of the control fiber and 8.3m of the LFM fiber. The input energy coupled into the fiber cores was 15μJ. 977nm pump light from a 10W diode laser array was counter propagated through the fiber to pump the Yb^{3+} ions. The diode light was pulsed at 10Hz for 1ms timed to precede the arrival of the signal light. In figure 2 below, we show the amplified output energy of the two fibers on the left hand side measured with a Molectron energy meter. As expected they produce roughly the same output energy as a function of pump diode current. In right hand side however, we plot the percentage of the signal power contained in the first stokes spectra as measured with an Ocean Optics fiber coupled spectrometer. Here we see, the LFM fiber shows significantly less Raman energy build up as a function of diode current than the control fiber. This is in agreement with what we expected from the design. In addition, we achieved greater than 0.6mJ output pulses from the LFM amplifier with less than 5% of the energy in the Raman spectral band by utilizing pulses stretched to 3ns. With straightforward scaling of Yb^{3+} doping concentration to reduce the amplifier length, increasing the core size to 50μm and increasing the pump energy an optimized design could yield output pulses with greater than 10mJ of energy and virtually no degradation due to stimulated Raman scattering.

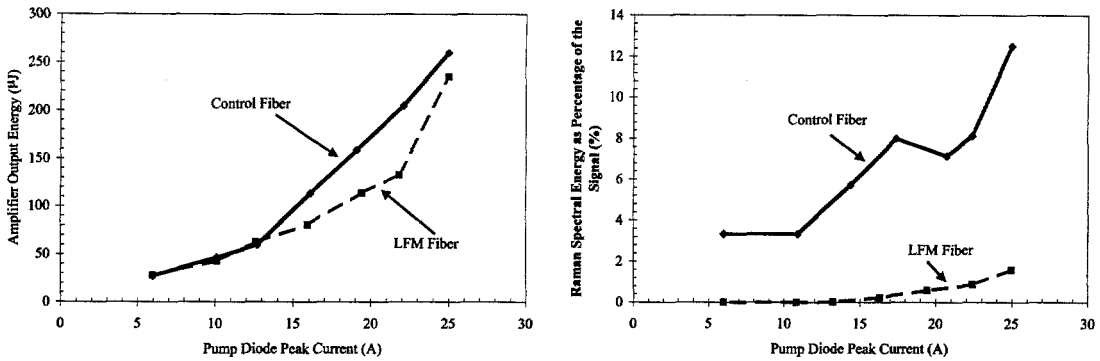

Fig. 2: Left: output energy vs. pump diode current for the step index control fiber and the LFM fiber. Right: Raman peak spectral power as a function of the pump diode current for the same fibers.

This work was performed under the auspices of the U.S. Department of Energy by the University of California, Lawrence Livermore National Laboratory under Contract No. W-7405-Eng-48.

1) A. Galvanauskas, Z. Sartania, M. Bischoff, "Millijoule femtosecond all-fiber system", CLEO 2001, Baltimore, Md., paper CMA1
2) M.E. Fermann, "Single-mode excitation of multimode fibers with ultrashort pulses", Optics Letters, vol. 23, pp. 52, (1998)
3) A. K. Ghatak, I. C. Goyal, R. Jindal, "Design of waveguide refractive index profile to obtain flat modal field" SPIE Proceedings vol. 3666, pp. 40 (1998)

High Power 938nm Cladding Pumped Fiber Laser

Jay W. Dawson, Alex Drobshoff, Zhi Liao, Raymond J. Beach, Deanna M. Pennington, Stephen A. Payne
Lawrence Livermore National Laboratory, PO Box 808, Livermore, CA 94551
Phone: (925) 422-1617, FAX: (925) 422-5928, email: dawson17@llnl.gov

Luke Taylor, Wolfgang Hackenberg, Domenico Bonaccini
European Southern Observatory, Karlschwartzchild Strasse 2, 85748 Garching-bei-Muenchen

ABSTRACT

We have developed a Nd:doped cladding pumped fiber amplifier, which operates at 938nm with greater than 2W of output power. The core co-dopants were specifically chosen to enhance emission at 938nm. The fiber was liquid nitrogen cooled in order to achieve four-level laser operation on a laser transition that is normally three level at room temperature, thus permitting efficient cladding pumping of the amplifier. Wavelength selective attenuation was induced by bending the fiber around a mandrel, which permitted near complete suppression of amplified spontaneous emission at 1088nm. We are presently seeking to scale the output of this laser to 10W. We will discuss the fiber and laser design issues involved in scaling the laser to the 10W power level and present our most recent results.

1. INTRODUCTION

It has long been a challenge to achieve high power laser or amplifier operation of the $^4F_{3/2}$-$^4I_{9/2}$ transition of neodymium based laser media because of the 3-level nature of the transition and competition from the $^4F_{3/2}$-$^4I_{11/2}$ 4-level transition. Multi-watt operation on this transition has recently been achieved in crystal hosts such as YAG and YVO_4 [1]. However, laser or amplifier operation of the $^4F_{3/2}$-$^4I_{9/2}$ transition in glass hosts or optical fiber hosts to date has been limited to power ranges on the order of 100mW [2]. Silica glass hosts offer many advantages over their crystal counterparts, such as broader tuning ranges (900nm to 950nm) and for specific material composition, more favorable branching ratios for the $^4F_{3/2}$-$^4I_{9/2}$ transition [2]. Optical fiber hosts also offer the potential of using wavelength dependent bend induced losses to create a distributed filter to suppress laser action on the $^4F_{3/2}$-$^4I_{11/2}$ transition [3]. We are developing this amplifier as a 938nm source for sum-frequency mixing with a 1583nm high power erbium fiber laser to achieve high power 589nm light for guide star applications for astronomy [4].

2. 938nm CHALLENGES

There are a number of challenges to be overcome in order to get high power operation of the $^4F_{3/2}$-$^4I_{9/2}$ transition in an optical fiber. Because the desired 3-level transition is competing with an undesired 4-level transition, pumping to transparency guarantees large gain in an undesired wavelength band. Further, cladding pumping, the standard method for achieving high output power from a fiber laser or amplifier is not intrinsically compatible with 3-level laser systems as the pump and signal beam do not have high overlap and thus it is difficult to achieve high inversion in the laser media. However, the materials with the best branching ratios (nearly pure fused silica) are also the ones into which neodymium is the least soluble. This increases the attractiveness for an optical fiber host due to the potential of long interaction lengths, which are preferred for low doping concentrations.

Of particular concern is the neodymium concentration level at which significant quenching occurs. We obtained several samples of standard neodymium-doped optical fiber with varying concentrations for characterization for use in our amplifier. The samples were co-doped only with germanium to maximize long wavelength emission at 938nm [2]. We were also able to obtain samples of the preforms from which these fibers were drawn. Using the preform samples we measured the upper state lifetime of the laser transition. In all samples, we found there was a 0.4-0.8μs component (due to quenched sites) and a 470μs component (due to active sites). By comparing the relative strengths of these

components we were able to estimate the percentage of ions that were quenched or not likely to contribute to the gain. A second measurement of small signal absorption at 905nm and small signal gain at 905nm with nearly complete inversion (achieved by pumping a short length of fiber in the core with 650mW of 830nm pump light from a Ti:Sapphire laser) was made on the optical fibers. This measurement followed the techniques used by Giles to characterize rare earth doped optical fibers for modeling [5] and permitted an independent estimate of the number of quenched sites. The second measurement also permitted us to understand the gain and absorption spectrum of our fiber samples. The results of the quenching measurements are plotted in figure 1 below.

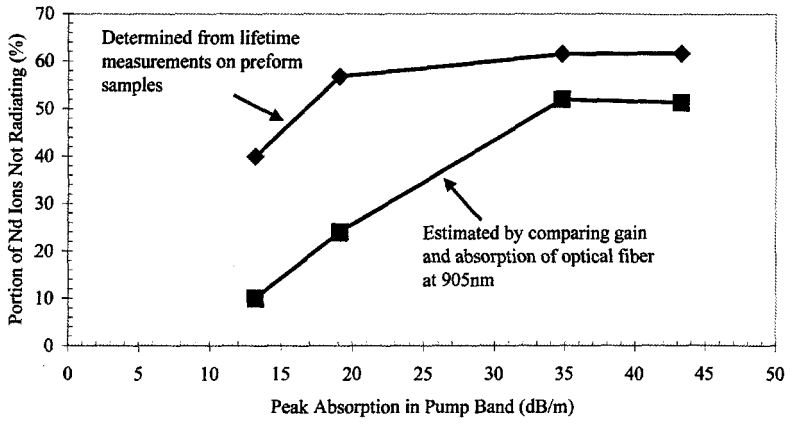

Figure 1: Estimate of Nd ion quenching in germanium codoped silica fiber samples as a function of peak absorption in the pump band.

In figure 1, one observes the optical fiber and the preform from which it came have the same general trend with respect to quenching vs. concentration. However, it appears, the optical fiber as drawn shows significantly better performance than would be expected from the preform measurement alone. We speculate that the effect of quenching during the fiber draw improves the distribution of neodymium ions in the lattice and thus reduces the number of quenched neodymium ions.

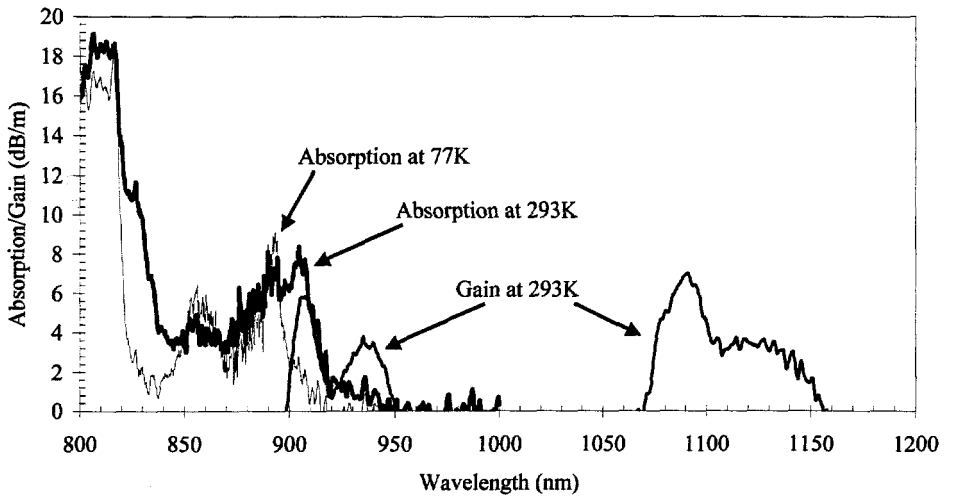

Figure 2: Absorption of a Nd-doped fiber with quenching at room temperature and 77K and gain at room temperature.

In figure 2, typical absorption and gain spectra for the fibers are plotted. Data below 800nm has been suppressed. Because, the fiber core is not single mode below 800nm there were unacceptably high errors in the data in that region. We have also measured the fiber absorption at 77K. The absorption in the 920nm-950nm region, of particular interest to our application, is virtually eliminated at 77K. Thus, the transition is effectively a 4-level transition when the fiber is cooled, making it much more compatible with cladding pumping. Liquid nitrogen cooling of a bulk laser gain media, would be difficult to achieve in a practical laser application. However, the fiber amplifier is much better suited to immersion in liquid nitrogen as it can be coiled and bent easily. This provides for a simple and robust means to isolate the remaining amplifier components such as the coupling optics for the signal and pump beams from the 77K temperatures. A fluorinated glass pump cladding ensures the guiding properties of the optical fiber would operate essentially the same at 77K as at 293K.

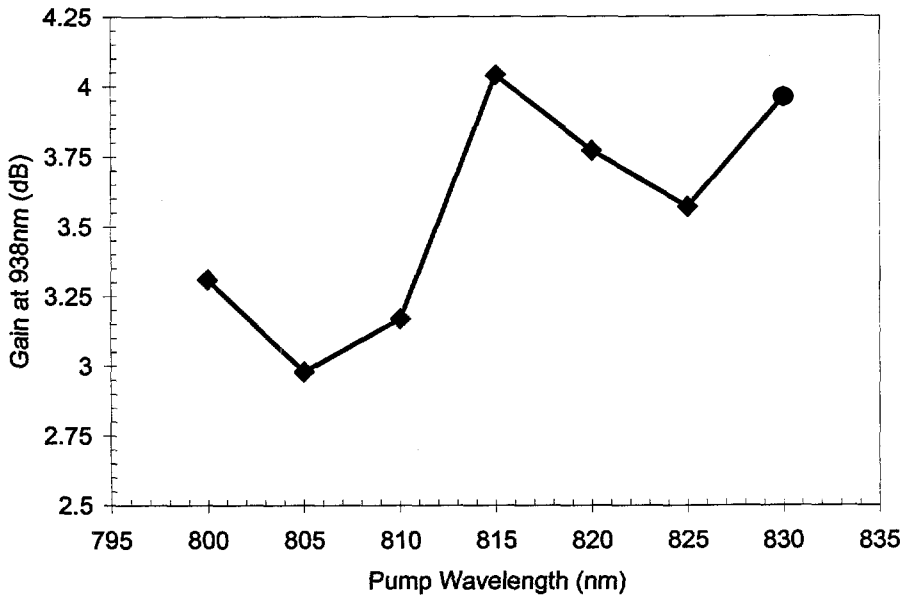

Figure 3: Gain at 938nm vs. pump wavelength for constant absorbed pump power.

We measured gain vs. pump wavelength for a short (~1m) piece of Nd fiber that was core pumped at room temperature (figure 3). Intriguingly, at a pump wavelength around 815nm the gain at 938nm suddenly jumps upwards. This is consistent with changes in the absorption spectra as a function of concentration, which show a distinct peak at 816nm emerging as the Nd concentration is lowered. This suggests that the unquenched Nd ions have a spectra that is different and distinct from the quenched Nd ions. This implies that while it may or may not be practical to reduce the Nd concentration sufficiently to completely eliminate quenching, it may be possible to mitigate the impact of quenching via careful pump wavelength selection.

As mentioned above, the 1088nm transition is a 4-level laser transition and the 938nm transition is 3-level. These transitions are competitive, with the 938nm transition having an obvious disadvantage due to its 3-level nature. For cladding pumping, this disadvantage is exaggerated. For our case, we constructed a cladding pumped fiber with a 0.22NA, 200μm pump clad and a singlemode 7.5μm core with absorption and gain spectra as detailed in figure 2 above. A 200m piece of this fiber would absorb most of the light in the pump cladding. If we use our measured gain and absorption spectra at 77K, 195K (this was not shown in figure 2) and 293K and an effective inversion approximation, we can estimate the gain at 1088nm for a constant 16dB gain at 938nm as a function of temperature. This estimation is detailed in table 1 below.

	77K	195K	293K
Average Inversion	0.0229	0.1006	0.212
938nm Gain (dB)	16.03	16.02429	16.016
1088nm Gain (dB)	31.602	138.828	292.56

Table 1: Theoretical estimate of gain at 938nm and 1088nm vs. temperature.

We see that at room temperature, our cladding pumped amplifier has little to no hope of being effective at 938nm, due to extremely high gain at 1088nm. At 195K (dry ice sublimation), the situation is improved, but still extremely bad. At 77K, the 1088nm gain is still high, but there is some hope of introducing compensating losses at 1088nm that will permit preferential operation at 938nm. We also note that operation at 77K "freezes out" any quenched ions that may have absorption at 938nm.

The issue of gain competition from the 1088nm transition remains, however. Most optical fiber amplifiers are coiled, by choosing the appropriate bend radius for the coiling we can create high loss at 1088nm with minimal losses at the 938nm signal wavelength. To understand this better, we measured the bend losses of the fiber at 938nm and 980nm and compared them to losses expected from theory [6]. We also used the theoretical expressions to what the losses would be at 1088nm. These results are shown in figure 4 below.

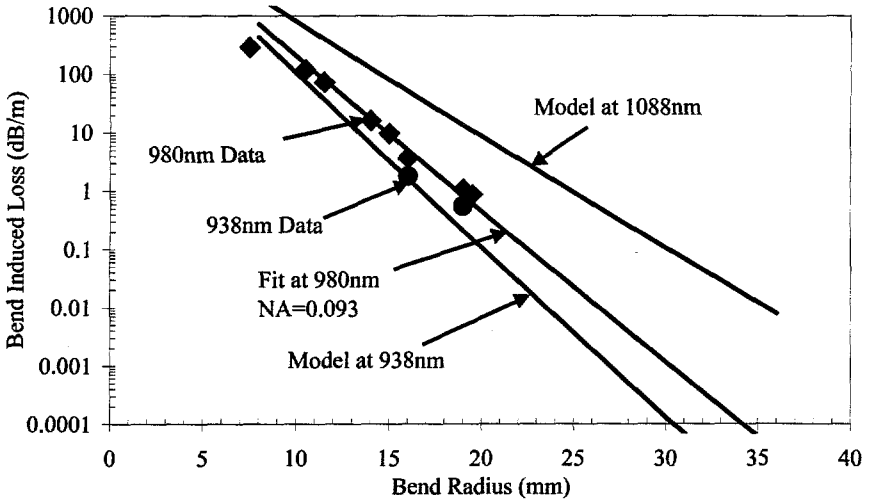

Figure 4: Measured bend loss (dB/m) as a function of bend radius (mm) for 980nm and 938nm (points). A bend loss model has been fit to the data (lines). The fiber numerical aperture was used as a fit parameter and a value of 0.0932 was found to provide the best fit. An independent measurement of the numerical aperture from the manufacturer found a value of 0.09.

For ~24mm bend radius, it appears from the plot above that we could generate >200dB of loss at 1088nm with less than 2dB of induced loss at 938nm for a 200m long fiber. What is not shown however, is that the pump cladding we employed also experienced losses upon coiling, which limited the effective bend radius we could use for coiling the entire fiber to >35mm. To overcome this issue, we chose to induce bend loss at one end of the amplifier and pump from the other end. We close this section by noting that future work will explore fiber designs that permit 938nm cladding pumped fiber amplifiers to operate at room temperature.

3. SYSTEM DEMONSTRATIONS

Utilizing the knowledge from our investigations of the Nd doped optical fiber, we have constructed a master oscillator, power amplifier system configuration using cladding pumped Nd doped fiber amplifiers. Our amplifiers were cooled to

77K and had lumped bend losses at the input to suppress 1088nm parasitics. A schematic of the system is shown below in figure 5.

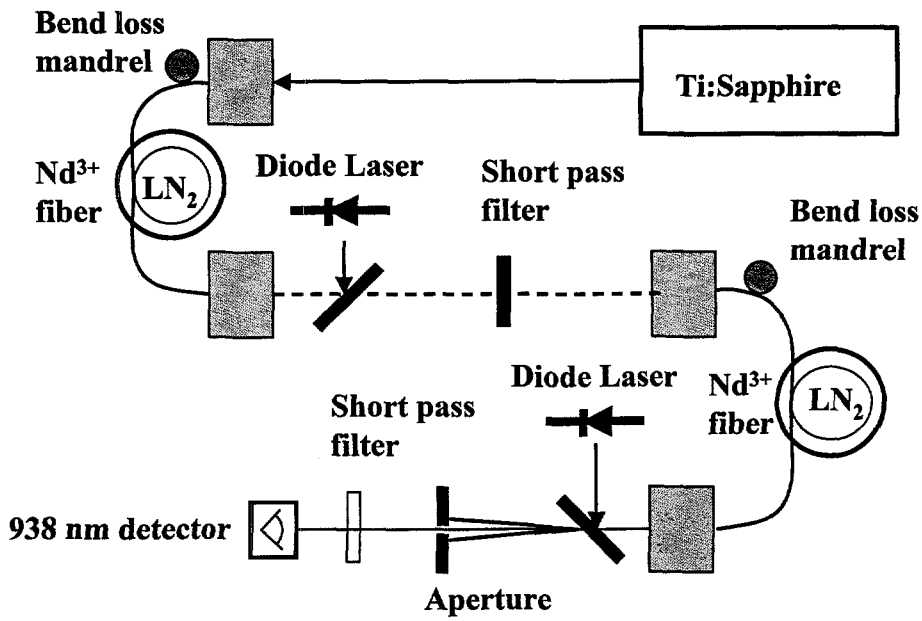

Figure 5: Schematic of the 938nm cladding pumped optical fiber system.

In figure 5 above, a two-stage amplifier configuration was employed to maximize the output power of the amplifier. The same type of fiber was used in each stage. The fiber was 100m long in the first stage and 200m long in the second stage. The core of the fiber employed had loss and gain characteristics as measured and reported in figure 2 and bend loss characteristics as reported in figure 4. The active fiber had a fluorinated outer region providing a 0.22NA, 200μm diameter pump cladding. The core had a neodymium doped germano-silicate material composition and was 7.5μm in diameter with an NA of 0.09. A peak small signal pump wavelength absorption of 19dB/m at 810nm was measured for light propagating in the core of the fiber. A short pass filter was employed between stages of the amplifier to eliminate amplification of 1088nm ASE from the first stage in the second stage. The 938nm signal power and 1088nm parasitic powers were determined by measuring the output power of the fiber at the power meter with and without the short pass filter and employing knowledge of the loss of the filter at 938nm and 1088nm. The bend mandrels employed were 19mm in radius and 10turns of fiber were wound onto each mandrel. 25W 808nm LIMO laser diodes were employed for the pumps. In the case of the 100m long amplifier, there was a significant amount of transmitted pump light. A Ti:Sapphire laser was used as the master oscillator. The Ti:Sapphire had an output power of around 500mW, good beam quality and a large effective linewidth, such that stimulated Brillioun scattering was not a system issue, despite long fiber lengths and high optical powers. An aperture at the output prevented cladding light from the fiber from striking the power meter. The output power from the second stage amplifier at 938nm and 1088nm is shown in figure 6 below.

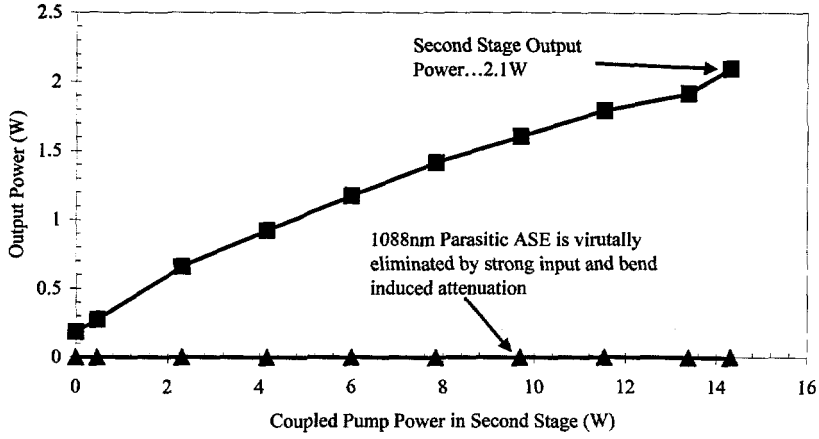

Figure 6: Output of 938nm amplifier system.

We note above that the total coupled pump power was only about 14W. There were significant losses in the dichroic mirrors we employed to combine the pump and signal wavelengths and the coupling optics were also not optimized. An additional 10W of coupled pump power would have brought the output power up to closer to 3W! We also note that the amount of observed parasitic power at 1088nm was minimal on the scale of the output power of the 938nm light. For configurations in which no bend loss was employed, we observed 1088nm output power greater than that observed at 938nm.

As discussed in the introduction, our goal in developing the 938nm laser system is to sum-frequency mix it with a high power 1583nm lasers system in order to generate 589nm light for laser guidestar applications. We have done so, using two fiber lasers as shown in the schematic in figure 7 below.

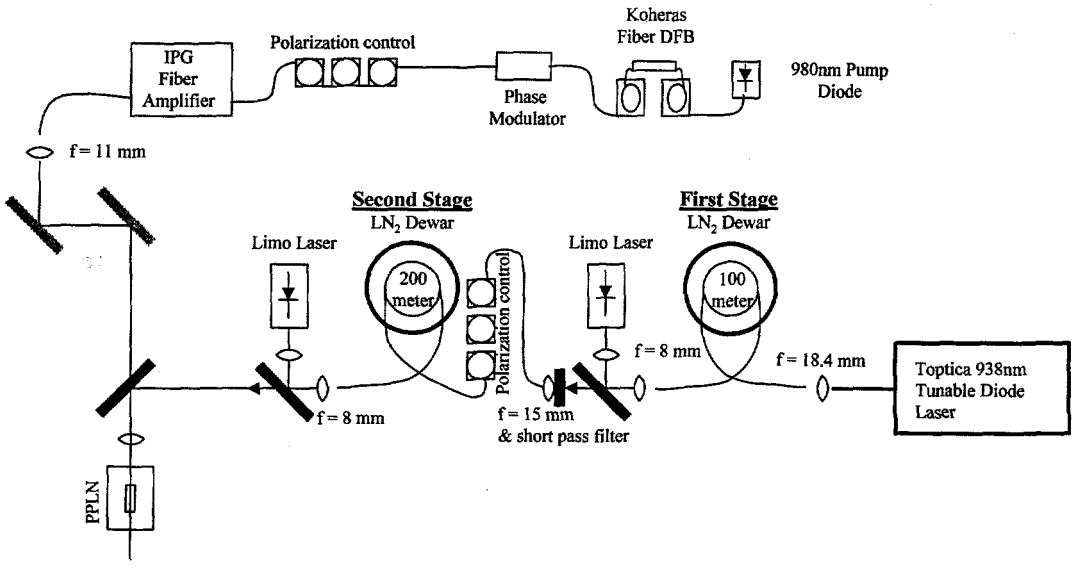

Figure 7: Schematic of the 589nm fiber laser source.

In figure 7 above, our 1583nm laser system was built entirely of commercially available components and consisted of a Koheras fiber DFB laser master oscillator with an output power at 1583nm of about 3mW. This light was passed through a phase modulator, which increased the bandwidth to about 100MHz. The light then went into a 10W IPG L-Band erbium doped fiber amplifier. The output power of this system was measured to be 10W at 1583nm when the amplifier was turned fully on. For the sum frequency mixing experiments, however, the amplifier output was limited to about 2W. The 938nm system configuration was essentially the same as that described in figure 5 above. The exception being that the Ti: Sapphire laser was replaced with a Toptica 938nm external cavity laser diode, with an internal tapered semi-condutor laser that could put out up to 400mW of 938nm light with a noise broadened bandwidth of about 500MHz. Due to the reduced 938nm input power and poorer beam quality resulting in poorer fiber coupling, the revised system had a 938nm output power less than 1W for the sum-frequency mixing experiment. Nevertheless, when the 938nm light was combined in the PPLN (5cm long crystal, 9.45μm period) with the 1583nm light, we observed a strong 589nm output. This is shown in figure 8 below, where we have plotted 589nm output vs. PPLN crystal temperature.

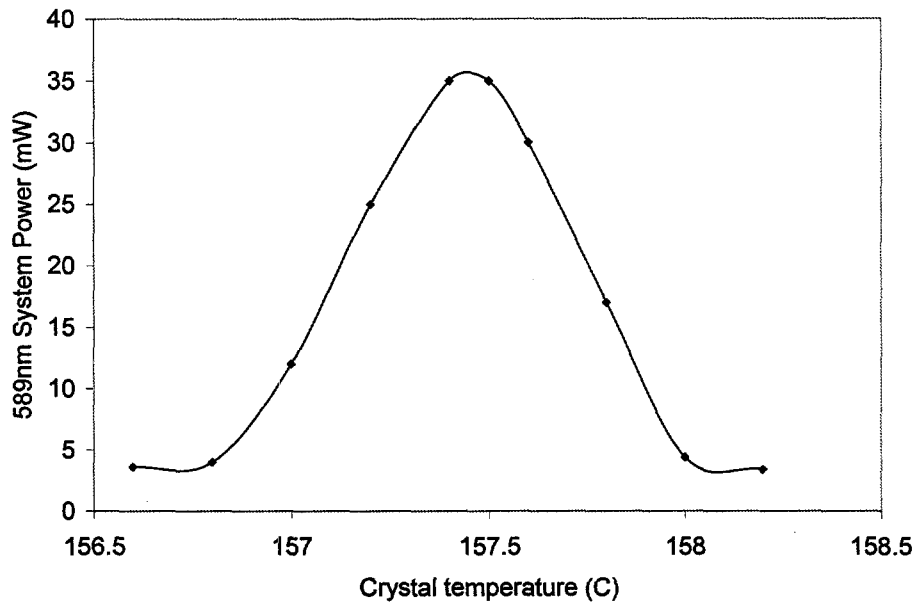

Figure 8: 589nm output power from fiber laser sum-frequency mixing vs. PPLN crystal temperature. Input power was 2W at 1583nm and 0.7W at 938nm.

We are working to improve the performance of the 938nm system using the Toptica laser diode, which should permit much higher 589nm output powers.

4. CONCLUSIONS

While a good result of 2.1W of output power at 938nm has been obtained, much can be done to improve this result in future design iterations. In particular, understanding of the quenching of neodymium sites was not complete until after the cladding pumped fiber had been obtained. A fiber with small signal absorption of 10dB/m at 810nm would suffer much less from pump losses due to quenching according to the data presented in figure 1. Furthermore, the amplifier fiber in question was much longer than desired resulting in high passive losses due to high scattering out of the fiber core, which is typical in rare earth doped optical fibers. We are presently redesigning our amplifier fiber to minimize

quenching and passive losses, which should improve both the amplifier output power and efficiency and reduce its length and corresponding susceptibility to stimulated Brillouin scattering. We are also seeking to eliminate the bend induced loss in the pump cladding, which will permit smaller bend radii to be employed across the entire amplifier and thus increase the amount of loss at 1088nm, while minimizing the loss at 938nm. We believe the combination of these re-design efforts will result in a system capable of operation at 10W of output power at room temperature.

This work was performed under the auspices of the U.S. Department of Energy by the University of California, Lawrence Livermore National Laboratory under contract No. W-7405-Eng-48, and has been supported in part by the National Science Foundation Science and Technology Center for Adaptive Optics, managed by the University of California at Santa Cruz under cooperative agreement No. AST-9876783.

REFERENCES

1. P. Zeller and P. Peuser, "Efficient, multiwatt, continuous-wave laser operation on the $^4F_{3/2}$-$^4I_{9/2}$ transitions of Nd:YVO_4 and Nd:YAG," Optics Letters **25**, 34-36 (2000)
2. P. Dragic and G. Papen, "Efficient amplification using the $^4F_{3/2}$-$^4I_{9/2}$ transition in Nd-doped silica fiber," IEEE Phot. Tech. Lett. 11, 1593-1595 (1999)
3. C. Swift and A. Harris, "Bend loss in neodymium-doped fiber lasers," Journal of Lightwave Tech. 16, 428-432
4. SPIE guidestar talk, Penningon et al.
5. C. Giles and E. Desurvire, "Modeling erbium-doped fiber amplifiers," Journal of Lightwave Tech. 9, 271-283
6. L.B. Jeunhomme, "Single-mode fiber optics: Principles and applications," 2nd edition, section 3.3.2 (Marcel Dekker, New York, NY 1990)

Phase-Locked Antiguided Multiple-Core Ribbon Fiber

Raymond J. Beach, Michael D. Feit, Scott C. Mitchell, Kurt P. Cutter, Stephen A. Payne, Richard W. Mead, Joseph S. Hayden, David Krashkevich, and David A. Alunni

***Abstract*—We report on the first experimental demonstration of a scalable fiber laser approach based on phase-locking multiple gain cores in an antiguided structure. A novel fabrication technology is used with soft glass components to construct the multiple core fiber used in our experiments. The waveguide region is rectangular in shape and comprised of a periodic sequence of gain and no-gain segments having nearly uniform refractive index. The rectangular waveguide is itself embedded in a lower refractive index cladding region. Experimental results confirm that our five-core Nd-doped glass prototype structure runs predominately in two spatial antiguided modes as predicted by our modeling.**

***Index Terms*—Clad pumping, fiber lasers, multicore fiber, phase locking, waveguides.**

I. Introduction

THE DEVELOPMENT of double-clad fiber has brought fiber lasers to the forefront of possible approaches for high beam quality, high average power laser sources [1]. Using a cladding-pumped geometry with a single-mode core, individual fibers have been demonstrated at greater than 100 W of average power [2]. These single-core results are irradiance limited by output facet damage and the onset of deleterious nonlinear optical interactions. Scaling to higher powers requires the area of the laser beam to grow. Two general approaches are actively being investigated for power scaling while preserving single spatial-mode output: 1) large mode area fibers in which the core area is a specially index-engineered waveguide structure [3], [4], and 2) multiple cores which are phase locked to give a single spatial-mode output beam. A number of different techniques have been investigated for phase locking multiple core structures such as evanescent coupling [5], diffractive coupling (Talbot plane methods) [6], [7], and 1-to-N-way phase-locking techniques [8]. With the evanescent technique, the field energy is localized on the gain cores, and nearest neighbor cores are coupled to each other via their evanescent (exponentially decaying) fields. This technique, originally used with multistripe diode lasers [9], has been described in several papers and recently used to phase lock an isometric configuration of seven gain cores in a cladding-pumped fiber [10].

Manuscript received August 28, 2002; revised January 3, 2003. This work was supported by the U.S. AFRL, Albuquerque, under Contract L-8958.1, and by the U.S. Department of Energy under Contract W-7405-ENG-48.

R. J. Beach, M. D. Feit, S. C. Mitchell, K. P. Cutter, and S. A. Payne are with the Lawrence Livermore National Laboratory, Livermore, CA 94551 USA (e-mail: beach2@llnl.gov).

R. W. Mead is with Collimated Holes, Inc., Campbell, CA 95008 USA.

J. S. Hayden, D. Krashkevich, and D. A. Alunni are with Schott Glass Technologies, Inc., Duryea, PA 18642 USA.

Digital Object Identifier 10.1109/LPT.2003.809943

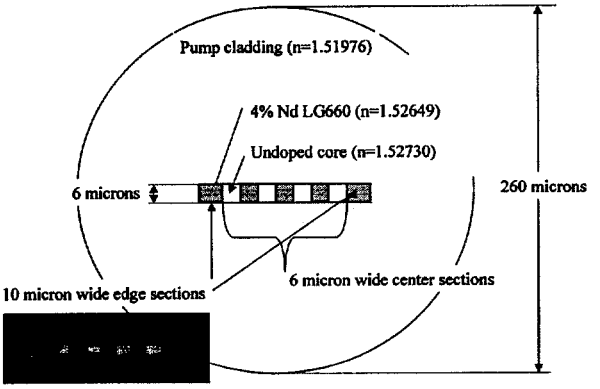

Fig. 1. Cross-sectional diagram of antiguided ribbon fiber structure showing the starting refractive indices of the bulk glass used to construct the fiber preform. Inset photograph shows the waveguide region of the fiber.

II. Experimental Demonstration

The main purpose of this letter is to report on what we believe is the first demonstration of antiguiding to phase lock multiple cores in a fiber structure. Because the eigenmode is delocalized across all gain cores in this scheme, all cores communicate with all other cores and we anticipate scalability will be more favorable than with evanescently coupled structures. Our choice of an antiguided structure is based on an analysis we recently presented on a scalable ribbon fiber concept [11], where we showed that a constant index waveguide region with a periodically modulated gain profile was preferred for ensuring single spatial-mode operation. Single-mode operation is desired so that a static phase corrector alone, placed in the near field of the ribbon laser's output, can optimize the phase across the aperture and result in a high Strehl ratio beam [11]. Fig. 1 depicts a cross-sectional view of the prototype Nd-doped ribbon fiber that we used in our experiments. This structure was fabricated by constructing a fiber preform using bulk LG-660 undoped, and 4% Nd-doped Silicate Schott glasses. The starting refractive index values of the various component glasses were, 1.519 76 for the pump cladding, 1.526 49 for the doped waveguide glass, and 1.527 30 for the undoped waveguide glass. To construct the preform, square and rectangular parallelepiped waveguide component pieces were fabricated and then placed in a cut-out section of the outer cylindrical cladding that was split in a clamshell configuration. The entire preform was then pieced together and held in place by inserting it in a hollow glass containment tube on which a vacuum was pulled during drawing. The preform was first drawn to cane having an outer diameter of 5 mm to facilitate the removal of the outside containment tube, and then the cane

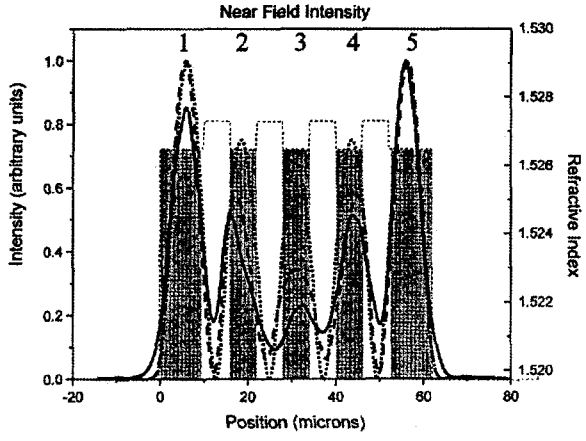

Fig. 2. Near-field measured and model-predicted irradiance profiles. The dotted line is our model-predicted Mode 5. The dashed line is our model-predicted incoherent superposition of Mode 5 and 6 together. The solid line is the experimentally measured near-field lineout. The shaded areas denote those regions doped with Nd^{3+}. The scale on the right references the refractive index profile, shown as a light dotted line.

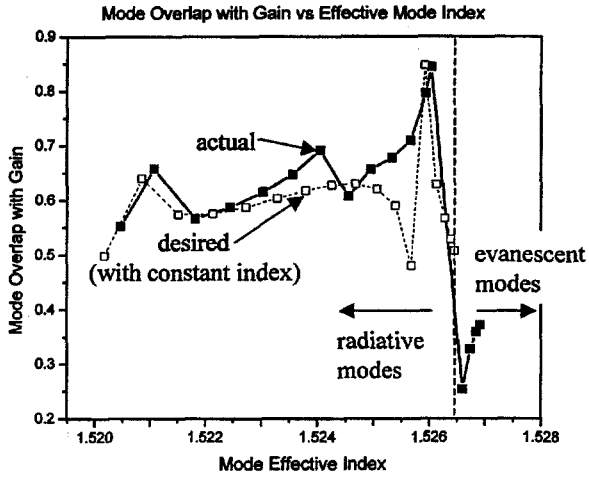

Fig. 3. The dark line is a plot of mode overlap with the gain-loaded portion of the fiber against the effective index value for the various modes supported by the waveguide structure shown in Fig. 1. The dots represent the individual modes. The dashed line is the calculated mode overlap for a waveguide structure similar to the one shown in Fig. 1, but optimized with constant index across the waveguide region.

was drawn to fiber having a final outer diameter of 260 μm. No polymer coating was applied to the fiber.

The spatial-mode structure of the ribbon fiber's output beam was characterized using an end-pumping geometry in which a fiber coupled 808-nm diode array served as the pump source. The output of the diode was imaged into the 260-μm diameter outer cladding of a 1-m-long piece of the fiber having both of its ends polished normal to the fiber axis and uncoated. The pump, which single-passed the fiber, was transmitted through a dichroic mirror contacting the fiber and having high transmission at 808 nm and high reflectivity at 1064 nm. The absorption coefficient of the Nd-doped cores is 5.6/cm at the 808-nm pump wavelength. The 1-m length of fiber was straight and supported by a V-groove machined in a piece of aluminum for the characterizations reported here. Fig. 2 shows a horizontal lineout of the near-field intensity distribution of the fiber superimposed on the index structure of the waveguide. Although this near-field intensity profile was found to be very repeatable, we did observe that arbitrarily bending or otherwise placing stress on the fiber could alter it significantly. Also shown in Fig. 2 are our model-predicted irradiance profiles calculated using the formalism presented in [11] and discussed below. For the index structure shown in Fig. 2, we have also calculated the entire mode spectrum supported by the waveguide as shown in Fig. 3, where mode overlap with the gain region is plotted against mode effective index value. In Fig. 3, radiative modes are defined as those with a harmonic dependence everywhere in the waveguide region, and evanescent modes as those with a harmonic dependence in some areas of the waveguide and an exponential dependence in others, depending on whether the mode index is below or above the local refractive index of the structure, respectively.

To fit our model-predicted modes to the measured near-field irradiance profile we have considered the highest gain mode alone (fifth from the right in Fig. 3), as well as an equal intensity incoherent superposition of the two highest gain modes together (fifth and sixth from the right in Fig. 3). These model-predicted near-field profiles are overlaid with the experimental data in Fig. 2, demonstrating that the two mode superposition replicates the prominent features of the experimental profile better than does the single mode alone. This is not surprising as the fifth and sixth modes are the highest gain modes supported by the structure, but are not well discriminated from each other in their gain overlap values of 0.84 and 0.80, respectively. We believe the remaining disagreement between the experimental results and the model-calculated near-field irradiance profiles can be ascribed to a lack of detailed knowledge of the true refractive index profile of the fiber. The specific refractive index values of the various glass components used in the fiber are known to depend in detail on the cooling rate of the glass during redraw [12], as well as the stress induced in the structure during fabrication, both being uncharacteristic for the glasses used here. While simultaneous operation in two spatial modes is evident here, we note that if a constant index throughout the waveguide region were to be obtained, then the gain discrimination between the most preferred and next most preferred mode would be greatly increased. This is shown in Fig. 3 by the dashed line and open dots, plotting mode overlap against mode effective index for the case of a constant refractive index value of 1.526 49 across the entire waveguide region. In this optimized case, the gain overlap of the two highest gain modes is calculated to be 0.85 and 0.64, substantially better than the mode discrimination in our present fiber.

Fig. 4 shows a horizontal lineout of the experimental far-field irradiance profile of the fiber. Also shown in Fig. 4 is a far-field profile corresponding to just the first and fifth near-field lobes as defined in Fig. 2. In this case, an appropriate mask in the near field blocks all but the selected near-field lobes. The far-field profiles were generated by directly focusing the appropriately masked near-field output of the ribbon fiber onto a camera charged-coupled device and digitizing the images, shown as inset photographs in Fig. 4. Also shown in Fig. 4 are the model-

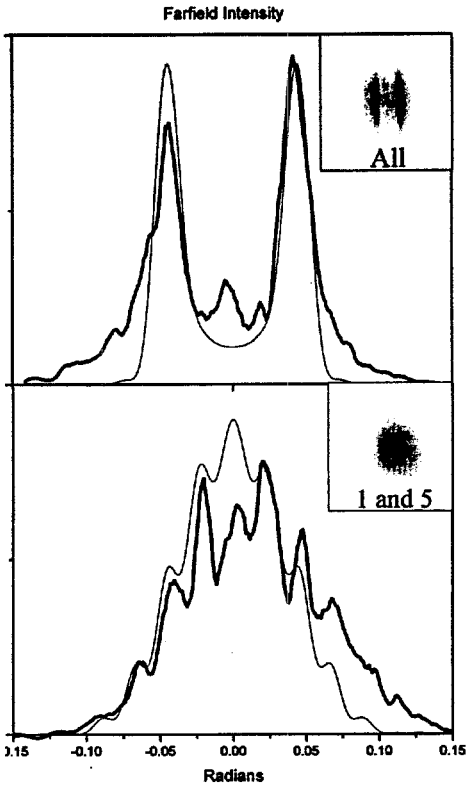

Fig. 4. Darker lines correspond to line outs of the experimentally measured far-field irradiance profiles shown in the inset pictures, and the lighter lines correspond to the model calculated profiles as described in the text. Top figure is the far field from the entire aperture. Bottom figure is the far field from near-field Lobes 1 and 5 only.

calculated far-field profiles generated by propagating the appropriately masked model-calculated near field. Evident in Fig. 4 is agreement between the principal features of the measured and modeled far-field profiles indicating there is coherence across the lasing aperture of the ribbon fiber. Contributing to the remaining disagreement between model and experiment is our limited knowledge of the detailed refractive index values of the various waveguide components as discussed above, as well as a possible admixture of modes beyond the two used in our modeling due to mode-to-mode scattering [13]. Finally, we characterized the vertical axis (narrow dimension) emission from the ribbon fiber, measuring the M^2 parameter [14] in this dimension to be 2.4, in reasonable agreement with our model prediction of two captured modes in this dimension.

We have also used a 15-cm section of the ribbon fiber as the gain element in a laser oscillator to assess the energetic performance of our antiguided structure, primarily to ascertain the passive loss of the structure under lasing conditions. A 4% reflective output coupling was investigated using the uncoated end of the fiber as the output coupler, and then 10%, 20%, and 30% reflective output couplings were investigated by contacting various flat mirrors to the output end of the fiber. For 4% reflectivity, the measured slope efficiency was 0.24 W/W referenced to the absorbed pump power, and the peak optical–optical efficiency was 0.25 W/W at an absorbed pump power of 3.2 W. System performance using the 10%, 20%, and 30% reflective output couplers was almost constant with a slope efficiency of 0.32 W/W and a peak optical–optical efficiency of 0.25 W/W. Setting the passive loss of the fiber at 0.005/cm, we could reproduce this energetics behavior using a model based on a previously published analysis of end-pumped laser systems [15]. A 1-ms pump pulse was used in these characterizations, and the output radiation from the fiber was observed to be unpolarized with a spectrum extending from 1059 to 1069 nm.

III. Conclusion

We have reported what we believe to be the first demonstration of antiguiding as a mechanism to phase lock a multiple core fiber laser. This demonstration was made using a five-core ribbon fiber structure that was fabricated using a novel soft glass fabrication technology. Although our prototype structure ran predominately in two antiguided modes rather than the desired single spatial mode because of varying refractive index across the waveguide, our experiments have demonstrated that our basic understanding of the optical physics of the device is correct. The benefit of our soft glass approach over a fused silica approach is that it greatly simplifies the fabrication of complicated fiber preforms. However, this advantage has to be weighed against the refractive index control possible with soft glasses. In any case, the soft glass preform has yielded a prototype fiber that has demonstrated the essential novel device physics of a new class of structures. Due to the delocalized nature of their eigenmodes, antiguided structures similar to the ribbon fiber reported here, but with constant index across their waveguide region are being evaluated as potential routes to extremely high power single spatial-mode radiation.

Acknowledgment

The authors would like to thank W. Krupke, J. Dawson, and Z. Liao of LLNL, and L. Brasure and N. Brilliant of the Air Force Research Laboratory (AFRL) for many useful conversations.

References

[1] H. Zeller, U. Willamowski, A. Tunnermann, H. Welling, S. Unger, V. Reichel, H.-R. Muller, J. Kirchof, and P. Albers, "High-power cw neodymium-doped fiber laser operating at 9.2 W with high beam quality," *Opt. Lett.*, vol. 20, p. 578, 1995.

[2] V. Dominic, S. MacCormack, R. Waarts, S. Sanders, S. Bricknese, R. Dohle, E. Wolak, P. S. Yeh, and E. Zucker, "110 W fiber laser," *Electron. Lett.*, vol. 35, no. 14, p. <AUTHOR: PAGE NUMBERS?>, 1999.

[3] J. Limpert, A. Liem, T. Gabler, H. Zellmer, A. Tunnermann, S. Unger, S. Jetschke, and H. R. Muller, "High-average-power picosecond Yb-doped fiber amplifier," *Opt. Lett.*, vol. 26, pp. 1849–1851, 2001.

[4] H. L. Offerhaus, N. G. B. Roderick, and D. J. Richardson, "High-energy single-transverse-mode Q-switched fiber laser based on a multimode large-mode-area erbium-doped fiber," *Opt. Lett.*, vol. 23, pp. 1683–1685, 1998.

[5] N. N. Elkin, A. P. Napartovich, A. G. Sukharev, V. N. Troschieva, and D. V. Vysotsky, "Direct numerical simulation of radiation propagation in a multicore fiber," *Opt. Commun.*, vol. 177, pp. 207–217, 2000.

[6] N. N. Elkin, A. P. Napartovich, A. G. Sukharev, and V. N. Troschieva, "Effect of small misalignments and the parameter spread on the optical modes of a multicore fiber laser with a spatial filter," *Quantum Electron.*, vol. 32, pp. 264–270, 2002.

[7] M. Wrage, P. Glas, D. Fischer, M. Leitner, D. V. Vysotsky, and A. P. Napartovich, "Phase locking in a multicore fiber laser by means of a Talbot resonator," *Opt. Lett.*, vol. 25, pp. 1436–1438, 2000.

[8] E. K. Gorton and R. M. Jenkins, "Theory of 1-N-way phase-locked resonators," *Appl. Opt.*, vol. 40, pp. 916–920, 2001.

[9] D. Meyhuys, K. Mitsunaga, L. Eng, W. K. Marshall, and A. Yariv, "Supermode control in diffraction-coupled semiconductor laser arrays," *Appl. Phys. Lett.*, vol. 53, p. 1165, 1988.

[10] P. K. Cheo and G. G. King, "Clad-pumped Yb : Er codoped fiber lasers," *IEEE Photon. Technol. Lett.*, vol. 13, pp. 188–190, Mar. 2001.

[11] R. J. Beach, M. D. Feit, R. H. Page, L. D. Brasure, R. Wilcox, and S. A. Payne, "Scalable antiguided ribbon laser," in *Proc. J. Opt. Soc. Amer. B 19*, 2002, pp. 1521–1534.

[12] H. J. Hoffmann, W. W. Jochs, and N. M. Neurtoth, "Relaxation phenomena of the refractive index caused by thermal treatment of optical glasses below T_g," in *Properties and Characteristics of Optical Glass.* Bellingham, WA: SPIE, 1988, vol. 970.

[13] M. E. Fermann, "Single-mode excitation of multimode fibers with ultrashort pulses," *Opt. Lett.*, vol. 23, pp. 52–54, 1998.

[14] A. E. Siegman and S. W. Townsend, "Output beam propagation and beam quality from a multimode stable-cavity laser," *IEEE J. Quantum Electron.*, vol. 29, pp. 1212–1217, Apr. 1993.

[15] R. J. Beach, "CW theory of quasithree level end-pumped laser oscillators," *Opt. Commun.*, vol. 123, pp. 385–393, 1995.

Symmetric Inertial-Confinement-Fusion-Capsule Implosions in a Double-Z-Pinch-Driven Hohlraum

G. R. Bennett,[1] M. E. Cuneo,[2] R. A. Vesey,[2] J. L. Porter,[2] R. G. Adams,[2] R. A. Aragon,[2] J. A. Caird,[3] O. L. Landen,[3] P. K. Rambo,[2] D. C. Rovang,[2] L. E. Ruggles,[2] W. W. Simpson,[2] I. C. Smith,[2] and D. F. Wenger[2]

[1]*Ktech Corporation, 2201 Buena Vista SE, Suite 400, Albuquerque, New Mexico 87106-4265*

[2]*Sandia National Laboratories, P.O. Box 5800, Albuquerque, New Mexico 87185-1193*

[3]*Lawrence Livermore National Laboratory, P.O. Box 808, Livermore, California 94551*

An inertial-confinement-fusion (ICF) concept using two 60-MA Z pinches to drive a cylindrical hohlraum to 220 eV has been recently proposed. The first capsule implosions relevant to this concept have been performed at the same physical scale with a lower 20-MA current, yielding a 70 ± 5 eV capsule drive. The capsule shell shape implies a polar radiation symmetry, the first high-accuracy measurement of this type in a pulsed-power-driven ICF configuration, within a factor of 1.6–4 of that required for scaling to ignition. The convergence ratio of 14–21 is to date the highest in any pulsed-power ICF system.

In the hot-spot ignition approach to indirect drive inertial confinement fusion (ICF), a spherical capsule containing cryogenic deuterium-tritium (DT) fuel is uniformly compressed by intense Planckian x-ray radiation to high temperature and density [1]. The temporal profile of the radiation temperature is designed so that the majority of the fuel is imploded along a low entropy adiabat, and a high-temperature low-density hot spot (created by coalescing shocks at the center) of low fuel mass surrounded by cool, high density DT is attained. With a sufficiently high ion temperature T_{ion} and areal density at the hot spot, 3.56 MeV α particles from the $D + T \rightarrow n + \alpha$ reaction are produced and then slowed. By depositing kinetic energy along their path, the α particles bootstrap T_{ion} up to 60 keV, thus initiating a radially propagating burn wave in the main fuel region, leading to ignition. The radiation field must be sufficiently uniform to drive the capsule to high convergence with minimal shell distortion. Such fields are contained by a high-Z radiation case, or hohlraum, and can be generated by, for example, multiple laser beam irradiation of the cavity wall [1]. Recently, a high-yield (HY) double-Z-pinch-driven hohlraum ICF concept has been proposed [2] that shares some similarities to the laser-driven cylindrical hohlraum ICF approach. Here, two axially located Z pinches at either end of a cylindrical "secondary" hohlraum, each driven by a separate 60-MA power feed, replace the laser beams as the energy source, creating a 220 eV hohlraum radiation temperature.

In this Letter, ICF capsule implosions and polar radiation symmetry measurements at 70 ± 5 eV in a 20-MA, single-power feed variant (but same physical scale) of this high-yield double-Z-pinch-driven hohlraum concept [3–5], on Sandia National Laboratories's Z accelerator [6], are reported for the first time. These represent the first capsule implosions in a Z-pinch-driven hohlraum with a fixed wall, and the high-accuracy polar radiation symmetry measurement is the first in a pulsed-power-driven ICF configuration. The measured polar radiation symmetry in an initial computer-optimized hohlraum was within a factor of 1.6–4 of that required to scale to ignition and HY. The capsule-convergence ratio (Cr) in a deliberately nonoptimized hohlraum was Cr = 14–21, the highest yet demonstrated in a pulsed-power-driven ICF system. In this work, the double-pinch hohlraum exhibits time-averaged radiation drive asymmetries, $\langle \Delta I \rangle / I$ [3,7], at the capsule, that are sufficiently low to be of near-term interest in the U.S. ICF program; i.e., $\langle \Delta I \rangle / I = 6 \pm 1$ [%] at the 70 ± 5 eV (FW84%M = 13–16 ns, full-width at 84% maximum) capsule drive temperature on Z. While this drive uniformity is not at the ignition-relevant requirement of $\langle \Delta I \rangle / I = 0.73\%$ [3,8], detailed simulations indicate that the increased hohlraum wall albedo α at the higher, HY-relevant 220 eV (FW84%M = 12.5 ns) capsule drive would scale the measured $\langle \Delta I \rangle / I$ to reduced levels; i.e., 1.2%–2.9% (within a factor of 1.6–4 of 0.73%). These calculations include the effects of the different case-to-capsule ratios in the HY design and the current implosions.

In the high-yield concept relevant to these experiments, each axial Z pinch is located within a separate primary hohlraum at either end of the central secondary hohlraum containing the 5-mm diameter cryogenic fusion capsule [Fig. 1(a)]. Upon stagnation, kinetic and magnetic energy is efficiently converted to x rays, thus creating, after thermalization, near-Planckian radiation fields in the secondary and both primary hohlraums [4]. With an overlap of reemission radiation from both primaries and the secondary hohlraum walls, the capsule is driven by a 220 eV radiation temperature with a flux uniformity dependent on the primary and secondary hohlraum

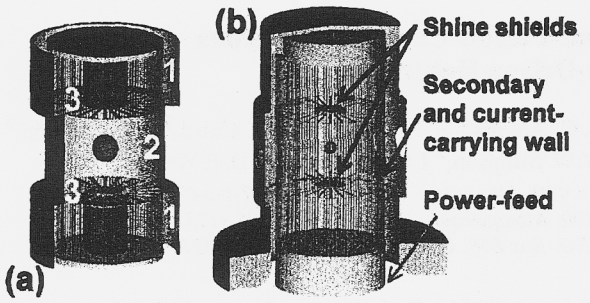

FIG. 1 (color). (a) High-yield dual power-feed double-Z-pinch-driven hohlraum ICF driver configuration, where each Z pinch is powered by a 60-MA current. Direct pinch emission and reemission from the primary hohlraum wall [1] flow into the secondary hohlraum [2] through a beryllium return-current array [3]. (b) The Z accelerator 20-MA, single power-feed variant is at a similar physical scale.

geometry, with little sensitivity to mm-scale-length structure in the pinch emission [2,9–11]. On the Z accelerator, the recently developed single-power feed variant of this geometry (the advanced, glueless load design [3]), at the same physical size [3–5], drove the capsule implosions reported here with a 70 ± 5 eV radiation temperature. In this case [Fig. 1(b)], electrical power enters through a single 3-mm anode-cathode gap in the lower primary hohlraum and current runs the outside length of the secondary hohlraum to drive the upper pinch. Both pinches are 10-mm in length and are formed from a single tungsten wire array [3].

To attain modest convergence with sufficient shell stability in the 70 ± 5 eV drive field on Z, 2.15-mm diameter glow discharge polymer plastic capsules of 59-μm wall thickness and 0.85-mg wall mass were used. With a 1 ATM air gas fill, the calculated peak convergence ratio based on the gas cavity boundary was 23 at the 75 eV upper level of the drive temperature. Each capsule was mounted between two vertical (or horizontal) 0.35-μm thick formvar ($C_5H_8O_2$ at 1.19 gm/cc) layers, and the target was radiographed normal to the z axis of the cylindrical symmetry.

Point projection x-ray imaging with the Z-Beamlet Laser (ZBL) [12] system provided the capsule implosion diagnostic [13]. With a 140 μm FWHM Gaussian x-ray spot (600 ps FWHM laser pulse width), the 4.8× magnification point projection imaging scheme provided a single 6.7 keV (predominantly Fe He_α) x-ray image of the imploding capsule with 120–150 μm spatial resolution, over a 3-mm diameter field of view. The 6.7 keV backlighting energy was chosen because it provided good shell contrast over a wide capsule-convergence ratio range. Two time-resolved transmission-grating spectrometers measured the upper and lower primary hohlraum temperatures (± 5% measurement error for each primary) on selected shots [3–5].

The secondary hohlraum length and shine shield diameter were optimized (using power balance inferred on shot Z766 [3]) to provide the most symmetric time-averaged capsule polar radiation drive using a 2D time-dependent radiation view factor code OPTSEC [9,10]. The fixed primary hohlraum geometry and the fixed secondary hohlraum diameter provided the optimization constraints. Because of the hohlraum cylindrical symmetry, the radiation drive can be expressed in terms of Legendre polynomials, P_n. The P_2 to P_8 even mode Legendre polynomials were minimized when averaged over the drive pulse with a 15.6-mm length, 18.476-mm inside diameter, and 6.5-mm diameter shine shields. Using the measured upper and lower primary hohlraum temperatures on shot Z829 (slight nonideal pinch balance throughout the drive), OPTSEC inferred the time-integrated radiation flux asymmetry to be $\langle \Delta I \rangle / I =$ 2.8% (or 1.9% for "best center" asymmetry, discussed later), with a peak secondary temperature of 68 ± 4 eV.

Figure 2(a) displays a typical capsule preshot radiograph, and Fig. 2(b) shows the Z830 capsule implosion image taken 10 ± 1.3 ns after peak primary radiation temperature. For comparison, Fig. 2(c) is shot Z837 (discussed later) captured at 22.5 ± 1.3 ns in an nonoptimized hohlraum. For Z830, the initial to final radii of minimum shell transmission, Cr, is 1.83 ± 0.04. Figure 3 plots the capsule's right-hand side (rhs) radius of minimum transmission as a function of polar angle (in Fig. 3 the 0° point is the capsule bottom; for clarity, error bars are shown for only every 30° increment). Also plotted is the result of a 2D LASNEX [14] simulation using as input the OPTSEC-inferred 2D time-dependent drive asymmetry and drive temperature from shot Z829. The relevant a_1-a_4 coefficients are listed, along with an error estimate from changing the two primary temperatures by 2.5% in opposite directions (i.e., +2.5% on upper primary and −2.5% on lower, and vice versa). The Legendre

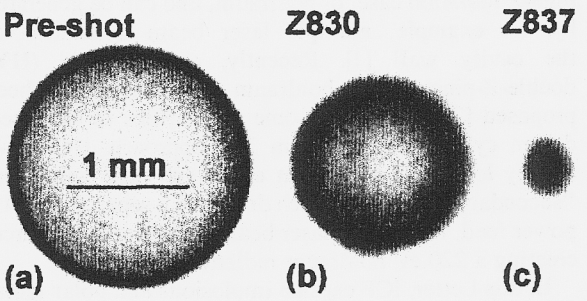

FIG. 2. (a) Preshot radiograph of a typical capsule. (b) Z830 capsule implosion image at 6.7 keV taken at 10 ± 1.3 ns after peak primary radiation temperature. (c) Capsule implosion Z837 image (also at 6.7 keV) in a "nonoptimized" hohlraum captured at 22.5 ± 1.3 ns. Although distorted, it is an example of moderate convergence.

coefficient a_0 of the simulated result was adjusted slightly to allow a clearer comparison between the dominant mode features. Also note the capsule left-hand side is not included in Fig. 3 because a faint axial feature overlies that side of the capsule [see Fig. 2(b)] and interferes with the analysis. However, because of cylindrical symmetry in the hohlraum geometry it is sufficient here to study only the rhs. The axial feature was caused by having apertures in current-carrying surfaces, but was reduced on later shots (e.g., Z837 [Fig. 2(c)] and Z839 [Fig. 4]) by applying thin mylar windows over the backlighter apertures.

The image analysis plotted in Fig. 3 indicates that $\langle \Delta r \rangle / r$ [3,15], the shell distortion from sphericity, is 4.4 ± 0.8 [%], corresponding to deflections of 25 μm, within the 10% limit of the 120–150 μm spatial resolution that an interference can generally be tracked. An 18th order Legendre polynomial fit, with the a_1-a_8 coefficients listed in Fig. 3, also gives $\langle \Delta r \rangle / r = 4.4 \pm 0.8$ [%]. The center around which r is defined is not the original capsule center, since a finite P_1 undoubtedly occurred; rather, it is the best center where the sum of $r(\theta)\cos(\theta)$ and the sum of $r(\theta)\sin(\theta)$ are simultaneously minimized. To infer the resultant drive asymmetry, the relation [3,8]

$$\langle \Delta r \rangle / r = (7/8)(\langle \Delta I \rangle / I)(\mathrm{Cr} - 1) \qquad (1)$$

is used. $\langle \Delta I \rangle / I$ is as defined earlier [7] except now using the best center of the drive asymmetry. Detailed 2D LASNEX simulations indicate that Eq. (1) is reasonably accurate, throughout the Cr range considered here, for any particular low mode drive asymmetry spectrum of *sufficiently* small amplitude; e.g., from a pure P_1 to a more complex combination of P_1, P_2, P_3, and P_4. (In the case of a pure even mode asymmetry, the best center of $\langle \Delta r \rangle / r$ and $\langle \Delta I \rangle / I$ is the original origin.) Therefore, using $\langle \Delta r \rangle / r = (7/8)(\langle \Delta I \rangle / I)(\mathrm{Cr} - 1)$ where $\mathrm{Cr} = 1.83 \pm 0.04$ and $\langle \Delta r \rangle / r = 4.4 \pm 0.8$ [%], the inferred drive asymmetry (best center) is $\langle \Delta I \rangle / I = 6.1 \pm 1.1$ [%]. With a respective factor of 2.8 and 1.38 reduction in even and odd mode drive asymmetry at the 220 eV ignition-relevant temperature [3], it is possible to determine the effective high-yield drive asymmetry, as follows: Given that $\langle \Delta r \rangle / r$ and $\langle \Delta I \rangle / I$ are linearly related, then the Legendre polynomial fit coefficients can be scaled by a factor of 1/2.8 (even) and 1/1.38 (odd). As a result $\langle \Delta r \rangle / r$ is reduced to 2.1%, thus implying $\langle \Delta I \rangle / I = 2.9\%$, which is a factor of 4 of the high-yield requirement of 0.73% [3,8]. If a perfect power balance for the dual-power feed is also considered, then the odd mode shell distortion coefficients would be zero (the even mode coefficients would change very slightly). In this case $\langle \Delta r \rangle / r = 0.9\%$, implying $\langle \Delta I \rangle / I = 1.2\%$; i.e., a factor of 1.6 of the HY requirement. Given that a dual power feed may not necessarily guarantee ideal power balance, however, the Z830 inferred drive symmetry can be best described as being within a factor of 1.6–4 of that required for HY.

On the basis of this analysis, the "optimum" secondary hohlraum geometry clearly requires additional optimization through further experimentation and modeling to meet the HY symmetry-scaling requirement. (In this pursuit, improved x-ray backlighter imaging spatial resolution of the capsule, possibly using advanced laser-backlit grazing-incidence imaging systems for the very highest spatial resolution at much higher Cr [16,17], is required.) However, it is encouraging that such low shell distortions were measured, and a highly uniform drive was inferred, in these initial experiments.

Figure 4 shows a plot of the average radius of minimum transmission for Z830 and Z831 (68 ± 4 eV), Z839 (72 ± 4 eV), and Z833 (75 ± 4 eV) with the corresponding 1D LASNEX predictions at the relevant drive temperatures (and accounting for the 140-μm FWHM Gaussian x-ray spot). Bearing in mind the ± 4 eV uncertainty in the measured drive, the close agreement here between

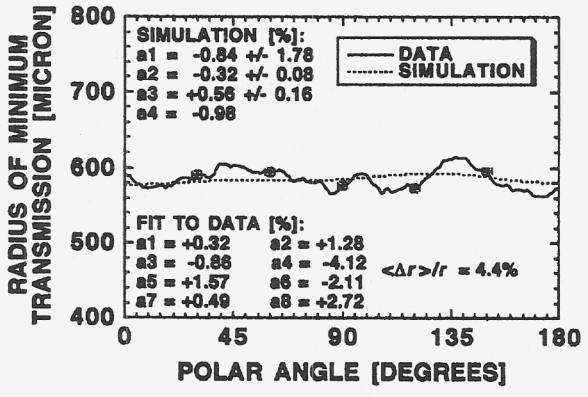

FIG. 3. Radius of minimum transmission vs polar angle for the right-hand side of the Z830 capsule, compared with simulation. The first eight coefficients of an 18th order Legendre polynomial fit to the data are shown.

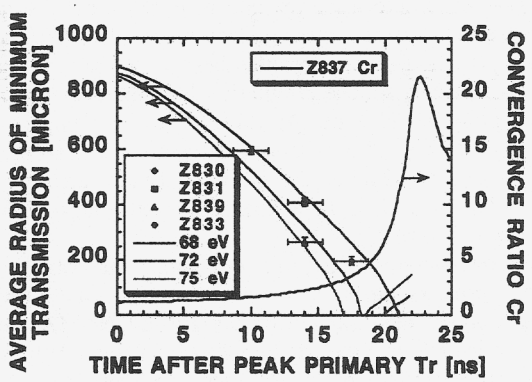

FIG. 4 (color). Z837 capsule convergence ratio vs time and average radius of minimum transmission vs time trajectory for other shots.

simulation and data confirms previous measurements and models of hohlraum energetics and secondary coupling [4,5] and suggests that the first order capsule physics is well understood. Z837 [Fig. 2(c)], captured at 22.5 ± 1.3 ns, was driven in a shorter, 13.0-mm length, but otherwise identical secondary hohlraum to Z830. Although the hohlraum geometry was deliberately not the optimum (part of a geometric symmetry control study to be reported in a later publication), evident in the "equator-hot" core shape, the capsule reached a moderate convergence. The measured Z837 primary temperatures were postprocessed in OPTSEC to provide input to a 2D LASNEX capsule simulation. With a 67.6 eV peak capsule drive temperature, the simulated capsule reaches a peak convergence ratio (based on gas cavity volume) of Cr = 21.6 at 22.7 ns, as shown in Fig. 4. The same simulation predicts a polar averaged peak shell density of 38 g/cm^3 and a polar averaged peak shell areal density of 0.24 g/cm^3.

To infer the Z837 [Fig. 2(c)] convergence ratio, horizontal and vertical lineouts of backlighter x-ray transmission (T) through the capsule were extracted. The $T = 0.5$ points were assigned asymmetric transmission error bars of 0 to −0.1, i.e., $T = 0.5$–0.4. These asymmetric error bars were the result of hole-closure plasma, from the primary and secondary hohlraum backlighter apertures [Fig. 1(b)], creating a nonflat, approximately linear backlighter flux that (without correction) tended to increase the apparent capsule transmission as the center was approached. Future experiments will attempt to eliminate completely these hole-closure plasma issues. The measured profiles were then overlaid onto the horizontal and vertical synthetic transmission profiles from the 2D LASNEX simulation (backlit with the 140-μm FWHM Gaussian x-ray spot). At a time of 22.3 ns the simulation simultaneously best matches the FWHMs of the horizontal and vertical profile data, and thus the equator-hot capsule shape. However, since a 0 to −0.1 transmission error bar has been assigned, it is equally important to determine the best fit to the same displacement points but at a transmission of 0.4. The horizontal and vertical synthetic profiles best match this point at 21.6 ns. Likewise, the simulation best matches the $T = 0.45$ point at 21.9 ns. At these times, all within the measured 22.5 ± 1.3 ns timing interval, the convergence ratios are Cr = 20.8 at 22.3 ns; Cr = 14.2 at 21.6 ns; and Cr = 17.1 at 21.9 ns. Thus, the convergence ratio of Z837 is inferred to be Cr = 14–21.

In conclusion, ICF capsule implosions and polar radiation symmetry measurements at 70 ± 5 eV in a 20-MA, single-power feed variant of the 220 eV, 60-MA, dual-power feed high-yield double-Z-pinch-driven hohlraum ICF configuration, but at the same physical scale, have been performed for the first time. The experiments, performed on Sandia National Laboratories's Z accelerator, represent the first ICF capsule implosions in a Z-pinch-driven hohlraum with a fixed wall. (Notably, this particular hohlraum configuration has the clearest path for meeting ignition-relevant symmetry requirements for pulsed-power systems [2,3].) Furthermore, the high-accuracy polar radiation symmetry measurement is the first in a pulsed-power-driven ICF configuration. When scaled from 70 to 220 eV, the radiation uniformity inferred from the capsule shell in the hohlraum geometry that was computer optimized to have optimum symmetry appeared to be within a factor of 1.6–4 of that required for ignition. An implosion imaged later in time indicated a capsule-convergence ratio of Cr = 14–21. Although the secondary hohlraum geometry was deliberately not the optimum in this case, the Cr attained is the highest yet demonstrated in any pulsed-power-driven ICF system.

The authors thank the Z and ZBL operations teams for technical support. Sandia is a multiprogram laboratory operated by Sandia Corporation, a Lockheed Martin Company, for the U.S. Department of Energy under Contract No. DE-AC04-94AL85000.

[1] J. Lindl, *Inertial Confinement Fusion* (Springer-Verlag, New York, 1998).
[2] J. H. Hammer *et al.*, Phys. Plasmas **6**, 2129 (1999).
[3] M. E. Cuneo *et al.*, Phys. Rev. Lett. **88**, 215004 (2002).
[4] M. E. Cuneo *et al.*, Phys. Plasmas **8**, 2257 (2001).
[5] M. E. Cuneo *et al.*, Laser Part. Beams **19**, 481 (2001).
[6] R. B. Spielman *et al.*, Phys. Plasmas **5**, 2105 (1998).
[7] $\langle \Delta I \rangle / I$ is the time-averaged drive asymmetry applied to a capsule. I is the drive flux averaged over the capsule surface, and $\langle \Delta I \rangle = [(I_{max} - I) + (I - I_{min})]/2$.
[8] This quantity includes a 8/7 adjustment compared with normal usage because $\langle \Delta I \rangle / I$, strictly speaking, does not replace the pressure asymmetry $\langle \Delta P \rangle / P$, since $\langle \Delta P \rangle / P = (7/8) \langle \Delta I \rangle / I$. This relation arises because, for low-Z ablators, the pressure is related to the radiation temperature (T) by $P \sim T^{3.5}$ [1], whereas from Stefan-Boltzmann $I \sim T^4$. Thus, $P \sim I^{3.5/4}$, implying $dP/P = (7/8) dI/I$.
[9] R. A. Vesey *et al.*, Bull. Am. Phys. Soc. **43**, 1903 (1998); **44**, 227 (1999); **45**, 360 (2000).
[10] R. A. Vesey *et al.*, in *Proceedings of the International Conference on Fusion Science and Applications (IFSA2001), Kyoto, 2001*, edited by K. A. Tanaka, D. D. Meyerhofer, and J. Meyer-ter-Vehn (Elsevier, Paris, 2002), p. 681.
[11] D. L. Hanson *et al.*, Phys. Plasmas **9**, 2173 (2002).
[12] G. R. Bennett *et al.*, Rev. Sci. Instrum. **72**, 657 (2001).
[13] S. M. Pollaine *et al.*, Phys. Plasmas **8**, 2357 (2001).
[14] G. B. Zimmerman and W. L. Kruer, Comments Plasma Phys. Control. Fusion **2**, 51 (1975).
[15] $\langle \Delta r \rangle / r$ is the instantaneous level of capsule shell distortion from sphericity. r is the radius of a sphere having the same volume as the distorted capsule, and $\langle \Delta r \rangle = [(r_{max} - r) + (r - r_{min})]/2$.
[16] G. R. Bennett, Appl. Opt. **40**, 4570 (2001).
[17] G. R. Bennett and J. A. Folta, Appl. Opt. **40**, 4588 (2001).

5. SOLID-STATE HEAT-CAPACITY LASER AND TESTS RESARCH ACTIVITY HIGHLIGHTS

DIODE-PUMPED ND:GGG LASER—FIRST LIGHT

Under the support of the U.S. Army's Space and Missile Defense Command, and in collaboration with industrial partners including Decade Optical Systems (DOS), Northrop/Grumman, and others, we are developing high-average–power (100-kW–class), diode-pumped solid-state, heat-capacity laser technology for applications in tactical short-range air defense missions.

As a proof-of-principle, we have built and delivered a 10-kW–class (13 kW actual) heat-capacity laser to White Sands Missile Range. This laser employed flashlamp pumping of the Nd:glass laser slabs. But to advance to a 100-kW–class laser, laser-diode pumping will be used for increased power and efficiency, and crystalline laser media for better thermal characteristics. The baseline design for such a laser uses Nd:doped gallium gadolinium garnet (GGG) as the laser medium and laser-diode pumping at 808 nm.

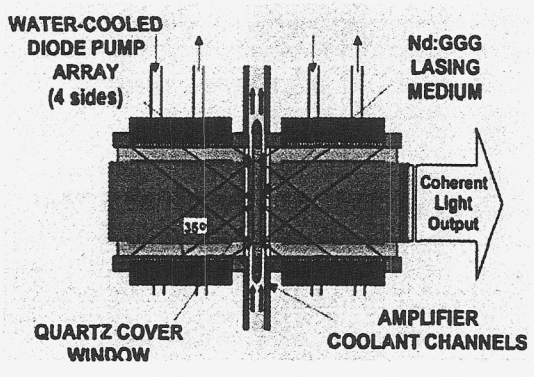

Figure 1. Schematic of the pump cavity. This is the fundamental building block of the diode-pumped Nd:GG laser system.

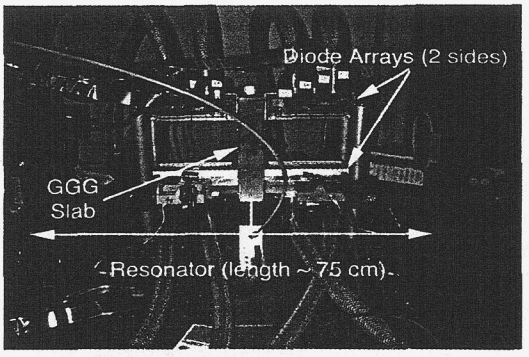

Figure 2. Photo of the half-size-slab experiment.

To establish a solid technical basis for such a laser, we have developed a half-scale testbed that utilizes a single Nd:GGG slab with an active region measuring 5×10 cm^2 in size and is pumped by four half-size laser diode arrays. A schematic of the laser is shown in Figure 1. The diode arrays consist of 28 SiMM (Silicon Monolithic Microchannel) "tiles" arranged in a 4×7 configuration and produce an average optical power of 4.2 kW/array. The pulse width is nominally 500 μs.

Figure 2 shows the experimental setup of the half-scale heat-capacity laser. In the middle, one can see the slab holder with the four pump arrays surrounding it. The entire laser system is extremely compact—the diode arrays shown are roughly 6 in. long and the entire cavity is only 75 cm long. We performed a series of experiments to verify the performance of this new laser. Optical gain coefficient, pump uniformity, output wavefront, and

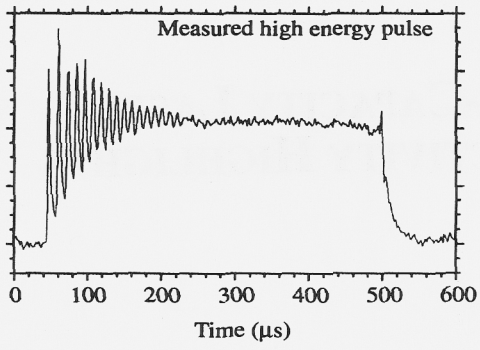

Figure 3. Typical laser output pulse, showing the presence of relaxation oscillations at the beginning of the pulse.

temperature rise in the lasing medium were measured to benchmark our temperature-dependent energetic model.

Using a stable resonator with low-output coupling, we obtained kW output from the half-scale system. At 200 Hz, over a ten-second run, we achieved an average power of 2.7 kW with an initial output in excess of 3 kW. The cavity consisted of a flat high reflector and an 85% reflectivity concave output coupler with a 10-m radius of curvature. No attempt was made to optimize either the output reflectivity or the curvature of the reflectors. Figure 3 shows a typical high-energy pulse from this system.

The average diode-array optical pump power used for this experiment was 13.3 kW and the overall diode electrical efficiency was 45%. Thus, the total electrical efficiency of the half-scale slab laser works is ~9%, a figure very near the 10% goal designed for the 100-kW mobile laser system. Using the output beam, we were able to penetrate a 1.5-mm-thick steel coupon in a matter of a few seconds (Figure 4).

In fiscal year 2003, we plan to activate the three-slab diode-pumped Nd:GGG testbed as a scientific prototype for the 100-kW system to be developed for battlefield defense. It is anticipated that this system will generate an output power in excess of 15 kW —greater than the nine-slab flashlamp-pumped system currently in operation at the Army's High Energy Laser Systems Test Facility (HELSTF).

— M. Rotter and S. Mitchell

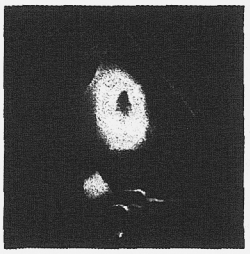

Figure 4. Frame taken from a movie showing the interaction of the laser beam with a steel coupon. The beam has punched through the coupon at this point.

COMPACT MICROCHANNEL-COOLED LASER-DIODE ARRAYS DELIVER OVER TENS OF KW/CM^2 ONTO THE WORKING SURFACE

Last year we reported the delivery of a 41-kW-peak-power diode array module constructed using LLNL Silicon Monolithic Microchannels (SiMMs) packages. In total, four of these modules (one of which is shown at right) are being delivered to the Solid-State Heat-Capacity Laser Project for optical pumping of a high-averagepower solid-state laser. These initial modules are being used for characterization and testing of a subscale laser slab. As reported earlier (see November 2001 LS&T Program Update), the SiMMs module brings unsurpassed average radiance (or brightness) capability to laser-diode arrays. This performance is attained through a unique combination of microscopic cooling channels in a silicon substrate that serve to remove waste heat, and precision microlenses that serve to condition the output radiation from the laser-diode bars that are mounted on the package (see Figures 5 and 6). The use of silicon as the solid material in the heat-conducting portion of the SiMMs package is critical. It makes possible the fabrication of thousands of tiny (~30-μm-wide) cooling microchannels in very close proximity to the heat-producing laserdiode bar arrays. The use of silicon also makes possible the precision location of multiple bars on a single substrate, allowing an array of precision-located cylindrical microlenses to be attached in a single step. Optimizing the performance of laser-diode bars was one of the primary considerations in the design of the SiMMs package. The aggressive cooling capability of the SiMMs package enables efficient operation of laser diode arrays in a very tightly packed geometry. The peak electrical efficiency of a SiMMs package is about 48%, converting nearly half of the electric input power into light output. Average exitance from the SiMMs laser-diode arrays operating in a CW mode is up to be 600 W/cm^2, which is ~3 times higher than available today. With microlens conditioning, the output

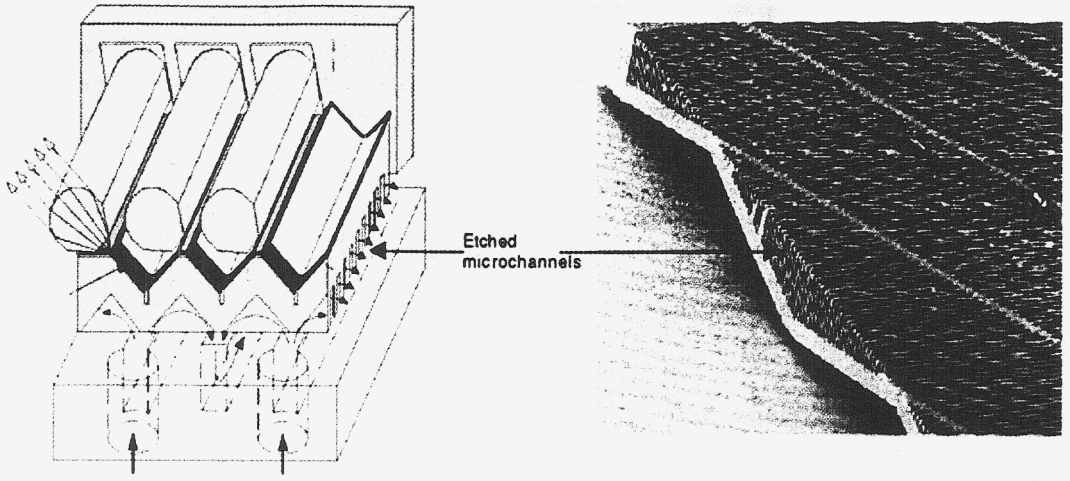

Figure 5. On the left is a cutaway sketch of s SiMMs package showing the location of the microchannels, which are fabricated into the silicon top layer of the package. On the right is an SEM photograph of a silicon wafer used in the SiMMs production showing the 30-μm-wide microchannels for cooling water that are fabricated using photolithography and anisotropic etching.

radiation from a SiMMs package is confined to an angular region of 6° by 0.6°, giving an unsurpassed average radiance capability of ~0.5 MW/cm^2-steradian. This technology is available for transfer to interested commercial enterprise. Initial testing of the laser modules is focused on characterizing pump light delivery efficiency and pump light uniformity delivered onto the Nd:GGG laser disks that comprise the gain medium of the heat-capacity solid-state laser. Part of this testing involves characterizing the radiation emitted by the modules.

The figure at top right shows the result of one test in which the output radiation from the module was focused onto a stack of steel plates having total thickness of 3 mm. After a brief exposure of ~5 s, a narrow slit (approximately 4 mm • 35 mm) was produced. During this exposure, the diode array was operated at a 10% duty factor (500-μs pulse width and 200- Hz pulse repetition frequency) and developed a peak power of 41 kW. The average power density at the focal spot on the steel plates during this test was estimated to be ~3 kW/cm^2. During

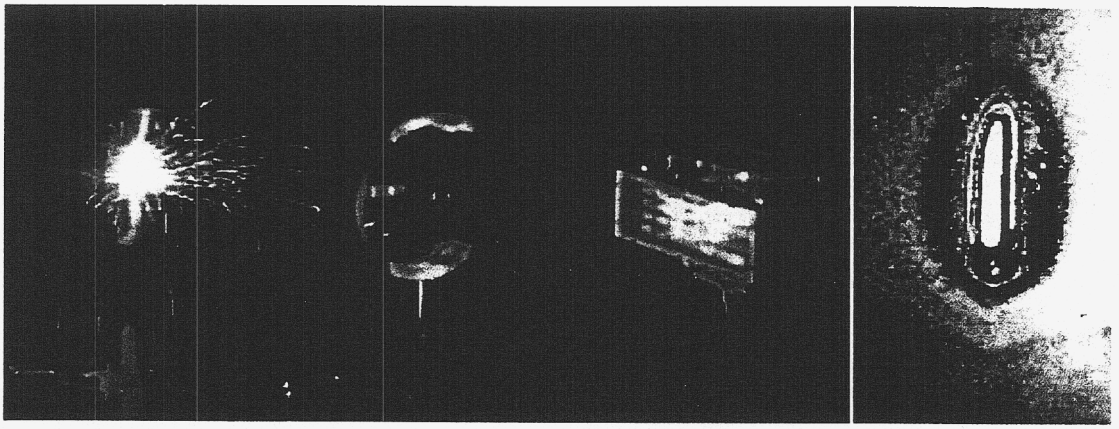

Figure 6. On the left is a 41-kW peak power SiMMs diode array operational with its output radiation focused onto a steel plate. This diode array is constructed from 28 closely packed SiMMs tiles. On the right is the hole that was burned through the steel plate.

the coming year, we plan on building a three-slab submodule of the ultimate 100-kW system. This submodule will use a total of 12 diode backplanes whose size will be twice what is currently used (56 ten-bar tiles per backplane). The total amount of peak diode power will be approximately 1 MW. Besides optical pumping of solid-state lasers, we are also evaluating possible applications of SiMMs modules to welding and surface treatment of materials. Areas of particular interest are brazing, heat-treatment, and surface hardening of metals. These material processing applications directly benefit from our SiMMs packaging technology because of the high irradiance—upwards of tens of kW/cm^2—that can be delivered to the working surface of samples. The SiMMs package represents a significant breakthrough in high-power diode-array packaging technology and enables the scaling of power from 2-D diode arrays to 100 kW or larger with extremely high brightness. Currently 840-kW arrays are in production for the heat-capacity laser program. When completed, these will be the most powerful average-power diode arrays in existence.

— R, Beach, B. Freitas, and M. Rotter

Modeling of High-Energy Pulsed Laser Interactions with Coupons

C. D. Boley and A. M. Rubenchik

Abstract

We describe a computational model of laser-materials interactions in the regime accessed by the solid state heat capacity lasers (SSHCLs) built at LLNL. We show that its predictions compare quite favorably with coupon experiments by the 10 kW SSHCL at LLNL.

1. Introduction

The development of a computational model of material interactions produced by solid state heat capacity lasers has been an area of intense activity. In this report, we describe such a model and discuss its application to coupon experiments with the 10 kW SSHCL. The experiments were performed at the High Energy Laser Systems Test Facility (HELSTF) at White Sands Missile Range. The laser produced pulses of high energy (at least 500 J) and long pulse length (hundreds of microseconds), at 20 Hz. Typical fluences on target ranged up to 1500 J/cm^2 per pulse, with peak intensities in the range of 1-10 MW/cm^2.

The experiments tested the capabilities of the laser for material removal and coupon melt-through. They were conducted both in ambient air and in the presence of Mach flow. The model generally showed quite favorable agreement with experiment. From the dependence on the material data, the model also indicated how a pulsed laser could achieve better energy deposition in this regime than a continuous (CW) counterpart.

The body of this paper describes the following topics, listed by section number:

(2) model in quiescent air,
(3) comparison with experiments in quiescent air,
(4) effects of air flow,
(5) comparison with experiments involving air flow,
(6) importance of material properties,
(7) advantage of pulsed lasers over CW lasers,
(8) conclusions and recommendations.

2. Model in quiescent air

First it is advantageous to note some phenomenology from the HELSTF experiments. Figure 1 shows dramatic streaks of ejected material, the visible radiation from which corresponds to a temperature of several thousand degrees. Simple estimates suggest that these are ejected liquid blobs heated during passage through the beam. (This shot is without air flow, which sweeps away the smaller blobs, as quantified later.) Also shown in Fig. 1 is the pattern of ejected metal remaining on an aluminum coupon after a few shots. The frozen lips on the sides of the holes again point to liquid ejection. Thus we expect liquid hydrodynamics to play a key role in the physics. In addition, if we estimate the maximum material removed by vaporization alone, we have

$$\Delta z \approx \alpha F / \rho H_v ,$$

where α is the typical absorptivity, F is the fluence, and H_v is the heat of vaporization. This shows that vaporization can account for only a fraction, of order 30%, of the observed material removal. Nevertheless, vaporization is not negligible. In addition, as seen below, it provides the recoil force for liquid expulsion. Therefore the model must describe the hydrodynamics of both liquid and vapor. Other important effects are heat transport in the solid and the interaction with the surrounding air.

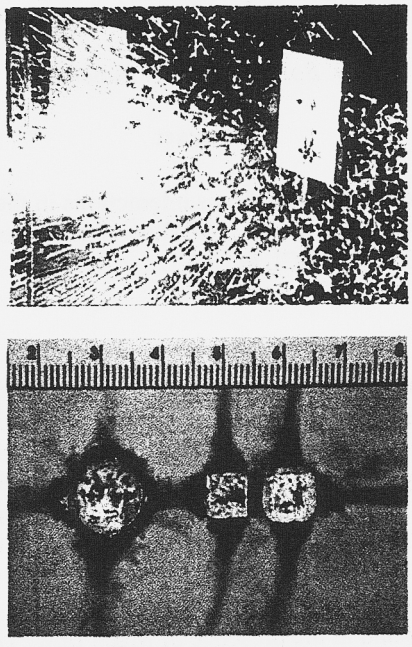

Fig. 1. Above: streaks emanating from a coupon during SSHCL shot without air flow. Below: sample debris patterns in an aluminum target.

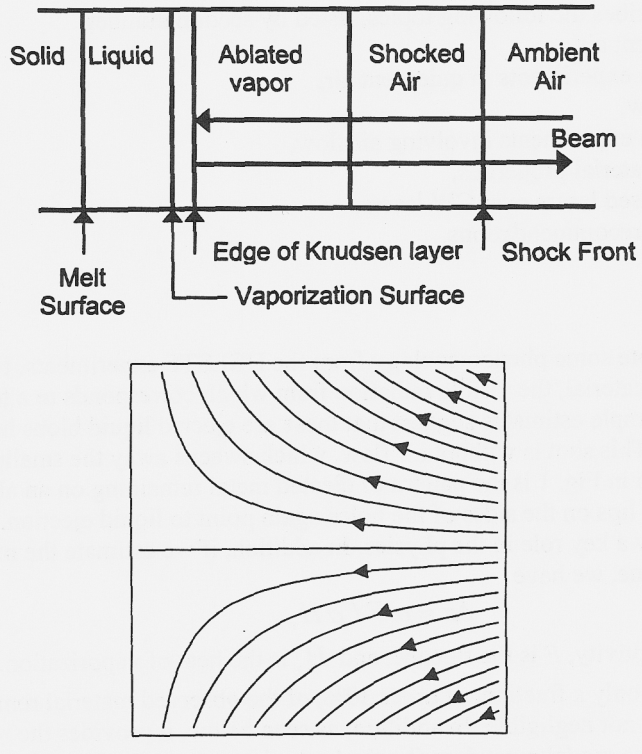

Fig. 2. Above: geometry of the model (not to scale). Below: streamlines in the liquid. The melt line is at the left, and the liquid surface is at the right.

For these purposes, we have used a computational model, called THALES, which has been developed intermittently over the past several years. It was first used, in a less advanced form, to model drilling by copper vapor lasers [1]. Later, it was used to model vaporization in beam dumps for a high-power laser [2]. These applications were at a sufficiently high intensity that material removal occurred via vaporization alone. The first use of the code to model SSHCLs was reported in [3]. Recently, we presented new capabilities of the model and selected results at a meeting [4] and at a workshop [5]. The new features include liquid hydrodynamics and some important effects of air flow.

The basic model is in one dimension, while the liquid hydrodynamics is handled in two dimensions. The geometry of the model, in the absence of air flow, is shown in Fig. 2. From left to right, the model describes heat conduction in the solid, a moving melt line, heat conduction and liquid motion in the melt, a moving ablation surface, a thin Knudsen layer of molecular flow [6], the hydrodynamically expanding vapor, a moving vapor/air boundary, the hydrodynamically expanding air, and a shock front. Reasonable estimates for temperature-dependent material properties (primarily the thermal conductivity and the material absorptivity) are employed, as discussed in Sec. 6. Since typical vapor temperatures are only a few thousand degrees, absorption in the vapor is negligible. In reality, absorption may occur in the ejected liquid blobs, but this is not considered here. In the presence of air flow, as noted later, the smaller blobs are swept away.

In the liquid model, the fluid is pushed inward (to the left) and toward the radial edges by the recoil pressure of the ablated vapor, as shown by the streamlines in Fig. 2. The fluid reaching the edges is assumed to be removed from the system. This picture is embodied in the following solution for 2D incompressible, potential flow [7]:

$$v_z(z,t) = -2\beta(t)[z - z_m(t)], \quad v_r(r,t) = \beta(t)r,$$

where z is to the right in the figure and $z_m(t)$ is the position of the melt surface. The function $\beta(t)$ responds to the central pressure just beneath the surface via

$$d\beta/dt + \beta^2 = (2/\rho a^2)\, p_0(t),$$

where ρ is the (constant) liquid density and a is the beam radius. Since the model does not describe the flow up the edges, it is most appropriate for shallow holes, such as those considered here.

3. Comparison with experiments in quiescent air

Now we turn to simulations of coupon experiments with the 10 kW SSHCL at HELSTF, first considering experiments in quiescent air. The pulse form used in the simulations is shown in Fig. 3. It has a FWHM of about 300 μs. In some experiments, it is stretched to about 680 μs by appropriate phasing of the flashlamps. Note the narrow initial spike, which rises to a peak intensity about an order of magnitude higher than that of the main part of the pulse. It accounts for about 5% of the pulse energy. Because of the multimode structure of the beam, the spatial profile is practically flat.

To illustrate the effects of liquid ejection, let us consider a pulse of about 470 J, with spot size 0.77 cm^2 (corresponding to a fluence about 610 J/cm^2), on a steel coupon. The calculated phase divisions within the coupon (i.e. regions of solid, liquid, and vapor), as functions of time, are shown in Fig. 4. The left-hand plot refers to a simulation without liquid motion. Here a melt layer of maximum depth about 60 μm opens up and then closes at about 1.5 ms. About 25 μm of material are removed, by vaporization. The right-

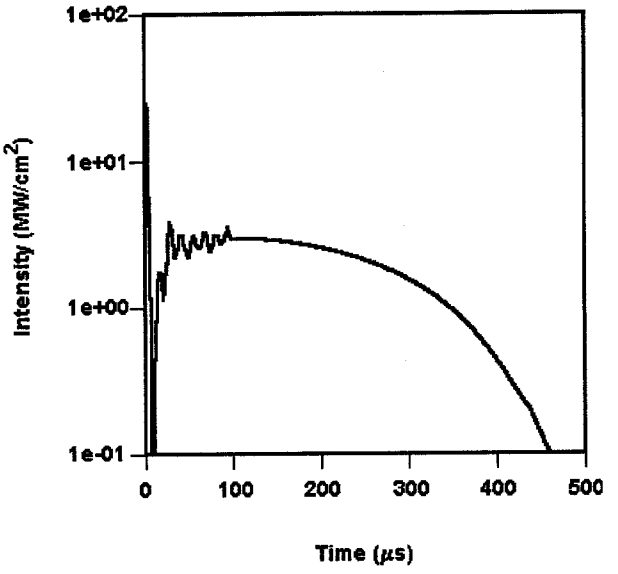

Fig. 3. Pulse shape of 10 kW SSHCL. The intensity corresponds to a fluence of 900 J/cm^2.

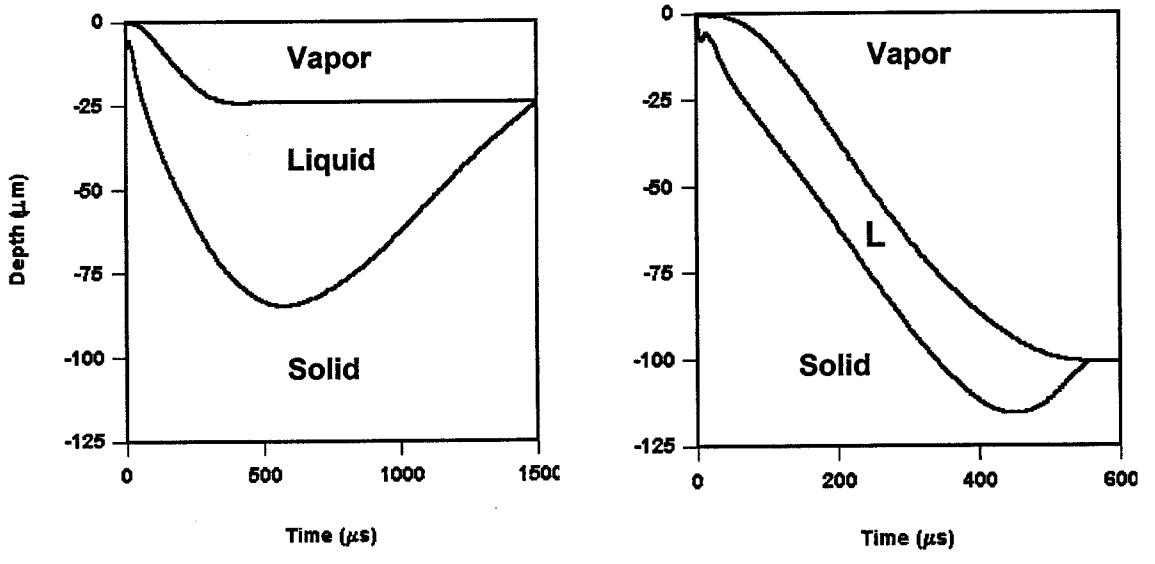

Fig. 4. Model predictions of phase divisions in coupon without liquid hydrodynamics (left) and with liquid hydrodynamics (right).

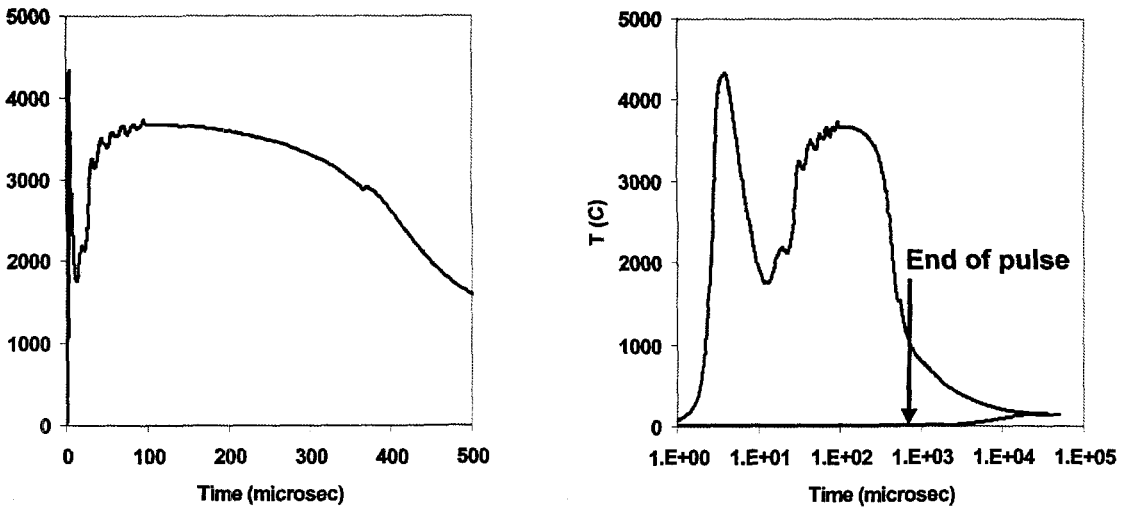

Fig. 5. Calculated temperature of the heated edge, for the second case of the previous figure. The plots give a short, linear time scale and a longer, logarithmic time scale. In the right-hand plot, the increasing line near 10 ms gives the temperature of the rear surface.

hand plot refers to a simulation with liquid motion. In this case, the melt layer remains fairly thin (no more than 25 μm), and appreciably more material is removed. The final ablation depth is about 100 μm. Thus in this case the inclusion of liquid motion in the model increases the material removal by about a factor of 4.

The calculated temperature of the front edge (solid or liquid) exposed to the beam is shown in Fig. 5. This is shown for the case of liquid ejection. Responding to the sharp initial spike in the pulse, the temperature quickly rises to about 4300 C, and then drops to somewhat less than 2000 C. During the main body of the pulse, it rises to about 3600 C, then drops over a period of several hundred microseconds to the melting temperature (1537 C, in this case). By the time of arrival of the next pulse, the temperature has decreased to about 145 C, corresponding to a net increase of 125 deg. Meanwhile, the temperature of the back edge has increased to about the same value. This is in accordance with 1-dimensional heat conduction, which is valid in steel on this scale of distances and times.

Now we turn to a series of experiments involving a single shot on a steel coupon. In this case, the diagnostics are the mass removal and the equilibrated coupon temperature. The shots have energies of about 500 J but different spot sizes, corresponding to fluences ranging from 155 to about 1100 J/cm^2. The coupon dimensions are 2x2x0.115 cm^3. Figure 6 shows the measured mass removal M as a function of fluence. For convenience, this has been divided by the spot area A. Thus if all the mass were assumed to be removed completely from the coupon, then the experimental Q* would simply be $F/(M/A)$, with F the fluence. Unfortunately, with data presently available, the fraction of removed mass leaving the coupon is not determined. It is certainly not true that all the liquid leaves, in view of the lips of frozen ejecta on the sides.

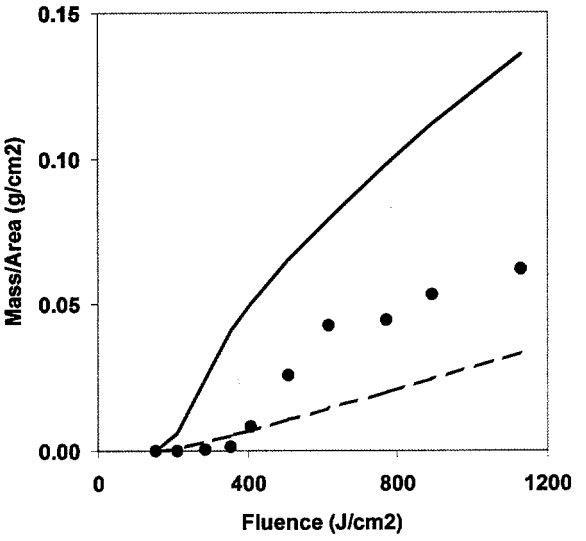

Fig. 6. Mass removal, per unit beam area, for a single pulse into a steel coupon, without air flow. The dots show data shots 020320x through 020320ag. The solid line and dashed lines give the prediction for the cases of all ejected liquid assumed to leave the coupon or assumed to return to the coupon, respectively.

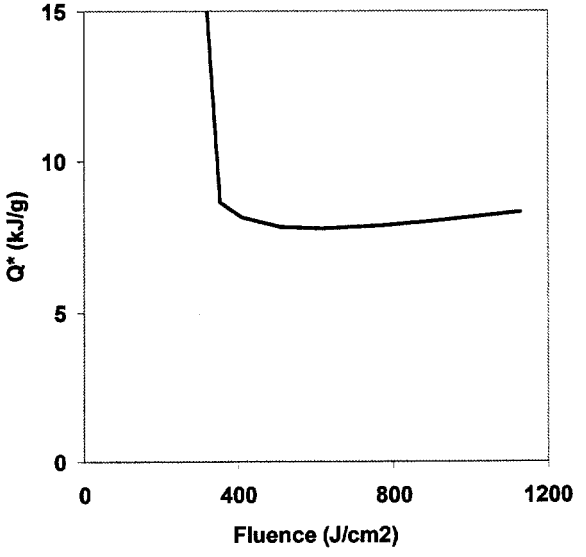

Fig. 7. Calculated Q* for the previous case.

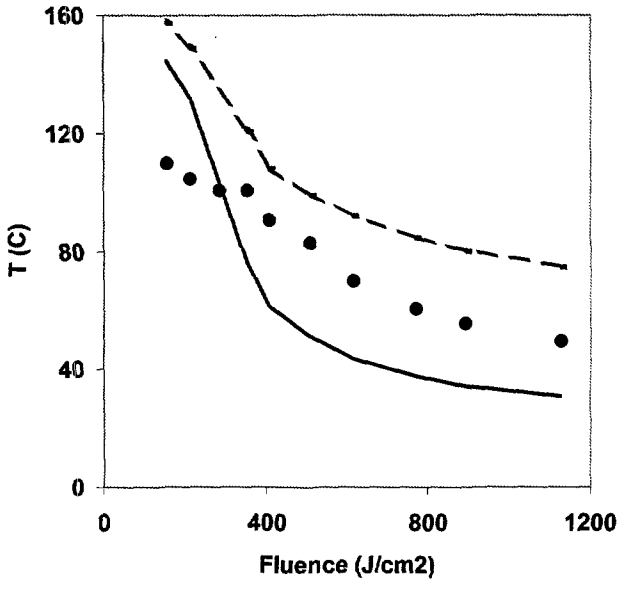

Fig. 8. Measured and calculated residual temperature of the coupon, for the same case as the previous two figures. The convention for solid and dashed lines is also the same.

The model predicts the hole depth but not the fraction of leaving or returning liquid ejecta. Thus Fig. 6 shows the predictions for the two cases of (1) all liquid leaving and (2) all liquid remaining. These bound the experimental results, as is appropriate. Since the actual hole depth is calculated by the model, a unique Q* can be calculated. As shown in Fig. 7, this has an extremely sharp decrease near the threshold for removal (about 300 J/cm^2), followed by a broad minimum near 7.8 kJ/g.

Figure 8 shows the measured equilibrated temperature versus fluence, along with the model predictions. It is interesting that the final temperature decreases as the fluence increases. The reason is that high-fluence shots invest more energy in removal. Similarly, the calculated residual temperature is lower when all liquid is assumed to leave the coupon. The calculations bound the data, except in the case of high residual temperatures. Here the data may be low because of experimental uncertainties.

Next we turn to experiments involving 1, 2, 3, or 4 successive pulses on a steel coupon. The diagnostics are again the mass removal and the coupon temperature. The energy per pulse, which gradually decreases with pulse number, is about 460 J. The fluence per pulse is about 1500 J/cm^2. Figure 9 shows the mass removal as a function of number of pulses. Also shown is the residual temperature. Each of these increases almost linearly with pulse number. The calculations again pertain to the cases of all ejected liquid leaving the coupon or else remaining on it. These are consistent with the data, which fall about midway between the two bounds.

As noted, the model gives an unambiguous prediction of the hole depth (and volume, since the hole is calculated as a cylinder or rectangular prism), but it does not predict the final location of the ejected liquid. The available diagnostics, on the other hand, give the coupon mass loss but not the actual shape of the hole. Limited microscopic measurements of the hole shape have been made at LLNL. These have been applied to the case of a single shot on an aluminum coupon, with a beam energy in the range

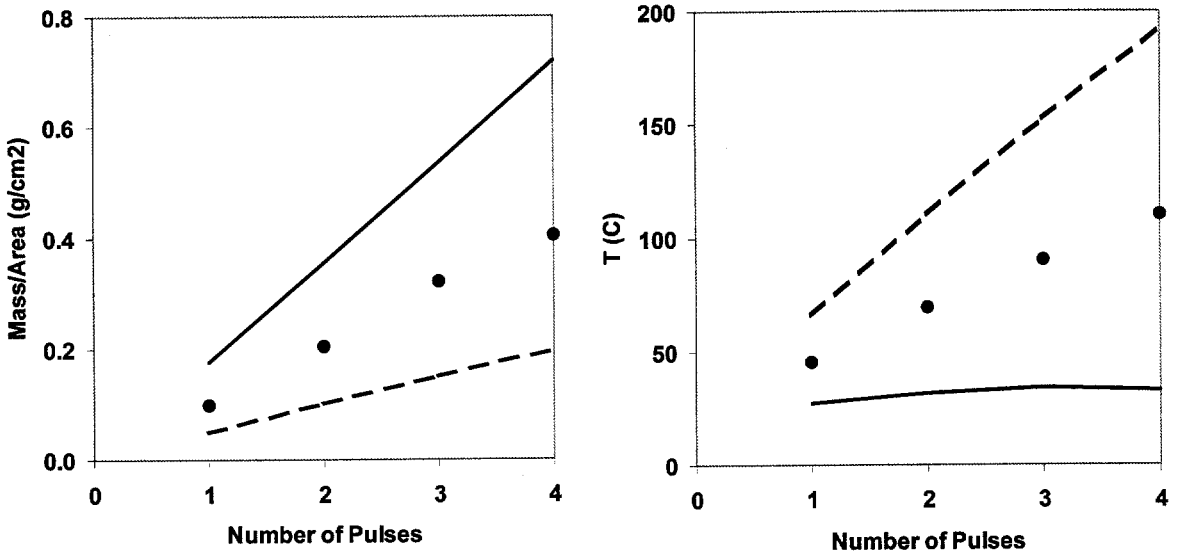

Fig. 9. Mass removal (per beam area) and residual temperature, for several shots on a steel coupon. The data correspond to shots 020423c through 020423f. As before, the solid lines show the model prediction if all ejected liquid is assumed to leave the coupon. The dashed lines give the prediction if all ejected liquid is assumed to return to the coupon.

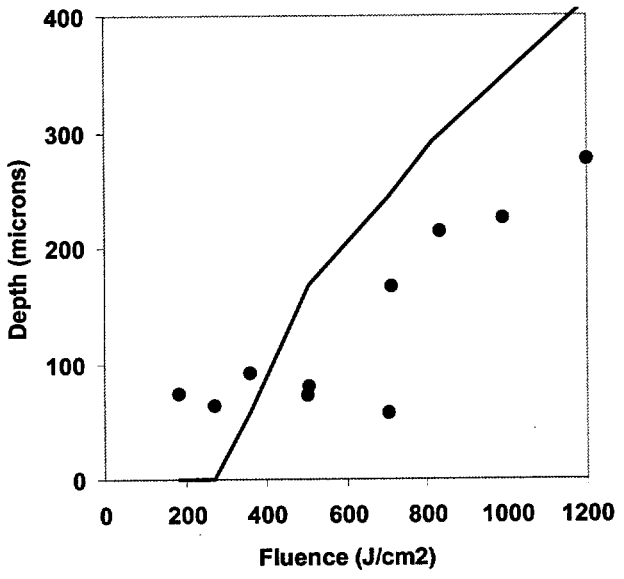

Fig. 10. Depth for single shots on an aluminum coupon, without air flow. The dots (shots 020319h through 020319q) are measurements with a microscope. The line is the model prediction.

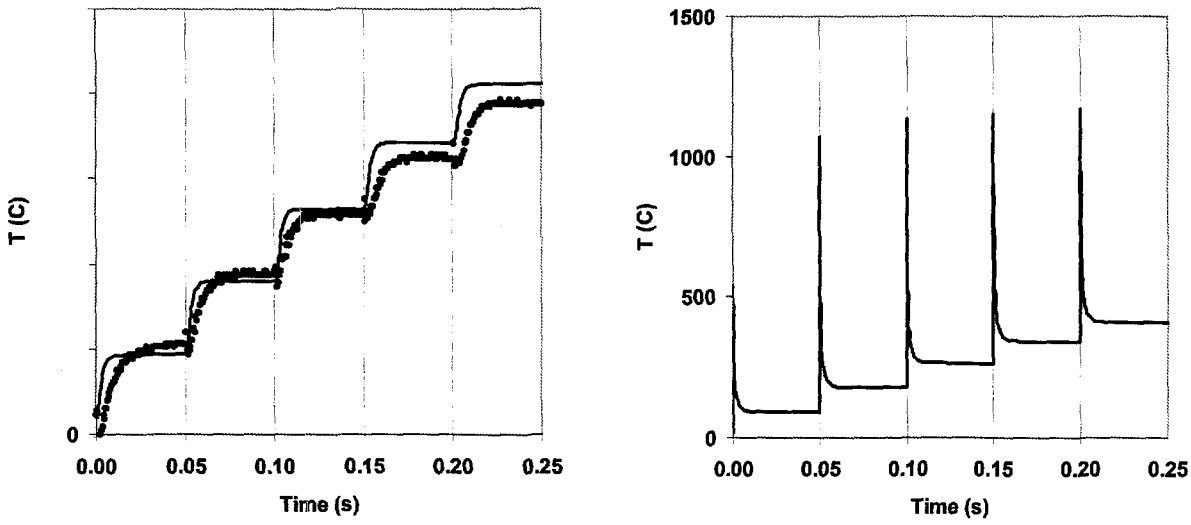

Fig. 11. Left: temperature of back surface of coupon, during 5 pulses on an aluminum coupon (500 J per pulse, spot size about 5 cm^2). Right: calculated front surface temperature.

500-600 J. The spot size is varied to give a fluence ranging from 180 to 1200 J/cm^2. The results are shown in Fig. 10. These show a constant depth of about 100 μm at low fluence (200-400 J/cm^2), followed by a gradual rise. Clearly the results at low fluence are not very precise, since other experience, such as visual observation and plume photographs, indicates a sharp threshold in fluence. This is also predicted by the model. With allowance for large error bars, the model appears consistent with experiment.

Now we consider an experiment giving the back face temperature during 5 successive pulses on an aluminum coupon. This is a large coupon, with dimensions 2"x5"x(1/16)". The fluence per pulse is about 100 J/cm^2, resulting in essentially no material removal. As shown in Fig. 11, the temperature of the back surface rises quickly for about the first 10 ms of each pulse and then remains nearly constant during the remaining 40 ms until the arrival of the next pulse.

The model calculations match this behavior fairly consistently. The calculated temperature rises more quickly than experiment, perhaps because of an inaccuracy in the thermal conductivity. The temperature becomes constant in time, in accordance with the constraints of a 1-dimensional calculation without losses. During the fraction of a second after the 5th pulse (not shown), the back surface temperature relaxes due to lateral conduction. The calculated behavior of the front surface temperature is very different, as shown in Fig. 11. It is driven very rapidly to a high value (500-1000 C) during a pulse. This is followed by a decay to a temperature comparable to that of the back surface. The fact that the temperature ratchets up has an important and favorable bearing on the absorbed energy, as will be discussed below.

Because of its large thermal diffusivity, aluminum exhibits significant lateral heat conduction. For this reason, we requested a long-time 3-dimensional thermal calculation by L. Hagler (LLNL). No hydrodynamical effects were needed, or modeled. Figure 12 shows the calculated back surface temperature versus time. The long-time falloff caused by lateral conduction is given correctly.

4. Effects of air flow

Air flow affects target interactions in a number of ways:

a) It removes small ejected droplets which shield the target.
b) It removes much of the melt layer.
c) It cools the target.
d) It supports target combustion.
e) It can break the target prior to melt-through.

All of these except for the third are favorable. We proceed to discuss them in turn.

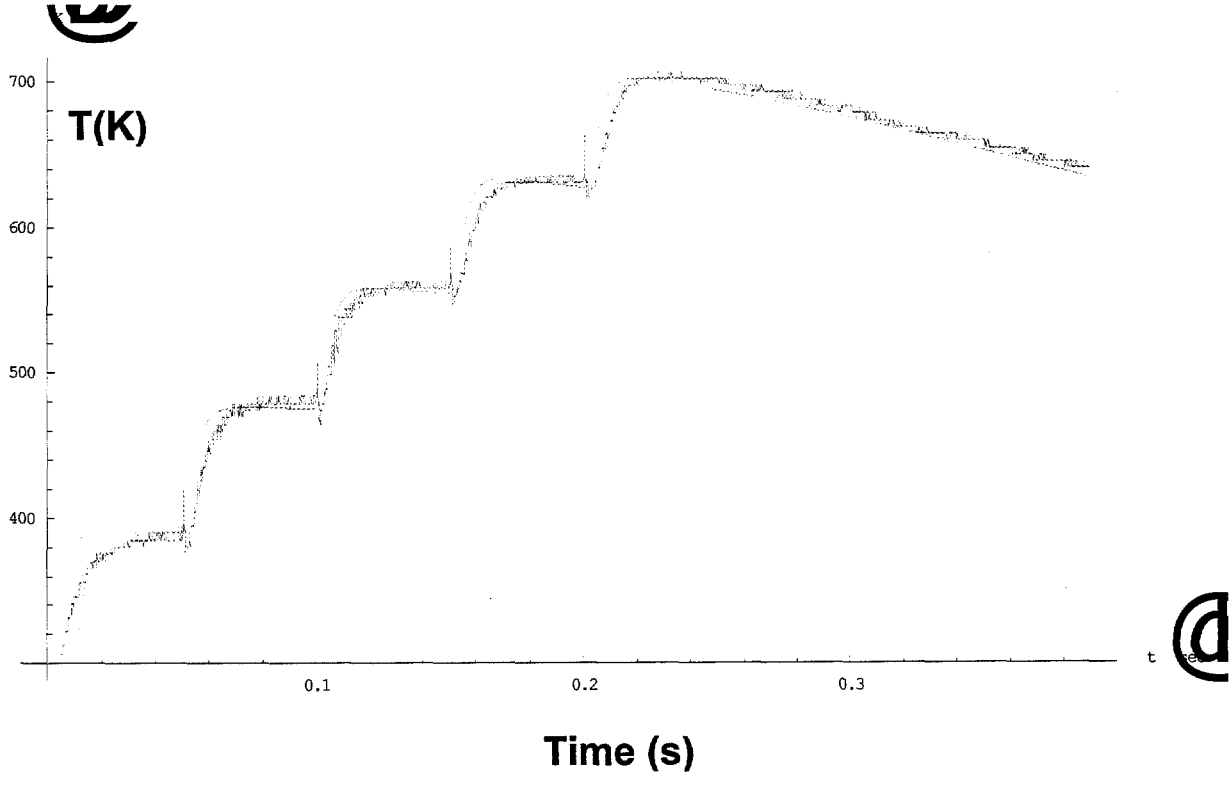

Fig. 12. Thin line: 3-dimensional ANSYS calculation of back surface temperature (K) of an aluminum coupon. The experiment is the same as in the previous figure. The solid line indicates the data.

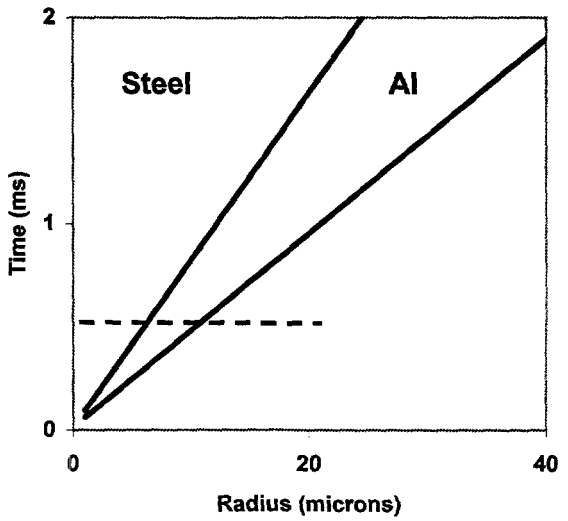

Fig. 13. Time required for wind at Mach 1 to remove a liquid particle from the beam, versus particle radius, for steel and air. The spot size is taken as 1 cm. The dashed line gives a typical pulse duration.

4(a) Removal of ejected droplets by air flow

The motion of a liquid droplet parallel to the target is governed by Stokes' law,

$$M\frac{dv}{dt} = 6\pi\eta_a r(u_a - v),$$

in which the particle has radius r, mass $M = (4/3)\pi r^3\rho$, and parallel speed v. The air has parallel speed u_a and viscosity η_a. From the solution of this equation, the distance moved within a time t is

$$x(t) = u_a\tau[t/\tau + \exp(-t/\tau) - 1],$$

where $\tau = (2/9)\rho r^2/\eta_a$ is a characteristic time. We have made the reasonable assumption that the initial parallel speed is much less than the wind speed. We are interested in the time to move a distance of the order of the spot size, say a. If this is appreciably less than the pulse duration, then the particle will have been removed from beam interactions.

There are two limiting cases, depending on whether the required time is much greater than, or much less than, the characteristic time τ. In terms of particle size, this translates into whether the radius is much less than, or much greater than, respectively, a characteristic radius $r_0 = (9a\eta_a/2\rho u_a)^{1/2}$. For steel or aluminum in air at Mach 1, this of order 1 μm. In the former case, the particle is sufficiently small to attain the wind speed almost immediately. The time required for removal from the beam is then just a/u_a. In the latter case, the particle is so sluggish that its speed can be neglected in comparison to the wind speed on the right-hand side of Stokes' law. Then its speed increases linearly with time, and the time required to move a distance a is

$$t = (2r/3)(a\rho/\eta_a u_a)^{1/2}.$$

This increases linearly with the particle size.

The removal time is plotted as a function of particle radius, for a spot size of 1 cm, in Fig. 13. The horizontal line denotes a sample pulse duration of 0.5 ms. Reading the intercepts along this line, we see that the maximum diameter removed is 12 μm for steel and 20 μm for aluminum. It should be noted that the particle size cannot exceed the depth of the melt, which will be shown to have this same order of magnitude.

4(b) Removal of melt layer by air flow

The pattern of air flow near the target is extremely complicated, since a turbulent boundary layer exists. Hence the effect on the melt layer can be described only approximately.

First we consider the parallel component of the wind. From elementary considerations, the shear stress at the top of the melt layer must match the shear stress produced by the wind. The form of the latter has been established in wind tunnel experiments. Using this, we have a condition of the following form at the liquid surface (cf. Fig. 14)

$$\eta \frac{\partial v_x}{\partial y} = f_s \rho_a u_a^2 ,$$

where η is the liquid viscosity and f_s is a skin friction factor. This factor is a slowly varying function of the Reynolds number of the air flow with respect to the spot size; it is of order 0.005. Since the liquid velocity vanishes at the bottom of the melt layer ($y = 0$), an approximation to the profile induced by the shear condition is

$$v_x(y) = f_s \rho_a u_a^2 \, y / \eta .$$

The melt at a depth y can be considered removed during a pulse time τ if $v_x(y) > a/\tau$, where a is the spot size. Thus the maximum melt depth is approximately

$$h_{\max} \approx \frac{a\eta}{f_s \rho_a u_a^2 \tau} ,$$

which is of order several tens of microns for our conditions. The actual depth would be expected to be less than this because of shear stress enhancement by surface modulations. In practice, we use a maximum depth of 30 μm for steel. It should be noted that, at a shallow depth such as this, Kelvin-Helmholtz waves are strongly damped and cannot resonate with the wind.

Next we turn to the component of wind normal to the surface, which is important in nearly head-on engagements. This generates an additional pressure that can be estimated from gas kinetics. The pressure is of the order

$$p = (1/2)\rho_a u_{an}^2 ,$$

with u_{an} the normal component. For air of Mach 0.9, this is about 0.6 bars.

Along the target surface, the momentum balance has the form

$$\eta \frac{\partial^2 v_x}{\partial y^2} = \frac{\partial p}{\partial x} ,$$

as depicted in Fig. 15. The variation in pressure occurs above the heated region and has a characteristic length of the spot size a. For melt of depth h, the parallel liquid speed at the surface is approximately

$$v_x \approx \frac{h^2 \rho_a u_{an}^2}{6\eta a} ,$$

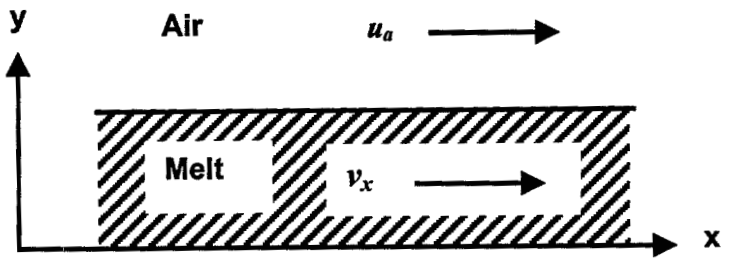

Fig. 14. Geometry of melt removal by the component of wind parallel to the target surface.

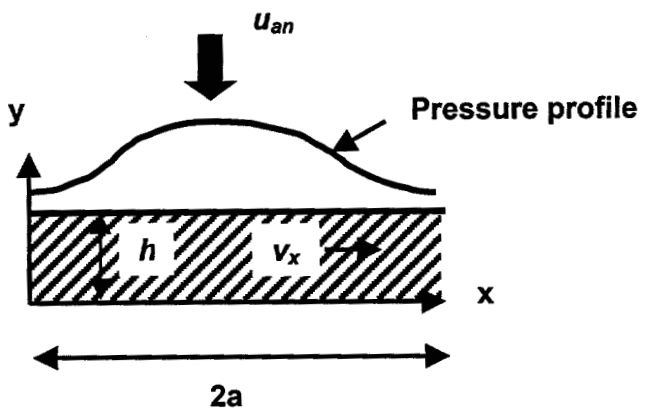

Fig. 15. Geometry of melt removal by the normal component of the wind.

with the factor of 6 roughly accounting for profile effects. This velocity results in melt removal. For Mach 0.9 air blowing on a 1-cm spot of depth 100 μm, the melt removal time is about 1 ms. Vortices in the wind will enhance the melt removal, by increasing the local pressure gradients. Melt removal by the parallel component of the wind is accounted for in an approximate manner in the model. Removal by the perpendicular component has not yet been implemented.

4(c) Cooling by air flow

Again we are dealing with a turbulent air boundary layer, so the considerations are necessarily qualitative. The cooling rate due to the wind is proportional to the difference in surface temperature and air temperature:

$$Q = \gamma\,(T - T_a),$$

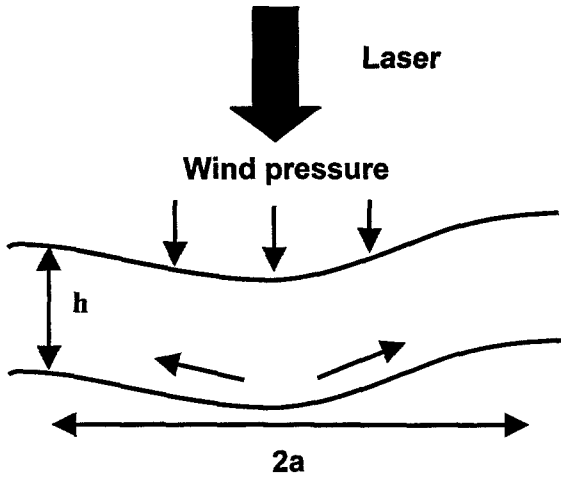

Fig. 16. Breaking of target by wind pressure.

with the heat transfer coefficient γ depending on details of the boundary layer. Wind tunnel experiments give an expression of the form

$$\gamma = \beta(\mathrm{Re})\,\rho_a\,C_{pa}\,u_a,$$

which equals about 0.16 W/(cm^2 K) for Mach 1 air past a spot size of 1 cm. Thus if the surface temperature is 2000 C, the resulting cooling rate is about 0.3 kW/cm^2. This is inconsequential during a pulse, but it can be significant between pulses. This treatment has been implemented in the model.

4(d) Target combustion

Air can support exothermic reactions in steel and aluminum, leading to a dramatic increase in target damage. We defer the discussion of this important effect to the experimental analysis in Section 5. The effect has not yet been implemented in the computational model.

4(e) Breaking of the target prior to melt-through

The additional pressure p from the normal component of wind can break the target before melt-through. For typical targets with a thin metallic skin of thickness h, the back of the skin will be put into tension by pressure on the front (Fig. 16). The important point is that the tensile stress on the back scales with the spot aspect ratio as $T \sim p(a/h)^2$. For a spot size of 1 cm and a thickness of 1 mm, the stress intensification factor is 100. This increases with material removal. The drop in material strength with temperature can then produce breaking before melt-through. Stainless steel, for example, has a tensile strength of about 100 bars at 1000 C. This important effect has not yet been implemented in the computational model.

5. Comparison with experiments involving air flow

We now turn to HELSTF experiments with flow past the face of the coupon at Mach 0.9. First we consider single pulses, having approximate energy 500 J but various spot sizes, on a steel coupon. The resulting fluence is in the range 140-2000 J/cm^2. The mass loss measurements, along with the calculated

Mitigation of Tensile Weld Stresses in Alloy 22 Using Laser Peening

Hao-Lin Chen, Kenneth J. Evans, Lloyd A. Hackel, Jon E. Rankin, Robert M. Yamamoto
Lawrence Livermore National Laboratory

Anne G. Demma, Adrian T. DeWald, Matthew J. Lee, Michael R. Hill
University of California, Davis

SUMMARY

Ensuring the structural integrity of the waste package (WP) closure weld is a major development task in support of the Yucca Mountain Project (YMP). A series of tests were performed at the Lawrence Livermore National Laboratory (LLNL) in cooperation with the University of California, Davis (UC Davis) on Alloy 22 base metal and weld coupons to characterize the effects the Laser Peening (LP) process has on these material configurations.

The test results show that the laser peening process produces peak values of compressive residual stress of several hundred MPa. Residual stress remains compressive to a depth on the order of 5 mm into Alloy 22 parent and weld material. This will significantly improve the material's resistance to stress corrosion cracking. In addition, electrochemical polarization tests show that an Alloy 22 laser peened surface corrodes at a much-reduced rate as compared to an untreated surface.

The development at LLNL of very high-energy pulsed laser systems has allowed the laser peening process to advance from a laboratory tool to a true production equipment status. An initial engineering study has concluded that this laser peening process can be readily deployed in a remote, radioactive environment and be fully compatible with the YMP surface facilities, which includes reliability and operational maintainability requirements. Laser peening times of a few hours per disposal container (DC) can be maintained, commensurate with the operational timeline for the entire closure system.

The Laser Peening System is an industrially viable process. Commercial jet engine components have undergone the laser peening process to increase their operational lifetime several fold. A production system built jointly by LLNL and their industrial partner, Metal Improvement Company (MIC), was put into commercial service in May 2002. This production process has received Federal and Canadian Aviation Administration (FAA and CAA) certification as commercial aircraft utilizing the laser peening process are in use today. Over $120 million in commercial aircraft parts have been treated utilizing laser peening, affecting $6 billion in aircraft and saving $30 million per month in aircraft maintenance costs. Significant cost benefits of this scale are anticipated with the application of laser peening for the Yucca Mountain Project (YMP).

As a consequence of this work, a new method for measuring the cross-sectional residual stresses in the welded Alloy 22 plates was used. The contour method was employed which provides a full two-dimensional cross-sectional map of the residual stress. In addition, the slitting method of measuring residual stresses was also utilized to provide complementary understanding and result verification. Details on both of these stress measurement techniques are included in this report.

INTRODUCTION

The goal of the Yucca Mountain Project (YMP) is safe permanent disposal of high-level nuclear waste. One of the many technical challenges to this plan is the design of the Engineered Barrier System (EBS) including the waste package that will contain the radioactive waste. One potential failure mode of the waste package is stress corrosion cracking (SCC), which occurs when three criteria simultaneously exist. These criteria are a potentially corrosive environment, a material susceptible to SCC, and the presence of tensile residual stresses at the surface of the material. While many design decisions have been made to attempt to minimize the occurrence of the first two conditions, it is necessary to control the third condition, the presence of tensile residual stresses. These stresses occur as a result of a variety of manufacturing techniques, including welding. While most of the residual stresses due to the welding of the waste package can be mitigated through solution heat-treating, the final closure weld, which occurs after the radioactive waste has been placed in the waste package, must be treated to eliminate the presence of tensile residual stress near the surface.

Laser peening is a commercially proven technology that has been shown to create compressive residual stress in both unstressed materials, as well as materials containing tensile surface residual stresses generated by welding. Lawrence Livermore National Laboratory (LLNL) has developed the laser peening process and the associated hardware for use by the YMP. Upon completion of the engineering and testing phases, LLNL will transfer the laser peening technology to U.S. industry and assist the DOE in developing vendors to supply production units to be installed at the YMP facilities.

The overall testing effort is divided into two phases:

Phase I of this project consisted of a study into the effectiveness of laser peening in generating compressive stress in small Alloy 22 (UNS N06022) base metal coupons and converting tensile stress in Alloy 22 welds into compressive residual stress. Particular emphasis was placed on optimization of process parameters to achieve compressive residual stress at greater depths than has currently been demonstrated. The process parameters studied included the laser irradiance (power per area), the laser pulse duration, the number of peening layers, the effect of the ablative layer (described below), and the effect of part thickness. Additionally, the effect of two process parameters, the number of peening layers and the effect of the ablative layer, was evaluated by measuring general corrosion resistance of peened and unpeened Alloy 22 coupons with an electrochemical polarization method. This initial effort ($95,000) was started in August 22, 2002 and completed on September 30, 2002.

Phase II ($70,000) of this project was started on September 14, 2002. Using the parameters determined from the initial phase (and listed in Appendix A), five welded flat plate specimens (three plates, 3/8 inch thick and two plates, 1 inch thick) were laser peened at LLNL. These peened plates, identified as Stress Mitigation Welded Specimens, were shipped to qualified YMP suppliers (Chalk River Neutron Diffraction facility, and Lambda Research Inc.) for residual stress measurements.

This report summarizes technical achievements made in **Phase I.** It is evident from this work that laser peening is a mature technology for YMP to effectively mitigate the potential for stress corrosion cracking in Alloy 22 welds. Upon receipt by Bechtel SAIC (BSC) of **Phase II** data from the qualified suppliers, test results will be analyzed and discussed by LLNL.

METHODS

Laser Peening

Laser peening was performed with LLNL's high-energy, flash lamp pumped, pulsed Nd-glass laser with SBS phase conjugation. The laser system (shown in Figure 1) is a 150 W unit with an output of 25 J/pulse at 6 Hz. This is 25 times the pulse rate of competing technologies suitable for laser peening, which leads to a corresponding decrease in processing time and expense. A laser of similar design is currently being operated (five days per week and 24 hours a day) at Metal Improvement Company's Laser Peening Facility to peen turbine blades for the aerospace industry.

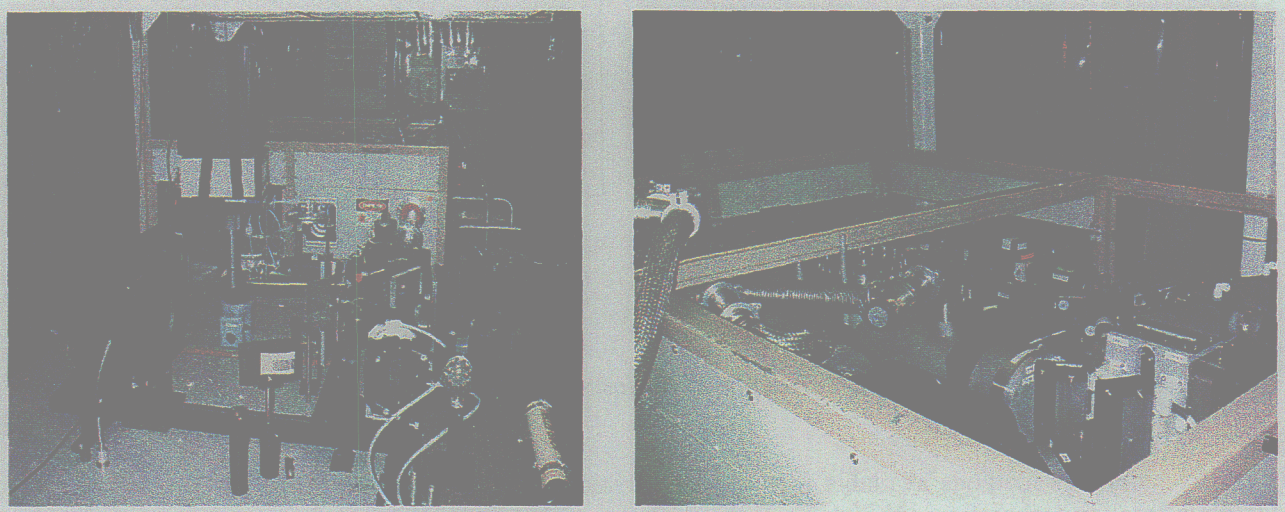

Figure 1: Laser system at Lawrence Livermore National Lab

The following table summarizes the general operating parameters of the LLNL laser peening system:

Table 1: Laser system operating characteristics

Parameter	Variable	Value
Laser pulse energy	**E**	**up to 25 J**
FWHM (full width half maximum) pulse duration	**t**	**20 ± 6 ns**
0-50% rise time	**t_{r50}**	**3 ± 1 ns**
Peening spot shape (laser cross section at target)	**(none)**	**nominally square**
Spot edge dimension	**d**	**2 to 5 mm**
Spot uniformity (energy variation over the central 80% of the spot area)	**m**	**≤ ± 20%**

Laser peening requires only a nominal cleaning and degreasing of the surface to remove residue from fabrication and transport, prior to processing. The process is shown schematically in Figure 2. The surface of the substrate is covered with an ablative layer, typically tape or paint, which serves the dual purpose of providing insulation between the laser pulse and the workpiece, and acts as the material source for plasma generation in the laser peening process. Alternatively, the surface of the workpiece can be ablated directly if desired, eliminating the need for the tape layer. On top of the absorption layer is a thin, inertial layer, typically a laminar fluid flow, transparent to the laser light that acts as a tamper, or as a confinement "cover" for the pressure that will develop. When the laser beam illuminates the surface, it is absorbed and rapidly forms high intensity plasma. The expansion of the plasma is confined by the tamping layer and builds to a pressure of roughly a million pounds per square inch. This high pressure results in a shock wave that travels into the workpiece, straining the material. Since the laser intensity is tailored to create a shock that is above the yield strength of the metal, a permanent compressive residual stress is induced. Thus the process can very effectively convert tensile stresses in the metal to strong and relatively deep

compressive stress. Fundamentally, this is the same process employed by shot peening; laser peening develops stress far deeper into the part than shot peening however, while causing less surface damage.

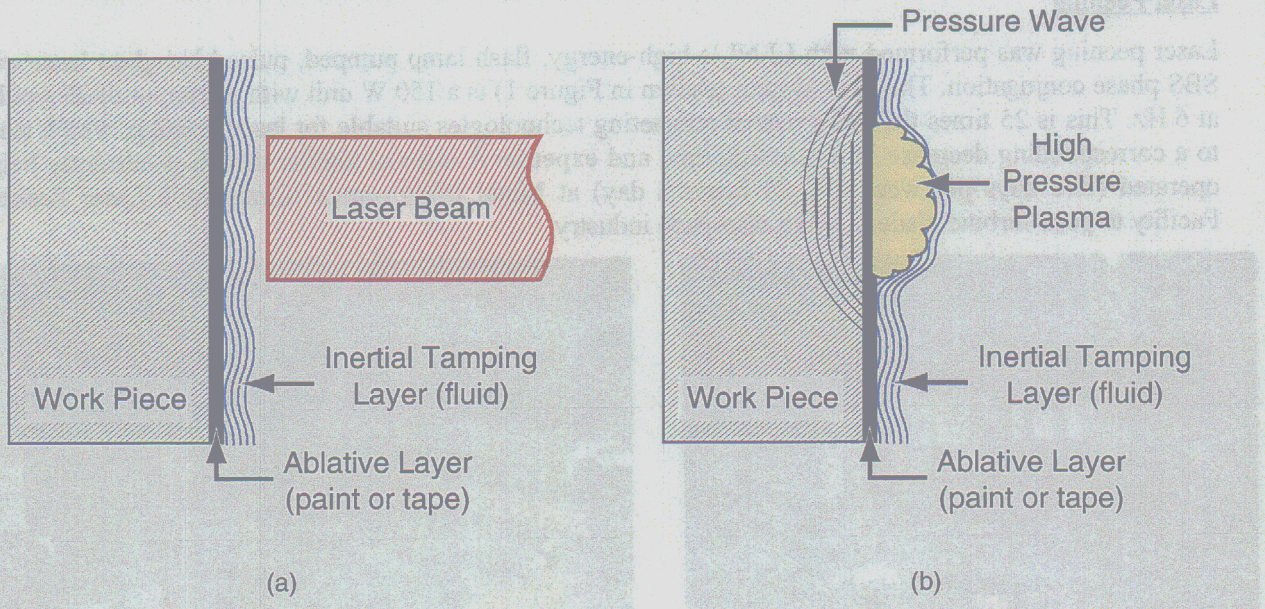

Figure 2: Schematic of the laser peening process

Measurement of Residual Stresses

There are numerous methods available for measuring residual stress in metals. Some of these methods include diffraction techniques, either using x-ray or neutron sources, or physical measurements of strain, including the slitting, contour, ring core or hole drilling methods. LLNL does not have the capability to readily make these measurements on site. TEC Materials Testing Laboratory (TEC) was contracted to perform residual stress measurements using the x-ray diffraction (XRD) technique. The XRD results showed a large amount of scatter that may be caused by the large and non-uniform grain structure of Alloy 22. Additional attempts were made to measure the stress profile (through the depth) of laser peened Alloy 22 coupons using mechanical methods. Dr. Michael R. Hill and his students (from the University of California, Davis) used the slitting and the contour methods to measure these residual stress profiles. These methods are summarized below, and discussed in more detail in Appendix B.

X-ray diffraction: Residual stress measurements were made by TEC on Bragg-Brentano geometry diffractometers, with the data collected by step scanning using computer controlled diffractometers instrumented with scintillation or solid state Si (Li) detector systems to eliminate background fluorescence. The macroscopic residual stresses are then calculated from the strain measured in the crystal lattice by employing x-ray elastic constants determined empirically. Residual stress measurements on Alloy 22 coupons were made at the surface and several depths beneath the surface. The various depths are exposed by electropolishing techniques. X-ray diffraction data obtained as a function of depth are then corrected for the influence of the penetration of the radiation into the subsurface stress gradient. The residual stress calculated at each depth beneath the surface of the sample is corrected for stress relaxation due to the removal of stressed material by electropolishing.

Microhardness measurements: Another possible method for estimating the depth of residual stress in treated components is through the measurement of the material hardness. Vickers microhardness scans were performed at LLNL on a LECO 400-G3 hardness tester through the depth of the part on a surface cut by wire electric discharge machining (EDM), and subsequently polished. This method does not quantify residual stress but is assumed to act as an indicator of cold work. Comparing the relative depth of

cold work between coupons is then assumed to represent the relative depth of residual stress. The orientation of the hardness scan relative to the part is shown in the following figure.

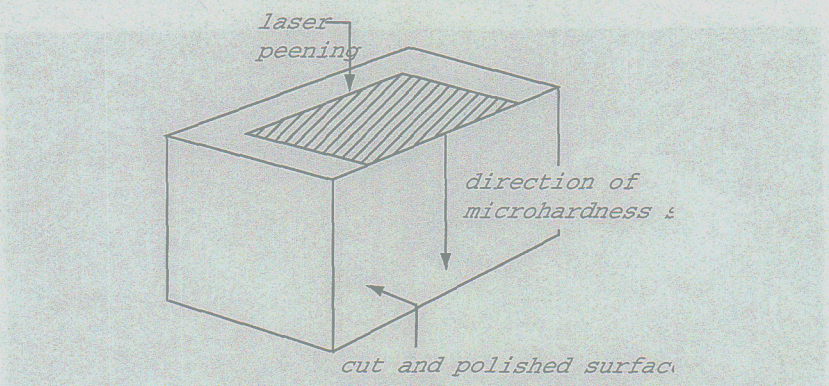

Figure 3: Schematic of microhardness measurements

Slitting method: The general procedure for slitting (also called the crack compliance method) (Prime, 1999) is to gradually extend a slit into the specimen surface and measure near-slit strain as a function of slit depth. Strain due to slitting is measured using metallic foil gages placed near the slit and the slits are cut using wire EDM. Strain versus slit depth data are then input to an inverse elastic analysis to compute the variation of pre-slit residual stress with depth from the surface (i.e., the stress profile). The method assumes elasticity and an invariant stress distribution along the axis of the slit (both valid for these measurements), and provides a one-dimensional, through thickness measurement of the residual stress present in the body, prior to the slitting experiment. Please refer to the attachment in Appendix B for a complete description of the slitting method (Hill, 2002).

Contour method: In this method, the component of interest is cut in two using wire EDM. Following cutting, the cut surfaces on each of the two halves of the part are measured (typically with a coordinate measuring machine) to determine the surface profile normal to the cut. The original residual stresses are then calculated from the measured surface contour using a straightforward finite element model. The elastic material properties of Alloy 22 were required for the calculation and these were assumed to be $E = 207$ GPa and $\nu = 0.3$ (as found in the Hastelloy 22 product information pamphlet). The contour method is a powerful tool for measuring residual stresses in welds, since it provides a two dimensional map of the stress component normal to the cutting plane. While it does assume elastic response, it allows for stress variation along both directions within the cutting plane. Please refer to the attachment in Appendix B for a complete description of the contour method (Prime, 2001).

The x-ray diffraction method was primarily used to measure the residual stress on the surface of Alloy 22 samples, where the mechanical release methods have limited capability. Slitting and surface contour methods were used selectively to determine the residual stress profile (in depth) beneath the surface of base metal and welded samples.

Alloy 22 Weldment Coupons

The effects of laser peening were evaluated in actual Alloy 22 weldments using samples fabricated from a butt-welded 33 mm (1.3 inch) thick Alloy 22 plate, D-22 (HT 059902CL1, welded by Framatome Technologies Inc.). The initial plate was approximately 813 mm (32 inch) long (longitudinal) and 201 mm (7.9 inch) across (transverse). This plate was cut into four 190 mm (7.5 inch) long, full-width samples, and two of these were used in this work

Laser peening was applied to one surface of one sample. The peened region was centered on the weld and was 76 mm (3 inch) long and 100 mm (4 inch) wide. A picture of half of each sample is shown in Figure 4, after cutting in half, as required by the contour method. The cutting of the specimens was performed on a Sodick AQ325L linear motor driven wire EDM by a commercial vendor, and

measurement of the cut surfaces was performed on a high-precision Leitz PMM 12106 coordinate measuring machine (CMM) at LLNL. A complete description of the contour method is given in Appendix B.

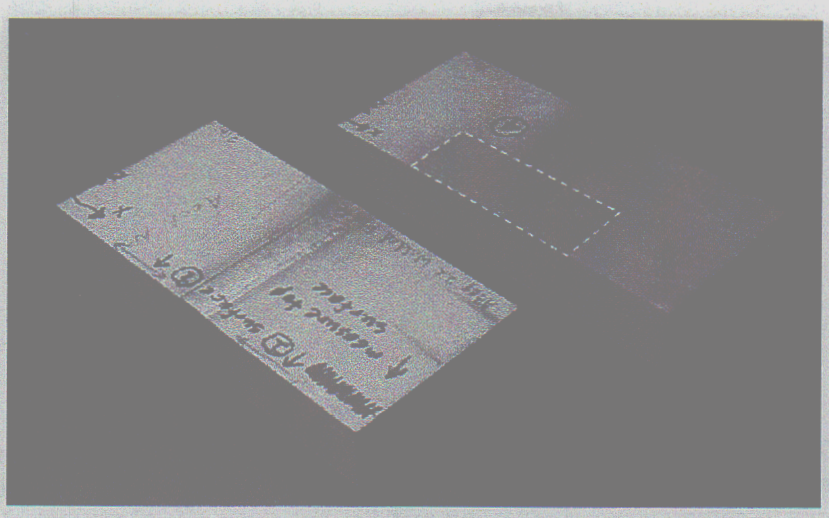

Figure 4: Unpeened (left) and laser peened (right) samples following sectioning required by the contour method (the peened region is rectangular and is indicated by a dashed line).

Alloy 22 Base Metal Coupons

A parametric study of laser peening residual stresses as a function of several process parameters was performed in Alloy 22 base metal specimens. The baseline method for measurement of residual stresses in this study was the slitting method; comparison measurements of through thickness residual stress profile, along with measurements of surface residual stress for a number of laser peening conditions were made with x-ray diffraction. Additionally, microhardness measurements were made on three coupons previously measured with slitting, to determine the value of the microhardness technique.

There are numerous parameters that play a role in determining the residual stress state in a laser peened material. In this study, the following parameters were investigated:

- Laser irradiance (power per area)
  - 13.5 mm thick coupons were treated with irradiances of 7 and 10 GW/cm^2;
- Number of peening layers
  - 9.5 mm thick coupons were treated with 2, 5, and 10 layers of peening
  - 20.8 mm thick coupons were treated with 10 and 20 layers of peening;
- Effect of a backing plate, which is typically used to support relatively thin coupons during laser peening
  - 9.5 mm thick coupons were treated with and without a backing plate
- Effect of the ablative layer:
  - Peening was applied to a 13.5 mm thick coupon with the standard aluminum tape ablative layer applied between each layer of peening
  - Peening was applied to a 13.5 mm thick coupon without aluminum tape (coupon surface is ablated directly) for 10 layers, followed by two additional layers with normal aluminum tape ablative layer
  - Peening was applied to a 13.5 mm thick coupon without aluminum tape for 12 layers

Corrosion Testing

Electrochemical polarization tests were carried out in a Simulated Acidified Water (SAW) solution at a nominal temperature of 90°C and pH of 2.7. Tests were performed on Alloy 22 base metal specimens with 2, 4, and 10 layers of laser peening, along with corresponding control coupons polished at the same time, but with no laser peening. De-aeration with pre-purified N_2 was performed 1-hour prior to testing as well as throughout the test at a flow rate of 100 cc/min. Scan rates were maintained to the ASTM standard value of 0.1667 mV/s.

RESULTS

Alloy 22 Weldment Coupons

The following contour plot of the longitudinal component of residual stress in the unpeened sample shows typical trends for a double-sided butt weld (Figure 5a). Tensile stresses at the weld center are largest just below the weld surface and are smallest at the mid-thickness. Residual stresses on the top and bottom weld surfaces are tensile at the weld center and gradually become compressive outside the weld bead. The maximum tensile stress is similar to reported values of the tensile yield strength of Alloy 22 plate.

A contour plot of residual stress in the laser peened sample shows a region of large and uniform compressive stress within the peened area (Figure 5b). Outside the peened area, residual stresses are similar to those in the unpeened sample.

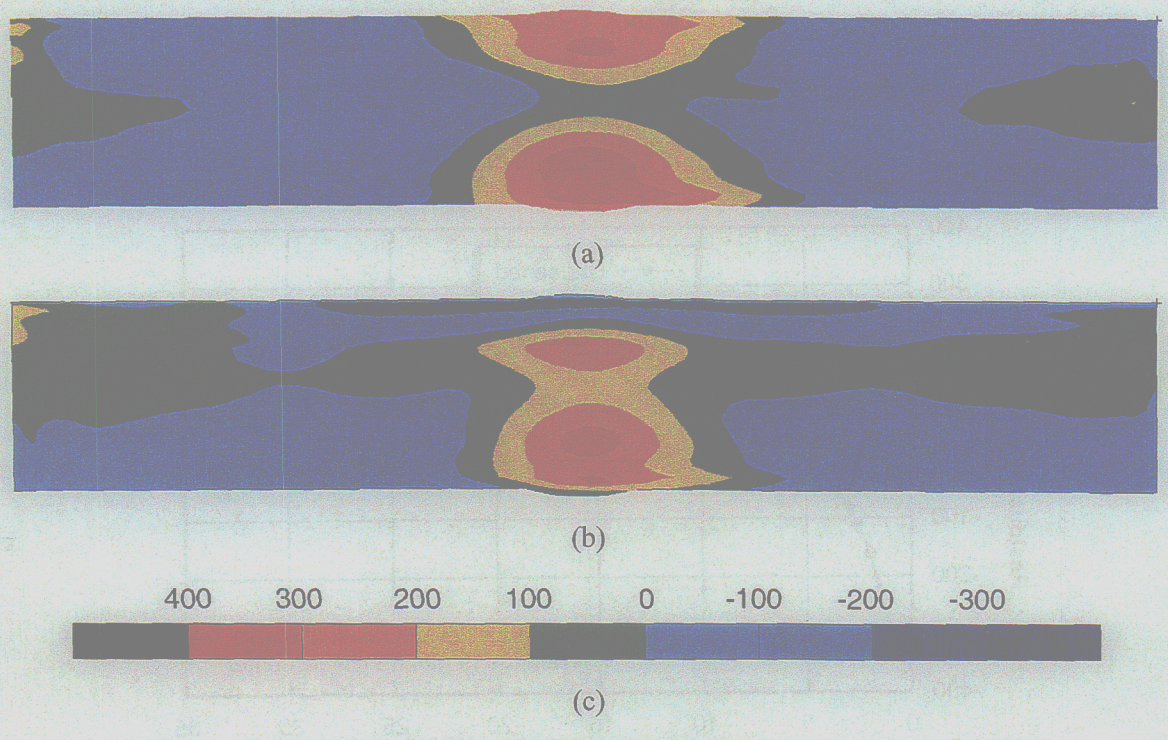

Figure 5: (a) Longitudinal component of residual stress present in the weld before laser peening, (b) Longitudinal component of residual stress present in the weld after laser peening surface treatment (laser peened surface is on the top of the figure), (c) Color map for residual stress magnitude (MPa)

Line plots of longitudinal residual stress versus depth from the surface more precisely illustrate residual stress in the unpeened weld and the effect of peening (Figure 6 through Figure 8). Line plots were prepared at three locations in the weld: at the center of the weld bead (Figure 6), at the right weld toe (Figure 7), and outside of the welded region (30 mm (1.2 inch) from the weld center, Figure 8). These

plots clearly show the effect of laser peening, and indicate that it produces deep compressive stress in both weld and base metals and at the geometrically discontinuous weld toe.

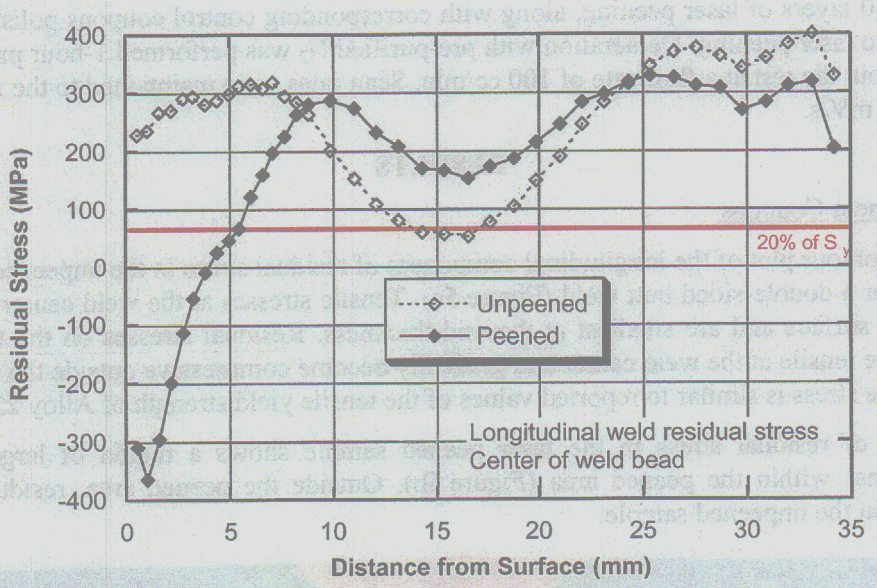

Figure 6: Longitudinal component of residual stress at the center of the weld bead with and without laser peening

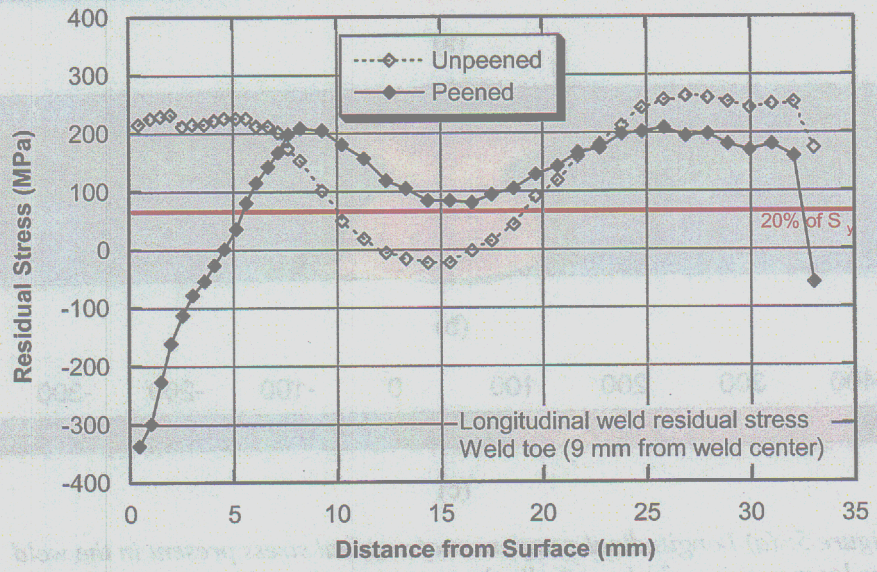

Figure 7: Longitudinal component of residual stress at the right weld toe, with and without laser peening

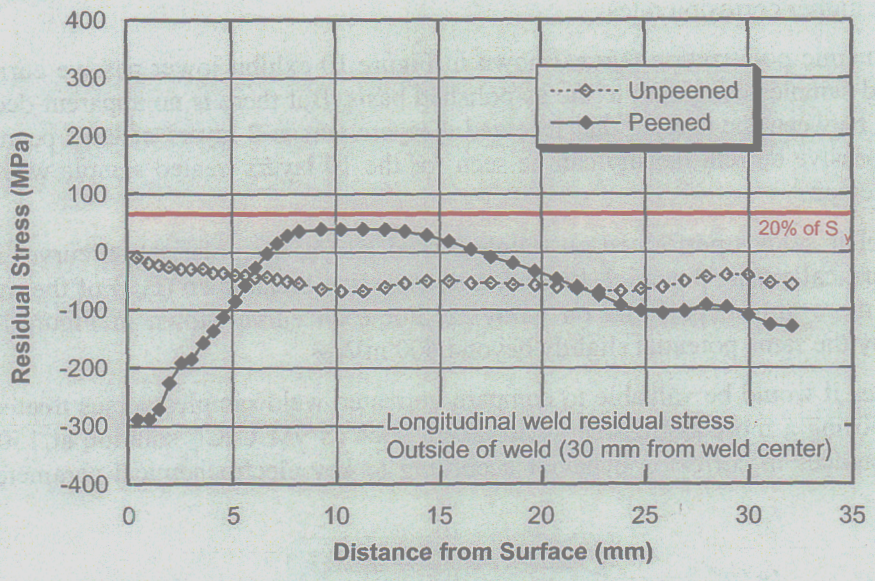

Figure 8: Longitudinal component of residual stress outside the weld region (30 mm from the weld center) with and without laser peening

Corrosion Testing

Electrochemical polarization results thus far have shown an increase in corrosion resistance for laser-peened Alloy 22 base metal samples relative to their untreated counterparts. This increase in corrosion resistance can be assessed according to a lower average corrosion rate obtained using the polarization resistance method. Figure 9 is a comparison of average corrosion rates of various Alloy 22 sample types exposed to a Simulated Acidified Water (SAW) medium at 90°C. In each case 1 hour of open circuit monitoring occurred before polarization resistance experiments were carried out. The number to the far right in parentheses refers to the quantity of trials performed on each sample type. The values shown in Figure 9 should not be perceived as absolute corrosion rates but rather relative values to provide a means of comparison.

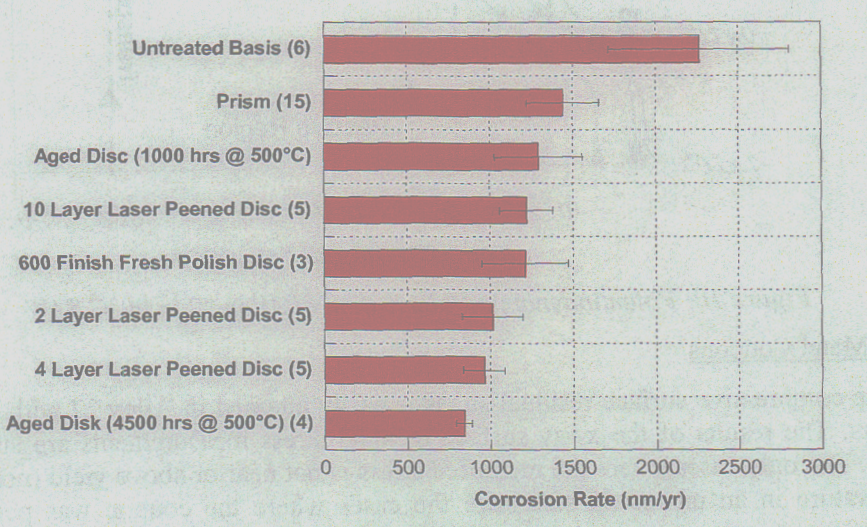

Figure 9: Average Corrosion Rates obtained for Alloy 22 in 90°C SAW

According to Figure 9 average corrosion rate values are approximately the same for the 2 layer, 4 layer, and 10 layer laser peened surfaces. But in general, average corrosion rates for the untreated basis used in this study show higher corrosion rates.

The potentiodynamic polarization curves shown in Figure 10 exhibit lower passive current densities for the laser-peened samples compared to the as polished basis. But there is no apparent decrease in passive current density between the sample that received 4 layers versus 2 layers of laser peening. However, a slightly lower passive current density can be seen for the 10 layers treated sample when examining the active-passive region.

Contrary to similar studies performed on stainless steel alloys, the polarization curves in Figure 10 are devoid of any critical pitting potential. Instead, a transpassive breakdown (E_{crit}) of the metal is the result of imposing a more anodic potential on Alloy 22. For each curve shown in Figure 10 transpassivity occurs at roughly the same potential slightly beyond 600 mV_{SSC}.

For future studies it would be valuable to compare untreated weld samples versus treated weld samples. In addition, choosing a more aggressive environment such as 9M $CaCl_2$ solution at 150°C may exhibit significant differences in corrosion behavior according to key electrochemical parameters such as E_{corr} and E_{crit}.

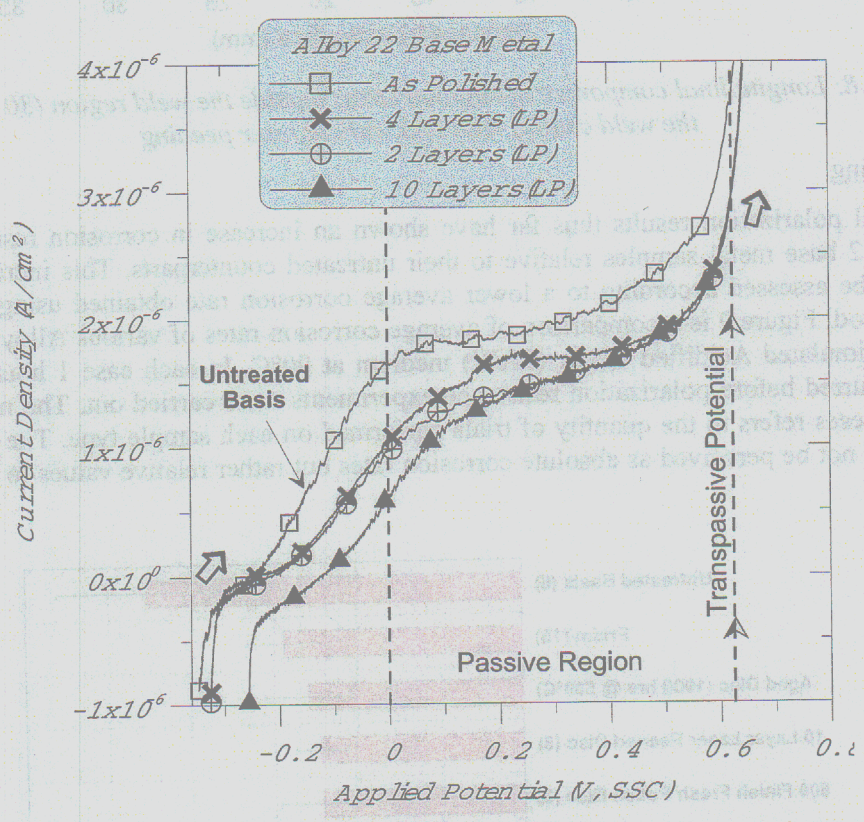

Figure 10: Potentiodynamic Polarization of Alloy 22 in 90°C SAW

Alloy 22 Base Metal Coupons

High magnitude compressive surface residual stress is easily attained in Alloy 22 with a wide variety of laser parameters. The results of the x-ray surface residual stress measurements are summarized in the following table. The only cases where the measured stress is not near or above yield (nominally 372 MPa at room temperature in an unworked state) are the cases where the coupon was peened without the ablative layer of tape (explained further below). Note that the magnitude of the surface stress is not the

most important criteria for this application; it is more desirable that the residual stress extends deep into the part.

Table 2: Surface residual stress measurements by x-ray diffraction

Treatment	First X-ray Surface Residual Stress Measurement (MPa)	Second X-ray Surface Residual Stress Measurement (MPa)
15 ns, 12 GW/cm^2, 1 layer	**-360±26**	**N/A**
15 ns, 12 GW/cm^2, 2 layers	**-430±30**	**N/A**
15 ns, 12 GW/cm^2, 3 layers	**-430±30**	**N/A**
15 ns, 12 GW/cm^2, 4 layers	**-430±30**	**N/A**
25 ns, 10 GW/cm^2, 10 layers	**-372±20**	**N/A**
25 ns, 10 GW/cm^2, 10 layers without tape, followed by 2 layers with tape	**-377±21.5**	**-179±18.3**
25 ns, 10 GW/cm^2, 12 layers without tape	**-23±15.9**	**-107±16.1**

The residual stress profiles presented in Figure 11 through Figure 15 were measured using the slitting method. Figure 11 shows the effect of laser irradiance on the residual stress state generated by laser peening. The surface residual stresses are comparable for both values of laser irradiance investigated, but treatment with 10 GW/cm^2 drives residual stress to approximately 3 mm, or about 50% deeper than 7 GW/cm^2. More data are currently being collected for coupons peened with 7, 10, and 13 GW/cm^2, with consistent laser spot size and pulse lengths to obtain a more complete data set.

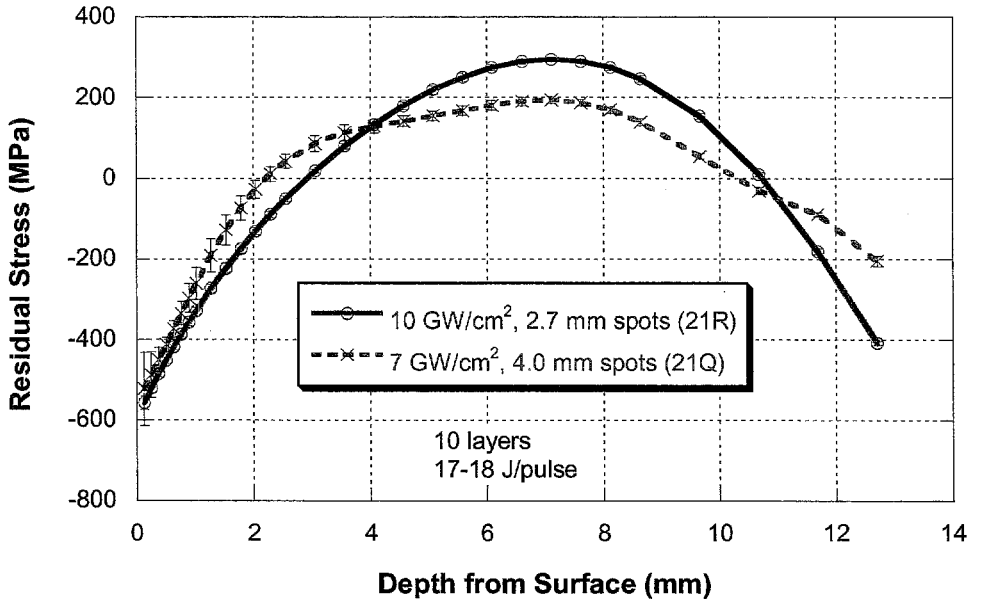

Figure 11: Residual stress versus depth as both spot size, and irradiance (power per area) are varied in 13.5 mm coupons

The interaction between the number of peening layers and the residual stress profile is under continuing investigation. Additional measurements of residual stress with 2 and 4 layers of peening will be made in 20.8 mm thick coupons to evaluate and compare the effect of the number of peening layers in a single specimen geometry. The current results indicate that in thin coupons (approximately 9 mm thick) residual stresses do not increase significantly in magnitude by increasing the number of peening layers (Figure 12). Likewise, the increase in residual stress magnitude in 20.8 mm coupons (Figure 13) is small when the number of peening layers is increased from 10 to 20.

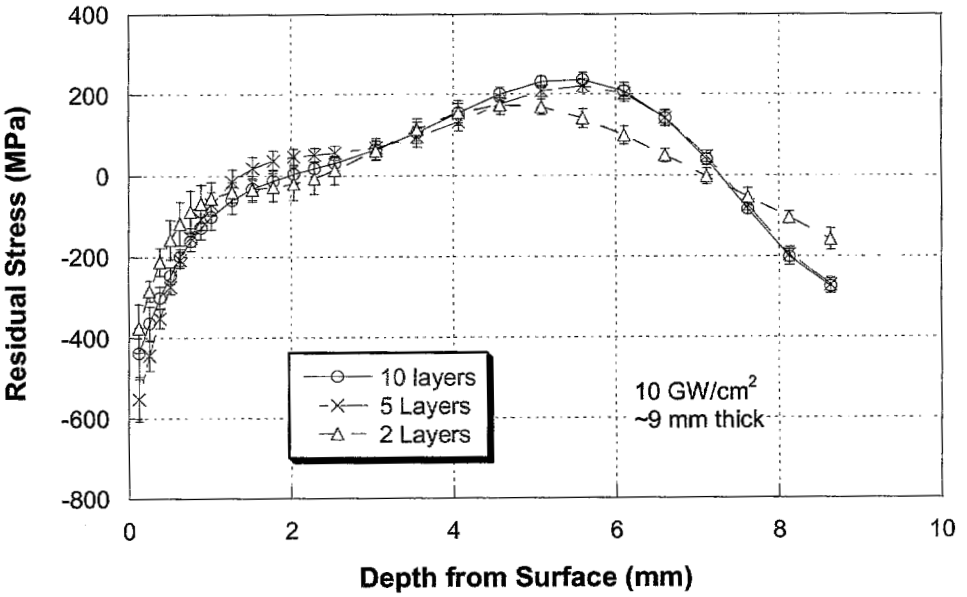

Figure 12: Residual stress versus depth as a function of number of peening layers in 9 mm coupons

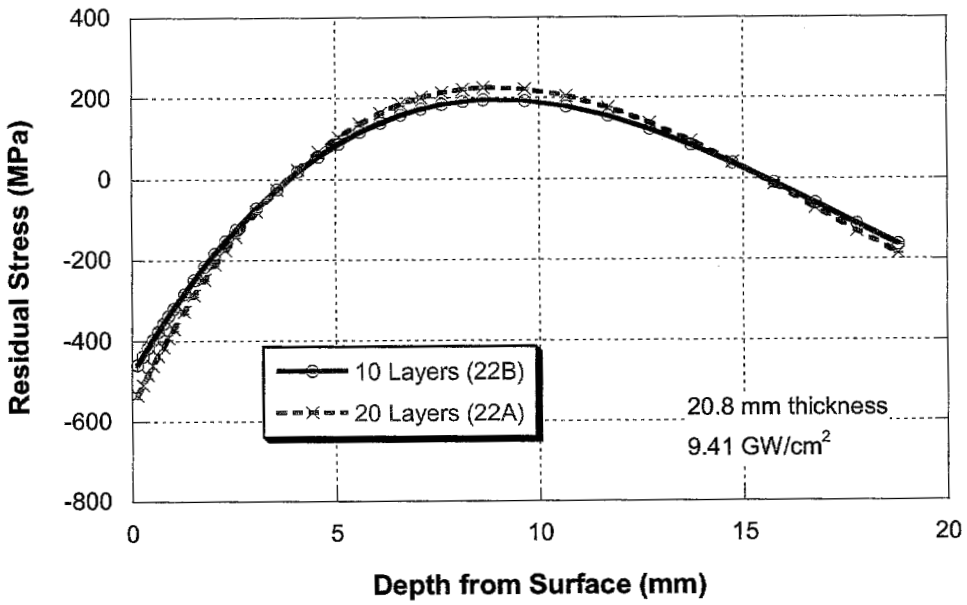

Figure 13: Residual stress versus depth as a function of number of peening layers in 20.8 mm coupons

The stress profile when the ablative tape layer is used only on the last two layers is not significantly different from the normal peening, where tape is used on every layer (Figure 14). Peening without taping between each layer would represent a significant savings in processing time, therefore cost. Peening without taping at any time results in a lower magnitude stress near the surface, although still compressive. The through depth residual stress measurements by the slitting method were augmented by surface stress measurements by x-ray diffraction method, the results of which are listed in Table 2. While the values of residual stress are lower in magnitude for coupons processed without an ablative coating between each layer of peening, they do remain compressive. When tape is used on the last two layers, the surface stress is approximately the same as for normal peening.

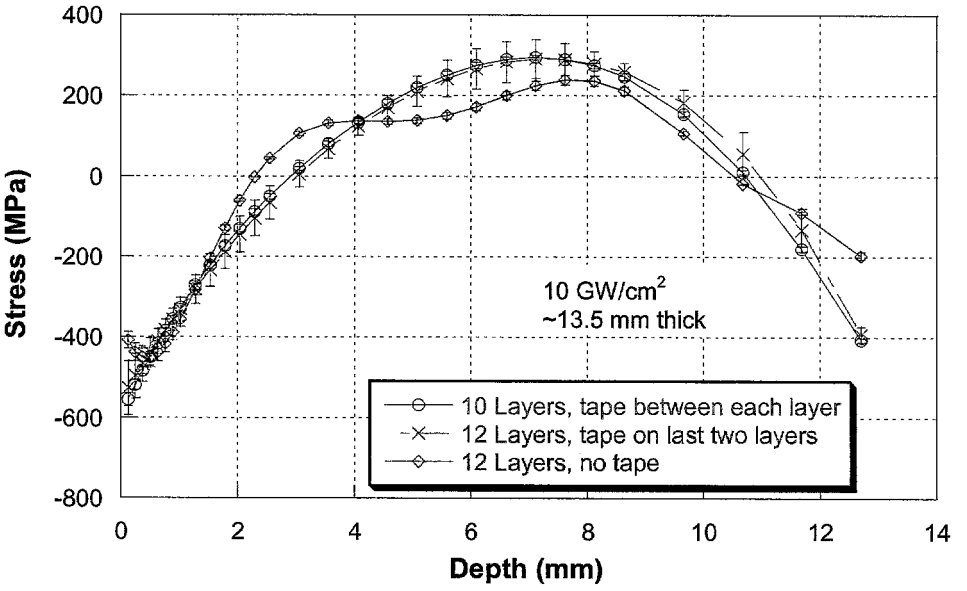

Figure 14: Residual stress as a function of depth with different protocols in applying the ablative layer

The presence of a backing plate does appear to play a significant role in the final residual stress state in thin coupons. While the surface stress is higher in magnitude without a backing plate, compressive stress reaches a slightly greater depth when a backing plate is used (Figure 15). While research is continuing to quantify this effect, this result agrees with the findings regarding depth of residual stress as a function of coupon thickness, which is discussed below.

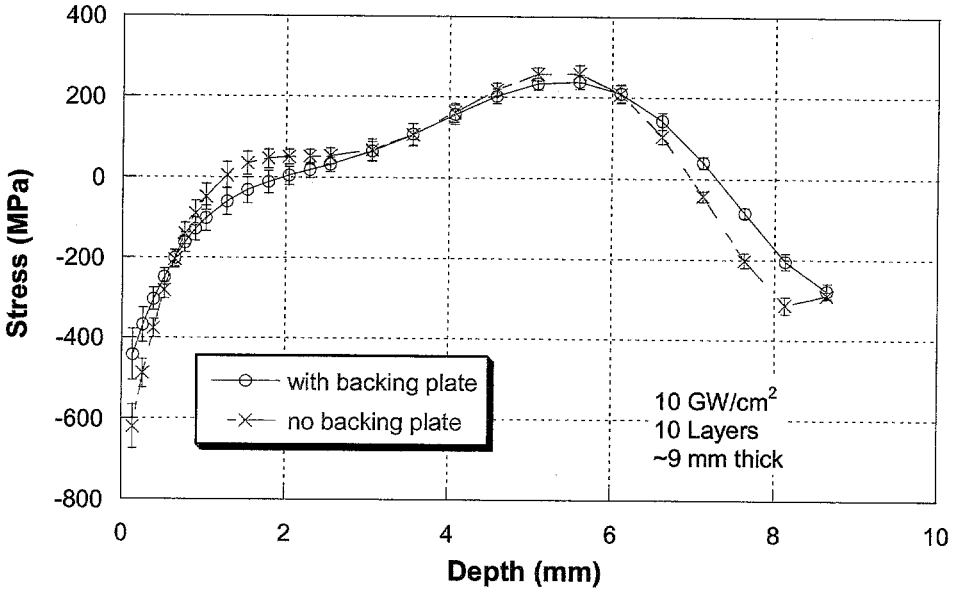

Figure 15: Residual stress as a function of depth for parts processed with and without the support of a backing block

Comparison of Residual Stress Measurement Methods

Measurements of residual stress as a function of depth performed using x-ray diffraction and layer removal provided data from which no conclusions could be drawn (Figure 16). There is no identifiable relationship between the number of peening layers and the resultant residual stress, nor do the results provided by x-ray diffraction seem physically plausible.

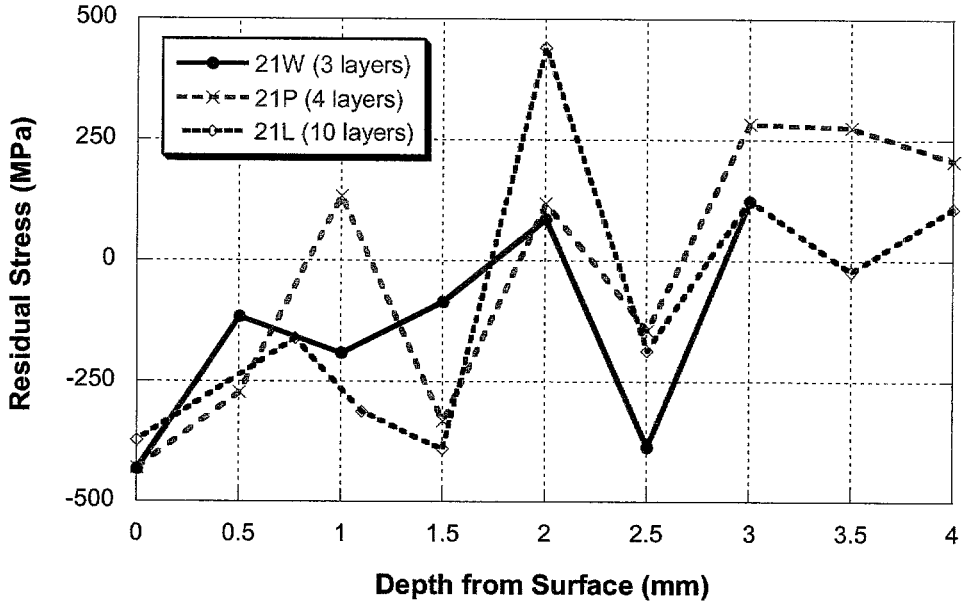

Figure 16: Residual stress as a function of depth for different numbers of peening layers, measured with x-ray diffraction

A direct comparison of the residual stress data measured by x-ray diffraction and slitting methods suggests that there is less inherent error in this application when using the slitting method (Figure 17). Measurements were made on two identically prepared coupons with the two methods. It is evident that the data from the slitting method pass through the trend of the x-ray data, and provide a more reasonable stress result. Additionally, slitting provides a residual stress record through nearly the entire thickness of the part, which would be costly and time consuming to attempt with x-ray diffraction.

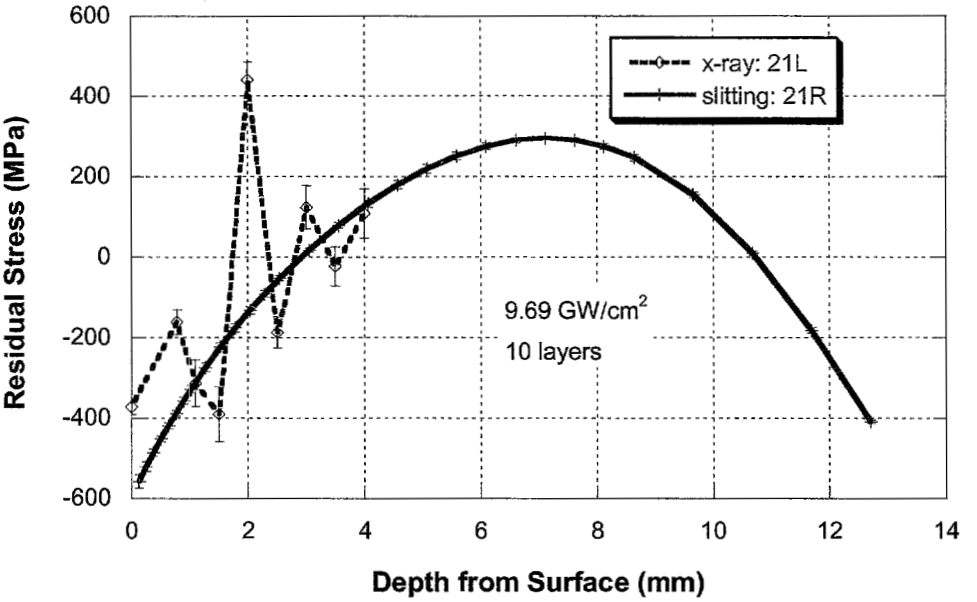

Figure 17: Residual stress with depth as measured by the slitting method and x-ray diffraction

Microhardness scans were performed through the depth on the cut and polished surfaces of three laser peened coupons (Figure 18). There is a significant hardness elevation through the first 2.5 mm in all three coupon thicknesses. The hardness continues to drop through approximately 9 mm in the thinner, 14 mm coupon; in the 20 mm coupons, the hardness appears to drop through the entire measurement depth. The unsmooth variations present in the data, along with the fact that the technique does not provide a measurement of residual stress, reduce the efficacy of this method for inspecting processed Alloy 22 coupons. For reference, results from the slitting method indicate that compressive residual stress extended to approximately 4 mm in the 20 mm thick coupons, and to approximately 3 mm in the 14 mm coupon.

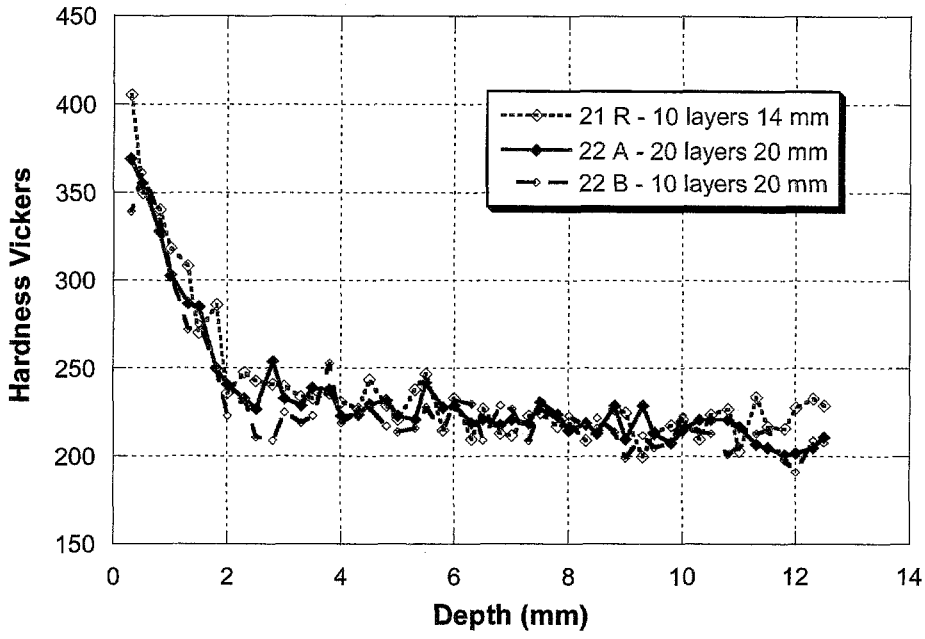

Figure 18: Microhardness traverses in three laser peened coupons

DISCUSSION

Alloy 22 Weldment Coupons

The depths of compressive stress in the laser peened samples were quantified from the line plots of residual stress versus depth measured with the contour method. Depth of compressive stress was determined in two ways, from both the depth at zero residual stress and the depth at a tensile stress equal to 20% yield strength. The yield strength of the welded material was assumed to be 372 MPa (54 ksi), which is the room temperature yield strength in un-welded plate, as reported by a material vendor (found in the Hastelloy 22 product information pamphlet). The depths of compressive residual stress in the peened weld, from each of the depth definitions and at each position where a line plot was prepared, are given in Table 3.

Table 3: Summary information on depth of compressive stress

Location	Zero crossing (mm)	20% yield crossing (mm)
Weld bead center	**4.0**	**5.6**
Weld bead toe	**4.6**	**5.7**
Outside of weld region	**6.8**	**Does not exceed**

The line plots also illustrate an expected trend that indicates consistency between the two residual stress measurements. Since the two welded samples were removed from the same long weld, and the weld was likely prepared by welding continuously along the length, the two samples should have contained the same residual stresses before peening. Further, the earlier small coupon residual stress measurements suggest that the laser peening process employed does not plastically deform material more than 15 mm from the peened surface. Therefore, stresses more than 15 mm from the peened surface should be similar in the unpeened and peened welds. Considering the equilibrium conditions of elasticity theory, peening residual stress is equilibrated by uniform tension and bending across the thickness of the welded plate. It

should therefore be expected that residual stresses in the unpeened and peened welds, at distances more than 15 mm from the peened surface, should differ by only a linear function with depth. This trend is evident in Figure 6 through Figure 8, and is quite clear when the difference in residual stress between peened and unpeened samples is plotted.

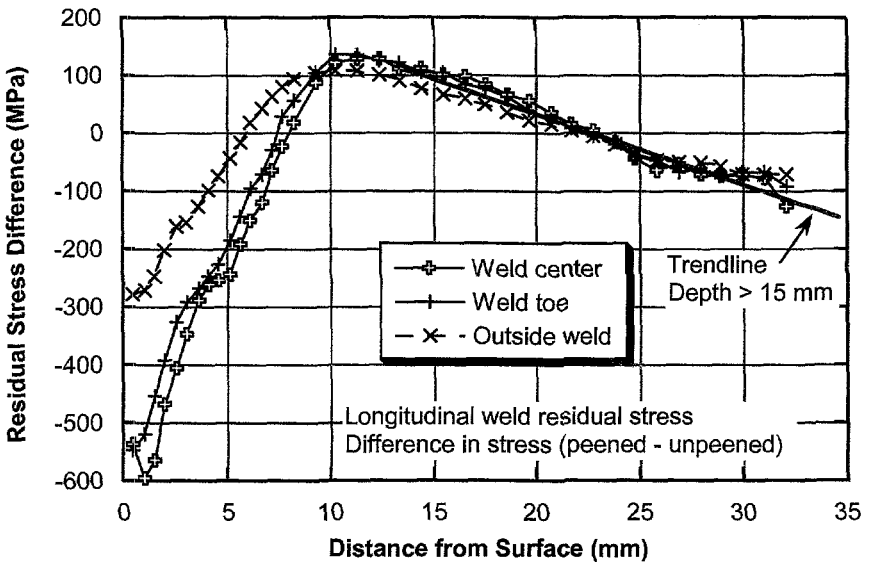

Figure 19: Difference between the longitudinal component of residual stress in laser peened and unpeened weld samples, at various positions transverse to the weld

The change in stress between the peened and unpeened coupons (as shown in Figure 19) also indicate that laser peening has a larger effect in regions of initially tensile weld residual stress. This may be due to the effect of initial tensile weld residual stress on the mechanism of plastic deformation induced by laser peening, or by a limit to the maximum level of compressive stress that can be introduced by laser peening. The latter possibility is supported by the fact that the maximum compressive residual stresses in Figure 6 through Figure 8 are nearly equal.

Corrosion Testing

Decreasing the general corrosion rate of Alloy 22 is a very favorable effect of the laser peening process. Models of the corrosion of YMP waste packages suggest that up to 5 mm of the waste package surface could be removed by general corrosion over the design life of 10,000 years (Farmer, 2000). To mitigate the potential for SCC, the compressive residual stress generated by laser peening must be deep enough to ensure that the new, exposed surface remains in a state of compressive stress, even after thousands of years of general corrosion. If the general corrosion rate is slowed dramatically, 5 mm of compressive residual stress will mitigate the potential for SCC for a significantly longer time.

Alloy 22 Base Metal Coupons

The results of the slitting method measurements in specimens of various thickness show that the depth of compressive residual stress is directly affected by the thickness of the coupon undergoing laser peening. Since the stresses in an unloaded part must exist in equilibrium, tensile stress must occur inside the part, to balance the compressive stress induced by laser peening. Laser peening can attain deeper residual stresses in a thick section than in a relatively thinner one. This is demonstrated in the figure below, which plots the depth of compressive residual stress, quantified as the point where the measured stress profile passes through zero stress, versus four different specimen thicknesses investigated (note that for the

fourth point, the depth of residual stress is reduced to 6 mm from 6.8 listed in Table 3; the material was in a state of compressive stress prior to peening because of the welding process. At a depth of 6 mm, the residual stress after peening is equal to the level present prior to peening). All the specimens shown were peened with the same laser parameters. The trend is close to linear through all the specimen sizes, indicating that the attainable depth of residual stress is driven by part geometry, as well as the surface treatment.

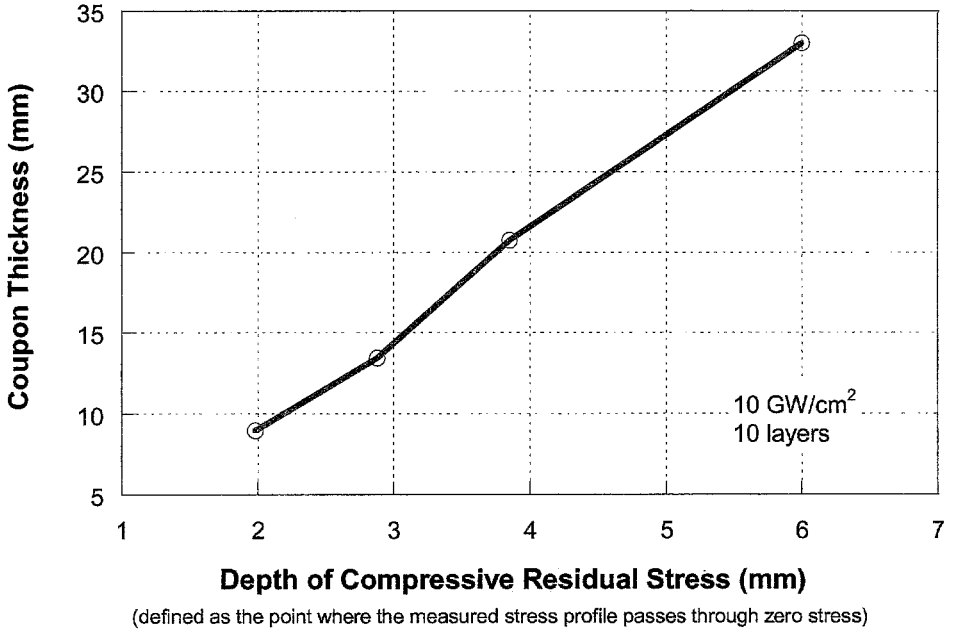

Figure 20: Depth of compressive residual stress as a function of coupon thickness

Understanding this result is critical; the attainable depth of residual stress relies heavily on the thickness and geometry of the part undergoing laser peening. It is very challenging to drive compressive residual stress through more than a quarter of a simple plate thickness, since a substantial portion of the cross section is required to react the effects of the compressive residual stress introduced by laser peening. In a geometry like the stress mitigation welded coupons, where a relatively thin plate is supported by sizable welded backing structure, deeper compressive residual stresses could be achieved in a similar plate thickness; the backing structure will increase the effective cross sectional area, thereby increasing the depth of compressive residual stress that can be supported. Note that in the current waste package design, the outer lid will be 25 mm thick (Plinski, 2001). From Figure 20, the current laser peening settings should be able to generate compressive residual stress to a depth of close to 5 mm, or perhaps greater because the outer lid is supported by substantial material.

Comparison of Residual Stress Measurement Methods

Of the four methods used to quantify the depth extent of residual stress in both Alloy 22 weldments and base metal coupons, the mechanical release methods, the slitting and contour methods, provide the most satisfactory results. These methods use equipment commonly available in precision machine shops and yield powerful data with relatively little expense. Release methods are particularly effective in this application, since diffraction methods are difficult to implement in welds due to microstructural variations between the weld and parent material. X-ray diffraction does provide data for surface residual stresses that can't be measured with the release methods; however, the principal figure of merit for a residual stress state for this application is depth of residual stress, rather than surface level. As shown in Figure 17, x-ray did not provide reasonable results for this measurement. The fourth method used in this work, the

microhardness technique, makes the broad assumption that hardness can be related directly to the residual stress state, which is not the case. Approximations of the total depth of plasticity from the microhardness data (the depth where the microhardness plateaus) do correlate with estimates of depth of plasticity based on the residual stress profile, as discussed above in reference to Alloy 22 weldments.

CONCEPTS FOR DEPLOYMENT OF LASER PEENING AT YUCCA MOUNTAIN

The Laser Peening System can commence operation after conclusion of the GTAW (Gas Tungsten Arc Welding) of the closure lid to the Disposal Container (DC). This would include completion of the weld surface examination/volumetric inspection (SE/VI) (Knapp, 2001). All Laser Peening operations would be conducted at the Surface Facilities and are an integral part of the Closure Cell Control System.

The Laser Peening System is divided into three main parts: the laser system, the laser transport system and the laser beam control/scanning system. The following will describe each of the three subsystems that comprise the Laser Peening System.

Laser System

The laser system is a system of optics, amplifiers, electronics and ancillary equipment all designed and integrated to produce a high quality, high reliability laser beam. Figure 1 provides photos of such a system currently working at Lawrence Livermore National Laboratory (LLNL). A typical laser system would be enclosed is a Class 1000 clean room, temperature controlled to ± 2 degrees C, and include additional subsystems such as a chilled water circulation system, a pulse forming network system, power supplies and a dedicated control system.

The laser system utilizes many standard "off the shelf" components to maximize system reliability, providing a cost efficient package without sacrificing system performance. The majority of the laser system components reside on an optical table, exhibiting a footprint on the order of a few office desks placed side by side. The entire laser system is stationary and can be easily accessed for any routine maintenance that may be required since it is not located in the hot cell area. Lawrence Livermore National Laboratory has deployed several of these laser systems which have demonstrated their robust design and high reliability.

An example of such a laser system is one presently in use by the Metal Improvement Company (MIC). LLNL and MIC have established a Cooperative Research and Development Agreement (CRADA) with one another that utilizes the laser peening process to significantly extend the lifetime of turbine blades used on large commercial aircraft. This system was put into commercial service in May 2002 and has treated over $120 million in commercial aircraft parts, affecting $6 billion in aircraft and producing a savings of $30 million per month in maintenance costs. In addition, this laser peening process has received Federal and Canadian Aviation Administration (FAA & CAA) certification.

The type of laser described above is a flashlamp pumped laser. This is the baseline laser type that would be used for the laser peening process at Yucca Mountain. Nominal laser peening process parameters are shown in Table 1. No technical development work of the laser peening process is required of the flashlamp pumped laser system to support the activities that feed directly into the YMP license application. Several baseline engineering activities would help support the optimization of the laser peening process for Alloy 22 welds and waste package performance. This engineering work would help support the license application and would include the following:

- Determine the laser peening parameters that would be required to induce the appropriate level of compressive residual stress in the Alloy 22 closure weld to meet the required waste package performance
    1. Determine the stress distribution inside the weld, at the weld boundary and at the heat affected zone; optimize the laser peening power and number of peening layers to reduce the stress variations across the welded surface.
    2. Develop procedures to peen canisters with no tape or with a single layer of tape used on the final layer of the laser peening process.
    3. Determine the minimum number of peening layers required to induce the required level of compressive stress in the Alloy 22 closure weld.
- Confirm that the optimized laser peening process does not result in any adverse metallurgical effects on the long term performance of Alloy 22
    1. Determine the metallurgical properties of laser peened Alloy 22 base metal and weld metal.
    2. Determine the corrosion rate of laser peened Alloy 22 base metal and weld metal.
- Determine laser beam tapering (or 'feathering') to minimize the transition from peened to non-peened areas, which could affect long term material performance
    1. Develop how the compressive residual stress profile could be changed using various coating and taping material thicknesses.
    2. Measure the compressive residual stress distribution across the peened and unpeened areas using x-ray and the surface contour method.

The above engineering activities would require several man-years of effort but could be completed in a relatively short period of time. A detailed cost estimate is required to provide an accurate assessment of the manpower required and the corresponding schedule for these activities.

The evolution of laser systems at LLNL allows for increased performance, reductions in both footprint and cost without any negative impact to system reliability or maintainability. An example of such a system is shown in Figure 21. Sponsored by the Space Missile Defense Command (SMDC) in Huntsville, Alabama, the purpose of this laser system is to provide in a very compact and high reliability package, sufficient power on target to destroy an incoming missile on the battlefield. This laser system utilizes "diode pumping" to develop the required amount of power in a very small footprint.

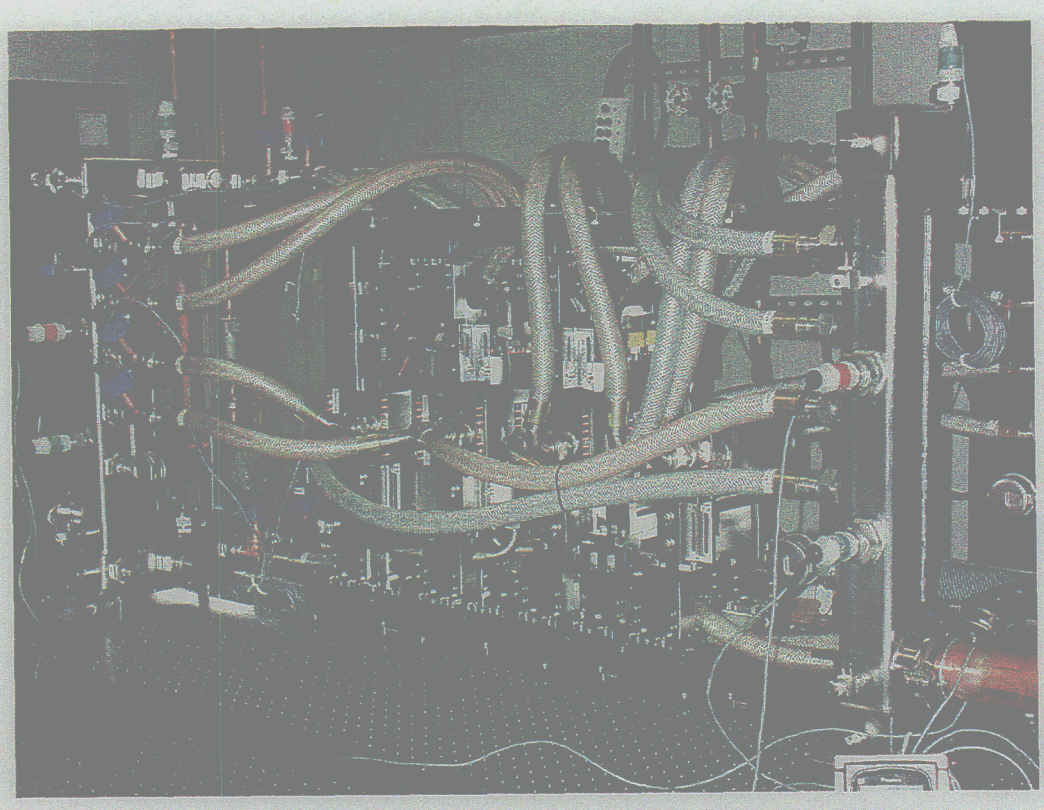

Figure 21: *The Solid State Heat Capacity Laser System (SSHCL)*

An extension of this diode pumped technology could be developed for the Laser Peening System. Current operational flashlamp pumped laser peening pulse rates could be increased an order of magnitude if not more to reduce laser peening time. In addition, laser power (utilizing diode pumped technology) could be enhanced to promote present system energy densities utilizing a larger spot size. This would again contribute to a reduction in laser peening time without any detrimental effect in performance.

Laser System Configuration Options:

- Flashlamped Pumped Laser System – present baseline configuration.
- Diode Pumped Laser System – significantly enhance performance, smaller footprint, increase laser pulse repetition rate.
- Multiple Lasers working simultaneously – decrease laser peening time, increase reliability.

Laser Transport System

The laser transport system takes the laser beam from the laser system and optically transports the laser beam into the hot cell area through a hermetically sealed optical window. This is done via a series of optical elements. Figure 22 shows conceptually the laser transport system; transporting the laser beam from its clean room into the hot cell area where the DC is located. Turning mirrors are shown to depict the type of pathway the laser beam would require, accounting for both transverse and elevation changes.

Engineering activities would include the design of the optical transport system using remote control for use in the hot cell environment. Included would be the development of the process certification method for hot cell operation.

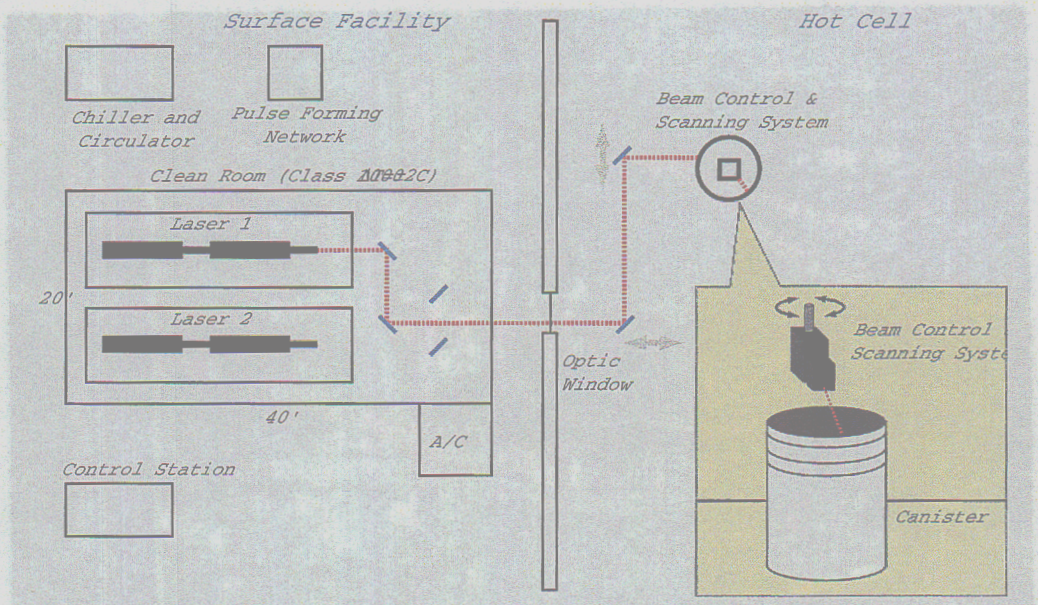

Figure 22: Laser Beam Transport System – Basic Schematic

Laser Transport System Configuration Options:

- Series of optical elements– present baseline configuration.
- Multiple laser beam paths – decrease laser peening time, increase reliability.

Laser Beam Control/Scanning System

The laser beam control/scanning system is the third major part of the total Laser Peening System. This portion of the system can be configured in several ways. The system would be incorporated into the laser peening end effector and properly aligned and indexed as it is attached to the Closure Gantry Manipulator (CGM). In this option the Disposal Container (DC) maintains a vertical axis of orientation, identical to the orientation used in the GTAW closure weld process (Knapp, 2001). Figure 23 depicts this concept as the laser beam, directed via the laser transport system, rotating about the centerline of the stationary DC during the laser peening process.

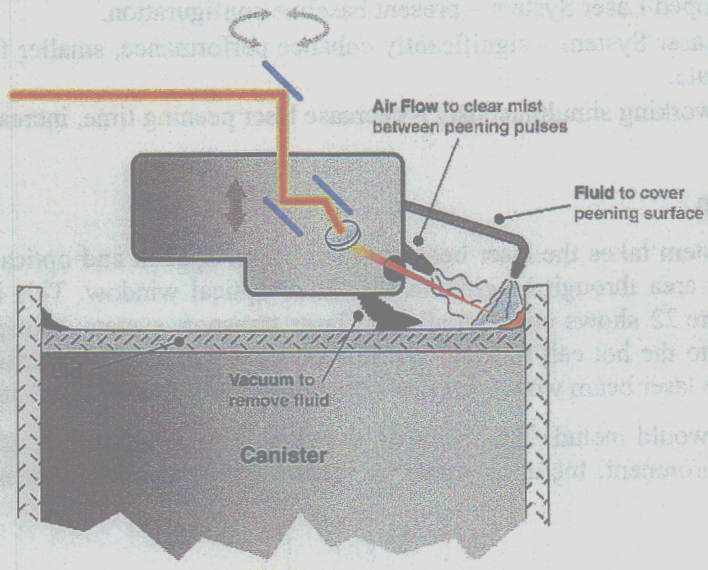

Figure 23:Vertical Orientation Laser Beam Control/Scanning System

Another configuration could have the laser peening beam held stationary in its end effector while the disposal container (DC) is rotated about its vertical axis. This would be accomplished by the DC resting on a small turntable that rotates about its vertical axis. Although this type of concept was eliminated from consideration for the GTAW process due to the small total run out tolerance required, the laser peening system is appreciably less sensitive to turntable run out and consequently could utilize such a system. At the present time, there is approximately 20% overlap of laser peened areas to ensure that all areas are fully and completely peened. This overlap allows for the type of small turntable run out that might be experienced in a turntable driven system. Benefits for this type of system would include a mechanically simpler and consequently more reliable laser peening system without sacrificing the laser beam on-target requirement.

Another Laser Beam Control/Scanning System concept again utilizes a stationary laser beam as the DC is rotated about is horizontal axis. Figure 24 provides a conceptual understanding of this type of system. The DC is rotated so that the laser beam peens the weld in a circular geometry as it is rotated about its horizontal axis. Gravity is used as an aid to help direct the tamping fluid required during the laser peening operation into a suitable collection container as it circulates through the closed loop system.

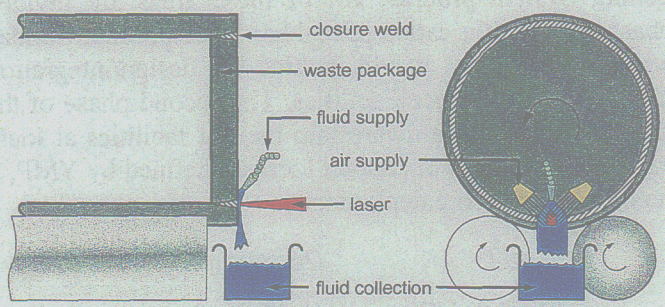

Figure 24:Horizontal Orientation Laser Beam Control/Scanning System

This concept, which once again deploys a stationary laser beam, has an additional advantage of being able to use multiple laser beams simultaneously. Envision as an example, 4 identical laser beams located around the circumference of the closure weld at the 4 positions of a clock; the 3, 6, 9 and 12 o'clock positions. Each of the 4 laser beams would operate in unison and would peen its corresponding quadrant worth of weld, equating to a total laser peening time of 25% of the original. This would greatly decrease the time the DC was in the hot cell area and consequently, the overall cost to provide a complete and verified closure weld. The multiple laser beam concept could also be applied to a DC mounted in a vertical axis orientation as shown in Figure 23, but the logistics of bringing in multiple laser beams from above the DC utilizing the present end effector concept seems somewhat more complicated than the horizontal axis option, but a configuration that nevertheless could be developed.

In addition to exploring different types of system configurations, investigations into the use of alternative tamping fluids would be a part of the Science & Technology (S&T) activities. This work, as an example, would identify and test new types of tamping fluids suitable for hot cell operation and optimize the laser peening process parameters using these newly selected tamping fluids.

Laser Beam Control/Scanning System Configuration Options:

- Vertical Orientation Utilizing CGM End Effector – present configuration.
- Vertical Orientation with rotating DC – increase laser system reliability.
- Horizontal Orientation Utilizing a Stationary Laser Beam – increase system reliability.
- Multiple Lasers working simultaneously – decrease laser peening time, increase reliability.

After the laser peening process has been concluded, the laser peened weld joint and parent material need to be examined to ensure that the process has been done properly. Several non-destructive test methods could be employed to verify the integrity of the peened areas. High energy X-Ray radiography and phased ultrasound measurement are two potential test methods. In addition, a correlation between the depth of the compressive stress versus the percent cold work of the material could be used to determine the final residual stress profile of the peened areas. Test specimens (comparable to the Almen strips used in other peening applications) could also be used to verify the performance of the laser peening operation. Using the contour method of measuring residual stress in these test coupons would provide additional support that the proper level and depth of compressive stress have been achieved.

The above discussion on laser peening deployment at Yucca Mountain outlines the baseline laser peening process using a flashlamp pumped laser, coupled with standard optical elements and a stationary disposal container with vertical axis orientation. Additional discussion is centered on variations to this baseline concept and the type of engineering activities and science and technology activities that would enhance overall baseline performance and process efficiency.

The following is a (non-exhaustive) summary table describing several examples of potential activities in support of the Laser Peening System process. All of these areas are divided into two phases; the design/proof of concept phase and the fabrication of real hardware phase to validate the proposed concept. The design phase (as shown in the table) would include the design/integration of the Laser Peening System into the overall Closure Weld Surface Facilities. The second phase of the work scope (yet to be estimated) would incorporate the process hardware into the test facilities at Idaho National Engineering and Environmental Laboratory (INEEL), or at another location defined by YMP, so that the entire system would be fully checked out and tested before deployment.

Activity Description	*Benefit*	*Duration*	*Effort*
Diode Pumped Laser	Perf/Reliability	18-24 months	2 man-yrs
Multiple Laser Beams	Perf/Reliability	12-18 months	1 man-yr
Vertical/Horizontal DC Orientation	Perf/Reliability	12-18 months	2 man-yrs
Baseline Engineering Design to support LA	Optimized Performance	12-18 months	6 man-yrs
Laser Beam Control System Integration	Reliability & Maintainability	18-24 months	4 man-yrs

SUMMARY

The most important findings of this work are as follows

- Laser peening produces compressive residual stress to depths on the order of 5 mm in actual Alloy 22 weldments
- The primary residual stress measurement methods used in this study, the slitting method and the contour method, produce consistent, powerful results efficiently and cost effectively. Both of these methods can be qualified, and the process has been started for the contour method.
- Preliminary results indicate that laser peening increases the general corrosion resistance of Alloy 22.
- There are a variety of options available for remote deployment of laser peening in a radioactive environment

REFERENCES

Farmer, J, et al, 2000, "Modeling and Mitigation of Stress Corrosion Cracking in Closure Welds of High-Level Waste Container for Yucca Mountain", ASME.

Hill, M.R., Lin W-Y., 2002, "Residual Stress Measurement in a Ceramic-Metallic Graded Material", J. Eng. Mater. Technol., **124**, p. 185.

Knapp, M.C., 2001, "Waste Package Project FY-01 Closure Methods Report", Bechtel SAIC Company, LLC, Las Vegas, NV.

Plinski, M.J., 2001, "Waste Package Operations Fabrication Process Report", Bechtel SAIC Company, LLC, Las Vegas, NV.

Prime, M.B., 1999, "Residual stress measurement by the successive extension of a slot: The crack compliance method", Appl. Mech. Rev., **52**, p. 75.

Prime, M.B., 2001, "Cross-Sectional Mapping of Residual Stresses by Measuring the Surface Contour After a Cut", J. Eng. Mater. Technol., **123**, p. 162.

APPENDIX A

The peening parameters actually employed in the peening of the 3/8 and 1 inch welded plates are summarized in the following table:

Table 4: Laser peening process parameters used

Parameter	Value
Laser pulse energy (at part)	**14 J**
FWHM (full width half maximum) pulse duration	**25 ns**
Spot dimension	**2.3 by 2.5 mm**
Irradiance (power per area)	**9.7 GW/cm^2**
Spot overlap (between successive spots)	**10%**
Number of layers	**10**
Layer overlap (between successive layers)	**20%**
Ablative layer	**Al tape, 2 layers**

The plate assemblies laser peened at LLNL had the following identification numbers:

Table 5: Plate identification

Plate thickness (in)	Part Number
3/8	**HT XX2213BC E1B**
3/8	**HT XX2213BC E2B**
3/8	**HT XX2213BC E3B**
1	**HT XX2246BG F1B**
1	**HT XX2246BG F2B**

The plates were mounted to an X-Y material handling stage positioned so that the weld bead ran in a horizontal direction. A PC running LabView controlled the planar movement of the stage. The fixturing of a welded plate is shown in the figure below.

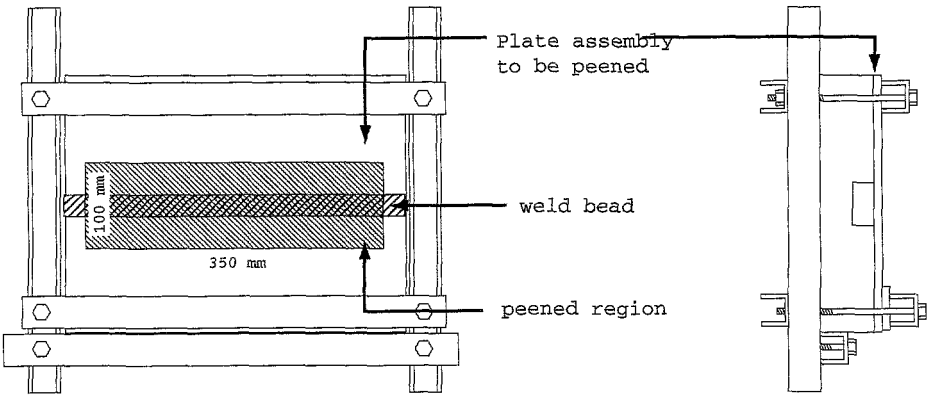

Figure 25: Schematic of the fixturing of the stress mitigation welded coupons

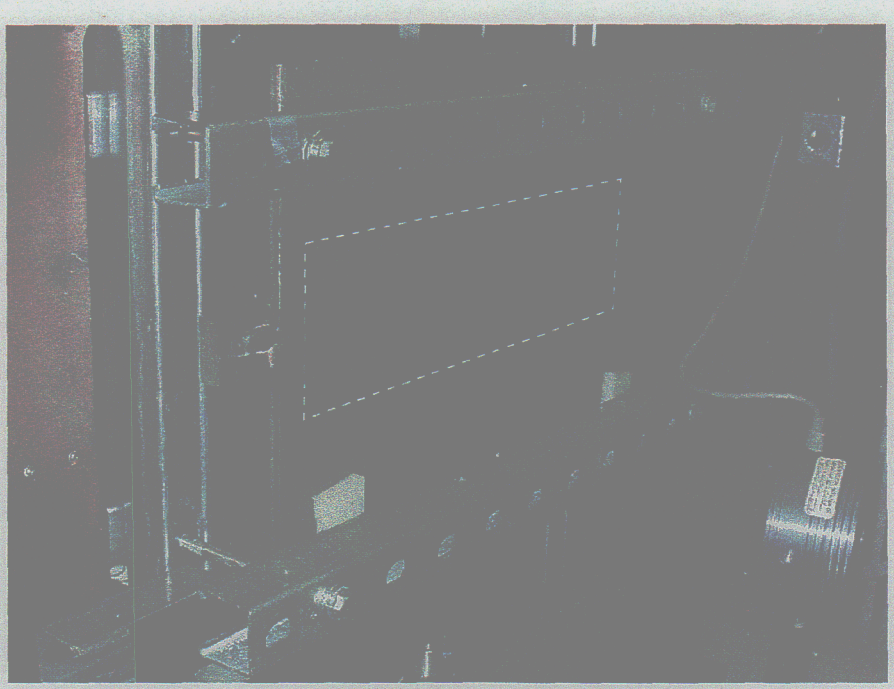

Figure 26: Photograph of the stress mitigation welded coupons; the laser peening is indicated by a dashed rectangle parallel to the weld bead.

Prior to peening, the plate was cleaned with acetone and ethyl alcohol, and dried with a heat gun. Two layers of aluminum tape were applied after the plate was dry. Between layers of peening, the used tape was removed, the surface was re-cleaned, and new tape was applied.

A fixed plexiglass shield was erected to minimize blowback of peening debris towards the delivery lens in the laser system. Additional protection was provided by 'puffing' compressed air across the processing area to clear debris from the beam path between laser shots. Two of the stress mitigation welded specimens are shown in Figure 27.

Figure 27: Stress mitigation welded coupons. The plate on the left is 3/8 inch thick and the one on the right is 1 inch thick

APPENDIX B

The following journal articles, "Residual Stress Measurement in a Ceramic-Metallic Graded Material" (J. Eng. Mater. Technol., 2002) and "Cross-Sectional Mapping of Residual Stresses by Measuring the Surface Contour After a Cut" (J. Eng. Mater. Technol., 2001) give technical details and experimental applications for the two mechanical release residual stress measurement methods used in this work, the slitting method and the contour method respectively.

The effects of process variations on residual stress in laser peened 7049 T73 aluminum alloy

Jon E. Rankin and Michael R. Hill[2]
Mechanical and Aeronautical Engineering Department,
University of California, Davis, CA USA

Lloyd A. Hackel,
Laser Science and Technology Program,
Lawrence Livermore National Laboratory, Livermore, CA USA

Abstract

This paper reports measurements of the distribution of residual stress with depth from the surface in laser peened coupons made of a high-strength aluminum alloy. Residual stresses were measured using slitting (also known as the crack compliance method). Measurements were made on several coupons to: compare laser peening (LP) and shot peening residual stresses; ascertain the influence of LP parameters on residual stress; determine whether tensile residual stress existed outside the peened area; assess the variation of residual stress with in-plane position relative to the layout of the laser spots used for peening; and, determine the importance of a uniform spatial distribution of laser energy within the spot. Residual stress 0.1 mm from the surface due to LP and shot peening were comparable and the depth of the compressive stress for LP was far greater than for shot peening. Variations of most LP parameters did not significantly alter residual stress at shallow depths, but greater laser energy and larger layer overlap increased residual stress at depths between 0.2 and 0.6 mm from the surface. Residual stresses adjacent to the peened area were found to be compressive. Decreased levels of surface residual stress were found when laser spots had a non-uniform distribution of laser intensity.

Keywords

Laser peening, surface treatment, residual stress, fatigue

Introduction

Laser peening is an emerging surface treatment, capable of imparting compressive surface residual stress and thereby improving the resistance of components to fatigue failure. While the general mechanical concept is similar to conventional shot peening, laser peening (LP) offers certain advantages. First, LP leaves a more desirable surface than does shot peening (SP). In stainless steel, LP has a reduced occurrence of strain-induced phase transformation compared with SP, thereby leaving a surface more resistant to corrosive attack [1]. In aluminum, LP may also leave an improved surface, which would reduce the occurrences of surface lapping, folds, and other undesirable features that occur with SP [2]. The improved surface condition should therefore result in improved resistance to crack initiation. Second, while LP and SP create residual stresses of similar magnitude, the compressive stresses extend far deeper from the surface for LP [3], thereby offering improved resistance to the growth of near-surface, macroscopic cracks. These two characteristics can therefore lead to significant improvements in the fatigue life of treated components.

These potential advantages of LP point to the need to further understand the effects of this process for a wide range of materials and geometry. This is especially the case since recent advances in laser science and technology [4-6] have enabled LP to become cost effective for a wider variety of components. This work presents measurements of the distribution (or, "profile") of LP-induced residual stress with distance from the surface under a variety of processing

[2] Corresponding author, Mechanical and Aeronautical Engineering Department, University of California, Davis, CA 95616, USA, (530) 754-6178, (530) 752-4158 (FAX), mrhill@ucdavis.edu

conditions for a high strength aluminum alloy used in aerospace structure (7049 T73). We refer to measurements of residual stress throughout the paper; technically, however, released strain was measured while residual stress was computed.

While potential improvements in fatigue life make LP an attractive process, its adoption will likely depend on verifying its performance relative to competing surface treatments. Because SP is the most commonly used surface residual stress treatment for aerospace structure, the effects of LP are often compared to the effects of SP (e.g., [3, 6]). Considering that the beneficial effects of either type of peening on fatigue life are primarily due to the near-surface residual stress field, the first objective of this paper is to compare the residual stress profile produced by LP to that produced by SP in 7049 T73 aluminum.

The residual stress profile due to LP is influenced by several process parameters. One basic process parameter is the fluence of the laser pulse (laser energy per spot area). A second important parameter is the size of the laser spot. A third important parameter is the number of layers of peening applied to a component and, for multi-layer peening, a fourth important parameter is the spatial offset, or "overlap", from one peening layer to another. These parameters have been investigated to various degrees in a number of materials. Smith et al [7] reported the effects of fluence and the number of peening layers on the residual stress profile in Ti-6Al-4V. Peyre and Fabbro, with various co-authors, have studied the effects of fluence and the number of peening layers on the residual stress profile in aluminum alloys [3, 8], as well as the effect of layer overlap on *surface* residual stress in stainless steel [9]. Despite these efforts, the influences of process parameters, particularly spot size and layer overlap, on the resulting residual stress profiles produced by LP are not wholly understood. Therefore, the second objective of this paper is to assess the variation of the LP-induced residual stress profile in 7049-T73 aluminum with changes in laser energy, laser spot size, and layer overlap.

Surface treatments like LP are most often applied to specific, highly stressed locations of a component. Typical application areas include mechanical joints, notches, fillets, and other abrupt changes in cross section. While compressive surface residual stress is imparted within a peened area, tensile surface residual stress may result outside the peened area, which may have deleterious effects on component performance. To determine whether tensile surface residual stress exists adjacent to the peened region, the third objective is to examine the in-plane variation of the residual stress profile adjacent to a laser peened area.

The scale of laser peening is large compared with the mechanisms of fatigue crack initiation, and this may have an influence on the ability of LP to improve fatigue life. Spatial, in-plane variations of residual stress induced by shot peening may be expected to be on a scale of approximately 0.1 mm, due to the small size and small amounts of penetration of the shot [2]. In contrast, the LP spot size is on the order of 3 to 10 mm, so that relatively large-scale, in-plane variations of residual stress may exist and may influence potential fatigue life improvements. For this reason, the fourth objective of this paper is to investigate the in-plane variation of the residual stress profiles within a laser peened region.

Despite efforts to the contrary, a potential exists for laser optics to become misaligned, or otherwise degraded, resulting in a non-uniform spatial distribution of energy within the laser spot. While such problems can be detected on-line [4] and subsequently corrected, it is nevertheless important to investigate the effect of laser spot variation on the resulting residual stress profiles. The final objective is therefore to examine the in-plane variations of the residual stress profiles for a surface peened with intentionally altered laser spots, and to compare the residual stresses to those occurring for a normally peened surface.

Methods

The objectives described above were addressed by measuring residual stress in a series of coupons peened in various ways. Residual stresses were measured by relaxation, using the slitting method (also called the compliance method or the crack compliance method) [10]. In the following section, the slitting method is presented in general and then experimental details are provided for the present set of experiments. A set of seven peened samples and fifteen measurement locations is then described, which together address the objectives just stated.

The Slitting Method

The general procedure for the slitting method is to gradually extend a slit into the specimen surface and measure near-slit strain as a function of slit depth. Strain released perpendicular to the slit was measured using a metallic foil gage placed near the slit (Figure 1). The slits were cut incrementally in depth using wire electrical discharge machining (EDM). The strain versus depth data were then used to compute the variation of the pre-slit residual stress component normal to the slit face with depth from the surface (i.e., the stress profile).

Solving for the residual stress profile from measured strain data requires the solution of an elastic inverse

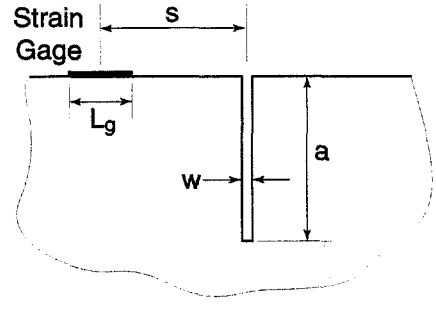

Figure 1: Strain gage installation schematic

problem. The inverse problem is solved by first representing the unknown residual stress profile in the Legendre polynomial basis, and then finding the coefficients of the basis from the measured strain data. For these near-surface residual stress measurements, all terms in the polynomial series were included (this is not the case when measuring through thickness stress distributions, as the zeroth and first order Legendre polynomials do not satisfy equilibrium). Taking x as the coordinate along the depth direction, the unknown residual stress profile $\sigma_{RS}(x)$ was written as a sum of Legendre polynomial terms $P_j(x)$, each with a corresponding amplitude A_j

$$\sigma_{RS}(x) = \sum_{j=0}^{m} A_j P_j(x) \tag{1}$$

where, m is the order of the highest term in the polynomial series. A solution of the equations of elasticity is then developed to relate the stress given by a particular basis function (with unit amplitude) $P_j(x)$ to strain at a near-slit gage location, as described below. If residual stress were given exactly by the basis function $P_j(x)$, the strain that would occur at cut depth a_i is provided by the elasticity solution. This strain is an element C_{ij} of a compliance matrix $[C]$ defined as

$$C_{ij} \equiv \varepsilon(a_i)\Big|_{\sigma = P_j(x)}. \tag{2}$$

Solving the elasticity problem for all basis functions and all cut depths, and invoking the principle of elastic superposition, results in a linear system relating basis function amplitudes to strain as a function of cut depth

$$\varepsilon(a_i) = \sum_{j=0}^{m} C_{ij} A_j \tag{3}$$

or, using matrix notation

$$\{\varepsilon\} = [C]\{A\} \tag{4}$$

where the braces $\{\bullet\}$ denote a vector and the brackets $[\bullet]$ denote a matrix. Given this system, and strains measured experimentally during cutting, the amplitudes of the stress expansion are found by inversion of Equation (4) in a least squares sense

$$\{A\} = \left([C]^T[C]\right)^{-1}[C]^T\{\varepsilon_{meas}\} \tag{5}$$

where $\{\varepsilon_{meas}\}$ is a vector of measured strain data. With the amplitude vector $\{A\}$ determined, the stress state existing prior to cutting is obtained from Equation (1).

The polynomial order for the stress expansion m was selected for each set of measured strain data by considering the root mean square of the error between measured strain and the fitted strain of Equation (4), as a function of an assumed order of stress expansion m. Preliminary strain fits were computed for Legendre polynomial series of order zero through seven (i.e., m in Equations (1) and (3) was varied from 0 to 7, so that the polynomial series had one to eight terms). Low-order polynomial series generally exhibited high strain fit error, and increasing order decreased error only for a limited number of terms. The numerical condition of the inverted matrix in Equation (4) also becomes poor with increasing number of terms, so that error in experimental data can have a significant impact on the measured residual stress when an unduly large number of terms is taken in the stress expansion. Therefore, the number of terms must be selected to ensure a good fit to the measured strain while not needlessly amplifying experimental errors. In this work, the optimal order of polynomial series was determined by plotting the root mean square of the strain fit error versus series order m, and selecting the order at which the error reached a plateau [11]. Once the order was selected, single-standard-deviation error bounds were found for the residual stresses using statistical methods [12] based on a standard error in measured strain equal to the larger of the root mean square strain fit error or the expected precision of the strain measurement system (3 με). Further aspects of order selection and error analysis for slitting were recently discussed by Hill and Lin [11].

A software program was used to determine the elements of the compliance matrix $[C]$ of Equation (4). This program embodies the elasticity solution originally published by Cheng et al [13] with improved integration and geometric accuracy [14, 15]. The solution assumes a slit of finite width w is cut to depth a in a semi-infinite half-space, and provides strain averaged over a given gage length L_g, where the gage center lies a distance s from the slit center (Figure 1). Inputs to the software code included experimental values of L_g, s, w, and slit depths a_i, as well as the elastic properties of the aluminum, which were assumed to be $E = 70.0$ GPa and $\nu = 0.33$ [16]. Output of the software program was routed to a general matrix and data analysis package [17] for determination of the basis function amplitude vector $\{A\}$ and the measured residual stress, as well as for error analysis.

Experimental Details

Careful attention was paid to several aspects of the experiments. Strain gages had a gage length of 0.79 mm. A waterproofing system consisted of a layer of acrylic covered by a layer of paraffin wax and was applied to protect each strain gage. Both the adhesive and coatings were carefully masked during application to ensure at least 0.5 mm overlap of each coating, which was found to be crucial for reliable water resistance and accurate strain measurement. The slit center to gage center distance s was nominally 1.8 mm, which allowed room for these coatings.

Wire EDM was used for slitting to specified increments of depth. The final slit depth ranged from 1.3 to 2.0 mm, and slitting was performed while the specimen was bathed in de-ionized water. Initial experiments used 0.20 mm wire, which produced a slit approximately 0.25 mm wide, and strain data were gathered at nominal depth increments of 0.102 mm. In an attempt to improve the measurement

resolution near the material surface, further experiments used 0.10 mm wire, which produced a slit approximately 0.12 mm wide. In these cases, the slit depth increments were 0.025 mm for the first six depths, 0.051 mm for the next seven depths, and then 0.102 mm for the remaining depths. Because the slit width was accounted for in the elastic solution, it was assumed to have a minimal impact on the measured stress. The smaller wire did allow smaller increments of depth to be cut, therefore improving near-surface resolution.

Transduced strain gage signals were produced by a commercial Wheatstone bridge and were recorded by hand. Cutting was halted prior to each strain reading to avoid interference from stray voltages produced by the cutting equipment.

After cutting was completed, the strain gage coatings were chemically and mechanically removed and measurement sites were examined under magnification. Digital images were captured at 50X optical magnification and had a resolution of approximately 530 pixels/mm (0.0019 mm/pixel). Digital photogrammetry was used to determine the slit width w, gage location s, and the final slit depth a_{max} for each measurement site. The measured slit width and gage location at each measurement site provided input to the stress computation. The measured maximum slit depth was used to adjust the intended slit depths to account for any offset between the depth axis of the EDM wire and the surface of the coupon. An offset was defined as the measured maximum slit depth minus the intended maximum slit depth, and this offset was added to each intended slit depth to arrive at a set of adjusted slit depths, which were used in the stress computation.

Coupon and Measurement Site Descriptions

Seven coupons were used to address the five objectives described above. These coupons were cut from a single 7049 T73 aluminum forging. Shot peening was performed by a commercial provider (Metal Improvement Company Inc., Paramus, NJ, USA) to AMS-S-13165, using 0.48-0.71 mm cast steel shot, 200% coverage, and 0.010A-0.014A Almen intensity. Laser peening was performed on a novel Nd:glass, flash lamp pumped laser which incorporated SBS phase conjugation. The laser system was capable of an average power of 150 W, a pulse width of 10 to 100 ns, a pulse energy of up to 25 J, and a repetition rate of up to 6 Hz. Details on a similar laser system were previously reported by Dane et al [4] and a discussion of its use for LP was reported by Hammersley et al [6].

The LP parameters used for each coupon are listed in Table 1. (which also has a listing of the measurement sites on these coupons, described below). Initial measurements of residual stress were made on treated rectangular surfaces with planar dimensions 9.5x50 mm and with coupon thickness of 25 mm (coupons 5ST and 6LT). All other coupons were 9.5 mm thick and had planar dimensions at least 25x38 mm.

While the coupon geometries varied slightly, an effort was made to limit the effects of coupon and slit geometry on measured stress. The stress computation relies on an elastic solution for a slit in a semi-infinite half-space in plane strain, and several geometric constraints were developed to approximate the geometry and boundary conditions of the elastic solution. The slit depth a_{max} was made small compared to the sample thickness to approximate an infinitely thick body (the greatest slit depth was 20% of the coupon thickness). The slit length was extended across the entire coupon and measurement locations were more than $2a_{max}$ along the slit from the coupon edges to approximate a plane strain condition. Multiple slits cut on the same coupon were remote from each other and from coupon edges to approximate a planar infinite body (the smallest perpendicular distance between slits or coupon edges was $6a_{max}$). In addition to these constraints, measurement sites were at least one laser spot size inside the peened area to assure that the full peening-induced stress fields were measured (except when specifically investigating stress near the edge of the peened area).

Residual stress profiles were measured at fifteen sites on the seven coupons. Example coupons, slit locations, and strain gage locations are shown in Figure 2. Measurement sites are defined by the locations of both the slit and the strain gage. For example, site 1 on coupon 4A (Figure 2(a)) is horizontally located at the strain gage, although the measurement is a weighted average of any residual stress variation that may exist along the line of the slit [18]. Site 1 is vertically located at the slit, because stress release occurs there, and no averaging occurs along this direction, providing a spatial resolution approximately equal to the slit width. A schematic representation of all measurement sites within the laser peening fields is shown in Figure 3. Note that the figure shows the sites relative to the laser spot layouts employed in peening and does not indicate the proximity of the sites to one another. Each site is denoted by a double ellipse, where the center indicates the measurement location and the major axis lies along the slit direction, indicating the direction along which spatial averaging should be expected.

The collection of coupons and measurement sites (Table 1 and Figure 3) was capable of addressing the five objectives of the present work. Results at sites 0-S and 0-L allow for a general comparison between residual stress profiles due to SP and LP. Measurements at sites 1, 2, and 3 compare the effects of laser pulse fluence and laser spot size on the residual stress profiles. Comparison of results at site 0-L and site 1 shows the effect of a reduced second-layer pulse width (18 ns for site 0-L and 12 ns for site 1; the difference of 1 ns in the first pulse widths was assumed to be insignificant). Comparison of results for site 2 with those of site 7a shows the effect of layer overlap. Results at sites 4, 5, and 6 show the in-plane variation of the residual stress profile adjacent to the laser peened area. Results for sites 7a,

Table 1: Experimental coupons and strain gages

Coupon	Site	Fluence (J/cm^2)	Pulse width		Size (mm)	Overlap (%)	Purpose or Effect
			1 (ns)	2 (ns)			
5ST	0-S	--	--	--	--	--	SP residual stress
6LT	0-L	60	18	18	5	10	Compare LP to SP
4A	1	60	17	12	5	10	Shortened second pulse
	2	45	17	12	5	10	Reduced laser energy
4AT	3	60	17	12	3.2	10	Reduced spot size
6AT	4	45	17	12	5	50	At edge of LP area
	5	45	17	12	5	50	1.25 mm beyond LP area
	6	45	17	12	5	50	2.5 mm beyond LP area
6A	7a	45	17	12	5	50	Center of layer 2 spot
	8a	45	17	12	5	50	In layer 2 spot
	9a	45	17	12	5	50	Edge of layer 2 spot
7AT	10a	45	17	12	5	50	Clean, edge of layer 2 spot
	11a	45	17	12	5	50	Clean, center of layer 1 spot
	12a	45	17	12	5	50	Attenuated, edge of layer 2 spot
	13a	45	17	12	5	50	Attenuated, center of layer 1 spot

8a, 9a, and 11a reveal the in-plane variations of the residual stress profile within the peened area.

The effect of degraded or damaged optics was investigated by intentionally altering the spatial distribution of laser energy within the spots. With the current laser system [6], the most common problem is a reduced amount of laser energy in one corner of the square laser spot. To simulate such degradation under controlled conditions, one corner of the laser spot was intentionally attenuated (i.e., masked) and LP was performed in an otherwise normal manner. Coupon 7AT contained two laser peened areas, each 22.5 mm square, one area peened with normal spots and the other peened with attenuated spots. The attenuated area within the laser spot was 1.5x1.5 mm and is shown, together with the measurement sites within this peened area, in Figure 3(d). Comparison of results at sites 10a and 11a with those at sites 12a and 13a shows the effect of a non-uniform spatial distribution of energy within the laser spots.

Results

The photogrammetric measurements for each measurement site are shown in Table 2. The nominal gage placement was 1.80 mm from the center of the slit, and the measured position varied from 1.51 mm to 2.03 mm. The differences between the intended and actual gage positions are due to inaccuracies in gage installation and in placement

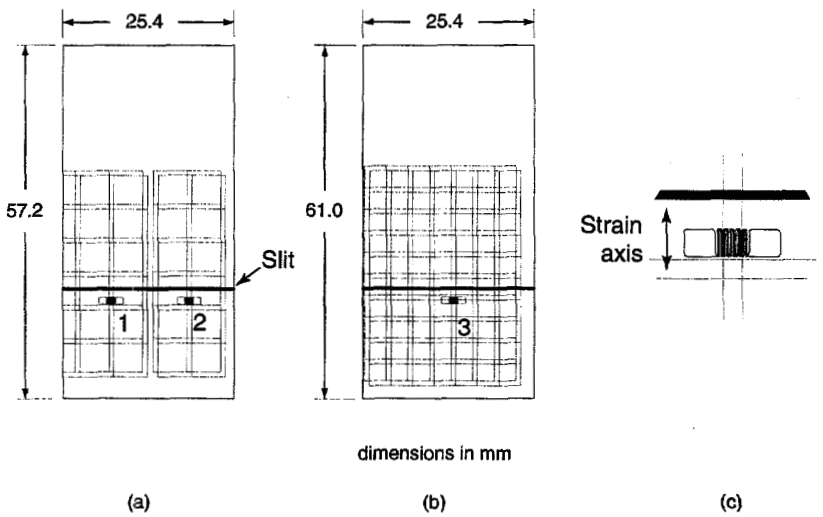

Figure 2: Examples of laser peened coupons, slits, and strain gage locations: (a) coupon 4A having two levels of laser fluence (left side 60 J/cm^2, right side 45 J/cm^2), (b) coupon 4AT with smaller laser spots, and (c) larger view of slit and strain gage

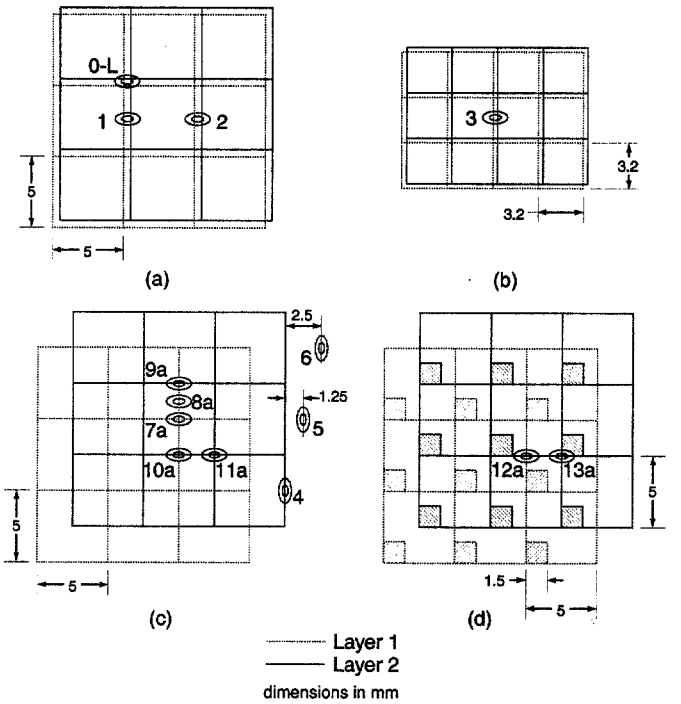

Figure 3: All measurement sites relative to peening fields: (a) 10% overlap and 5x5 mm spot, (b) 10% overlap and 3.2x3.2 mm spot, (c) 50% overlap and 5x5 mm spot, (d) 50% overlap and 5x5 mm spot with a 1.5x1.5 mm corner attenuation as indicated with cross hatching

of coupon relative to the wire in the EDM machine. The slits exhibited typical amounts of over-cut observed for wire EDM, being 0.02 to 0.06 mm wider than the EDM wire (after accounting for differences in wire size). Cut depths varied from the intended depths by between 0.01 and 0.11 mm due to inaccuracies in placement of the coupon relative to the EDM wire. As stated above, measured gage positions, measured slit widths, and adjusted cut depths were used in the stress determination for each measurement site. The difference between the nominal and actual geometry had significant effects on the calculated stress, as discussed below.

Figure 4 shows measured strain data for sites 0-S and 0-L and the strain fit from the inverse elastic analysis. Although data and fits are shown for only two measurement sites, other sites exhibited similar trends in measured strain and similar agreement between measured and fitted strains. Note that the strain trends for these two measurement sites cannot be used to directly infer relative levels of residual stress since the geometry varied for these two measurement sites (Table 2) and this influences strain release due to slitting.

Stress profiles for SP and for variations in LP process parameters show interesting trends (Figure 5). Results at site 0-S compared with those at site 0-L indicate that compressive residual stress extended far deeper into the surface for LP than for SP (Figure 5(a)). These results also show that SP generated a larger compressive residual stress close to the surface for these laser settings. Decreasing the pulse width of the second-layer laser pulse from 18 to 12 ns increased the near-surface residual stress to a similar magnitude to that produced by SP (compare Figure 5(a) and (b)). Reducing the laser fluence from 60 to 45 J/cm^2 resulted in residual stress that was of similar magnitude near the surface, but that decreased more rapidly with distance from the surface (Figure 5(b)). Laser spot sizes of 3.2 and 5.0 mm produced very similar residual stress profiles (Figure 5(c)). Coupons

Table 2: Gage position s, slit width w, and cut depth a_{max} for each strain gage

Coupon	Site	s (mm)	w (mm)	a_{max} (mm)
5ST	0-S	1.51	0.25	1.41
6LT	0-L	1.73	0.25	1.28
4A	1	1.65	0.12	2.00
	2	1.63	0.12	2.03
4AT	3	2.03	0.13	2.02
6AT	4	1.91	0.15	2.02
	5	1.95	0.15	2.04
	6	1.93	0.16	2.07
6A	7a	1.54	0.13	2.02
	8a	1.69	0.12	2.07
	9a	1.71	0.13	2.01
7AT	10a	1.78	0.12	2.01
	11a	1.77	0.11	2.01
	12a	1.69	0.13	2.02
	13a	1.85	0.12	2.02

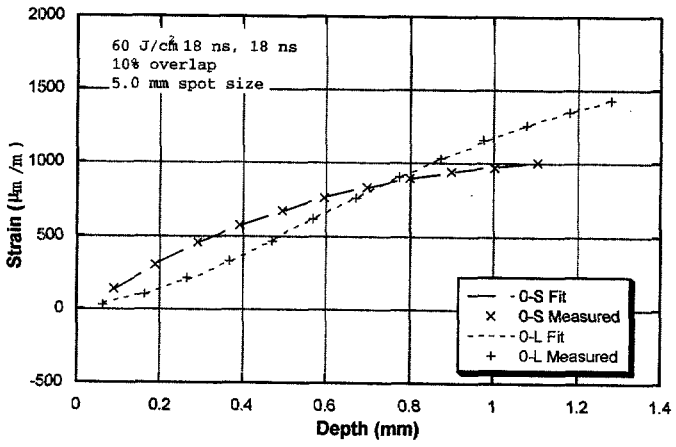

Figure 4: Measured strain and strain fits for sites 0-S and 0-L

treated with 10% and 50% layer overlap had similar levels of residual stress close to the surface, but the residual stress decreased more rapidly with depth for 10% overlap (Figure 5(d)).

The two most important characteristics of a stress profile may be the residual stress close to the surface and the depth that the compressive residual stress extends into the material. These two characteristics were quantified by interpolating the graphical results of Figure 5 at common points. For near-surface stress, residual stress at 0.10 mm was found. To quantify the depth of significant compressive residual stress, the depth where the residual stress first reached -50 MPa was found. With the exception of site 0-L, all sites had the same level of residual stress 0.10 mm from the

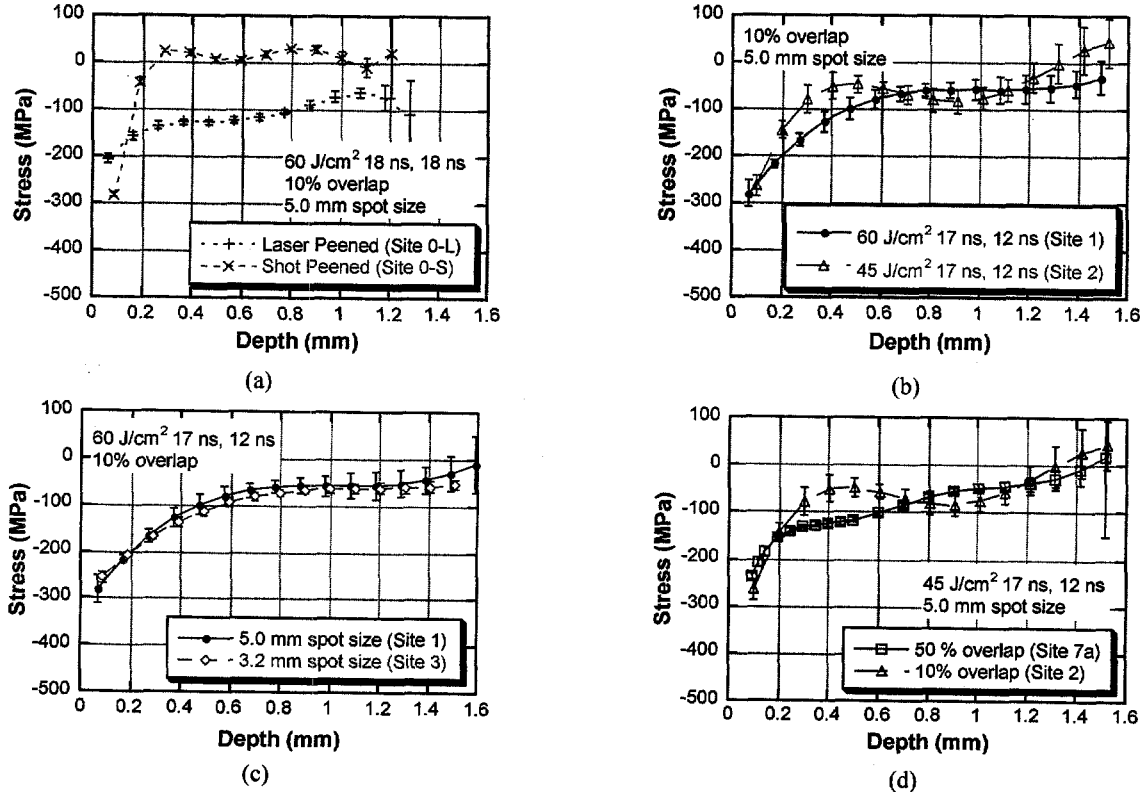

Figure 5: Comparison of peening processes: (a) SP vs. LP (b) effect of fluence; (c) effect of spot size; (d) effect of layer overlap

surface, to within experimental uncertainty (Table 3). The compressive residual stress at the LP sites exceeded -50 MPa over a depth between 0.45 and 1.57 mm, which was a factor of 2.5 to 8.7 deeper than occurred for SP (Table 3).

Stress levels outside the peened area were significantly lower in magnitude than stresses within the peened area (

Figure 6). Both near and below the surface, the magnitude of the residual stress decreased monotonically with distance from the laser peened area. No tensile residual stresses were measured outside the peened area. Measured residual stress at site 4 has more uncertainty near the surface than occurs at other measurement sites, due to difficulty in fitting the measured strain. It is suspected that gage coating material interfered with the EDM cutting at this site, so that initial slit depths were smaller than would otherwise occur. Even with the larger uncertainty at site 4, there was a significant decrease in residual stress outside the laser peened area.

Variations of the residual stress profile with in-plane position inside the peened area were limited to the near-surface region (Figure 7). The inset to Figure 7 summarizes the measurement sites for the four stress profiles presented in the figure. The highest surface residual stress was found at the edge of a layer two spot (site 9a), but because results were not available for all sites at shallow depths, it is not possible to make a definitive conclusion about which location had the highest or lowest stress at shallow depths. In the region between 0.10 and 0.20 mm, the largest stresses occurred at the center of a layer 2 spot (site 7a) with the difference between sites being as much as 100 MPa. Below 0.60 mm, all locations had similar stress profiles.

The effects of corner attenuation were also limited to the near-surface region (

Figure 8). At the edge of a layer-two spot (sites 10a and 12a), residual stresses at depths less than 0.30 mm were significantly altered by corner attenuation, with the attenuated site having much lower stress close to the surface. At the center of a layer-one spot (sites 11a and 13a), near-surface residual stresses were unaffected by corner attenuation. At depths greater than 0.30 mm, the stress profiles were similar at both sites, with or without corner attenuation.

Discussion

To investigate the variations of residual stress that may occur in laser peening, this paper presented measurements of the profiles of residual stress with depth from the surface for a variety of laser process parameters and at a variety of positions with respect to the laser spots. The major findings were that: 1) significant LP compressive residual stress extended far deeper into the material than SP compressive residual stress, 2) LP residual stress at a depth of 0.10 mm was less than or similar to that found for SP, depending on the laser parameters, 3) LP residual stresses at depths less than 0.20 mm were not significantly affected by most laser peening parameters, 4) higher fluence and larger layer overlap increased LP residual stresses at depths between 0.2 and 0.6 mm, 5) near-surface tensile residual stresses were not found adjacent to the laser peened area, and 6) variations in the residual stress profiles with in-plane position and variations due to degraded laser spots were limited to depths less than 0.60 mm. Before discussing the importance of these results, some choices made in planning this work and in reducing the experimental data should be discussed.

Although slitting was used in this study to measure residual stress, other techniques could have been used and may have had certain advantages. X-ray diffraction (XRD) might have been used to measure the in-plane surface residual stress variation, and might have been able to measure residual stress closer to the surface. Since the current results revealed in-plane spatial variations of LP residual stress near the surface, XRD would need to be carried out using a small x-ray spot to avoid in-plane averaging. XRD could also have been used to measure the profile of residual stress with depth, using layer removal and correcting results for stress redistribution. However, the model commonly used to account for stress redistribution [19] assumes a uniform in-plane residual stress state. When designing this test program, errors due to the lack of in-plane stress state uniformity could not be estimated because

the in-plane variations were unknown. Although the slitting method also suffers from averaging along the slit, it was attractive due to the lack of averaging normal to the slit. The slitting method also had the advantage of good performance for steep depth-wise stress gradients [10],

Site	Condition	Near Surface Residual Stress (MPa)	Depth of Compressive Residual Stress (mm)
0-S	Shot Peened	-256 ± 9	0.18
0-L	60 J/cm^2 18 ns 18 ns	-188 ± 9	> 1.30
1	60 J/cm^2 17 ns 12 ns	-263 ± 29	1.33
2	45 J/cm^2 17 ns 12ns	-263 ± 21	0.45
3	60 J/cm^2 17 ns 12ns (3.2 mm)	-253 ± 12	1.57

Table 3: Summary of near surface residual stress and depth of compressive residual stress

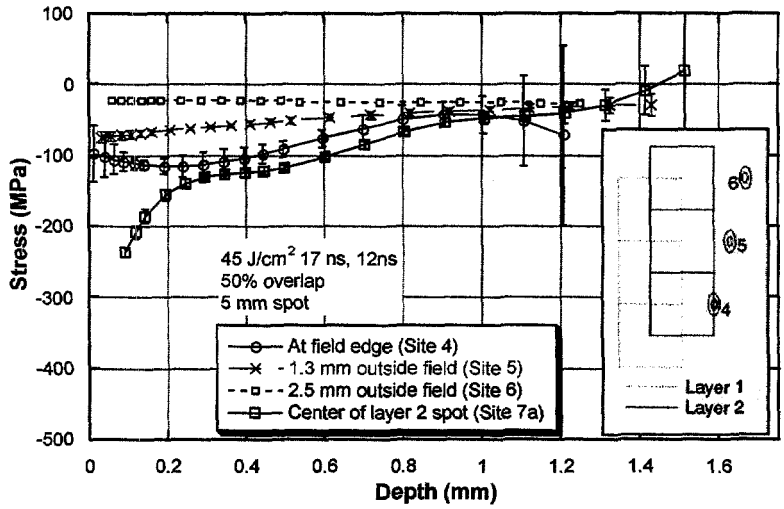

Figure 7: Residual stress adjacent to a laser peened area

whereas XRD can produce erroneous results in such cases [20].

It may be beneficial to combine XRD with slitting to measure the in-plane and in-depth variations of residual stress due to LP. In this study, there was difficulty in obtaining accurate results very close to the surface (depth less than about 0.07 mm) for two reasons. The first reason was that the largest numerical uncertainties for the slitting method occur near the beginning and end of the slit. The second reason was that repeatedly cutting to shallow depths was difficult because coatings used to protect the strain gage physically prevented the wire from contacting the coupon surface. Therefore, initial slits were of various depths. Although slit depth variations were accounted for in the stress computation, they did result in measurements at various depths and in an inability to obtain near-surface results in a few cases (e.g., site 8a). Despite the anticipated difficulties with XRD discussed above, some of these difficulties may be less significant at shallow depths. For example, the effect of in-plane stress variations on layer-

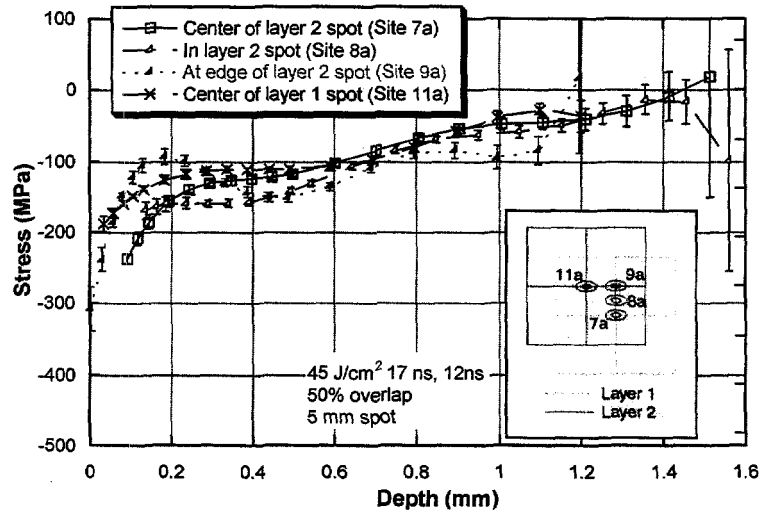

Figure 6: In-plane variations of the residual stress profile

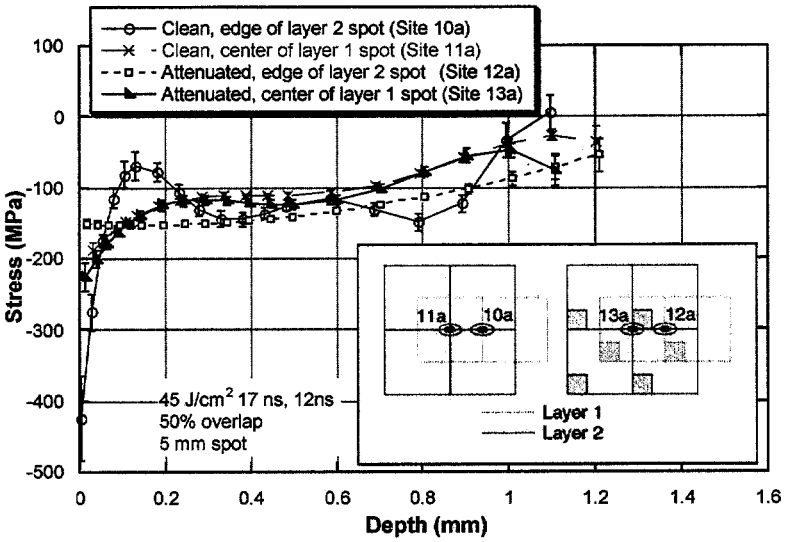

Figure 8: Comparison of residual stress profiles with and without corner attenuation

removal corrections may be insignificant for depths that are small compared to the spatial scale of the in-plane stress variations. It may therefore be beneficial to employ slitting and XRD at duplicate sites, and to combine diffraction results near the surface with slitting results at greater depths.

When formulating the compliance matrix [*C*], an analytical elasticity solution was employed, but it would have also been possible to use the finite element method. In finite element solutions, a small number of elements can be removed to simulate the extension of the slit, and slit-face tractions can be used to simulate the effect of the residual stress basis functions on near-slit strain (e.g., [10, 11]). To account for experimental variations in s, w, and a_i when using the finite element approach, one would need to adjust the finite element mesh for each variation of geometry. Alternatively, one could interpolate the results of a single finite element run to account for variations in s and a_i, assuming that small variations of w do not significantly affect the solution. A significant advantage of the analytical elasticity solution was that it could generate compliance matrices for different geometries more rapidly than a finite element mesh could be revised (i.e., s, w, and a_i were inputs to the software program invoking the solution and they could be easily changed).

The use of the measured strain gage position and offset slit depths had a significant effect on the computed residual stresses. To illustrate the effects of measured gage position and offset slit depths, the stress computation was repeated for two measurement sites. For site 0-S, the analysis was repeated using the intended gage position $s = 1.8$ mm and the offset slit depths. Residual stresses at all depths were affected, with the largest differences near the surface (Figure 9). For site 0-L, the analysis was repeated using the intended slit depths and the measured value of s. Near-surface stresses were again significantly affected (Figure 10). It is therefore advisable to measure gage position and final cut depths following slitting experiments, and for the measurements to be included in stress computations.

Several of the key findings mentioned above may have important implications for potential LP applications. Compared with SP, compressive surface residual stresses due to LP were of similar magnitude near the surface (Table 3) and extended far deeper into the surface of the component (Table 3, Figure 5(a)). The greater depth of compressive residual stress that occurred with LP should serve to enhance fatigue performance to a greater degree than occurs with SP. In fact, enhanced fatigue performance has been shown for laser peened coupons in a number of fatigue studies involving SP and LP [3, 6, 8, 21].

Near-surface residual stresses due to LP were significantly affected by only a single LP parameter. Residual stress at depths less than 0.20 mm were significantly increased when the second-layer pulse width was decreased from 18 to 12 ns (compare results at site 0-L and site 1 in Figure 5 and Table 3). Since this made the near-surface stress as large as that found for SP, the shorter second-layer pulse duration was advantageous. All other laser parameter variations produced little change in the near-surface stress (Figure 5 and Table 3), indicating that near-surface stress was robust to variations of laser fluence, spot size, and layer overlap.

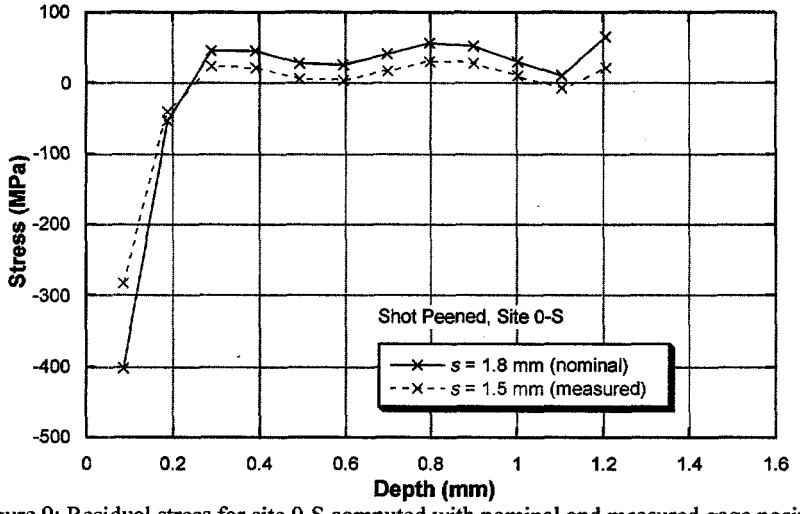

Figure 9: Residual stress for site 0-S computed with nominal and measured gage position

Residual stresses at depths between 0.20 mm and 0.60 mm were significantly affected by both laser fluence and layer overlap. Larger compressive residual stresses were found in this depth range with increased laser fluence and with increased layer overlap. The amount of the residual stress increase for both parameters was greatest near a depth of 0.40 mm and was approximately 75 MPa in each case.

The variations in the residual stress profiles caused by the variations of LP parameters should have implications on the fatigue performance of peened components. Improvements in fatigue life due to surface treatments like SP and LP are mainly due to the compressive residual stresses they impart. When considering the effects of surface treatment on fatigue life, it is useful to consider the phases of crack initiation and crack propagation separately. Fatigue crack initiation usually takes place very near the surface, and is therefore most influenced by the magnitude of the near-surface residual stress [22]. Since the variations of laser fluence, overlap, and spot size investigated here did not produce a significant change in the level of residual stress at depths less than 0.20 mm, LP should be a robust method for increasing lifetime to fatigue crack initiation. One possibly confounding issue, however, is that fatigue cracks may initiate away from the surface when high levels of compressive surface stress exist in a shallow layer [23, 24].

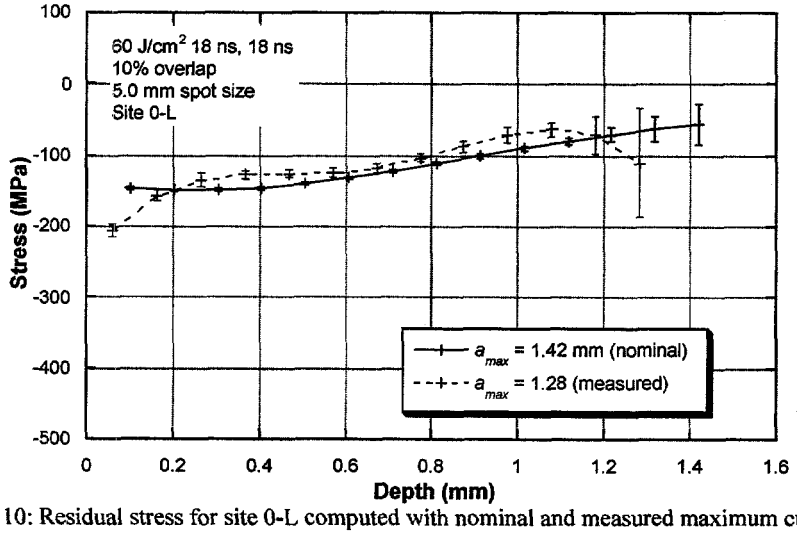

Figure 10: Residual stress for site 0-L computed with nominal and measured maximum cut depth

The influence of surface treatment on fatigue crack propagation is due to the contribution of residual stress to the total stress intensity factor (which is also affected by the applied cyclic loading). This contribution is most often quantified using the weight function [25], which shows that the contribution is linearly affected by the residual stress magnitude and non-linearly affected by the shape of the residual stress profile. While a weight-function analysis is beyond the scope of the present work, it can be stated unequivocally that residual stresses resulting from LP with higher fluence and larger layer overlap would have a larger contribution to the stress intensity factor because they have higher levels of compressive stress (Figure 5(b) and (d)). Components peened at higher fluence and larger overlap should therefore exhibit a longer crack propagation lifetime.

The effects of the LP variations on total fatigue life may depend on the level of loading. For highly loaded components that exhibit short to intermediate fatigue lifetimes (e.g., 10^3 to 10^5 cycles), life is mostly spent in crack initiation [26, 27]. The LP process variations should therefore not play a significant role in fatigue life improvements offered by LP for highly loaded components. For components carrying lower loads and exhibiting long lifetimes ($> 10^6$ cycles), a significant portion of the life is spent in crack propagation [26, 27]. The LP variations may therefore have a significant effect on fatigue life improvements for lightly loaded components. Since the effects of the LP variations are expected to be different for the crack initiation and crack propagation phases, their impacts on total fatigue life should depend on the level of loading. A fatigue test program would be required to validate this hypothesis, but such a program would likely require a large number of coupons to understand the effects of LP process variations in the presence of the stochastic nature of the fatigue process.

The fact that tensile surface residual stress was not found adjacent to the laser peened area suggests that LP should not have detrimental effects on fatigue performance. While compressive residual stress near the surface is desirable, tensile residual stress must exist at some other locations within the body to satisfy equilibrium. The results here suggest that the residual stress component perpendicular to the edge of the peened area is compressive on the surface adjacent to a laser peened area, suggesting that tensile stresses are limited to the component interior. Interior tensile residual stresses are of less concern because crack initiation is mainly a near-surface phenomenon due to the presence of surface roughness, oxidizing atmosphere, and higher stresses (when bending or torsion loadings exist) [22, 26]. However, the results here may not be representative of what may occur in other geometries or for other residual stress components. Other research has investigated the residual stress component parallel to the edge of the peening field and found it to be tensile near the surface, outside the peened region [28]. The effect of residual stresses outside the peened region on fatigue performance would therefore depend on the direction of the applied stress in relation to the edge of the peened area. When the applied stress is perpendicular to the edge of the peened area, residual stresses outside the peened region should be of little concern.

The variations of the residual stress profiles with in-plane position were limited to depths less than 0.60 mm. These measurements were a first attempt to quantify the variation of the residual stress profile in the peened area. Three of the locations investigated lie along the boundary between two layer-one spots, starting at the center of a layer-two spot (site 7a, Figure 7 inset) and progressing out to the edge of a layer-two spot (sites 8a and 9a). At a depth of 0.10 mm, the results indicate that higher compressive residual stress existed at the center of a layer-two spot (site 7a) than at the edge (site 9a). Residual stress at a depth of 0.10 mm and at the center of a layer-one spot (site 11a) fell between those at the other sites. Results at shallower depths were not available at all sites due to the experimental difficulties described above. In summary, the results show that in-plane variations of the residual stress profile do exist within the laser peened area, and this suggests that fatigue cracks may initiate and grow at preferred locations (i.e., at locations of lower stress magnitude). It would therefore be of value for LP fatigue test programs to include a component of fractography to determine whether in-plane variations of residual stress lead to preferred sites for crack initiation and growth. This information would also provide supporting evidence for the stress variations reported here, which have been found from a limited number of experimental measurements.

The variations of residual stress due to degraded laser spots were limited to shallow depths. Near-surface residual stress at the edge of a layer-two spot was significantly less when laser spots had attenuated corners (compare site 10a with site 12a,

Figure 8). When the corner was attenuated, the level of near-surface stress at this location was significantly less than at any other location peened with normal laser spots (Figures 5 and 7). The fact that corner attenuation had little effect on residual stress at one location in the laser peened field (compare sites 11a and 13a), but a marked effect at another location (compare sites 10a and 12a) is non-intuitive. Future work should be directed at verifying this result, since the current work presents only limited experimental results. If attenuated laser spots lead to a reduced level of near-surface stress, this may lead to a preferred location for crack initiation, as just described. It therefore would be advisable to take steps to ensure a uniform spatial distribution of energy within the laser spots, which was a particular advantage of the laser system employed in this work [4].

Acknowledgements

Thanks are due to Fritz Harris of the Metal Improvement Company Inc. for helpful discussions, to John Halpin of Lawrence Livermore National Laboratory (LLNL) for laser engineering, to Laurie Lane of LLNL for

laser peening, and to Greg Cook of Woodland Precision Technology for EDM. Michael B. Prime of the Los Alamos National Laboratory generously provided software implementing the elastic solution for strain near a finite width slit. UC Davis received financial support from Metal Improvement Company Inc. and LLNL received financial support from the National Center for Manufacturing Sciences (USA).

References

[1] P. Peyre, X. Scherpereel, L. Berthe, C. Carboni, R. Fabbro, G. Beranger, C. Lemaitre, Mater. Sci. Eng. A280 (2000) 294.

[2] P. K. Sharp, G. Clark, The Effect of Peening on the Fatigue Life of 7050 Aluminum Alloy, Defence Science & Technology Organisation, Victoria, Australia, 2001

[3] P. Peyre, R. Fabbro, P. Merrien, H. P. Lieurade, Mater. Sci. Eng. A210 (1996) 102.

[4] C. B. Dane, L. E. Zapata, W. A. Neuman, M. A. Norton, L. A. Hackel, IEEE J. Quantum Electron. 31 (1995) 148.

[5] C. B. Dane, L. A. Hackel, J. M. Halpin, J. Daly, J. Harrisson, F. Harris, High-throughput laser peening of metals using a high-average-power Nd:glass laser system, in: S. Nakai, L.A. Hackel, W.C. Solomon (Eds.), High-Power Lasers In Civil Engineering and Architecture, Society of Photo-Optical Instrumentation Engineers, Bellingham, WA, 2000, pp. 211-221.

[6] G. Hammersley, L. A. Hackel, F. Harris, Opt. Lasers Eng. 34 (2000) 327.

[7] P. R. Smith, M. J. Shepard, P. S. Prevéy, A. H. Clauer, J. Mater. Eng. Perform. 9 (2000) 33.

[8] P. Peyre, P. Merrien, H. P. Lieurade, R. Fabbro, Surf. Eng. 11 (1995) 47.

[9] X. Scherpereel, P. Peyre, R. Fabbro, G. Lederer, N. Celati, Modification of electrochemical properties of stainless steel by Laser Shock Processing, in: M.H. Aliabadi, C.A. Brebbia (Eds.), Proceedings of the International Conference on Computer Methods and Experimental Measurements for Surface Treatment Effects, WIT Press, Southampton, UK, 1997, pp. 83-92.

[10] M. B. Prime, Appl. Mech. Rev. 52 (1999) 75.

[11] M. R. Hill, W. Lin, J. Eng. Mater. Technol. 124 (2002) 185.

[12] P. R. Bevington, D. K. Robinson, Data Reduction and Error Analysis for the Physical Sciences, 2nd ed, McGraw-Hill, New York, 1992, pp. 115-138.

[13] W. Cheng, I. Finnie, J. Eng. Mater. Technol. 115 (1993) 220.

[14] M. B. Prime, I. Finnie, J. Eng. Mater. Technol. 118 (1996) 410.

[15] W. Cheng, I. Finnie, M. Gremaud, M. B. Prime, J. Eng. Mater. Technol. 116 (1994) 1.

[16] J. R. Davis (Ed.), ASM Specialty Handbook - Aluminum and Aluminum Alloys, ASM International, Materials Park, OH, 1993, p. 695.

[17] MATLAB, 5.3.0.10183 (R11), The MathWorks, Inc, Natick, MA, 1999.

[18] W. Cheng, I. Finnie, Ö. Vardar, J. Eng. Mater. Technol. 113 (1991) 199.

[19] M. G. Moore, W. P. Evans, SAE Transact. 66 (1958) 340.

[20] P. S. Prevéy, X-ray diffraction characterization of residual stresses produced by shot peening, in: A. Niku-Lari (Ed.) Shot Peening Theory and Application, IITT-International, Gournay-Sur-Marne, France, 1990, pp. 81-93.

[21] A. H. Clauer, Laser Shock Peening for Fatigue Resistance, in: J.K. Gregory, H.J. Rack, D. Eylon (Eds.), Surface Performance of Titanium, TMS, Warrendale, PA, 1996, pp. 217-230.

[22] J. O. Almen, P. H. Black, Residual Stresses and Fatigue in Metals, McGraw-Hill Book Company, Inc, New York, NY, 1963, p. 59.

[23] D. W. Hammond, S. A. Meguid, Eng. Fract. Mech. 37 (1990) 373.

[24] M. Larsson, A. Melander, R. Blom, S. Preston, Mater. Sci. Technol. 7 (1991) 998.

[25] A. P. Parker, Stress intensity factors, crack profiles, and fatigue crack growth rates in residual stress fields, in: J.B. Wheeler (Ed.) Residual Stress Effects in Fatigue, ASTM STP 776, American Society for Testing and Materials, Philadelphia, PA, 1982, pp. 13-31.

[26] D. K. Benson, Surface treatments for fatigue strengthening, Achievement of High Fatigue Resistance in Metals and Alloys, ASTM STP 467, American Society for Testing and Materials, Baltimore, MD, 1970, pp. 188-208.

[27] B. R. Sridhar, K. Ramachandra, K. A. Padmanabhan, J. Mater. Sci. 31 (1996) 5953.

[28] J. J. Ruschau, R. John, S. R. Thompson, T. Nicholas, J. Eng. Mater. Technol. 121 (1999) 321.

6. SPECIAL PROJECT: LASER MATERIAL PROCESSING RESARCH ACTIVITY HIGHLIGHTS

LASER PEENING IMPROVES CORROSION RESISTANCE AND MITIGATES TENSILE RESIDUAL STRESSES IN ALLOY 22

Under the support of Bechtel SAIC and in collaboration with the University of California at Davis and Metal Improvement Company, we are developing a laser peening process for application to radioactive waste storage.

DOE has been charged with designing, constructing, and operating a facility at the Yucca Mountain Project's (YMP) Nevada site to permanently store the nation's high-level radioactive waste. In addition to the natural barriers at the Nevada site, a number of engineered barriers are being designed to help the facility meet its containment goal. Foremost among these is the waste package, which will be fabricated from Alloy 22, a material highly resistant to corrosion. Our current work has focused on mitigating the potential for stress corrosion cracking (SCC) by eliminating the near-surface tensile residual stresses resulting from welding processes, and evaluating the corrosion resistance of laser-peened Alloy 22.

Parametric studies covering many of the laser peening conditions have resulted in an improved treatment plan and the deepest residual stresses we have produced to date. Examples of two-dimensional residual stress fields in peened and unpeened Alloy 22 weldments, measured with the contour method, are shown in Figure 1. Laser peening converts the near-surface longitudinal (along the weld) tensile residual stress present in the unpeened plate into deep, compressive residual stress.

Measurements of residual stress were made for various coupon thicknesses. Figure 2 shows the depth of compressive residual stress vs coupon thickness. These depths of residual stress, on the

Figure 1. Results of contour residual stress measurement in a peened and unpeened Alloy 22 weld. Laser peening turned high tensile residual stress into near-yield-level compressive residual stress at the part surface.

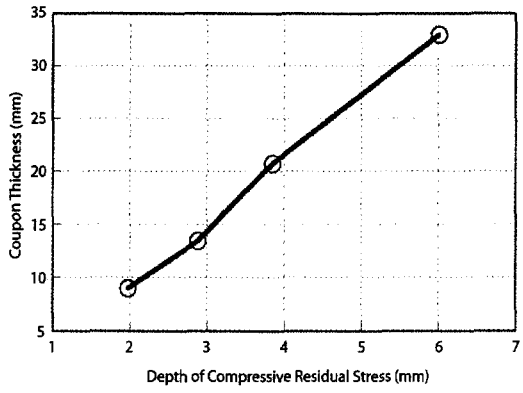

Figure 2. Depth of compressive residual stress vs. part thickness for a range of Alloy 22 coupons.

order of 20% of the part thickness for the range tested, far exceed the capabilities of conventional shot peening and other methods used in industry. This deep compressive stress serves to inhibit the process of SCC, which occurs in a tensile stress field.

In addition to SCC, over the long time scales considered for the YMP, general corrosion of the waste package could also occur. It is difficult to accurately measure the rate of Alloy 22 corrosion in the laboratory, since the most aggressive chemical environments cause limited corrosion in Alloy 22, even over multi-year test protocols. One method of evaluating a material's corrosion resistance (without waiting for it to corrode) is by measuring the surface potential with electrochemical polarization tests. Material scientists working for YMP at LLNL have used this method to compare the corrosion rate of peened and unpeened Alloy 22 coupons. Preliminary relative rates shown in Figure 3 indicate that laser-peened Alloy 22 will corrode more slowly than Alloy 22 alone; note that these values should be compared to one another, rather than construed as absolute corrosion rates. Because of the large depth of compressive stress, laser-peened material will continue to inhibit SCC even after several millimeters of material are removed through general corrosion. These beneficial characteristics, in conjunction with its noncontact (hand's-off) nature, make laser peening a good candidate for YMP to improve the corrosion resistance and lifetime of storage canisters.

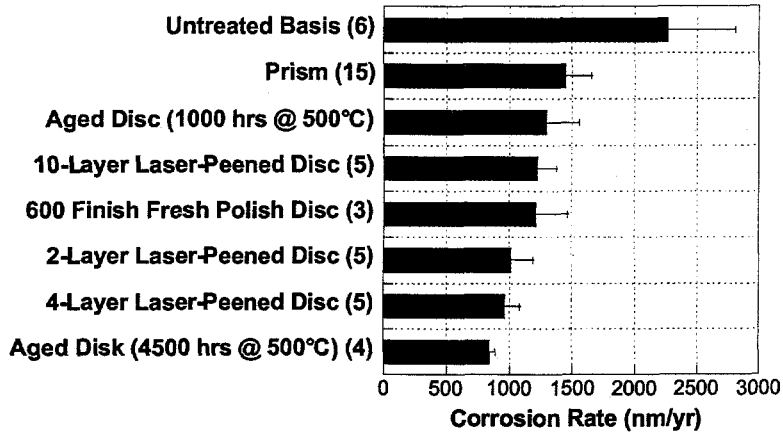

Figure 3. Relative corrosion rates of Alloy 22 coupons in different conditions, including three different laser peening treatments.

While the YMP development work continues, laser peening was also introduced this past year into commercial production by Metal Improvement Company, our Cooperative Research and Development Agreement partner. The laser peening system was deployed to solve a serious fatigue failure problem in high-value commercial jet engine components. Since commercial introduction in May 2002, aircraft worth billions of dollars are now in service with laser-peened parts—saving millions of dollars per month in aircraft maintenance costs, millions more in parts replacement costs, and all the while greatly enhancing safety. Significant cost benefits of this scale are also anticipated with the application of laser peening for the YMP.

— J. Rankin, B. Yamamoto, A. Dewald, and K. Evans

LASER PEENING IMPROVES FATIGUE LIFE OF ALUMINUM COMPONENTS FOR USAF

Under the support of USAF's Aging Landing Gear Life Extension Program, LS&T is working with UC Davis, the Ogden Air Logistics Center Landing Gear Engineering Branch (OO-ALC/LILE), and Metal Improvement Company, Inc. (MIC) to evaluate the advantages of applying laser peening to improve the performance of landing gear components for the USAF. Using test coupons made from the same high strength aluminum alloy (7049-T73) as the trunnion,

we systematically studied the effects of laser peening on the fatigue life and stress corrosion cracking (SCC) characteristics of a trunnion, which is part of the main landing gear on the USAF's T-38 aircraft. The results clearly show that laser peening can significantly improve the fatigue life of this component while at the same time improving the resistance to SCC.

Since the trunnions are currently treated with a SP treatment, an additional goal of this study was to compare the two surface treatments and to also investigate the potential effects of applying laser peening to previously shot peened specimens. Fatigue tests at three different load levels near the service stress were performed. All three surface treatment techniques (LP, SP, and SP+LP) increased the fatigue life of the test specimen but the greatest benefits appear to come from the laser peening treatment (Figure 4). Additionally, the benefits of each of the surface treatments increased at longer fatigue lives (lower maximum stress).

Stress corrosion cracking tests were performed on C-ring specimens made from 7075-T6 aluminum. The same surface treatments as above were used for the SCC tests (LP, SP, SP+LP) along with a control case of no surface treatment. The untreated C-ring specimens all showed clear evidence of SCC and cracked in half in the caustic environment after a few days (11, 13, and 23 days) while none of the treated specimens cracked throughout the entire test duration of 60 days. Although this test was not conclusive in ranking the benefits of LP over SP with regard to SCC, but it did clearly show that LP is an effective tool to enhance the SCC performance of untreated specimens.

We are currently performing similar laser peening and fatigue tests on actual T-38 trunnions. Since the fatigue coupons were specifically designed to have a fatigue performance similar to the T-38 trunnion it is expected that a similar life extension is achievable on the actual part. The estimated cost savings to the USAF (due to a reduction in the replacement costs and maintenance and inspection time) will be on the order of tens of millions of dollars.

— A. Demma, M. Lee, A. DeWald, J. Rankin, H.-L. Chen, M. Hill, and L. Hackel

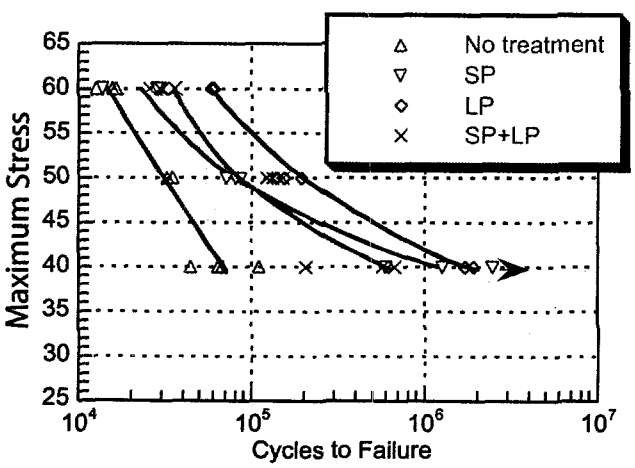

Figure 4. Stress life plot for 7049-T73 small coupon fatigue tests.

DISCLAIMER

This document was prepared as an account of work sponsored by an agency of the United States Government. Neither the United States Government nor the University of California nor any of their employees, makes any warranty, express or implied, or assumes any legal liability or responsibility for the accuracy, completeness, or usefulness of any information, apparatus, product, or process disclosed, or represents that its use would not infringe privately owned rights. Reference herein to any specific commercial product, process, or service by trade name, trademark, manufacturer, or otherwise, does not necessarily constitute or imply its endorsement, recommendation, or favoring by the United States Government or the University of California. The views and opinions of authors expressed herein do not necessarily state or reflect those of the United States Government or the University of California, and shall not be used for advertising or product endorsement purposes.

This work was performed under the auspices of the U.S. Department of Energy by University of California Lawrence Livermore National Laboratory under Contract W-7405-ENG-48.

This report has been reproduced directly from the best available copy.

Available to DOE and DOE contractors from the
Office of Scientific and Technical Information
P.O. Box 62, Oak Ridge, TN, 37831
Prices available from (615) 576-8401, FTS 626-8401

Available to the public from the National Technical Information Service,
U.S. Department of Commerce, 5285 Port Royal Rd., Springfield, VA 22161

March 2003

UCRL-ID-134972-02
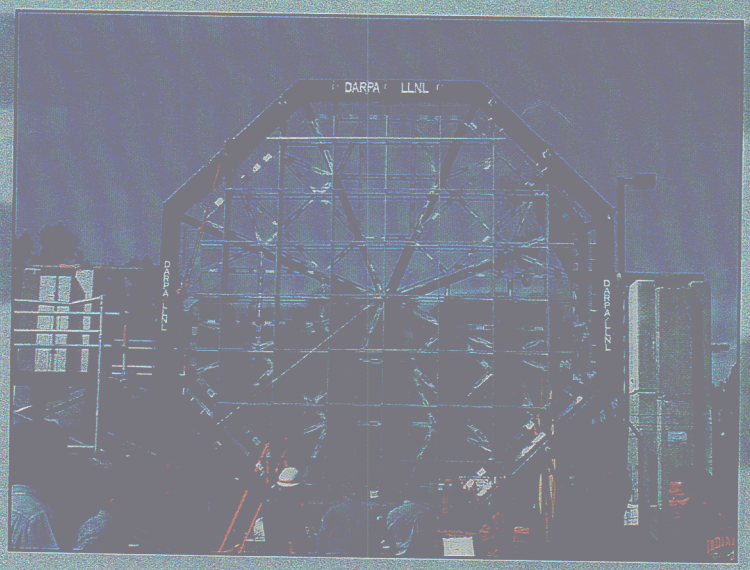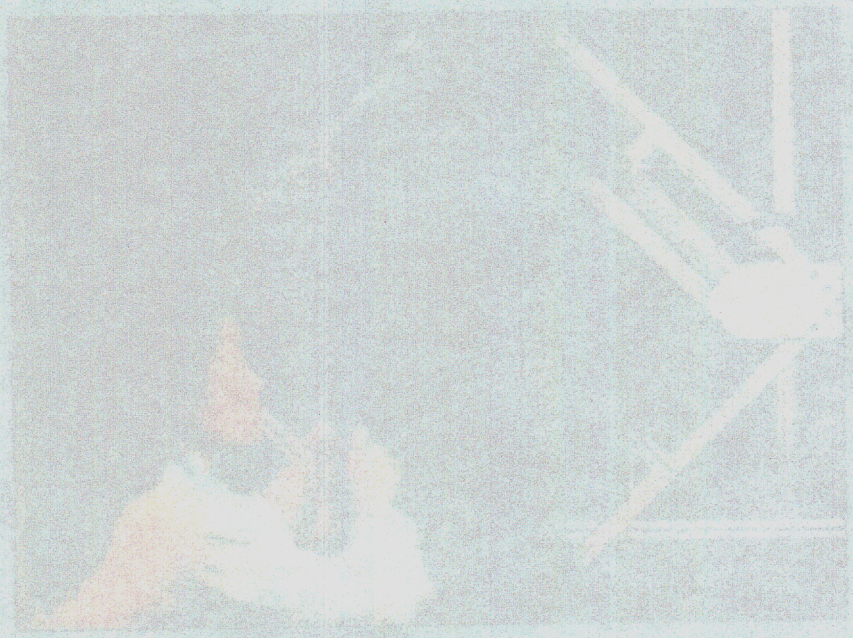
University of California
Lawrence Livermore National Laboratory
Laser Programs
PO Box 808 • Livermore, CA • 94551
Visit our NIF Programs Website at *http://www.llnl.gov/nif/*